

21st Aerospace Mechanisms Symposium

(NASA-CP-2470) THE 21ST AEROSPACE
MECHANISMS SYMPOSIUM (NASA) 356 p Avail:
NTIS HC A16/MF A01 CSCL 20K

N87-29858
--THRU--
N87-29882
Unclas
0098662

H1/39

*Proceedings of a symposium hosted by
Lyndon B. Johnson Space Center
Houston, Texas
April 29-May 1, 1987*



NASA Conference Publication 2470

21st Aerospace Mechanisms Symposium

*Proceedings of a symposium cosponsored by
National Aeronautics and Space Administration,
the California Institute of Technology, and
Lockheed Missiles and Space Company, Inc.,
and hosted by Lyndon B. Johnson Space Center
April 29-May 1, 1987*



National Aeronautics
and Space Administration

Scientific and Technical
Information Branch

1987

PREFACE

This document represents the proceedings of the 21st Aerospace Mechanisms Symposium, which was held at the NASA Johnson Space Center (JSC) on April 29 to May 1, 1987.

This symposium is jointly sponsored by the National Aeronautics and Space Administration, the California Institute of Technology, and the Lockheed Missiles and Space Company, and is concerned with the problems of design, fabrication, test, and operational use of aerospace mechanisms. The symposium provides a forum for personnel active in the field of mechanisms technology as well as a source of information for others with an interest in this area. The symposium rotates annually between the eight NASA Centers and attracts papers and attendees internationally. This was the third symposium to be held at JSC in the 21-year history of this organization.

The 24 papers included in these proceedings were published in general as received from the authors with minimum modification and editing. Information contained in the individual papers is not to be construed as being officially endorsed by NASA.

Also included as an appendix to this report is a summary of the panel discussions related to future trends and directions in mechanism technology which were held during the 20th Aerospace Mechanisms Symposium at the NASA Lewis Research Center in Cleveland, Ohio, on May 7 to 9, 1986.

PRECEDING PAGE BLANK NOT FILMED

CONTENTS

Section	Page
Preface	iii
Organizing Committee	ix
Program	xi

SESSION I

Chairman: Mr. Donald C. Wade, NASA Johnson Space Center

Folding, Articulated, Square Truss Robert M. Warden, AEC-Able Engineering Co.	1
The Design and Development of a Two-Dimensional Adaptive Truss Structure Fumihiro Kuwao, Shoichi Motohashi, Makoto Yoshihara, and Kenichi Takahara, Toshiba Corporation, and Michihiro Natori, Institute of Space and Astronautical Science	19
A Microgravity Isolation Mount D. I. Jones, A. R. Owens, R. G. Owen, and G. Roberts, University College of North Wales, and D. W. Wyn-Roberts and A. A. Robinson, European Space Technology Centre	35

SESSION II

Chairman: Dr. Nathan D. Watson, NASA Langley Research Center

AKM Capture Device William D. Harwell, NASA Johnson Space Center	55
Grabber Arm Mechanism for the Italian Research Interim Stage (IRIS) Edmondo Turci, Aeritalia Space System Division	65
Development of a Standard Connector for Orbital Replacement Units for Serviceable Spacecraft Ellen F. Heath, Matthew A. Braccio, Steven D. Raymus, and David W. Gross, Astro-Space Division, RCA Aerospace and Defense	81

SESSION III

Chairman: Mr. Henry Kaupp, NASA Johnson Space Center

The Design and Development of a Mobile Transporter System for the Space Station Remote Manipulator System Thomas W. Carroll, Rockwell International	93
---	----

Section	Page
Telerobotic Work System: Concept Development and Evolution Lyle M. Jenkins, NASA Johnson Space Center	103
Traction-Drive, Seven-Degree-of-Freedom Telerobot Arm: A Concept for Manipulation in Space D. P. Kuban and D. M. Williams, Martin Marietta Energy Systems, Inc.	111

SESSION IV

Chairman: Mr. James I. McPherson, McDonnell Douglas Corp.

Experiences of CNES and SEP on Space Mechanisms Rotating at Low Speed G. Atlas, SEP, and G. Thomin, CNES	131
Common Drive Unit R. C. Ellis, R. A. Fink, and E. A. Moore, Sperry Space Systems .	145
A Reactionless Precision Pointing Actuator Peter Wiktor, Jet Propulsion Laboratory	165
The Design of Worm Gear Sets Andrea I. Razzaghi, NASA Goddard Space Flight Center	175

SESSION V

Chairman: Mr. James D. Phillips, NASA Kennedy Space Center

Pointed Telescope Subassembly for the UARS High Resolution Doppler Imager Robert D. Renken, Ball Aerospace Systems Division	195
Passive Isolation/Damping System for the Hubble Space Telescope Reaction Wheels Martin D. Hasha, Lockheed Missiles & Space Co.	211
A Multipurpose Satellite Ejection System Michael B. Moore, NASA Marshall Space Flight Center	227
A CAD/CAE Analysis of Photographic and Engineering Data S. Michael Goza and Wayne L. Peterson, NASA Johnson Space Center	235

SESSION VI

Chairman: Mr. Barry S. Leonard, Lockheed Missiles & Space Co.

The Preloadable Vector Sensitive Latch for Orbital Docking/Berthing William R. Acres and John J. Kennedy, NASA Johnson Space Center	247
---	-----

Section	Page
Space Station Based Options for Orbiter Docking/Berthing Daniel J. Hoover, Rockwell International	261
An Electromechanical Attenuator/Actuator for Space Station Docking LeBarian Stokes, Dean Glenn, and Monty B. Carroll, NASA Johnson Space Center	275
SESSION VII	
Chairman: Mr. David Wyn-Roberts, European Space Technology Centre	
Space Station Lubrication Considerations Lubert J. Leger, NASA Johnson Space Center, and Keith Dufrane, Battelle Columbus Laboratories	285
GIOTTO's Antenna De-Spin Mechanism: Its Lubrication and Thermal Vacuum Performance M. J. Todd and K. Parker, European Space Tribology Laboratory . .	295
Anatomy of a Bearing Torque Problem Damon D. Phinney, Ball Aerospace Systems Division	315
Space Station Alpha Joint Bearing Michael R. Everman and P. Alan Jones, AEC-Able Engineering Co., and Porter A. Spencer, Lockheed Missiles & Space Co.	329
Appendix - Summary, 20th Aerospace Mechanisms Panel Discussions, NASA Lewis Research Center, May 8, 1986	347

ORGANIZING COMMITTEE

The papers presented at the Symposium were selected and reviewed by the Organizing Committee. Authors are responsible for the content and the technical accuracy of their respective papers. The committee was composed of the following personnel:

General Chairman	Charles W. Coale Lockheed Missiles & Space Company
Administrative Chairman	David F. Welch California Institute of Technology
Operations Chairman	Joseph F. Wilson Lockheed Missiles & Space Company
Host Center - NASA Johnson Space Center, Houston, Texas	
Chairman	Jerry E. McCullough
Vice Chairman	Gordon Rysavy

Committee Members

Erik K. Antonsson	California Institute of Technology
Richard H. Bentall	European Space Technology Centre
Kenneth C. Curry	Jet Propulsion Laboratory
Charles R. Darwin	NASA Marshall Space Flight Center
David F. Englebert	NASA Ames Research Center
Harvey H. Horiuchi	Jet Propulsion Laboratory
Carl D. Lamb	NASA Marshall Space Flight Center
Stewart H. Loewenthal	Lockheed Missiles & Space Company
Ronald E. Mancini	NASA Ames Research Center
James D. Phillips	NASA Kennedy Space Center
Douglas A. Rohn	NASA Lewis Research Center
William C. Schneider	NASA Johnson Space Center
Bowden W. Ward, Jr.	NASA Goddard Space Flight Center
Nathan D. Watson	NASA Langley Research Center

David Wyn-Roberts

European Space Technology Centre

Advisory Committee

Paul W. Bomke

Jet Propulsion Laboratory

Aleck C. Bond (Ret.)

NASA Johnson Space Center

Thomas F. Bonner, Jr.

NASA Johnson Space Center

H. Mervyn Briscoe (Ret.)

European Space Technology Centre

Otto H. Fedor

Lockheed Space Operations Company

Angelo Giovannetti (Ret.)

NASA Ames Research Center

Allen J. Louviere

NASA Johnson Space Center

Frank T. Martin (Ret.)

NASA Goddard Space Flight Center

Peter A. Minderman (Ret.)

NASA Kennedy Space Center

James H. Parks (Ret.)

NASA Langley Research Center

Alfred L. Rinaldo (Ret.)

Lockheed Missiles & Space Company

PROGRAM

WEDNESDAY, 29 APRIL 1987

- 8:30 Wednesday Authors Breakfast
 Royal Banquet Room A, Sheraton Kings Inn
- 9:00 REGISTRATION AND COFFEE
 Auditorium Lobby, Building 2, Johnson Space Center
- 10:00 INTRODUCTORY REMARKS
 Mr. Jerry E. McCullough, Host Chairman
 NASA Johnson Space Center
 Dr. Charles W. Coale, General Chairman
 Lockheed Missiles & Space Co., Sunnyvale, CA
- CENTER WELCOME
 Dr. Aaron Cohen, Center Director
 NASA Johnson Space Center
- 10:30 SESSION I
 Mr. Donald C. Wade, Session Chairman
 NASA Johnson Space Center
- Folding, Articulated, Square Truss
 Robert M. Warden, AEC-Able Engineering Co., Goleta, CA
 - The Design and Development of a Two-Dimensional Adaptive Truss Structure
 F. Kuwao, S. Motohashi, M. Yoshihara, and K. Takahara, Toshiba Corporation, Kanagawa, Japan
 M. Natori, Institute of Space and Astronautical Science, Tokyo, Japan
 - Microgravity Isolation Mount
 D. I. Jones, A. R. Owens, R. G. Owen, and G. Roberts, University College of North Wales, Bangor, Gwynedd, Great Britain
 D. W. Wyn-Roberts and A. A. Robinson, European Space Technology Centre, Noordwijk, The Netherlands
- 11:45 LUNCH
- 12:45 SESSION II
 Dr. Nathan D. Watson, Session Chairman
 NASA Langley Research Center, Hampton, VA
- AKM Capture Device
 William D. Harwell, NASA Johnson Space Center, Houston, TX

- Grabber Arm Mechanism for the Italian Research Interim Stage (IRIS)
Edmondo Turci, Aeritalia, Space Systems Group, Torino, Italy
- Development of a Standard Connector for Orbital Replacement Units (ORU) for Serviceable Spacecraft
E. F. Heath, M. A. Braccio, S. D. Raymus, and
D. W. Gross, RCA/GSD/Astro-Electronics, Princeton, NJ

2:00 COFFEE BREAK

2:10 SESSION III

Mr. Henry Kaupp, Session Chairman
NASA Johnson Space Center

- Design and Development of a Mobile Transporter System for the Space Station Remote Manipulator System
Thomas W. Carroll, Rockwell International, Downey, CA
- Telerobotic Work System - Concept Development and Evolution
Lyle M. Jenkins, NASA Johnson Space Center, Houston, TX
- Traction-Drive, Seven Degree-of-Freedom Telerobot Arm: A Concept for Manipulation in Space
D. P. Kuban and D. M. Williams, Oak Ridge National Laboratory, Oak Ridge, TN

3:25 COFFEE BREAK

3:35 PANEL SESSION "ROBOTICS FOR SPACE"

Mr. Stuart H. Loewenthal, Moderator

- Lockheed Missiles & Space Co., Sunnyvale, CA
- Prof. Susan Hackwood, University of California, Santa Barbara, CA
- Dr. Geoffry Marks, Astro Aerospace Corp., Carpinteria, CA
- Dr. Byron Purves, Boeing Aerospace Corp., Huntsville, AL

6:00 WELCOMING RECEPTION

Royal Banquet Room, Sheraton Kings Inn

THURSDAY, 30 APRIL 1987

7:00 Thursday Authors Breakfast

Royal Banquet Room A, Sheraton Kings Inn

8:00 SESSION IV

Mr. James I. McPherson, Session Chairman
McDonnell Douglas Corp., Houston, TX

- Experiences of CNES and SEP on Space Mechanisms Rotating at Low Speed
Gerard Atlas, SEP, Vernon, France
Georges Thomin, CNES, Toulouse, France
- Common Drive Unit
R. C. Ellis, R. A. Fink, and E. A. Moore, Sperry Space Division, Durham, NC
- A Reactionless Precision Pointing Actuator
Peter Wiktor, Jet Propulsion Laboratory, Pasadena, CA
- The Design of Worm Gear Sets
Andrea Razzaghi, NASA Goddard Space Flight Center, Greenbelt, MD

9:40 COFFEE BREAK

9:55 SESSION V

Mr. James D. Phillips, Session Chairman
NASA Kennedy Space Center, FL

- Pointed Telescope Subassembly for the UARS High Resolution Doppler Imager
Robert D. Renken, Ball Aerospace Systems Division, Boulder, CO
- Passive Isolation/Damping System for the Hubble Space Telescope Reaction Wheels
Martin D. Hasha, Lockheed Missiles & Space Co., Sunnyvale, CA
- A Multipurpose Satellite Ejection System
Michael B. Moore, NASA Marshall Space Flight Center, AL
- A CAD/CAE Analysis of Photographic and Engineering Data
S. Michael Goza and Wayne L. Peterson, NASA Johnson Space Center, Houston, TX

11:35 LUNCH

12:45 SESSION VI

Mr. Barry S. Leonard, Session Chairman
Lockheed Missiles & Space Co., Sunnyvale, CA

- The Preloadable Vector Sensitive Latch for Orbital Docking/Berthing
William R. Acres and John J. Kennedy, NASA Johnson Space Center, Houston, TX

- Space Station Based Options for Orbiter
Docking/Berthing
Daniel J. Hoover, Rockwell International, Downey, CA
- An Electromechanical Attenuator/Actuator for Space Station
Docking
LeBarian Stokes, Dean C. Glenn, and Monty B. Carroll,
NASA Johnson Space Center, Houston, TX

2:00 BREAK

2:15 PANEL SESSION "LARGE SPACE STRUCTURES"

Mr. Stuart H. Loewenthal, Moderator

Lockheed Missiles & Space Co., Sunnyvale, CA

- Mr. John Coyner, Martin Marietta Aerospace Co., Denver, CO
- Mr. Robert Crawford, General Research Corp., Santa
Barbara, CA
- Mr. Don McCutchen, NASA Johnson Space Center, Houston, TX

3:30 PREVIEW - Evening Activities

EVENING SOCIAL ACTIVITIES

5:00 Bus to Galveston

6:00 Elissa Tour

7:30 Colonel Cruise/Dinner

FRIDAY, 1 MAY 1987

8:00 Friday Authors Breakfast
Royal Banquet Room A, Sheraton Kings Inn

9:00 SESSION VII

Mr. David Wyn-Roberts, Session Chairman

European Space Technology Centre, Noordwijk, The
Netherlands

- Space Station Lubrication Considerations
Lubert J. Leger, NASA Johnson Space Center, Houston, TX
Keith Dufrane, Battelle Columbus Laboratories, Colum-
bus, OH
- GIOTTO's Antenna De-Spin Mechanism: Its Lubrication and
Thermal Vacuum Performance
M. J. Todd and K. Parker, European Space Tribology Labo-
ratory, Risley, Cheshire, England
- Analysis of a Bearing Torque Problem
Damon D. Phinney, Ball Aerospace Systems Division,
Boulder, CO

- Space Station Alpha Joint Bearing
Michael R. Everman and P. Alan Jones, AEC-Able Engineering Co., Goleta, CA
Porter A. Spencer, Lockheed Missiles & Space Co., Sunnyvale, CA

10:40 COFFEE BREAK

10:55 NASA JOHNSON SPACE CENTER OVERVIEW
Mr. William J. Huffstetler, Jr., NASA Johnson Space Center
PRESENTATION OF HERZL AWARD
Dr. Paul W. Bomke, Jet Propulsion Laboratory, Pasadena, CA
CLOSING REMARKS
Mr. Joseph F. Wilson, Operations Chairman
Lockheed Missiles & Space Co., Sunnyvale, CA

12:00 LUNCH

1:00 TOUR OF NASA JOHNSON FACILITIES

FOLDING, ARTICULATED, SQUARE TRUSS

Robert M. Warden*

ABSTRACT

A larger, stronger deployable boom has been developed to handle the requirements of larger, heavier payloads in space. The main components of the boom and its deployer are described and their functions explained. Desirable features of the boom are identified and physical properties are reported.

INTRODUCTION

The new generation of experimental payload is larger and more complex than ever before and requires larger and stronger support structures. For example, the Tethered Satellite Experiment is a 590 kg (1300 pound) sphere designed to be deployed 100 km (62 miles) out of the Shuttle, much like trolling with a very large fishing pole (Figure 1). The deployable boom which is the subject of this paper is the "fishing pole". The boom is contained in a canister which is 76 cm (30 inches) in diameter by 152 cm (60 inches) tall (Figure 2). When power is applied to the system, the boom gently pushes the satellite away from the shuttle. When fully deployed, the boom is approximately 12 m (40 feet) long. The boom is unique not only in that it is the largest and strongest of its kind but also the design has many features with other potential applications.

Requirements

The basic requirement was for a compact structure which would deploy the payload away from the shuttle, support the tether during the experiment, and retract the payload when the experiment is finished. A total of 70 electrical conductors must run the full length of the structure while maintaining electrical continuity at all times. The system must retain near full strength and stiffness during deployment and retraction and be able to stop and reverse at any time.

* AEC-Able Engineering Co., Goleta, California

Additional requirements are as follows:

Table I: Requirements

Diameter	1.00 M	(39.0 in) max
Retracted Length	1.52 M	(60.0 in) max
Deployed Length	12.0 M	(480 in) min
Deployed Strength	6779 N-m	(6.0 x 10 ⁴ in-lb) ult
Deployed Stiffness	4.45 x 10 ⁵ N-m ²	(1.55 x 10 ⁸ lb-in. ²)
Operating Temp	-75 °C +65 °C	(-103 °F) (+149 °F)
Survival Temp	-150 °C +120 °C	(-238 °F) (248 °F)
Life Cycles	160 min	

Existing designs were found to be inadequate for this application. Coilable fiberglass booms stowable in the allowable envelope could not be made with enough stiffness or strength. They were also limited in the number of electrical wires they could support and their rotating base required some sort of derotator or slip-ring assembly. Most such folding structures rely on numerous latches and often have a large "dead band" or free play due to the hinge pins.

The new design incorporates pretensioned joints to eliminate dead band and no latches are used at all. Electrical cables are stored flat and are not subject to any twisting or sharp bends during operation. No slip rings are needed as the mast does not rotate to allow the mechanism to function.

SYSTEM DESCRIPTION

Boom

The boom is a four-sided structure which is designed to fold into a flat package for storage (Figure 3). The structure has an excellent compaction ratio of 7.2% which means that a 40-foot-long mast will retract to a length of less than 35 inches.

The geometry of the boom is based on cubical units called "bays". Each bay is designed to fold independently of the others but all of the bays are connected together to form a continuous structure from top to bottom. The individual bays open or close sequentially to deploy or retract the boom. The deployment mechanism will be described after the mast.

An important feature of the mast is that only one bay is in transition at a time. This provides a very stable system in that the mast develops full strength and stiffness even when only partially deployed. Another important feature is that the mast stacks flat without rotating. This makes it easier to handle electrical cables and simplifies alignment.

At each end of a bay is a rigid, "square frame" which controls the square shape of the mast (Figure 4). In the retracted position, the square frames are stacked flat, separated by stacking buttons to provide a load path during launch.

The vertical (or longitudinal) members are called "longerons" and are hinged at mid-bay to allow the square frames to stack when the mast is retracted. The mid-bay elbow joint of the longeron is held straight when deployed by a flexible fiberglass "bow" (which acts as a compression spring) pushing on the joint and "diagonal cables" pulling on the joint. The fiberglass bow also helps deploy the mast in other applications which will be discussed later.

The diagonal cables are tensioned between the square frames and the mid-bay elbow joints across the four faces of the boom. This has the desirable effect of pretensioning all of the joints in the mast and eliminating any dead band.

The key to deploying or retracting the boom (or specifically, each bay) is the mid-bay elbow joint. Controlling this joint causes the bay to open or close. The longerons must fold to allow the square frames to stack flat. To do this, a force is applied at the joint which is opposite to, and greater than, the compressive load of the fiberglass bow. When this force is simultaneously applied to all four joints in a bay, the longerons fold as the bows are compressed. Half of the diagonal cables remain taut to control the folding longeron geometry while the other half become slack and simply fold out of the way.

When closed, a bay is, in effect, slightly spring-loaded to deploy by the force in the fiberglass bow. This force increases rapidly as the bay opens so deploying the bay mainly involves easing the mid-bay elbow joint into place. This process is discussed later in the transition section. Note that no latches are necessary in the deployment or retraction of the boom.

Electrical Cables

Since this boom is used to push an experiment away from the Shuttle, electrical cables must be provided to connect the experiment to the Shuttle.

Seventy conductors grouped into twisted, shielded pairs and twisted, shielded triplets were needed to run the full length of the boom to the experiment. To make a thinner package, a ribbon cable configuration was used instead of a round bundle. The ribbon cables were prefolded over a relatively small radius and then clamped to the boom (Figure 5). By offsetting the cable attachment point from the hinge line, the cable lays flat when retracted but becomes effectively "too long" for the bay when deployed so that it bends over a large radius which increases the life of the wires. Four different ribbon cable assemblies can be handled this way (one on each face of the boom) and power leads can thus be separated from signal wires.

The cables are folded with the longerons and stored flat between the retracted bays. There is no increase in the height or diameter of the retracted boom because of the addition of the cables.

Canister

The canister is divided into three main sections: the storage shell, the elevating mechanism, and the transition section (Figure 6). Guide rails run the entire length of the canister to prevent the boom from rotating.

The storage shell contains and supports the retracted boom during handling and launch. It is made of thin aluminum sheet, rolled and welded into a cylinder and supported at each end by machined aluminum rings. The structural interface to the Shuttle support structure is a large mounting ring located near the top of the storage shell. The electrical connector brackets for the electrical leads that run up the boom and for the canister harness are mounted to the lower ring.

The elevating mechanism is a large nut with four helical threads machined on the inside. At the corner of each square frame of the boom is a small roller which can engage in the thread of the nut. The nut is driven by a spur gear on its lower end that also acts as the mechanical support to the rest of the canister. The nut is rotated causing the boom to deploy or retract depending on the direction of rotation.

On other mechanisms using the same deployment principle, large-diameter bearings are used on the top and bottom of the nut for support (Figure 7). Because the bearings are made of steel and the nut is made of aluminum, thermal interference problems occur at high or low temperatures due to different coefficients of thermal expansion. These problems increase with the diameter to such an extent that the free play required to accommodate a large bearing results in excessive dead band.

To solve this problem, a new approach has been taken. A combination gear and bearing race of hard-anodized aluminum is attached to the nut. In place of a continuous bearing, localized bearing support blocks are used. Because all of the large-sized parts are made of aluminum (including the boom), the problem of differential thermal expansion is minimized and clearances can be made much closer. The localized bearings are made of steel but are now of such a small size as to be less affected by thermal extremes. The wedge shape of the ring gear allows the bearings to take axial as well as radial loads. The bearing blocks are mounted to the top of the storage shell and are braced to the main mounting ring. In this way, most of the load from the boom is transferred directly from the nut to the mounting ring.

Transition Section

The transition section is an area which overlaps the elevating mechanism and the storage shell and contains the device that changes the boom between fully deployed and fully retracted.

By incorporating a special guide, the action of deploying and retracting the boom by the elevating nut is also used to open and close the bays as they pass through the transition section. The shape of this guide resembles an "S" and is called the S-track (Figure 8).

As defined before, the mid-bay elbow joint controls the opening and closing of the bay and therefore a slider block was added to the joint to slide along the S-track.

When the boom is being retracted, the elbow-joint slider engages the S-track causing the longeron to fold and the bay to close. The bottom of the S-track follows the motion of the extension and the bays are sequentially closed and stored in the storage shell area of the canister.

When the boom is being deployed, the force from the fiberglass bow onto the elbow joint is reacted by the S-track. The top of the S-track is curved to gently ease the elbow joint into place. After a bay is opened, its base is engaged by the elevating nut which lifts it out of the canister. Since the bottom of one bay is the top of the next one, as a bay is lifted out of the canister, the following bay is going through transition. In this way the bays are sequentially opened in a continuous motion.

The S-track design is an excellent deployment/retraction device because it:

- uses no moving parts
- works continuously in either direction
- is reversible at any time
- uses the motion of the boom for power
- occupies minimal area
- is automatically synchronized with the boom.

VARIATIONS AND OTHER APPLICATIONS

The elevating mechanism for this system is the large rotating nut but another method can also be used. Variations of this boom have been designed and built which are self deploying and lanyard controlled. This method of deployment results in a much lighter and smaller system but full strength and stiffness are not obtained until the boom is fully deployed. A larger version of this boom based on a 2.7 M (108 inch) cube has been built and tested for large-scale applications such as the space station. Although this type of boom is difficult to build smaller than a 16" cube, the upper limit to size is limited by the size of the launch vehicle.

CONCLUSION

The boom and deployment mechanism for the tethered satellite program have been designed, built, and qualification tested. The tests included operation at high and low temperature as well as loading to determine strength and stiffness. Results of this testing show that the mast meets all of the imposed requirements.

This boom was developed to satisfy the need for a larger and stronger deployable structure that can stow in minimal volume. The design goals were achieved by using this unique and recently patented folding boom. Fabrication and acceptance testing are currently in progress for a flight system scheduled to launch in 1988.

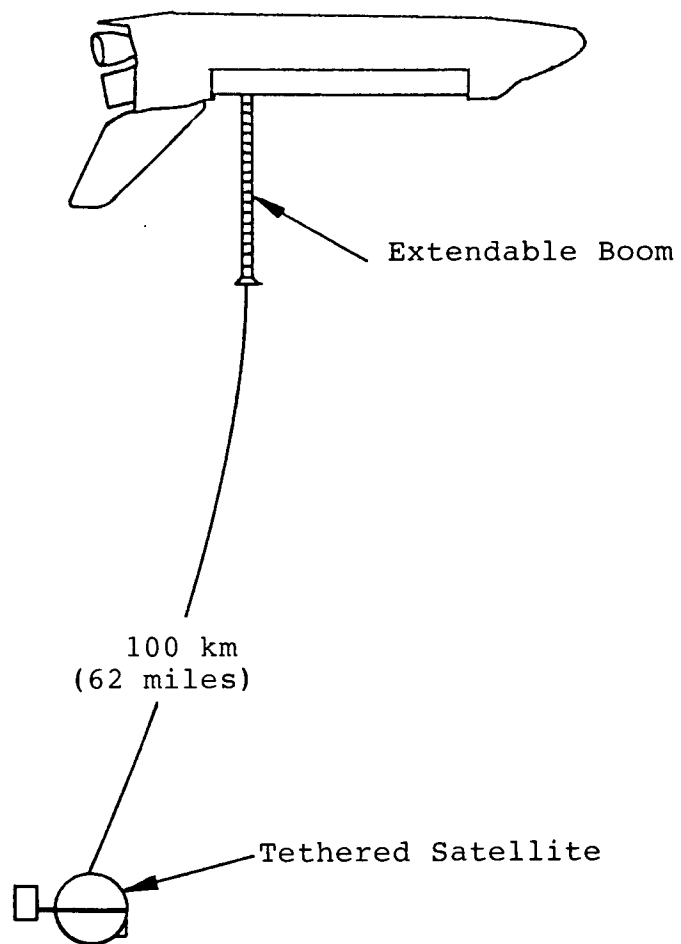


Figure 1: Tethered Satellite Experiment

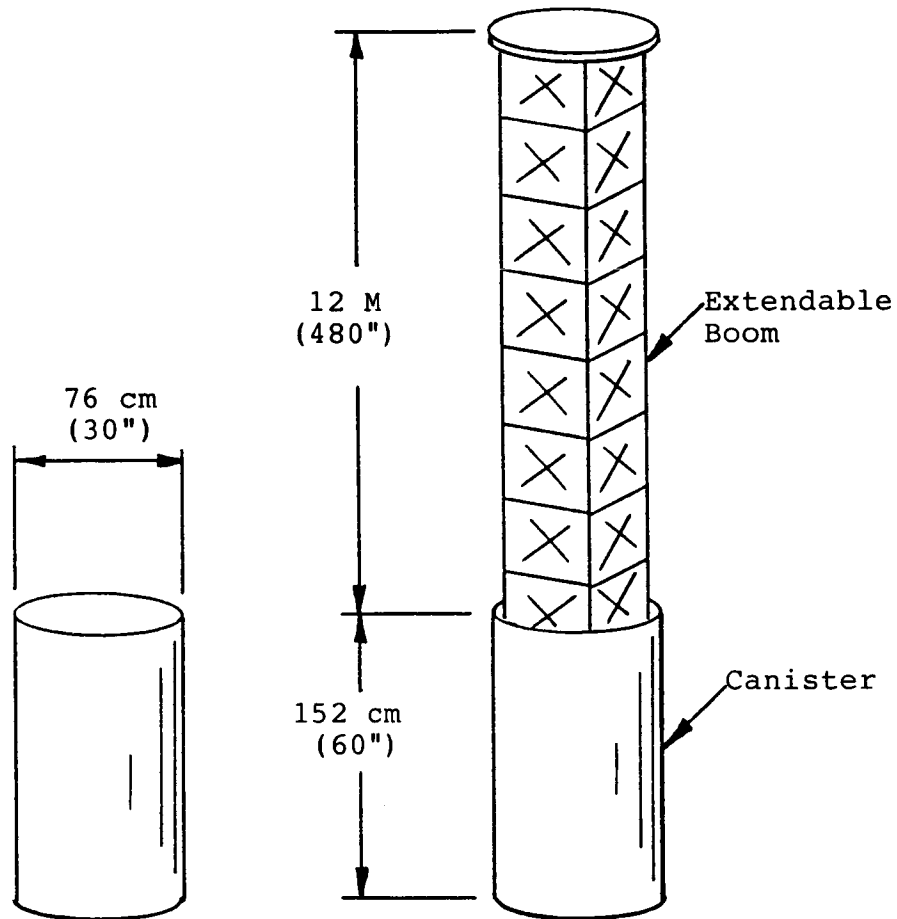


Figure 2: Envelope Dimensions

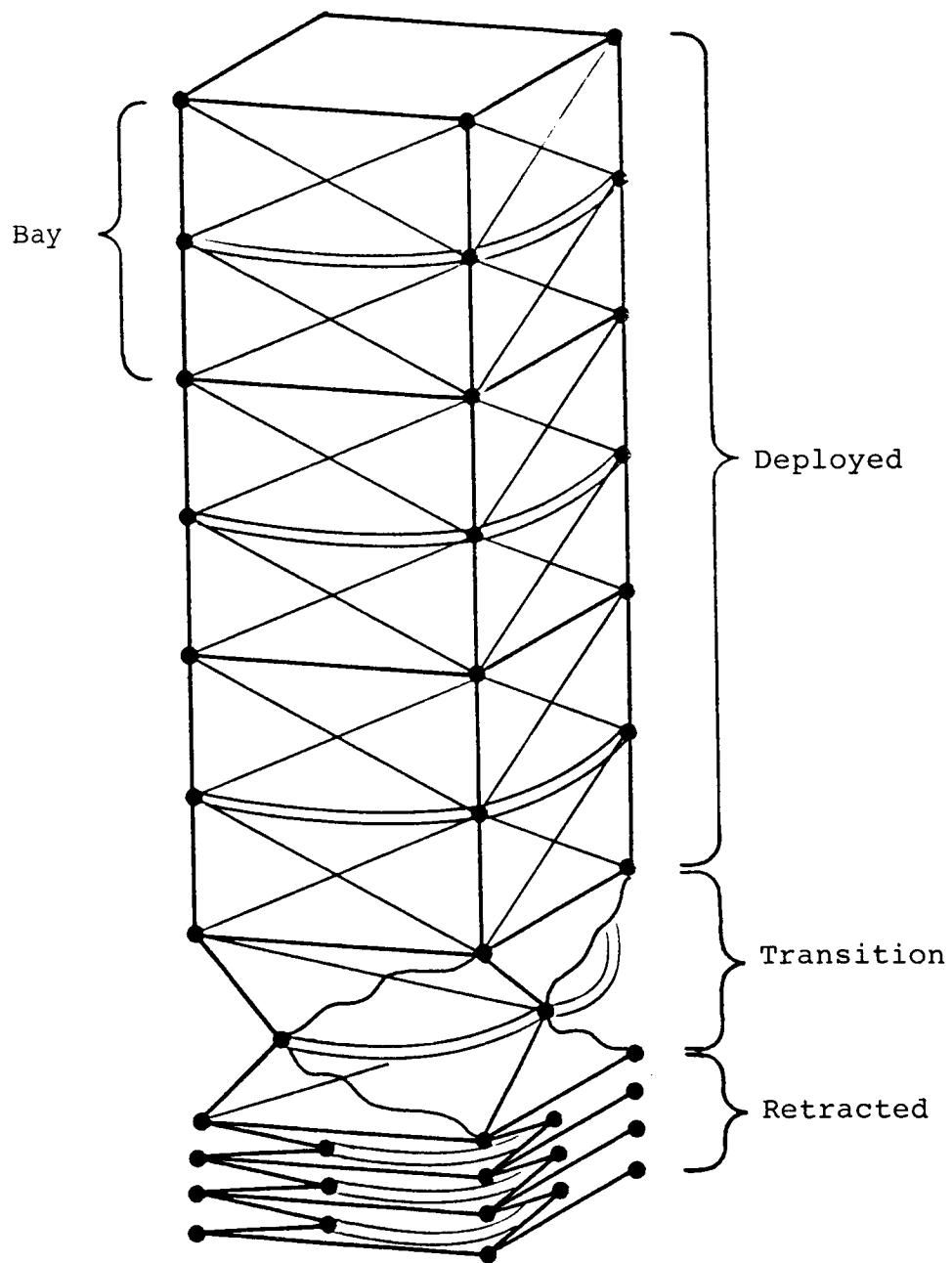
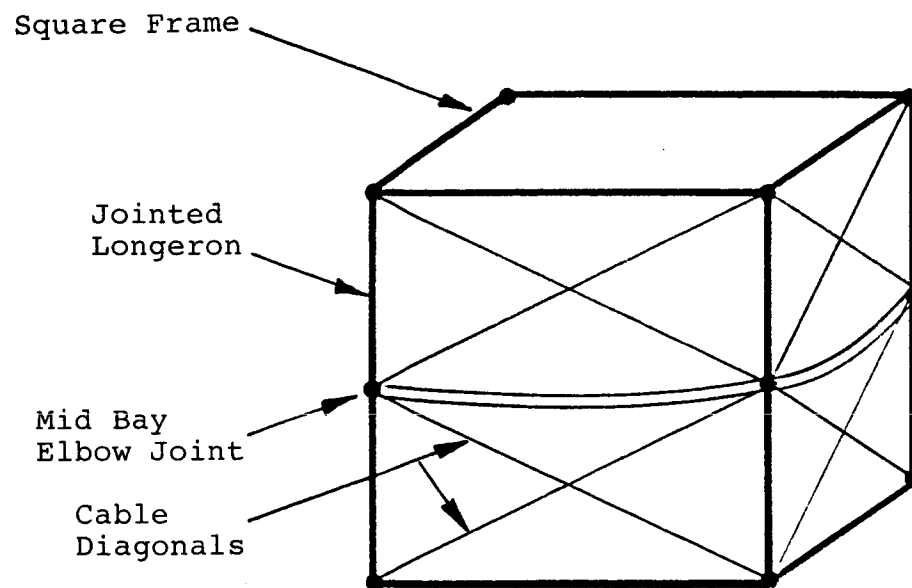
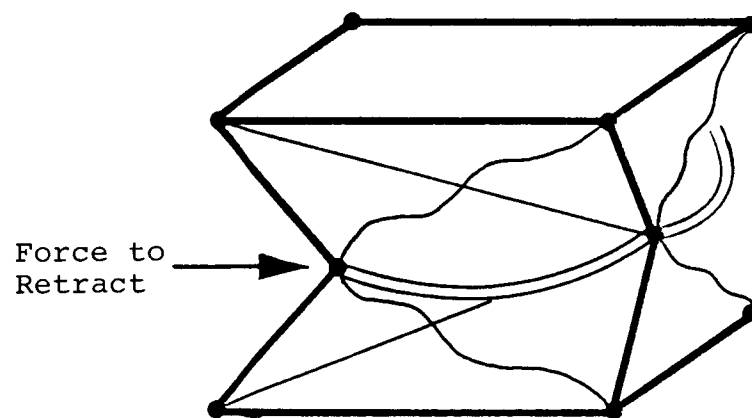


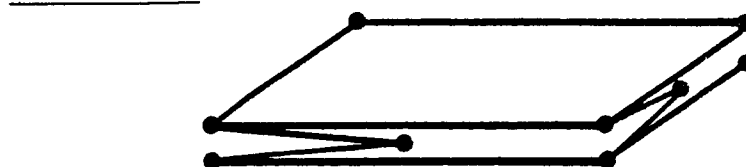
Figure 3: Boom Description



OPEN BAY

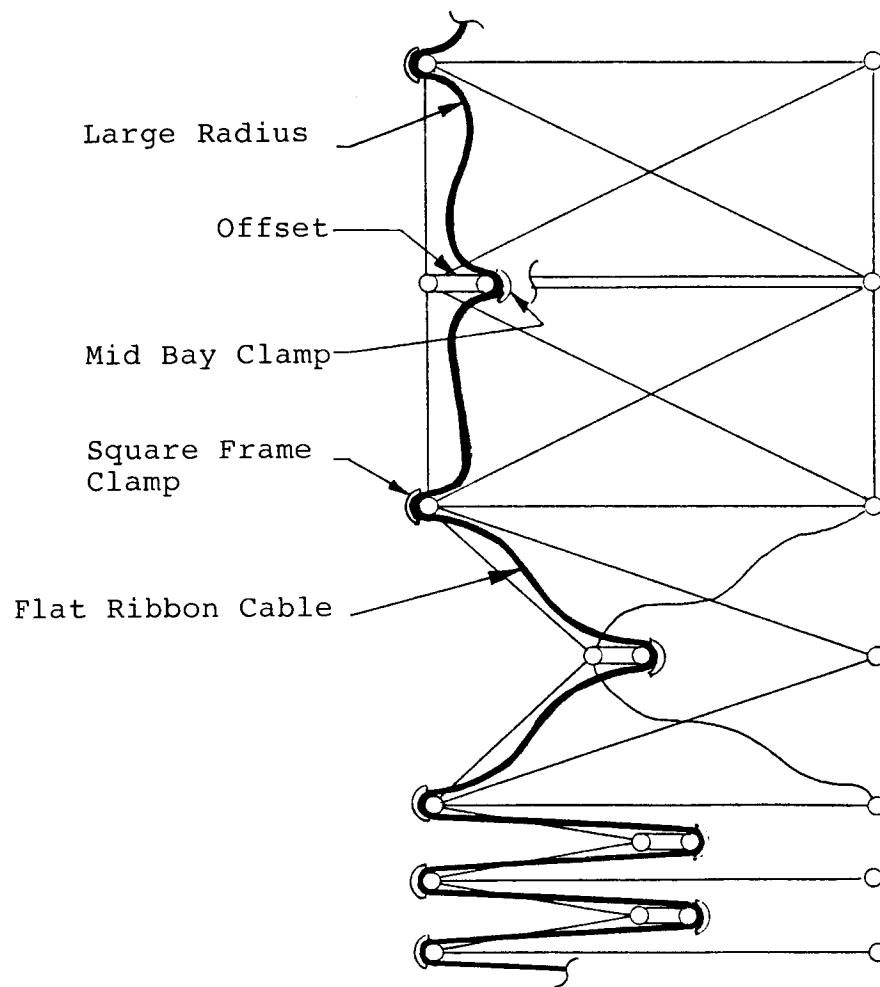


TRANSITION



CLOSED BAY

Figure 4: Bay Components



One Face Only Shown

Figure 5: Electrical Cable

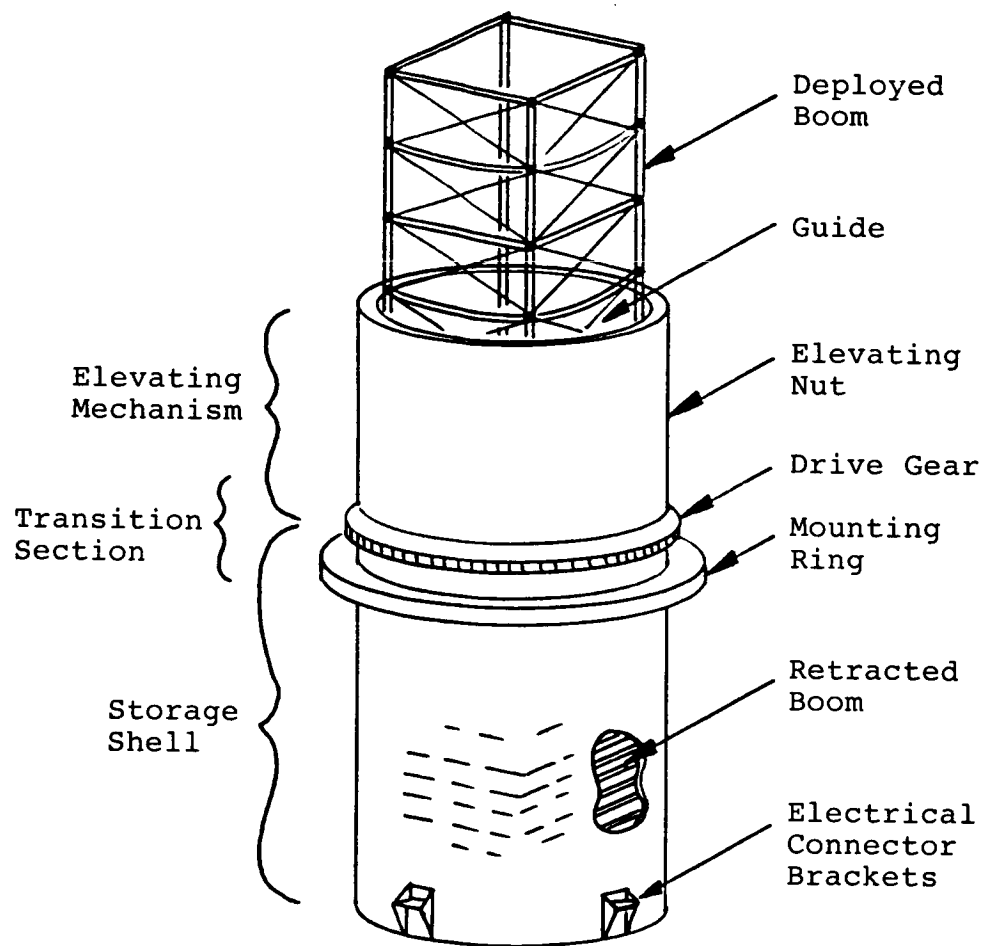


Figure 6: Canister Description

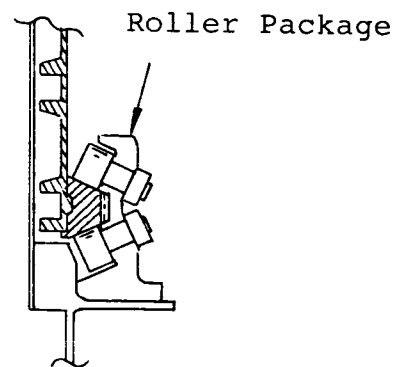
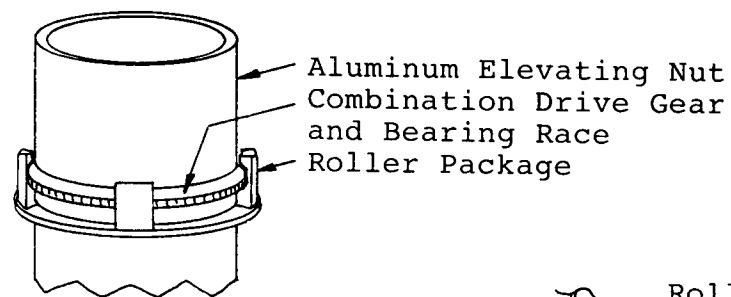
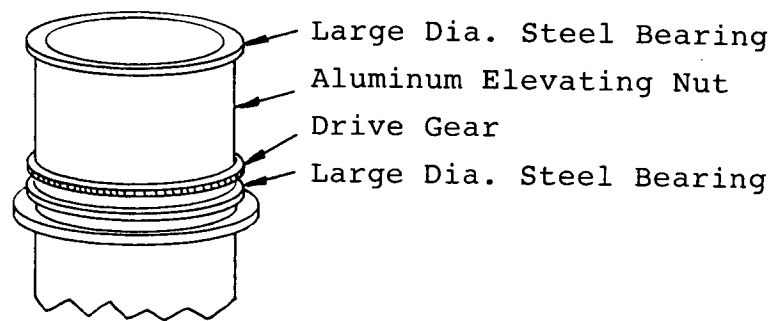


Figure 7: Bearing Comparison

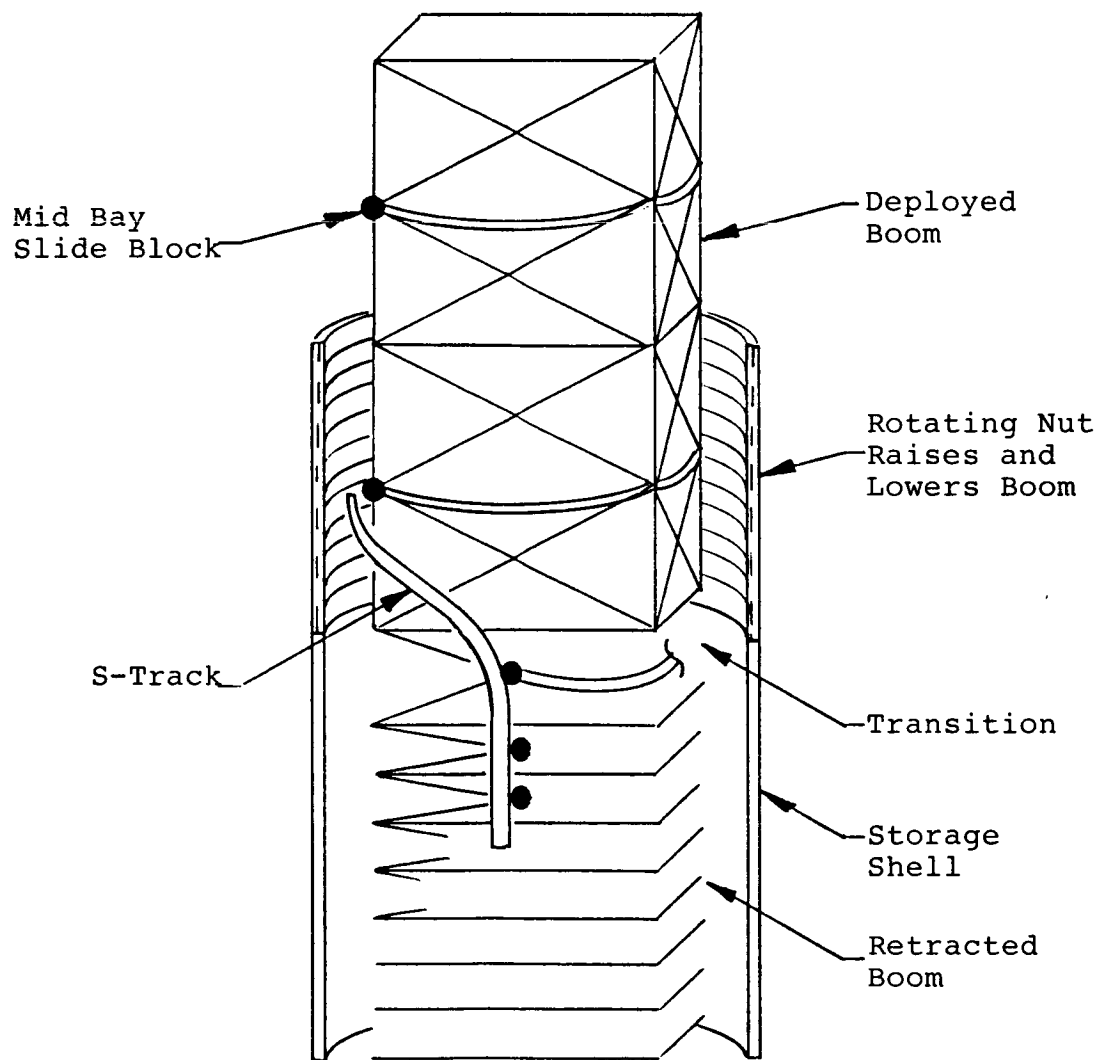


Figure 8: S-Track Function

ORIGINAL PAGE IS
OF POOR QUALITY

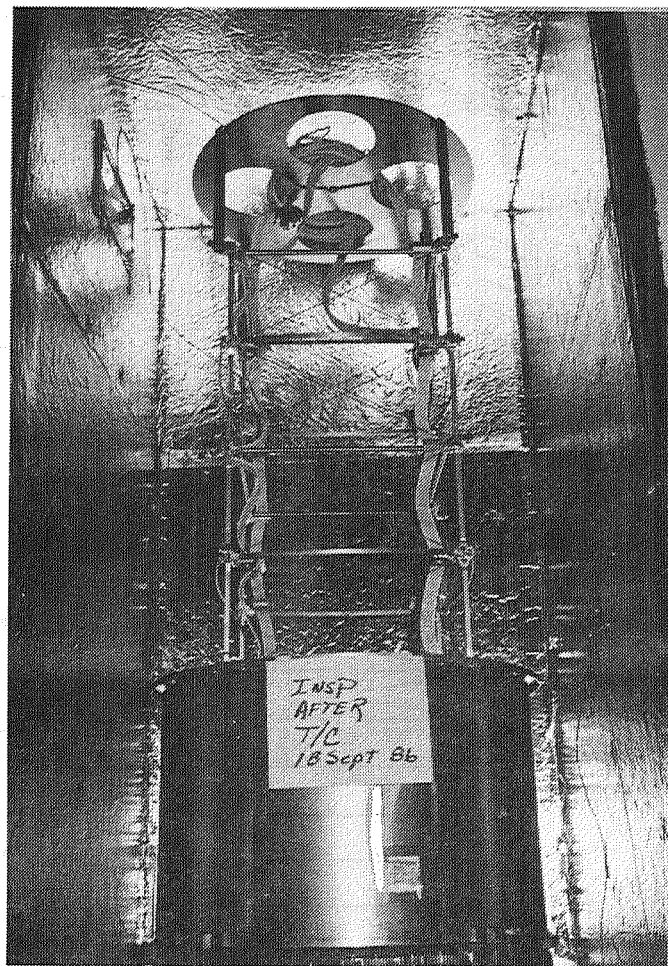


Figure 9: Boom Deployed in Thermal Chamber

ORIGINAL PAGE IS
OF POOR QUALITY

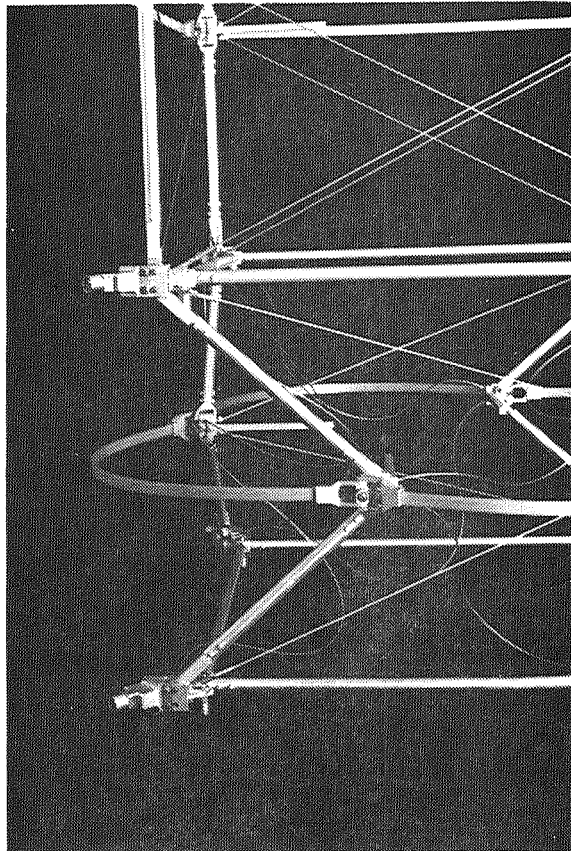


Figure 10: Bay in Transition

THE DESIGN AND DEVELOPMENT OF A TWO-DIMENSIONAL ADAPTIVE TRUSS STRUCTURE

Fumihiro Kuwao*, Shoichi Motohashi*, Makoto Yoshihara*,
Kenichi Takahara** and Michihiro Natori***

Abstract

The functional model of a two-dimensional adaptive truss structure which can purposefully change its geometrical configuration is introduced. The details of design and fabrication such as kinematic analysis, dynamic characteristics analysis and some test results are presented for the demonstration of this two-dimensional truss concept.

1. Introduction

An adaptive structure is a new type of space structure which can purposefully vary its geometric configuration and mechanical characteristics through geometric change of some component members in order to adapt to mission requirements and environmental conditions. This new structural concept appears to be applicable for use in many kinds of space structures; for example, in the control of geometry and vibration characteristics or for adjustment on orbit to compensate for the uncertainty in ground testing of large space structures.

One-dimensional adaptive truss-beam structures have already been studied (Refs. 1-3), and their application to space crane arms and to control of configuration and vibration characteristics has been proposed. They effectively use the properties of a statically determinate truss structure for their adaptivity.

In the near future two-dimensional truss structures will become important for planar space structures, such as large space antennas and space platforms. Various adaptive, two-dimensional truss structures have already been introduced and evaluated from the view point of both geometrical adaptivity and control of vibration characteristics (Ref. 5,6). In applications of space structures, some kinds of curved surfaces including paraboloids are important. There are two ways for obtaining a curved-surface, truss concept from a flat one. One is the bending concept in which the length of surface members is changed from that of the original flat structure, and the other is the shear concept in which the length of diagonal members is changed. The former is suitable for regular octahedral elements and the latter is suitable for cubic elements (Ref. 5).

The sheared deployable, cubic element, which is shown in Figure 1, displays the simple means of changing its configuration. In Figure 1, doubly-marked members change their length telescopically, while the members which are marked by a circle are folded when the cubic element is stowed. This sheared, deployable, cubic element can change its configuration by changing the length of the four diagonal members telescopically.

One example of a two-dimensional adaptive truss structure, which was introduced in Ref. 5 because of wide adaptivity for various configurations and ease of fabrication, is shown in Figure 2. The deployment stages are presented in Figure 2 (a)-(c). Figure 2(d) is a parabolic cylindrical surface. Figure 2(e) is a

- * Toshiba Corporation, Komukai Works
1, Toshiba-cho, Komukai, Saiwai-ku, Kawasaki-shi, Kanagawa, 210 JAPAN
- ** Toshiba Corporation, Research and Development Center
4-1, Ukishima-cho, Kawasaki-ku, Kawasaki-shi, Kanagawa, 210 JAPAN
- *** Institute of Space and Astronautical Science
4-6-1 Komaba, Meguro-ku, Tokyo, 153 Japan

paraboloid , while Figure 2(f) is a hyperbolic paraboloid. In this example some of the cubic elements are modified by elimination of diagonal members to maintain a statically determinate truss structure (Ref. 7).

In this paper, the functional model of the two-dimensional adaptive truss structure, shown in Figure 2, is introduced. The details of design and fabrication of this model, kinematic analysis of various configurations, dynamic analysis, and test results are presented.

2. Kinematic analysis

Generally speaking, kinematic analysis is very important in the design and development of deployable structures, especially in determining the mechanical degrees of freedom and the offset position of hinges. Two types of kinematic analyses are performed to design the functional model.

First, a wire frame model which does not consider the diameter of members is studied. This analysis is very useful in understanding the kinematic behavior of the functional model while moving between the stowed and deployed configurations. There are two types of diagonal members which change their length telescopically. One is the so-called $\sqrt{2}$ diagonal member which changes its length in the range:

$$\begin{aligned}\sqrt{2}a & : \text{ deployed configuration} \\ 2a & : \text{ stowed configuration} \\ & \text{ where } a : \text{ the length of the vertical member.}\end{aligned}$$

The other type is the so-called $\sqrt{3}$ diagonal member which changes its length in the range:

$$\begin{aligned}\sqrt{3}a & : \text{ deployed configuration} \\ a & : \text{ stowed configuration.}\end{aligned}$$

The type of deployment under consideration is shown in Figure 2 (a)-(c).

Second, an analysis is performed on a solid model which includes the offset positions, the definition of kinematic degrees of freedom and the shape of the hinges. The analysis is performed using the Computer-Aided-Engineering (CAE) program GEOMOD. This method of design and analysis is very practical for obtaining highly efficient and reliable mechanism designs. In kinematic analysis, numerical problems in solving the simultaneous non-linear equations can occur, as the number of the independent kinematic loops increases. Therefore, precise kinematic analysis was performed only for typical elements of the functional model. The deployment of the configuration of Figure 1 (a)-(b) was analyzed by this method.

3. Shape control

The functional model, which depends on the shear concept, can form the following quadratic surfaces by changes in the length of the diagonal members telescopically.

Circular Cylindrical surface:

$$y^2 + z^2 = r^2$$

r : the length of radius

Parabolic Cylindrical surface:

$$z = y^2/2c$$

c : the focal length

Circular paraboloid:

$$z = (x^2 + y^2)/2c$$

Hyperbolic paraboloid:

$$z = (x^2 - y^2)/2c$$

To form the quadratic surface starting from the deployed planar truss, additional strokes of the diagonal members are necessary. As the actuator for the diagonal members of the functional model, a single ball-screw has been used (for reasons of simplicity, reliability, and cost), and the maximum possible stroke of the diagonal member is shorter than the length of the vertical member. Thus for the functional model, the stroke of the diagonal members limits the retrieval function, as described in section 6.

4. Dynamic characteristics control

A two-dimensional adaptive truss structure will be able to change its vibration characteristics by changing the configuration of the structure as shown in Figure 2. It is a very important characteristic of the two-dimensional adaptive structure. To verify the change of vibration characteristics, finite element method (FEM) models, which have 337 grid points and 474 bar elements with the pin flag options for simulating hinges, have been made using NASTRAN for the configurations shown in Figure 2 (Case 1), namely plane, circular cylindrical surface, paraboloid and hyperbolic paraboloid. In these models, the focal length of the hyperbolic paraboloid is about four times as long as the vertical member length, 3000 mm; the radius of the circular cylindrical surface is three times as long as the vertical member length, 2100 mm; and the focal length of the paraboloid is about three times as long as the vertical member length, 2000 mm. Eigenvalue problems were solved by the modified Householder's method after reducing the original degrees of freedom to three translation degrees of freedom at every corner point, using the Guyan reduction method. The boundary condition is free-free.

The natural frequencies are listed in Table 1 and the first mode shape is shown in Figure 3. The first mode shape of the planar configuration is very similar to that of a free-free square plate, but the higher mode shapes are not similar. The natural frequencies of the lower modes for the curved configurations are slightly lower than those of the planar configuration.

For the configuration shown in Figure 2, to obtain the paraboloid surface, half of the $\sqrt{3}$ diagonal members are shortened and half of the $\sqrt{3}$ diagonal members are extended. With the configuration of Figure 4 (Case 2), two types of paraboloid can be formed. One is formed by shortening the $\sqrt{3}$ diagonal members and the other is formed by extending the $\sqrt{3}$ diagonal members.

From the point of view of vibration characteristics, it appears that the former paraboloid has higher natural frequencies than that of the latter. To verify this idea, natural frequency analysis was performed in the same manner as Case 1. The natural frequencies are listed in Table 2, and the first mode shape is shown in Figure 4.

In the planar configuration (Fig 4a), the first and the third natural frequencies are slightly lower than those of Case 1. But the paraboloid by shortening the diagonal members has higher natural frequencies than that of the paraboloid by extending the diagonal members. This is a very interesting characteristic of a two-dimensional adaptive truss structure. Both paraboloids have the same surface shape, but the vibration characteristics are different.

The arrangement of members in Case 2 was selected for the functional model.

5. Functional model

The dimensions of the functional model, which is shown in Figure 5, are approximately 3.5 m x 3.5 m x 0.7 m in the deployed configuration. The model consists of the truss structure and the actuator/control modules.

The truss structure consists of the following members:

36 vertical members	:	diameter 20 mm
120 lateral members	:	diameter 10 mm
36 diagonal members	:	diameter 20 mm
18 battren wires	:	diameter 2 mm

In the concept design phase wires have been used in place of diagonal members in the upper and lower surfaces of the model to reduce the weight of the truss. These members provide inplane shear stiffness.

The hinges consist of the following:

184 pin-joints
128 two degree-of-freedom hinges
36 telescopic hinges.

Figure 6 shows one of major joints.

The truss has 36 actuators which change the length of those diagonal members with telescopic joints. The actuator consists of a ball-screw and a small DC servomotor with a speed reducer and encoder. The actuators are controlled by a micro-computer (INTEL 8086 equivalent) to change the configuration of the truss as shown in Figure 2. The functional block diagram of the actuator/control modules is shown in Figure 7. The micro-computer sends the reference values of the length and deployment rate of diagonal members to 36 drivers through GPIB (General Purpose Interface Bus). The drivers control the actuators in respect to both position and angular rate using feedback of the encoder signal.

6. Preliminary test results

The deployment/retrieval functional test was performed with a constant angular velocity of 0.5 deg/sec between the vertical member and the lateral member. The behavior of deployment/retrieval is very smooth on the floor with 18 casters. Figure 8 shows the "stowed" configuration at $\theta = 40$ deg where θ is the angle between the vertical and lateral member; $\theta = 0$ deg corresponds to a perfectly stowed configuration, while $\theta = 90$ deg denotes the fully deployed configuration.

The functional model can actually be stowed up to $\theta = 25$ deg. However, gravity effects in the ground test require support cables to compensate the gravity force when θ is smaller than 40 deg. The stowing functional test to $\theta = 25^\circ$ will be performed with support cables.

The shape control test was performed on the floor also. The plane shape of the functional model was changed to the cylindrical surface configuration successfully. Figure 9 shows the cylindrical surface which is formed by the grid points of the upper surface. The shape control test for the paraboloid and the hyperbolic will also require support cables.

7. Concluding remarks

In early 1987, a modal survey for verification of vibration characteristics and the shape control tests for the paraboloid and the hyperbolic paraboloid with the support cables will be performed.

References

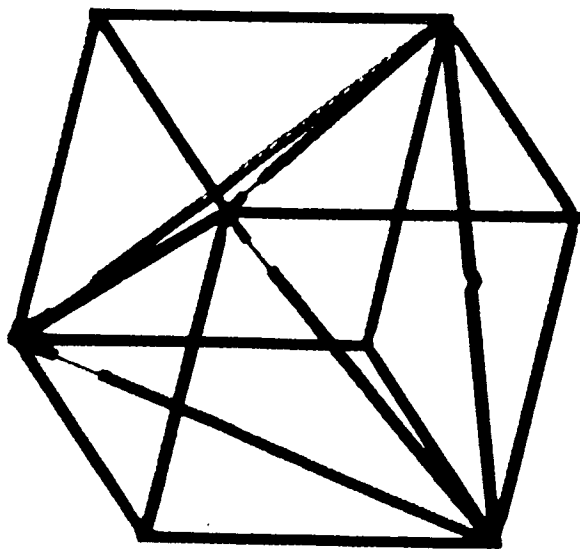
1. K. Miura, H. Furuya & K. Suzuki: Variable Geometry Truss and Its Application to Deployable Truss and Space Crane Arm, IAF-84-394, 35th Cong. Internatl. Astron. Fed., Lausanne, Oct. 1984; also *Acta Astronautica*, 12,7/8 (1985), 599-607.
2. M.D. Rhodes & M.M. Mikulas, Jr.: Deployable Controllable Geometry Truss Beam, NASA TM-86366 (1985).
3. K. Miura & H. Furuya: An Adaptive Structure Concept for Future Space Applications, IAF-85-211, 36th Cong. Internatl. Astron. Fed., Stockholm, Oct. 1985.
4. M. Natori & K. Miura: Deployable Structures for Space Applications, AIAA-85-0727, AIAA/ASME/ASCE/ASH 26th SDM Conf., Orlando, April 1985.
5. M. Natori, K. Miura & H. Furuya: Deployable Surface Truss Concepts and Two-dimensional Adaptive Structures, Proc. 15th Internatl. Symp. Space Technology and Science, Tokyo 1986, 503-508.
6. M. Natori, K. Iwasaki & F. Kuwao: Adaptive Planar Truss Structures and Their Vibration Characteristics, AIAA-87-0743, AIAA/ASME/ASCE/ASH 28th SOM Conf., Monterey, April 1987.
7. M.S. Anderson & N.A. Nimmo: Dynamic Characteristics of Statically Determinate Space Truss Platforms, AIAA-85-0819, AIAA/ASME/ASCE/ASH 26th SDM Conf., Orlando, April 1985; also *J. Spacecraft*, 23 (1986), 303-307.

Table 1. Natural Frequency (Case 1)

Mode	Natural frequency (Hz)			
	Plane configuration	Hyperbolic paraboloid	Cylindrical surface	Paraboloid configuration
1	19.45	18.48	16.03	16.19
2	22.19	19.45	20.26	20.89
3	27.96	25.69	20.43	20.92
4	28.03	25.69	27.80	23.39
5	28.65	27.62	30.99	27.14
6	41.06	36.03	36.13	30.17
7	41.76	37.53	37.59	35.85

Table 2. Natural Frequency (Case 2)

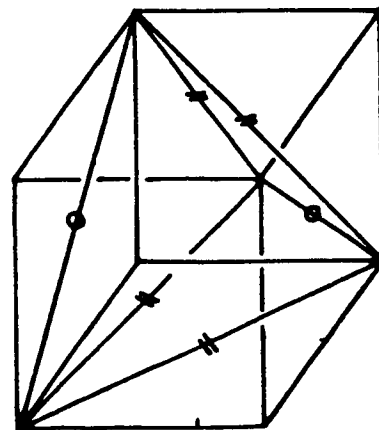
Mode	Natural frequency (Hz)		
	Plane configuration	Paraboloid configuration	
		$\sqrt{3}$ members extended	$\sqrt{3}$ members shortened
1	17.09	16.73	15.25
2	22.83	23.52	16.59
3	25.36	24.63	18.47
4	28.45	26.85	21.41
5	33.11	32.58	21.49
6	45.92	40.84	32.10
7	48.73	41.47	34.59



(a) Deployed Configuration
(Solid Model)



(b) Stowed Configuration
(Solid Model)



(c) Arrangement of Hinges

H: Telescopic hinge
O: Folded hinge

Figure 1. Sheared Deployable Cubic Element

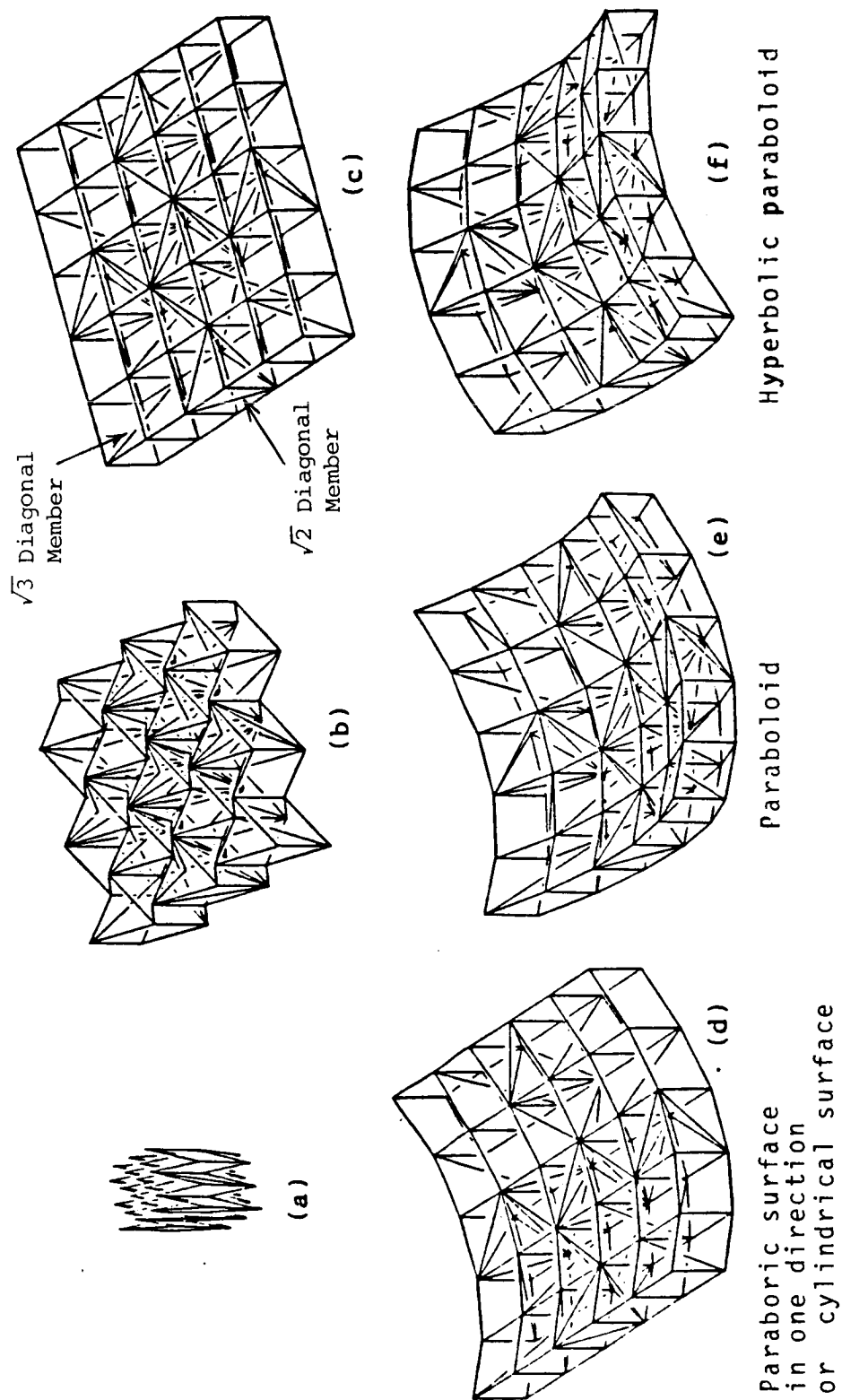
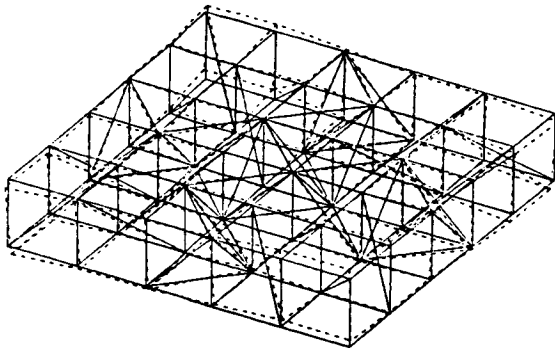
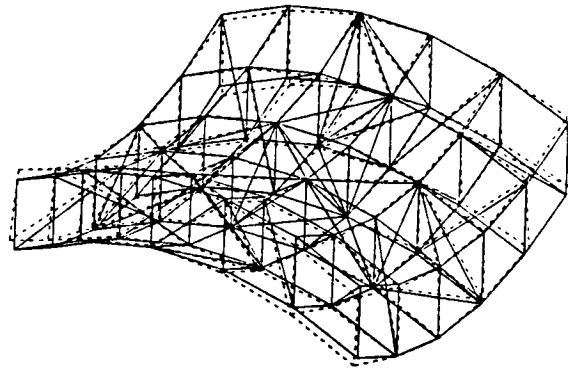


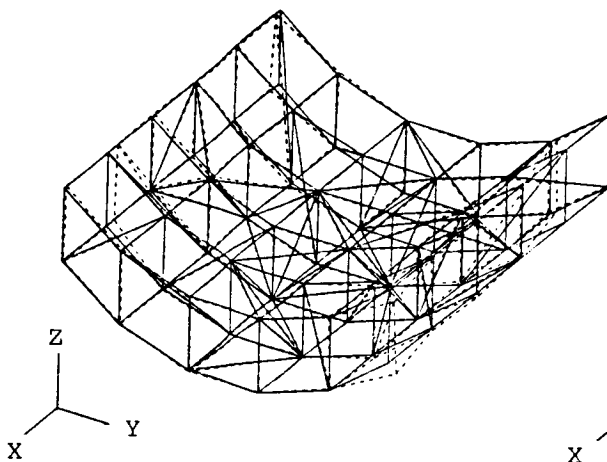
Figure 2. Two-Dimensional Adaptive Truss Structure (Functional Model)



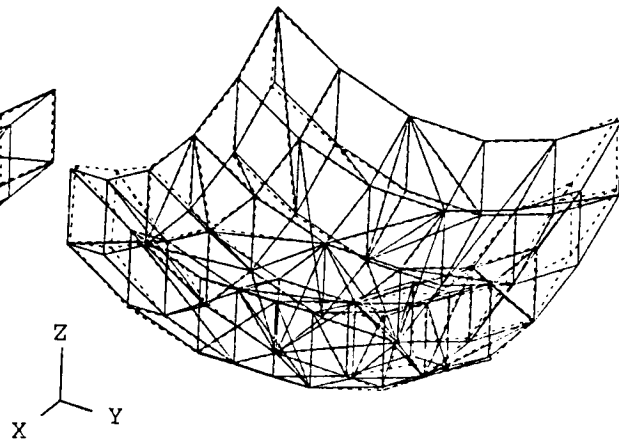
(a) Plane Configuration



(b) Hyperbolic Paraboloid Configuration

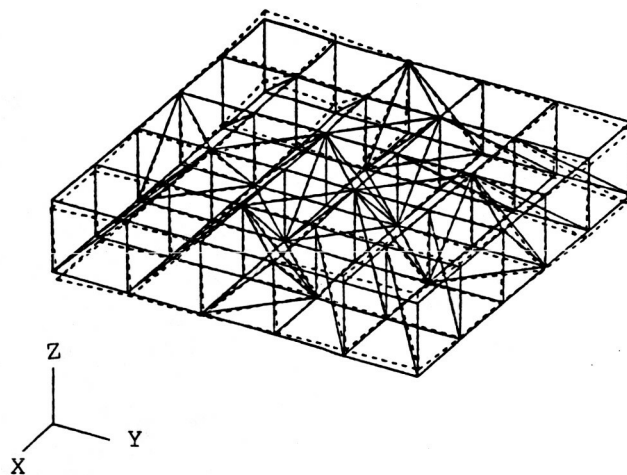


(c) Cylindrical Surface Configuration

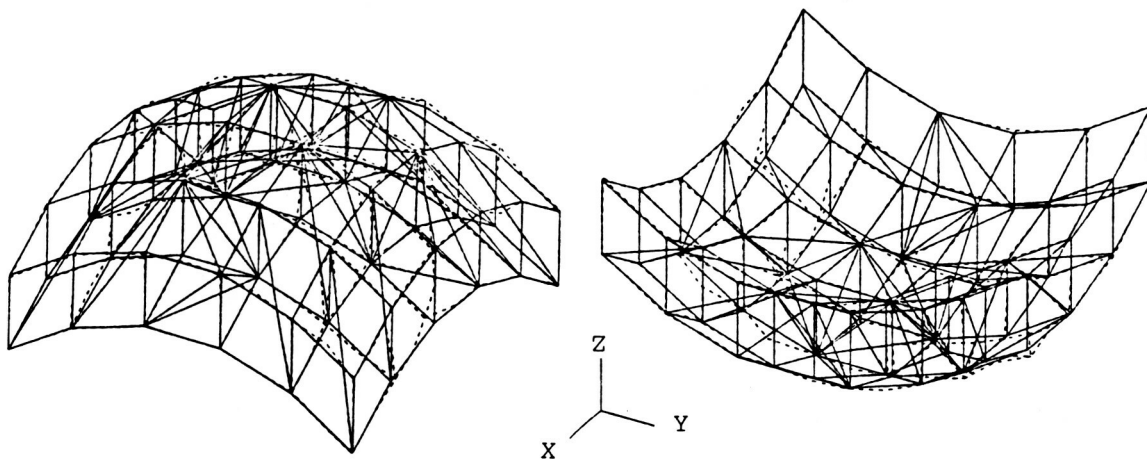


(d) Paraboloid Configuration

Figure 3. First Mode Shape (Case 1)



(a) Plane Configuration



(b) Paraboloid Configuration
($\sqrt{3}$ Members Extended)

(c) Paraboloid Configuration
($\sqrt{3}$ Members Shortened)

Figure 4. First Mode Shape (Case 2)

ORIGINAL PAGE IS
OF POOR QUALITY

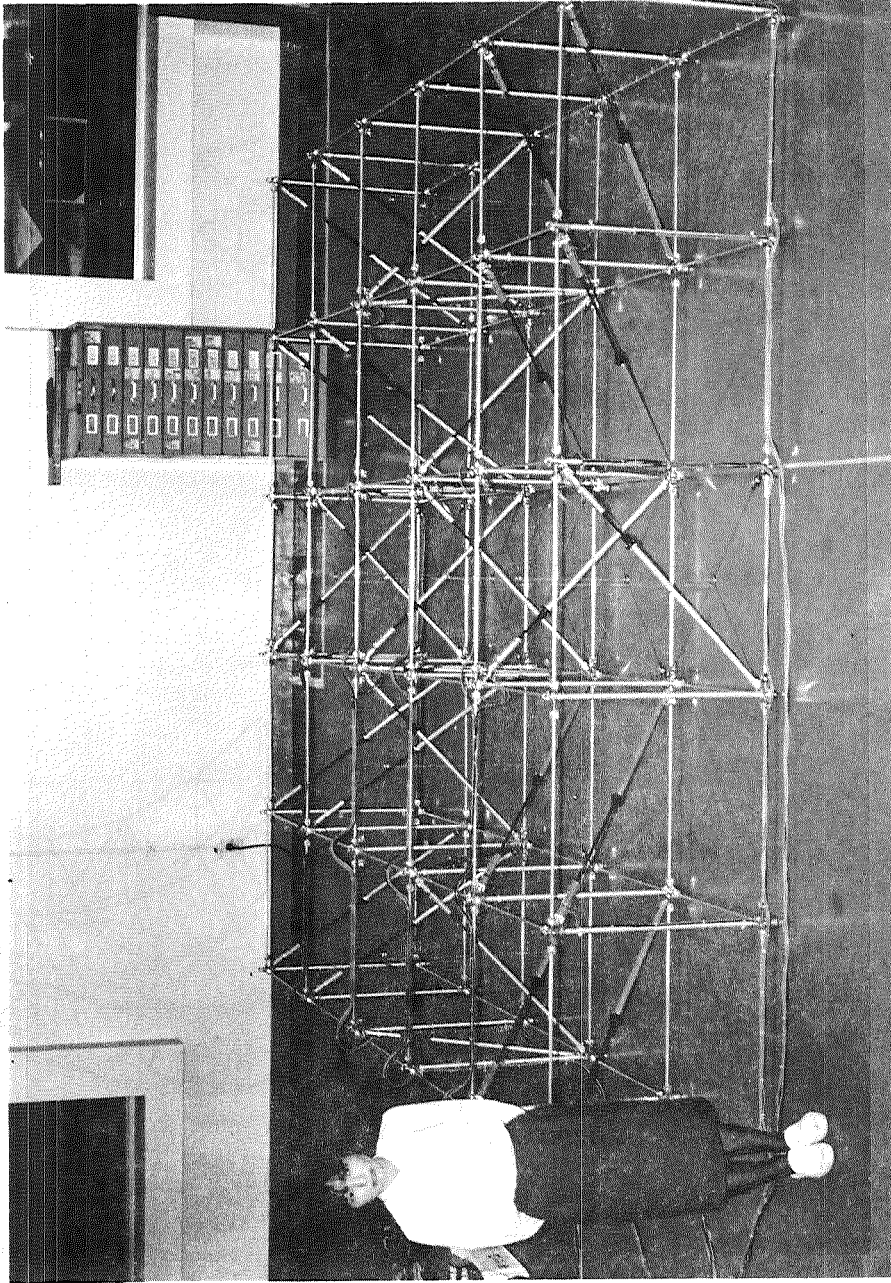


Figure 5. Functional Model of Two-Dimensional Adaptive Truss

ORIGINAL PAGE IS
OF POOR QUALITY

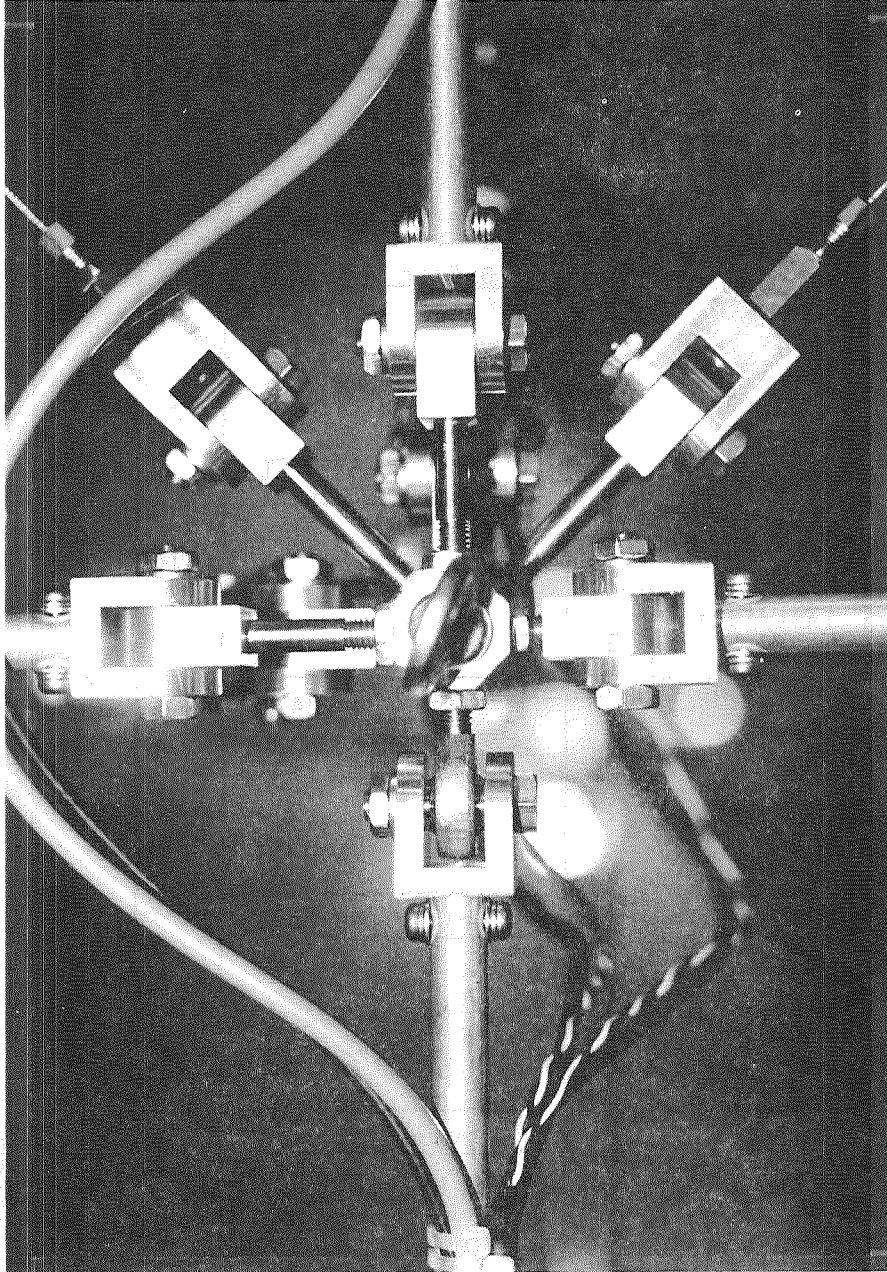


Figure 6. One of Major Joints (Functional Model)

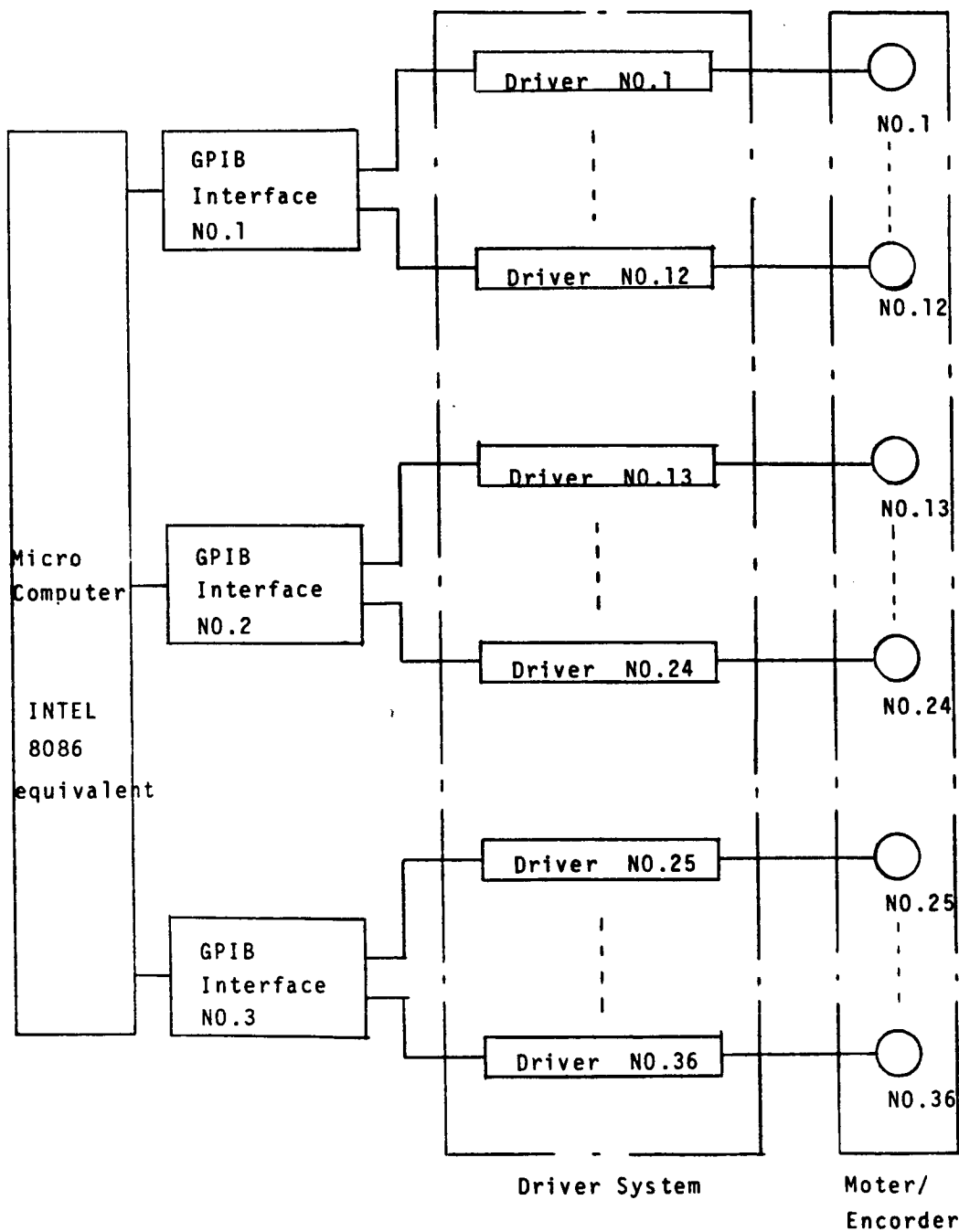


Figure 7. Functional Block Diagram of the Actuator/Control Modules

ORIGINAL PAGE IS
OF POOR QUALITY

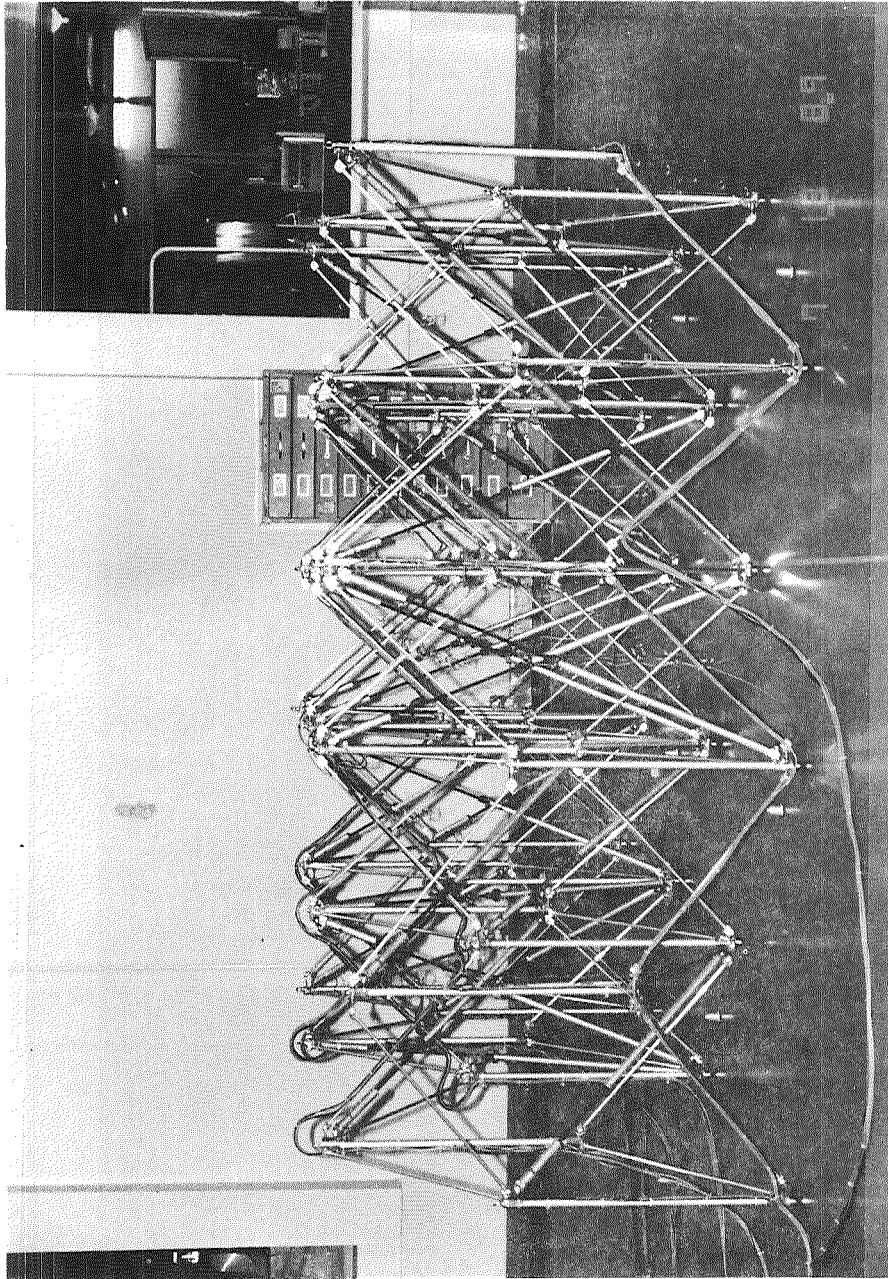


Figure 8. Stowed Configuration at $\theta=40$ deg (Functional Model)

ORIGINAL PAGE IS
OF POOR QUALITY

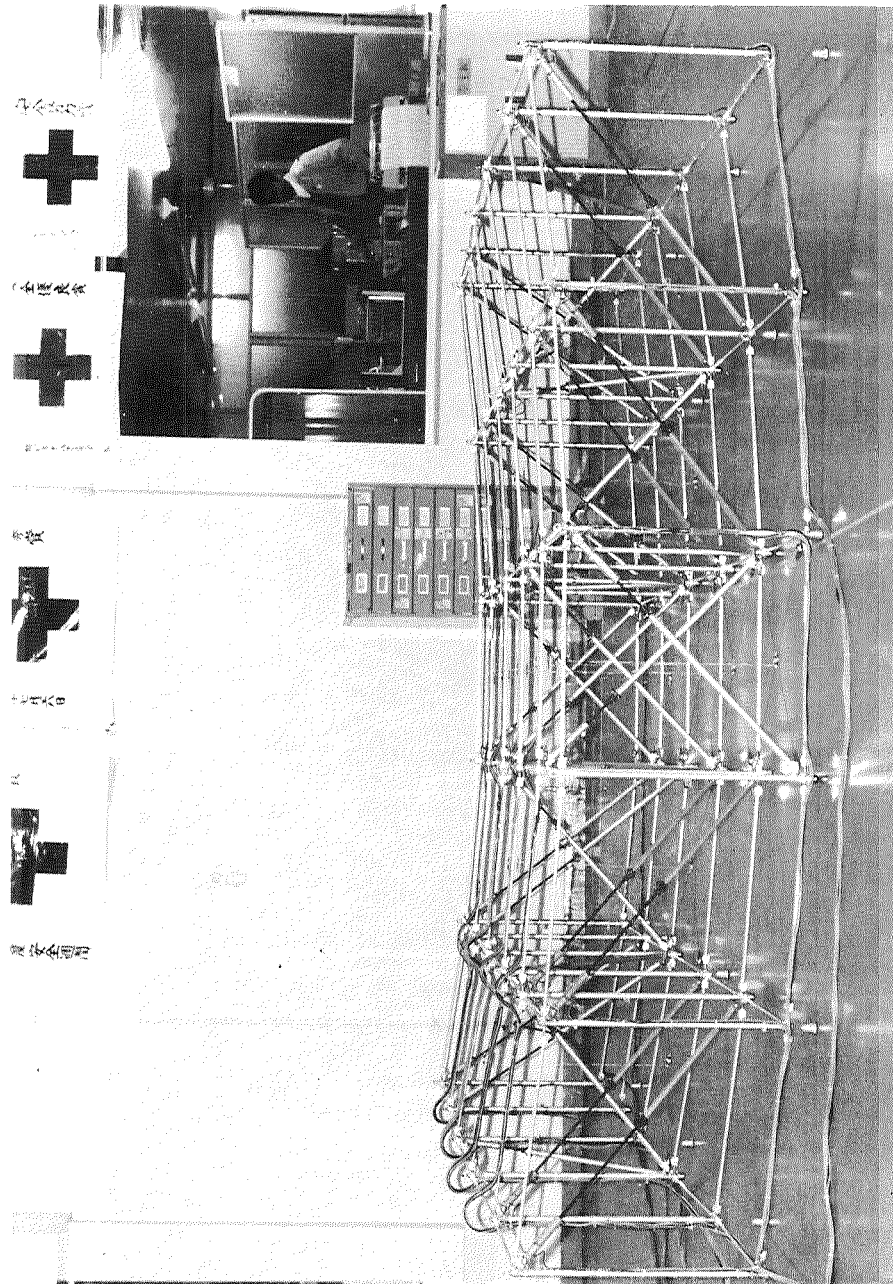


Figure 9. Cylindrical Surface Configuration (Functional Model)

A MICROGRAVITY ISOLATION MOUNT

D. I. Jones, A. R. Owens, R. G. Owen, G. Roberts, *
D. W. Wyn-Roberts & A. A. Robinson. **

ABSTRACT

In this paper we discuss the design and preliminary testing of a system for isolating microgravity sensitive payloads from spacecraft vibrational and impulsive disturbances. The Microgravity Isolation Mount (MGIM) concept consists of a platform which floats almost freely within a limited volume inside the spacecraft, but which is constrained to follow the spacecraft in the long term by means of very weak springs. The springs are realised magnetically and form part of a six degree of freedom active magnetic suspension system. The latter operates without any physical contact between the spacecraft and the platform itself. Power and data transfer is also performed by contactless means. Specifications are given for the expected level of input disturbances and the tolerable level of platform acceleration. The structural configuration of the mount is discussed and the design of the principal elements, i.e. actuators, sensors, control loops and power/data transfer devices are described. Finally we describe the construction of a hardware model that is being used to verify the predicted performance of the MGIM.

INTRODUCTION

It has long been proposed that the microgravity environment of Earth orbit has advantages for experimental work in the fields of fluid science, organic and inorganic materials preparation and the life sciences. Wilhelm [1] reviews some of the preliminary work which has already been performed in materials processing. If space manufacture is to achieve commercial viability then further research is required now to establish suitable processing techniques which take full advantage of the unique on-orbit environment. It has been established [2] that many of the proposed processing techniques are critically dependent upon achieving lower levels of microacceleration than exist in current spacecraft. The experience gained in Europe on Spacelab will be applied to achieving a low level microgravity environment for experimenters on the Columbus programme in cooperation with the U.S. Space Station.

The factors which determine the microgravity environment have been identified [3] and may be classified by frequency range as follows:

- 1) quasi-static, external disturbances due to aerodynamic drag and gravity gradient effects.

* University College of North Wales, Bangor, Great Britain.

** European Space Technology Center, Noordwijk, The Netherlands.

- 2) Low frequency vibration sources, e.g. responses of large flexible elements (solar arrays, antennae), crew motion, spacecraft attitude control, robotic manipulators.
- 3) Medium/high frequency vibration caused by on-board equipment (motors, pumps etc.)

Disturbances in class 1 are minimised by careful consideration of spacecraft orbital altitude and mass distribution; generally it is thought that a quasi-static level of the order of $1\mu g$ is achievable. Lower values may be possible by reducing the effects of aerodynamic drag by active acceleration control using thrust compensation.

Isolation of the experimental payload from class 3 disturbances is relatively straightforward and a passive, mechanical suspension would probably suffice since the microgravity requirement is less stringent in this range.

In many ways, the most difficult disturbances to deal with are those in class 2. The concept of a Man-Tended Free Flyer (MTFF) is currently being investigated by ESA as part of its Columbus programme. Here, microgravity payloads requiring infrequent crew attention are placed aboard an autonomous, unmanned free flyer. This offers extended periods free from the disturbances associated with the Space Station, the Flyer returning periodically to the Space Station for servicing. Vibration due to on-board equipment may still be a problem. The difficulty of access, if human intervention is required, is also a drawback.

In the case of the Columbus attached Pressurised Module (PM), additional disturbances occur due to the continual presence of men and due to vibrations transmitted from the Space Station itself. Therefore, especially the PM but also quite possibly the MTFF require a suspension mechanism which isolates payloads from class 2 and class 3 disturbances but which is controlled to maintain a long-term position adjacent to its supporting frame. Here we propose a Microgravity Isolation Mount (MGIM) for this purpose.

The MGIM consists of support frame and a platform for mounting the experiment. Frame and platform are separated by actively controlled isolators.

In this paper we discuss what levels of acceleration are allowable on the platform and what levels are present on the supporting frame. A design proposal for the MGIM is then presented and its component parts discussed. Finally, we assess the potential performance of the MGIM and give experimental results from a preliminary rig which has been constructed to verify actual operational capabilities.

REQUIRED ACCELERATION LEVELS.

Studies of the microacceleration levels required for successful experimentation have shown that the class 2 frequency band is critical. Curve (a) in Fig.1 shows a sinusoidal specification of acceptable acceleration levels, based on the envelope of several curves given by Tiby & Langbein [5]. Their curves were derived from theoretical models which indicate that the allowed acceleration exhibits a constant limit at low frequencies and a square law dependency at high frequencies. Curve (b) is the design specification for Eureka [6] while curve (c) is the proposed specification for the U.S. Space Station [7]. Taking into account each of these curves, we formulated Fig.2a as an appropriate specification for our work. Below 1.5 Hz a constant level of $10^{-5}g$ is specified as the minimum to be achieved while between 1.5 Hz and 15 Hz an f^2 variation, compatible with Fig.1a, is assumed. Above 15 Hz a $10^{-3}g$ upper limit is imposed in consideration of practical constraints such as damage to delicate instrumentation. A supplementary (dotted) curve in Fig.2a continues the f^2 variation down to the $10^{-6}g$ level and represents the ultimate objective of our work.

Our guideline sinusoidal characteristic for the translational vibration of the supporting frame is shown in Fig.2b. In practice this vibration characteristic will be produced by several different sources, such as spacecraft subsystems (pumps, steerable antennae etc.), crew motion and thrusters which will interact on the nonlinear dynamic components of the spacecraft structure. The result will be a random combination of impulsive and periodic signals with broadband "noise" as a base and probably containing spectral peaks related to the natural modes of the spacecraft structure. Since modelling of such a complex system is a considerable task in itself, and in view of the paucity of measured data (especially in the lower frequency range), Fig.2b was adopted as an envelope which encompasses all these effects. An f^2 variation is assumed below 3 Hz and a constant limit of $10^{-1}g$ above 3 Hz. In fact, comparison with known characteristics for other transportation systems [4] shows it to be a worst case since it exceeds considerably the expected on-orbit vibration environment. This is supported by [2] where the measured acceleration data presented for the D-1 mission rarely reaches $10^{-2}g$ except during orbit trim burns.

Combining figures 2a and 2b gives the transmissibility function, Fig.2c which shows that below 0.03 Hz it is permissible for the platform to follow the outer frame and this defines the break frequency required of the MGIM. This corresponds to a maximum amplitude of approximately 4 mm which is an important parameter in designing the MGIM actuators. Above this frequency at least a -40dB/decade roll-off is required, up to 1.5 Hz, to maintain the platform acceleration at or below $10^{-5}g$.

STRUCTURAL DESIGN

Our preliminary design study is based on the structural concept shown in Fig.3 where the payload is affixed to a central platform. The platform is to be controlled in six degrees of freedom so that it remains at a cen-

tral position within its supporting frame. For the purposes of the present study, it has been assumed that the unit fits into a cube of about 1 m side and has a maximum mass of approximately 200 kg, but this does not mean that other configurations cannot be accommodated. Both platform and supporting frame should be as rigid as possible and the platform should be well-damped so that any high frequency modes will decay quickly. In conflict with this, low platform weight is desirable so that payload mass is maximised. This can be achieved with a platform having a closed-cell honeycomb internal structure with a stainless steel surface skin. The central platform allows easy access to the payload and is adaptable to various sizes and shapes of experiment modules. A locking mechanism is provided which clamps the platform securely for periods of launch and manoeuvre.

Modules containing actuators and sensors are situated at each corner, the actuators acting together to control translational motion and differentially to control rotational motion. With this configuration the actuators act directly on the platform and a modular construction facilitates assembly.

Any combination of platform and payload will have an uneven mass distribution and estimates were made of the following parameters:

- i) the total mass of the platform and payload,
- ii) the position of the centre of mass relative to the geometric centre,
- iii) the moments of inertia about the principal axes,
- iv) the orientation of the principal axes relative to the reference axes.

For simplicity, the analysis was confined to a two dimensional representation with the geometric centre taken as the origin.

Figures 4 and 5 show how the five parameters vary as payload asymmetry increases.

In a case thought to be typical of a platform/payload combination, Fig.4 shows a heavier experiment on the right hand side having drawn the centre of mass up and across to the right. The total platform mass is 95 kg with the centre of mass pulled 9 cm radially away from the origin. The principal axes are only rotated by about 9°.

In the previous case, platform and payload are assumed to have a uniform density of 320 kg/m³ but in Fig.5 the shaded area represents a solid block of aluminium. This probably represents an extreme case of asymmetry. The total mass is now 150 kg with the radius of the centre of mass pulled to 20 cm from the origin and the principal axes rotated by 14°.

More accurate computation of these parameters is desirable but two tentative conclusions may be drawn from these results:

- i) Insisting that experiment packages be configured such that they conform to a 10 cm envelope for centre of mass displacement does not place unreasonable constraints on mass asymmetry,
- ii) The moment on the platform, due to the line of action of the actuators not being through the centre of mass, will induce angular motion (and amplification of linear acceleration at the periphery). By far the major contributor to this moment is the translation of the centre of mass; orientation of the principal axes is relatively unimportant.

ELECTRICAL POWER, COOLING AND DATA TRANSMISSION.

The connections between platform and supporting frame must perform three separate functions:

- i) supply of electrical power to the platform,
- ii) transport of cooling fluid to and from the platform,
- iii) transmission of control and data signals.

Any physical connection will form a compliant element between the frame and platform thus introducing direct transmission of vibration. It is therefore crucial to investigate to what extent these functions can be performed without recourse to a direct umbilical link.

Electrical power transmission may be substantial for some experiments such as crystal growth from a melt in a furnace. We have assumed a load rating of 1 kW and investigated the use of a transformer with loose-coupled secondary to effect power transmission. Fig.6 shows that the primary winding is wound onto the core of the transformer in the usual manner, but the secondary winding has a 7 mm clearance in all directions between the core and former. A prototype of this transformer has been constructed, the primary winding being driven with a square wave derived from a 150 V d.c. supply by a MOS transistor bridge. The secondary is connected directly to a bridge rectifier and smoothing capacitor with resistive load. Power transfer of 1 kW with good regulation properties has been successfully achieved [8].

Cooling the payload is the most difficult task. Applying the Stefan-Boltzmann law of radiation shows that for the 6 m² surface area of our unit, a surface temperature of 46°C. results from dissipating 1 kW with an ambient temperature of 20°C. It is likely that these figures represent a pessimistic case and could be improved upon by:

- i) placing one of the MGIM walls adjacent to the spacecraft outer skin to take advantage of a reduced ambient temperature,
- ii) changing the MGIM shape from a cube to "flatter" proportions giving an improved ratio of surface area to volume,
- iii) reducing the input power needed to maintain furnace temperature by means of improved thermal insulation.

For greater power levels, forced liquid cooling is the only realistic method requiring flexible tubing between frame and platform. For the specification given previously, the limit of stiffness for this tubing is of the order of 2-3 N/m and careful dynamic characterisation would be required when designing such an umbilical. It is worth stating that the thermal problem exists whatever method of vibration isolation is being considered.

The non-contact transmission of data presents little problem and we have demonstrated an infra-red optical link operating at over 100 kbit/s - more than adequate for the expected 100 Hz sampling rate. A source/receiver distance of 30 mm and lateral movement up to a radius of about 30 mm can be tolerated even in the presence of fairly high levels of ambient light.

Clearly, there is an advantage from the point of view of vibration isolation in operating the MGIM as a wholly non-contact system. The preceding discussion indicates that it is also feasible to maintain platform services in such a way and so we proceed to discuss how non-contact vibration control may be achieved.

ACTUATORS AND SENSORS.

The sensors referred to in Fig.3 are non-contact devices. There are eight sensors sited to measure platform displacement relative to the outer frame. They operate as differential capacitance bridges detecting the movement of a central plate affixed to the platform, as shown in Fig.7. Stray capacitances from the sensing plates and connecting leads to ground, and between the primary and secondary windings of the transformer, are eliminated by guard techniques. Conventional phase sensitive detection yields a linear d.c. output which is independent of the dielectric constant of the gap and, by making the central plate much larger than the two sensor plates, is sensitive to motion in one axis only.

The actuators must also be non-contact devices; they are effectively small linear motors as shown in detail in Fig.8. Rare earth permanent magnets establish a flux density in the bore of the stator. A thin, planar armature inserted into the bore produces force on the platform in one direction while allowing free movement along the other two directions to the limits of the bore gap. It has been estimated [4] that each actuator must provide approximately 0.01 N of force. The actuator shown in Fig.8 has a 72 conductor armature and a stator bore flux density of 0.14 T.

Fig.9 is its measured characteristic showing that a force of 0.01 N is achieved with about 30 mA of armature current. Evidently, the power requirements are very low and the actuator does not appear to be a limiting factor in this application.

CONTROL TECHNIQUES.

A one degree of freedom analysis shows that, for the case of a low umbilical stiffness, acceptable system performance can be obtained in a straightforward manner using platform position sensing only. The block diagram of the control loop for one axis is shown in Fig.10. Its transfer function is given by:

$$\frac{y}{x} = \frac{s + \gamma}{s^3 + \alpha s^2 + s + \gamma}$$

where the parameters α and γ are related to the chosen natural frequency, the system mass and specified control loop gains by the following substitutions:

$\omega_0^2 = C/M$	where:	$\omega_0 =$ system natural frequency
$\alpha \omega_0 = a$		$a, b =$ lead-lag time constants
$\gamma \omega_0 = bc$		$M =$ platform + payload mass
		$C =$ feedback loop gain

Assuming that $\alpha/\gamma = 30$, computer simulation has shown [8] that the frequency response of equation (1) agrees well with the requirement of Fig.2.

In order to assess system performance in the case where the centre of mass is not coincident with the platform's geometric centre, a two degree of freedom model was simulated - see Fig.11. Here the platform is in plan view and is controlled by two actuators at either corner exerting forces F_1 and F_2 . Sensors at these points measure the gaps x_1 and x_2 . Linear motion is confined to the x direction. The moments are given by $F_1 l_a$ and $F_2 l_b$, respectively, and induce an angular displacement, θ , about the z axis. The control loops for the actuators are as shown in Fig.10 and are independent; no control loop is implemented for explicit control of rotation.

Fig.12 shows the step response of the two platform ends, assuming a 7 cm displacement of the centre of mass in the y direction. Curves a and b show that the overshoot of the two ends are different due to the asymmetry but still exhibit acceptable damping. Curve c shows the response of the centre of mass for comparison. The peak angle induced is shown in Fig.13 to be limited to an acceptable value of 0.26 milli-radians. Fig.14 shows

the variation of the peak angle for greater displacements of the centre of mass. This preliminary simulation indicates that rotational effects do not compromise the MGIM performance and we now intend to investigate this further with a six degree of freedom model for various actuator/sensor configurations.

EXPERIMENTAL VERIFICATION

In order to obtain experimental verification of the performance of our proposed design we have constructed two test rigs where the platform is supported on an air bed giving very low values of friction.

The first test rig consists of two parallel air tracks holding a platform of approximately 8.5 kg weight and giving 5.5 mm of free movement as shown in Fig.15. Actuators and position sensors, similar to those described previously, are used to control the platform motion. The digital compensator is designed for 0.5 Hz bandwidth and incorporates integral control since it is necessary to counteract the disturbance forces from the air jet system and any levelling mis-alignment of the air track.

Fig.16 shows the sinusoidal acceleration frequency response of the platform to an imposed vibration of the supporting frame. It does not quite conform with the expected frequency response (dotted line), due to the resonant peak at 0.5 Hz. Nevertheless, it is quite clear that the rig is isolating the platform successfully from high frequency vibration while maintaining its position adjacent to the supporting frame at low frequency.

This result encouraged us to construct a second test rig which has a heavier platform and extends control to three degrees of freedom. In order to avoid the imperfections associated with the first rig, this second rig was built to a higher standard so that a lower bandwidth controller could be employed and allowing testing of our non-contact "umbilical" technology.

The rig consists of a heavy slate plinth and surface plate on which are mounted four air pads - see Fig.17. These support a 35 kg platform of honeycomb construction, giving free motion in the horizontal plane. Surrounding the platform is an outer frame which is free to move in one axis and is driven by a vibrator. The actuators and position sensors are mounted between the platform and outer frame and allow ± 5 mm of movement in each horizontal axis. As shown in Fig.18, power supply to the on-board electronics is by means of auxiliary secondaries on the loosely coupled transformer to give 5V and ± 12 V d.c. A servo-accelerometer (Sundstrand QA 1400) is mounted at the platform extremity to measure acceleration in either the x or y axes. Data from this is passed via a programmable analog anti-alias filter (under control of the on-board computer) before being sampled at 100 Hz and digitised with 12 bit resolution. This data is then passed back to external instrumentation via the optical data link. A further two-way optical link allows external control of the on-board FORTH computer, which is responsible for data acquisition, as well as switching a 1 kW dummy load.

The digital lead/lag compensators are implemented for the three channels (x,y, θ) on an MC6809 microprocessor sampling at 100 Hz. Controller outputs are applied to the actuator coils by power operational amplifiers.

As well as its performance in vibration isolation, this rig will allow us to test the effects of:

- i) centre of mass displacement,
- ii) transformer power level changes producing disturbance forces on the platform,
- iii) other actuator/sensor configurations,
- iv) other control strategies,
- v) the acceleration spectrum with a stochastic vibration input.

CONCLUSIONS.

To date our study has concentrated on formulating a design concept for the MGIM. In this paper we have discussed the required performance specification and outlined the mechanical structure and the design of functional components of an MGIM capable of achieving this.

The one degree of freedom test rig has largely confirmed the potential of our design. We now intend to concentrate on using the three degree of freedom test rig to demonstrate further the MGIM technology outlined here. In conjunction we are preparing a six degree of freedom computer model of the MGIM in order to design multivariable control laws and assess the impact of offset centre of mass on system performance.

REFERENCES.

- [1] Wilhelm, J.P.
"Industrial Research Opportunities in Space".
IEEE EASCON '84, 17th Annual Electronics & Aerospace Conf.,
Sept. 10-12, 1984.
- [2] Hamacher, H., Merbold, U. & Jilg, R.
"The Microgravity Environment of the D-1 Mission".
Proc. 37th IAF Conference, Innsbruck, 1986. Paper IAF-86-268.
- [3] Olsen, R.E. & Mockovciak, J.
"Operational Factors Affecting Microgravity Levels in Orbit".
Jour. Spacecraft, Vol. 18, 2, 1981, pp. 141-144.

- [4] Jones, D.I., Owens, A.R. & Owen, R.G.
"Microgravity Isolation Mount: Design Report".
Report of a study performed under ESTEC contract No. 6380/85 by
U.C.N.W., Bangor.
- [5] Tiby, C. & Langbein, D.
"Allowable g-levels for Microgravity Payloads".
Report of a study performed under ESTEC contract No. 5504/83 by
Battelle Institute, Frankfurt.
- [6] Eilers, D.
"Microgravity Conditions for Orbiting Platforms".
Annual DGLR Conference, Germany, 1983.
- [7] Teledyne Brown Engineering
"Low Acceleration Characterization of Space Station Environment".
Report prepared for N.A.S.A., Marshall Space Flight Center, Oct. 1985.
- [8] Jones, D.I., Owens, A.R. & Owen, R.G.
"A Microgravity Isolation Mount".
Proc. 37th IAF Conference, Innsbruck, 1986. Paper IAF-86-270.

ACKNOWLEDGEMENTS.

The work presented here was performed as part of ESTEC contract No. 6380/85/NL/AN.

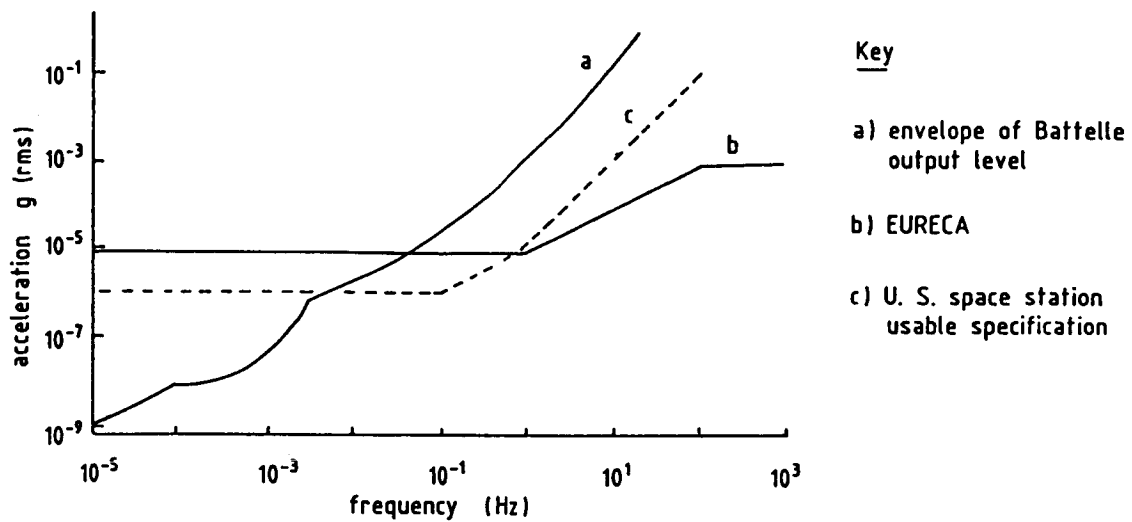


Fig.1 Relationship between sinusoidal specifications.

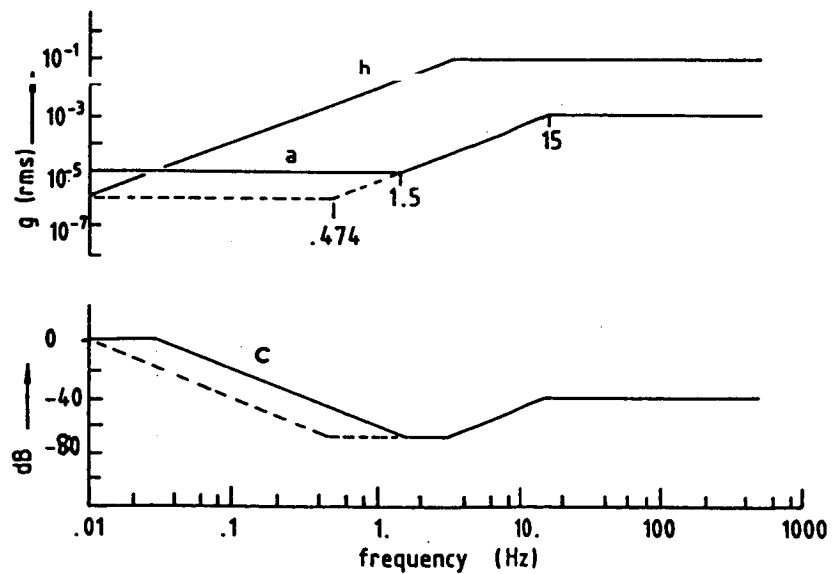


Fig.2 Assumed sinusoidal specification.

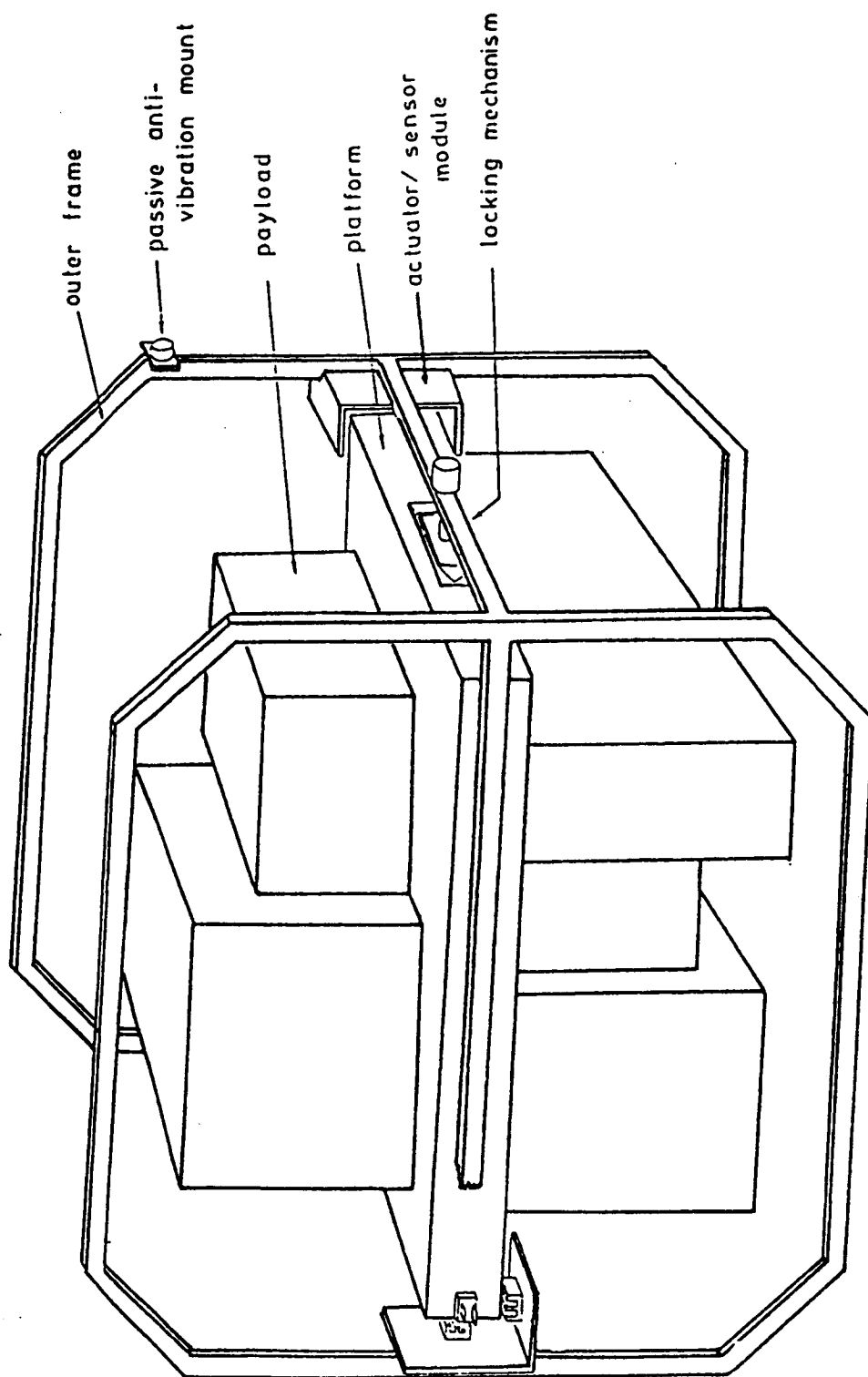


Fig.3 Structure of microgravity isolation mount.

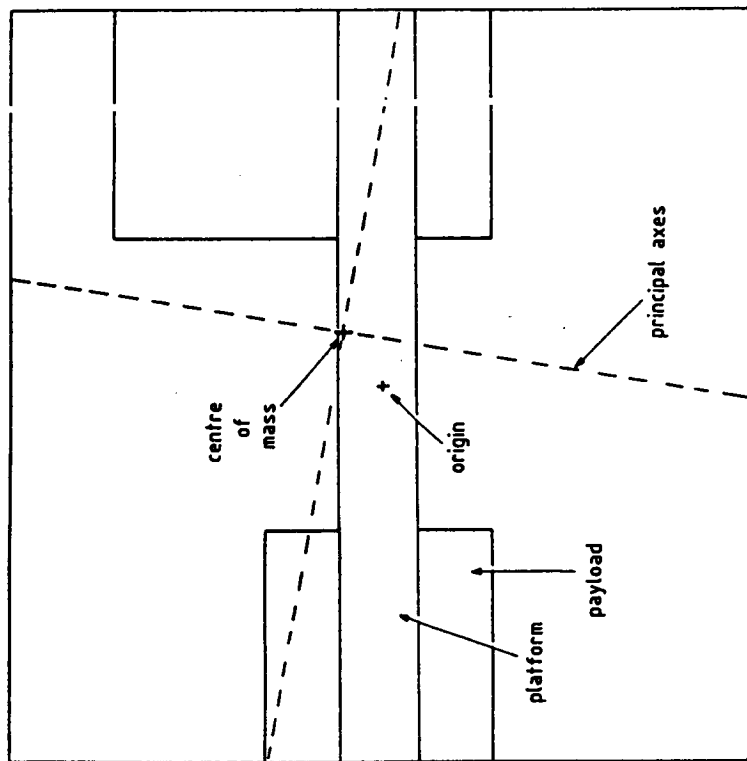


Fig.4 Platform/payload mass distribution
typical case.

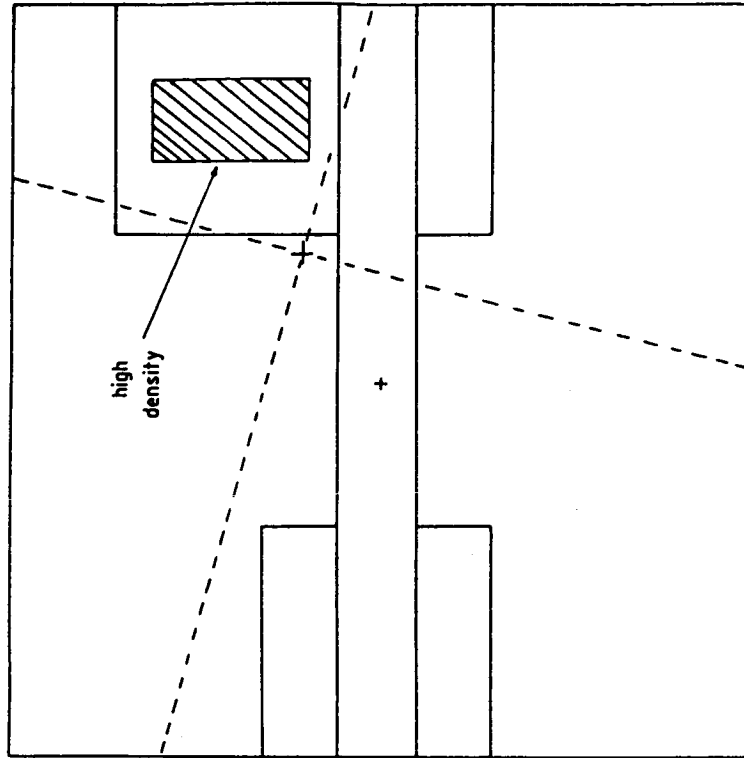


Fig.5 Platform/payload mass distribution
asymmetric case.

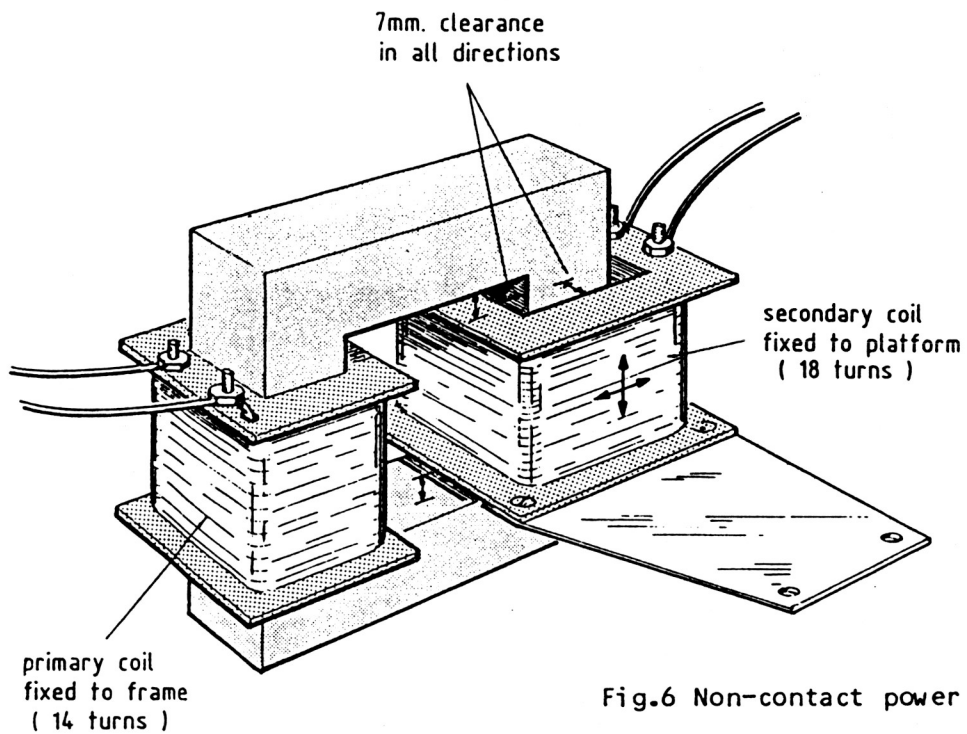


Fig.6 Non-contact power transformer.

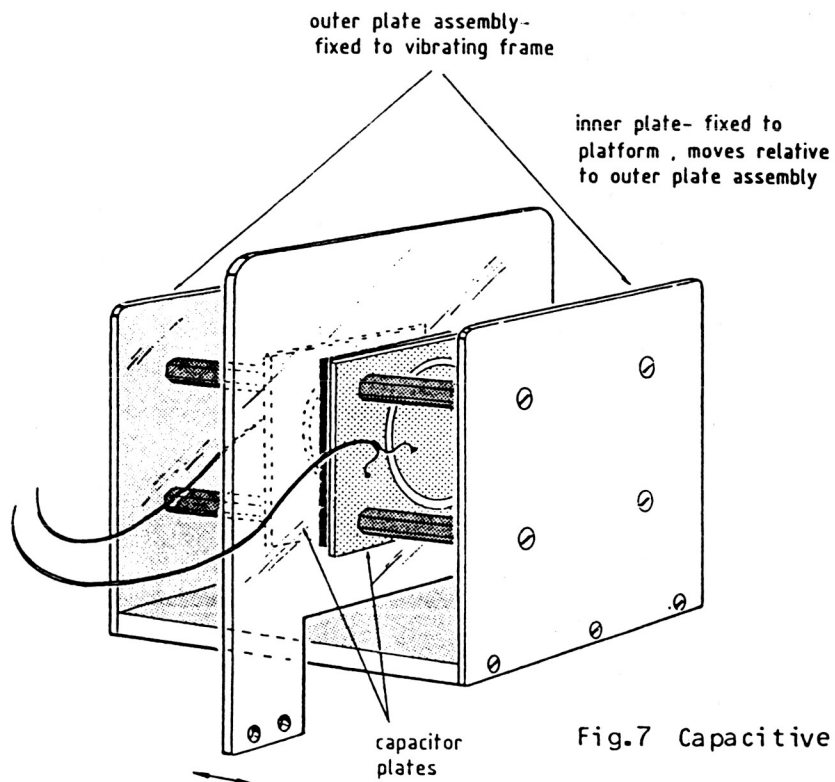


Fig.7 Capacitive position transducer.

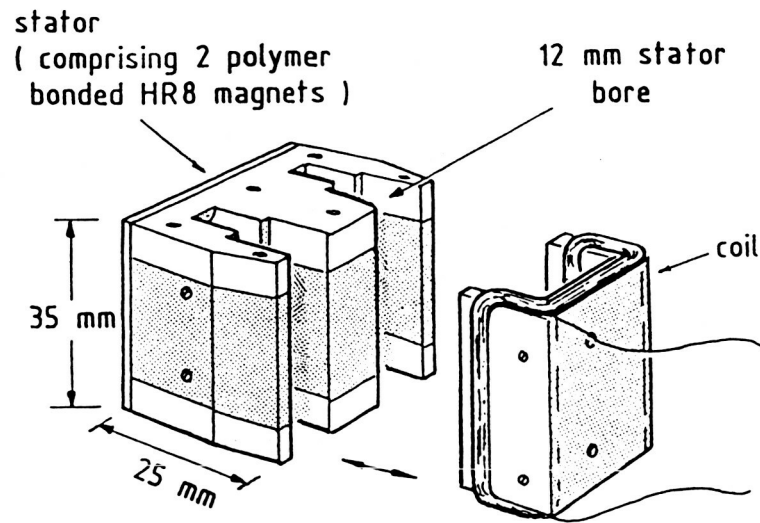


Fig.8 Actuator.

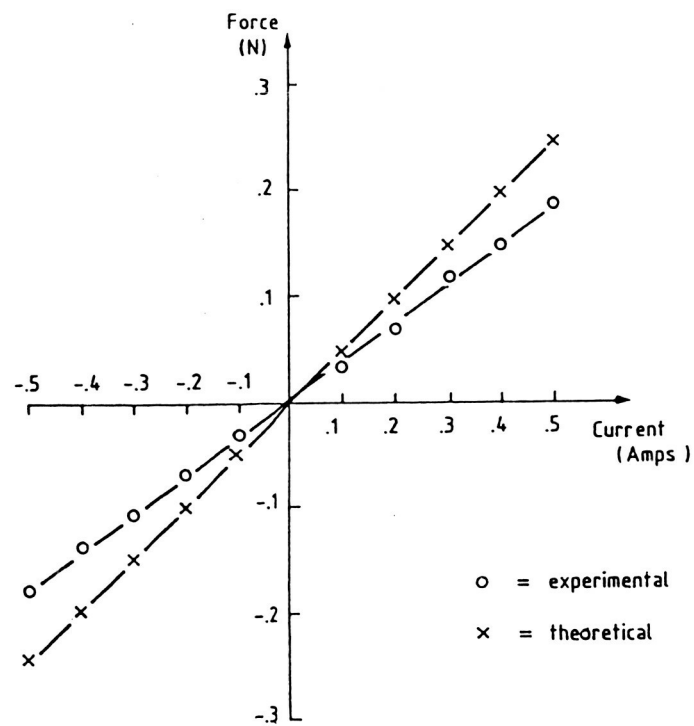


Fig.9 Measured force characteristic of actuator.

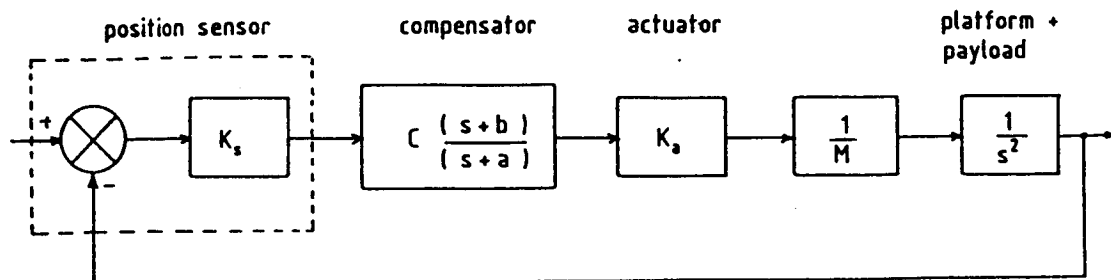


Fig.10 Block diagram of control loop.

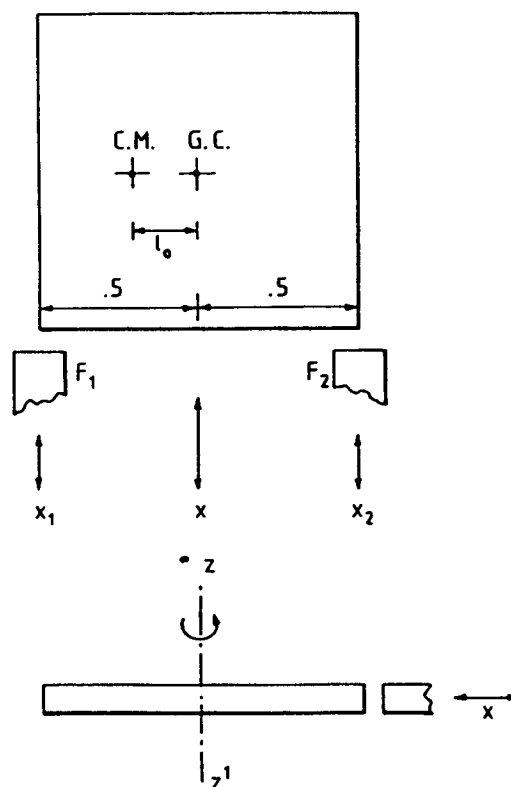
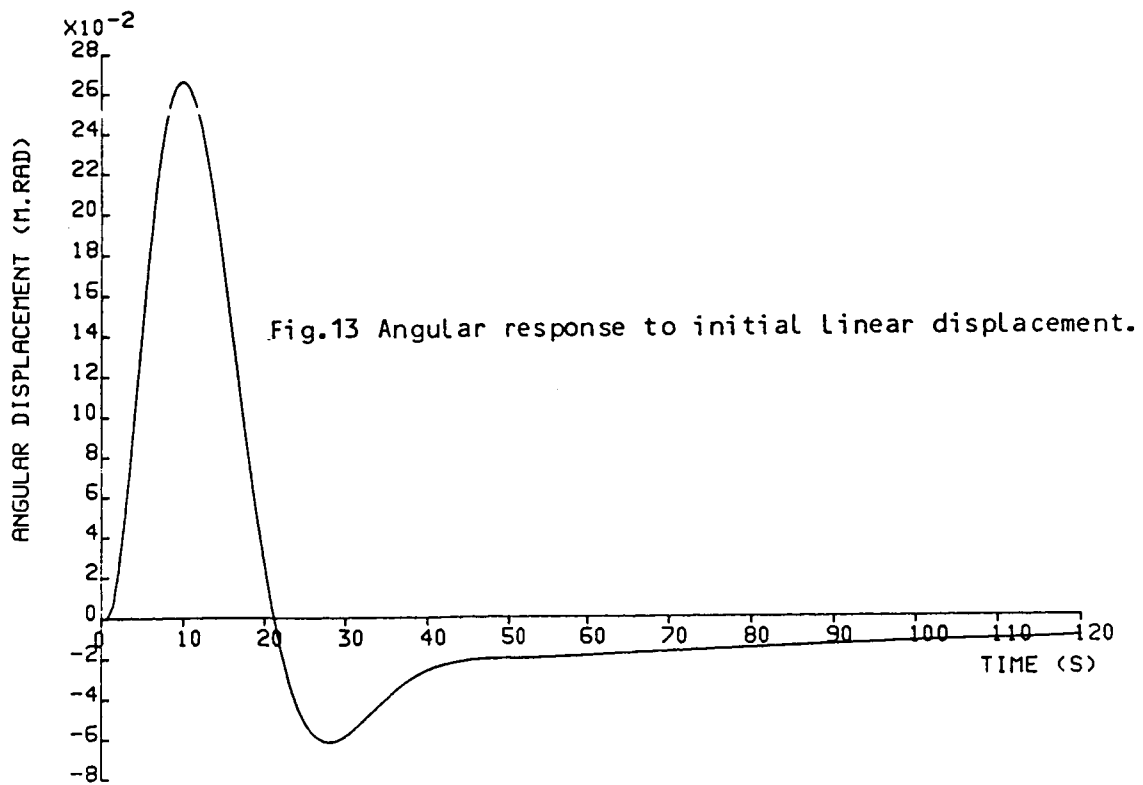
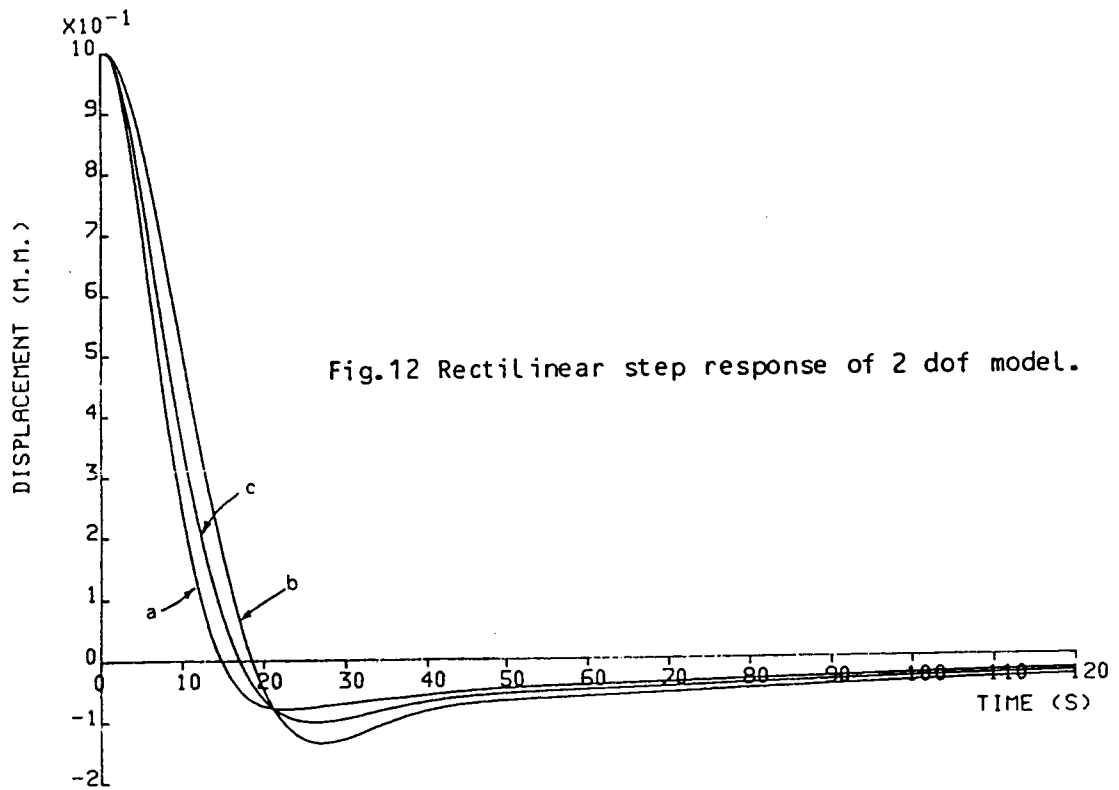


Fig.11 Two degree of freedom model.



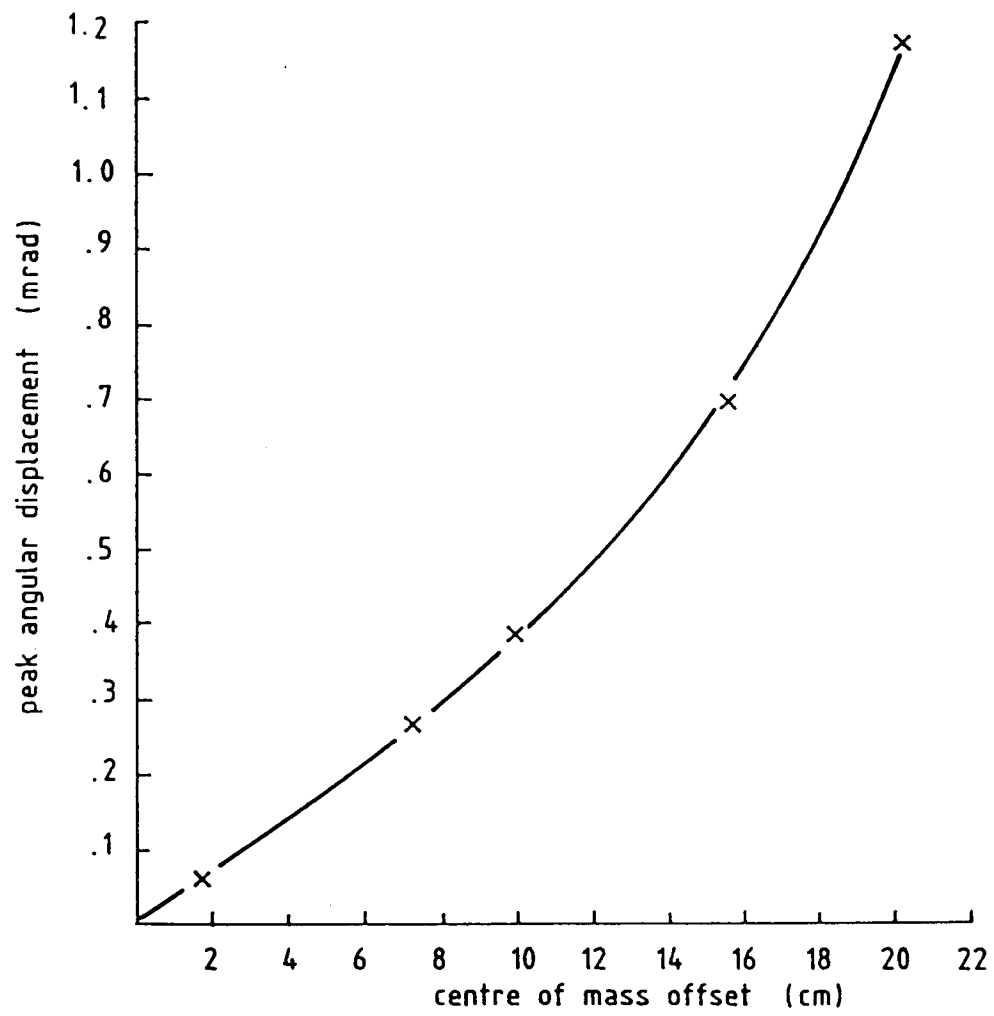


Fig.14 Variation of peak angle with centre of mass.

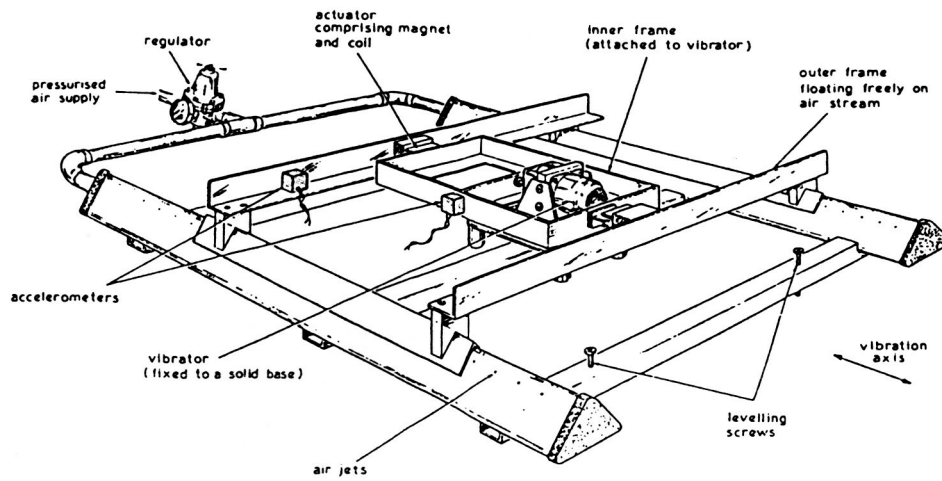


Fig.15 One degree of freedom test rig.

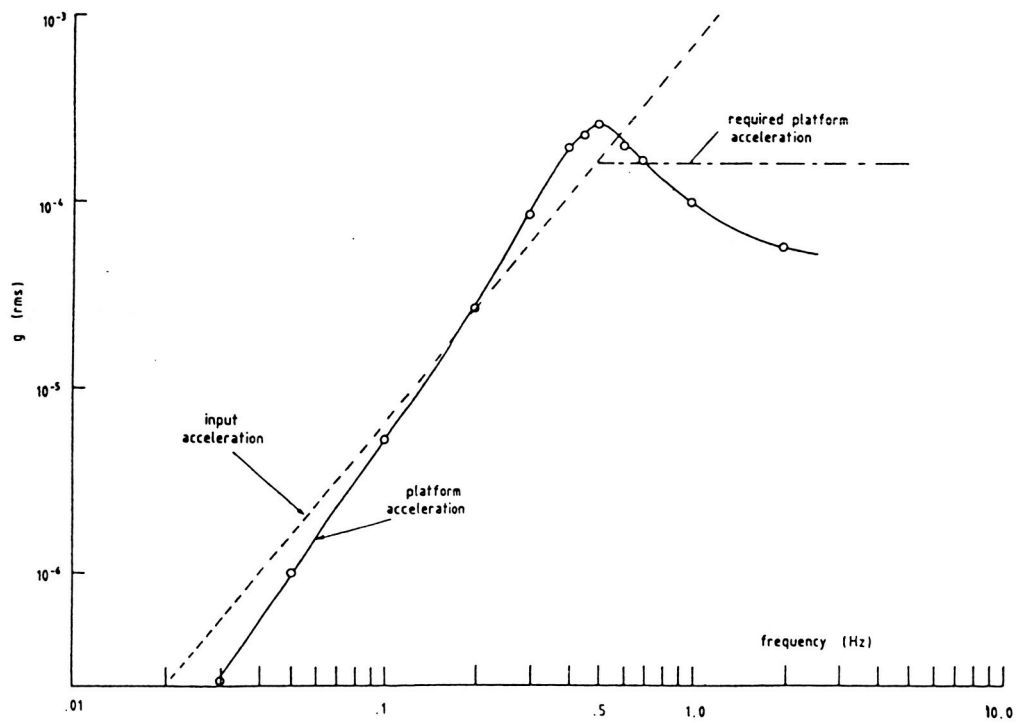


Fig.16 Measured results from 1 d.o.f. test rig.

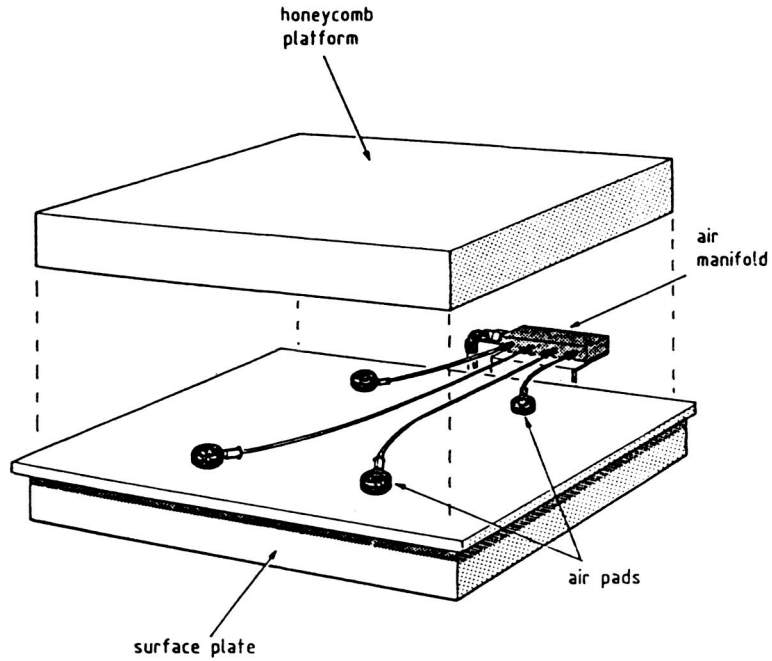


Fig.17 Three degree of freedom test rig.

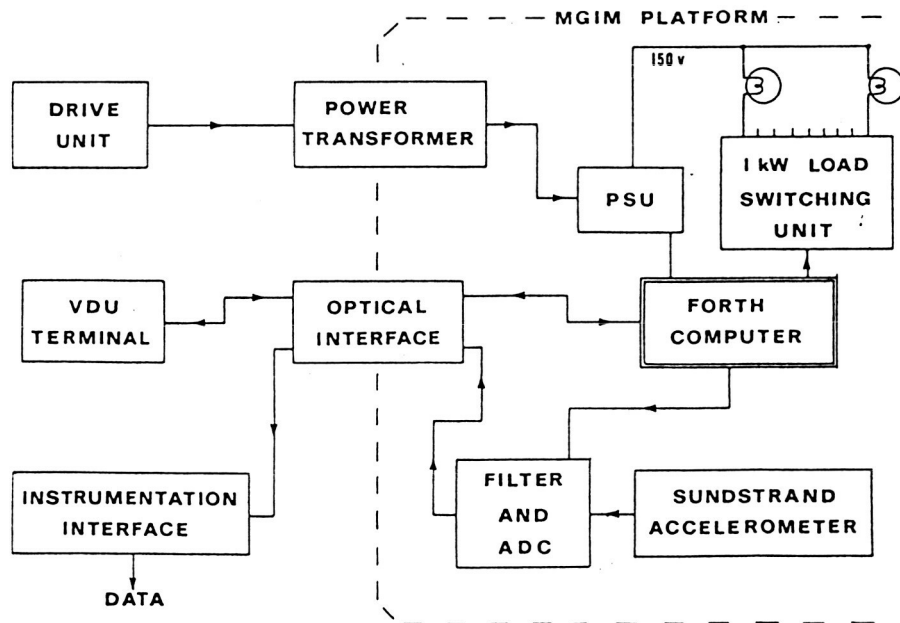


Fig.18 Instrumentation for 3 d.o.f. test rig.

AKM CAPTURE DEVICE

William D. Harwell*

Introduction

The Westar and Palapa satellites were built by Hughes Aircraft of California. They were both of the Hughes HS376 series and identical in external configuration. Both satellites were launched from the orbiting Shuttle during mission STS 41-B in February, 1984. Soon after launch, the Payload Assist Modules on both satellites failed, placing them in useless orbits. In an effort to recover them and the considerable investment each satellite represented, NASA and Hughes undertook the Satellite Retrieval Mission. The mechanism used to capture each of the errant satellites was the AKM (Apogee Kick Motor) Capture Device (ACD) - also referred to as the "Stinger".

Mechanism Requirements

The AKM Capture Device (ACD) had three interface requirements: interface with the Manned Maneuvering Unit (MMU) for transportation to and stabilization of the spacecrafts; interface with each satellite for retrieval; and finally, interface with the Shuttle's Remote Manipulator System (RMS or "robot arm") for satellite transport back to the Orbiter's payload bay. The majority of the design requirements were associated with the capture and release of the satellites. In addition to these unique requirements, the general EVA (Extra-Vehicular Activity), RMS grapple, and RMS manipulation requirements applied. These requirements included thermal, glare, snag, RMS runaway and crewman safety considerations. Finally, a host of contingency features were also needed.

Mechanism Description

The "Stinger" was an EVA crewman operated device which attached to the arms of the MMU. So configured, the crewman flew the MMU/Stinger assemblage from the payload bay to the spinning satellite and aligned himself with the spin axis of the satellite's motor nozzle. He then flew the probe of the Stinger into the nozzle, through the throat, and into the empty motor casing. By actuating a lever on the ACD's control box, a debris cover extended - releasing three independently sprung toggle fingers inside the motor casing. This constituted a "soft-dock." The crewman then operated a threaded shaft which retracted the probe, bringing its fingers into contact with the material surrounding the nozzle throat, as shown in figure 1. The retraction also brought the Stinger's 41 inch diameter ring into contact with the satellite's separation ring, creating a compressive loading of the satellite's nozzle throat and separation ring. This constituted "hard-dock." The astronaut then

*NASA Lyndon B. Johnson Space Center, Houston, Texas.

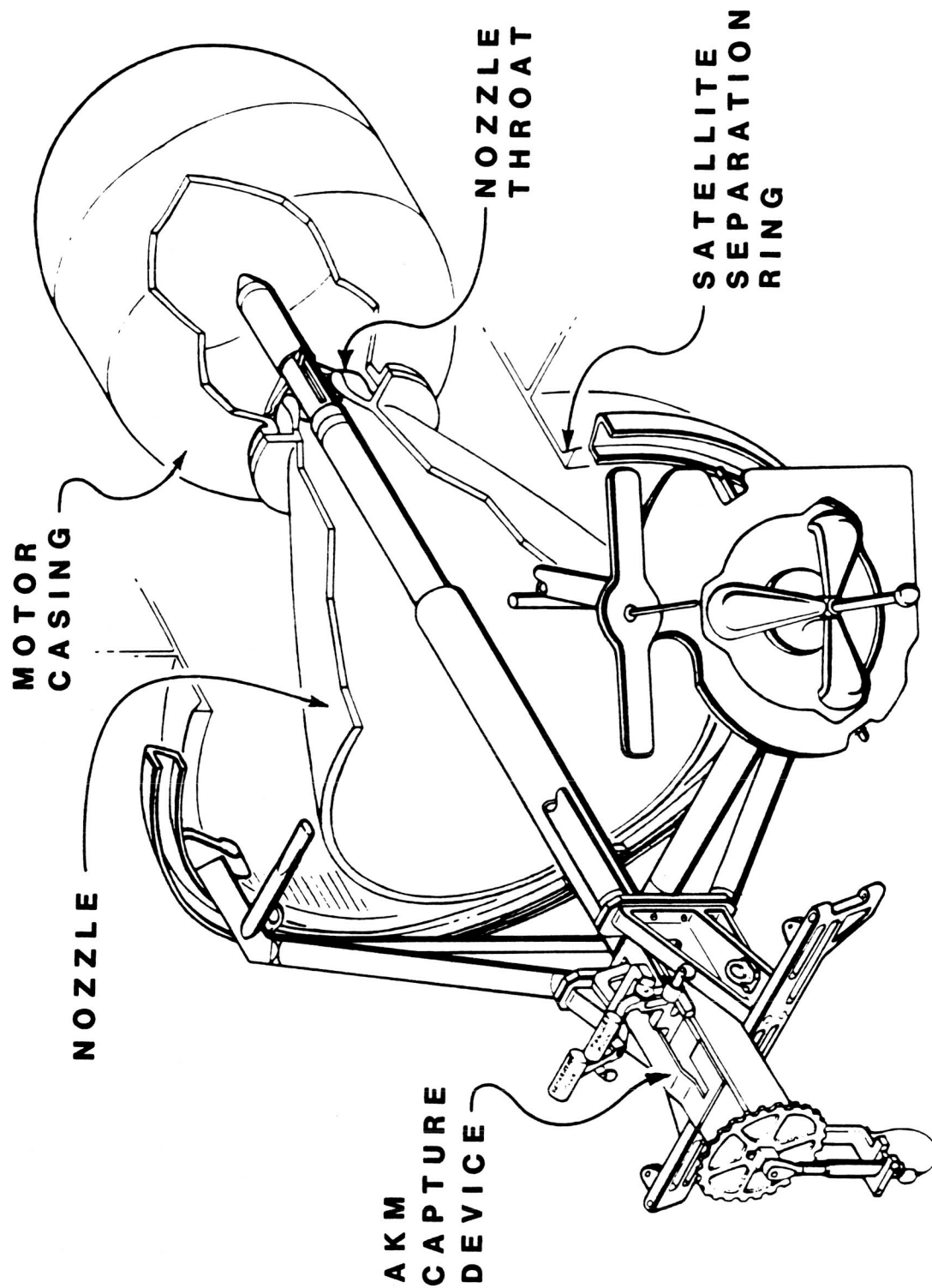


FIGURE 1
AKM CAPTURE DEVICE - ENGAGED

used the MMU's propulsion system and onboard logic to stabilize the satellite for RMS grapple.

Once the satellite was grappled and returned to the payload bay, a number of tasks were performed to prepare it for berthing. Upon completion of these tasks, the crewman actuated a lever which released the probe from the end of the Stinger. The probe remained in the motor casing for the remainder of the mission. The astronaut then re-stowed the remainder of the ACD.

ACD Mechanisms and Controls

The AKM Capture Device (ACD) is comprised of a number of component mechanisms and mechanical controls. These are grouped into four major assemblies (see figure 2), which are; the Probe, Control Box, Support Structure, and Grapple Fixture. Each will be discussed individually.

PROBE ASSEMBLY

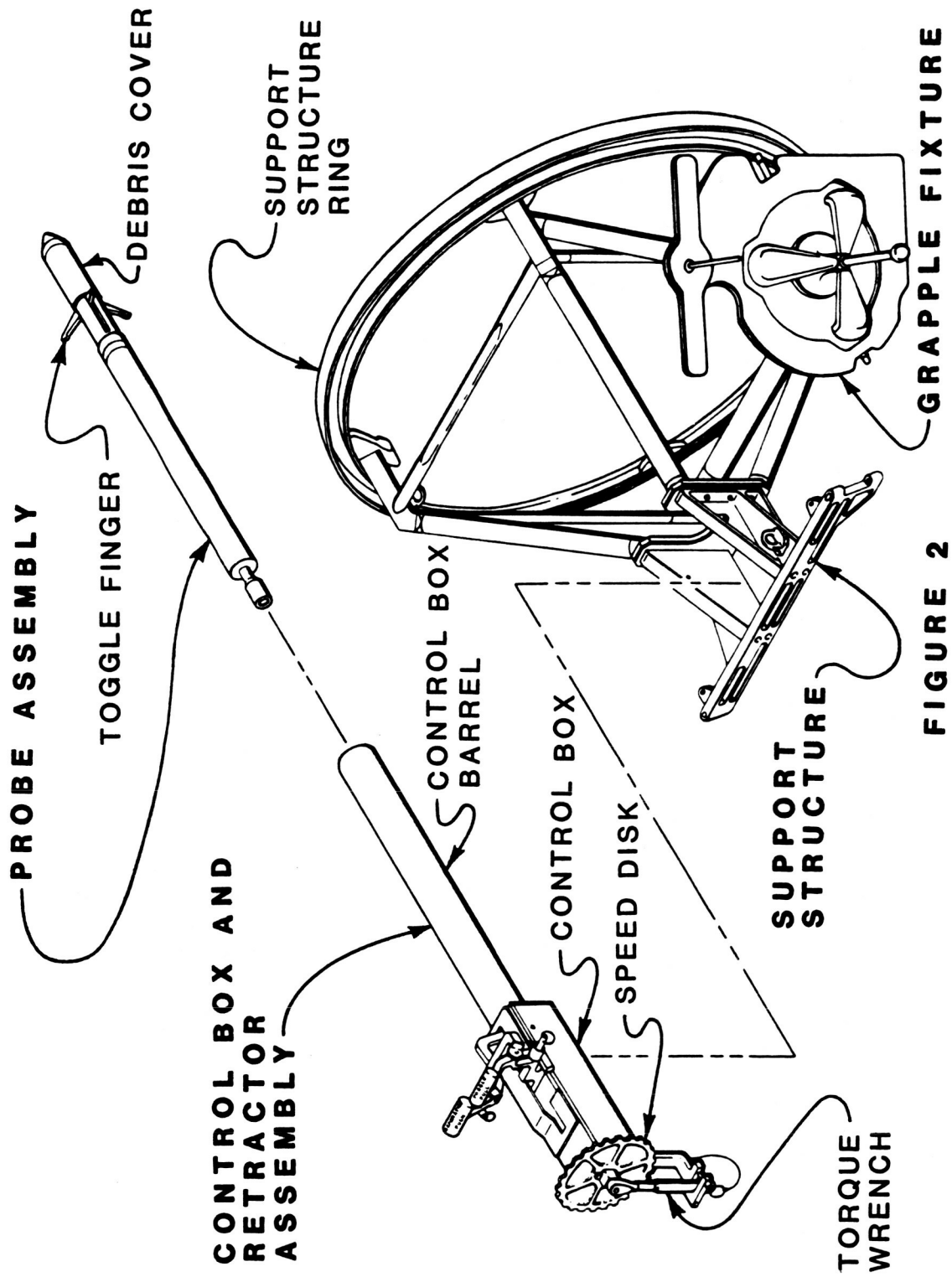
The Probe Assembly consists of the following components:

- Toggle Finger and Block Assembly
- Debris Cover
- Debris Cover/Toggle Finger Release Mechanism
- Control Box Interface

Toggle Finger and Block Assembly - Three toggle fingers spaced radially around a circular pivot block comprised this assembly. Each finger rotated independently about its pivot from the bias of a torsion spring, thereby increasing the reliability of the assembly. Any single finger was capable of withstanding the loads generated during the capture and handling. Thus, a three-fold failure (no finger opening) had to occur to prevent the preliminary capture or "soft-dock" and subsequent "hard-dock". In addition, the torsion springs which controlled the fingers were sized such that the Manned Maneuvering Unit's (MMU's) thrusters could override and close them if the astronaut prematurely deployed the debris cover prior to penetrating the throat.

Debris Cover - The debris cover was necessary for several reasons. The first was due to uncertainties about the condition of the nozzle throat. The throat was made of a carbon composite which deteriorated to some extent as the fuel was burned. The possibility that particles remaining in the area of the throat could contaminate the ACD toggle assembly and reduce the chances of capturing the satellites dictated the need to protect the toggle assembly. Secondly, the debris cover was given a conical leading profile to help guide the ACD as the probe traveled along the nozzle and through the throat. Finally, the debris cover encased the toggle fingers prior to deployment. Each toggle finger was biased to rotate outward as the cover opened.

ORIGINAL PAGE IS
OF POOR QUALITY



AKM CAPTURE DEVICE - EXPLODED VIEW

Debris Cover/Toggle Finger Release Mechanism - The debris cover was attached to a shaft which was deployed by a preloaded compression spring. The end of the shaft was held by a pair of latches which were actuated by a rod in the control box. When actuated, the rod opened the latches releasing the shaft and debris cover, and thereby, the toggle fingers.

Control Box Interface - Each of the satellites were spinning about their axes as they floated in space. The MMU's arms were not designed to withstand the torque associated with despinning the satellites. In an effort to reduce this torque, it was specified that the probe assembly not transmit any torque. This required that it be attached to the control box by a rotating interface. To simplify the design, it was also decided the toggle fingers would not be closed once deployed. Instead, the Stingers' probe assemblies would remain in the satellites. They could be removed rather easily by hand once the satellites were returned to earth. This required that the probe assembly be removeable. Finally, the actuator rod from the control box had to enter the probe to operate the Debris Cover/Toggle Finger Release Mechanism. To accomodate these requirements the shouldered interface on the end of the probe was designed - see figure 2. This interface will be discussed further in the control box portion of this paper.

CONTROL BOX

The ACD's control box was designed primarily for the purposes of deploying the toggle fingers, applying the clamping load, and releasing the probe assembly. However, in addition to these primary functions, several contingency features were provided. Each will be discussed in this section. The control box will be broken down into the following systems for purposes of discussion:

- Probe Actuator System
- Retractor System
- Probe Release System

Probe Actuator System - the function of this system was to deploy the debris cover, thereby releasing the toggle fingers. System elements included the actuator rod, the connecting linkage, and the toggle lever. Operationally, the astronaut would pull the toggle lever at the appropriate time, causing the actuator rod to enter the opening at the end of the probe. Inside the probe, the actuator rod opened latches which held the debris cover shaft. A preloaded compression spring in the probe then extended the cover - a motion which also released the toggle fingers. The secondary responsibilities of this system were to verify the cover had extended and to overcome any binding of the debris cover that may have occurred. The total rotation of the toggle lever was 60 degrees. Of this, the first 15 degrees of motion fired the debris cover. The remaining rotation drove the actuator rod into the cavity the debris cover shaft had vacated, verifying (by the absence of the shaft) deployment of the cover and toggle fingers. Any resistance to complete

rotation of the toggle lever indicated the cover did not open completely, if at all. By applying force to the toggle lever the crewman could force the actuator rod forward against the end of the debris cover shaft. This relieved any binding that might have occurred, thereby deploying the cover.

Retractor System - To provide clearance for the toggle fingers to swing outward and to accommodate variances within the throat's surface, the trailing end of the debris cover traveled approximately 4 inches past the plane of the inner throat before its deployment. When the fingers opened, the Stinger and satellite were loosely, but positively coupled. To complete the capture, this coupling had to be rigidized. By retracting the probe into the barrel of the control box, the fingers engaged the material surrounding the throat as the support structure ring came into contact with the satellite's separation ring. The components of the retractor system accomplished this task.

The retractor consisted of a large threaded shaft with a speed disk and a ratcheting, break-over torque wrench on the control box end. The other end was connected through the probe release system to the probe. The initial probe retraction was accomplished by rotating the speed disk, a large circular wheel, until the fingers contacted the throat. This eliminated a significant amount of ratcheting. The final Stinger-to-satellite rigidization was accomplished by operating the torque wrench until it broke over - indicating that a preset clamping force had been achieved. Finally, the retraction system served as a backup to the probe release system. This feature will be discussed in the next section.

Probe Release System - To rigidly attach the probe to the control box while permitting it to rotate, as discussed in the probe's control box interface section, a unique arrangement was implemented. Three, 3/8 inch bearing balls were placed in slots, equidistantly spaced around a bearing sleeve (see figure 3). A second sleeve, the retainer sleeve, slid over the bearing sleeve. A portion of each ball protruded through the inner diameter of the bearing sleeve when the retainer sleeve was closed. These ball segments fit radially around the groove on the end of the probe, preventing it from coming out. The inner diameter of the bearing sleeve and a close tolerance bushing held the probe concentrically in the control box barrel. When the probe release lever was pushed forward, the retainer sleeve slid back. This exposed a groove in the retainer sleeve which permitted the balls to travel out into their respective slots as the probe was removed. Thus, the probe release system provided probe containment while acting as a bearing.

A normal probe release has just been described. However, contingency provisions were made for the situation in which the probe binds and will not release. The probe release system, as mentioned earlier, was connected to the large retractor screw in the control box. When the ACD is securely clamped to the satellite, the retractor is

ORIGINAL PAGE IS
OF POOR QUALITY

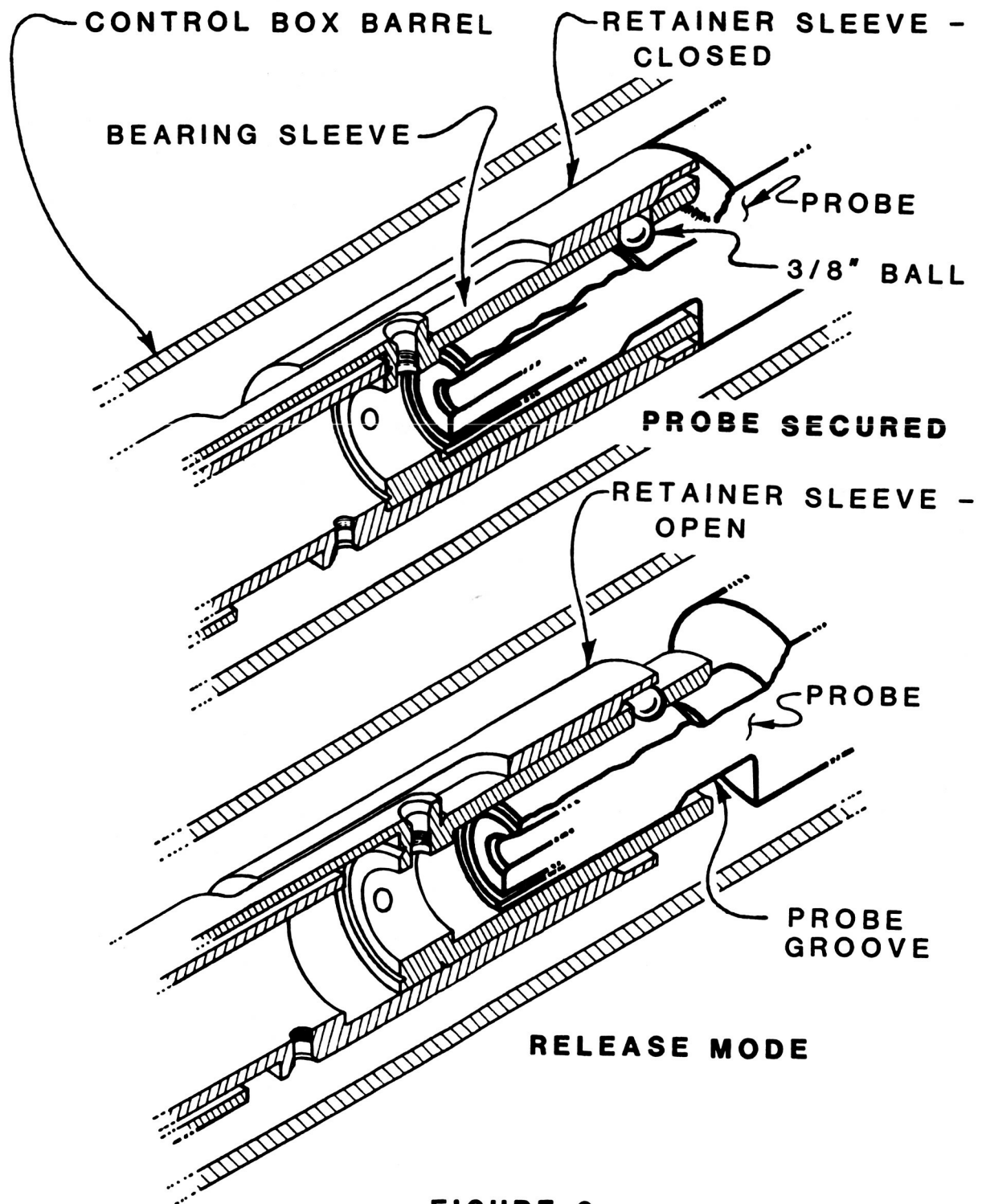


FIGURE 3
PROBE RELEASE SYSTEM

capable of retracting the probe several more inches. If the probe does not slip out of the control box barrel as planned, further operation of the torque wrench will forcibly withdraw the bearing sleeve from the end of the probe, provided the retainer sleeve is slid back. Since the ACD removal from the satellite was necessary for mission success a third method of removal was also incorporated. It involved the removal of the support structure from the control box and will be discussed in the support structure section of this paper.

ACD SUPPORT STRUCTURE

During transportation back to the Shuttle and preparation for berthing, RMS manipulations caused a variety of forces, torques, and moments to be exerted on the ACD. These loads were the results of accelerating and decelerating the satellite, ACD, MMU, and suited crewman combination about the payload bay. Of greater significance was the possibility that while connected to the RMS, an arm runaway could occur. The significantly higher loads that a runaway could create represented the worst load case, and therefore, became the design load criteria by which the support structure was designed. Other considerations in the support structure's design were the MMU's arm bracket and ACD control box interfaces and the protection of the satellite's separation ring.

The ACD's MMU interface was a simple bracket design which mated with the existing MMU arm brackets. The control box interface, however, required a stable attachment of the support structure to the control box which could be easily disassembled for contingency purposes, should the probe not release from the ACD. The separation ring on the bottom of the satellite was the means by which the berthing hardware was attached. If the stinger could not be removed, the spacecraft could not be returned to earth. The control box interface consisted of a cradle into which the control box assembly slid and two attach bolts. The bolt heads mated with the power screwdriver - a battery operated EVA screwdriver capable of generating high torques. If required the bolts and, thus, the structure could be removed from the control box. The entire control box and probe assembly could then be pushed into the motor casing and nozzle, providing clearance for the satellite berthing adapter.

It was specified that the satellite's aluminum separation ring not be damaged during capture. Relative motion between it and the ACD's ring during retrieval could create surface damage that could prevent or hinder proper attachment of the berthing adapter. To eliminate this possibility, four spring-loaded silicone rubber pads were added to the support structure's legs. As the ACD was tightened on the satellite, these pads came into contact with the separation ring, precluding any damage.

GRAPPLE FIXTURE

Issues arose concerning MMU propellant consumption, time required to transport a satellite back to the payload bay by means of the MMU, possible throat deterioration, and the need to effectively handle the satellite while

it was prepared for berthing. Two satellites were to be captured. A considerable amount of propellant would be expended if the astronaut were to fly out to each spacecraft, capture and stabilize it, and return each to the Shuttle by means of a single MMU (the second MMU was primarily a backup unit). Additionally, this process required a considerable amount of time in a timeline which was already very long. The possibility of throat deterioration, as previously noted, was present since the carbon throat was thought to be brittle. Forces generated during transportation could cause some throat breakage and subsequent lack of handling control of the satellite. Finally, once back in the payload bay, the satellite had to be manipulated to prepare it for berthing. This required some stable means of supporting the spacecraft.

These concerns prompted the decision to use the Shuttle's Remote Manipulator System (RMS) to transport and manipulate the MMU/ACD/satellite/crewman assemblage. To accommodate RMS capture, a flight standard grapple fixture was attached to the support structure of the Stinger. Once the satellite was captured and stabilized, the RMS operator grappled the assemblage and returned it to the Orbiter. During the berthing preparations, the MMU crewman remained in place, continually monitoring the satellite for excessive movement which would indicate throat deterioration. If excessive motion occurred, he would operate the torque wrench on the ACD's control box, applying more compressive loading. This, in turn, would rigidize the spacecraft/ACD interface to bring the satellite back under control.

Conclusion

The ACD's were designed, fabricated and certified in seven months. In November of 1984, during two separate EVA's on mission STS 51-A, two separate Stingers were used to successfully capture the Westar and the Palapa satellites. They were returned to earth and refurbished (by Hughes Aircraft) for resale.

GRABBER ARM MECHANISM FOR THE ITALIAN RESEARCH INTERIM STAGE (IRIS)

Edmondo Turci*

ABSTRACT

Two deployable arms, named "grabbers," were designed and manufactured to provide lateral stability of the perigee spinning stage which will be deployed from the Space Shuttle cargo bay. The spinning stage is supported by a spin table on a cradle at its base. The Italian Research Interim Stage (IRIS), which is being developed under an Italian "Consiglio Nazionale delle Ricerche/Piano Spaziale Nazionale" (CNR/PSN) contract, is designed to carry satellites of intermediate mass up to 900 kg. The requirements are defined and the mechanism is described. Functional test results are presented.

INTRODUCTION

A grabber arm mechanism was designed to latch, at the upper level, the perigee spinning stage in the Space Shuttle cargo bay. This constraint will be remotely disengaged before the spinning and deployment of the stage. The mechanism consists of a set of rotating arms which enables a pin to engage and disengage with a mating socket. The withdrawal of the arm must give enough clearance to allow safe deployment of the stage. The technique is well known: a rotating plate enables a pin to engage in a socket, using a connecting rod and a motorized crank lever. This set of links provides a good lateral stiffness, as required, when the pin is forced into the socket. However, if there is a misalignment of the pin and the socket, then a high force is needed to lock the mechanism in position. This will cause high insertion forces on the interface structure with a consequent increase in mass.

GRABBER ARM MECHANISM

In order to achieve better locking performance and to save mass, a toggle action has been introduced into the linkage. (See fig. 1.) The grabber arm is driven upwards by a crank lever until it comes to rest against the interface structure. The crank continues to rotate forcing the toggle arms to expand. The toggle arms in turn move the sleeve upwards forcing out three swinging latches (pawls), which centralize the grabber pin in the socket. The mechanism then goes overcenter, locking the pin in position. The toggle arms are kept in position by springs (bottom washers) until the locking phase. The gap between the socket and the pin is large enough to allow for any relative displacement which could occur in the space environment. The pawls will still force the pin into the central position and the locking action of the toggle will provide a stiff connection.

*Aeritalia Space System Division, Turin, Italy.

Because of possible tangential misalignment after rotation of the spin table (i.e., in case of an aborted mission, the grabber must reengage the perigee stage before return of the Space Shuttle), a significant insertion force could occur. The grabber pin has a conical shape and is dry-lubricated to minimize this force.

The crank lever is driven by a geared stepper motor. Two sets of microswitches monitor the position of the crank lever.

Adjustment of the grabber pin is provided by rotating the two conical components; this eliminates misalignment due to manufacturing tolerances.

MECHANICAL INTERFACES AND LOADS

Cradle/Perigee-Stage Interface Characteristics

As already mentioned, after the grabber is inserted, the pin diameter is increased by the expansion of the pawls until the socket diameter is reached. During this phase, there is the capability to overcome (by means of the torque motor) any radial offset, up to a maximum of 1.5 mm, due to the space environment.

This capability is achieved by exploiting the cradle and tower (spinning stage and spin table) flexibility. The "y" direction stiffness is obtained from the IRIS mathematical model. Two different conditions are evaluated (fig. 2):

- With no grabber inserted, the system stiffness is minimum and is equal to 1620 N/mm.
- With one grabber inserted, the system stiffness is maximum and is equal to 5290 N/mm.

These values have been used for the calculation of the required motor torque characteristics assuming, as demonstrated by means of the NASTRAN model, that the stiffness along the x direction is lower.

Payload-Attachment-Fitting/Grabber Interface Characteristics

The payload attachment fitting (PAF) consists of an annular plate containing both bushings (sockets), which must offer a high resistance to the acting load. For this purpose, a hard Custom 455 alloy has been used. The grabber stiffness along the x and y directions can be considered approximately equal since the bearing and the plate are very stiff. It can be assumed that the grabber stiffness depends mainly on the deflection stiffness of the pawls.

Grabber/Cradle Interface Characteristics

To interface the grabber and the cradle, two fork brackets have been used. Each bracket has been joined to the cradle structure via four "HI-LOKS," which give a precise connection in both clearance gap and preload.

This connection is not removable and transmits high loads without depending on friction.

The motor is joined to the cradle by means of an attach fitting structure (fig. 3).

The stiffness of the crank lever attachment point, with the motor assembled to the cradle, has been calculated relative to the hinge pin. The minimum required stiffness is low and is easily satisfied by the motor attach fitting and cradle structure.

Flight Loads

The ultimate loads exchanged by the cradle and the PAF through the grabber are, in case of landing, a compression force of 95 000 N (on one grabber) and a tangential force of 58 000 N for both landing and lift-off cases. These loads are derived from the IRIS system coupled-analysis finite-element model. A thermal analysis at system level and local analysis complete the inputs for the grabber design.

KINEMATIC ANALYSIS OF THE GRABBER ARM

The kinematic relationships of the linkage and the functional relationships of the forces acting on each part of the grabber have been investigated.

A fundamental hypothesis used is that concerning the tribological properties. A generalized friction coefficient has been used (molybdenum disulfide (MoS_2) - bonded solid lubricant in vacuum) for all the contact surfaces. Manufacturer's data sheet (and MIL-L-25504) shows values of friction coefficient of 0.05 for Hertz pressures comparable to those foreseen on the main critical parts. In order to comply with a more realistic distribution of pressures and other uncertainties, a value of $f = 0.15$ has been considered.

The model to be used for the linkage depends on the particular position reached by the articulated quadrilateral.

- Deployment: The gear motor rate is constant and the grabber head is driven toward the socket (on the PAF) up to the first contact. The required torque must only overcome the friction on the bearing due to the preload force and the grabber weight (ground tests).
- Spin-table misalignment recovery: The insertion of the grabber head into the socket initiates the misalignment recovery. The gear motor rate is still constant but additional torque is required because of the misalignment of the spin table with respect to the grabber position. The force along the insertion axis must not open the pawls until full insertion has been reached. The upper

spring washer and pawls are designed to ensure this condition.

- Pawls expansion and locking:

The head of the grabber has been fully introduced in the socket. From this moment, any further rotation of the crank lever overcomes the elastic reaction of the upper spring washers forcing the internal sleeve upwards to open the pawls. As soon as the pawl is in contact with the socket, further expansion requires the crank lever to overcome the "system stiffness." That is, the complete IRIS spinning stage is forced to move by the expansion of the pawls.

The main points investigated were as follows.

Toggle Action

The toggle arms operate as a device which assures the mechanical lock of the grabber head into its proper hole. The model is sketched in fig. 4a. The locking is due to the overcenter position reached. This overcenter has a permanent equilibrium position, which is kept by the connection rod.

Expandable Head

The expandable head contains the locking and unlocking parts of the grabber. This occurs when the grabber plate is stopped and the internal levers are in movement. The model used is sketched in fig. 4b/c. The locking action can be considered as three successive phases:

- The pawl expansion begins and both upper and bottom spring washers are deflected until the gap is zeroed.
- The radial offset between socket and pin begins to be overcome. In the counteract worst condition, only one pawl works and develops the necessary force to the system stiffness.
- The radial offset has been completely recovered and the final position of the toggle arms has been reached. All three pawls are in contact within the socket. The bottom spring washer ensures that an adequate pressure is applied by each pawl on the socket internal surface. If the radial offset is zero, the pressure forces on each pawl are symmetrical and do not depend on the system stiffness. The grabber is then fully locked.

Free Expansion of the Pawls

This analysis evaluated the optimum profile of the pawls and the sleeve, and the axial contact forces. Because of the complexity of the profiles, a numerical computation was carried out.

The axial force on the sleeve and the pawl deflection vs. sleeve displacement in the free condition are represented in the diagram of fig. 4c.

Drive Torque

Evaluation of the drive torque on the crank lever from the withdrawn position to full locked position is a primary task of the analysis. The drive torque " C_M " will vary with the crank lever angle " ϕ " as shown in fig. 5. The phases considered were:

- Deployment
- Misalignment recovery (insertion)
- Locking
- Unlocking

The assumptions were:

- The deployment considers a constant drive motor angular rate, gravity, and friction torque on the grabber bearings. Inertia is neglected.
- The misalignment recovery assumes a spin-table friction torque of 50 N-m and a misalignment error of 15 mm (equivalent to a degree of rotation).
- The locking phase considers a radial offset (max 1.5 mm) and a nominal system stiffness (6600 N/mm) with one grabber inserted (worst case). The motor still maintains an unpowered torque to react flight loads (30 N-m).
- The locking/unlocking phase utilizes a generalized friction coefficient ($f = 0.15$).

MATERIAL USED IN THE GRABBER MECHANISM

The grabber plate was made from 7075 aluminum alloy. This choice is due to thermal displacement of the cradle interface fork brackets. The cylindrical tube, the cone, the eccentrics, and the crank lever are 15-5-PH steel. The pawls and the sleeve are Inconel 718 hardened with thick chromium coating. The socket is Carpenter Custom 455. The thermal properties of the materials are adequately matched. All sliding parts are dry-lubricated with resin-bonded solid-film molybdenum disulfide of the type available today for space applications. Functional tests were conducted early in the development to verify local conditions of the sliding parts at appropriate Hertz contact pressure and coefficients of friction. Chromium coatings were introduced during these preliminary tests. The rotating hinges of the grabber plate utilize space-qualified bushings.

REDUNDANCY PROVISIONS

Redundancy has been incorporated into the grabber design to prevent single-point failures from making the grabber inoperative. The motor has two isolated redundant windings and electronic control units. The design uses a brushless permanent-magnet stepper so that none of the problems associated with contacting electrical interfaces in vacuum can occur. The speed reducer uses the harmonic drive concept (Schaeffer Magnetics). The upper and lower spring washers can provide enough force even when a single spring has failed. Rotating parts are bushed and designed to last one order of magnitude times the required life. Three switch mechanisms have been used for any of the two extreme operating conditions (withdrawn, locked).

The structural elements which are not redundant will be investigated extensively during qualification and fracture analysis tests.

MOTOR AND INTERFACE CHARACTERISTICS

Each grabber has an actuator that is joined to the cradle structure by means of an attach fitting. This consists of two straps and a motor support at the junction to the cradle. (See fig. 3.) The actuator comprises the following major elements: (1) motor, (2) speed reducer, (3) output flange, (4) motor housing, (5) frame, and (6) bearings. The stepper motor uses samarium-cobalt magnets and is three-phase "y" connected, designed for six-state bipolar drive.

The drive scheme sequentially excites each of the three motor phases in a bipolar mode, thus producing the required six magnet states that result in stepwise motion of the motor. By reversing the order, direction of rotation is reversed. Maximum rate is 300 steps per second. The available torque on the shaft is normally 200 to 240 N-m and 110 N-m when a failure on the windings has been introduced. The motor has been fully space qualified by Schaeffer Magnetics under Aeritalia specification.

DEVELOPMENT TESTS

In June/July 1985, a grabber development prototype was tested. The test utilized a fixture simulating the cradle/spinning-stage interfaces, including spin-table movement. (See fig. 6.)

The stiffness of the structure was simulated by springs and appropriately dimensioned plates and rods. The crank shaft was rotated manually, the torque and crank angles being measured at each step.

The main scope of this test was to confirm the maximum torque needed and to verify the tribological improvements introduced on the development prototype. (Chromium coating on pawls and sleeve was not used in the preliminary tests.)

Five tests have been performed with different values of radial offset (ϵ_r) and spin-table misalignment recovery (ϵ_c). The test results are given in table I.

Significant findings were made when comparing the results of test no. 4 with the theoretical values as shown in fig. 5:

- The spin-table misalignment recovery required a drive torque of 25 N-m (crank angle 100/110 deg) from both calculated and measured methods.
- The maximum measured drive torque in locking operation was 52 N-m, whereas the calculated value was 89 N-m.

The following explanation is suggested. The assumed generalized value of the friction coefficient $f = 0.15$ is conservative where high contact pressures are applied; that is the case of the locking operation. The value $f = 0.15$ is correct when moderate contact pressures are applied; that is the case during the insertion for misalignment recovery.

As a resin bonded solid film MoS_2 has been used on sliding surfaces, a more realistic analysis should consider $f = 0.05$ where high contact pressures are applied and $f = 0.15$ where moderate pressures are applied.

When the grabber was disassembled, there was no evidence of crushing or coating removal.

QUALIFICATION TESTS

Thermal vacuum and fracture mechanics tests are programmed to be completed by the middle of 1987.

Thermal Vacuum Test

The qualification grabber model will be installed on a test fixture simulating the attachment point of the cradle structure and the PAF coupling section. The test fixture is similar to that used for the grabber development test modified to support the electric motor and suitable to be used in a thermal vacuum chamber.

The test article assembled on the test fixture will be placed in a test suspension allowing its fitting inside the vacuum chamber. Cryogenic shrouds and a set of infrared lamps will be inserted in order to obtain the

required cold and hot conditions during the test. Fig. 7 illustrates the thermal vacuum test setup showing both the grabbers and the test fixture.

The test article equipped with a set of strain gauges and thermocouples will be subjected to a set of complete functional cycles in nominal and misaligned positions. The thermal cycling profile will be repeated as many as 35 times including spring and motor failure simulations. Determining functional life in the thermal vacuum environment and establishing capability of the tribological processes are the objectives of the test.

Load and Fracture Mechanics Tests

The grabber will be loaded utilizing mechanical interfaces and jacks to reproduce lift-off and landing conditions. A standard fracture mechanics procedure will be applied to the model grabber. These tests will complete the qualification test program.

CONCLUSION

The design described in this paper proved to be a suitable method to provide stiff structural constraints. Very good locking performance was achieved leading to mass savings since low insertion forces on the interface structure were required.

The grabber has been designed to a high level of reliability over a broad spectrum of environments. State-of-the-art technologies and lubricants have been used throughout.

TABLE I.- DEVELOPMENT TEST RESULTS: TORQUE VS. CRANK ANGLE

a. Engagement

Test 1; ϵ_r - 0 mm, ϵ_c - 0 mm		Test 2; ϵ_r - 0.5 mm, ϵ_c - 15.5 mm		Test 3; ϵ_r - 1 mm, ϵ_c - 15.5 mm		Test 4; ϵ_r - 1.5 mm, ϵ_c - 15.5 mm		Test 5; ϵ_r - 1.8 mm, ϵ_c - 15.5 mm	
Angle, deg	Torque, N-m	Angle, deg	Torque, N-m	Angle, deg	Torque, N-m	Angle, deg	Torque, N-m	Angle, deg	Torque, N-m
-22	2.2	105	10	95	10	95	25	107	10
-5	2.4	115	12	107	25	103	25	115	31
10	3	123	15	115	13	111	10	123	39
25	3.6	130	12	123	13	119	13	130	49
40	4.6	140	32	132	34	123	34	138	70
55	8	150	15	138	30	130	49	Locked	0
70	9	180	0	150	0	138	52		
85	10	Locked	0	Locked	0	150	0		
95	10					Locked	0		
111	9								
119	11								
130	12								
140	41								
Locked	0								

b. Disengagement

Test 1		Test 2	
Angle, deg	Torque, N-m	Angle, deg	Torque, N-m
Un- locked	-4	Un- locked	-5
150	9	140	8
130	7	130	8
107	8	119	8
90	8	111	8
70	5.5	70	4
55	4.4	40	0
40	3.3		
25	2.4		
10	1.6		
-22	1		

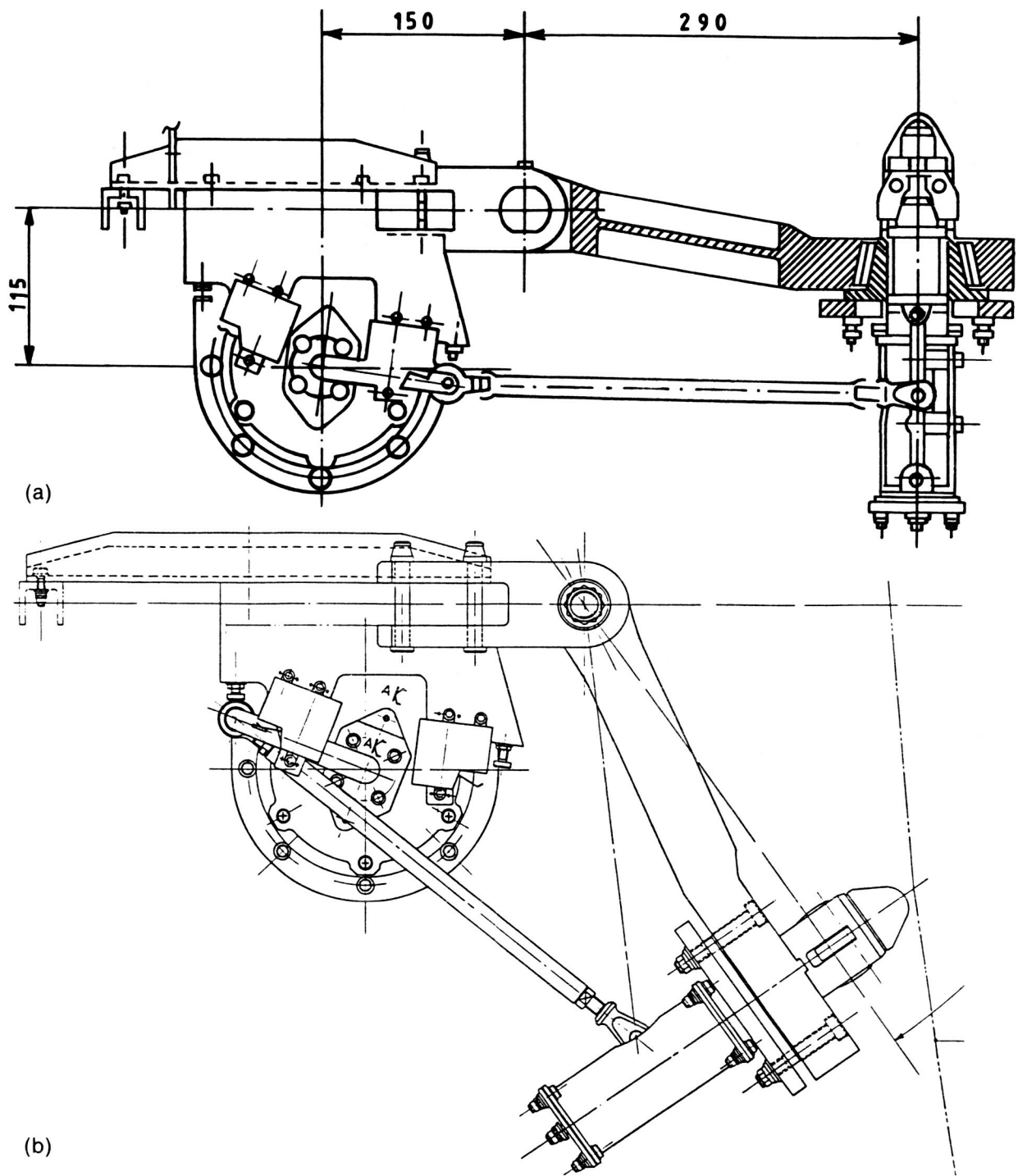
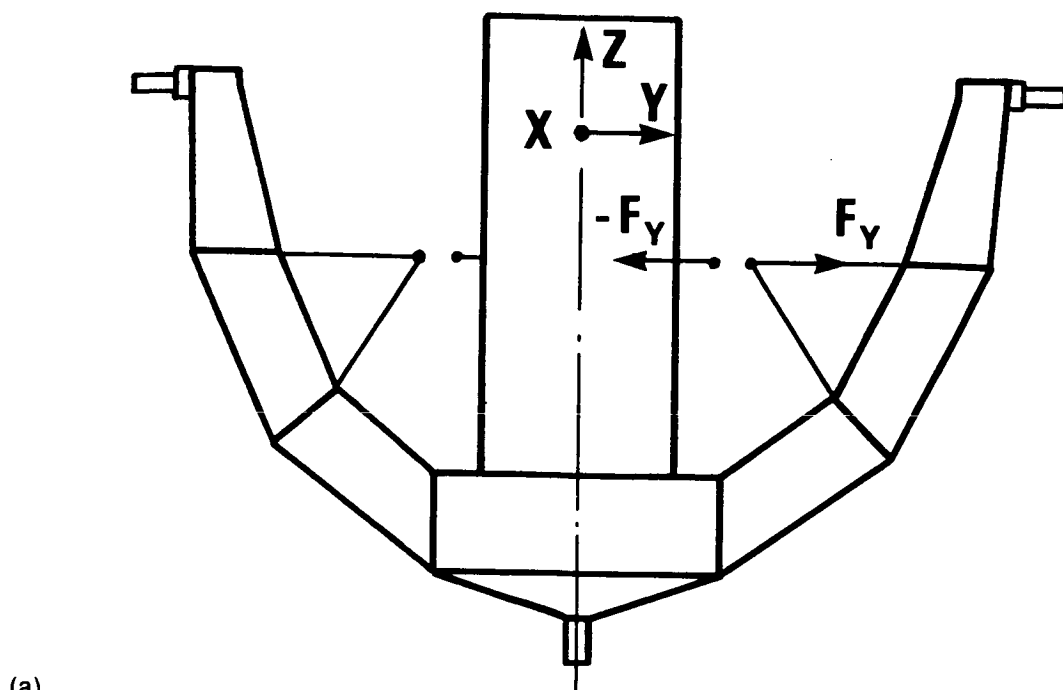
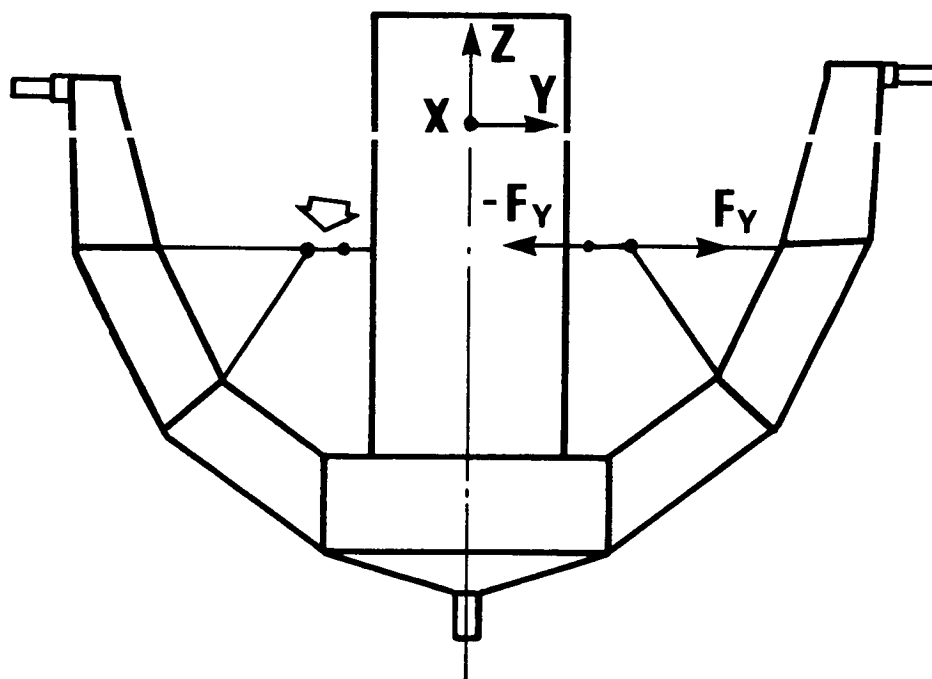


Figure 1. Grabber arm configuration (dimensions in millimeters).
 (a) Deployed. (b) Withdrawn.

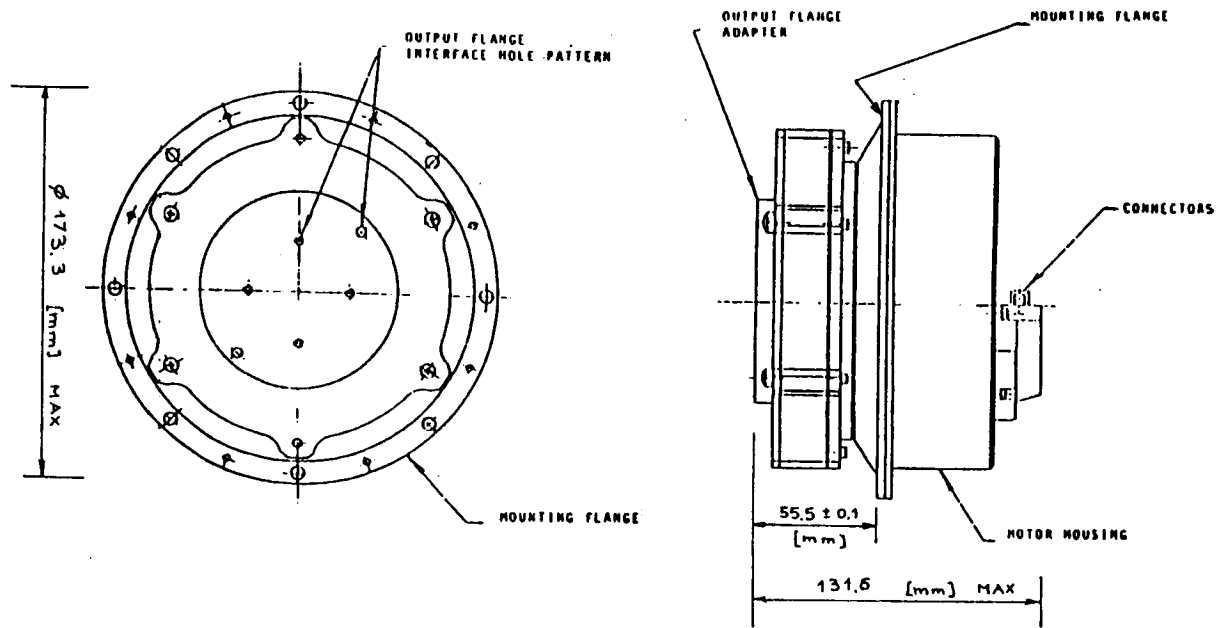


(a)



(b)

Figure 2. Cradle and spinning stage: grabber constraints. (a) Both grabbers open. (b) Both grabbers inserted.



GRABBER ACTUATOR

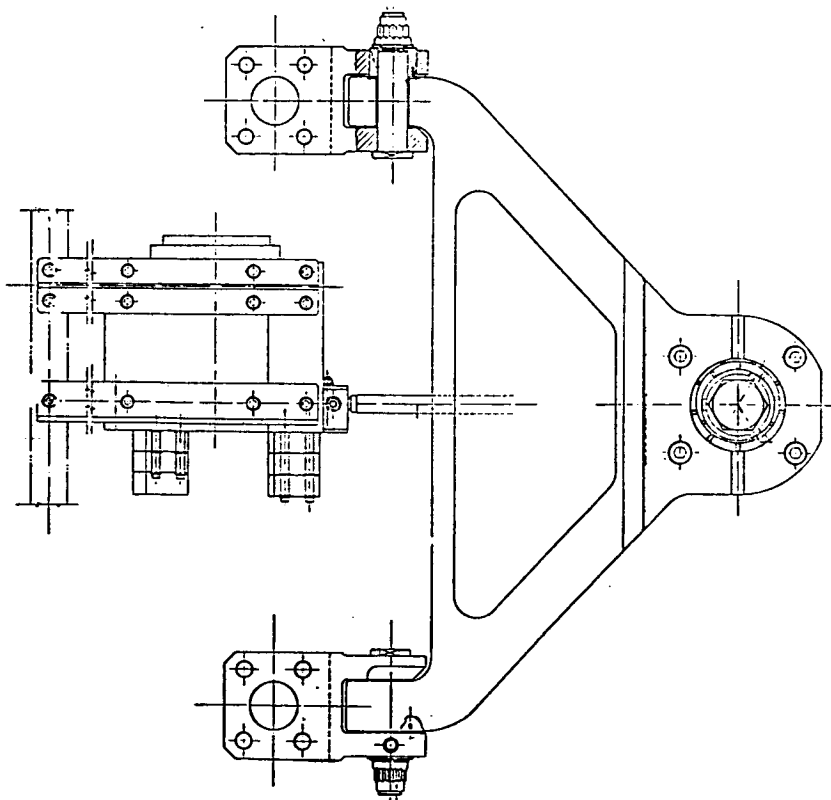


Figure 3. Grabber actuator and mechanical interfaces.

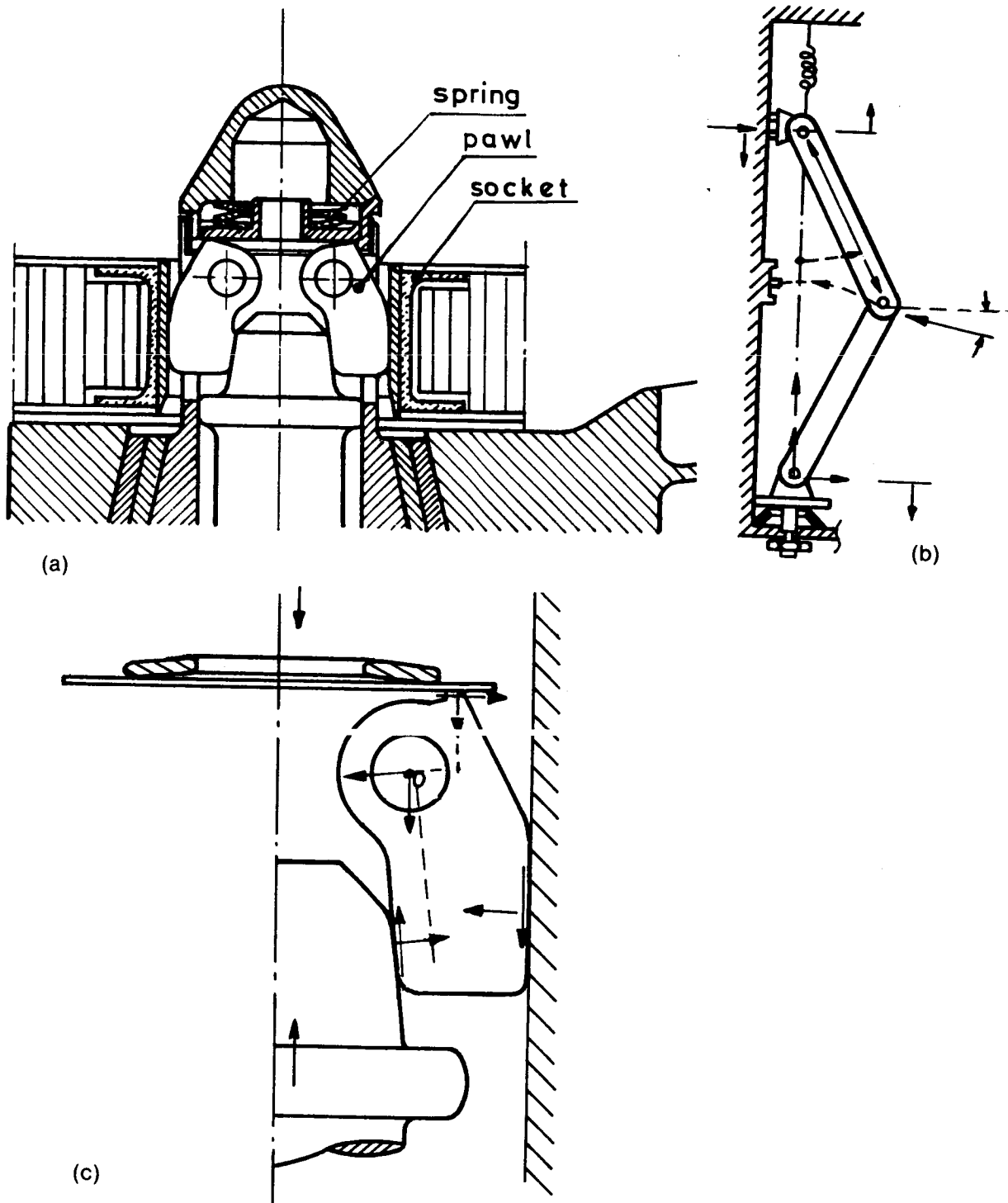


Figure 4. Linkages of the expandable grabber head. (a) Expandable grabber head. (b) Toggle arms. (c) Sleeve and pawls.

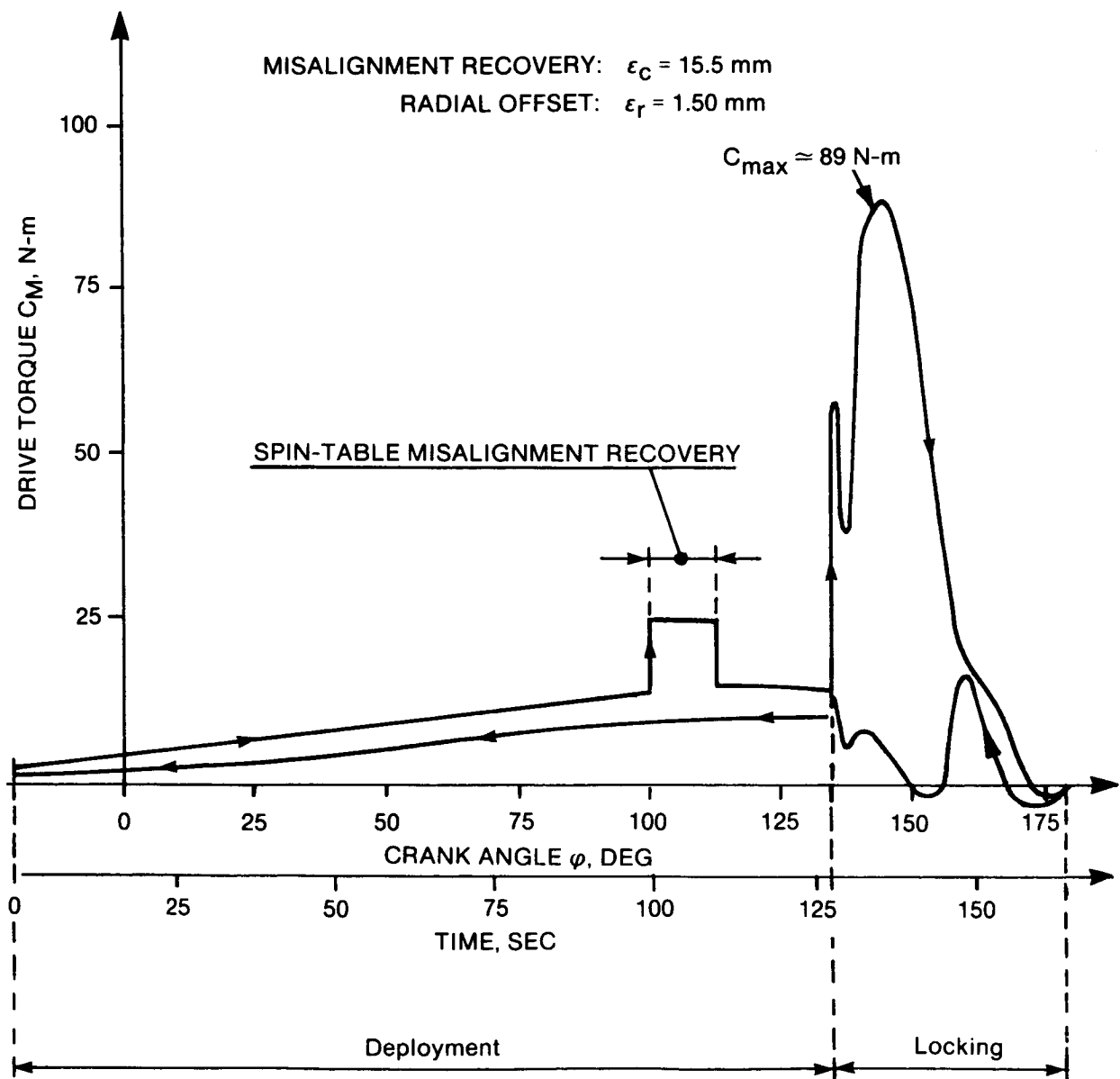


Figure 5. Drive torque versus crank rotation: diagram.

ORIGINAL PAGE IS
OF POOR QUALITY

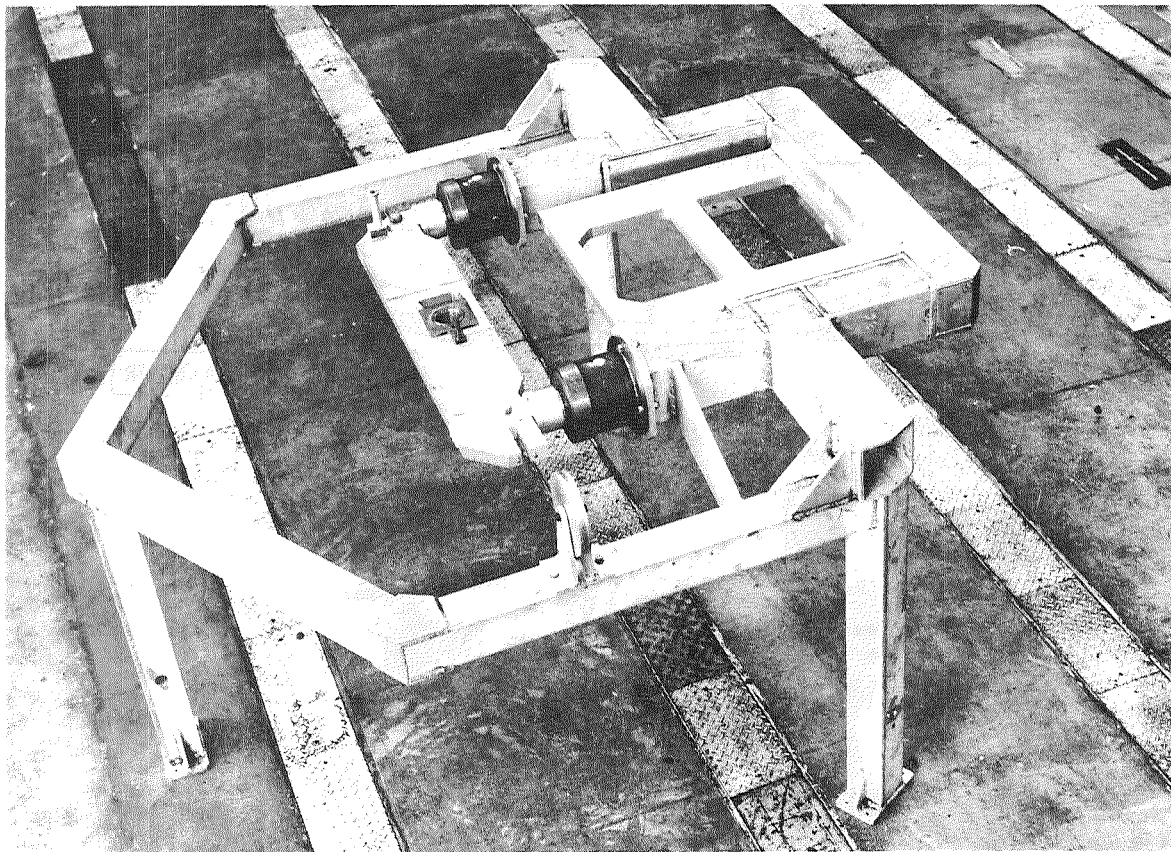
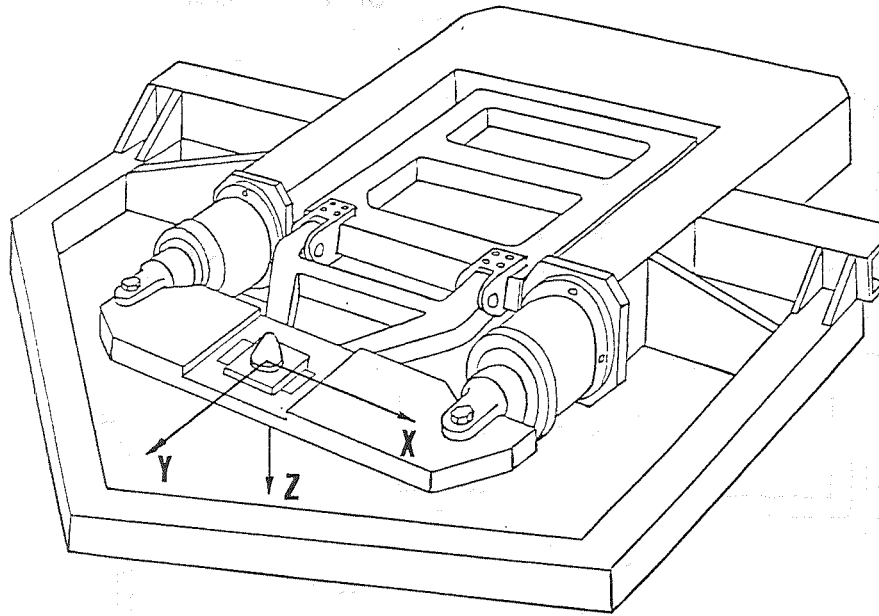


Figure 6. Test fixture simulating cradle/spinning-stage interfaces.

ORIGINAL PAGE IS
OF POOR QUALITY

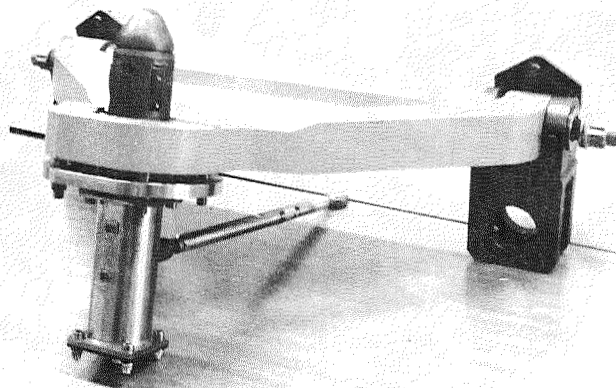
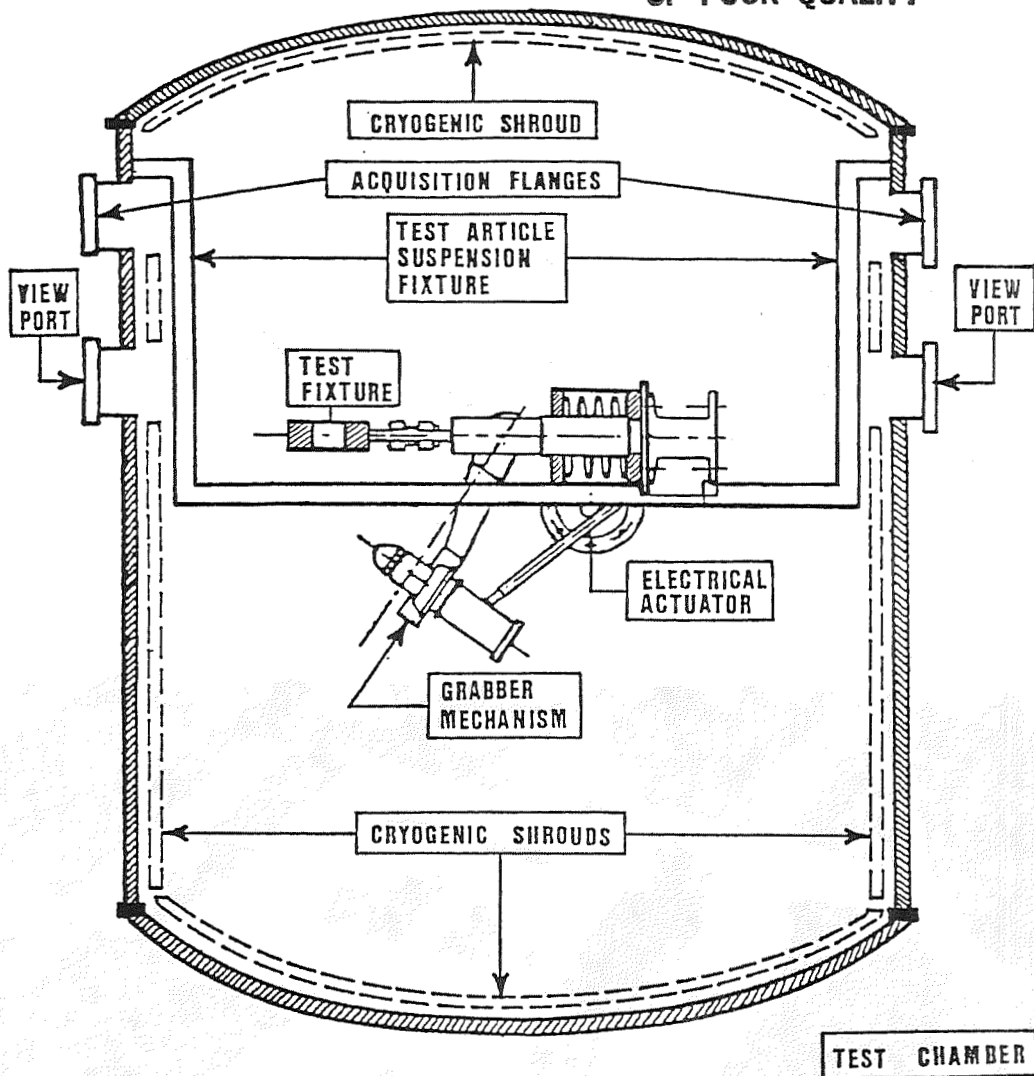


Figure 7. Thermal vacuum test setup and test item.

DEVELOPMENT OF A STANDARD CONNECTOR FOR
ORBITAL REPLACEMENT UNITS FOR SERVICEABLE SPACECRAFT

Ellen F. Heath, Matthew A. Braccio,
Steven D. Raymus, and David W. Gross*

ABSTRACT

The current trend for spacecraft to be serviceable and repairable in orbit has led to a modular approach to satellite subsystem design. Spacecraft equipment, such as, sensors, tape recorders, computers, transponders, batteries, etc., housed in discrete modular units--called Orbital Replacement Units (ORUs)--can be attached and detached to the spacecraft as needed. The interface between the ORU and the spacecraft is crucial. The projected use of robotics and the need for a common mechanism capable of performing several functions puts many constraints on the design of the interface. Astro-Space Division has designed and developed such an interface mechanism--called the Standard Interface Connector (SIC)--that mates the ORU to the spacecraft. The SIC also provides for the flow of fluids, data, and power between the module and spacecraft. The baseline design presented in this paper can be configured to provide various attachment schemes. Tests on SIC models have demonstrated the functionality of the design and its compatibility with current robotics.

INTRODUCTION

Early servicing of spacecraft will almost certainly be done by extra vehicular activity (EVA) crewmembers, using tools such as NASA's Module Servicing Tool (MST). Later, the Space Station Orbital Maneuvering Vehicle (OMV) repair vehicle will permit in-orbit servicing, using the same connector mechanism with a robot arm under supervisory control. Making the ORU exchange process autonomous provides a more cost-effective, repeatable operation than one requiring astronaut intervention. This, however, places more restrictions on the design of the interface between the modules and spacecraft. It must be compatible with existing and proposed robotic systems; provide a stable mount for delicate instruments; and provide for power, data, and fluid transmission across the interface.

SIC DESIGN

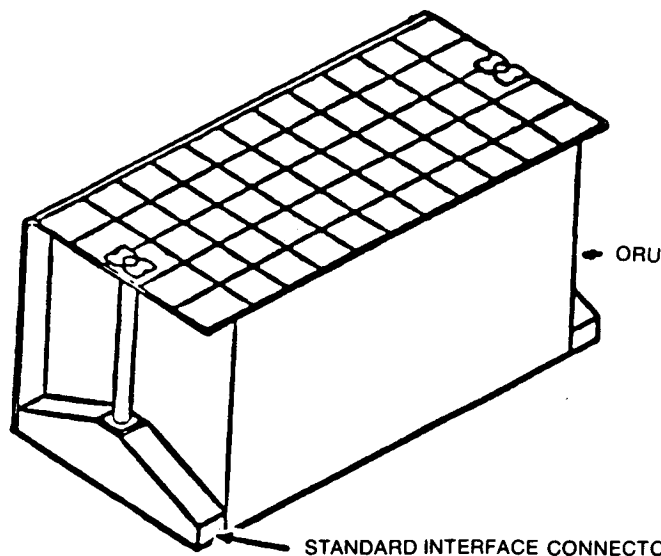
Several candidate SIC designs were established as the result of trade-offs of more than ten connector concepts. The factors that drove the design are as follows:

- The SIC must be robot friendly, yet suitable for extra vehicular activity (EVA) astronauts.

*Astro-Space Division, RCA Aerospace and Defense, East Windsor, N.J.

- The SIC design must be applicable to payloads, ORUs, and perhaps in the case of the Space Station, payloads attached to its structural framework.
- The SIC must perform several functions: assist in aligning the ORU to the platform, mate utility connectors, and provide proper mechanical attachment to ensure pointing accuracy.
- Alignment, attachment, and connector mating must be accomplished simultaneously with one actuation.
- The platform must be able to accommodate ORUs and payloads of different sizes and shapes. A platform with no protrusions would allow for a flexible layout of replaceable units. Therefore, the SIC mating ports had to be designed so that the ORUs could be flush with the platform surface.
- The mechanism housing must be usable as a transport handle.

The candidate SIC designs are variations of a baseline, the only differences being each tie-down configuration. The general arrangement is shown in Figure 1. The baseline design, based on proven technology of NASA's Multi-mission Modular Spacecraft (MMS) project, relies on the concept of a load-spreader beam transmitting loads to restraint pins at its corners. The load-spreader beam houses the mechanism through which all connections are initiated and achieved. A handle extending from the upper surface of the load-spreader beam is compatible with a modified MST and thus can be used by an astronaut or robot. A centrally located preload bolt--also of MMS heritage--is mated with a funnel-shaped socket on the platform and provides initial



7-0016

Figure 1. General Arrangement: ORU/SIC Configuration

alignment and attachment. Once the screw makes contact with its mating socket on the platform, turning it drives a carrier containing all connectors into position. Preload, obtained by tightening the screw, is transmitted through the load-spreader beam to the two nearest corners of the ORU. The preload provides mounting restraint points for the ORU. Greater detail on the locations of attachment devices and connectors on the load-spreader beam and the spacecraft platform are shown in Figure 2. This baseline connector design satisfies requirements for simplicity and efficiency, because all functions providing alignment, attachment, and utility connection are housed in one load-spreader beam.

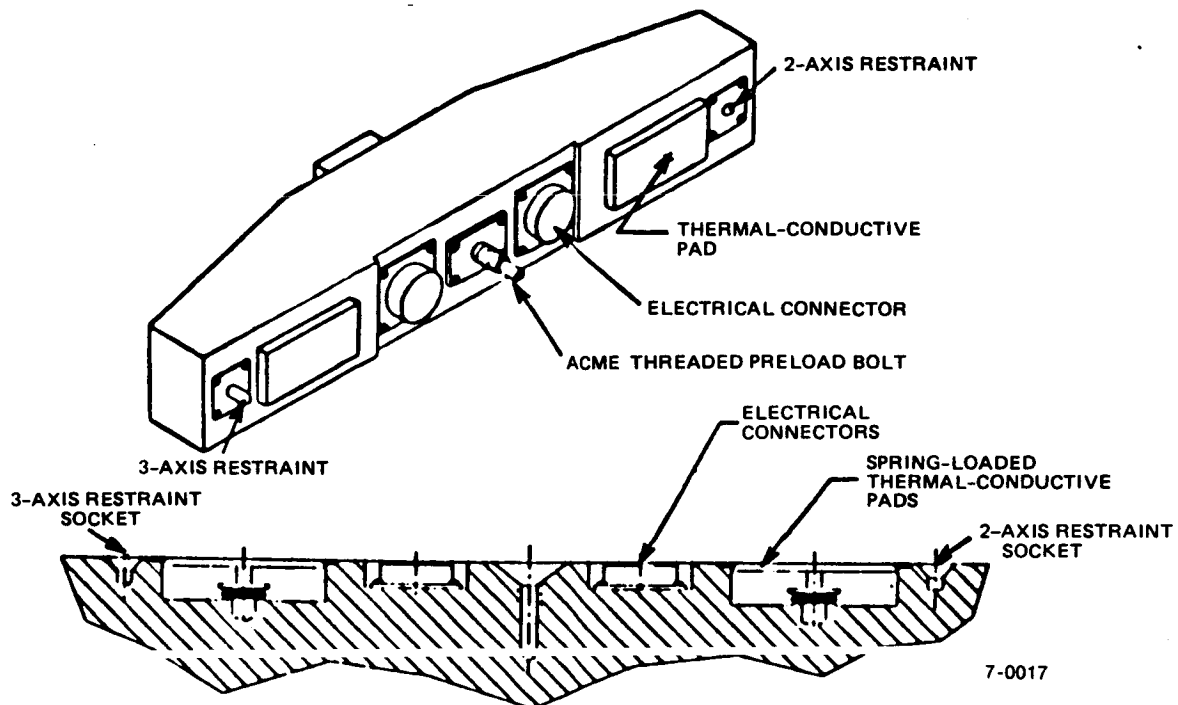


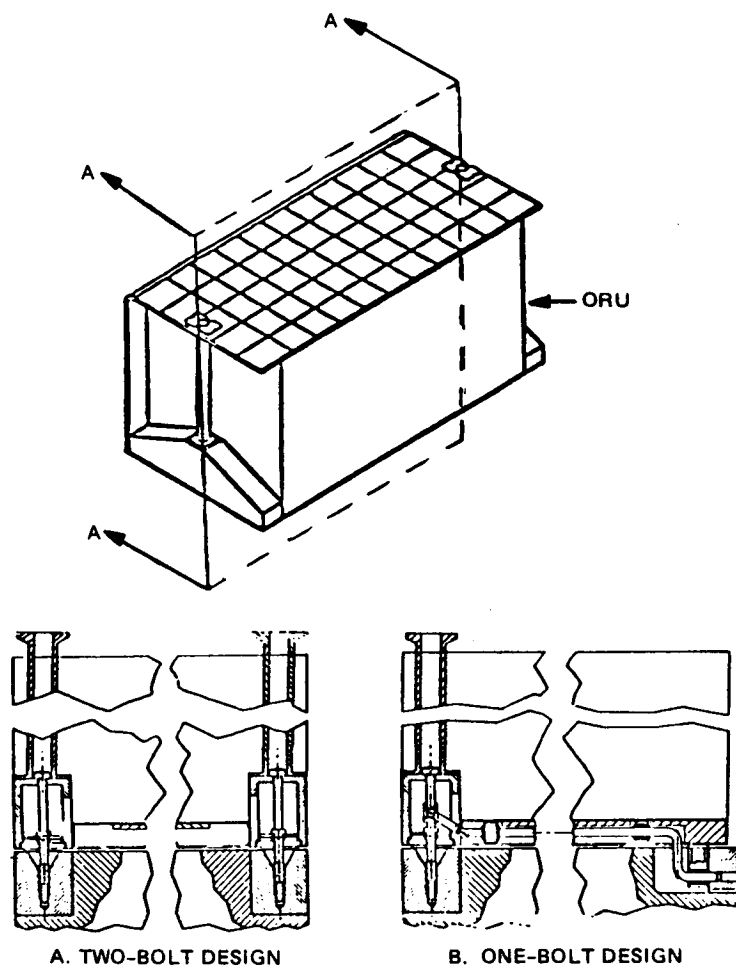
Figure 2. SIC-to-Platform Interface

The candidate designs were derived from all possible attachment configurations of the baseline design. The preferred configuration for the Space Station platforms is an ORU having an SIC at each end, giving it a four-point mount. If the two-axis and three-axis restraint pins are eliminated from one SIC, a three-point mount results. Another variation of a three-point mount is obtained with only one SIC when a push rod assembly is added. The advantages of the three-point mount are many:

- the mounting is statically determinant
- it provides the minimum number of points required to constrain the six degrees of freedom of the structures
- it prevents differential bending or thermal expansion from inducing loads in the structures

- it makes single action attachment possible because the turning of one bolt activates all three restraint pins

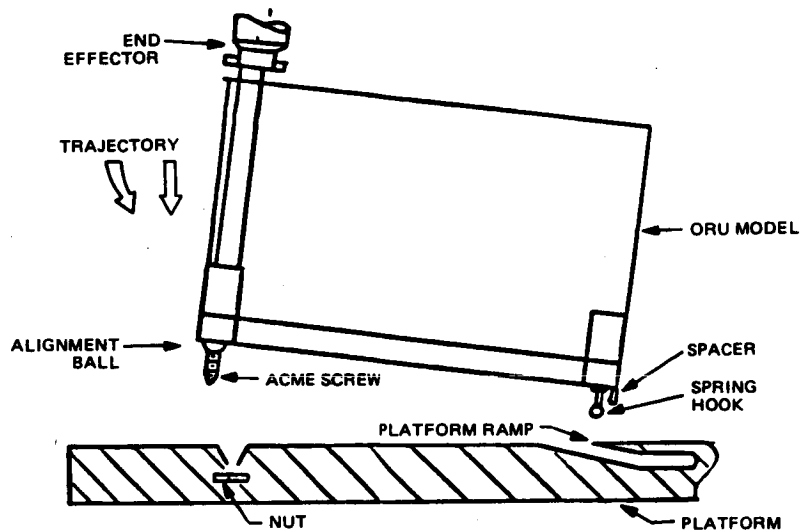
A cut-away drawing of these variations is shown in Figure 3. A three-point mount can be achieved without the push-rod assembly using a spring-loaded pin and ball that has been forced into a socket, as shown in Figure 4. The major disadvantage of this design is that it requires a robotic servicer to perform a cocking movement. A final three-point mount configuration being considered locates the SIC at right angles to the baseplate, as shown in Figure 5. The turning bolt directly draws the ORU into position at the edge of the spacecraft platform. However, flexibility of platform layout is limited by this design, because all ORUs or payloads require a platform edge to attach to.



7-0018

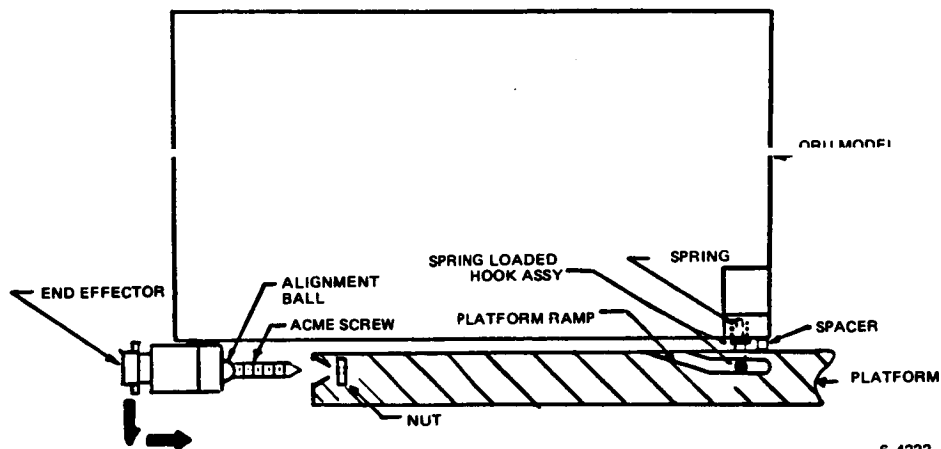
Figure 3. Variations of the Baseline SIC Design

The virtues of the baseline SIC design include flexibility, efficiency, simplicity, cost-effectiveness, ease of operation, and universality of application. The fact that the design permits a vertical (normal) approach to the platform yields flexibility in planning for platform layout; also, payloads



6-4228

Figure 4. Active/Passive Three-Point Support



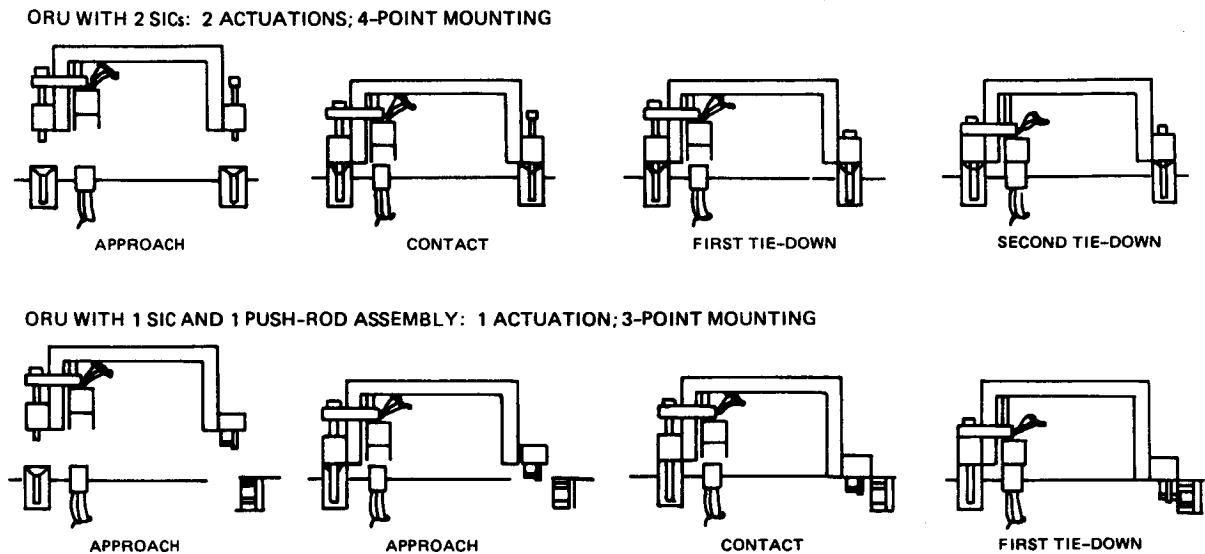
6-4222

Figure 5. SIC: Edgemount Variation

and ORUs can be located in tight spaces between other modules. In addition, this type of mounting requires only translational motion from a robotic teleoperator, making it efficient for automated servicing. Figure 6 shows the simplicity of the attachment procedure for the two-SIC variation and the push-rod assembly variation.

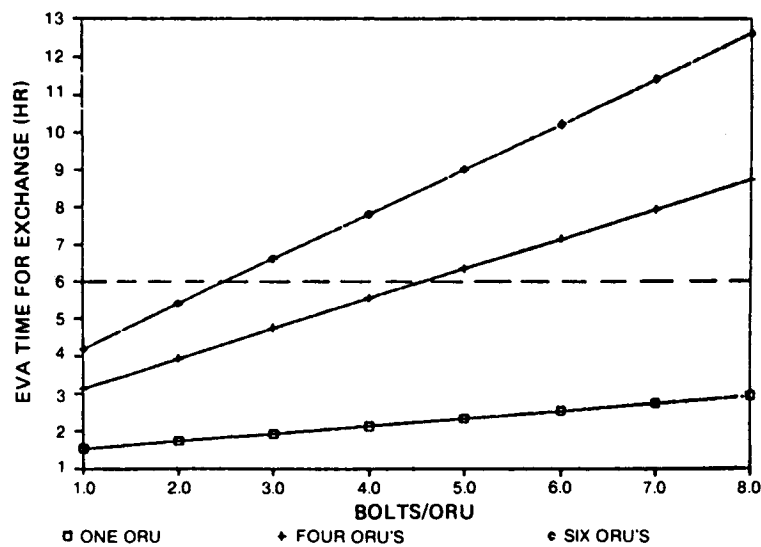
Efficiency is increased by the fact that at least two mounting points are loaded for each bolt turned. This is especially important for servicing by an astronaut because it has a direct effect on the number of ORUs that can be exchanged, because it is a time-critical operation. A trade study on

this subject indicated that, to exchange as many as six ORUs in the six-hour EVA time frame, the design could allow only two bolts per ORU, as plotted in Figure 7.



7-0020

Figure 6. Attachment Procedure for Two Variations of the SIC Baseline



7-0022

Figure 7. Results of Trade Study on ORU Exchange Times in EVA

A major benefit of the SIC is that it can be fitted with a variety of connectors, including specialized coaxial connectors, multipin electrical connectors and heat conduction pads. Figure 8 shows a load spreader beam fitted with heat pipe disconnects as well as electrical connectors.

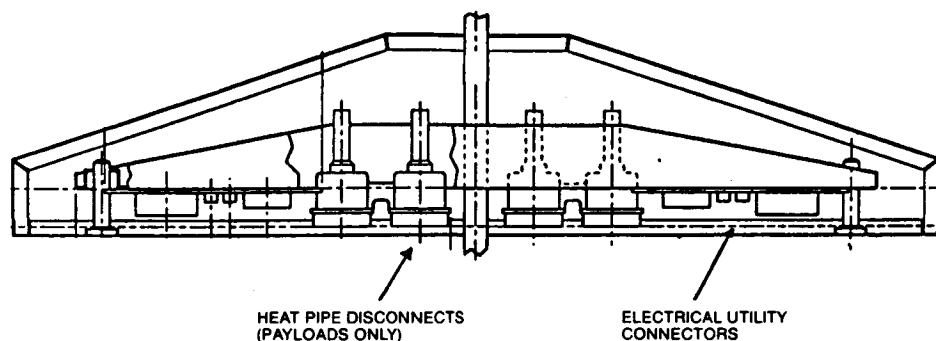


Figure 8. SIC Assembly with Heat Pipe Disconnects

7-0023

FABRICATION AND TEST

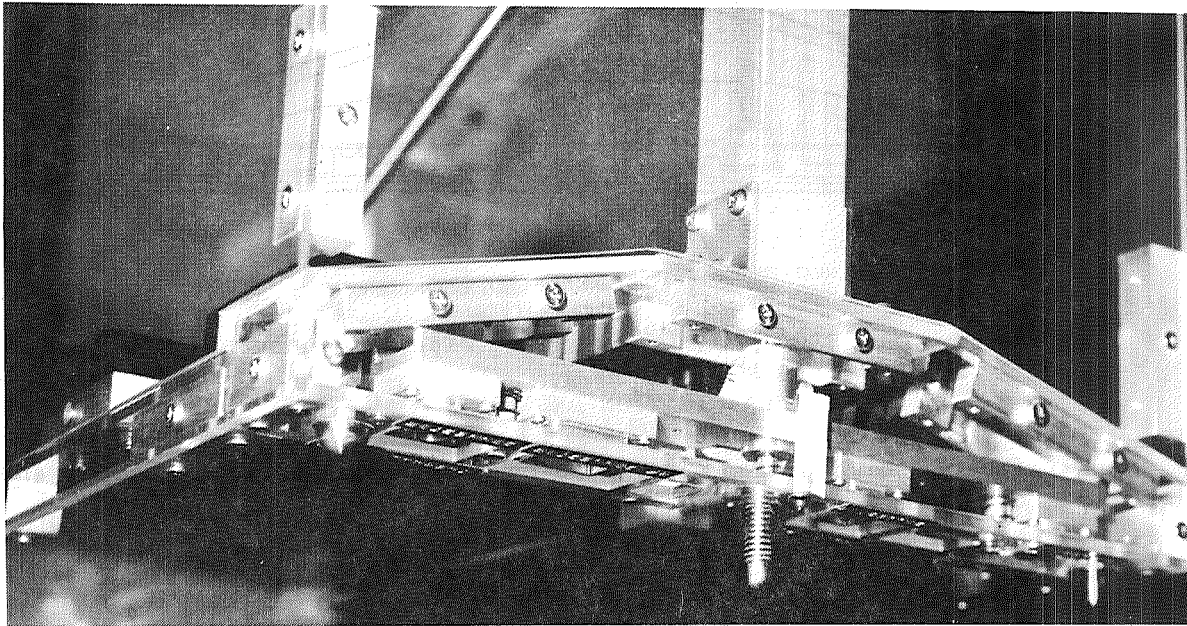
A multifaceted test program was developed for the baseline design, and three types of models were fabricated.

Half-Size Model

In the first stage--design feasibility test--a half-size ORU model demonstrated the basic functionality of the design and its compatibility with available robotics. The robot at RCA's Advanced Technology Laboratory (ATL) was used for this test. The design configuration was that of a three-point mount using a load-spreader beam at one end of the ORU combined with the push-rod and shear-pin assembly. This variation carried the greatest risk of all the concepts, yet also the important potential for single-action attachment, i.e., loading all three restraint points by turning one screw. The model was built of plexiglass to view the working parts, which were made of aluminum. A close-up of the load-spreader beam with the screw and sliding connector plate is shown in Figure 9. The model consisted of the load-spreader beam with push-rod assembly attached to a baseplate and the whole covered with a shroud. A plexiglass stowage mockup contained the mating parts. Because this test emphasized robot handling, greatest attention was given to the design and fabrication of the attachment screw, its mating socket, the restraint pins and sockets, the connector plate, and the gripper plate that interfaces with the robotic end effector. Working connectors were not used. A platform mock-up was also built for this test, complete with mating parts and two mock ORUs to delineate the ORU insertion space.

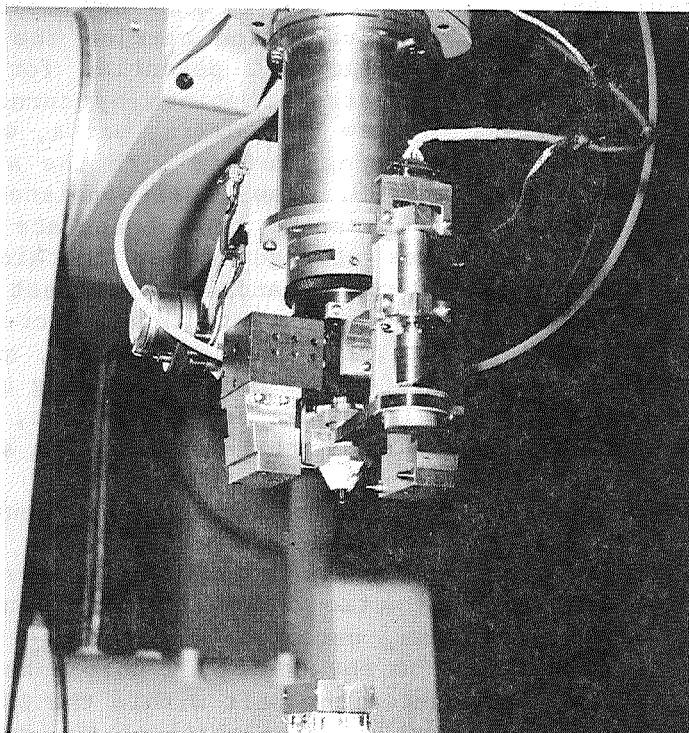
The test of the half-size ORU/SIC was coordinated with engineers at the robotics facility at ATL. First, a special end effector for their PUMA 762 was adapted from a standard true-parallel jaws gripper to provide for alignment adjustment and the bolt turning action. An alignment cone with adjoining V-blocks, mounted inside the jaws, permitted angular and lateral alignment. An allen wrench protruding from the center of this cone was turned by a motor-driven belt to loosen and fasten the bolt within the ORU/SIC handle. The end effector and the corresponding gripper plate of the handle are shown in Figure 10. In addition, a miniature CCD camera was fixed to the back side of the end effector for targeting.

ORIGINAL PAGE IS
OF POOR QUALITY



86-5-230C

Figure 9. View of SIC Plexiglass Model Showing Load-Spreader Beam and Sliding Connector Plate

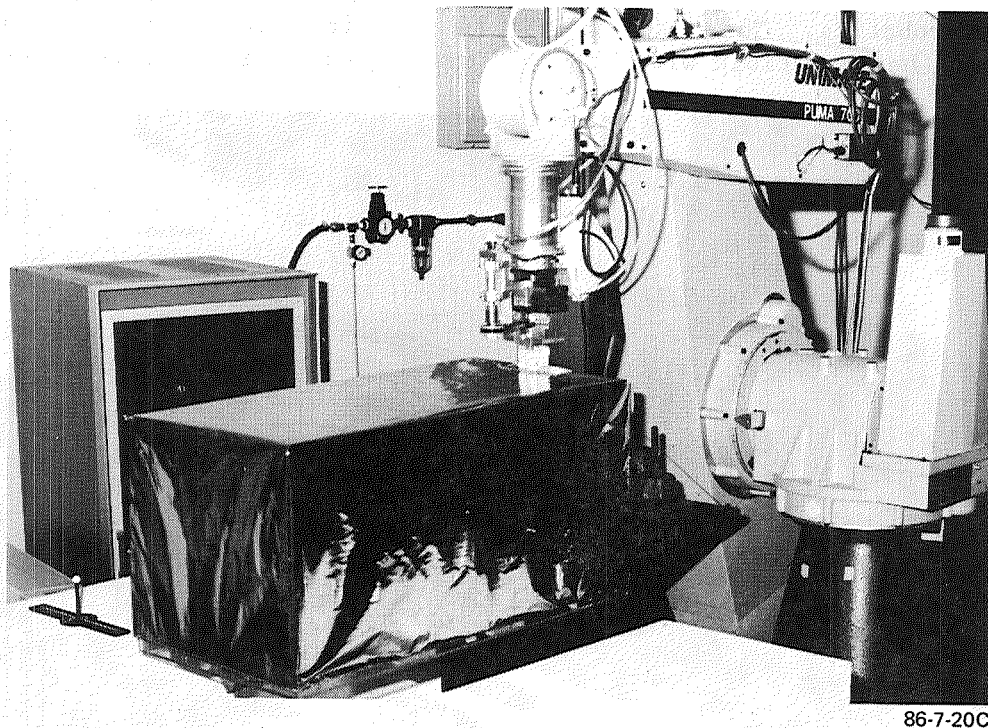


86-7-30C

Figure 10. Parallel Jaws Gripper Adapted for ORU Exchange at ATL

ORIGINAL PAGE IS
OF POOR QUALITY

A six-axis force/torque sensor was situated between the end effector and the robot arm. The alignment mechanisms acted in cooperation with this sensor by means of a compliance control loop. Software written for the test provided the operator the choice of performing the ORU exchange via preprogrammed instructions or manual joy stick control. The operator was located in a separate control room with a view into the robotics lab. Cameras and TV monitors provided remote viewing. An interactive voice control system activated the preprogrammed task segments and the camera position controllers. Using a combination of automated and manual operations, the operator successfully directed the robot to release the model from its stowage location, carry it to the platform mock-up, maneuver it into its mounting position between adjacent ORUs, and firmly attach it to the platform. The entire operation took an average of 4.5 minutes. Figure 11 shows the model about to be inserted onto the platform mock-up by the robot.



86-7-20C

Figure 11. ORU Insertion onto Platform by PUMA 762 Robot

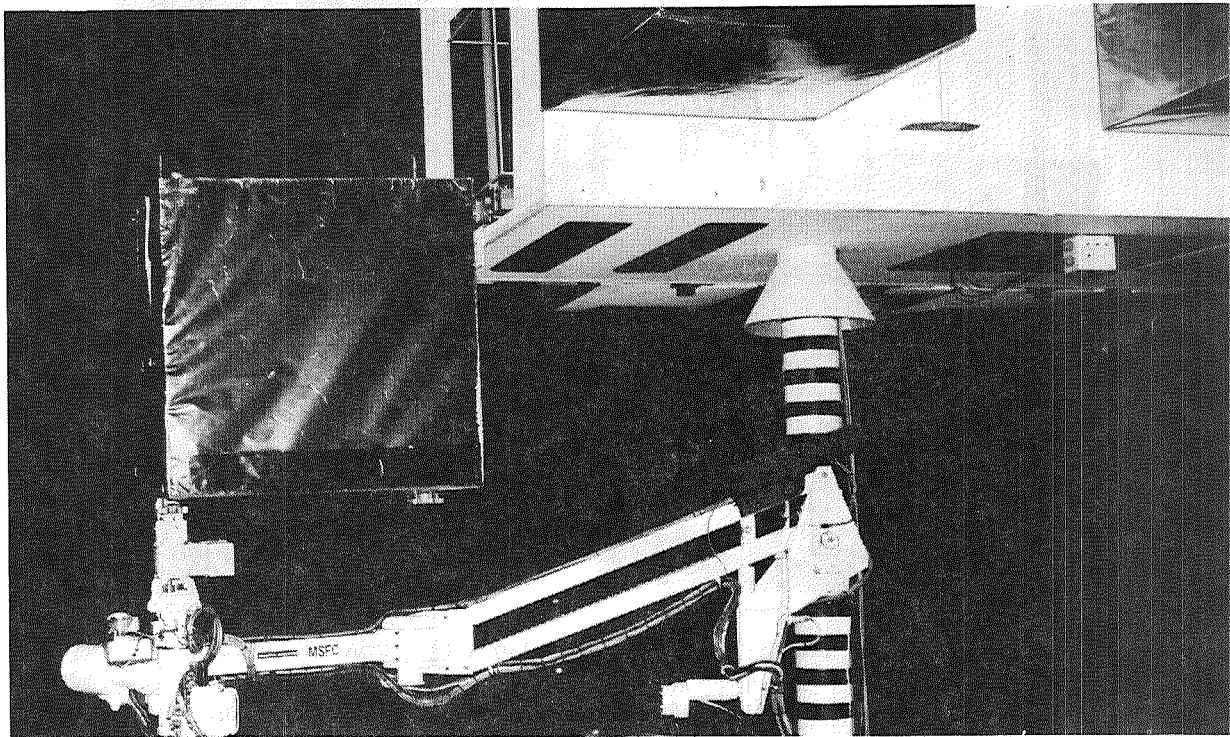
After successful completion of the test of the three-point mount configuration, the model was reconfigured to represent a payload requiring six mounting points. The push-rod assembly was replaced with four additional bolts around the periphery of the baseplate, and their corresponding sockets in the stowage mock-up. This configuration was designed to be handled by a "dual-arm" robot with appendages that cooperate with each other.

A PUMA 560 was added to the robotics laboratory; the newly introduced robot and the original PUMA 762 communicated and worked cooperatively with each other, just as a dual-arm robot would. They effectively carried out the payload exchange scenario.

ORIGINAL PAGE IS
OF POOR QUALITY

Full-Size Mechanical Test Model

To conduct proof-of-concept testing in a more realistic, space-servicing environment, full-scale ORU exchanges were effected in a NASA robotics facility. In a cooperative effort with Goddard Space Flight Center (GSFC) and Marshall Space Flight Center (MSFC), automated exchanges of four ORU/SIC designs were performed using the engineering test unit of the Integrated Orbital Servicing System (IOSS) as shown in Figure 12. This system, located at MSFC in Huntsville, Alabama, depicts the servicing kit of the Orbital Manuevering Vehicle (OMV) docked to a space platform mock-up with three ORUs. The test ORU model could be used to represent a two-actuator (see Figure 13), one-actuator (similar to that tested at ATL), one-actuator edge-mount, or one-actuator advanced technology SIC configuration. These last two designs were considered purely experimental and were meant to take advantage of advanced robotics. The model was 30 in x 30 in x 30 in and weighed a mere 11.5 lb to be compatible with the IOSS wrist-joint torque limit of 60 ft-lb.

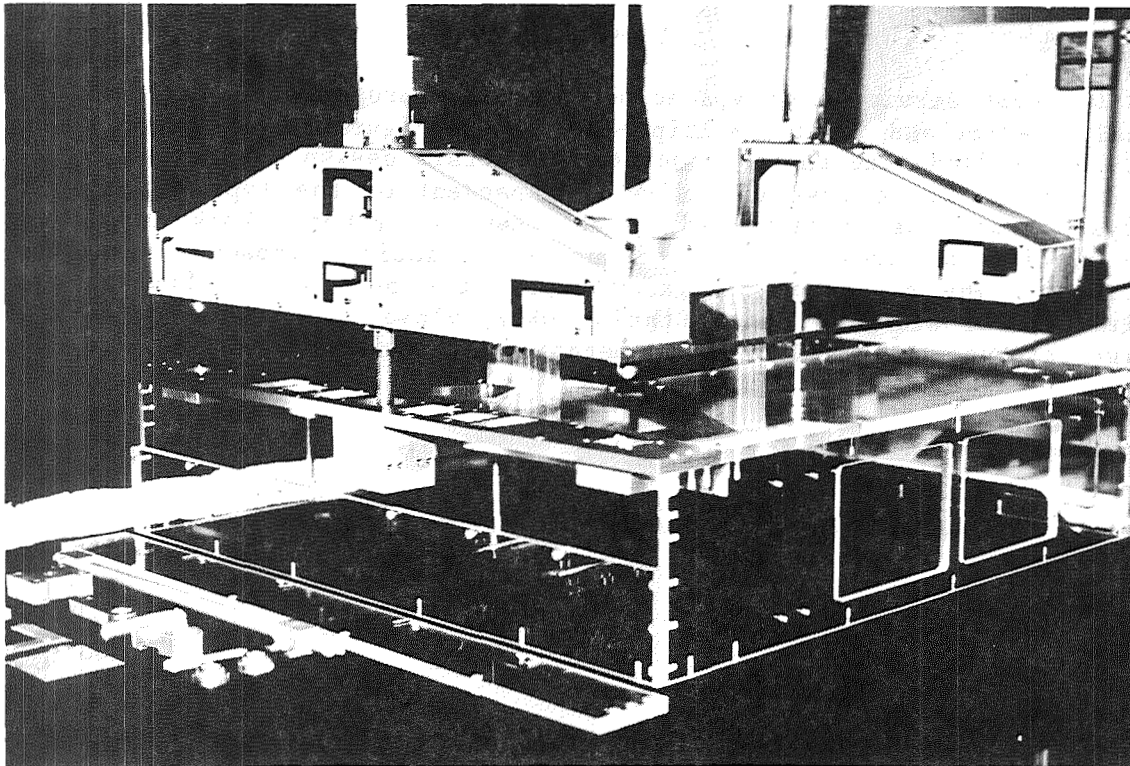


87-1-527C

Figure 12. IOSS Engineering Test Unit with Astro-Designed ORU Model

The test involved exchanging each ORU/SIC variation between the space platform mock-up and the OMV stowage rack using the 13-foot IOSS servicer arm. A mock-up of the NASA Module Servicing Tool (MST) was used as an end effector throughout; however, the edgemount was exchanged using the end effector that was integral to the IOSS arm. This was done to demonstrate other servicing tool designs.

ORIGINAL PAGE IS
OF POOR QUALITY



86-9-153C

Figure 13. SIC Mechanical Test Model: Two Load-Spreader Beam Variation

These tests demonstrated the functionality of each ORU/SIC design and showed that exchanges of each could be performed using only the passive compliance of the servicer arm. Experience from this test will aid in design refinement and will become a means of extrapolating to future space-servicing scenarios.

Full-Size, Lightweight Model for EVA Simulation

Finally, to ensure that the robotically optimized ORU design is compatible with EVA operations, a full-size, lightweight model was fabricated. This test addressed the issues of visibility and ease of insertion by an astronaut. A foamboard model was fitted with hardware representing the attachment screw and alignment cone, and was equipped with a detachable MST mock-up. The model was also equipped with guides to assure that the screw would be inserted in its socket. An appropriately sized box represented the insertion space expected to be available. Although the model was lightweight, it was suspended from the ceiling with springs to simulate a 0-g environment. The MST mock-up gave the person handling the model a feel for the distance and placement of the model from the handles of the tool an astronaut would use. The knowledge gained from this test will be used to enhance the baseline design for test at a 0-g environment such as one of NASA's neutral buoyancy facilities.

CONCLUSION

In-orbit servicing of spacecraft has been proposed to increase operational lifetime and provide multiple-payload configurations. Viable concepts must be verified, and their impact on spacecraft design determined. Servicing methods must be cost effective, independent of the type of payload or subsystem, and easily performed by astronaut or robot. Work at Astro has made significant progress in defining a realistic approach to spacecraft servicing. The connector design concepts have been established as strong candidates for standard Space Station ORU/payload attachment devices. The design incorporates simplicity of operation and versatility of use.

THE DESIGN AND DEVELOPMENT OF A MOBILE TRANSPORTER SYSTEM FOR THE SPACE STATION REMOTE MANIPULATOR SYSTEM

Thomas W. Carroll*

ABSTRACT

This paper describes the analyses, selection process, and conceptual design of potential candidate MobileTransporter (MT) systems to move the Space Station Remote Manipulator System (SSRMS) about the exposed faces of the Space Station truss structure. The actual requirements for a manipulator system on the space station will be discussed, including potential tasks to be performed. The SSRMS operating environment and control methods will be analyzed with potential design solutions highlighted. Three general categories of transporter systems will be identified and analyzed. Several design solutions have emerged that will satisfy these requirements. Their relative merits will be discussed, and unique variations in each system will be rated for functionality.

INTRODUCTION

The National Space Transportation System (NSTS) Shuttle Orbiter makes use of a highly-refined Shuttle Remote Manipulator System (SRMS) to perform various on-orbit manipulative tasks such as deployment and retrieval of orbiter payload bay packages and satellites, space structural assembly, and remote servicing and maintenance. This system was designed to handle payloads no larger than those that could be transported in the orbiter payload bay. The typical mission length was to be on the order of two weeks or less, with potential for complete refurbishment of the SRMS between flights, so the SRMS is presently an orbital replacement unit (ORU) in itself, with no provisions for on-orbit repair.

The NASA Space Station presents an entirely new arena for a manipulator system. The expected station lifetime of up to 30 years, the large potential payloads of up to 120,000 Kg. (the shuttle orbiter), and the limited on-orbit servicing capabilities dictate a new approach to a manipulator system. The harsh environment of long-term exposure to atomic oxygen, severe extremes of heat and cold, and the conditions of a vacuum and zero gravity require elaborate engineering analyses and studies for the development of space-borne manipulator systems. Limited station power resources necessitate energy-efficient systems design. NASA has requested that the National Research Council of Canada, in conjunction with Spar Aerospace Limited of Toronto, Canada, redesign existing manipulator systems to form a Space Station Remote Manipulator System (SSRMS) that will satisfy these new requirements.

One of the present forms of the SSRMS is 17.4 meters in length, and weighs approximately 860 Kg, which is significantly larger than the present shuttle orbiter manipulator system. This SSRMS features a double-ended end effector configuration, and has seven degrees of freedom due to replacing the standard shoulder with a three-axis end effector / wrist assembly. Higher power and data transfer rates (end effector to payload) with potential for thermal and fluid transfer are special requirements to be considered. The re-designed end effector operates as a standard three-wire snare, or as a shoulder mount with side-attachment latches for the required base stiffness. The new mounting configuration of this and other SSRMS designs, and the larger overall size and mass, place special design constraints on potential transporter candidates. These requirements will be discussed as transporter design drivers, and an evolutionary series of transporter concepts will be presented and discussed.

*Rockwell International, Space Station Systems Division, Downey, California

SPACE STATION MANIPULATOR SYSTEM TRANSPORTER REQUIREMENTS

NASA has outlined a series of basic requirements for a manipulative system on the space station, and the Canadian government and U.S. contractors have responded with variations in designs to bring down the development costs and enhance performance. The following requirements have been defined:

- I The Mobile Transporter (MT) and attached Mobile Remote Servicer (MRS), which together comprise the Mobile Servicing Center (MSC), shall be capable of traversing all designated space station truss faces. To accomplish such motion, the mobile transporter shall be capable of- (a) straight traverse along a clear truss face, (b) direction changing within tight quarters, and (c) plane changing (from one face to another) at any clear area on the truss structure.
- II The MSC shall have the capability to move and manipulate payloads of >100,000Kg (orbiter).
- III The MSC shall have the capability of self-contained operation for periods of up to 6 hours.
- IV The MSC shall be able to be controlled from an EVA station on the MSC or from the station.

These are examples of the basic requirements that have been the design drivers throughout the definition stages of the MSC development. Many of these "requirements", such as an on-board battery system for 6 hours of independent operation, are open to discussion as to their actual need for a potential system, but are presented as a departure point for design studies. Some of the responsibilities of the MSC will be berthing/deberthing of the Orbiter, Orbital Maneuvering Vehicles (OMV's), Orbital Transfer Vehicles (OTV's) and other free-flying platforms, removing payloads from the Orbiter, transporting and installing the payloads to the desired truss location and retrieving payloads for Earth return. As the name implies, a major function of the MSC will be maintenance and servicing of the Space Station and associated payloads, as well as transportation of various payloads and experiments.

The Mobile Servicing Center consists of four parts, the Mobile Transporter, the "utility platform" or base structure, the Space Station Remote Manipulator System (SSRMS) and the end effector(s). Figure (1) shows a current baseline design under study. This MSC concept utilizes the Canadian-developed "utility platform" / SSRMS structure in conjunction with a dual-drawbar push pull transporter.

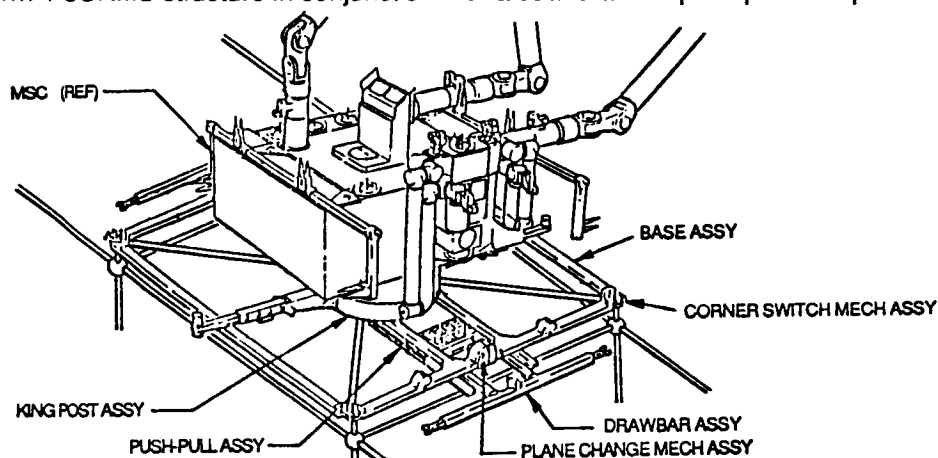


FIGURE 1- MOBILE TRANSPORTER AND MOBILE SERVICING SYSTEM

The MSC will be controlled either IVA from a pressurized module or by EVA from the MSC utility platform. Primary control is envisioned from the pressurized module. Since most of the MSC's functions are envisioned as being automatic, the need for EVA assistance during standard payload activities is minimized. One version has the Mobile Transporter operating in an independent mode without the need for attachment to, or control by an attached MSC structure. This could allow separate operations for the transporter as a "truck" to support various station operations.

As a servicing center, the MSC will provide other services to the payloads. Some of these services are: providing a support structure for the payloads during transportation, providing video and lighting for the verification of payload installation, maintenance and servicing tasks, providing manipulative arms for maintenance, servicing and refurbishment tasks, and providing checkout of the payload before deployment. These particular requirements have been subject to much discussion, as have others concerning operational speed, method of attachment, method of propulsion, degrees of freedom, controllability, autonomy, system mass, maintainability, and other factors, but we have used the above four requirements as a baseline for our discussion of various concepts.

EARLY MOBILE REMOTE MANIPULATOR SYSTEM (MRMS) CONCEPTS

Many concepts of manipulator propulsion to move about the surface of the space station have been analyzed and discarded for various reasons. A natural attachment and propulsion scheme has centered around a wheeled transporter traversing upon attached rails. While quite simplistic in nature, these concepts involve the attachment of a high-mass rail system at all points where the MSC is expected to operate. Curved rails or switches must be mounted at all turning and plane change locations. Even the variation of a monorail system requires an extensive rail system, and the high stresses applied to a single rail can bring total system mass up to that of a dual rail system to compensate in strength. Figure (2) depicts a typical railed transporter system.

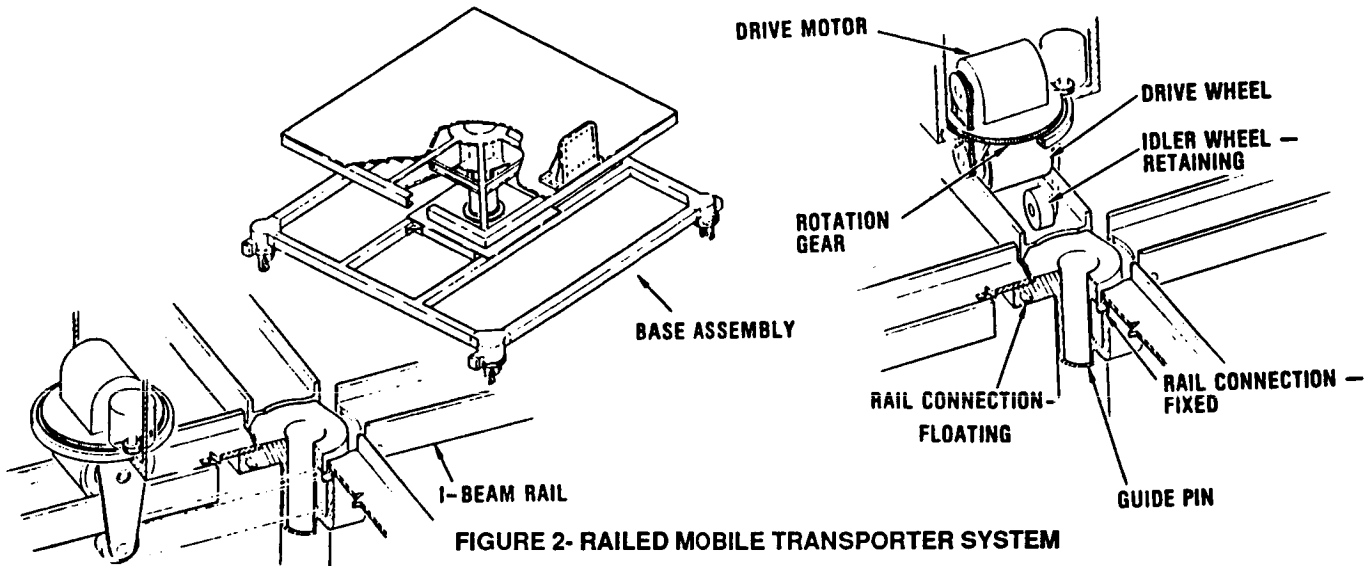


FIGURE 2- RAILED MOBILE TRANSPORTER SYSTEM

One solution to the massive rail dilemma is to use transporter attachment points at the truss node fittings. Small knobs or rings can be "grasped" by the transporter system as it traverses each fitting point, thus saving the mass of continuous rails. The problem lays in how to design a mechanism that can successively grasp each node fitting for continuous travel on the truss surface, or for turning and changing planes, and yet have a secure attachment to the station structure. One concept used rings similar to boat oarlocks, with a small slot in the top, to allow javelin-shaped rails attached to a transporter base to pass through. The rings were drawn inward by a discontinuous drawbar mechanism for traversing. Turns and plane changing was difficult with this concept. Figure (3) depicts the "javelin / ring" transporter concept.

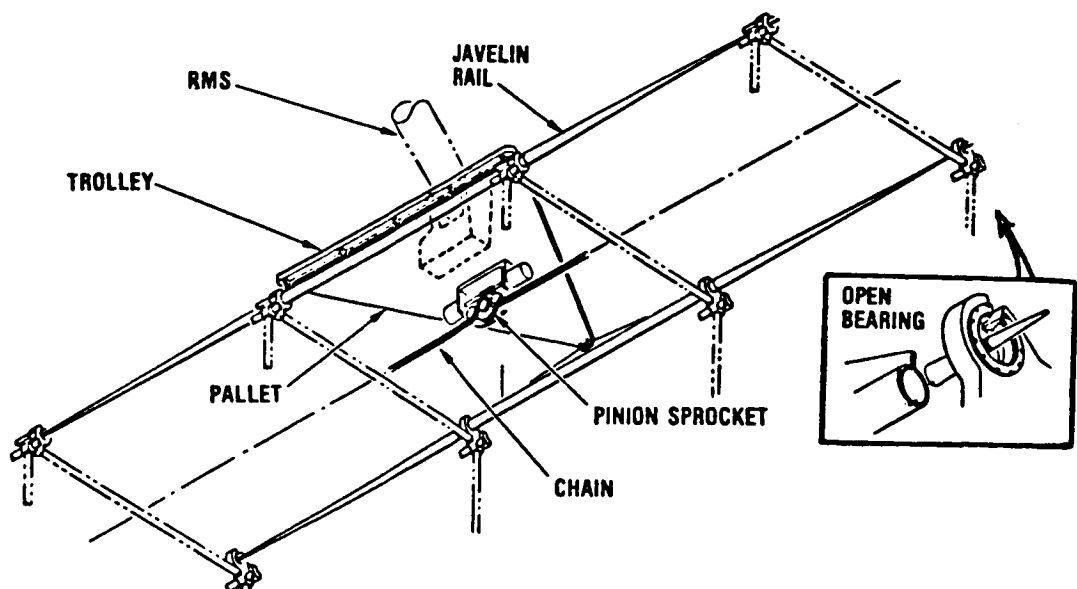


FIGURE 3- RAILED / JAVELIN TRANSPORTER

Later concepts centered on the use of 9cm diameter mushroom-shaped node "guide pins" developed by NASA Langley as the transporter attachment points. These 9cm high, 0.4 Kg pins are drawn through slotted rail assemblies in many concepts developed over the past two years, and remain the prime attachment scheme for most MSC systems under development. Many discontinuous and continuous motion drawbar transporter concepts, several endless belt crawler transporters, and an RMS-propelled transporter variation make use of these or similar pins for attachment. Figure (4) depicts the transporter node guide pin developed at NASA Langley.

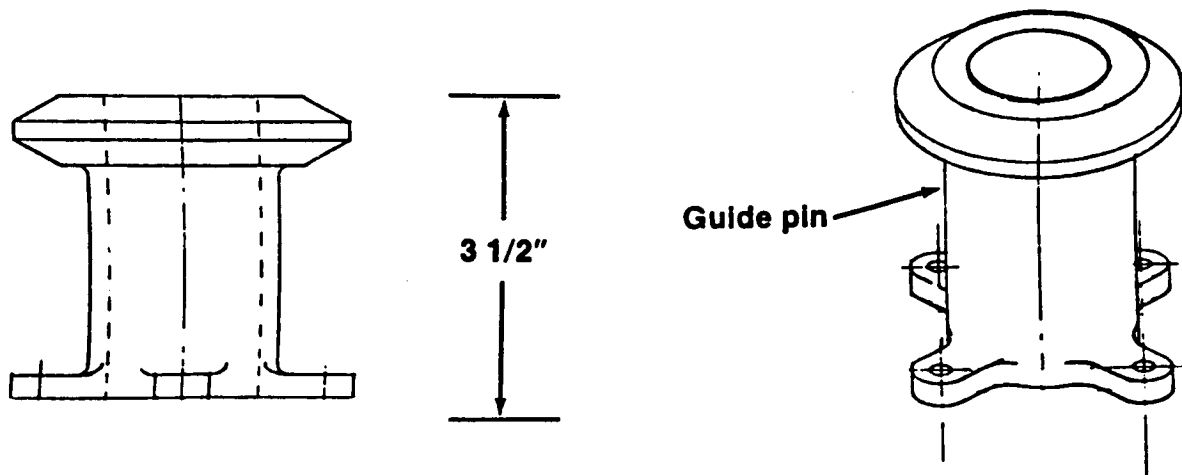


FIGURE 4- NASA MSC TRANSPORTER NODE GUIDE PIN

The use of the node guide pin scheme as an attachment point, and means of motivation for an MSC transporter, requires some sort of grasping mechanism for the widely spaced pins. Most concepts use a discontinuous motion to grab successive pins in the traversing motion. Dispensing with the idea of grasping robotic pincers reaching for the node pins, one concept made use of the cross-country ski traversing method of placing one ski after the other, with a special bottom coating to keep the ski from sliding back. The MSC transporter uses two sliding rails to surround each node guide pin, with an eccentric jamb bar or ratchet to hold each rail in position on the pins. Figure (5) illustrates this concept.

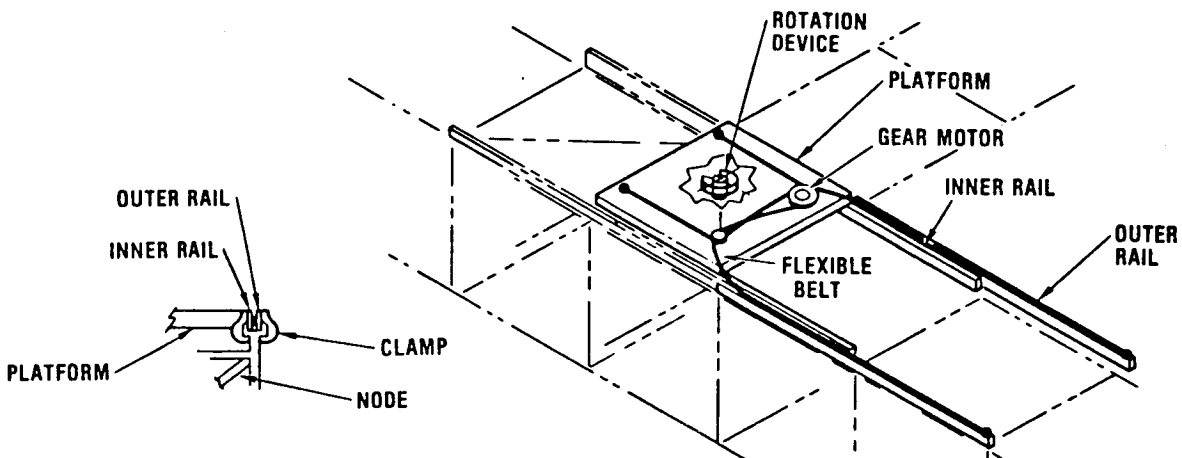


FIGURE 5- SLIDING RAIL MSC TRANSPORTER

NASA Langley determined that a continuous and firm attachment to the truss structure was of prime importance in the design of a mobile transporter. Using the mushroom-shaped guide pin shown in Figure (4) as an attachment base, Langley devised the push-pull transporter, (sometimes called the Track-layer) as a simple method of moving a manipulator system base about the truss surfaces. The push-pull transporter uses slotted rails through which the guide pin heads pass. A rack-and-pinion actuated, or similar mechanism drawbar mechanism reaches out, attaches to, and draws inward each successive node guide pin. The resulting motion is start/stop in action, but the required mechanisms are simple. In-plane turning is accomplished by the use of four "corner switches" that direct the motion of incoming node pins. The corner switches and drawbar mechanism are rotated 90°, and the guide pins are drawn inward from the new direction. Plane change is accomplished by truss-mounted "flip platforms" that rotate the transporter over the side of the truss structure. Figure (6) illustrates the Push-pull Transporter concept.

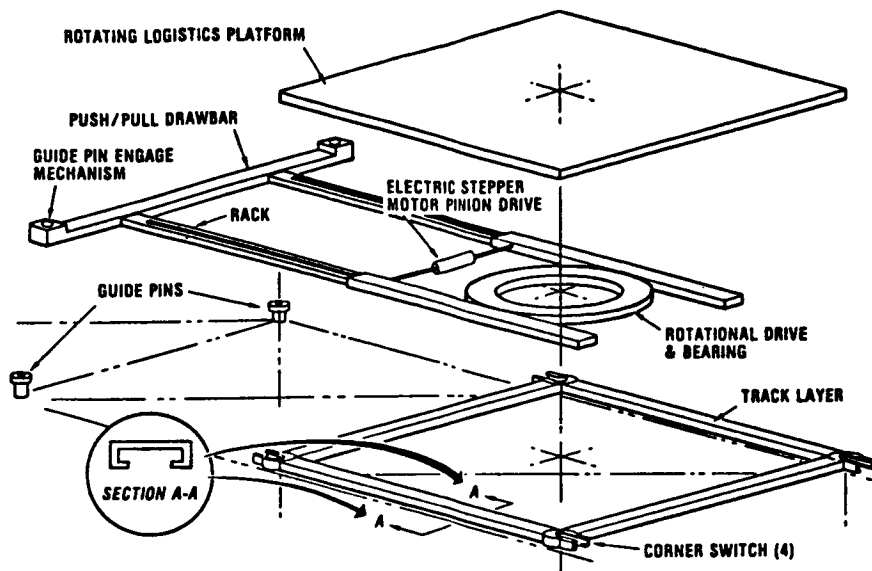


FIGURE 6- NASA LANGLEY PUSH-PULL MOBILE TRANSPORTER

Using the NASA Langley concept of solid attachment to the truss structure by having slotted rails securely surrounding the node guide pins, one improvement was to eliminate the discontinuous motion of the node pin drawbar assemblies. One concept makes use of dual endless toothed belts encased in split rail assemblies. The smooth, continuous motion belts grasp the "moving" pins and bring them into the slotted rail assemblies. Since this method can not make use of the corner switch direction-changing method, four forks grasp the base of the node pins, and the clamshell rails open to allow the transporter to be lifted off of the pins for turning by a turret assembly. Plane changing uses swiveling node pins or the plane change mechanisms mentioned later. The attachment is solid, and the motion smooth, but this concept uses fairly complex mechanisms. Figure (7) depicts the split rail crawler transporter.

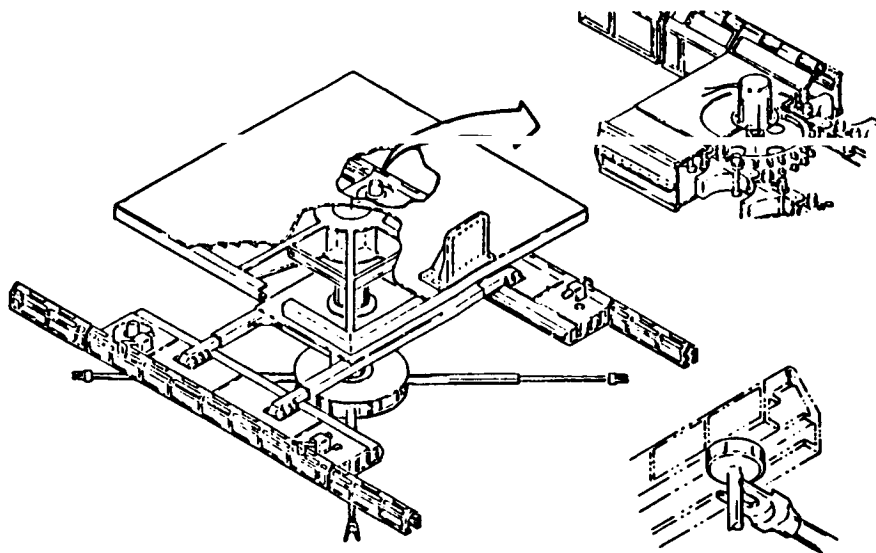


FIGURE 7- ENDLESS BELT SPLIT RAIL CRAWLER MOBILE TRANSPORTER

The complexity of some of the mobile transporter concepts caused many designers to take a long, hard look at ways to eliminate excess mechanisms. It was decided that the MSC contained an eloquent piece of machinery in itself, - the RMS manipulator arm. Why not use this already-developed device as the motion-producing mechanism for traversing throughout the station real estate? No plane change or direction changing mechanisms were required. The RMS-Propelled concept was born. This transporter concept moved along in "inch worm" fashion, -attaching, detaching, and re-attaching the end effector to produce traversing motion, plane-change, or turning. Later versions used a three or four point attachment fixture securely attached to the end effector for stiffness.

Problems arose in simulations with controlling such complex motion,- especially in turning and plane changes. Trying to attach and re-attach even a single point end effector became a control nightmare. The NSTS RMS, or even the re-designed SSRMS was not designed for this repeated operation. The standard NSTS RMS was difficult to reverse and use the end effector as an elbow joint for every other traverse step, and the end effector joint was too weak for large payloads when used as a "shoulder". Another problem was where did one place a payload of any size, batteries, and the EVA astronaut. Figure (8) depicts the RMS-Propelled "Inch-worm" concept.

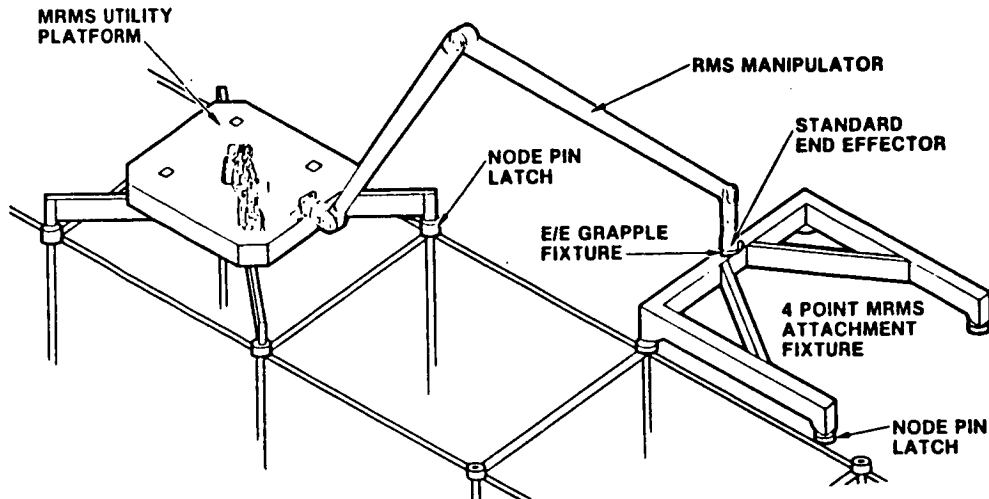


FIGURE 8- RMS-PROPELLED "INCH WORM" MSC TRANSPORTER

The requirements for a mobile transporter system were starting to be defined. Solid attachment, smooth motion, versatile functionality and low complexity driven by the number one factor- *low cost*, were the drivers that resulted in the dual push-pull transporter with on-board plane change mechanisms. The above-mentioned MSC transporter concepts seemed either too complex, poorly functional, or produced a discontinuous motion that disturbed the space station μG environment.

The Langley push-pull transporter seemed a good departure point, for it offered solid attachment to the truss at all times,- even during turning and plane change. The mechanisms were simple and could be made redundant for fail-safe operation. The transporter mass was low, and the base structure was adaptable to various configurations of MSC superstructure. The discontinuous motion produced by the drawbar assembly remained the design problem.

One has only to look at how you climb a ladder to envision how this motion can be smoothed out. You do not remove both hands from the ladder to reach for the next rung (at least not more than once). Each hand reaches for a new rung in a smooth, continuous motion as your body glides up the ladder. Your feet are doing this same motion at the other end. This concept was applied to the push-pull transporter with the drawbar split into two, separately-controllable node-pin grasping drawbars. The uneven stress of having only one node pin attached remained a problem. Figure (9) depicts the Split Dual Drawbar concept.

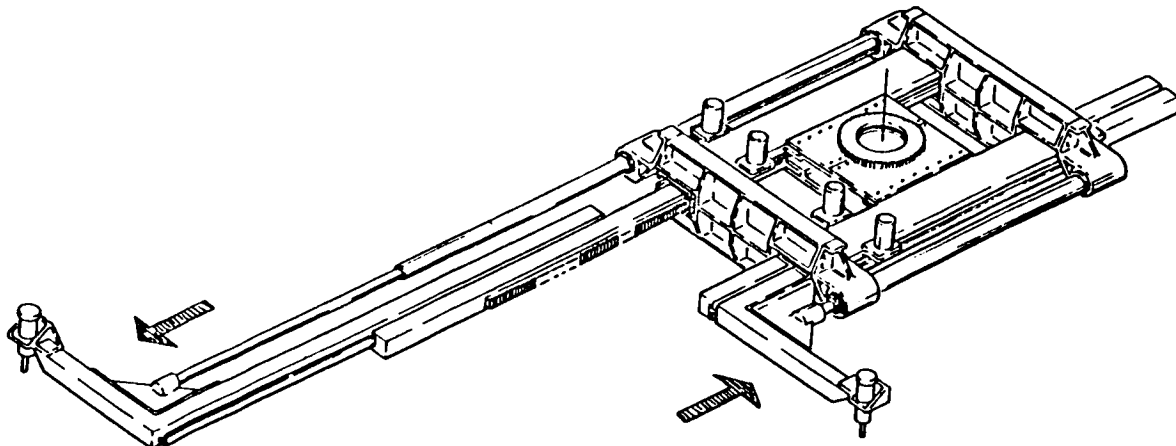


FIGURE 9- SPLIT DUAL DRAWBAR TRANSPORTER CONCEPT

The uneven stress that a single attachment point drawbar has on the truss members and the transporter body itself was the main driver to add a second dual drawbar assembly to the push-pull concept. This second assembly created a more massive transporter, but these more rigid drawbars did not twist the truss structure on traverse, and control was the same. This second drawbar assembly is placed at the other end of the transporter, with the wider bars of one fitting outside the narrower bars of the other. The dual drawbar design uses the same corner switches as the Langley concept, but this design does not require a slot in the top for a guide pin withdrawal pin to slid into. The guide pins are grasped below the node guide pin head by retractable fork assemblies. It is these retractable forks that allow the drawbars to rotate beneath the slotted rails and the guide pin heads. Plane change mechanisms mounted on the sides of the slotted rail assemblies allow plane change maneuvers at any clear point on the truss structure. Figure (10) depicts the basic dual-drawbar mobile transporter concept.

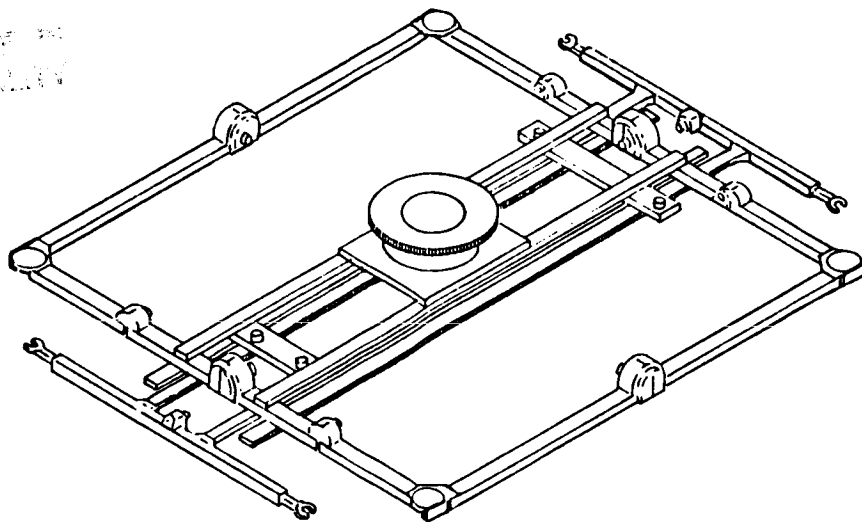


FIGURE 10- DUAL DRAWBAR PUSH-PULL MOBILE TRANSPORTER

Let's show a little more detail on how this design works and how it differs from the others. This basic design will work for an Independently-Controlled Mobile Transporter (ICMT), as well as the Mobile Transporter for the Canadian-supplied MSC System. The addition of a battery system, internal and EVA controls, a thermal control system, and a control link to the station, can create an independent transporter system able to function away from the MSC. Figure (11) depicts the functional layout of this concept.

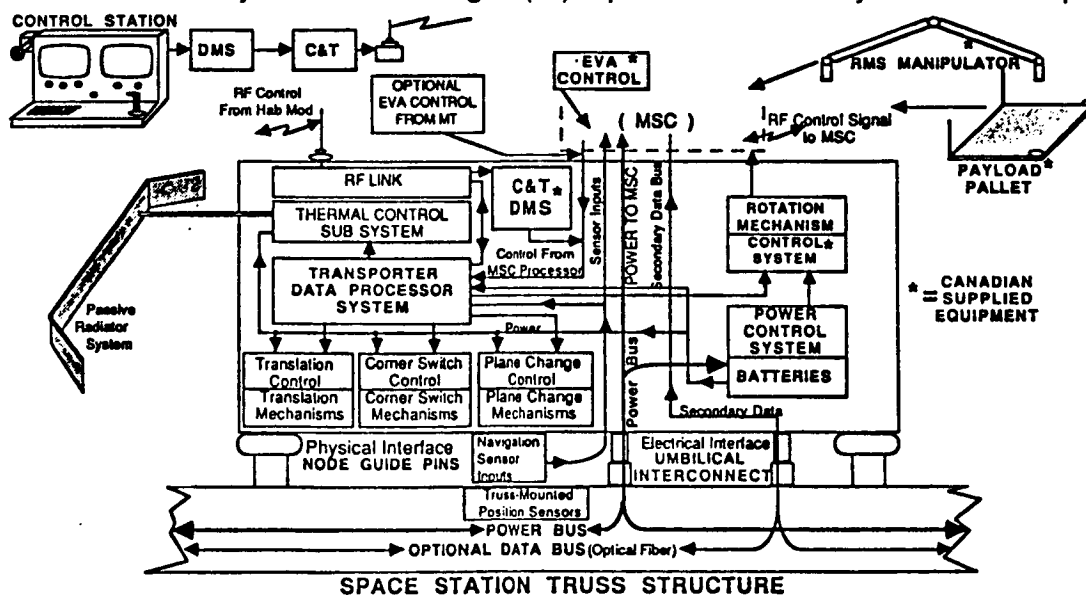


FIGURE 11- PUSH-PULL MOBILE TRANSPORTER FUNCTIONAL LAYOUT

The independent controllability feature of this mobile transporter concept will allow the MSC to function as a separate entity in manipulative operations, as well as the transporter. These two separate major subsystems of the MSC System contain the battery / PMAD systems to afford operations away from the station power bus. Charging for both power systems is normally accomplished through the Mobile Transporter umbilical connection to the station, but the MSC can be connected directly for charging or independent operations. DMS and control information is also available at these umbilical ports.

SPACE STATION DUAL PUSH-PULL MSC MOBILE TRANSPORTER CONCEPT FEATURES

Some of the features that have made the dual push-pull concept desirable are the self-contained plane change mechanisms, the dual drawbars for eliminating discontinuous motion, and the drawbar fork assemblies that allow easy rotation and simple corner switch construction. These features help bridge the gap between that basic driver, - *COST* , and achieving the goal of functionality.

Having to rely on dedicated plane change mechanisms attached to various locations on the space station was self-defeating in two aspects. The mass and resulting cost was a negative feature, and the MSC / transporter was constrained to these operations only at points where the mechanism was installed. Some of these location-dependent mechanisms included "flip platforms" to allow the transporter to drive itself over a 90° edge of the truss, and dedicated swivel node guide pins that were driven by actuators on-board the transporter. It became apparent that all plane change functions should be accomplished by an on-board mechanism. The most successful of these has been the rotating slotted rail section plane change mechanism depicted in Figure (12) and used on the dual push-pull transporter.

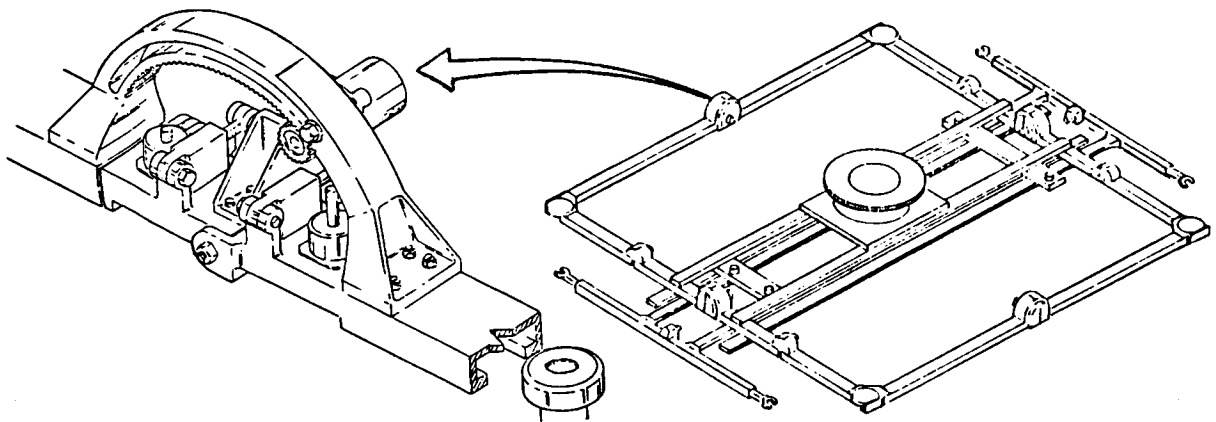


FIGURE 12- SELF-CONTAINED MOBILE TRANSPORTER PLANE CHANGE MECHANISM

Plane change is accomplished in the following manner:

- (a) At the desired point on the truss structure, the transporter makes a 90° turn maneuver. Actually, the transporter base / MSC remains in the same orientation, and only the drawbar and corner switch are rotated to the new direction.
- (b) One drawbar / fork assembly attaches itself onto the set of guide pins on the side of the truss opposite from where the transporter is to maneuver to.
- (c) This drawbar actuated by a rack-and-pinion, or similar actuator, drives the transporter halfway off the edge of the truss until the plane change mechanism straddles the other set of guide pins.
- (d) With one half of each P/C mechanism firmly locked onto the two "top" guide pins, the other half of the mechanism, with the guide pin lock jaws open, rotates 90° to enclose the other pins on the new truss face. The guide pin jaws now lock onto these pins. The transporter has not rotated at this time, - only one half of the P/C mechanism.
- (e) With the four guide pins securely attached to the P/C mechanism, the drawbar forks retract to release the other two guide pins. The drawbar retracts into the transporter.
- (f) At this point, the transporter is rotated 90° by the plane change mechanisms.
- (g) The opposite drawbar reaches out to the other two guide pins and the forks attach.
- (h) The "original half" of the P/C mechanism opens and releases the "top" guide pins, rotates 90°, and the other half of the mechanism releases the other two guide pins.
- (i) The drawbar now retracts the transporter onto the new truss face, and a turn maneuver is made to traverse on the new plane, or the maneuver is repeated for traverse on the "back" side.

In spite of the seemingly complex set of steps, this maneuver can be under total automatic sequence control, as all of the guide pins are found in the same orientation and location. Positional feedback on the actuators, and sensors in the fork grippers and plane change mechanisms can verify compliance with a pre-programmed maneuver sequence. These P/C mechanisms weigh less than 20Kg each, compared to hundreds of Kg in large dedicated platforms. Dual mechanisms, each with dual drives, and emergency manual actuation, provide redundancy for fail-safe operations. The low mass / compact design, with easy access to EVA activities, provides for on-orbit replacement in maintenance operations.

The split drawbar mechanism depicted in Figure (9) has evolved to the present concept of a forward and aft set of drawbars. A unique feature that arose from this dual configuration is the retractable forks on the drawbars. Besides allowing engagement / disengagement from the base of the guide pins, this arrangement allows the drawbar assembly to be placed below the corner switch / rail assemblies. Not only does this arrangement provide for a compact transporter, but pin engagement below the guide pin head, rather than at the top, does not require a slot in the top of the corner switch. The corner switch structure is already somewhat weakened by the slot in the bottom through which the node guide pin passes.

The feature of having a smooth, continuous motion is accomplished at the expense of having an extra drawbar assembly. Analyses have shown that a smooth acceleration to operating speed, a continuous traversing motion, and a smooth deceleration to a stop, have a dramatic effect on eliminating unnecessary μG levels. Figure (13) shows the smooth "ladder climbing" motion of the MT traverse.

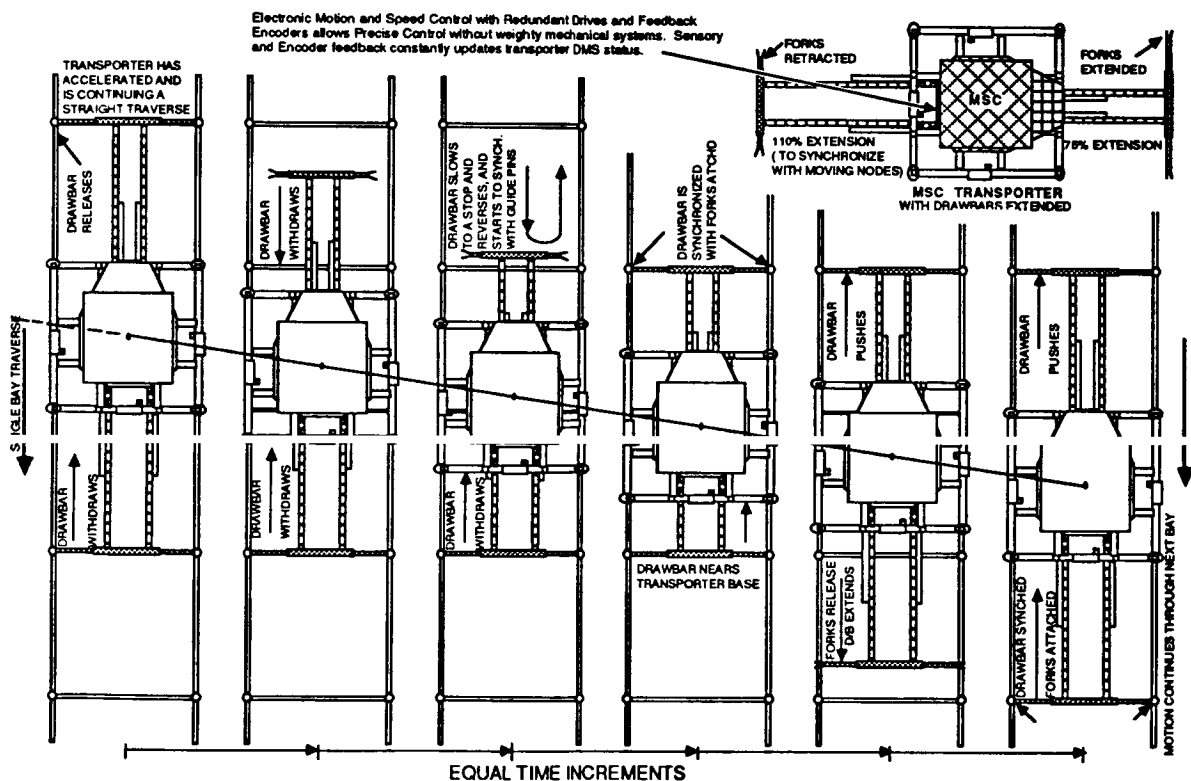


FIGURE 13- MOBILE TRANSPORTER DUAL DRAWBAR PRODUCES CONTINUOUS MOTION

Much design effort remains to create the fully-functional transporter system required for the space station. Co-ordination of the mechanical drives for synchronized motion in the traverse, interconnection of corner switch and plane change mechanisms in triple redundancy for fail-safe reliability, and the integration of a complete, self-contained transporter with the Canadian Mobile Remote Servicer for independent operations will require intense engineering efforts. Many NASA centers and contractors have collaborated to produce well thought designs to solve the manipulative and robotics requirements for the initial operational and growth configurations space stations. This paper has only touched on some of the major factors that were considered in the development of the preceeding Mobile Transporter concepts.

TELEROBOTIC WORK SYSTEM: CONCEPT DEVELOPMENT AND EVOLUTION

Lyle M. Jenkins*

The basic concept of a telerobotic work system (TWS) consists of two dexterous manipulator arms controlled from a remote station. The term "telerobotic" describes a system that is a combination of teleoperator control and robotic operation. "Work" represents the function of producing physical changes. "System" describes the integration of components and subsystems to effectively accomplish the needed mission. Telerobotics reduces exposure to hazards for flight crewmembers and increases their productivity. The requirements for the TWS are derived from both the mission needs and the functional capabilities of existing hardware and software to meet those needs. Conditions imposed by the space environment make the space telerobot different from remote operating systems in the manufacturing industry, the nuclear industry, and the offshore petroleum industry. The TWS is only one manifestation of a space robot. There are analogous concepts derived from different control options, missions, and development paths. The systems-development approach recognizes dynamic, state-of-technology progress and the need for flight tests to support ground tests in producing an operational space system.

The initial mission for development of the TWS concept was the repair and servicing of satellites from the Space Shuttle Orbiter. Potential missions include the construction of large space systems and the maintenance of these systems. The Space Station has become a particularly attractive potential application for a TWS [1]. The station size requires a number of Space Shuttle flights for construction. Extravehicular activity (EVA) by the flight crew is currently the primary mode of assembly. Assistance by a telerobot could enhance operational margins and reduce astronaut exposure to hazards. The functional capability of the TWS should be equivalent to the capabilities of an EVA astronaut in order to assume tasks that are currently designed for performance by the crew in space suits [2]. Equivalence in manipulative capability also provides for contingency backup by the EVA crewman.

Applications of any telerobot design to the space operational environment must recognize that robotic or autonomous modes will be closely monitored. The operator will intervene when circumstances become hazardous or when the robotic mode is baffled by a particular task. Nevertheless, the use of robotics is imperative for the most effective utilization of the flight crew [3]. The qualitative relationship of teleoperation to robotic

*Project Engineer, Lyndon B. Johnson Space Center, Houston, TX.

or automated performance of tasks in complexity and rate of accomplishment is illustrated in Figure 1. The objective of a smart adaptive space robot may be approached by designing for autonomous operations on simple tasks and increasing the capability to more complex tasks. An alternate approach is to use teleoperation with an inherent capability for performing complex tasks and incorporate supervisory and robotic techniques to increase the rate of performance. If a smart adaptive space robot is to be developed, evolution through teleoperation is the more conservative approach. Management regards teleoperation as a lower risk and as a potential backup to robotic performance. Teleoperation may be a slower path to a space robot because people tend to resist change and may continue to work in less productive modes. However, teleoperation evolution is a less restrictive approach than an autonomy evolution, which may require work site and task interface evolution as well.

The functions of telerobots in space are very different from the functions of terrestrial robots. Industrial robots are used in much more structured and repetitive operations. An industrial robot is highly productive when the task is well defined and the need for interaction with sensors is limited or easily characterized. The purpose of remote systems in the nuclear power industry is to preclude human exposure to an extremely hazardous environment. The adaptive potential of the human operator is used to accomplish complex and varied functions. In contrast to the conditions

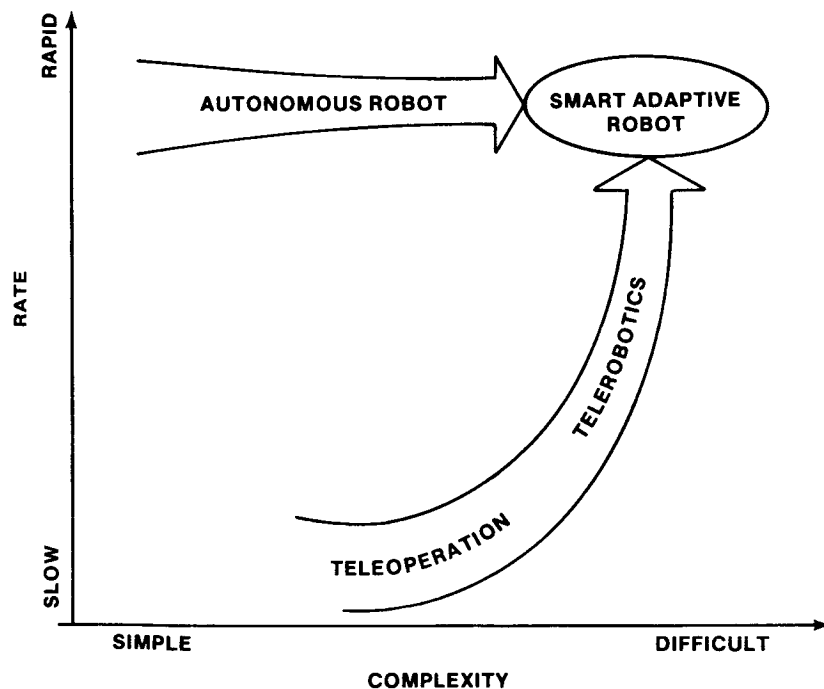


Figure 1. Robot capability development

in space robotics, operators are readily available and can be economically traded for system complexity. The remote operating vehicles in undersea applications also rely heavily on the operator's adaptive capability.

The idea for the use of TWS came from a study of the equipment needs for servicing satellites. Heretofore, EVA has been the primary resource for the performance of tasks in the repair and servicing of satellites. The highly successful Solar Max repair, the retrieval of Westar and Palopa, and the orbital refueling system demonstration confirmed the feasibility of using the Space Shuttle for in-flight maintenance of the orbiting vehicles. However, EVA by space-suited astronauts is risky and inefficient. The current flight rules require a buddy system as well as an intravehicular monitor. Also, just prior to extravehicular activity, crew members must breathe oxygen to prevent the adverse effects of the rapid decrease in air pressure. Though necessary for EVA, the breathing of oxygen and other preparations for cabin departure are nonproductive expenditures of crew time. The Space Shuttle's remote manipulator system (RMS) was designed for the deployment and retrieval of satellites, and it has no capability for dexterous tasks needed for servicing. In fact, the resolved rate control system for the RMS precludes tasks that constrain the motion of the arm. The addition of a force and moment sensor to the RMS is currently under development to provide limited RMS dexterity. The addition of small dexterous arms as an end effector for the large Shuttle arm (Figure 2) is the conceptual solution proposed by Grumman Aerospace Corporation (GAC) for enhancement of the RMS dexterity.

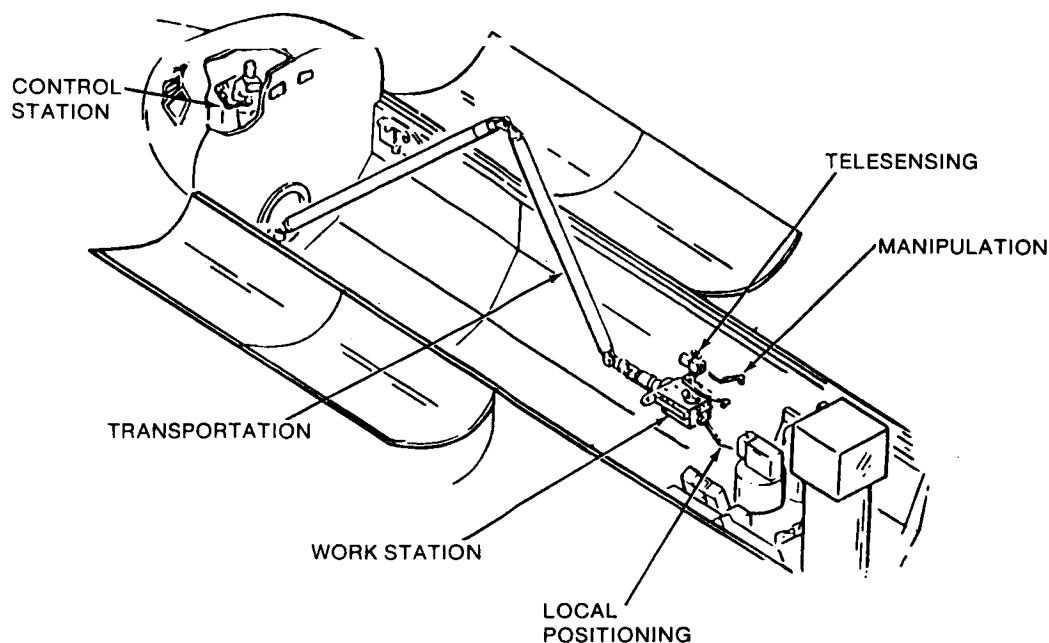


Figure 2. Definition of TWS systems

This initial concept was dubbed the "Telepresence Work System" and proposed to the Office of Aeronautics and Space Technology (OAST) as a technology development focus. During the same time, Martin Marietta Corporation (MMC) developed an analogous concept in their study of the remote orbital servicing system (ROSS) for use on the orbital maneuvering vehicle (OMV). Funding from the Office of Space Transportation Systems (OSTS) for satellite servicing equipment was applied to studies of the telepresence work system by Grumman and Martin. Subsequently, the studies were titled "Telerobotic Work System Definition Study." The basis for the name change was a recognition for the need for an evolutionary approach that would increase operator productivity. A telepresence system implies the objective of making the operator feel translated to the work site. The sensors and control modes would tend to enmesh the operator in the system. By emphasizing the telerobotic approach, the system design choices can enhance the evolution to robotic modes that expand productivity and place the operator in a supervisory capacity. The evolution from teleoperation to supervisory control to adaptive robotic control implies a capability to come back down the control scale to support robotic functions.

The contracted studies produced the telerobot concepts [4 and 5] illustrated in Figures 3 and 4. As might be expected from the EVA equivalency criteria, the resultant designs are strongly anthropomorphic.

The studies by GAC and MMC have concentrated on the satellite servicing functions and operation out of the Space Shuttle. The development plans

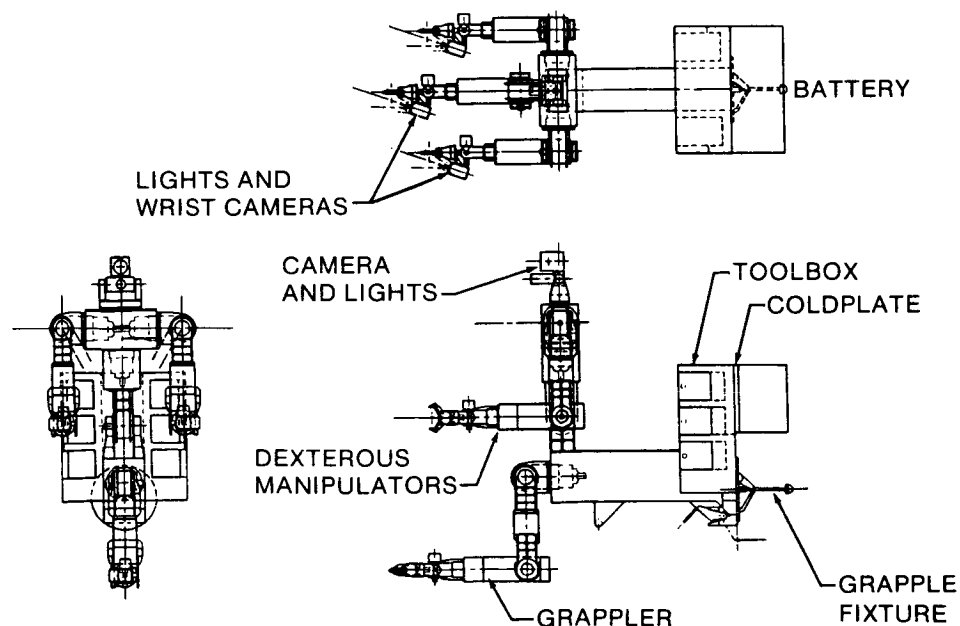


Figure 3. Grumman telerobot concept

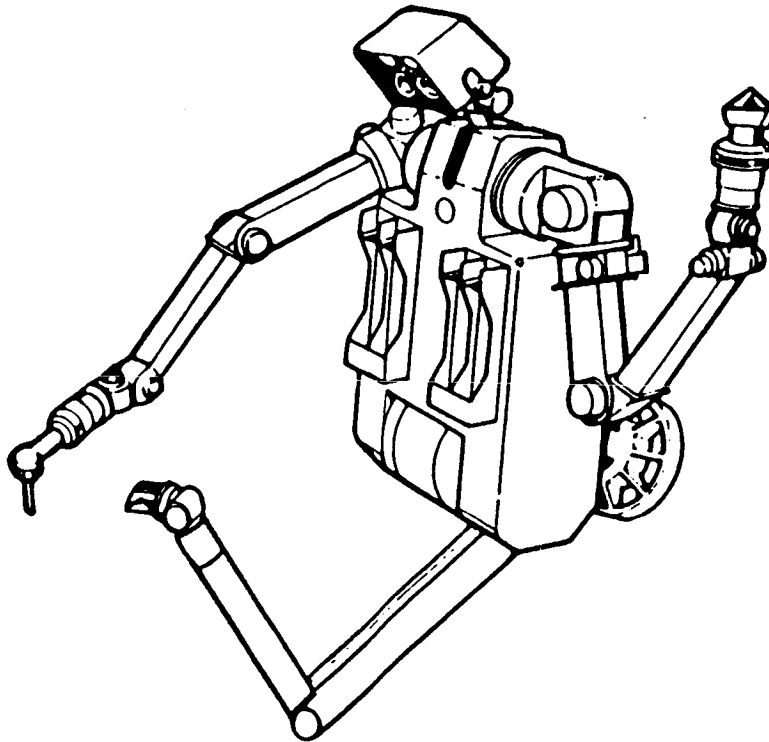


Figure 4. Martin telerobot concept

reflect the early need to demonstrate the feasibility and capability of a telerobot in these operations. However, development resources were expected to be severely limited in this mission application. Other missions were envisioned in the smart front end for the OMV and in the construction of the Space Station. Limited consideration was directed at these applications, although the functional capability to perform required tasks is little different from the satellite servicing tasks.

The development logic for the TWS is based on an evolutionary pattern. The potential development of technology can be expected to rapidly advance. Design features of subsystem modularity and robust computer capability should permit incorporation of technology enhancements with limited impact on the telerobot system. This approach is expected to be adopted for the flight telerobotic servicer program. The planning by the OAST is also consistent with the evolutionary approach for development of technology and the transfer of the technology to applications.

Much of the OAST program is concentrated in the telerobotic testbed at the NASA Jet Propulsion Laboratory (JPL)(Figure 5). Rather than a specific implementation of a set of ground test hardware, the testbed serves as a systems laboratory. The goal is to provide the necessary environment for resolving systems issues. There has been criticism that the equipment is

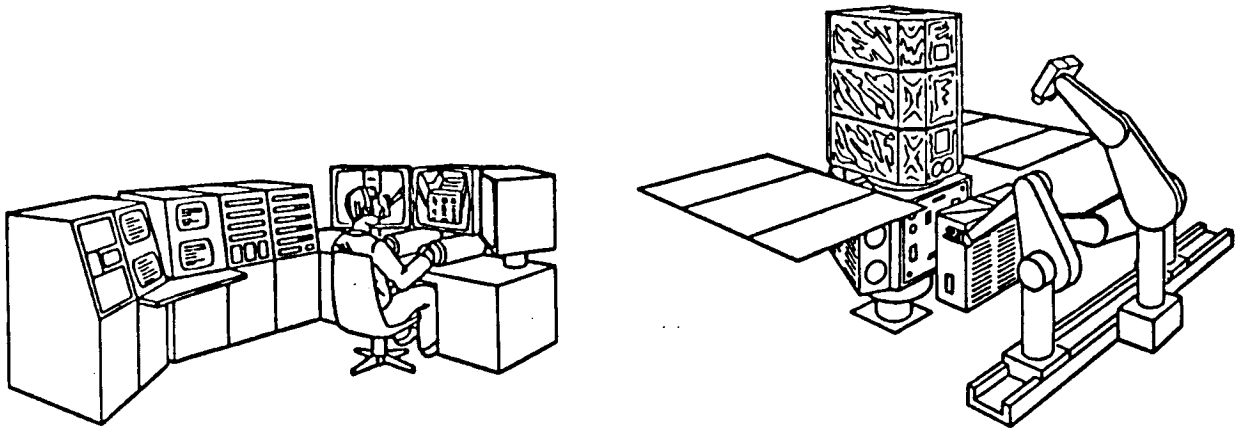


Figure 5. Telerobot demonstrator concept

largely state of the art. This view does not recognize the system-level considerations that must be examined in the light of the most advanced technology. Perhaps a valid criticism is the lack of zero-g simulations at JPL. Other facilities in NASA exist for effective simulation of the space environment, and these are being integrated into the overall program. Examples are the flat floors and neutral buoyancy facilities at Lyndon B. Johnson Space Center and Marshall Space Flight Center. Computer simulations are another way of evaluating operations. The validity of the ground simulations will eventually need correlation through test in the flight environment.

The categories for flight tests are: research, calibration of ground simulations, and development testing. Also, flight demonstrations may prove the technology ready for space applications and demonstrate task performance for specific missions. One aspect of research concerns human interaction with the displays and controls. The operation of controllers in zero-g depends on the type of control, the actuation forces, and the precision of positioning and movement relative to the axis system. To establish design parameters, researchers must evaluate the complex interaction of the controller with the physical characteristics of the manipulator arms. Force reflection is generally acknowledged to require less training in the performance of manipulation tasks on Earth. This has yet to be established for space operations. It will undoubtedly be dependent on the restraints of the operator. The operator's perception of the displays of various sensors may be biased by the environmental conditions.

It is generally recognized that the mechanisms used in manipulators and end effectors will react differently without the force of gravity either to bias the backlash in joints or to reduce the response to input forces. The mechanisms of the manipulator have critical interfaces in both directions, on the task side and on the operator/control side. At the task end, the objects being handled are not positioned and oriented by gravity. Assembly

tasks involving loose parts will require significant attention to control and positioning. There must be tethers or other positive attachments to preclude parts drifting off into space.

On the operator side of the system, the zero-g effects present a number of interactions relating mostly to the teleoperator mode of control. In the weightless environment, even the slightest force demands a response. For a force-reflection-type controller significant restraints will probably have to be provided. Restraints for a rate-type-controller may be as simple as guards or arm rests near the controller. The interactions between restraints and control inputs is a critical issue which needs additional testing.

Mechanisms perform differently in a zero-g environment. Backlash in joints and actuators may produce uncertainties that affect task performance. To take full advantage of the low loads on manipulator arms, the space design will be lighter and more flexible than analogous earthbound arms. The mechanisms and actuators also will be exposed to severe temperature extremes. Rejection of the heat generated by the actuators is not a trivial problem. Active thermal control systems are undesirable, leaving radiation of a duty cycle variable load by radiation as the prime mode. Heaters to maintain the lower limits of the performance envelope reduce available power and reliability. Interaction with the task will be particularly difficult to simulate on the ground.

A significant challenge in the development of a space telerobot will be to predict its effectiveness in an environment that combines a vacuum and a lack of gravity. The principal resource for such experiments is the Space Shuttle. However, because of the reduced number of Space Shuttle flights, it is difficult to obtain a listing on the payload manifest for this type of experimentation. Interfaces in the Orbiter cabin and the payload bay will limit the type and number of tests that can be used to validate ground simulations and to resolve several issues that are not amenable to simulation.

The development of a space telerobot represents a valuable resource in the performance of tasks in the unstructured and hazardous environment of space. As telerobotics proves itself in limited space applications, research will be initiated to expand its use, and technologies will develop rapidly to accommodate changing requirements. As a result of space pioneering, applications of telerobotics will extend to personal service functions for disabled and aged people and to hazardous situations such as are found in construction and agriculture.

REFERENCES

- [1] Jenkins, L.; and Olsen, R.: Remote Operating Systems for Space-Based Servicing. ASME Conference on Computers in Engineering (Las Vegas, Nev.), Aug. 1984.
- [2] Jenkins, L.: Telerobotic Work Systems Concepts. AIAA/NASA Symposium on Automation, Robotics and Advanced Computing for the National Space Program (Washington, D.C.), Sept. 1985.
- [3] Holcomb, L.; Larson, R.; and Montemerlo.: Overview of the NASA Automation and Robotics Research Program. AIAA/NASA Symposium on Automation, Robotics and Advanced Computing for the National Space Program (Washington, D.C.), Sept. 1985.
- [4] Telepresence Work System Definition Study. Grumman Aerospace Corporation, Contract NAS 9-17229, 1985.
- [5] Telepresence Work System Definition Study. Martin Marietta Corporation, Contract NAS 9-17230, 1985.

TRACTION-DRIVE, SEVEN-DEGREE-OF-FREEDOM TELEROBOT ARM:
A CONCEPT FOR MANIPULATION IN SPACE*

D. P. Kuban and D. M. Williams**

ABSTRACT

As man seeks to expand his dominion into new environments, the demand increases for machines that perform useful functions in remote locations. This new concept for manipulation in space is based on knowledge and experience gained from manipulator systems developed to meet the needs of remote nuclear applications. It merges the best characteristics of teleoperation and robotic technologies. This paper summarizes the report of a study performed for NASA Langley Research Center.¹ The design goals for the telerobot, a mechanical description, and technology areas that must be addressed for successful implementation will be presented and discussed. The concept incorporates mechanical traction drives, redundant kinematics, and modular arm subelements to provide a backlash-free manipulator capable of obstacle avoidance. Further development of this arm is in progress at the Oak Ridge National Laboratory.

INTRODUCTION

The national commitment to establish a permanent operating space station signifies that man has progressed beyond exploration of space to habitation in space. As the Space Station Program develops, remote manipulation will play a critical role in the successful use of space. Remote manipulation advances will increase the domain where useful work can be performed (e.g., polar orbits pose health hazards for extravehicular activity), and automated manipulation will reduce manpower requirements for construction and routine operations in space. As manipulators are developed for space, it is envisioned that the advanced mechanical, sensory, and control technologies generated to support this action will fertilize industrial robotic applications and improve terrestrial productivity. With these useful results in mind, the information presented here was developed to address the technical aspects of designing a manipulation system that could expand with the advances in sensory and control technology that are certain to occur within the next decade.

*Research sponsored by NASA Langley Research Center under Interagency Agreement Number 40-1553-85 with Martin Marietta Energy Systems, Inc.

**Martin Marietta Energy Systems, Inc., Oak Ridge, Tennessee

DESIGN GOALS

The Shuttle Remote Manipulator System (RMS) has demonstrated its usefulness in the capture, repair, and deployment of satellites. The large reach of this system makes it suitable for manipulation of sizable structures and objects in the microgravity of space. Smaller, more dexterous manipulation systems will be required to perform satellite maintenance, some aspects of space structure construction, and vehicle refueling operations. The purpose of developing a telerobotic work package for space application is to increase astronaut and system safety, productivity, and flexibility. Astronaut risks increase as the demand for extravehicular activities (EVA) time increases for large projects such as space station assembly, operation, and maintenance. A telerobotic remote handling system can accomplish many tasks in the time required for an astronaut to "breathe down" to prepare for EVA tasks. Telerobotic systems also make round-the-clock operations possible, while the operating crew remains safe within the orbiter or space station.

The focus of this effort is the development of a manipulator system capable of performing a range of manipulation tasks presently accomplished by astronauts during EVA. The manipulation capabilities of astronauts are significantly reduced as a result of the protective suit and its pressurization. In fact, the dexterity of the human hand is so diminished that an entire set of special tooling has been developed through the years for use in EVA tasks. The suited human arm, while bulky, does retain its kinematic redundancies, thereby allowing the arm to avoid obstacles and approach the worksite in a number of ways. The suited astronaut does have sensory and judgemental capabilities as yet unmatched in machines. The ability to deal with the unexpected and unanticipated is the strongest attribute of the EVA astronaut, and one which needs to be preserved in the space telerobot through transparent operator interfacing.

Several general performance goals result from the desire to provide EVA equivalence in a system suitable for space application. These are summarized below:

1. Force-reflecting replica master teleoperated control for demanding operations,
2. Sensory-driven robotic operations for anticipated events,
3. Redundant kinematics for local obstacle avoidance,
4. Dual arm system,
5. High bandwidth communications link with local intelligence,

6. Position or force control,
7. Graphic menu interface for operator interaction, and
8. Reliable and modular for rapid repair or reconfiguration.

Two fields of related technology are available to establish benchmarks for technical feasibility: Teleoperator systems have been used for many years to allow humans to remotely manipulate hazardous materials, and industrial robotics have recently experienced rapid expansion resulting from advances in control technology. These two technologies utilize different design approaches optimized for their respective modes of operation. Table 1 summarizes the key elements of these manipulation technologies and provides detailed performance goals for the space telerobot.

PAST REMOTE MANIPULATION EXPERIENCE

Over the past several years, the U.S. Department of Energy Consolidated Fuel Reprocessing Program has sponsored a world-leading teleoperation development program. Initially, a TeleOperator Systems SM-229 teleoperator was employed in the Remote System Development Facility (RSDF) for human factors experiments and special remote equipment developments.² A second system using the M-2 teleoperator from the Central Research Laboratories of Sargent Industries was integrated into the Remote Operation and Maintenance Demonstration (ROMD) facility.³ This system was used successfully to remotely operate a Fairchild satellite refueling coupling (see Fig. 1). Total task time was about 35 min with minimal practice training, compared with about 15 min for suited astronaut water-tank simulations. Teleoperation task time would be greatly reduced if the coupling was redesigned for remote operation. A third system, the recently developed Advanced Servomanipulator (ASM) system, designed to improve reliability and maintainability through gear drives and modular construction, is operating in the Advanced Integrated Maintenance (AIMS) Facility.⁴

These efforts have produced extensive information and experience of great value in developing new telerobotic systems. Some of the capabilities that have been developed include control techniques such as special compensation algorithms, and adaptive gain, as well as prediction of force-reflection thresholds and backdrivability characteristics. Equally important are the effects of different kinematics and different configurations on work task efficiency and obstacle avoidance. The space telerobot applies this experience to the general problems of space teleoperations.

Table 1. Space Telerobot Criteria Development

Good force-reflecting teleoperator	Good industrial robot
End effector speed 1 m/s Friction 1 to 5% of capacity (at expense of increased backlash) Medium to low backlash	End effector speed 1 to 2 m/s Friction 30 to 100% of capacity No backlash (at expense of increased friction)
Replica master control 25 to 50 mm deflection at full load 6 DOF and end effector	Teach pendant, keyboard Minimal deflection at full load (0.25 to 1 mm) 4 to 6 DOF and end effector
Bilateral position-position control for force reflection with man in the loop Relatively low inertia for minimum fatigue Kinematics approximately manlike	Force feedback with 6-axis end effector sensing High inertia for stiffness Kinematics mission dependent
Accuracy and repeatability not important 1:4 to 1:10 capacity/weight ratio Universal end effector	Accuracy and repeatability very important 1:10 to 1:40 capacity/weight ratio Interchangeable end effectors



End effector speed 1 m/s
Friction close to teleoperator, much lower than robot
Backlash close to robot, much lower than teleoperator

Replica master control preferable, joysticks and autonomy research possible
0.5 mm deflection at full load
7 DOF and end effector

Bilateral position-position control for force reflection
Low inertia compared to robots
Manlike kinematics for dexterity in teleoperation

1:4 capacity/weight ratio
Universal interface for NASA end-effector research
Capacity of 9 kg continuous, 14 kg peak

Arm cross section to reach inside 150 mm x 150 mm opening

THE TRACTION-DRIVE REDUNDANT KINEMATIC TELEROBOT

The kinematics ultimately determine the dexterity of the manipulator and dictate its mechanical complexity. Most available industrial robotic systems are composed of six or fewer degrees of freedom for position and orientation of the end effector. Complete position and orientation within the reach of a manipulator requires at least six degrees of freedom, three for positioning (usually associated with the shoulder and elbow), and three for orientation (usually associated with the wrist). The major goals for the kinematics of this new telerobot were EVA-equivalent operation, elimination of midrange singularities, and large volumetric coverage. To approach EVA-equivalent operation, the kinematics should be about 100 to 150% human size and provide local obstacle avoidance. This second feature is most easily accomplished by adding a redundant joint. More detailed justifications for the redundant kinematics are given by Hollerbach.⁵ The additional degree of freedom should be grouped with the positional joints to provide positional obstacle avoidance similar to the capabilities of the human arm. It should also be accomplished by simple mechanical methods. Achieving kinematic goals with a highly complex mechanical system would not be a successful solution. A more appealing solution would be simple enough to allow repeating the mechanism at each joint. This would allow using modular subassemblies, significantly reducing design and fabrication cost.

The results of these goals are a seven degrees-of-freedom arm mechanism that provides kinematic redundancy for obstacle avoidance. The telerobot is shown in Fig. 2 performing a satellite refueling operation (as demonstrated with the M-2) from the shuttle. This arm is constructed of three identical pitch/yaw joints which combine to provide shoulder, elbow, and wrist joints. An output roll at the wrist completes the system. This arrangement results in a kinematic structure whose inverse kinematics are easily found for path planning, provided that assumptions on the elbow location are made.⁵ The pitch/yaw joints are derived from the technology that was developed in the ORNL Advanced Servomanipulator (ASM) wrist (Fig. 3). The ASM wrist uses a triple-nested differential that provides three orthogonal, intersecting rotary axes. A simple manipulator element which results from using only the pitch and yaw motions is the basis for the replicated subassembly.

Comparison of the resulting volumetric coverage (see Fig. 4) shows that this arrangement offers extended reach over typical six degrees-of-freedom manipulators. The implementation limits singularities to the extremities of the motion range. In this position, the joints are operated at right angles to each other, a very unusual and awkward stance, therefore these singularities do not limit operations.

The telerobot can be reconfigured to approach the worksite from a number of different directions. Four standard working orientations are shown: anthropomorphic, over the wall, sidewinder, and under the table (Fig. 5). With this diversity of stances (multimorphic), obstacles in any position can be avoided. Additional joints can be attached or extending segments can be used to reconfigure the arm for exceptional work site constraints. Additionally, the reorientation of the lower arm allows presentation of the wrist in optimal manners for control of forces generated by the arm on the worksite.

Each joint assembly consists of a differential drive mechanism, two servomotors with speed reducers, two torque sensors, and two encoders. The speed reduction ratio through the differential is 3.75 to 1. All items are totally enclosed in a aluminum housing, as shown in Fig. 6, with outside dimensions of 430 mm long, 100 mm wide and 100 mm high. The assembly is estimated to weigh 12 kg. The most significant advantages of this mechanical system are low backdrivability, smoothness of operation, high stiffness, simplicity, zero backlash, built-in clutch protection, and output position encoding.

The differential drive mechanism has two inputs and two outputs that rotate about orthogonal axes. Force transmission through the differential drive mechanism is accomplished by traction drives. Unlike force transfer through gear teeth which generate torsional oscillation as the load transfers between teeth, force transfer through traction is inherently smooth and steady without backlash and relatively stiff in comparison.⁶ The elements of this traction differential drive can be seen in Fig 7. Two driving rollers provide input into the differential. A significant advantage in this setup is that each driven roller is required to transmit only one-half of the total torque necessary to make a particular motion. These rollers interface with two intermediate rollers which in turn drive the pitch/yaw roller about the pitch and yaw axes. The axis about which the pitch/yaw roller rotates depends upon the direction of rotation of the driving rollers. The pitch/yaw roller is driven about the pitch axis when the driving rollers rotate in opposite direction. When both driving rollers are rotated in the same direction, the pitch/yaw roller is driven about the yaw axis. The driving rollers and pitch/yaw roller are equipped with a belleville spring preload mechanism to ensure proper traction. The belleville spring preload mechanisms apply thrust loads on the driving rollers and pitch/yaw roller. This thrust load produces the normal load between the rollers necessary to provide adequate traction to transmit the required torque.

The rolling surfaces will be lubricated with traction fluids developed by NASA Lewis Research Center. These lubrication media will vary for space applications from those used in ground-base applications.⁷

The location of motors and the transmission of torque is a design consideration that ultimately affects system performance. The first design choice is between localized and centralized positioning of actuators. Centralized actuation minimizes the mass and inertia of the moving arm members, but it requires many linkages to transmit torque from the motor to the joint output. Centralized actuation has been used on most teleoperator systems for earth operations (Central Research Laboratories Model M-2, TeleOperator Systems SM-229, Oak Ridge National Laboratory ASM) to minimize inertia and reflected loads in these force-reflecting systems. In the microgravity environment of space, the mass of joint members does not place a continuous load on the preceding joints. Localized actuation reduces torque transmission elements and permits electrical rather than mechanical modularity at the expense of some increase in system inertia. Many robotic systems are constructed in this manner (the PUMA is the most recognized). For modularity and simplicity in a microgravity environment, localized actuators were selected.

Speed reduction and transmission of torque from motor to joint output affects the linearity of position and torque control as well as the reliability of the manipulator. The design choices for speed reduction/torque increase include direct-drive motors, planetary gearing, harmonic drives, and traction drives. Direct-drive motors do not provide a geometrically satisfactory alternative due to the large size necessary for the torque ranges required. Planetary gearing is compact, but suffers from backlash whose effects are difficult to control in a microgravity environment. Harmonic drives eliminate the backlash problem, but they inject a nonlinear torque ripple into the drive train as a result of their method of speed reduction. Traction drive reducers provide backlash-free and torque ripple-free speed reduction, and have been developed for space applications.

A commercially available planetary gear reducer has been selected to provide a speed reduction of 30:1, which permits backdrivability with a low force-reflection threshold. In future iterations, this reducer would be specially designed to meet the necessary requirements for space application. The performance characteristics, such as speed and load limits, can be varied simply by changing the reduction ratio of this reducer. Brush-type dc servo motors power the differential mechanism as shown in Fig. 6. These motors drive through speed reducers and torque sensors. The motors used are Inertial Motors Corporation Model M17B. Torque sensors used are GSE Corp. rotating torque transducers (Model 2025). Renco, Inc., optical encoders (Model R-60) are used for position information. Future developments could incorporate a precise Inductosyn for position encoding, but one is not readily available in the size necessary. These sensors provide the control system signals indicating the payload weight and location. Encoders

are located on the pitch and yaw axes to maximize accuracy. By locating these encoders directly at each joint axis, the possible traction slip through the differential rollers will not affect the positioning characteristics.

The joint assembly will be fabricated using common shop practices and tolerances. The traction rollers will be fabricated from high quality case- or through-hardened gear or bearing steel such as AISI 440C. The rolling surfaces will be polished to a 4-rms finish to ensure a long service life. The housing will be formed from an aluminum alloy, such as AISI 6061-T6, into a closed tubular cross section to provide minimum weight and maximum stiffness.

Cabling provisions have been made to eliminate use of external pigtailed and connectors. These provisions are illustrated in Fig. 6. A through passage within the differential mechanism contains the cabling arrangement. This cabling arrangement consists of a flat cable bundle, wound in two coils and positioned about the pitch and yaw axes within the through passage. These coils accommodate rotations about both the pitch and the yaw axes. The cabling arrangement is also equipped with electrical connectors positioned at each mounting interface. These connectors engage and disengage automatically as the joints are attached and detached.

The wrist roll mechanism is illustrated in Fig. 8. This mechanism has a motion range of $\pm 180^\circ$, a maximum velocity of 9 rad/s, and torque capacity up to 35 N·m. Its mechanical interface will accommodate many end effectors and incorporates a quick connect/disconnect attachment method similar to that on the ASM. Each end effector module will be modified or designed to be replaceable from the wrist. This capability also allows direct attachment of special tools to the wrist without using the end effector. Electrical connectors are also mounted in each interface surface. These connectors would engage and disengage automatically as the end effectors are attached and detached.

Each joint, weighing only 12 kg, has been designed to carry a 14 kg payload at a distance of 0.37 m from its orthogonal axis. The maximum no-load speed at this distance is 1.3 m/s. The arm's total reach using three identical joints of minimum length (400 mm) is 1.1 m when measuring from the shoulder pitch axis to the center of tong's grip. In this outreached position, the arm will comply under a 14 kg payload with a maximum deflection of 0.5 m while maintaining a total positional accuracy of ± 1.0 mm.

Computer-Aided Three-Dimensional Interactive Applications (CATIA) is a three-dimensional modeling package developed by Dassault Systems (France) and marketed by IBM. It was used to develop a kinematic model of the

telerobot. Figures 9 and 10 are CATIA plots of the model. Some of the CATIA modules used to develop these plots are kinematics, robotics, and solids.

The arm will be counterbalanced to simulate 0-g by using a single mass of approximately 20 kg. The mass is attached mechanically to the arm through an innovative arrangement of a four-bar linkage that counterbalances both shoulder and elbow joints. This arrangement has been chosen to minimize the additional inertia. The wrist will be electrically counterbalanced to further reduce the system's total inertia.

CONCLUSIONS

A concept for a space telerobot was developed for NASA Langley Research Center. This concept incorporates modular, replicated manipulator elements to provide redundant kinematics in a package approximately the size of a suited human. This telerobot will employ traction drive technology to eliminate backlash and reduce torque nonlinearities associated with available speed reduction mechanisms. The arm will be capable of teleoperated or robotic operation for maximum operational flexibility and reduced manpower.

Construction and maintenance of a space station is a significant challenge. The technology to augment human activities in this environment is available but not properly configured for the tasks at hand. Efforts toward development of an EVA-equivalent manipulator will return benefits for generations to come, both in space and on earth. A successful space manipulation system will expand the productivity and capabilities of man in this remote, challenging environment.

REFERENCES

1. H. L. Martin et al., "Recommendations for the Next-Generation Space Telerobot System," Oak Ridge National Laboratory, ORNL/TM-9951, March 1986.
2. M. M. Clark, W. R. Hamel, and T. V. Draper, "Human Factors in Remote Control Engineering Development Activities," 31st Conf. on Remote Systems Technology, Detroit, 1983.
3. J. N. Herndon et al., "The State-of-the Art Model M-2 Maintenance System," presented at the National Topical Meeting on Robotics and Remote Handling in Hostile Environments, American Nuclear Society, Gatlinburg, Tennessee, April 23-27, 1984.

4. D. P. Kuban and H. L. Martin, "An Advanced, Remotely Maintainable, Force-Reflecting Servomanipulator Concept," presented at the National Topical Meeting on Robotics and Remote Handling in Hostile Environments, American Nuclear Society, Gatlinburg, Tennessee, April 23-27, 1984.
5. John M. Hollerbach, "Optimum Kinematic Design for a Seven Degree of Freedom Manipulator," MIT Artificial Intelligence Laboratory, Cambridge, Massachusetts, 1983.
6. Stuart H. Loewenthal, Douglas A. Rohn, and Bruce M. Steinetz, "Application of Traction Drives as Servo Mechanisms," presented at 19th Aerospace Mechanisms Symposium, May 1985.
7. Rothbart, Editor, Mechanical Design and Systems Handbook-1985, Loewenthal, Zaretsky, Traction Drives, Chapter 34, 1985.

ORIGINAL PAGE IS
OF POOR QUALITY

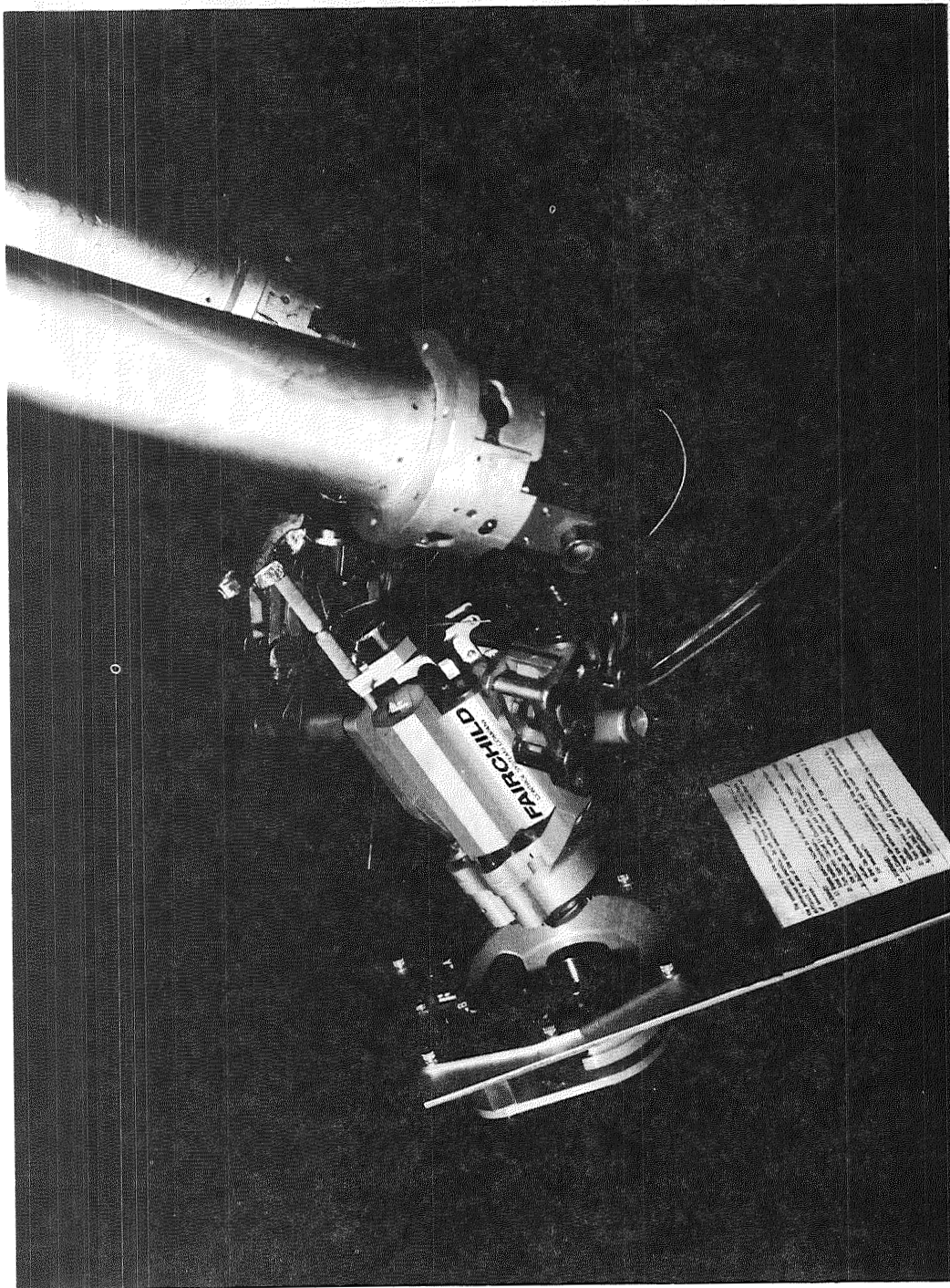


Fig. 1. N-2 operating Fairchild satellite refueling coupling

ORIGINAL PAGE IS
OF POOR QUALITY

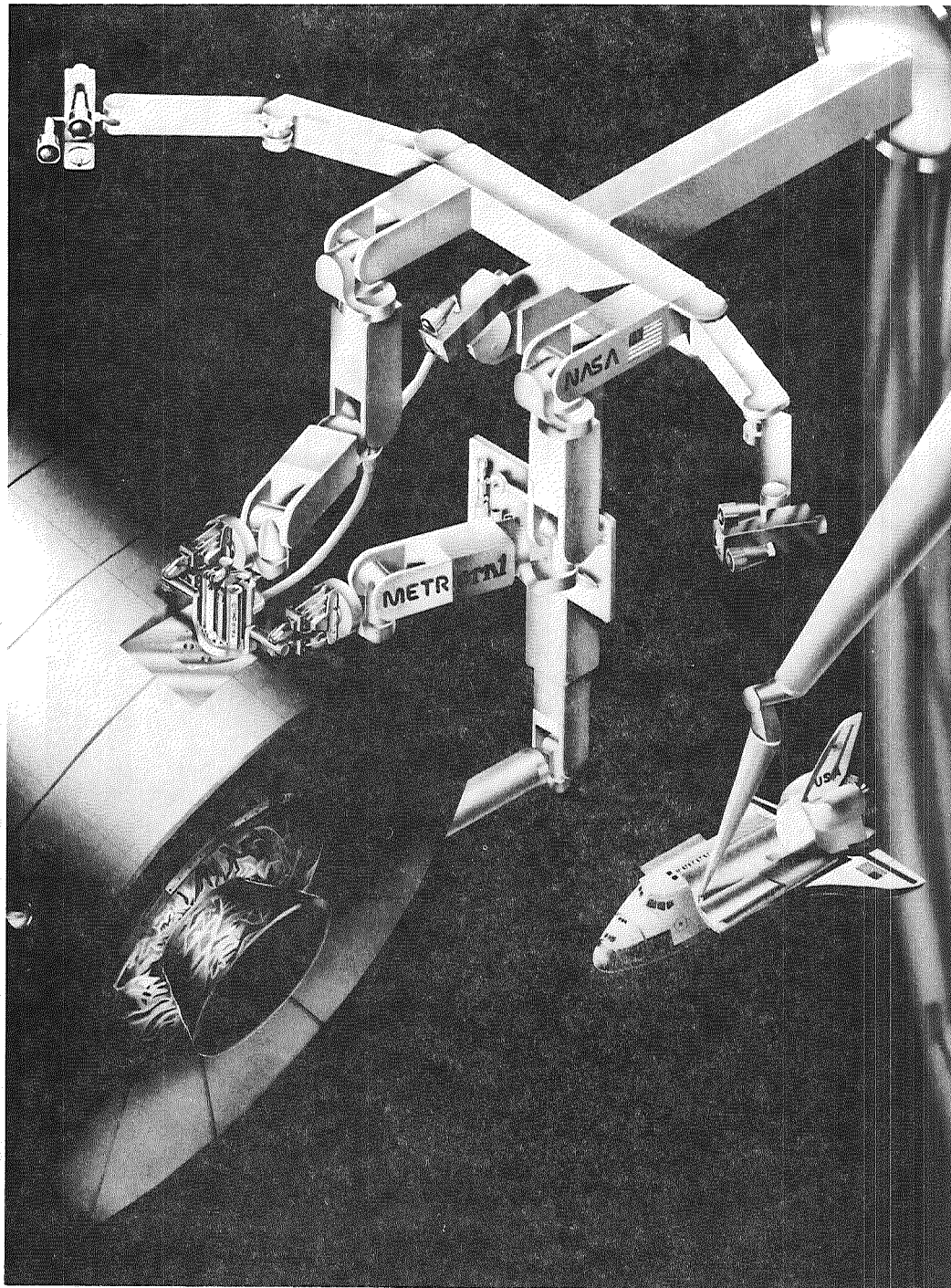


Fig. 2. Telerobot refueling satellite

ORIGINAL PAGE IS
OF POOR QUALITY

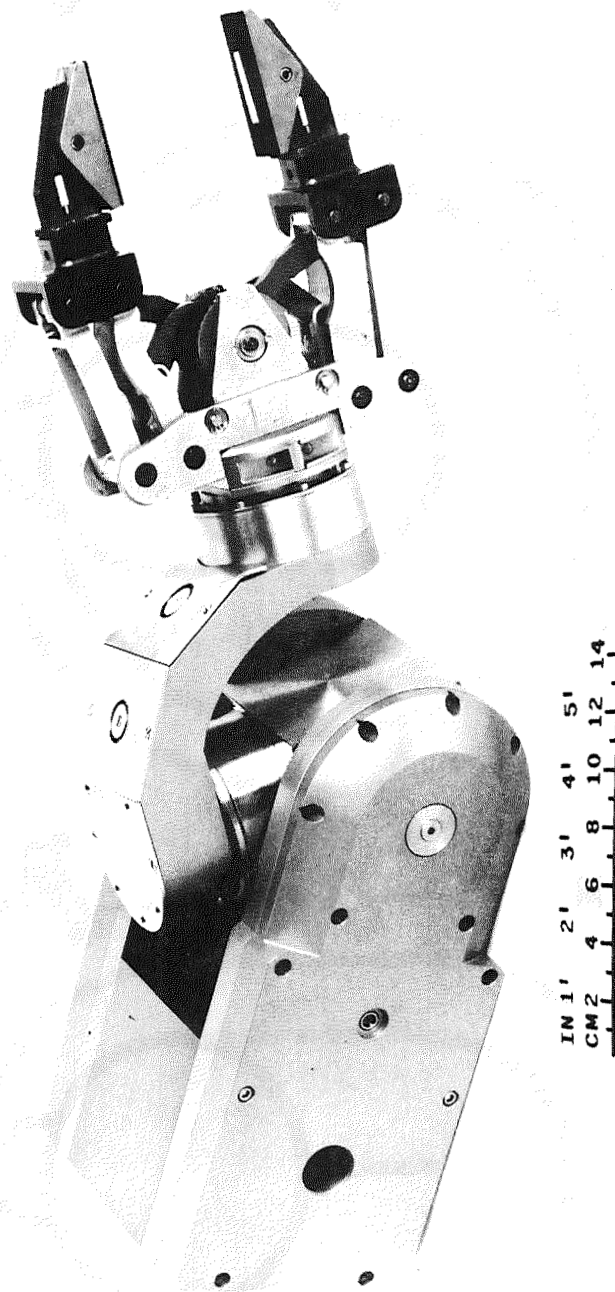
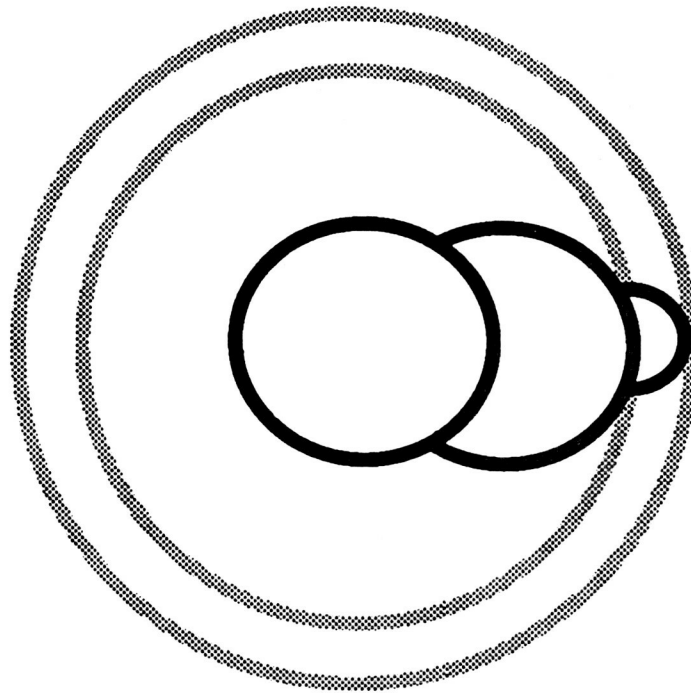


Fig. 3. ASH four degrees-of-freedom wrist

7 DOF



ASM

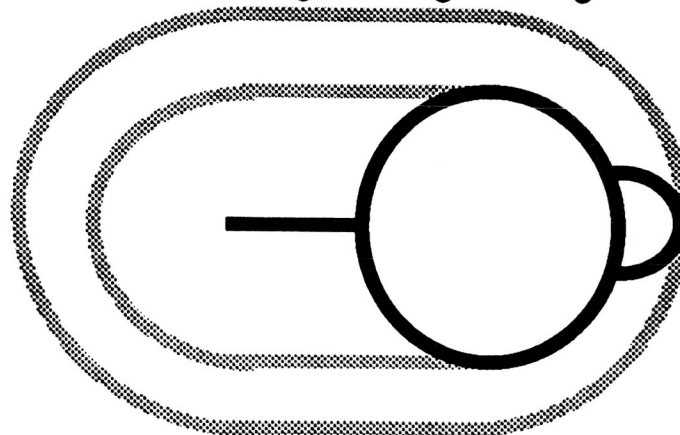


Fig. 4. Comparison of volumetric coverage: 7 DOF telerobot and ASM

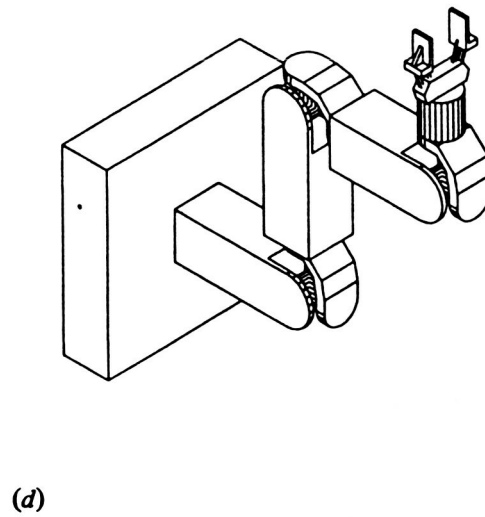
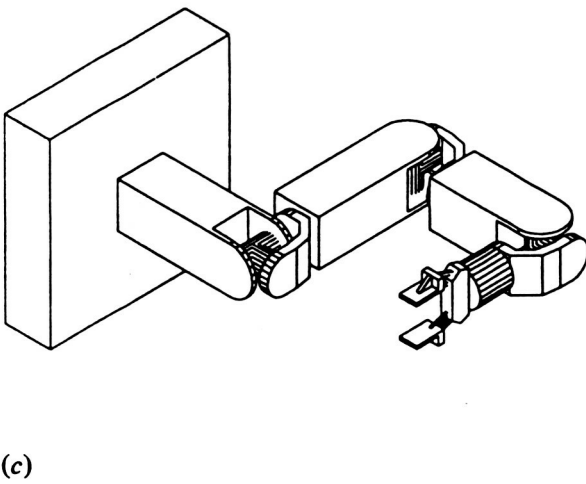
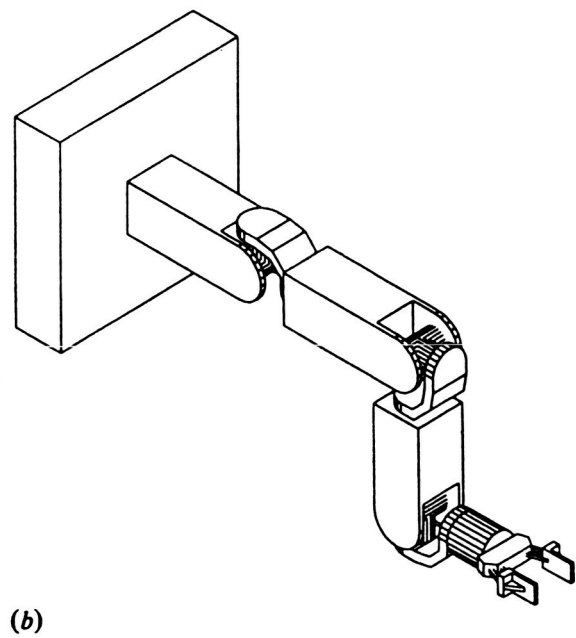
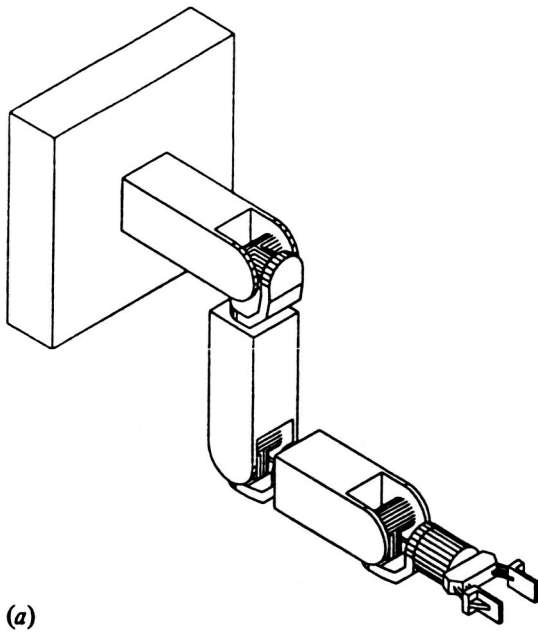


Fig. 5. Examples of kinematic dexterity and active reconfigurability:
(a) anthropomorphic, (b) over the wall, (c) sidewinder, and
(d) under the table

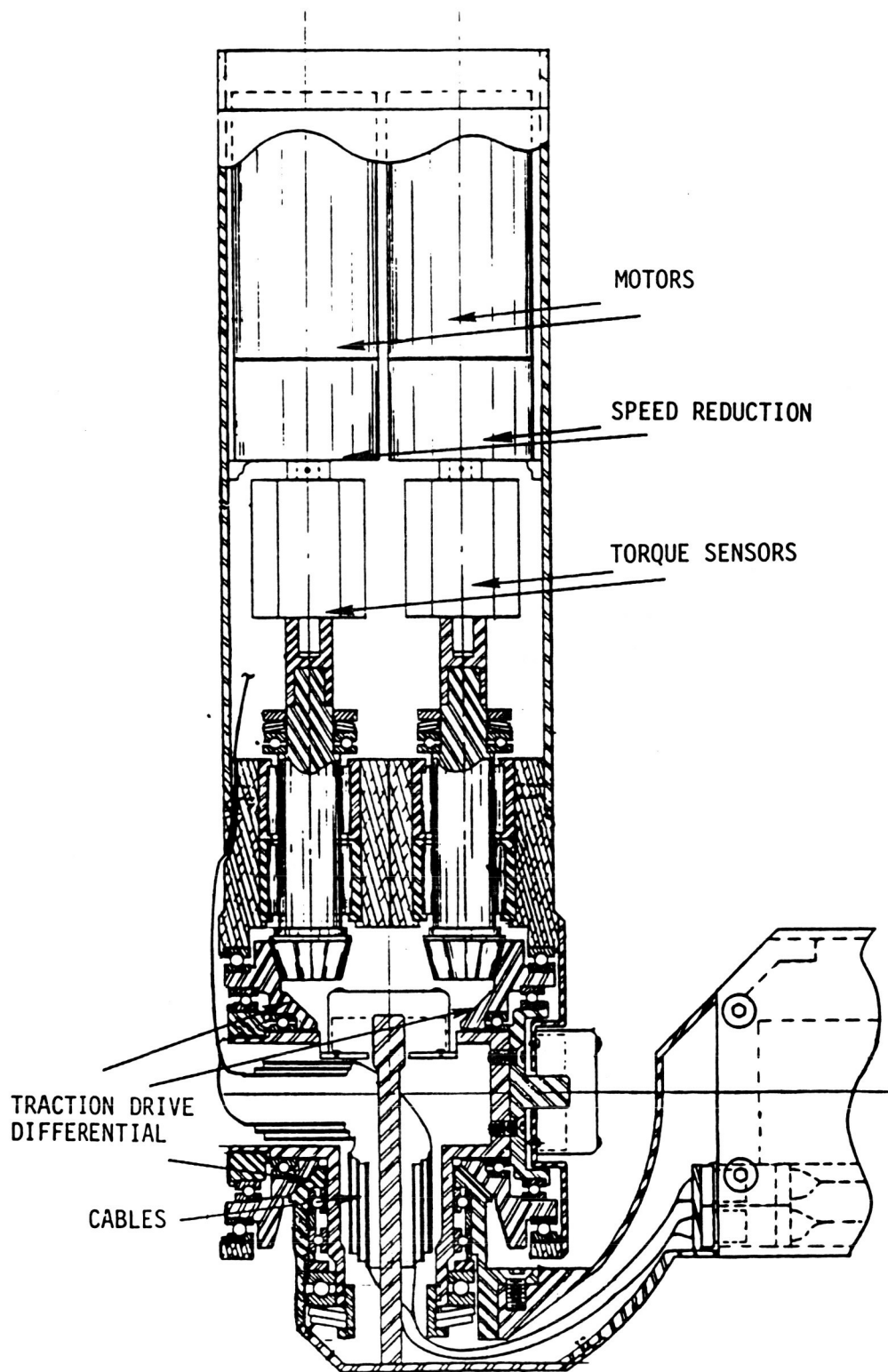


Fig. 6. Telerobot typical joint assembly

ORIGINAL PAGE IS
OF POOR QUALITY

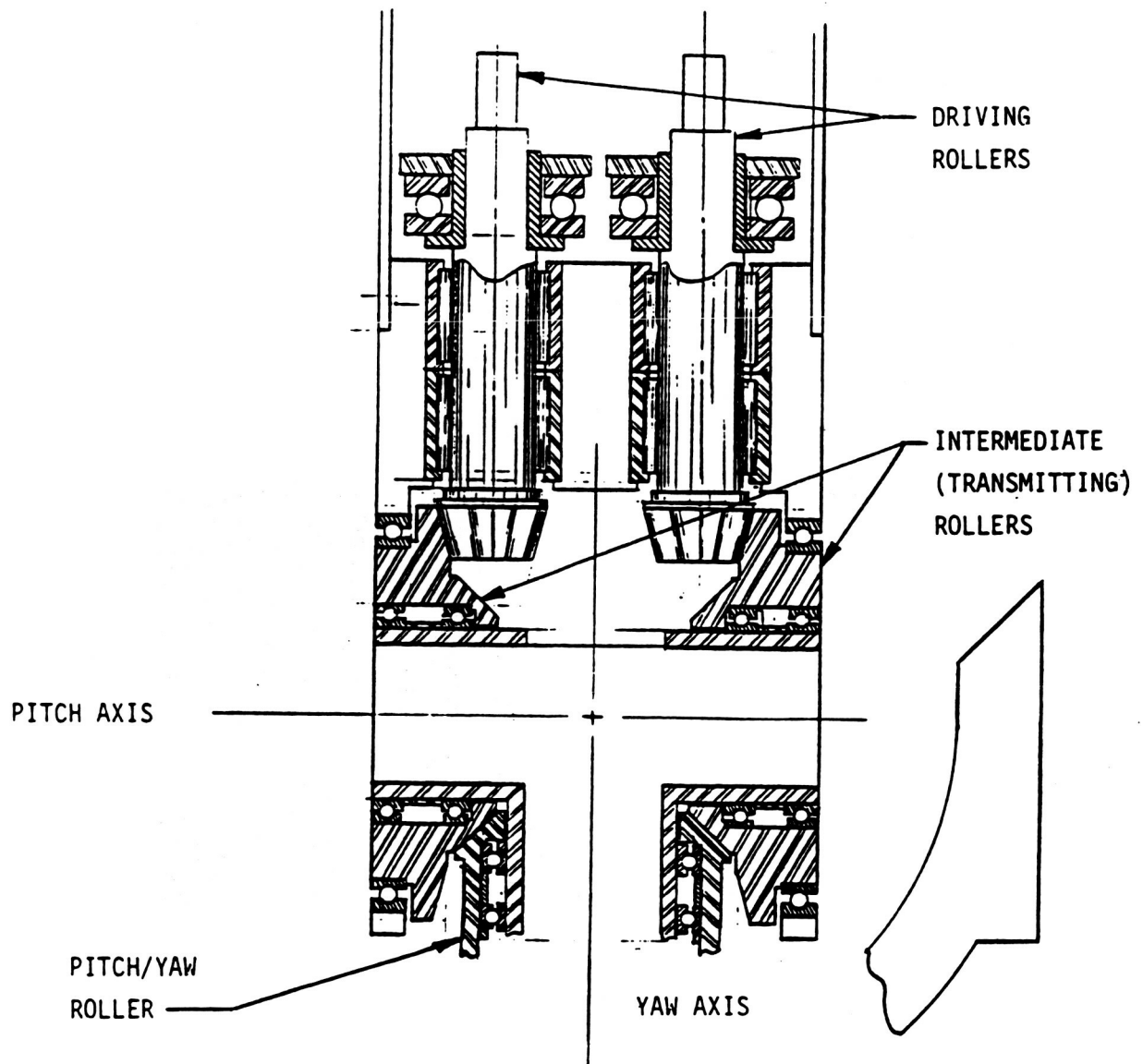


Fig. 7. Traction drive differential

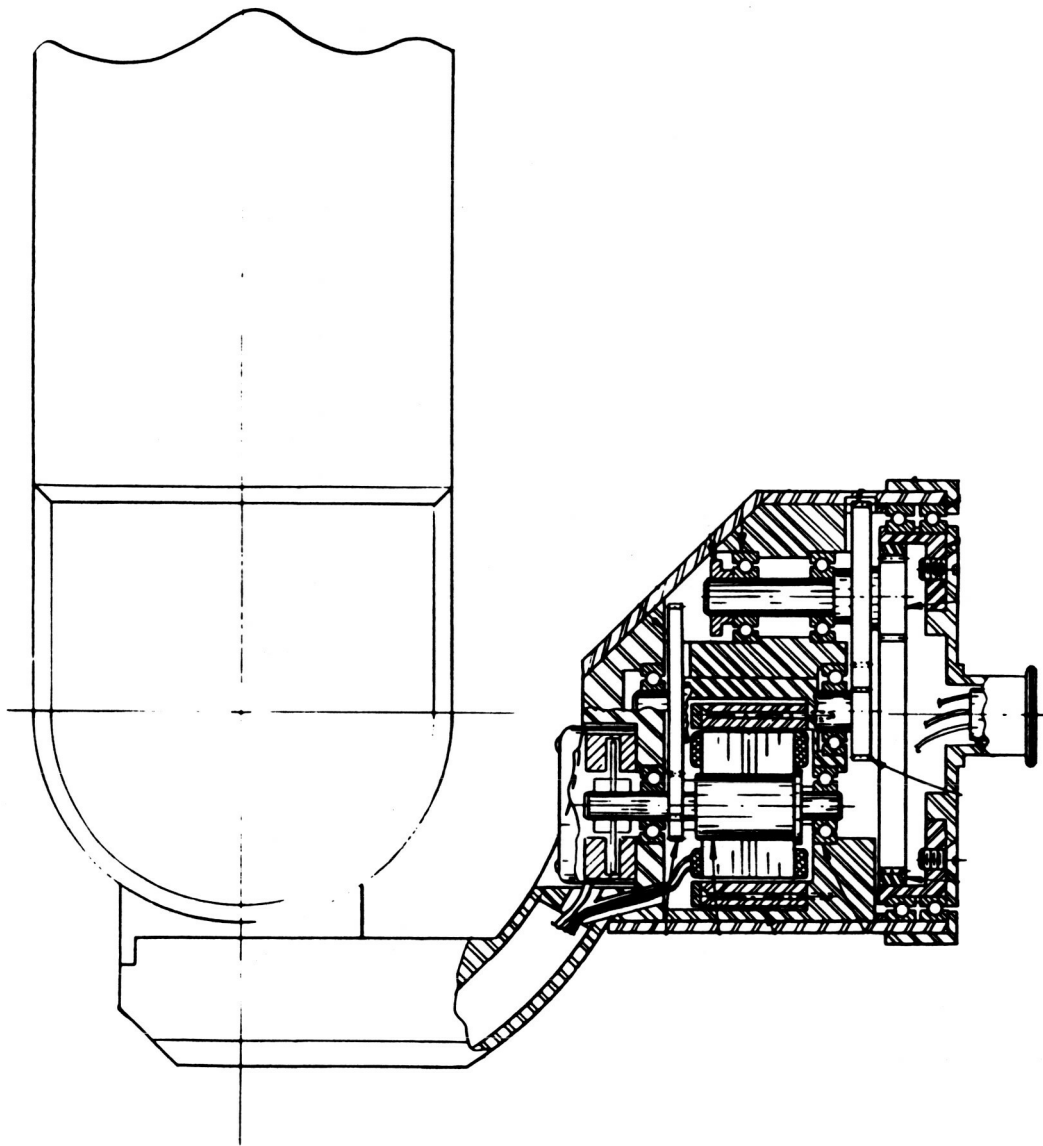


Fig. 8. Telerobot distributed wrist roll joint

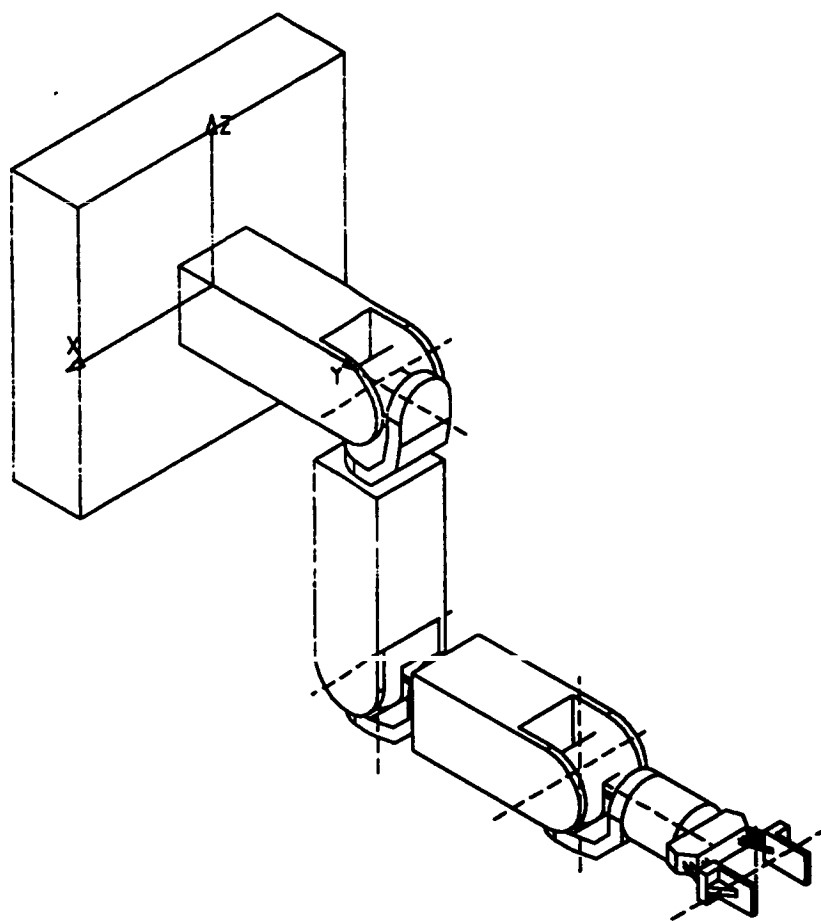
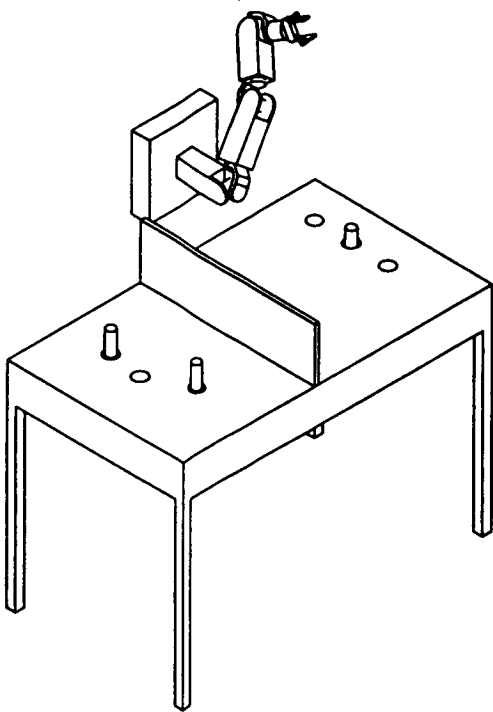
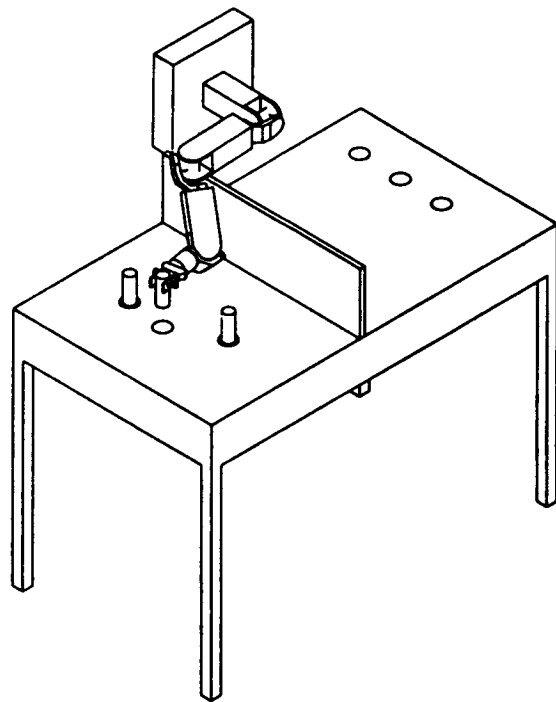


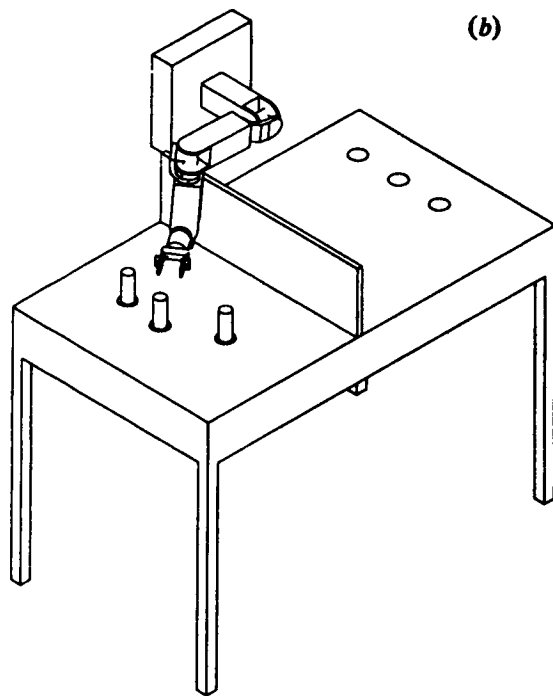
Fig. 9. Telerobot kinematic model



(a)



(b)



(c)

Fig. 10. CATIA simulation of telerobot performing task around an obstacle: (a) step 1, (b) step 2, and (c) step 3

EXPERIENCES OF CNES AND SEP ON SPACE MECHANISMS
ROTATING AT LOW SPEED

G. Atlas* and G. Thomin**

I INTRODUCTION

This paper describes some aspects of knowledge acquired in the field of space mechanisms by SEP and CNES in International and French National space programmes. The experience described centres on the development of the following major mechanism programmes :

- The MEGS (Mecanisme d'Entraînement du Générateur Solaire)

This is a solar array drive mechanism developed and flown under a CNES led programme and is now flying on the Earth Observation SPOT 1 satellite.

- The MOGS (Mecanisme d'Orientation de Générateur Solaire)

This is a Solar Array Drive designed by SEP under CNES contract and currently being developed for application in the EUTELSAT II programme.

For these mechanisms, the paper highlights key design areas and the mechanism performance obtained. Some test problems with the MEGS sliprings are discussed.

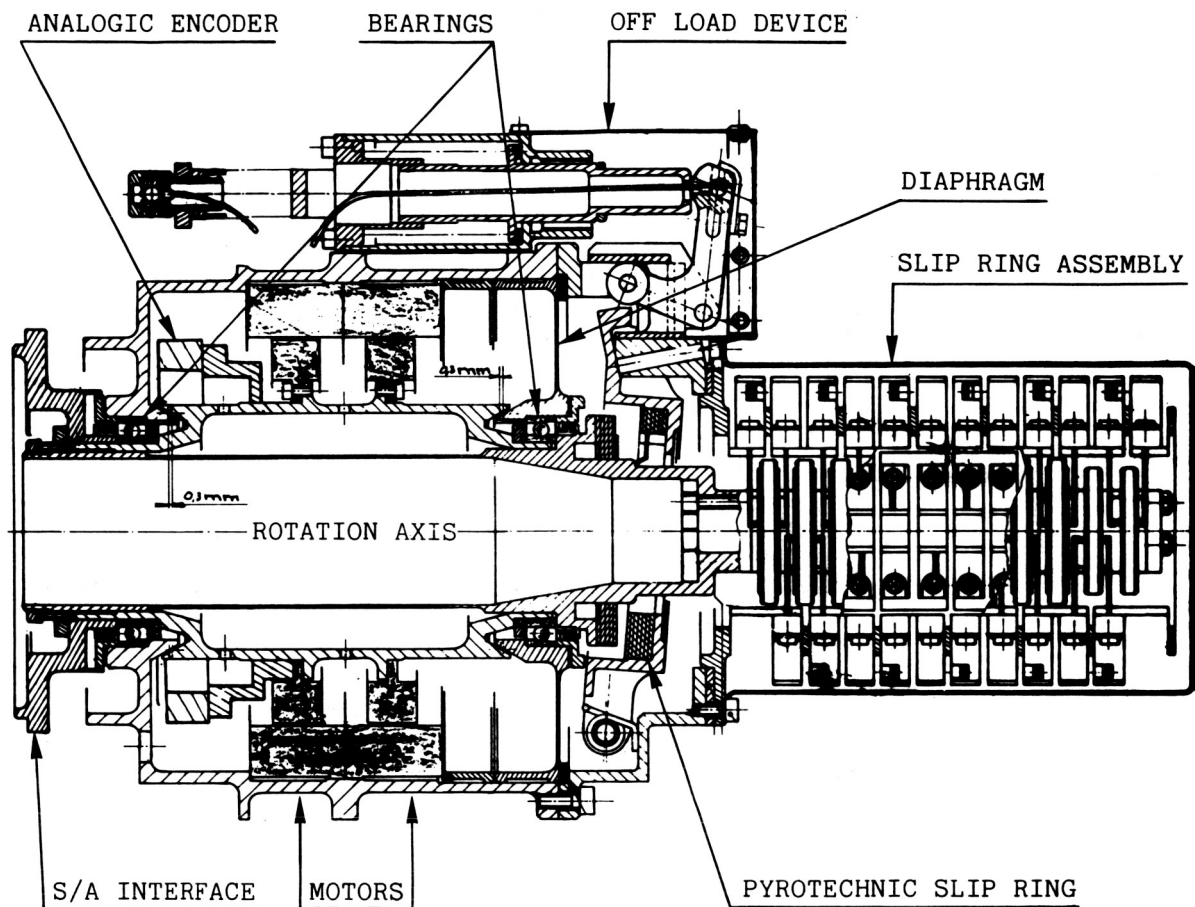
II THE MEGS (Mecanisme d'Entraînement du Générateur Solaire)

II-1 The Major Requirement

The SPOT Mission was to provide precise images of the Earth, these images having a resolution of 10 meters. This was a very severe requirement for the control stability of the satellite, and made large corresponding demands on the stability and uniformity of motion made by the MEGS. This speed stability was required to remain within 10% of the nominal speed of 1 rev/100 minutes (no stepping was allowed). Particularly important was the avoidance of frequencies between 0.15 and 0.2 Hz which might have excited the Solar Arrays. The MEGS is shown in Figure 1.

*Société Européenne de Propulsion (SEP), Vernon, France

**Centre National d'Etudes Spatiales (CNES), Toulouse, France



MEGS

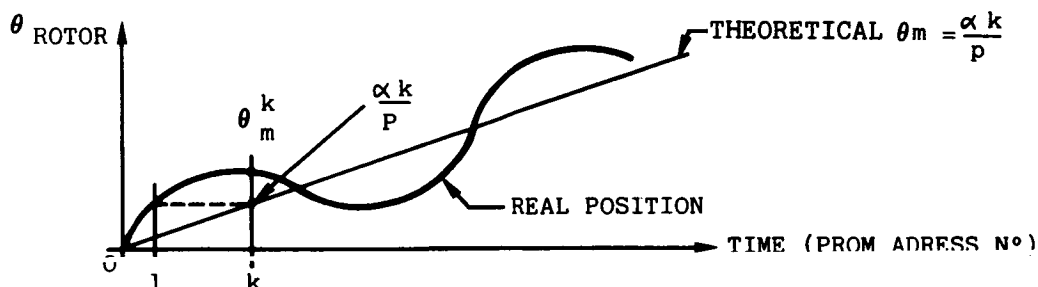
(Mécanisme d'Entraînement du Générateur Solaire)

Figure 1

II-2 The Drive System

In order to achieve these speed uniformity requirements, a direct drive design was chosen. The motor selected was a SAGEM variable reluctance stepper motor (nominal 1200 steps per revolution), but not driven in "stepping mode", but in "synchronous mode". This is achieved by applying, to adjacent motor coils, currents which vary sinusoidally in time, the current in adjacent coils being out of phase by π . This has the effect of moving the "detent position" of the motor progressively in the desired direction at, for a "perfect motor", a constant speed. However since the coils of the motor are not absolutely identical either electrically or physically, some small variation can occur. There can also be interaction with resistive torques arising from position or time dependant friction.

A similar synchronous drive technique was applied by SEP to the Despin Mechanism of the ESA Satellite GIOTTO. This Despin Mechanism is still operating successfully after the encounter with the Halley comet.



Schematic of variation in synchronous drive

Figure 2

As shown schematically in Figure 2, the sinusoidal current demand produces a constant speed with a certain speed modulation or error. The displacement is given by :

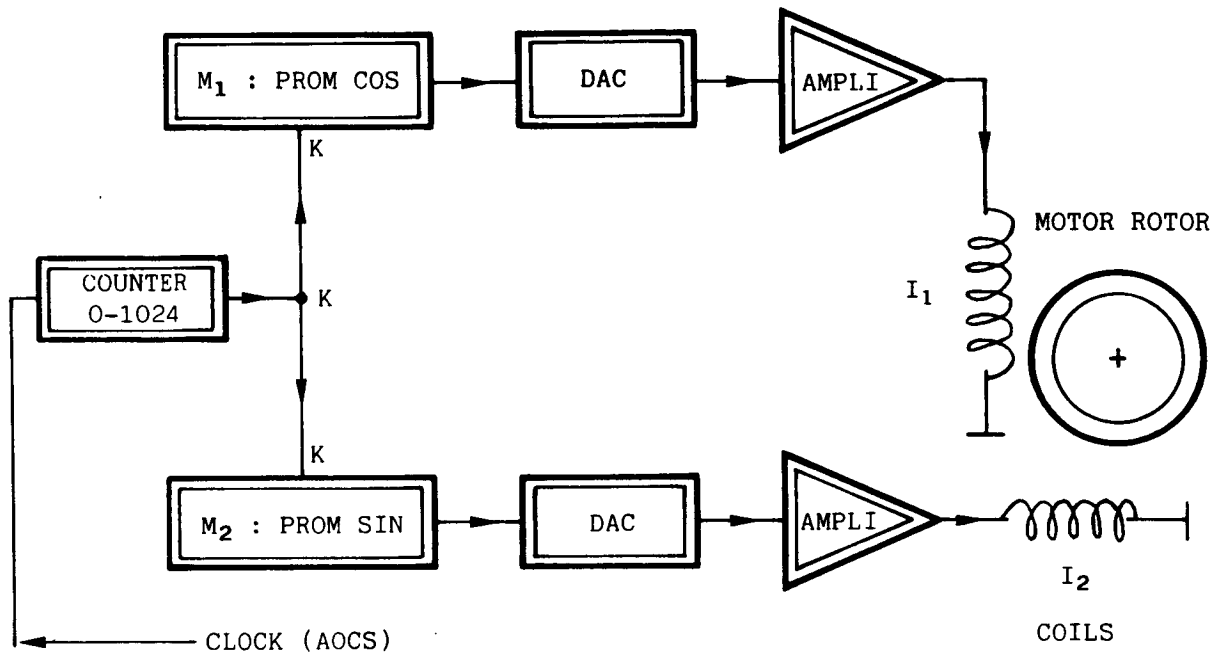
$$\theta_m = \frac{\alpha k}{p} + \mathcal{E}(\alpha k) + \delta = G(\alpha k)$$

where p = number of sinusoidal cycles per motor revolution
($p = 300$ for the SAGEM motor chosen).

δ is an irreducible random error and $\mathcal{E}(\alpha k)$ is due to miscellaneous defects in the control loop and the motor.

note that if the drive were perfect $\omega t = p \theta_m$
were θ_m is the angular motor position.

Figure 3 shows the circuit which was selected to provide the sinusoidal command ; PROMS provide the sinusoidal reference.



Circuit used to obtain a sinusoidal command current

Figure 3

The actual speed variation can be measured by means of a gyrometer mounted on the motor shaft. This has been performed during ground testing (ie without an attached inertia) and the results are shown in Figure 4.

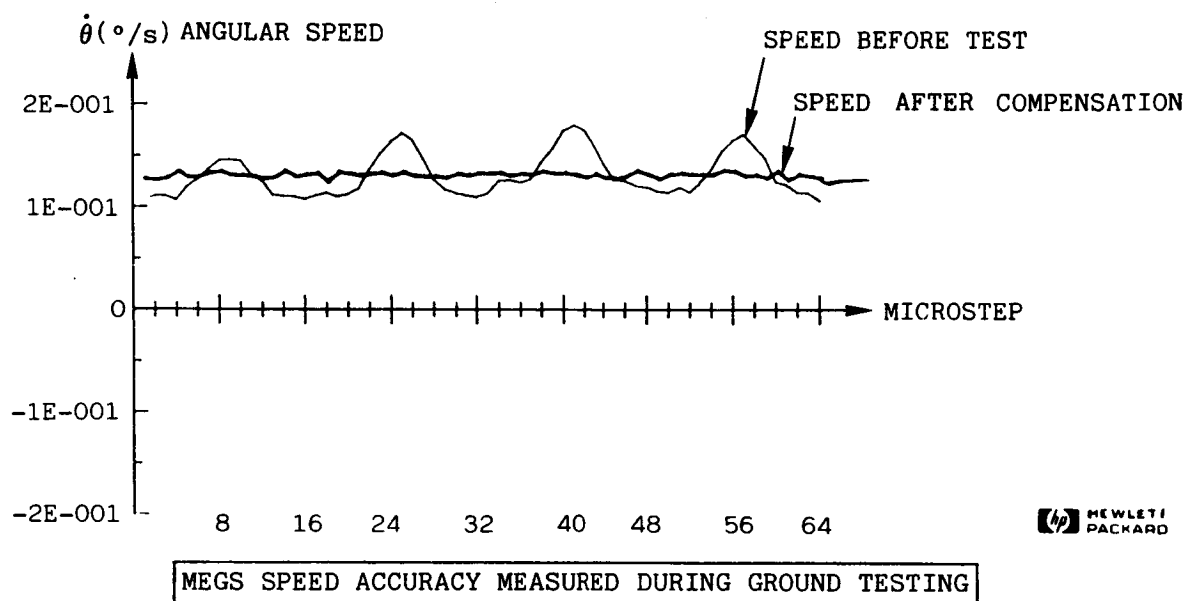


Figure 4

The larger of the two errors shown indicates the result when a pure sinusoidal current is utilised for the synchronous drive. Analysis of this result enables a modified, or compensated, "sinusoidal" drive profile to be derived which departs from the pure sinusoid and reduces the systematic errors. Thus the drive circuit PROMS contain the two functions.

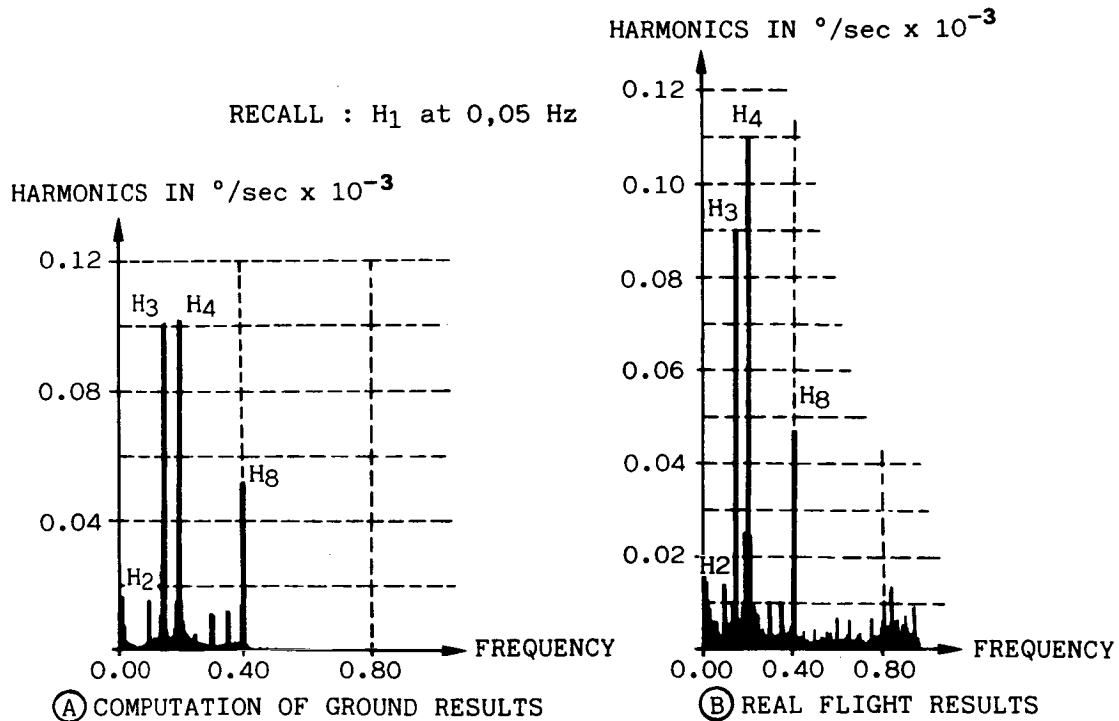
$$I_1 = I_0 \cos \alpha'_k \quad \text{and} \quad I_2 = I_0 \sin \alpha'_k$$

where α'_k is the compensated form of α_k ; $\alpha'_k = \alpha_1$ see figure 2.

Flight measurements have been made on the SPOT 1 satellite, and the results are shown in Figure 5 and Table 1, which also shows the results of ground testing in air. H1 to H8 represent the harmonics of the speed variation, expressed in percent, which were derived for the flight case at different orbit positions.

IN FLIGHT				ON GROUND + 20°C		
IN ORBIT POSITION	107 110°	140 200°	140 95°	MEASURE 1	MEASURE 2	MEASURE 3
H1 (%)	Noise			1.75	2.24	1.53
H2 (%)	0.73	0.65	0.64	0.53	0.83	0.36
H3 (%)	0.51	0.59	0.56	0.56	0.63	0.41
H4 (%)	2.43	2.02	2.41	0.63	0.73	1.26
H5 (%)	0	0.18	0.34	-	-	-
H6 (%)	0.53	0.37	0.56	-	-	-
H7 (%)	0.69	0.62	0.64	-	-	-
H8 (%)	3.33	2.69	3.23	2.67	2.96	2.77

TABLE 1 Comparison of flight and ground performance data



MEGS orbital performance measurements

Figure 5

It can be seen that H₁ is not measurable in the flight case and is in any event less than on ground. The reason for this change is not yet clear but could derive from a change in the compensation parameters.

H2, H3 and H8 are remarkably similar to the ground test results. H4, on the other hand, is significantly greater. It is thought that this change comes from the altered slipping friction torques in vacuum, which have the effect of modifying the equilibrium or detent position which the motor assumes during its movement. The effective torque of the motor around the detent position is shown in Figure 6.

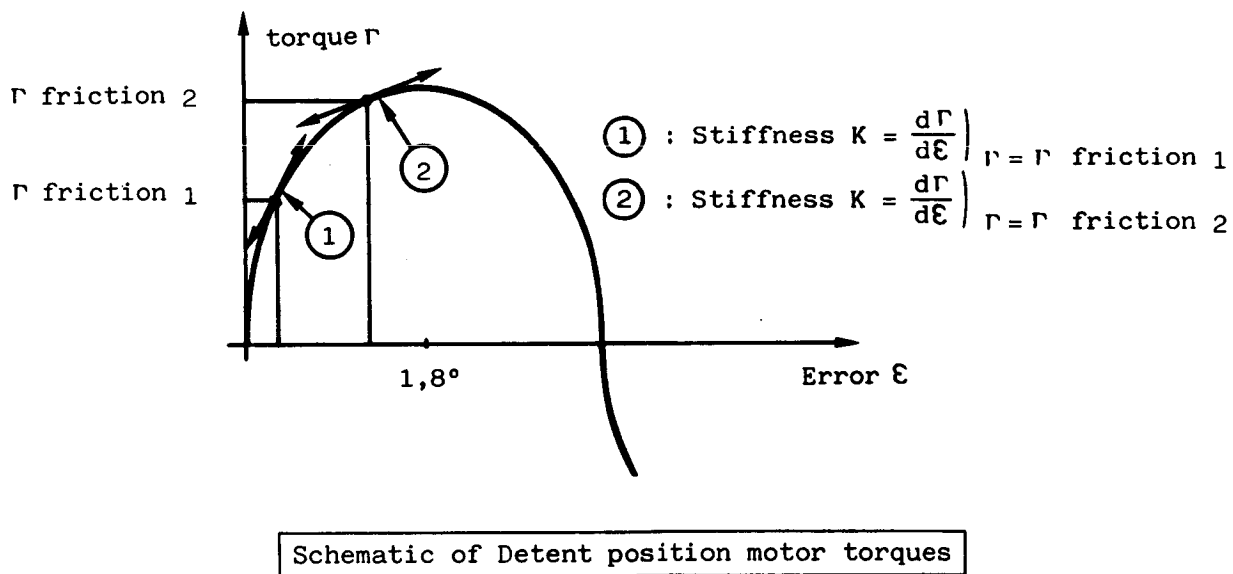


Figure 6

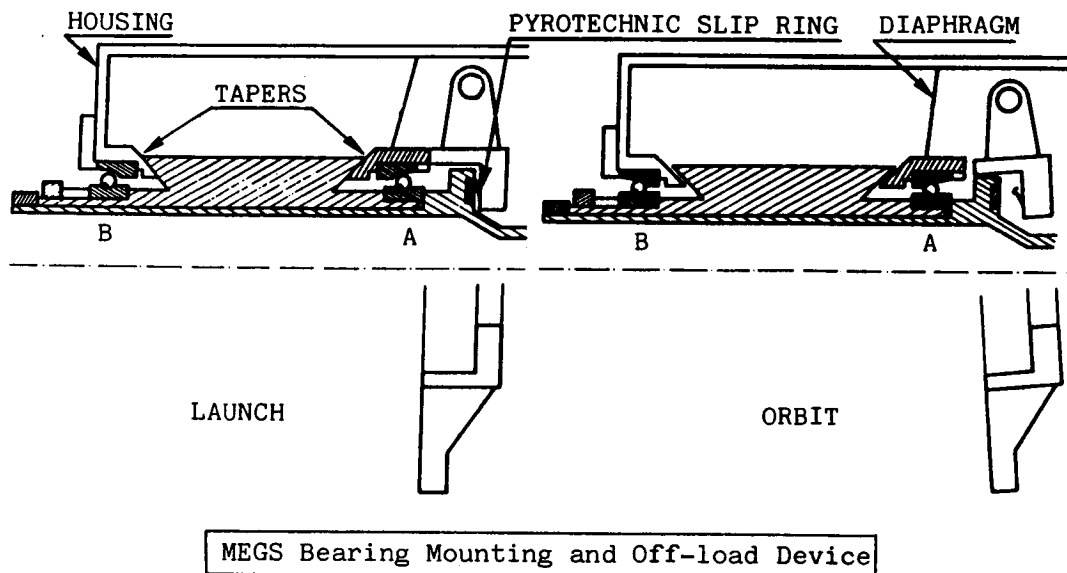
The motor torque acts against the rotor and is resisted by the frictional torques in the MEGS. If those torques change, due for example to an increase in friction of the bearings or the slipping unit, then the equilibrium point also changes, with consequent effect on the speed stability.

The change in H4 from an average, during ground testing, of 0.9% to an average of around 2.2% in flight can be correlated with the frictional change in the slirings. In fact there is an almost linear relationship between the resistive friction and the 4th harmonic such that a 0.1Nm change in friction equates with a 1% change in H4. The observed change in H4 is therefore thought to correspond with an expected change in friction of the MoS2/Ag/C brushes against the silver slipping where the nominal friction torque was 0.2Nm to 0.3Nm in vacuum compared with 0.4Nm to 0.6Nm in air.

II-3 Bearing Off-Load Device

Special attention was given to the protection of the bearings during launch, and maintaining the uniformity of their resistance torque in operation.

The bearings selected were 25 deg angular contact bearings SNFA SEA 55, lead lubricated according to an ESTL procedure (lead coated races with a lead bronze cage). This combination of bearing and lubrication is suited to low speeds with low wear, and gives a satisfactory low torque and low torque noise. Moreover, due to the dry lubrication, an accelerated life test can be done.



MEGS Bearing Mounting and Off-load Device

Figure 7

Figure 7 shows the installation of the bearings in the MEGS where it can be seen that they are mounted back to back, with the right hand bearing mounted in an axially compliant but radially stiff diaphragm (preload of 100 N). The diaphragm protects the bearing against thermally induced preload variations. In the launch configuration the off-load device separates the two bearings and prevents brinnelling. Operation of the off-load device also brings into contact the slirping which provides the signals for the pyrotechnics needed for the array and the MEGS off-load release.

II-4 Slipring Assembly

Because of the low torques requirement on the slip ring, a high diameter disc concept for the sliprings was abandoned in favour of a modular cylindrical assembly with a small external radius.

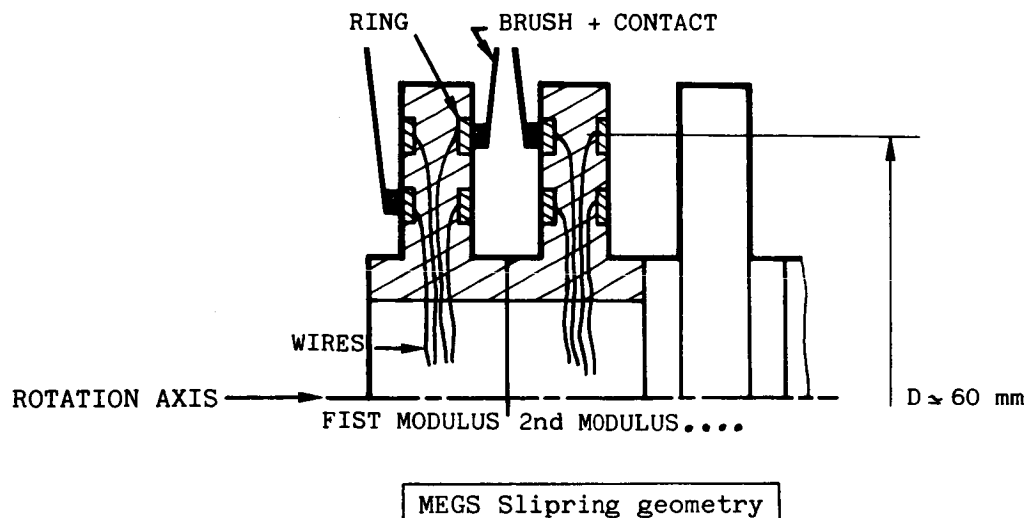


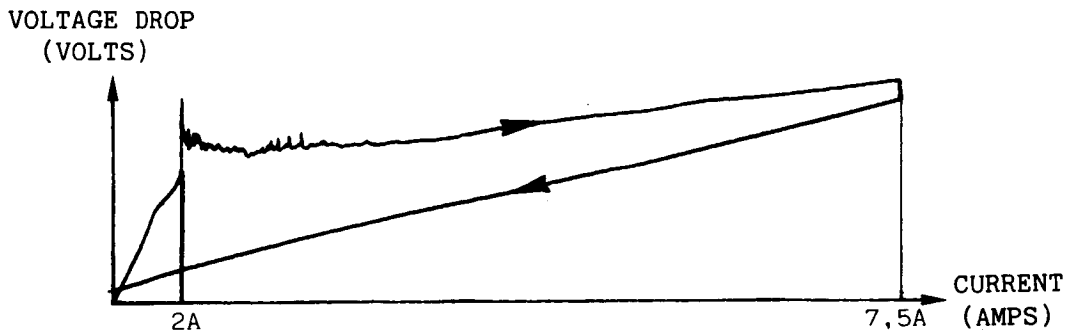
Figure 8

Figure 8 shows the principle of the slipring geometry. Note that the brush pressure is applied by means of a soft blade spring. This technique reduces the effect of temperature differentials and also allows for the 0.3mm displacement of the rotor when the off-load mechanism is applied. The slipring materials were chosen after a series of tests performed by CNES with material from Le Carbone Lorraine. The material chosen was Ag/Carbon/MoS₂ (12% MoS₂). As described above, the pyrotechnic sliprings were incorporated in the off-load device. In this way they did not contribute to the in-orbit frictional torques.

II-5 THE MEGS SLIPRING AGEING PROBLEM

One year after delivery of the MEGS, during integration testing on the SPOT 1 satellite at the MATRA facilities at Toulouse, anomalous values of contact resistance were found in both the pyrotechnic and the power/signal slipring assemblies. The problem was particularly severe for the pyrotechnic sliprings (which had to be tested before launch) where a typical value found was a 1000 ohm resistance compared with the expected performance of 1 ohm. Since the circuit was designed to cater for 40 mohms under a 7.5 amp nominal current, action was necessary to examine the phenomenon and find a remedy.

Although such a high contact resistance had not before been identified either at SEP or at MECANEX, Switzerland, where the sliprings were manufactured, some anomalies had been observed during tests to determine the "breakdown current" on the pyrotechnic slipring assembly.



EVIDENCE OF THE "DIODE EFFECT" DURING TESTING

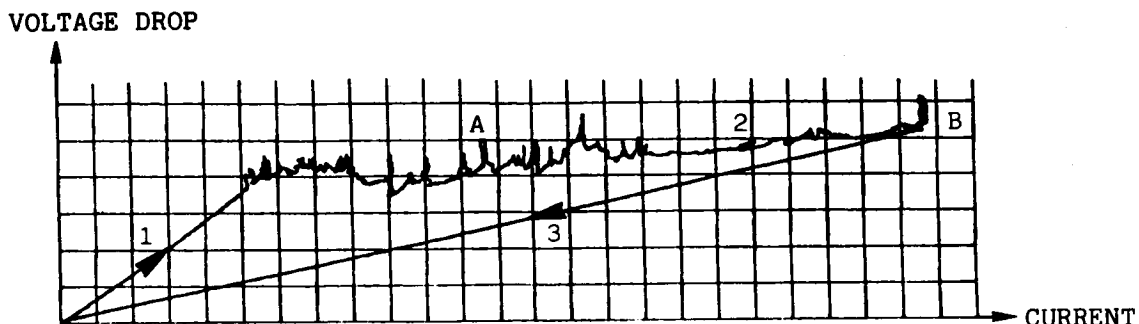
Figure 9

Figure 9 shows the results of such a test where it can be observed that the voltage drop that can be maintained across the slipring rises steeply until about 2 Amps has been applied and then "breaks away" rising only slightly for the remaining current rise to 7.5 Amps, the nominal current.

From these tests it appeared that there was some form of "diode" effect, the contact behaving normally after the nominal current was applied.

It was concluded that the high friction observed during integration was caused by a local pollutant which even if it were generated during ground use or storage would normally be rubbed off during operation by either mechanical or electrical action. The long storage prior to integration had enabled the pollutant to build up.

In order to check the electrical effect, a breakaway test was done on the "failed" unit where the current was increased up to the nominal current density of 30 A/cm². The results had uniformly the same character for all slipring circuits, and showed the features given in Figure 10, with some variation in the current at which the different stages in the phenomenon were observed.



Breakaway tests on MEGS sliprings

Figure 10

Referring to Figure 10, Phase 1 ($I < 0.5$ Amps for the power lines) indicates a normal resistance/current relationship. The peaks, such as that indicated by A in the figure, correspond to the burning off of the pollutant layer. Phase 2 is diode type behaviour and indicates a "semi conductor" presence, possibly a layer of Ag₂O or Ag₂S. At the point B, where the nominal current density is achieved, all the pollutant layer has been burnt off, and in Phase 3 the slipring shows a nominal performance, indicating that the contact area has been cleaned.

Although these tests showed that current alone could clean the surface and in actual fact gives a predominant effect, both current and movement are necessary to eliminate the Pollutant layer. The results also showed that the attainment of a critical "breakaway point" was necessary to achieve the cleaning function.

Following these investigations, the SPOT 1 MEGS sliprings were cleaned just prior to launch in 1986 and subsequently operated well within their specifications in orbit. Investigations are now being performed to investigate the origin of the pollutant layer and to identify materials that could be used to avoid the problem.

IV THE MOGS (Mecanisme d'Orientation de Générateur Solaire)

IV-1 The Major Requirements

Following the successful development of the MEGS it was decided by CNES to fund at SEP the design of a solar drive specifically for GEO applications.

The main requirements were :

- Low mass Mechanism	< 5 Kg	Electronic	< 2.5 Kg
- Load capabilities	800 N //	along rotation axis	
	1500 N \perp	perpendicular to axis	
	200 Nm \perp	perpendicular to axis	
- Power capability	6 kW	at 50 V	
- Accuracy	+/- 0.2 deg	at EOL	
- Life	10 years		

III-2 Technical description of the MOGS

Figure 11 shows a scheme drawing of the MOGS. In this design, to reduce the overall dimensions and mass, the slipring assemble is placed between the bearings which are SNFA SEA 55 angular contact bearings, lubricated by the ESTL lead lubrication process. The use of a diaphragm mounted bearing reduces the sensitivity of the mechanism to temperature variations whilst maintaining the high radial stiffness required by the application.

The power sliprings utilise 4 cylindrical modules, each with 6 rings capable of carrying up to 8 Amps. The same slipring and brush materials as for the MEGS are used for the power circuits but for the 20 signal circuits NEY ORO brushes sliding against gold rings are used.

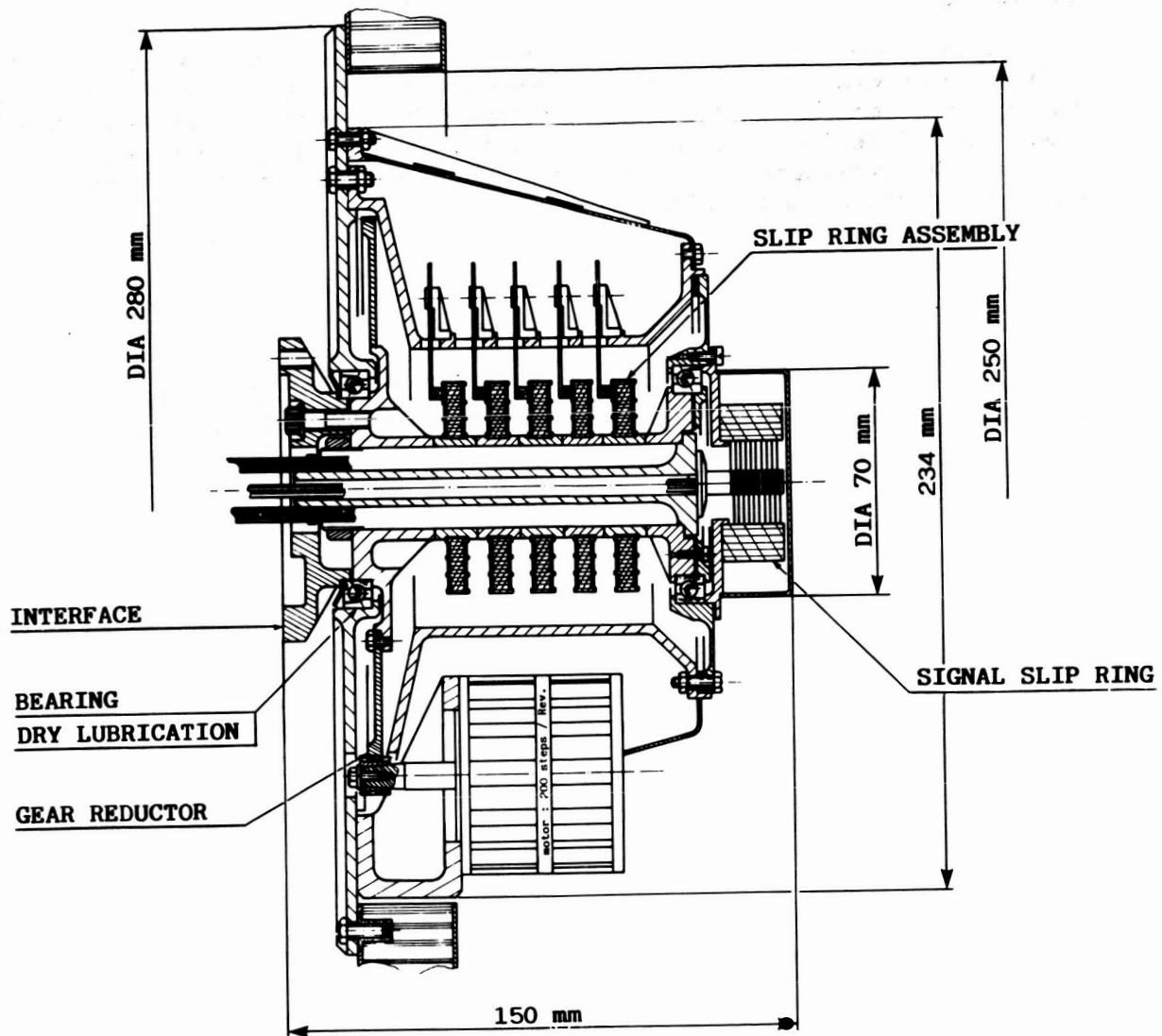
Although the MOGS design has benefited from the experience gained from the MEGS and GIOTTO Despin Mechanism programmes, the lesser importance of speed stability has meant a change in approach to drive control, and an off-shaft stepper motor is used, driven by a shaped pulse, to improve the dynamic characteristics.

The high pointing accuracy is achieved by use of a 200 step/rev MOORE REED stepper motor driving a 15:1 gear giving a shaft step of 0.12 deg (worse case backlash, including wear effect, is 0.08 deg). A magnetic encoder (+/- 0.1 deg accuracy), is fitted to the MOGS, allowing datum checking and the possibility for in-orbit reconfiguration on the satellite.

The gear system utilises a steel pinion rotating against a NUFLON-N treated steel gear. This combination was selected following load-representative vacuum testing at CNES and CETIM. Thus the whole MOGS is dry lubricated.

The effect of temperature differentials on the MOGS performance is minimised by the use of the diaphragm loaded bearing, the linking of the motor to the MOGS drive shaft by a flexible connection, and by the use of a special "constant gap device" which maintains the gear-pinion play at a constant value.

ORIGINAL PAGE IS
OF POOR QUALITY



MOGS

(Mécanisme d'Orientation de Générateur solaire)

Figure 11

IV CONCLUSION

This paper has described the salient features of two solar array drives whose development has been undertaken by SEP and CNES. The designs illustrate the radically different approaches which originated from the differing design requirements. A slipping problem occurred late in the development of the MEGS and the paper indicates how recovery action can be taken with this type of failure.

COMMON DRIVE UNIT

R. C. Ellis*, R. A. Fink*, E. A. Moore*

ABSTRACT

The Common Drive Unit (CDU) is a high reliability rotary actuator with many versatile applications in mechanism designs. The CDU incorporates a set of redundant motor-brake assemblies driving a single output shaft through differential. Tachometers provide speed information in the AC version. Operation of both motors, as compared to the operation of one motor, will yield the same output torque with twice the output speed.

INTRODUCTION

The CDU drive motors can be (and have been) designed to meet specific program needs. Two designs of the CDU are fully developed, qualified, and space proven by use in the Solar Max Repair Mission. The CDU's were used to drive retention latches for the multi-mission spacecraft (MMS) and also to rotate and tilt the MMS. Future usage of the CDU includes the following:

- ° Keel Latch Drive for the Space Telescope
- ° Umbilical Disconnect Mechanism for the Space Telescope
- ° Deployment and Stowage of Solar Array Wings for the EURECA Free-flying Platform
- ° Latches for the Upper Atmospheric Research Satellite

Common Drive Unit

The CDU consists of a differential gearhead and a set of two motor-brake assemblies. The motor-brake assembly of the original CDU design consisted of a three-phase AC motor, a three-phase AC brake, and a tachometer. Two configurations, 0001 and 0002, were designed and supplied. (See Figure 1.) Both configurations have output torque of 11 N-m. The output speed of the 0001 configuration is 8 rpm and of the 0002 configuration is 64 rpm. This was accomplished by using a smaller motor with a higher gear ratio for the 0001 unit. The most recent design (currently in qualification testing) incorporates a DC brush-type motor and a DC brake. (See Figures 2 and 11.)

* Sperry Space Systems, Durham, NC

Any type of motor-brake assembly could conceivably be used. Proposed CDU motor designs have included the following:

- A. DC brushless motors, including the drive electronics and additional planetary gearing
- B. DC brush motors with a torque limiting hysteresis clutch
- C. Stepper motors

DRIVE UNIT MECHANICAL DESIGN

The primary design goal of the CDU was to provide as much redundancy as reasonably possible. There are, therefore, two separate power paths with the only common element being the output shaft, which is also the planet carrier. There are numerous redundant features within each individual power path. A cross-sectioned layout of the unit is shown in Figure 3. The complete unit consists of a differential output driven by two spur gears, dual two stage planetary reductions and dual motors with integral friction brakes. The differential allows either of the two motors to be operated separately or together. If one motor fails, its brake will lock the motor shaft and allow output from the other motor.

The output shaft carries three pairs of planet gears turning on needle bearings, supported by carrier pins. The carrier pins are free to turn and act as bearings in the event the needle bearings seize. The planets alternately engage two internal ring gears. External ring gears mate with two spur gears. The ring gears are also supported by bearings that are free to turn if the bearing should seize. If the entire differential assembly malfunctions, output can still be provided by powering both motors. The differential then turns as a unit, without providing any gear reduction. If only one motor drives the differential, it produces a 2/1 reduction in speed, but a 2/1 increase in torque, so that the torque is the same as when both motors are powered.

Between the differential and each motor are two-stage planetary gear reductions. Each stage has a floating carrier with three posts supporting three planet gears on ball bearings. An internal ring gear is common to both stages. The ring gear was made as a separate part to simplify the design and fabrication of the spacer plate. The ring is trapped against a shoulder when the motor is installed, and an axial dowel pin at the ring O.D. prevents rotation.

All of the gears and bearings in the drive are lubricated with Braycote Micronic 601. This grease has good temperature and vacuum stability and has worked well in many of our space designs. All rubbing surfaces are coated with the grease, but

the amount is controlled to minimize the effects of high viscosity at extremely low temperatures and reduce any possibility of leakage from the unit.

The overall gear reduction ratio of the 0001 unit is 786.5 to 1. This is accomplished by an 11/1 planetary, a 5.286/1 planetary, a 6.765/1 spur stage, and the 2/1 differential. The unit had to produce a normal torque of 11 N-m and a stall torque of 36.7 N-m maximum. However, it also had to be operated into a hard stop. The mechanical parts were, therefore, designed to have adequate factors of safety at over twice the maximum stall torque, or 80 N-m.

The motor/brakes used on the drive unit are independent assemblies which are pretested and can be replaced if necessary without any adjustment or calibration.

AC MOTOR/BRAKE DESIGN

The AC motor used on this unit was based on a motor that was developed for the Shuttle Cargo Bay pallet latches. Those latches also used a dual motor/brake and differential design. Over 200 of those motors have been fabricated and shipped. Since the brake of a nonoperating motor must hold to allow the other motor to provide output through the differential, every feature of the brake was made redundant to ensure fail-safe operation.

Figure 3 shows a cross section view of the motor/brake. Referring to this figure, the following features should be noted.

- A. The motor rotor is a squirrel cage type for ruggedness and high reliability.
- B. The bearings are preloaded with a spring washer to 13-22 newtons (3-5 pounds) to provide for differential thermal expansion.
- C. The insulation system consists of polyimide coated magnet wire, polyimide impregnation, and polyimide film (all Class 220) for maximum compatibility and temperature resistance.
- D. The brake armature has a total of six springs to minimize the effect of failure of one spring.
- E. The brake disc is mounted on a splined sleeve which is mounted on a splined shaft to provide redundancy.
- F. The brake disc slides on a spline and is captured between the two friction surfaces resulting in no axial loading of the bearings.

- G. The armature pins slide in a self-lubricating polyimide bushing which can also slide in the pilot holes to provide redundancy.
- H. The solenoid is composed of six poles, each phase having two poles spaced 180° for balance.
- I. The bearings are sealed to minimize lubricant migration. Lubricant is Micronic 601 grease.
- J. The friction surfaces are separated from all lubricated surfaces by a five stage labyrinth seal.
- K. The friction surfaces and their bonding interface are slotted to create a "key" to prevent rotation in case of a bond failure.
- L. The back nut and internal screws are secured with a mechanical lock and a secondary adhesive lock.
- M. All materials are selected to minimize differential thermal expansion.
- N. The brake disc is aluminum to minimize rotating inertia.
- O. Connections between motor and brake wiring are made using terminals.
- P. All wiring and terminals are conformal coated.
- Q. The brake friction surfaces are composed of brake lining on brake lining to minimize wear and provide maximum stability of friction torque at ground ambient or space vacuum and temperature conditions.
- R. The brake has dual friction surfaces to provide required holding torque even if one surface is completely inoperative.

THERMAL DESIGN

The unit motor/brake has been designed and tested for operating temperatures from -71°C to $+176^\circ\text{C}$. Mechanical stresses due to thermal effects have been minimized by using 15-5PH stainless steel for motor housings, gears, and shafts. The inherent thermal stability permits nonoperational temperature exposure of -129°C without damage or performance degradation.

TACHOMETERS

The tachometer consists of a wound two-phase stator and a permanent magnet rotor. Both the output voltage and frequency varies linearly with rotational speed.

MOTOR/BRAKE MAGNETIC DESIGN

The motor size and design are controlled by the required torque output and the required brake operation. The final design required close coordination and integration of the motor and brake designs to ensure proper operation. Curves of the motor performance are shown for reference in Figures 4 through 7.

The shape of the speed-torque curve is dictated primarily by the ratio of rotor resistance to the motor reactance. To obtain good low slip (high speed) operation, low rotor resistance is required. Increasing the rotor resistance will result in increased stall torque until the peak torque is at stall. Further increases will cause reduced stall torque. The temperature sensitivity of the motor is also affected by the resistance/reactance ratio. With very low rotor resistance, the stall torque will increase at high temperature, since the rotor resistance increases with temperature. At high rotor resistance, the torque will reduce as the temperature increases. In addition, the high speed torque always reduces as the rotor resistance is increased. The rotor resistance was selected to minimize the stall torque temperature sensitivity as illustrated by Figures 5 and 6.

The stall torque for two phase operation is approximately two thirds the three phase torque. The torques at other speeds are also reduced; the amount depends on the final design parameter. For this design, the two-phase torque is greater than two thirds the three-phase torque at all speeds above stall.

The power factor of an AC induction motor is low at stall and increases to a peak at some speed, then reduces again as the speed increases further. Figure 4 shows the nominal performance at rated input, room ambient. The power factor peaks at approximately 68%. It is above 60% for all torque loads greater than 14 N-m and above 50% for all torque loads greater than 85 N-m. The efficiency peaks at 65% and is greater than 60% for loads between 4.3 N-m and 2 N-m. It is greater than 50% for loads between 0.2 N-m and 2.7 N-m. The current ranges from 2.18 amps to 0.46 amp.

Figure 5 shows the speed-torque output at -71°C for the voltage and frequency extremes. Both the stall torque and the maximum torque vary approximately 35% over these extremes.

Figure 6 shows the speed-torque output at +121°C for the specified voltage and frequency extremes. At this high temperature, the stall torque is also the peak torque and varies approximately 35%.

Figure 7 shows the speed-torque output at the conditions of minimum and maximum peak torque. The minimum peak torque occurs at minimum voltage, maximum frequency, and maximum temperature. Note that the stall torques are very nearly the same.

The design for the 0001 configuration is basically the same except scaled down for the reduced output.

The motor size required for either configuration, depends primarily on the required output duty cycle. The limiting constraint on the 0002 configuration is the heat dissipation in the rotor during stall or near stall operation. By designing the motor to have the maximum rotor temperature rise that can be safely handled during the specified 30 second stall condition, the size is minimized.

The brake must be designed so that the solenoid force is great enough to pull in at the low voltage, high temperature (i.e., minimum current) condition with two phases excited and also drop out with two phase removed at the other extreme (i.e., maximum current). For a conventional design, the force will vary as the square of the applied current and directly with the number of phases.

The general relation between the solenoid force and current in an unsaturated design is shown in Figure 8. This figure shows the force versus current for six conditions.

1. Three phase input, minimum gap (brake engaged).
2. Three phase input, maximum gap (brake released).
3. Two phase input, minimum gap.
4. Two phase input, maximum gap.
5. One phase input, minimum gap.
6. One phase input, maximum gap.

The minimum running current and the minimum and maximum stall current are drawn in and the following points are pertinent.

A. TWO PHASE INPUT, MINIMUM GAP, AT MINIMUM RUNNING CURRENT

The generated solenoid force must be great enough to hold the armature (i.e., must exceed the spring force).

B. ONE PHASE INPUT, MINIMUM GAP, AT MINIMUM RUNNING CURRENT

The generated solenoid force must be small enough for the spring to overcome to allow the armature to release and engage the brake.

C. TWO PHASE INPUT, MAXIMUM GAP, AT MINIMUM STALL CURRENT

The generated solenoid force must be great enough to overcome the springs and allow the armature to pull in.

D. ONE PHASE INPUT, MAXIMUM GAP, AT MINIMUM STALL CURRENT

The generated solenoid force must be low enough for the spring to prevent the armature from pulling in.

E. TWO PHASE INPUT, MAXIMUM GAP, AT MAXIMUM STALL CURRENT

The generated solenoid force must be great enough to overcome the spring and allow the armature to pull in.

F. ONE PHASE INPUT, MAXIMUM GAP, AT MAXIMUM STALL CURRENT

The generated solenoid force must be low enough for the spring to prevent the armature from pulling in.

By referring to the figure, it can be seen that the maximum force which the spring must overcome occurs at point "F". This establishes the minimum spring force. The minimum force which must overcome the spring force occurs at point "A" and establishes the maximum spring force. From the figure, the minimum spring force is more than 3 times the maximum spring force, an obvious impossibility.

Figure 9 shows the same conditions for a brake designed with a square saturation curve. The force variations are minimized by operating the solenoid in saturation at the stall current levels. With this type design, the maximum spring force is more than 40% greater than the minimum spring force, which is possible.

This allows the following brake operation:

3 Phase Operation

The brake will release when excitation is applied and engage when power is removed for all conditions of voltage, frequency, and temperature.

2 Phases Operation

The brake will release when excitation is applied and engage when power is removed for all conditions of voltage, frequency, and temperature.

1 Phase Operational

The brake will engage. Brake torque will be less than one-half the unexcited torque until excitation is removed.

DC MOTOR DESIGN

The motor assembly for the DC CDU is shown in Figure 10. Performance of the complete drive unit is shown in Figure 11.

The rotor incorporates a lamination stack, windings, commutator, and shaft. The insulation system is rated at 220°C. Labyrinth seals are used to avoid bearing contamination from brush wear particles.

The stator contains samarium cobalt permanent magnets; their extreme resistance to demagnetization assures consistent motor performance over the unit life. A band is bonded to the I.D. to protect the magnets during assembly, and prevent a potential magnet chip from entering the air gap, and possibly jamming the motor.

Brush holders are cartridge type, making the brushes easily replaceable without motor disassembly. This is important when determining wear rates in development and life testing.

Bearings are deep groove, double shielded, and lubricated with Braycote Micronic 601 grease.

MOTOR BRUSH COMPATIBILITY

The most important factors in a vacuum-rated motor design are the characteristics of the brush material. Sperry's preferred brush material has a low metallic content with molybdenum di-sulfide for vacuum lubrication. It was selected for low wear in a vacuum, but it's most important characteristic is the relatively high resistance of the wear debris. End-of-life insulation resistance is typically in the one megohm range. Other brush types with a high metallic content can cause significant current leakage paths to ground. In the extreme case, the brush debris can bridge between commutator bars, shorting out the motor.

Brushes wear due to two factors; mechanical friction and electrical arcing. The selected material has a low wear rate due

to friction but will wear very rapidly if arcing is significant. To maximize life, the motor is a very slow speed design (600 rpm). This minimizes wear due to friction and reduces arcing. To further reduce arcing, the motor was designed with 49 winding coils and 49 commutator bars, many more than normally used for a motor of this size. The result is a substantial reduction in inductance for each coil and lower voltages generated between adjacent commutator bars as the motor is commutated.

Motor testing confirmed the soundness of this design. Brush arcing was not visible in a dark room and wear in a vacuum was low. Motor life in a vacuum is approximately 400 hours. Another benefit is the long life under atmospheric pressure. From measured wear rates, the life was projected to be 40,000 hours. Thus, special precautions, such as nitrogen back-fill are not necessary or desirable.

DC BRAKE DESIGN

The brake is a fail-safe design which will disengage when power is applied. (Refer to Figure 11.) The brake has two friction material interfaces and is engaged by four compression springs. The brake armature slides approximately 0.015 cm on four pins. The pin sliding surfaces are redundant. The rotating disc is attached to the shaft by redundant splines. The brake has no mechanical single-point failure modes and could be electrically redundant with the addition of another energizing coil.

The friction material was developed by Sperry for the Shuttle Remote Manipulator Arm. It provides consistent torque (approximately +25%) under environmental extremes of pressure, temperature and humidity.

EMI FILTER

A DC motor produces conducted and radiated emissions due to current ripple in commutation, and brush arcing. This motor design has low current ripple and arcing due to the use of many coils and commutator bars. A relatively small EMI filter can be used effectively since the basic motor design is very quiet. Figure 10 shows the EMI schematic. Since the motor polarity must be reversed to change direction of rotation; the filter has been designed to be effective for either polarity.

TESTING EXPERIENCE

The AC drive units had one significant test problem. The original design included a three-phase thermal protector which was sensitive to motor temperature as well as input current.

During vacuum stall testing, the motor and brake windings overheated before the thermal protector tripped. To correct this, three small thermostats were placed in good contact with the motor windings. Selective screening was used to match thermostats since all three phases should be opened at approximately the same time.

The first DC drive units experienced a problem during random vibration testing as part of the qualification. The amplification at the brake pins was higher than expected, and the pins sheared. The pin was redesigned to have an enlarged diameter and to eliminate the shoulder. This design modification provided a safety factor of four at the qualification vibration level.

CONCLUSIONS

The CDU is a high reliability rotary actuator with many versatile applications in mechanism designs.

ORIGINAL PAGE IS
OF POOR QUALITY

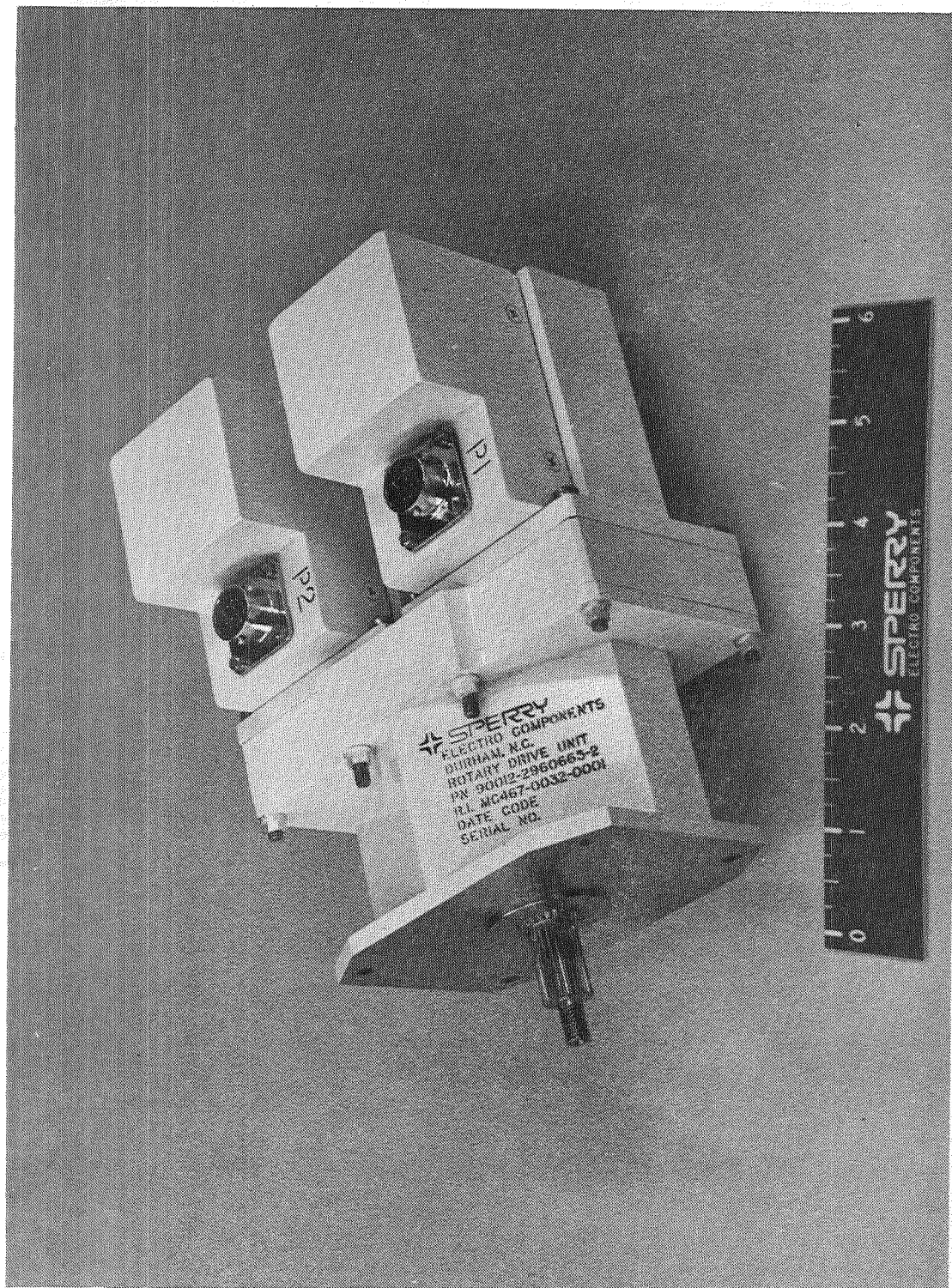


FIGURE 1

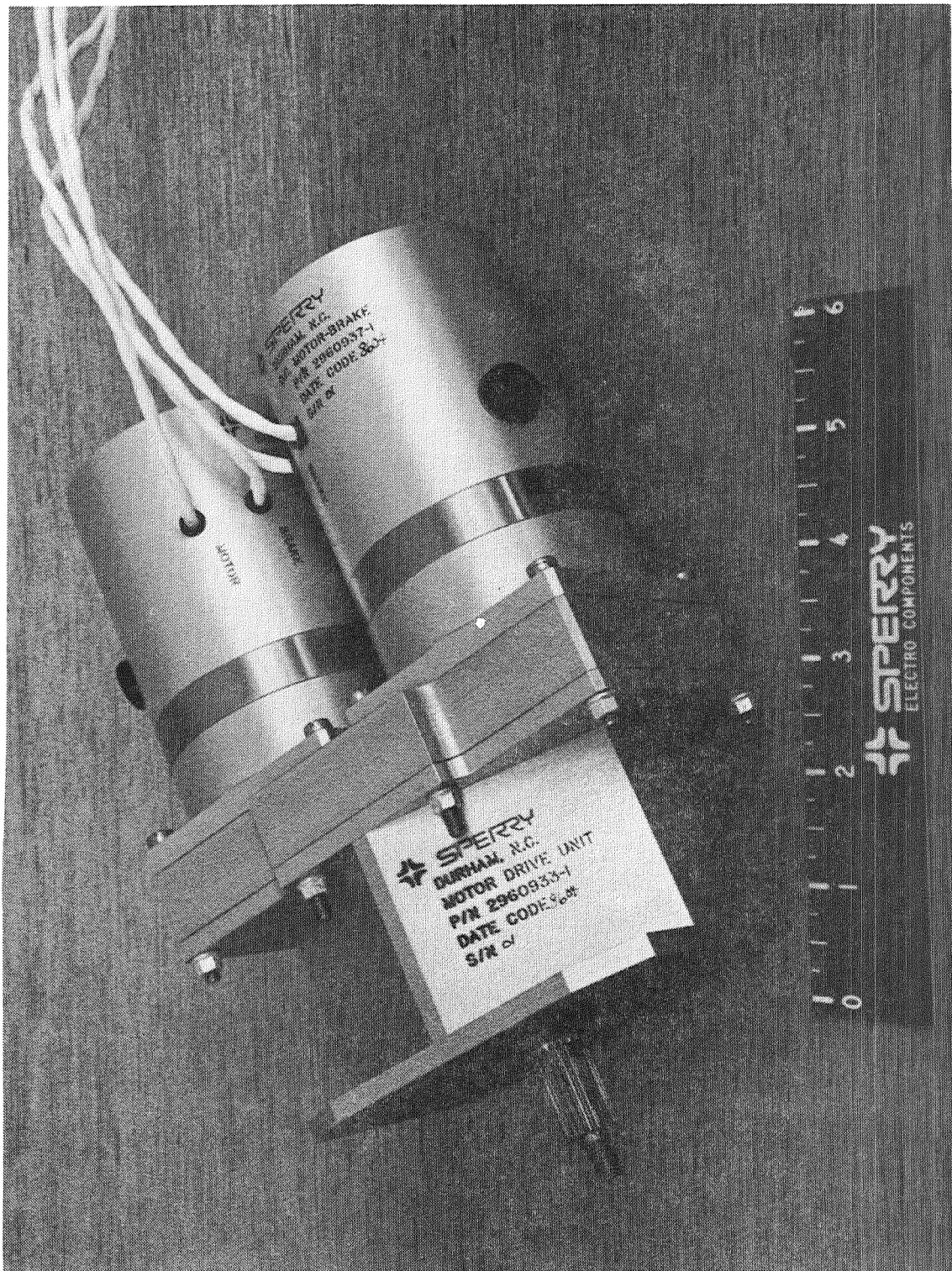


FIGURE 2

ORIGINAL PAGE IS
OF POOR QUALITY

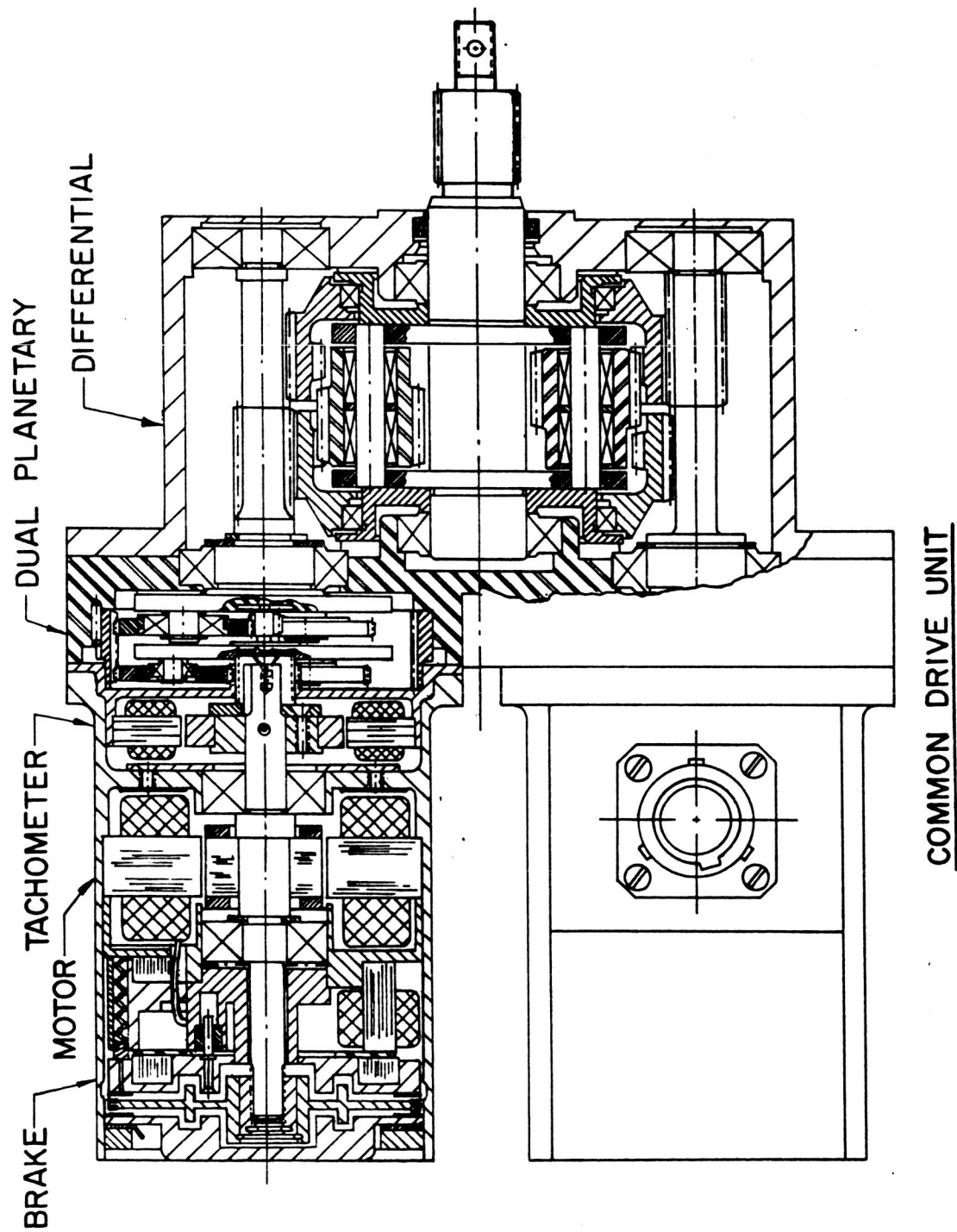


FIGURE 3

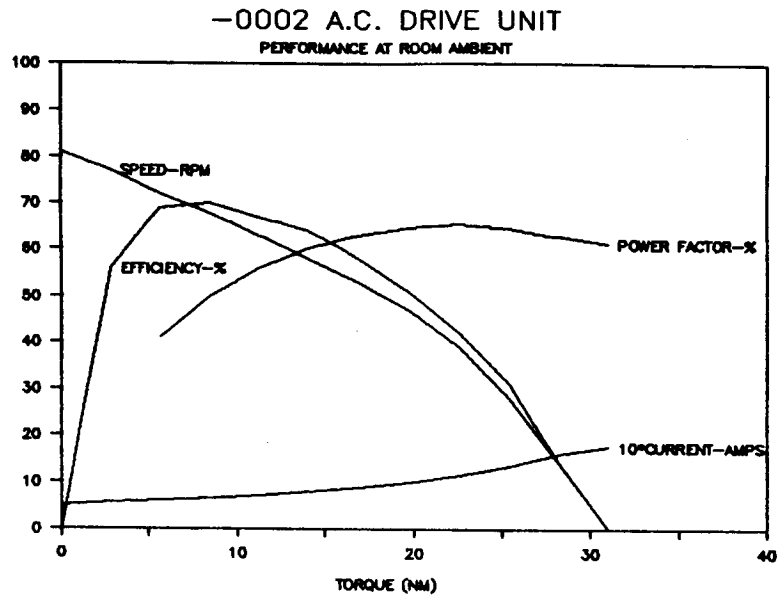


FIGURE 4

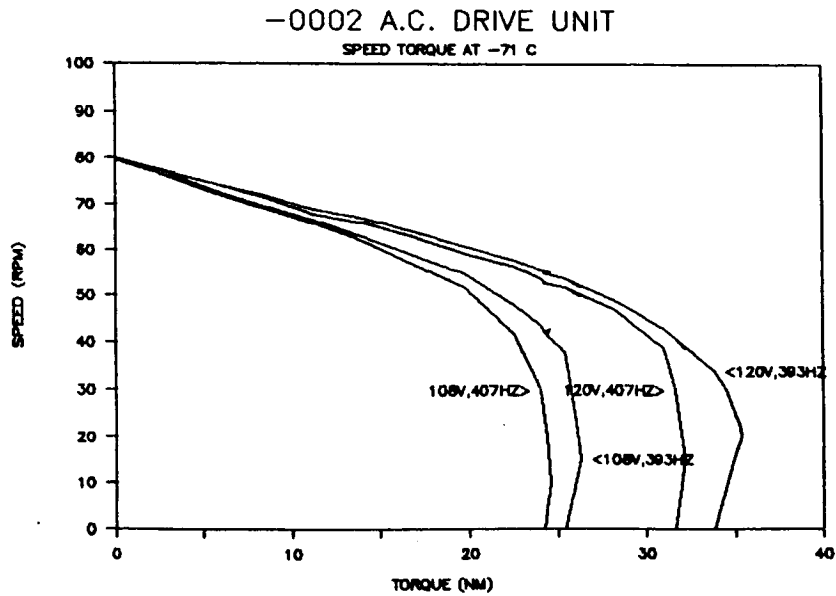


FIGURE 5

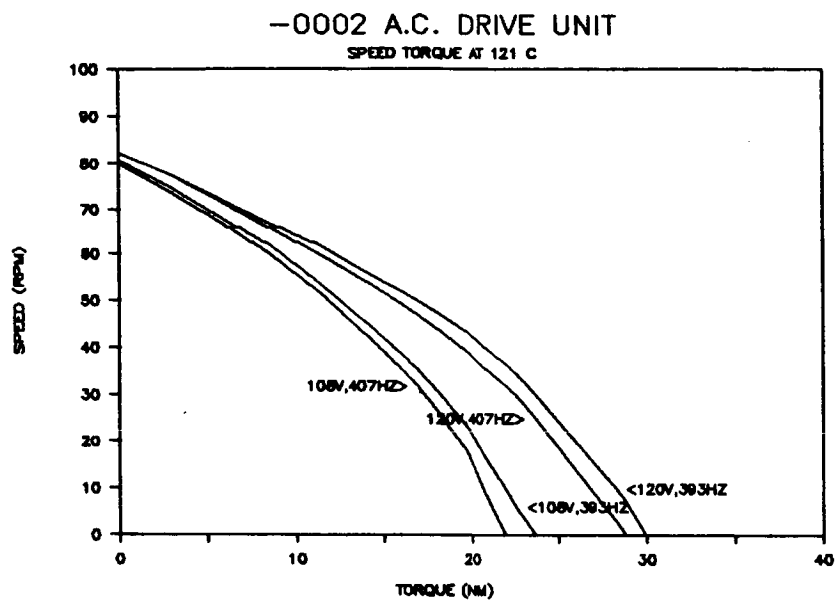


FIGURE 6

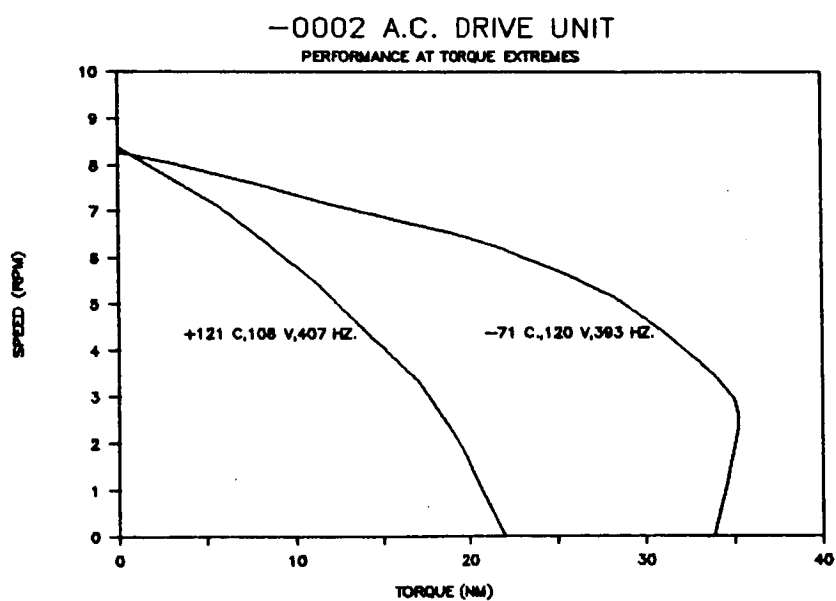


FIGURE 7

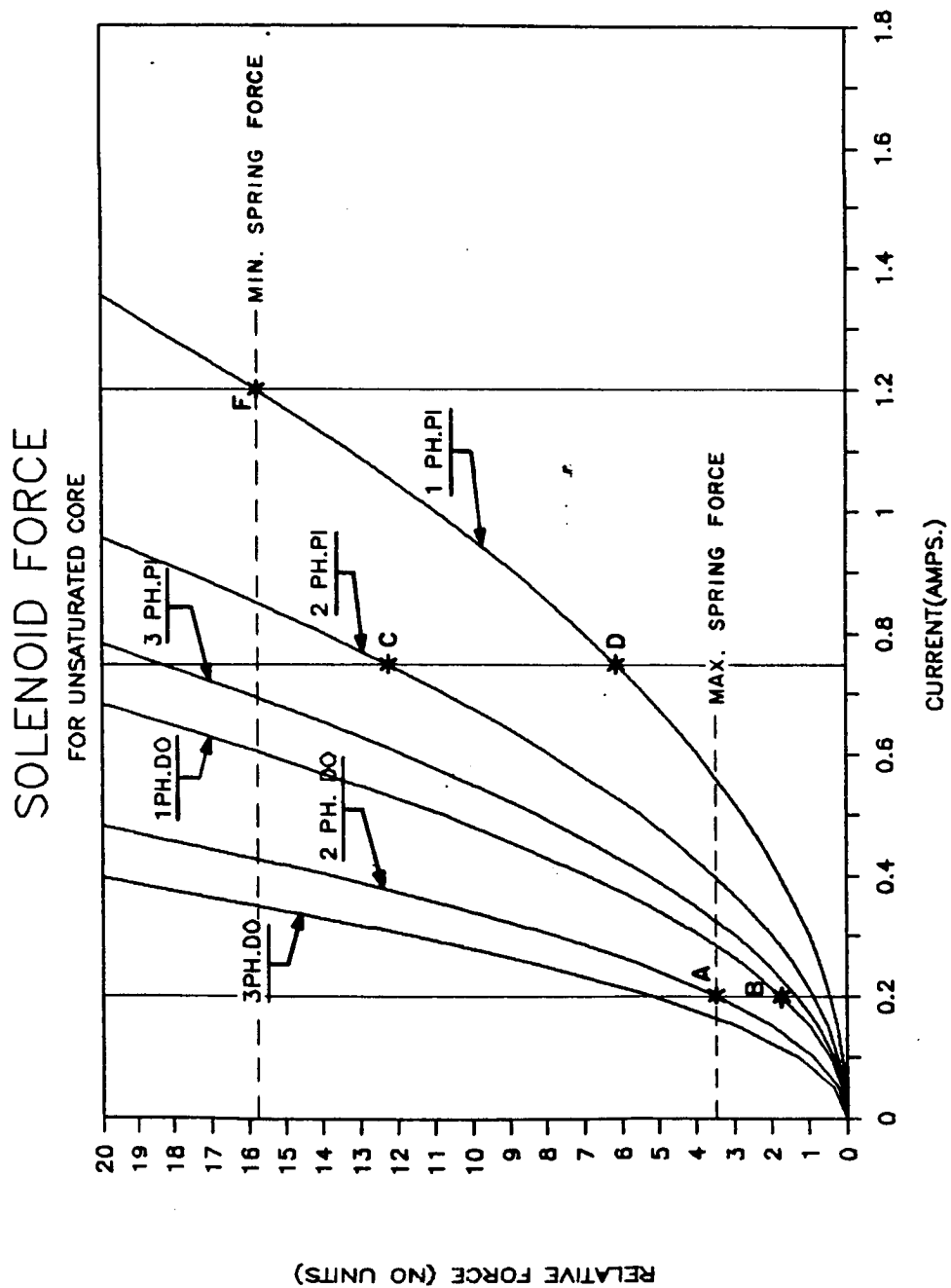


FIGURE 8

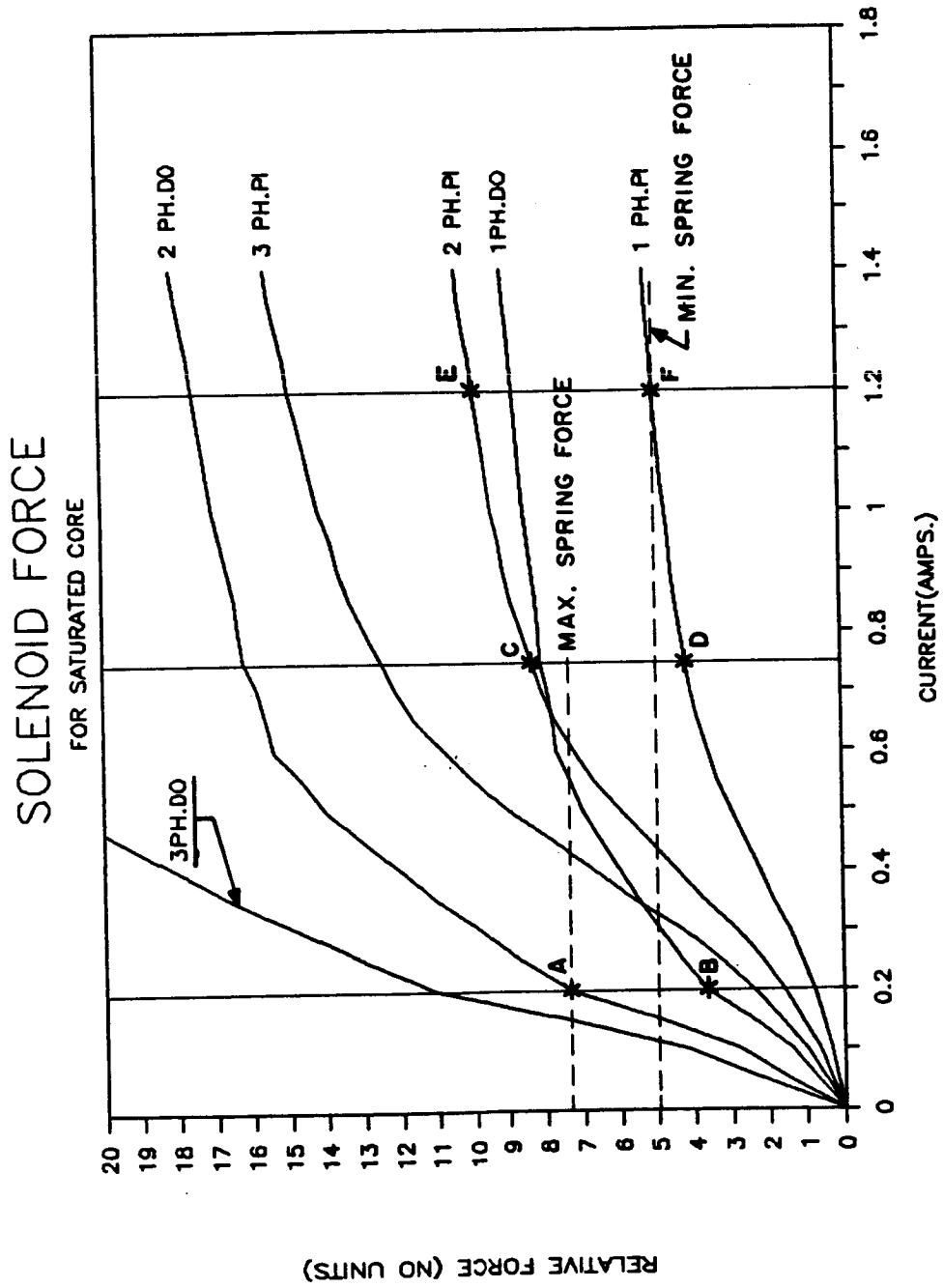
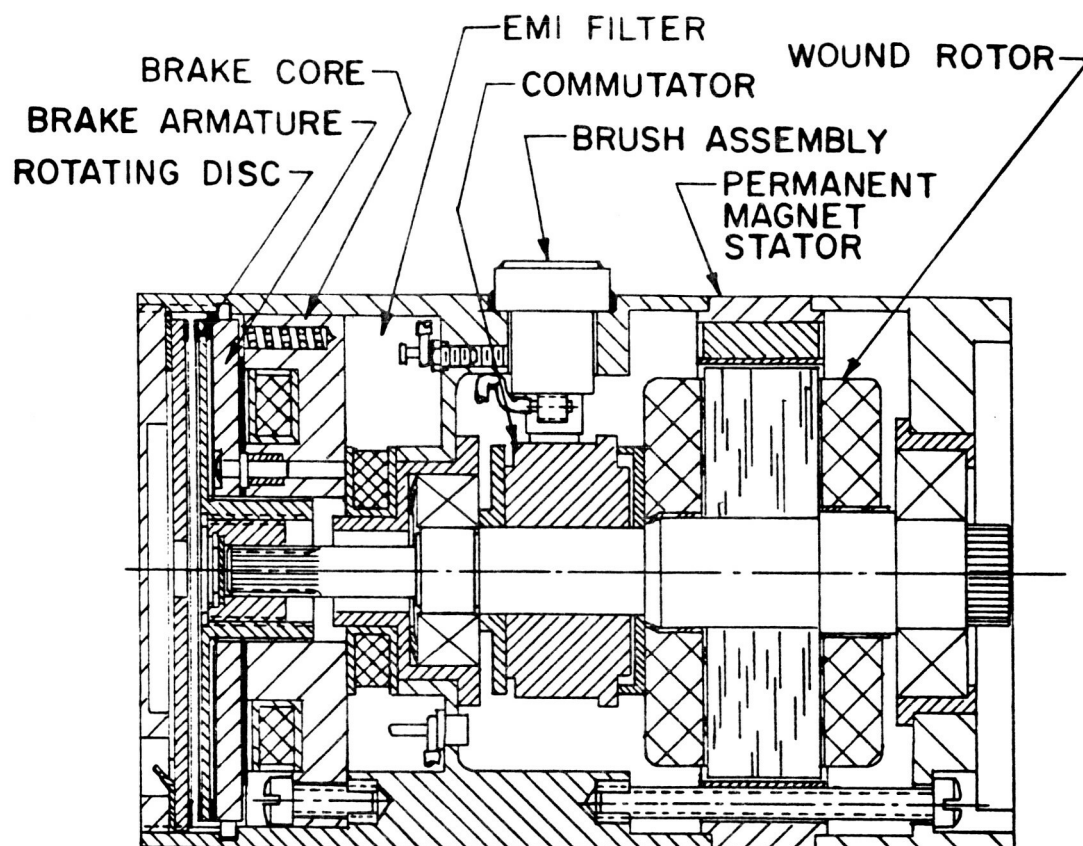
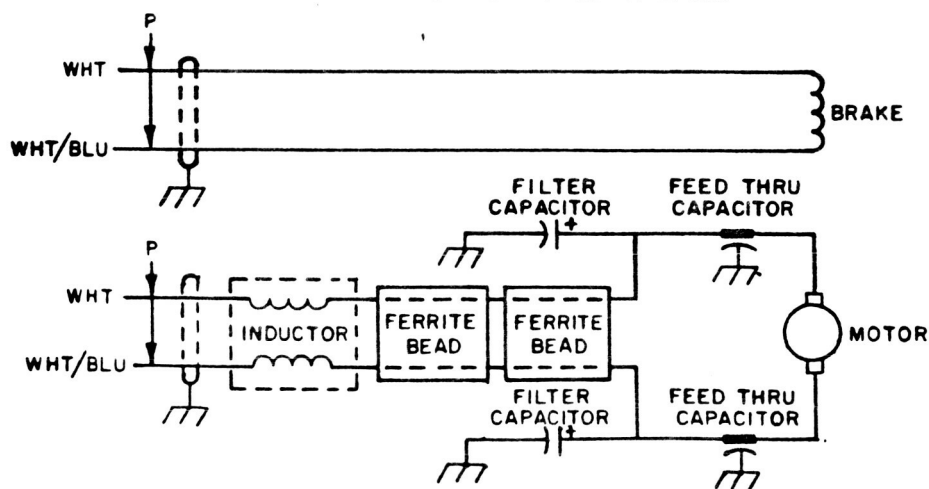


FIGURE 9



DC MOTOR/BRAKE



MOTOR/BRAKE SCHEMATIC

FIGURE 10

***** DC MOTOR PERFORMANCE *****

***** COMMON DRIVE UNIT *****

INPUT:

VOLTAGE:	24 MIN.	28 NOMINAL	32 MAX.
TEMP (C):	-68 MIN.	35 MAX.	
RESISTANCE:	108 OHMS @25C	5 TOL. (+,-)	
TORQ. SENS.:	0.52 NM/A	0.028 TOL. (+,-)	
DRAG TORQ.:	0.01 NM		
BRUSH DROP:	0.5 VOLTS		
GEAR RATIO:	786.		
GHD. EFF.:	0.87 PER UNIT		

OUTPUT:

	24V, 35C	28V, 25C	32V, -68C
VOLTAGE:	24	28	32
TEMPERATURE (C):	35	25	-68
NO-LOAD SPEED (RPM):	0.433	0.552	0.714
NO-LOAD CURR. (AMPS):	0.032	0.034	0.036
STALL TORQUE (NM):	55.15	78.72	166.5
STALL CURRENT (AMPS):	0.199	0.254	0.474
RESISTANCE (OHMS):	117.8	108	66.34

DC MOTOR PERFORMANCE

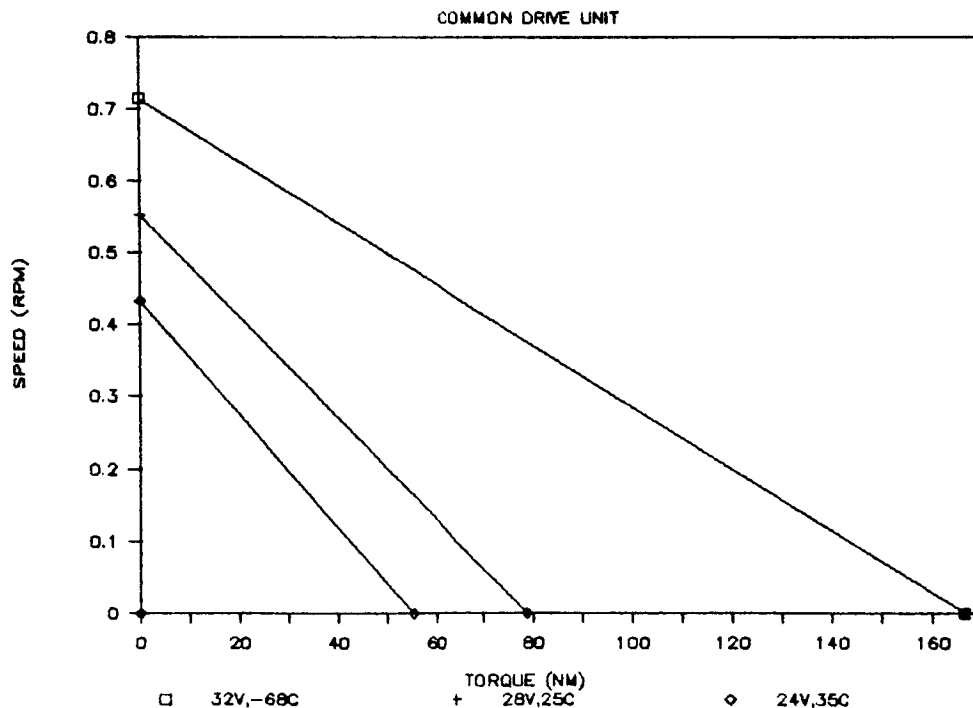


FIGURE II

A Reactionless Precision Pointing Actuator

Peter Wiktor*

This paper discusses the applications, design, control and testing of an actuator that provides the precise motion control of a gimbal platform without torquing against the basebody to which it is attached. The reactionless actuator described in this paper has been given the name "reactuator".

INTRODUCTION

The Voyager 2 spacecraft built by the Jet Propulsion Laboratory (JPL) flew by Uranus in January of 1986 and took spectacular high resolution pictures of its rings and moons. Due to the long exposure times required, the entire spacecraft was slewed to compensate for the relative motion between the spacecraft and the image. Voyager's cameras are mounted on a two axis gimballed platform which is controlled by two geared actuators. Voyager was not able to take advantage of the platform for image motion compensation since the actuators induce vibrations in the spacecraft which feed back and blur the camera images. A minimum of 30 seconds must be allowed for the spacecraft to settle down after a low rate slew of the platform before high resolution, no smear pictures can be taken. Experience with Voyager and other spacecraft has led JPL to pursue the development of reactionless gimbal actuators for the precise positioning of gimballed platforms [1,2,3]. An actuator of this type has been designed for a Space Shuttle based tracking system and is currently baselined for the Mariner Mark II class of interplanetary spacecraft [4].

In addition to exciting a spacecraft's flexible modes, the angular momentum imparted to a gimballed platform by a conventional direct drive or geared actuator induces a rotation of the whole spacecraft. This rotation must be taken out by the spacecraft's attitude control system. For example if the Mariner Mark II spacecraft had a conventional gimbal actuator an additional 50% of fuel beyond that required for attitude control would be needed to take out actuator induced rotation of the spacecraft [5]. The reactuator, on the other hand, decouples motion of the gimbal from the spacecraft. Gimbal control is independent of the spacecraft natural modes and spacecraft attitude control is independent of gimbal motion.

*Member Technical Staff, Guidance and Control Section, Jet Propulsion Laboratory, California Institute of Technology, Pasadena, California.

REACTUATOR SCHEMATIC

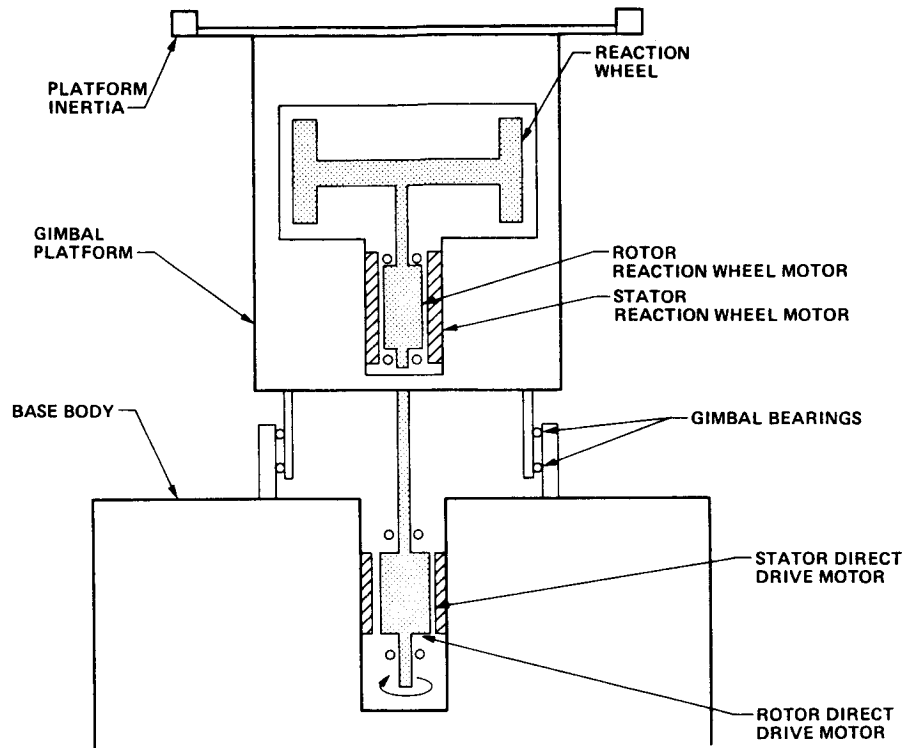


Figure 1

HARDWARE DESCRIPTION

There are two rotational loads imposed on a gimbal moving relative to a basebody: the inertial load and the loads in the joint imparted by bearing friction and cable torque between the gimbal and basebody. The reactuator shown schematically in Figure 1 has two motors to account for these loads. The reaction wheel (RW) motor cancels inertial loads and the direct drive (DD) motor handles loads in the joint. By properly distributing torque commands to each motor, the gimbal can be moved without imparting a reaction torque on the basebody. Providing a rigid body to torque against the reaction wheel permits high bandwidth platform control even if the gimbal is mounted on a flexible structure. The direct drive motor replaces the energy lost due to bearing friction and cable torque thereby preventing the reaction wheel from spinning up and saturating in speed.

In addition to two motors, the reactuator incorporates two angular position sensors as shown in the detailed cross section of Figure 2. The

sensors provide commutation signals for the brushless DC motors as well as position and velocity feedback for closed loop rate control. The components of the reactuator have been carefully selected to minimize self induced torque ripple. A detailed description of each component follows.

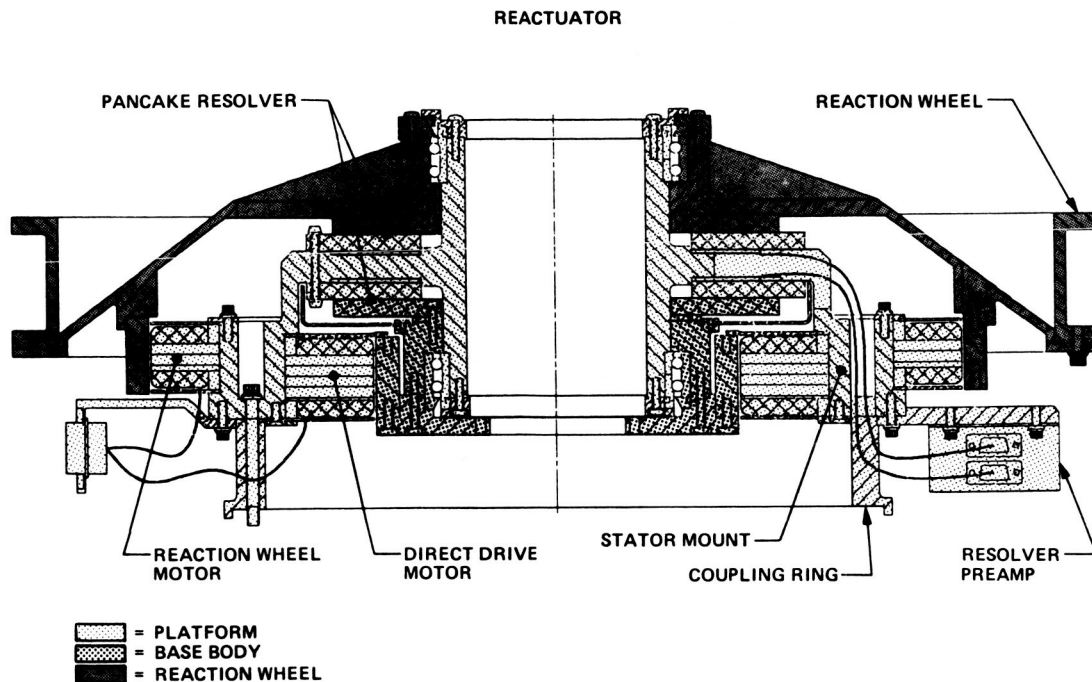


Figure 2

Bearings

The reaction wheel and gimbal are each supported on a duplex pair of stainless steel ball bearings. The bearings have a solid outer race and split inner race with customized preload, contact angle and raceway curvature. The reactuator housing is made of titanium to closely match the bearing's thermal coefficient of expansion.

Resolver

The position sensors are high accuracy ($\pm 29 \mu\text{rad}$) printed circuit pancake resolvers. Each resolver has two tracks, one with 256 poles and one with 254. The outputs of the two tracks are converted to 12 bit digital words by two hybrid resolver to digital converters [6] which also output an analog velocity signal. The digital words from the two tracks are correlated digitally to produce a 19 bit word that corresponds to

absolute position over one revolution. A built-in ferrite core transformer [7] allows the resolver to be interfaced to the stationary element. This eliminates the need for a slip ring or separate rotary transformer.

Motors

Two phase, 16 pole, brushless DC motors provide actuating torque for both the reaction wheel and the direct drive. The motors are designed to generate a sinusoidal back EMF signal with minimum harmonic distortion. Cogging torque is minimized by the use of a nickel iron lamination material.

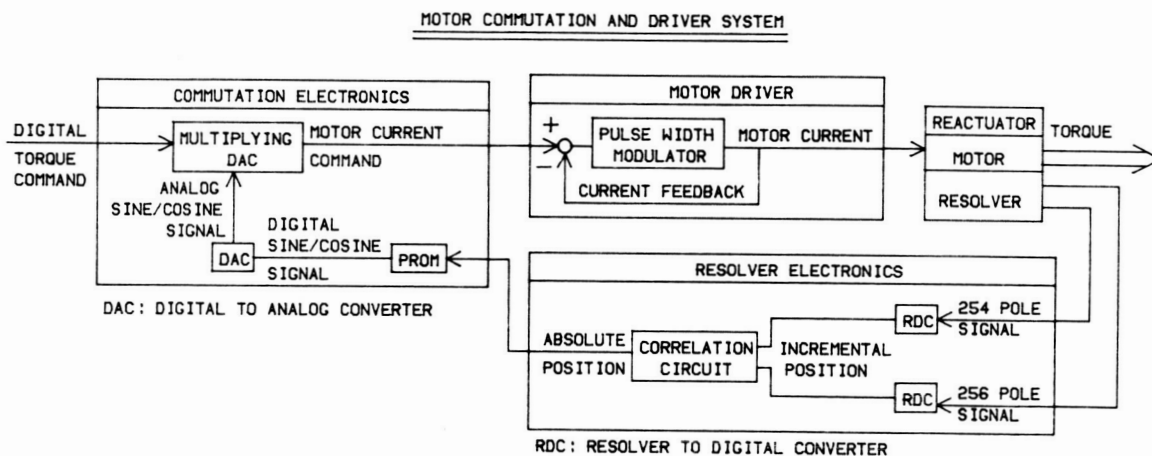


Figure 3

Motor Driver

The motor commutation and driver system is a hybrid of digital and analog circuitry as shown in Figure 3. It is designed to drive the motor with sinusoidally varying current resulting in minimum torque ripple. The digital absolute position signal from the resolvers addresses a sine signal that is stored in programmable read only memory (PROM). The output of the PROMs is converted into an analog signal and fed into a multiplying digital to analog converter (DAC). A digital torque word modulates the amplitude of the analog commutation signal and feeds it to a pulse width modulated (PWM) power amplifier [8]. The PWM driver is a closed loop amplifier that produces a current proportional to the commutation signal based on sensing and feeding back output current. The driver automatically compensates for variations in supply voltage as well

as back EMF and thus produces a constant peak torque independent of motor speed or voltage fluctuations. Since the commutation signal is stored in PROMs, it can easily be programmed to compensate for harmonic distortion in the back EMF signal as well as to precisely align the commutation signal with the motor poles.

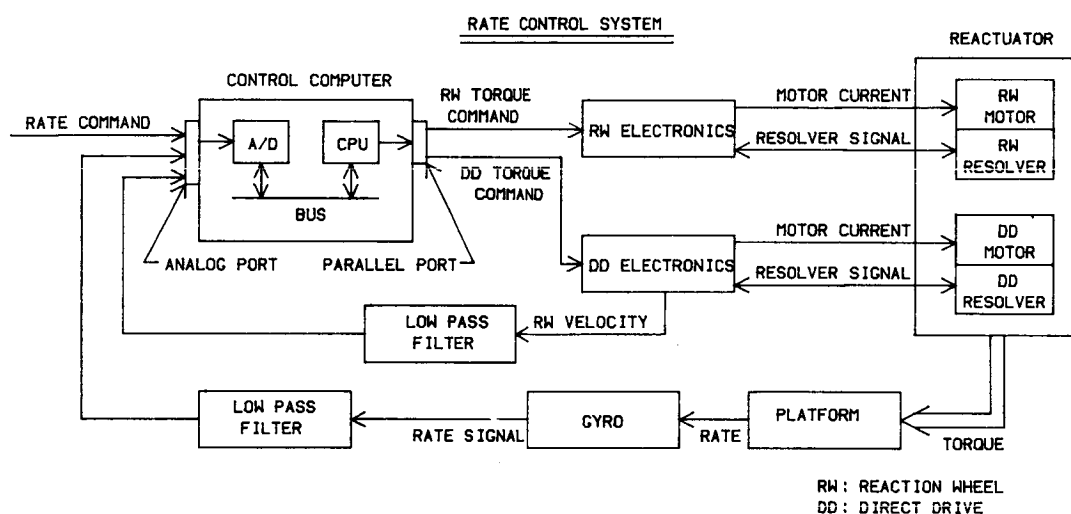


Figure 4

RATE CONTROL SYSTEM

The reactuator is used in a closed loop rate control system as depicted in Figure 4. The control system may be described by the following process. A digital computer receives rate commands and sends appropriate torque commands to the two motors to control platform rate as measured by a rate gyro. The computer also controls reaction wheel speed based on feedback from the reaction wheel resolver velocity signal.

The controller is designed to produce smooth, accurate platform response to rate commands. It must reject basebody disturbances as well as self induced vibration. Torque commands must be distributed to the two motors in such a manner as to produce the desired smooth response without causing the two motors to "fight" each other. The torque commands can be made independent by separating the control bandwidths for the two motors by one order of magnitude. The reaction wheel controller is tuned for high frequency disturbance rejection while the direct drive motor prevents reaction wheel speed saturation at a much lower bandwidth.

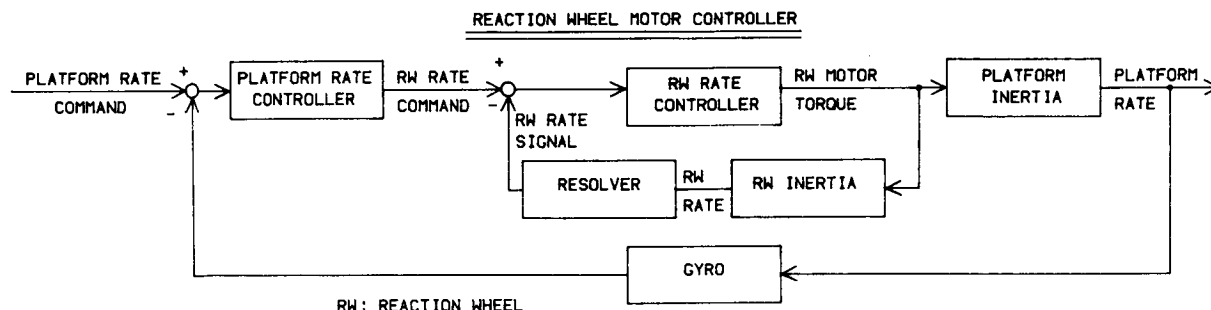


Figure 5

Reaction Wheel Motor Controller

The reaction wheel motor controller incorporates two loops as depicted in Figure 5. The outer loop compares the platform rate as measured by the gyro with the rate command. The resulting error signal goes through a filter which produces the reaction wheel rate command for the inner loop. This loop compares the commanded rate to the reaction wheel resolver velocity signal and sends the appropriate torque commands to the motor causing it to follow the commanded rate. Since this velocity signal has high bandwidth and relatively low noise, the inner loop rejects motor and bearing torque ripple thus producing a smooth reaction wheel rate.

The platform rate controller has the transfer function,

$$\frac{K_P S + K_I}{s^2}$$

The two integrators of this controller guarantee no steady state error to constant platform rate commands. The reaction wheel controller transfer function consists of a simple gain that produces well damped response to the rate feedback signal.

Direct Drive Motor Controller

If the reaction wheel's speed is such as to cancel the angular momentum of the platform and the direct drive motor's torque cancels bearing and cable torque, then the reactuator will exert no torque on the spacecraft. The direct drive motor controller depicted in Figure 6 is designed to achieve this result. The controller commands the direct drive motor to provide sufficient torque to drive the angular momentum of

the reaction wheel and the platform to zero. The direct drive controller has proportional plus integral gains that produce a well damped zero steady state error response.

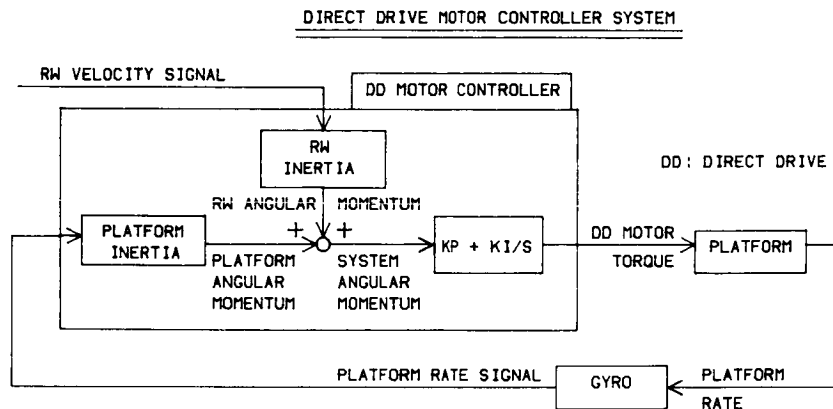


Figure 6

TESTING

A photograph of the reactor and rate control system breadboard is shown in Figure 7. The reactor breadboard is assembled out of JPL's Galileo spacecraft spare parts. It is mounted on an air bearing to simulate a spacecraft and to allow the effectiveness of the "reactionless" actuator to be monitored. The air bearing is isolated from ambient noise by a seismic isolation pier. Table 1 summarizes the key parameters of the breadboard system.

The system was first tested in an open loop. The air bearing was levitated and the reaction wheel motor was given a constant torque command. The gyro measured a platform disturbance of 280 $\mu\text{rad/sec}$ RMS induced by motor and bearing torque ripple. The rate loop around the reaction wheel motor (Figure 5) was closed to attenuate this disturbance. Again the air bearing was levitated but this time a constant rate command was given to the reaction wheel motor controller. The closed loop platform rate disturbance measured by the gyro was 12.3 $\mu\text{rad/sec}$ RMS. Integrating the velocity signal, the corresponding disturbance in terms of position was 7 μrad RMS. Comparing the open to closed loop platform response indicates that the controller exhibits a -27 db disturbance rejection to reaction wheel motor and bearing torque ripple [9].

ORIGINAL PAGE IS
OF POOR QUALITY

REACTUATOR BREADBOARD SYSTEM

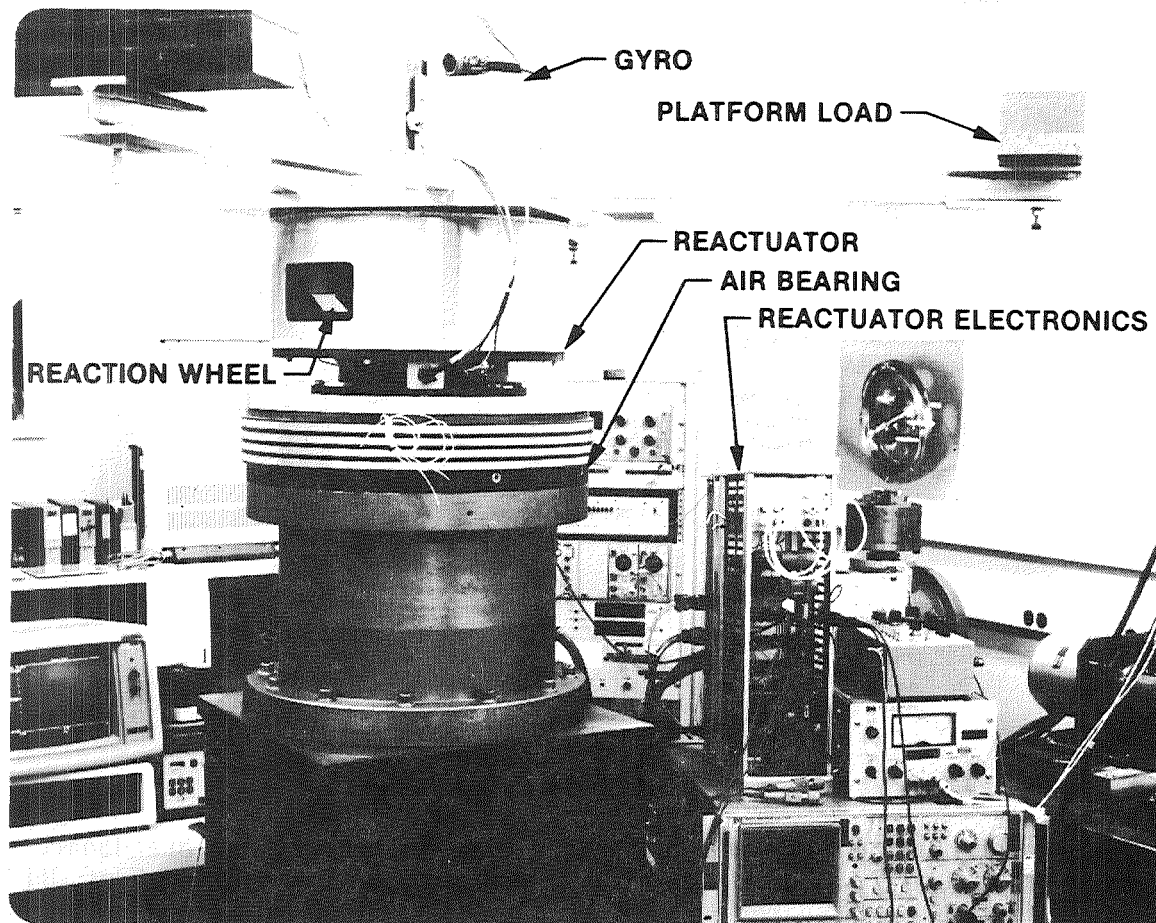


Figure 7

The breadboard reactuator is connected to the electronics by numerous cables. The torque from these cables causes the reaction wheel to accelerate until the motor torque saturates due to the back EMF generated by the motor. The direct drive motor controller which prevents the reaction wheel motor from saturating will be incorporated in the near future. The two motor actuator will then be tested to determine the effectiveness of the "reactionless" actuator. A flexible boom will be attached to the air bearing and the ability of the actuator to control the platform without exciting this boom will be determined. The flexible boom will also be used to intentionally induce basebody disturbances allowing the reactuator to demonstrate its ability to reject basebody disturbances.

TABLE 1

Breadboard Reactuator System Parameters

Gyro bandwidth	5.5 hz
Gyro peak rate	35 mrad/sec
Gyro noise	23 rad/sec RMS
Resolver bandwidth	30 hz
Resolver noise	4.6 mrad/sec RMS
Resolver peak rate	11.9 rad/sec
RW and DD motor drive voltage	45 volts
RW and DD motor driver bandwidth	400 hz
RW motor torque constant	5.21 Nm/amp
RW motor winding resistance	21.3 ohms/phase
DD motor torque constant	1.25 Nm/amp
DD motor winding resistance	33 ohms/phase
Platform inertia	56 Kg m ²
RW inertia	0.281 Kg m ²

RW: Reaction Wheel

DD: Direct Drive

CONCLUSION

It is practical to consider a reactionless actuator for the precise pointing of a gimballed platform on a basebody which has either low structural stiffness or a low moment of inertia. An actuator of this type allows the design of the gimbal controller to be completely independent of the basebody's structural dynamics. There are many applications for a reactionless actuator including the Space Station where it will be critical to precisely point various payloads without exciting the station's low frequency modes [10].

ACKNOWLEDGEMENTS

The Research described in this paper was performed by the Jet Propulsion Laboratory, California Institute of Technology, under contract with the National Aeronautics and Space Administration. It is the author's sincere pleasure to thank the Actuator and Inertial Sensors Group of the Guidance and Control Section at the Jet Propulsion Laboratory for their hard work, dedication and enthusiasm in developing the retractor breadboard.

REFERENCES

- [1] Schumacher, L.L., "The Integrated Platform Pointing and Attitude Control Subsystem (IPPACS) -- A Concept for Today and 2001", JPL IOM 343-82-412, May 17, 1982. (internal document)
- [2] Marchetto, C.A., "Precision Micro-Stepping Actuator", Eleventh Annual Symposium on Incremental Motion Control Systems and Devices, Chicago, IL, May 1982.
- [3] Sirlin, S. W. and Bell, C.E., "Soft Mounted Momentum Compensated Pointing System for the Space Shuttle Orbiter", SPIE Technical Symposium Southeast, Orlando, Florida, April 1986.
- [4] Bell, C.E. and Lehman, D.H., "Mariner Mark II: Spacecraft Control for the 1990's and Beyond", 33rd Annual Meeting American Astronomical Society, Boulder, Colorado, October 1986.
- [5] Schier, A.J., "Removal of Momentum Wheels From HPSP and the Resulting ACS Propellant Mass for the CRAF Mission", JPL IOM 343-86-1587, October 29, 1986. (internal document)
- [6] Bruce, I., "Replacing Tachometers With A Resolver-Tracking Converter Combination", Power Conversion and Intelligent Motion, Volume 12 Number, 11, November 1986.
- [7] Koerner, T., "Rotary Transformer for Inductosyn Excitation", JPL IOM 342-86-A-144, December 3, 1986. (internal document)
- [8] Salomon, P., "PWM Motor Driver Operating Description", JPL IOM 343-86-1795, October 13, 1986. (internal document)
- [9] Wiktor, P.J., "Pathfinder Breadboard Actuator Test Results", JPL IOM 343-86-1551, November 5, 1986. (internal document)
- [10] Sirlin, S.W. and Laskin, R.A., "Payload Isolation and Precision Pointing for the 1990's", Annual Rocky Mountain Guidance and Control Conference, Keystone, Colorado, February 2-6, 1985.

The Design of Worm Gear Sets

Andrea I. Razzaghi*

ABSTRACT

The purpose of this paper is to present a method for designing worm gear sets to meet torque multiplication requirements. First, the fundamentals of worm gear design are discussed, covering worm gear set nomenclature, kinematics and proportions, force analysis, and stress analysis. Then, a suggested design method is discussed, explaining how to take a worm gear set application, and specify a complete worm gear set design. The discussions in this paper will be limited to cylindrical worm gear sets that have a 90° shaft angle between the worm and the mating gear.

INTRODUCTION

Designing worm gear sets to meet torque multiplication requirements is a challenge because of the high friction in worm gearing. Friction is higher in worm gearing than in more conventional types of gearing, such as spur, bevel and conical, due to the sliding that occurs between the worm and the mating gear. Friction is very difficult to quantify because there are so many factors that affect it. The coefficient of friction depends on the material combinations, surface roughness, operating speeds, and the pressure, temperature, and viscosity of the lubricant.

The curves in Figure 1 show the dependence of the coefficient of friction on the sliding velocity between the worm and the mating gear, the material combination, and the lubrication. Curve A is for a cast-iron worm and mating gear. Curve B is for a case-hardened worm mating with a phosphor-bronze gear. Both curves are based on good lubrication. The curves indicate that the coefficient of friction increases as the sliding velocity decreases. Many more curves could be added to this graph for more combinations of materials and different lubrication. In aerospace applications where the sliding velocities are slow, and non-standard materials and lubricants are used, it is easy to see how the coefficient of friction for a particular application would be difficult to determine.

*NASA/Goddard Space Flight Center, Greenbelt, MD

WORM GEAR SET NOMENCLATURE

Figure 2 shows the nomenclature for worm gear sets as defined below.

Pitch Diameter

The pitch diameters of the worm, D_w , and of the gear, D_g , are tangent to each other and represent where the curved surfaces of the gear teeth and worm threads contact each other during operation. D_g is the diameter of the gear's pitch circle, and D_w is the diameter of the worm's pitch cylinder.

Center Distance

The center distance, C_d , is the distance between the center of the worm and the center of the gear when in mesh.

Root Diameter

The root diameter of the worm, R_{dw} , is the diameter to the root of the worm's threads; and of the gear, R_d , is the diameter to the root of the gear's teeth.

Outside Diameter

The outside diameter of the worm, O_{dw} , is the diameter to the tips of the threads; and of the gear, O_d , is the diameter to the tips of the teeth.

Circular Pitch

The circular pitch, P_c , is the spacing of gear teeth measured along the gear's pitch circle from a point on one tooth to a corresponding point on an adjacent tooth.

Normal Circular Pitch

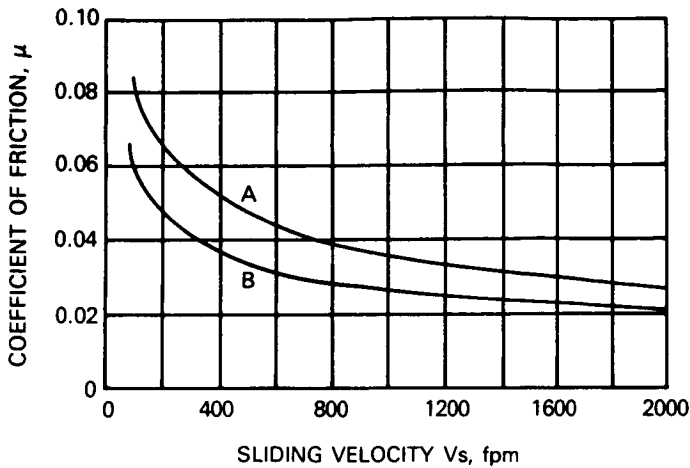
The normal circular pitch, P_n , is the circular pitch in the normal plane.

Tooth Thickness

The tooth thickness, T , is the thickness of the tooth measured along the pitch circle.

Addendum

The addendum, A_d , is the height of the gear tooth beyond the pitch circle.



CURVE A: CAST-IRON WORM AND GEAR
WITH GOOD LUBRICATION

CURVE B: CASE-HARDENED WORM AND
PHOSPHOR-BRONZE GEAR WITH
GOOD LUBRICATION

**FIGURE 1: REPRESENTATIVE VALUES OF
COEFFICIENT OF FRICTION FOR WORM GEARING**

SHIGLEY, JOSEPH EDWARD, *MECHANICAL ENGINEERING DESIGN* THIRD EDITION, McGRAW-
HILL BOOK COMPANY, 1977

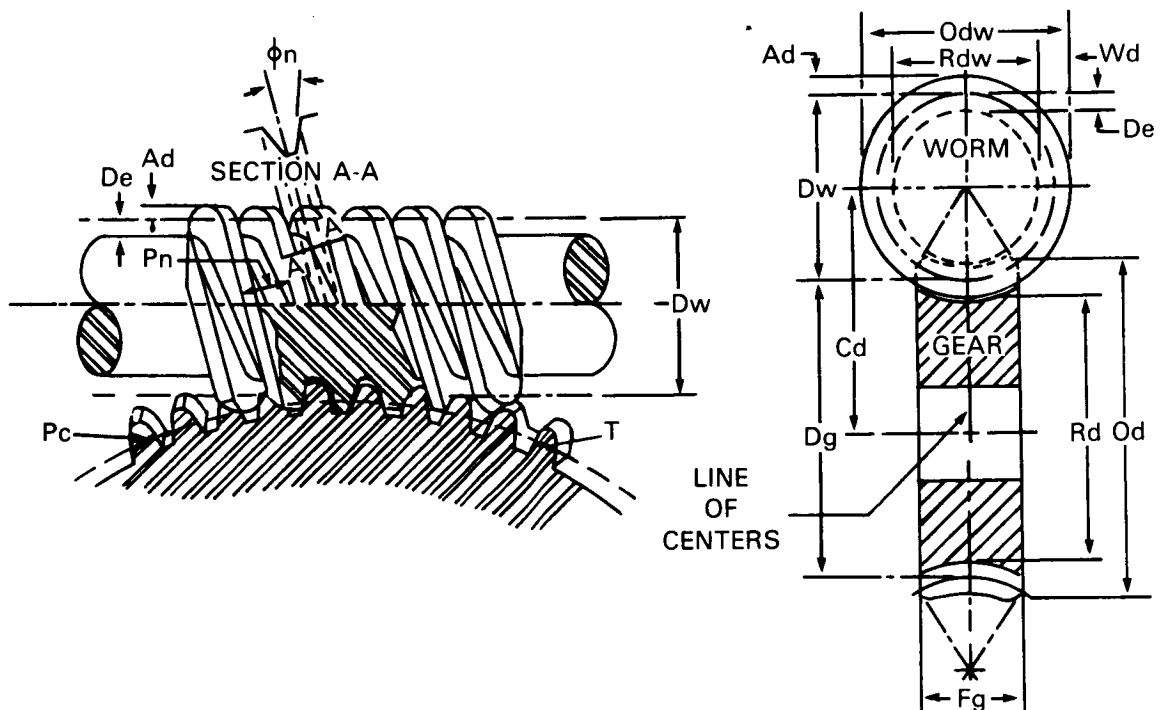


FIGURE 2: WORM GEAR SET NOMENCLATURE

Dedendum

The dedendum, D_d , is the depth of the gear tooth below the pitch circle.

Whole Depth

The whole depth, W_d , is the sum of the addendum and the dedendum.

Face Width

The face width of the gear tooth, F_g , is the width of the gear tooth measured on the pitch circle.

Normal Pressure Angle

The normal pressure angle, ϕ_n , is the angle, in the normal plane, between the line-of-action (common tangent to the base circle of the gear and base cylinder of the worm) and a perpendicular to the line of centers.

Gear's Helix Angle

The gear's helix angle, ψ_g , measured at the pitch diameter, is the angle between the teeth and the axis of rotation.

Figure 3 illustrates the developed pitch cylinder of a double-threaded worm, where A and B represent the two threads.

Lead

The lead of the worm, L , is the axial advance per revolution of the worm.

Lead Angle

The lead angle of the worm, λ , is the angle measured at the pitch cylinder, between the helix of the worm and the plane of rotation. When the shaft angle between the worm and gear is 90° , then λ is equal to ψ_g .

Axial Pitch

The axial pitch of the worm, P_a , is the linear pitch in the axial plane on the pitch cylinder. When the shaft angle is 90° , then P_a is equal to P_c .

The worm gear set is characterized by the gear ratio, and the gear is often characterized by the diametral pitch.

Gear Ratio

The gear ratio, Z_g , is the number of teeth on the gear, N_g , divided by the number of threads on the worm, N_w . The gear ratio is also the speed ratio and is equal to the input speed of the worm, S_w , divided by the output speed of the gear, S_g .

Diametral Pitch

The diametral pitch of a gear, D_p , is the number of teeth per inch on the pitch circle.

KINEMATICS AND PROPORTIONS

When designing a worm gear set, the designer's application will dictate certain parameters. The remaining parameters can be calculated using the following kinematic relations.

The diametral pitch of a gear is the number of teeth per inch on the pitch circle:

$$D_p = \frac{N_g}{D_g}$$

The circular pitch is the circular distance the gear advances on the pitch circle per turn of the worm:

$$P_c = \frac{\pi}{D_p}$$

The gear tooth thickness and the worm thread thickness are not necessarily equal, but for the purposes of this paper, will be assumed to be equal. The tooth thickness and the space between teeth will also be assumed equal. Their sum is P_c , so:

$$T = 1/2 P_c$$

The lead of the worm is the axial distance the worm advances per turn:

$$L = N_w P_a$$

When the shaft angle is 90° , the usual case, then:

$$P_c = P_a \text{ and}$$

$$L = N_w P_c = \frac{\pi N_w}{D_p}$$

Referring to Figure 3:

$$\tan \lambda = \frac{L}{\pi D_w}$$

$$\lambda = \tan^{-1} \left(\frac{L}{\pi D_w} \right)$$

Substituting in for L, λ can also be expressed:

$$\lambda = \tan^{-1} \left(\frac{N_w}{D_p D_w} \right)$$

The normal circular pitch is:

$$P_n = P_a \cos \lambda$$

Table 1 gives recommended pressure angles and tooth proportions for various lead angle ranges.

Table 1¹

RECOMMENDED PRESSURE ANGLES AND TOOTH PROPORTIONS FOR WORM GEARING

Lead angle, λ degrees	Pressure angle, ϕ_n degrees	Addendum, A_d	Dedendum, D_e
0-15	14 1/2	.3683 P_a	.3683 P_a
15-30	20	.3683 P_a	.3683 P_a
30-35	25	.2865 P_a	.3314 P_a
35-40	25	.2546 P_a	.2947 P_a
40-45	30	.2228 P_a	.2578 P_a

The whole depth of the gear tooth and of the worm thread is the sum of the addendum and the dedendum.

$$W_d = A_d + D_e$$

¹Shigley, Joseph Edward, Mechanical Engineering Design, Third Edition, McGraw-Hill Book Company, 1977.

The outside diameter is the sum of the pitch diameter and twice the addendum.

$$O_d = D_g + 2A_d$$

$$O_{dw} = D_w + 2A_d$$

The root diameter is the pitch diameter minus twice the dedendum.

$$R_d = D_g - 2D_e$$

$$R_{dw} = D_w - 2D_e$$

The recommended minimum face width of the gear tooth is, as illustrated in Figure 4, equal to the length of a tangent to the worm's pitch circle between its points of intersection with the outside diameter. Expressing F_g in terms of D_w and O_{dw} :

$$F_g \geq \sqrt{O_{dw}^2 - D_w^2}$$

FORCE ANALYSIS

Figure 5 shows the forces acting at the worm's pitch cylinder. W represents the force exerted by the gear. The gear tooth contacts the worm thread at their pitch diameters, at the normal pressure angle relative to the worm's axis of rotation, and at the gear's helix angle (equal to the worm's lead angle) relative to the gear's axis of rotation. The relative motion between the worm and gear teeth is pure sliding. The force W acting normal to the worm-thread profile produces a frictional force, $W_f = \mu W$, with component $\mu W \cos \lambda$ in the negative X-direction and $\mu W \sin \lambda$ in the positive Z direction.

The X-axis is tangent to the worm's pitch cylinder and parallel to the gear's axis of rotation. The Y-axis is parallel to the mutual radial axis between the worm and the gear. The Z-axis is tangent to the gear's pitch circle and parallel to the worm's axis of rotation. The X, Y and Z components of W , respectively, are:

$$W^X = W (\cos \phi_n \sin \lambda + \mu \cos \lambda)$$

$$W^Y = W \sin \phi_n$$

$$W^Z = W (\cos \phi_n \cos \lambda - \mu \sin \lambda)$$

²Shigley, Joseph Edward, Mechanical Engineering Design, Third Edition, McGraw-Hill Book Company, 1977.

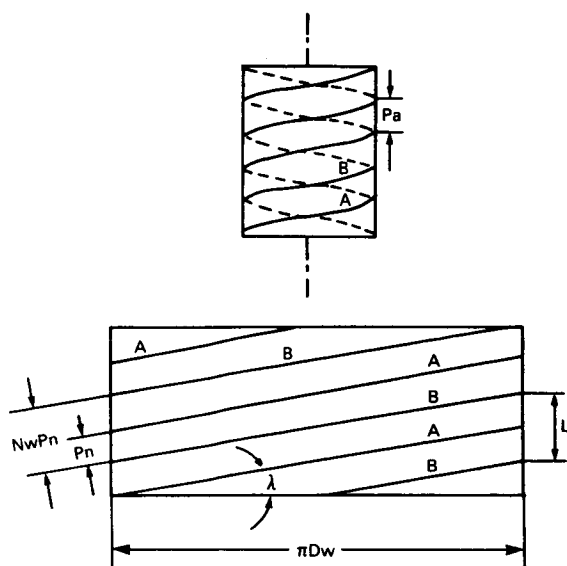


FIGURE 3: DEVELOPED PITCH CYLINDER OF WORM

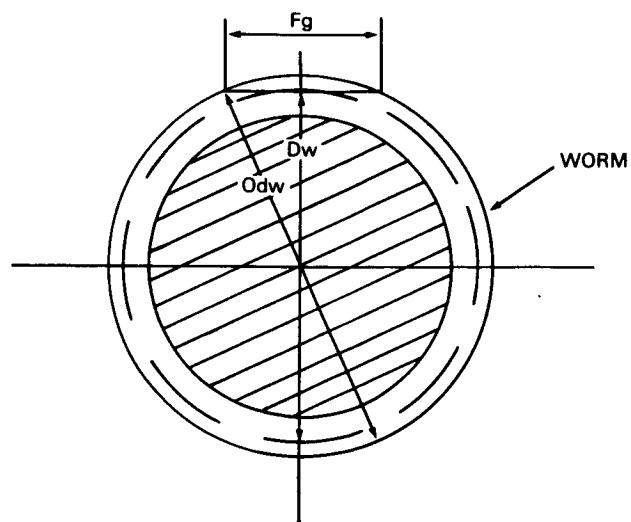


FIGURE 4: MINIMUM GEAR FACE WIDTH RECOMMENDATION

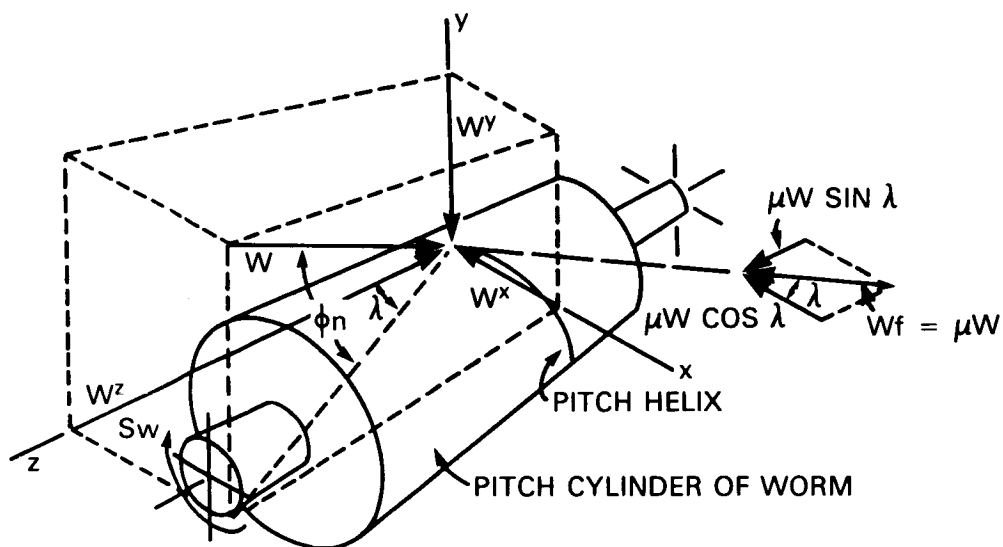


FIGURE 5: PITCH CYLINDER OF A WORM SHOWING THE FORCES ACTING UPON IT BY THE MATING GEAR

The tangential force on the worm is W^x , the radial force on the worm is W^y and the axial force on the worm is W^z . Since the gear forces are opposite the worm forces, the forces can be summarized as:

$$W_{wt} = -W_{ga} = W^x$$

$$W_{wr} = -W_{gr} = W^y$$

$$W_{wa} = -W_{gt} = W^z$$

where g denotes the forces acting on the gear, w denotes the forces acting on the worm, a denotes the axial direction, r denotes the radial direction and t denotes the tangential direction.

The torque input from the worm is the product of the worm's tangential force and its pitch radius :

$$T_w = \frac{W_{wt} D_w}{2}$$

Similarly, the torque output from the gear is:

$$T_g = \frac{W_{gt} D_g}{2}$$

The torque multiplication ratio is:

$$Z_t = \frac{T_g}{T_w} = \frac{W_{gt} D_g}{W_{wt} D_w}$$

Substituting the expressions for W_{gt} and W_{wt} into this expression:

$$\begin{aligned} Z_t &= \frac{-W (\cos \phi_n \cos \lambda - \mu \sin \lambda) D_g}{W (\cos \phi_n \sin \lambda + \mu \cos \lambda) D_w} \\ &= \frac{-D_g (\cos \phi_n \cos \lambda - \mu \sin \lambda)}{D_w (\cos \phi_n \sin \lambda + \mu \cos \lambda)} \end{aligned}$$

The efficiency of the worm gear set can be expressed as the absolute value of the torque ratio divided by the gear ratio:

$$Eff = \left| \frac{Z_t}{Z_g} \right|$$

Substituting N_g/N_w in for Z_g and the expression for Z_t :

$$\begin{aligned} \text{Eff} &= \left| \frac{N_w}{N_g} \left[\frac{-D_g (\cos \phi_n \cos \lambda - \mu \sin \lambda)}{D_w (\cos \phi_n \sin \lambda + \mu \cos \lambda)} \right] \right| \\ &= \left| \frac{N_w D_g}{N_g D_w} \frac{(\cos \phi_n \cos \lambda - \mu \sin \lambda)}{(\cos \phi_n \sin \lambda + \mu \cos \lambda)} \right| \end{aligned}$$

Dividing the numerator and denominator by $\cos \lambda$:

$$\text{Eff} = \left| \frac{N_w D_g}{N_g D_w} \frac{(\cos \phi_n - \mu \tan \lambda)}{(\cos \phi_n \tan \lambda + \mu)} \right|$$

Substituting $D_g D_p$ for N_g :

$$\text{Eff} = \left| \frac{N_w D_g}{D_g D_p D_w} \frac{(\cos \phi_n - \mu \tan \lambda)}{(\cos \phi_n \tan \lambda + \mu)} \right|$$

Substituting $\tan \lambda$ for $\frac{N_w}{D_p D_w}$:

$$\text{Eff} = \left| \frac{\tan \lambda (\cos \phi_n - \mu \tan \lambda)}{(\cos \phi_n \tan \lambda + \mu)} \right|$$

Simplifying:

$$\text{Eff} = \left| \frac{\cos \phi_n - \mu \tan \lambda}{\cos \phi_n + \mu \cot \lambda} \right|$$

The efficiency equation is a function of three parameters: pressure angle, lead angle, and coefficient of friction. Two of these are design parameters, ϕ_n and λ . The coefficient of friction, however, is dependent upon many factors and is very difficult to set in the design. Figure 6 shows the effect of the coefficient of friction on worm gear efficiency for the standard pressure angles, between $14\frac{1}{2}^\circ$ and 30° . The lead angle was held constant at $18^\circ 26'$. The graph shows a clear deterioration of efficiency as the friction increases, but very little change over the standard range of pressure angles. In Figure 7, the lead angle was varied within the range 5° to 45° , at 5° increments, and pressure angle was held constant at 20° . This graph shows that the efficiency drops off more drastically at the lower end of the lead angle range as friction increases. The optimum lead angle for maximizing efficiency is in the 35° to 40° range, but in actual practice lead angles above 25° are rarely used because they are difficult to manufacture.

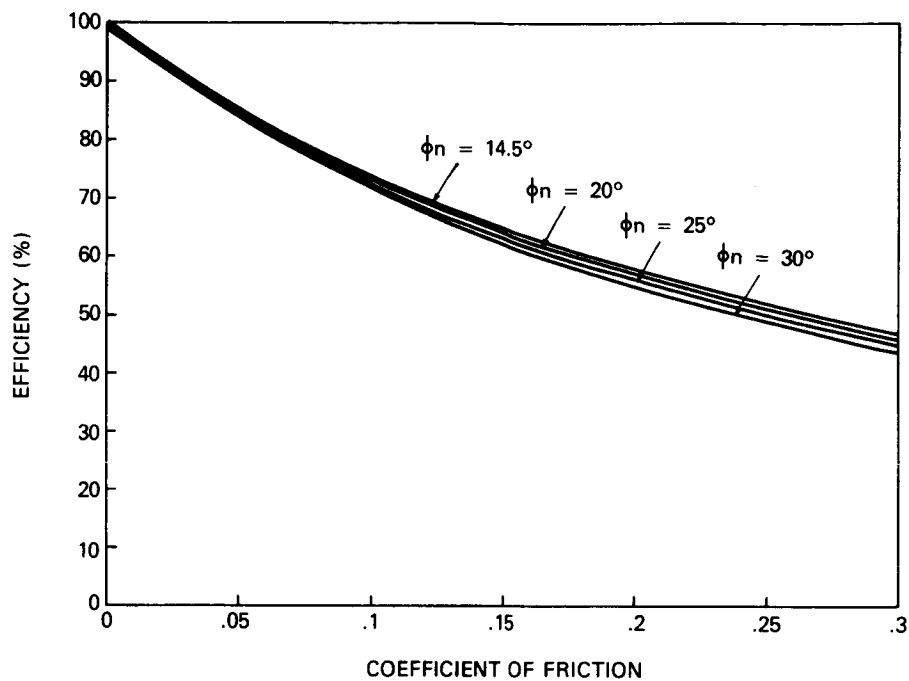


FIGURE 6: THE EFFECT OF THE COEFFICIENT OF FRICTION AND THE PRESSURE ANGLE ON WORM GEAR EFFICIENCY ($\lambda = 18^\circ 26'$)

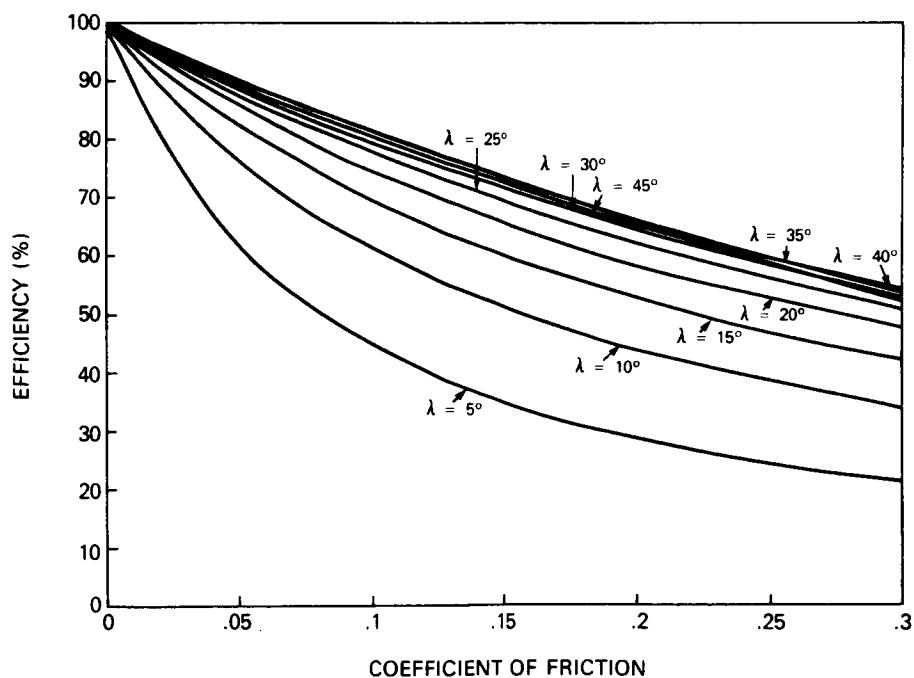


FIGURE 7: THE EFFECT OF THE COEFFICIENT OF FRICTION AND THE LEAD ANGLE ON WORM GEAR EFFICIENCY ($\phi_n = 20^\circ$)

The torque multiplication ratio can be expressed as the product of the efficiency and the gear ratio:

$$Z_t = Z_g \text{ Eff} = Z_g \left| \frac{\cos \phi_n - \mu \tan \lambda}{\cos \phi_n + \mu \cot \lambda} \right|$$

Figure 8 shows the effect of the coefficient of friction on the torque multiplication ratio for various gear ratios, with $\phi_n = 20^\circ$ and $\lambda = 18^\circ 26'$. As the gear ratio increases, the slopes of the curves increase proportionately. When friction is negligible, $Z_g = Z_t$. This, however, can never be assumed because friction is always present and difficult to estimate. Figure 9 shows an improvement over Figure 8 where λ , at 40° , is close to the optimum for high efficiency. Figure 10 shows the other extreme with $\lambda = 5^\circ$.

STRESS ANALYSIS

When worm gear sets are run at slow speeds, the bending strength of the gear tooth may become a principal design factor. Especially when using non-standard materials, the stress on the tooth should be checked to assure a good factor of safety. Since it is customary to make the worm threads out of a stronger material than the gear teeth, the worm threads aren't usually considered. Bending stress is difficult to determine because worm gears are thick and short at the two edges of the face and thin in the central plane. The Lewis stress equation, as follows, is usually used to approximate bending stress in worm gear teeth:

$$\sigma = \frac{Wgt}{F_g Y P_n}$$

where, Y, the form factor can be obtained from Table 2.

Table 2

LEWIS FORM FACTORS

Normal Pressure angle, ϕ_n , degrees	Lewis Form Factor, Y
14 1/2	.100
20	.125
25	.150
30	.175

POWER RATING

The velocity components in a worm gear set are shown in Figure 11. The worm velocity:

$$V_w = \pi \frac{D_w S_w}{12}$$

the gear velocity:

$$V_g = \pi \frac{D_g S_g}{12}$$

and the sliding velocity:

$$V_s = \frac{V_w}{\cos \lambda}$$

where V_w , V_g and V_s are expressed in fpm, D_w and D_g are in inches and S_w and S_g are in rpm. The AGMA equation for input - horsepower rating of worm gearing is (where W_{gt} and W_f are in lbs.):

$$H_p = \frac{W_{gt} D_g S_w}{12,000 Z_g} + \frac{V_s W_f}{33,000}$$

DESIGN METHOD

This section presents a suggested design method for worm gear sets when the primary requirement is torque output. Figure 12 shows a flow chart that summarizes the following discussion.

The designer must first look at the worm gear set application to determine the dimensional requirements. The designer usually starts with a center distance requirement. The American Gear Manufacturer's Association (AGMA) recommends the following minimum worm pitch diameter based on center distance:

$$D_w \geq \frac{C_d}{2.2} .875$$

Select a center distance, use the above relation to select a worm pitch diameter (rounding up a standard size), then calculate the gear's pitch diameter using:

$$D_g = 2 C_d - D_w$$

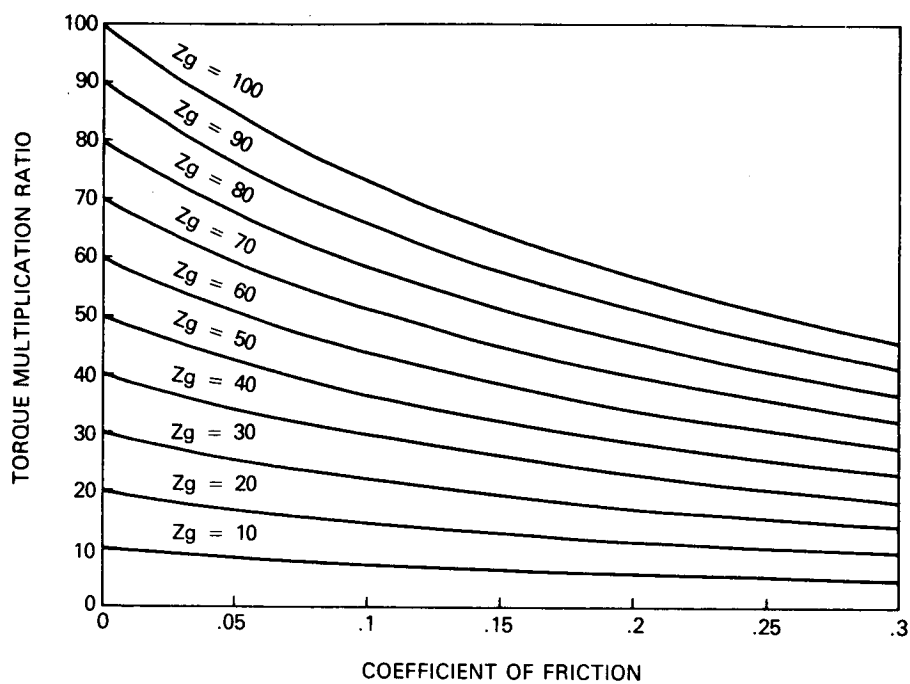


FIGURE 8: THE EFFECT OF THE COEFFICIENT OF FRICTION AND THE GEAR RATIO ON THE TORQUE MULTIPLICATION RATIO ($\phi_n = 20^\circ$, $\lambda = 18^\circ 26'$)

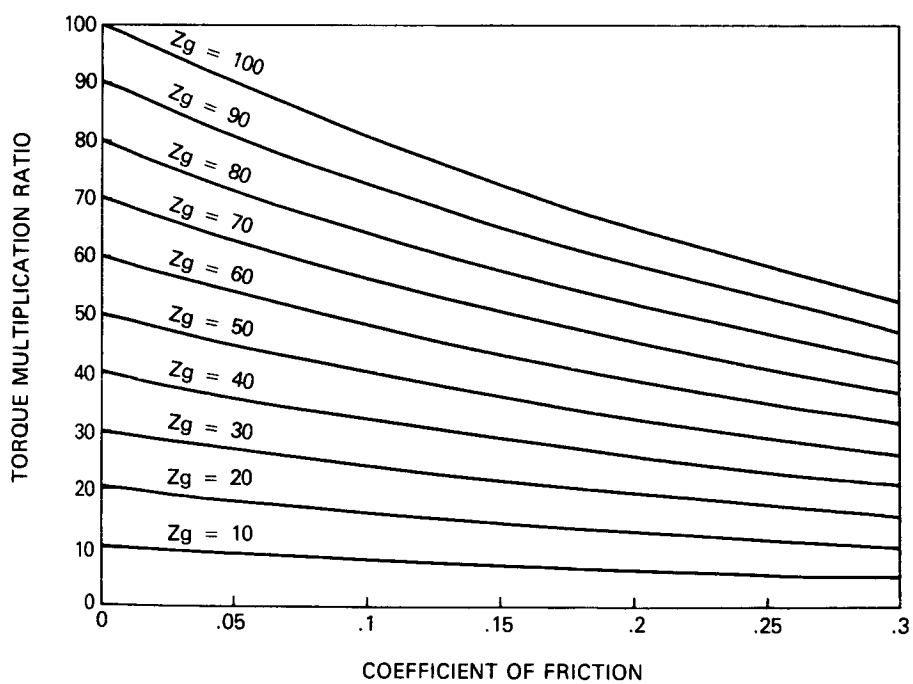


FIGURE 9: THE EFFECT OF THE COEFFICIENT OF FRICTION AND THE GEAR RATIO ON THE TORQUE MULTIPLICATION RATIO ($\phi_n = 20^\circ$, $\lambda = 40^\circ$)

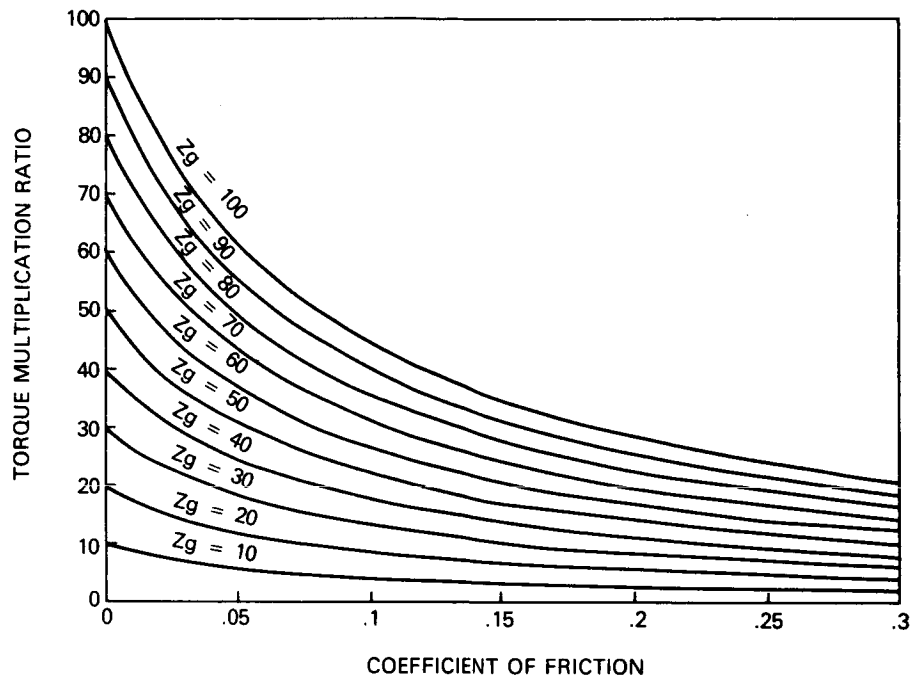


FIGURE 10: THE EFFECT OF THE COEFFICIENT OF FRICTION AND THE GEAR RATIO ON THE TORQUE MULTIPLICATION RATIO ($\phi_n = 20^\circ$, $\lambda = 5^\circ$)

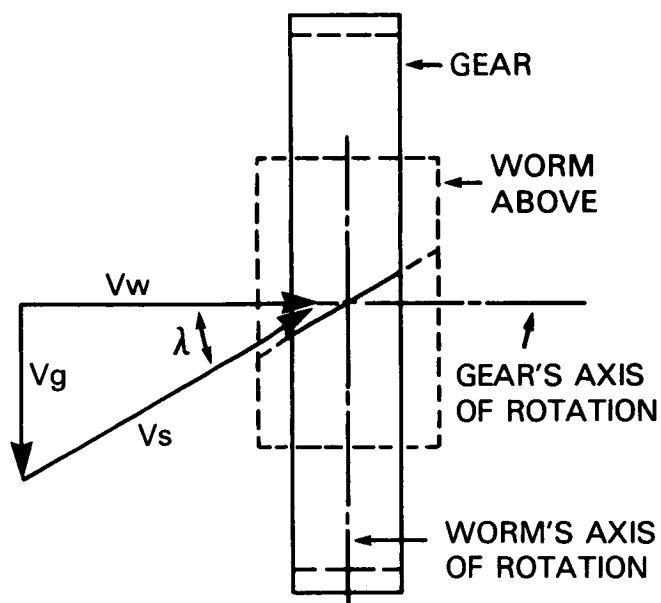


FIGURE 11: VELOCITY COMPONENTS IN WORM GEARING

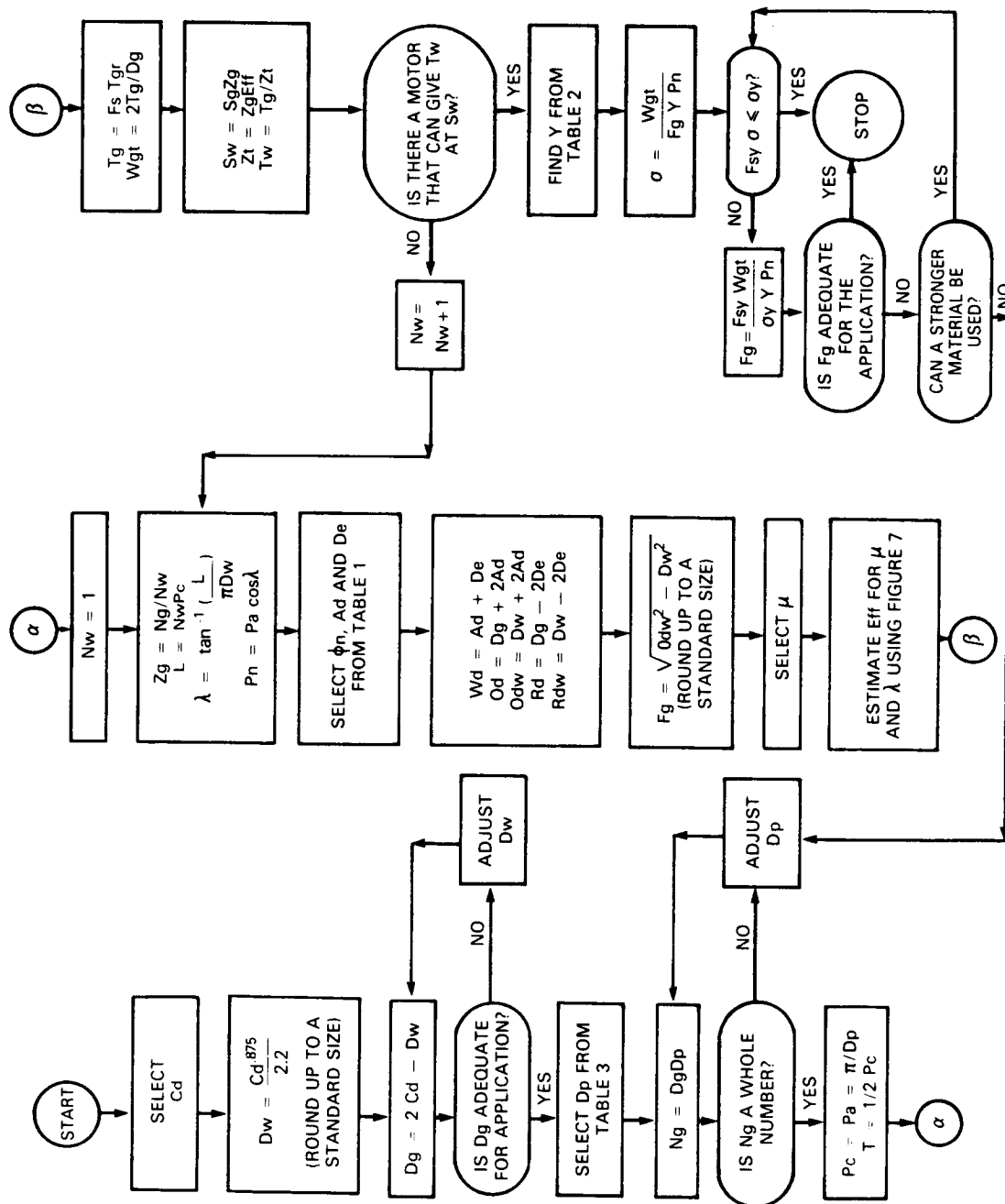


FIGURE 12: WORM GEAR DESIGN FLOW CHART

In any application, out of the three dimensions C_d , D_w and D_g , the magnitude of at least one will be dictated by the gear set application; the other two can be calculated using the above equations.

The designer must now select a diametral pitch for the gear. The diametral pitch determines how smooth the gear set runs. Although there are no standards established, a preference has developed among gear producers and users. Table 3 classifies preferred diametral pitches from coarse to ultra-fine. Use this table to make a selection appropriate for the worm gear set application.

Table 3

PREFERRED DIAMETRAL PITCHES

Class	Diametral Pitch D_p	Class	Diametral Pitch D_p	Class	Diametral Pitch D_p	Class	Diametral Pitch D_p
Coarse	1/2	Medium-Coarse	12	Fine	20	Ultra-Fine	150
	1		14		24		180
	2		16		32		200
	4		18		48		
	6				64		
	8				72		
	10				80		
					96		
					120		
					128		

Once the diametral pitch has been selected, the required number of teeth on the gear is calculated. Since N_g must be a whole number, D_p may have to be slightly adjusted. Now calculate the circular pitch, axial pitch, and tooth thickness.

Initially set the number of threads on the worm to one. Next, calculate the gear ratio, the lead, the lead angle, and the normal circular pitch. Use Table 1 to select pressure angle, addendum and dedendum; then calculate the whole depth, outside diameters, and root diameters. Finally, calculate the recommended minimum face width of the gear tooth (rounding up to a standard size).

At this point the designer must make the assumption of worst-case friction. Based on a knowledge of the materials, lubrication, operating speeds and environment, a conservative estimate of the worst-case coefficient of friction must be made. Once a coefficient of friction has been assumed, use the graph in Figure 7 to estimate the efficiency for the particular lead angle. Now, a safety factor, F_s , must be selected. When torque output of the gear set is the primary design parameter, and knowledge of the friction is limited, a conservative factor of safety must be used.

The required torque output, T_{gr} , must be adjusted by applying the factor of safety:

$$T_g = F_s T_{gr}$$

The required input speed is the product of the required output speed and the gear ratio:

$$S_w = S_g Z_g$$

To determine the required input torque, first calculate the required torque multiplication ratio:

$$Z_t = Z_g \text{ Eff;}$$

then divide the adjusted required output torque by the torque multiplication ratio:

$$T_w = T_g / Z_t$$

Now the designer has established the requirement that the drive motor must output a torque of T_w at a rpm speed of S_w . If this requirement is unsatisfactory, increase the number of threads on the worm and iterate until a reasonable motor requirement has been established.

Once the worm gear set has been sized, the designer must check the bending stress in the gear tooth. Use the Lewis equation to calculate the bending stress, σ . Select a factor of safety, F_{sy} , on the yield stress, σ_y , and compare $F_{sy} \sigma$ to σ_y . If $F_{sy} \sigma$ exceeds σ_y , calculate the required face width of the gear tooth to assure at least a factor of safety

of F_{sy} over σ_y . If this increase in F_g is unacceptable for the application, either consider a coarser gear and decrease D_p or consider using a stronger gear material.

CONCLUSIONS

The design of worm gear sets to meet torque multiplication requirements is a difficult task. The sliding that occurs between the worm and the mating gear causes high friction. When the sliding velocity is slow, as with many aerospace applications, the friction is high. Friction is dependent on many other factors including material combinations and lubrication. In aerospace applications of worm gearing, friction is especially difficult to characterize due to the use on non-standard materials and lubricants. Because the friction is difficult to quantify for a particular worm gear set application, the importance of conservative safety factors on torque output and material yield are strongly emphasized.

The suggested design method presented in this paper demonstrates how a worm gear set designer can start with the dimensional limitations of the application, and a torque output requirement, and develop a complete worm gear set design. The designer will likely perform several iterations before finding a design that is appropriate for the application, and also has attainable requirements for the drive motor. If the designer keeps the requirements and limitations in mind, and uses conservative factors of safety, this design method can be used to design a worm gear set able to deliver the required output torque.

POINTED TELESCOPE SUBASSEMBLY
FOR THE UARS HIGH RESOLUTION DOPPLER IMAGER

Robert D. Renken*

ABSTRACT

The Pointed Telescope Subassembly (PTS) consists of a telescope, its Coudé relay optics, a two-axis gimbal mechanism, and a cover/caging device. These components, their mechanisms, the requirements, and some of the trade-offs leading to the final design are described in this paper. The PTS supplies light to the interferometer of the High Resolution Doppler Imager (HRDI) to be used to study upper atmospheric wind velocity.

INTRODUCTION

The PTS is a major subassembly of the HRDI, an instrument which will be flown on the Upper Atmospheric Research Satellite (UARS). The PTS is being built for the University of Michigan by Ball Aerospace Systems Division (BASD). Its function is to gather light from the upper atmosphere and supply it to the interferometer using the telescope and relay optics which are mounted on a two-axis gimbal. The interferometer will measure upper atmospheric wind velocity by measuring the Doppler shift of the light. The PTS is on the side of the satellite facing the Earth, with its azimuth axis directed toward the Earth and its zenith axis perpendicular to it as shown in Figure 1. Each axis has its own bearings, motor, optical encoder, and flexible lead assembly. In addition, there is a telescope cover and caging mechanism. The design is now complete, hardware is being manufactured, and testing is scheduled for mid-1987.

REQUIREMENTS

The PTS is required to collect light from a specific region of the atmosphere as directed by the Principle Investigator. The telescope must have a wide field of view that is rectangular, 0.12 deg by 1.37 deg and a selectable narrow field of view that is 0.12 deg². The collected light is required to be routed through the gimbal to the interferometer. The telescope boresight placement is to be within 3 arc minutes. Position knowledge and repeatability are to be within 72 arc seconds for the zenith axis and 54 arc seconds for azimuth. During a typical scan operation, the telescope will be pointed to twenty different positions, each 3 arc minutes from the previous position. Required rotational travel is 350 deg for azimuth and 90 deg for zenith, although the zenith axis is rotated an additional 45 deg for caging.

* Ball Aerospace Systems Division, Boulder, Colorado

The telescope's cleanliness is extremely important, as is its stray light rejection ability, because any extraneous light introduced into the system masks the intended data. Environmental requirements are typical for space vehicles launched on the Shuttle. The gimbal mechanism is to be operated in the vacuum of space and protected from thermal extremes through the use of thermal blankets and heaters. The major structural requirement is that launch resonant frequencies be above 35 Hz; however, the control system requires at least 40 Hz during operation. Weight, although a serious consideration, did not prove to be a design driver.

TELESCOPE

A sectional view of the 7-in. off-axis modified Gregorian telescope and its baffle system is shown in Figure 2. The first three mirrors are all off-axis parabolas. Light is reflected from the primary mirror through the field stop to the secondary mirror, then through the Lyot stop to the tertiary mirror. Finally, the light is folded and imaged on the end of the fiber optics bundle. The fiber optics serves two purposes: it routes the light from the telescope to the zenith axis centerline, and it changes the beam shape from rectangular to circular. The entrance aperture of the fiber optics bundle is nominally 0.83 mm (0.033 in.) by 8.8 mm (0.349 in.) and contains 151 fibers. The exit aperture is round and is 3.05 mm (0.120 in.) in diameter. The fibers are made from fused silica and are coated with an antireflection coating. The telescope field-of-view selector is shown in Figure 3. When actuated, it places a narrower slit in front of the field stop. A brushless partial-rotation direct-current torque motor is mounted on flex pivots and used to rotate the slit to the narrow field-of-view position. Position is sensed by a light-emitting diode and photocell combination by placing a blade between them when the motor is actuated. The mechanism is returned to the wide field-of-view position by the spring force in the flex pivots. Thus, it is powered continuously to operate in the narrow field of view and, in the event of electrical failure, will automatically return to the wide position.

Stray light avoidance became a major design driver for the telescope. This consideration led to the selection of an off-axis design instead of a simpler on-axis design. It also led to the use of a proprietary black anti-reflective coating supplied by the Martin Company for the interior of the baffle. There is more experience in applying this coating, called Martin Black, to 6061 aluminum so this material was selected for the baffle. However, a sample of 5083 aluminum was coated with excellent results. The stray light consideration also led to stringent cleanliness procedures for both particles and films during assembly. These contaminants on mirrors scatter light and allow unwanted light into the system. Therefore, the baffle was thoroughly cleaned and vacuum baked prior to assembly. Once the telescope is assembled and optics are aligned, it will be covered and the cover is not to be removed except for functional testing in the assembly area and during thermal vacuum testing.

RELAY OPTICS

The relay optics transmits the light from the telescope fiber optics to the end of a light pipe at the input of the interferometer as shown in Figure 4. The light beam exiting the fiber optics expands in the shape of the cone with a 15-deg half-angle. The elliptical mirror (RM 1) collects the light and provides a beam that is nearly collimated. The light is then reflected with a series of flat mirrors through a field lens to a second elliptical mirror which reimages it on the end of the light pipe. Optically, the relay optics has several interesting characteristics: (1) the path length has two identical halves, with the field lens in the middle, (2) the two elliptical mirrors are identical, and (3) each elliptical mirror has one focal point on the end of the fiber optics (or light pipe) and the other focal point at the center of the field lens.

The relay optics concept chosen was the result of several design iterations. The original concept used light pipes throughout the drive with corners turned by small elliptical mirrors. In a later concept, the corners were turned by pairs of parabolic mirrors. These two concepts were not selected for several reasons. First, they would not transmit enough light. Second, we were concerned that a single broken light pipe would result in the failure of the experiment. Third, the spacing between the ends of the light pipes and the elliptical (or parabolic) mirrors was extremely critical, which meant that the structural thermal distortions would alter the amount of light transmitted. The system with mirrors is relatively insensitive to thermal distortion because the beam is nearly collimated, so separation distances become less critical. The beam is also relatively large, so small lateral or angular misalignments are less critical. Also, it transmits more light and is less susceptible to breakage.

All of the mirrors and the lens are mounted on solid pads which are machined to give tilt adjustment. They are mounted using oversize holes with pins that are bonded to prevent motion after final alignment.

ZENITH DRIVE ASSEMBLY

The zenith drive assembly is shown in Figure 5. The telescope is attached structurally to two short shafts which are supported by the zenith bearings. The bearings on one side of the telescope are a duplex pair, mounted face-to-face. There is a single radial bearing on the other side of the telescope. All bearings are mounted with light interference fits so that any possible mechanical shift during launch is avoided. Also, they are preloaded to remove internal freeplay. The duplex pair is manufactured with a preload of 58 newtons (13 lb). The radial bearing is also loaded axially to 58 newtons by a diaphragm. Because the preload on the radial bearing is reacted by the duplex pair, the two bearings in this pair are loaded unequally, one with more than 58 newtons, the other with less, but not less than zero.

There are several reasons for this zenith bearing configuration. The duplex pair is designed to support all axial launch loads, which means that one yoke arm needs to be stronger than the other because of the unequal loading. The duplex pair is mounted face-to-face to make it free to accept small angular misalignments. The single radial bearing was chosen to provide radial support to the telescope. The diaphragm limits axial loads and also gives this bearing the capability of accepting angular misalignment. The telescope is driven by a brushless two-phase dc motor mounted on one side. Angular position is given by a 16-bit optical encoder which is mounted on the other side. The motor is commutated electronically by taking the angular position from the encoder and generating the required sine and cosine current for the motor. Electrical connections are made with a flexible lead assembly which is mounted inside the optical encoder. Both the flexible lead assembly and optical encoder are purchased as modular components. They have their own bearings and are connected to the zenith axis with couplings that provide for some misalignment.

YOKE STRUCTURE

The structure connecting the zenith and azimuth drive assemblies is the yoke, shown in Figure 6. The configuration that was selected forms a riveted aluminum box beam, with two machined aluminum face plates connected by inner and outer skins which were formed from sheet metal. Caps are riveted to the tops of the arms to provide the interface to the zenith housings and doublers are riveted to the bottom to provide an interface to the azimuth drive shaft.

The riveted aluminum structure was selected after several other concepts were reviewed, including welded titanium, riveted titanium, and welded aluminum. The aluminum structure was selected because the design was driven by stiffness (i.e., the resonant frequency had to be held) rather than strength. The riveted, rather than welded, construction was selected even though it is slightly heavier, because riveting could be done in-house and no thermal residual stresses would be introduced. The riveted structure relies on the rivets to fill the rivet holes, to give a rigid structure and to avoid motion between the parts. A disadvantage of the aluminum is that it has to interface with the titanium bearing housings and shafts. Shrink fits are used at those interfaces that are tight enough so the fit never gets loose during thermal extremes.

AZIMUTH DRIVE ASSEMBLY

The azimuth drive assembly is shown in Figure 7. It consists of a shaft mounted on bearings supported by the housing and driven by a brushless dc torque motor. There is an optical encoder identical to the zenith encoder and a flexible lead assembly. Two angular contact bearings are used in a back-to-back configuration, preloaded to 267 newtons (60 lb) against each other with a diaphragm. The diaphragm is snubbed to limit its axial travel to 0.076 to 0.152 mm (0.003 to 0.006 in.) during launch. The optical path is through the center of the shaft, with the field lens supported by the shaft. As in the

zenith drive, interference bearing fits are used to preclude any possible shift during launch or thermal cycling.

This bearing mounting concept was selected after several designs were considered. The original design used the two bearings rigidly mounted against each other to achieve maximum stiffness. In this concept, preload is controlled by carefully machining the bearing clamping ring to within a few ten-thousandths of an inch. This concept is adversely affected by temperature changes unless the bearing separation distance is set equal to $D/\tan\beta$, where D is the bearing pitch diameter and β is the mounted contact angle. Preload in any solidly mounted bearing scheme is adversely affected if there are pronounced thermal gradients. In an attempt to eliminate the extreme sensitivity of the bearings to temperature changes and to mounting tolerances, a concept using a preload diaphragm was investigated. First, the diaphragm was placed in line with the bearing outer race. However, analysis showed that the drive became less stiff with the overall resonant frequency dropping approximately 5 Hz. Then, the plane of the diaphragm was moved to be in-line with the point at which the lines of contact converge as shown in Figure 8. Further analysis showed that with this concept, the resonant frequency dropped approximately 1 Hz. The concept was analyzed for the extremes of the bearing contact angle, which were found to have a negligible effect on resonant frequency.

COVER AND CAGING DEVICE

The cover serves both to shield the telescope aperture from dust and to cage the zenith and azimuth drives during launch. These devices are shown in Figure 9. The cover is sealed to the telescope with an O-ring seal and it has a filtered vent to allow the telescope to breathe. Early in the design phase, we recognized that even though the caging device would prevent gimbal rotation, there would still be motion during launch along the axis of the telescope. Therefore, the cover is allowed to float in this axis and is held against the telescope with a set of springs. The center of the cover also has a window and a light so the interferometer can be exercised with a known light source.

The caging mechanism is a double four-bar linkage which is stopped past top dead center. The linkage is driven by a motor gearbox assembly as shown in Figure 10. Two brush commutated dc motors drive a set of spur gears which turn the input crank of the linkage. This input crank and its associated link drive the other pair of links which rotates the cover. The springs that hold the cover in position also tend to drive the linkage to the caged and locked position. The motor gearbox is operated in the same direction of rotation for both caging and uncaging. The linkage input crank has a set of cam-actuated limit switches to sense its position and to shut off the motors at the end of travel.

The caging device is the only part of the PTS that has any redundancy. There are two dc torque motors, either of which will drive it to the open position. The gears and gearbox bearings have been deliberately oversized to

minimize the chances of their failure. All of the pins in the caging mechanism have redundant sliding surfaces so that any one could seize and not cause the linkage to fail. A secondary use for the redundant motor is as a speed limiter; its windings are shorted when the motor is unused and it limits the speed of the primary motor, which minimizes brush wear. The caging device still operates satisfactorily if this speed limiting feature fails.

For recaging, the PTS is dependent on the gimbal's ability to point the telescope at the cover. In the event of gimbal failure, the PTS structure and bearings would support re-entry loads. However, the telescope would not remain clean.

MATERIALS

Aluminum (alloy 5083 annealed) and titanium (composition 6Al4V) were the two primary structural materials for the PTS. The 5083 aluminum was used for telescope mirrors, the yoke, the adaptor, and the zenith housings. It was selected for these parts because dimensional stability was a concern and an annealed aluminum is relatively stable. Stiffness, not strength, was the primary structural concern. Because an annealed aluminum is more stable and as stiff as a tempered aluminum, the annealed material became a logical choice. The specific alloy 5083 was selected because strength remains a concern and it has a high yield strength in the annealed condition. For the mirrors, the aluminum was plated with nickel, then silver, and then coated with an anti-reflective coating. Titanium 6Al4V was used at all bearing interfaces, in the azimuth shaft and housing, and for the preload diaphragms. It was selected because its coefficient of thermal expansion nearly matches that of the bearing steel, and because of its low density, high strength, and good corrosion resistance. Other materials are 6061-T6 aluminum for the caging device and telescope baffle and both 440-C corrosion resisting steel and 52100 high chrome bearing steel in the bearings.

The bearings are lubricated with BASD's 36207 fluid lubricant, which is a polyfunctional ester with corrosion inhibitor/anti-wear additives. Creep is controlled by using low surface energy films on the material adjacent to the bearings. This lubricant was selected because of its low contamination potential. It also has corrosion inhibitors so the 52100 bearing steel could be used. The caging mechanism gearbox is lubricated with Braycoat 601 grease.

CONCLUSION

The design described in this paper proved to be interesting and challenging in a number of areas because of the required pointing accuracy and the optics. These factors, along with the environment, led to the use of state-of-the-art materials and lubricants. The telescope and gimbal are designed to operate in the space environment for a minimum of 2-1/2 years and I believe the design will meet this challenge. The hardware is now being assembled and the test program to qualify this design will start in the near future.

ACKNOWLEDGMENT

The author wishes to acknowledge the fine assistance of the Ball Aerospace Document Preparation Group, which was able to take the information given here and transform it into this paper. I also thank the Publications Department and the Word Processing Department, without whose aid this paper would not have been possible.

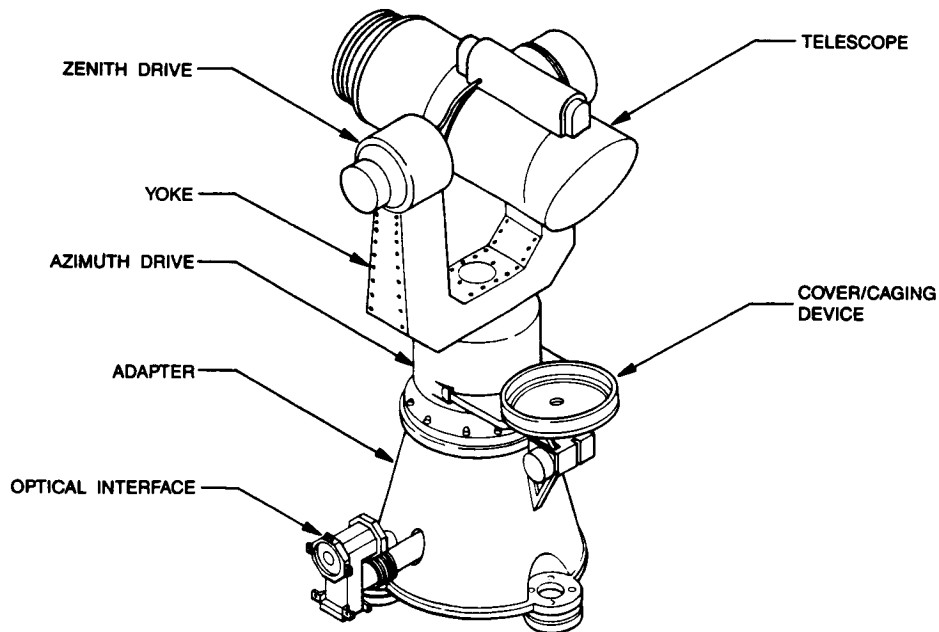


Figure 1 Pointed Telescope Subassembly

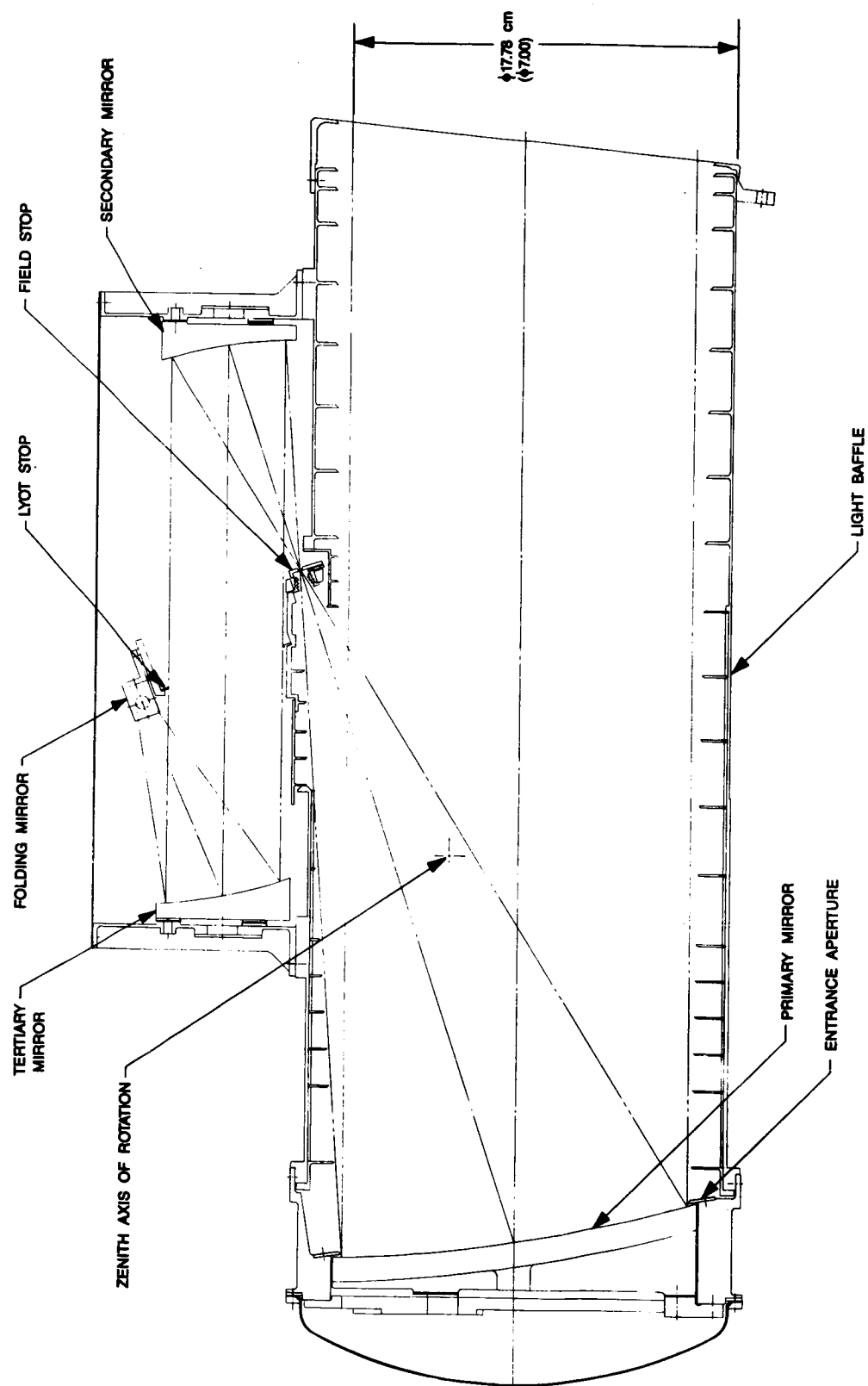


Figure 2 Telescope Cross Section

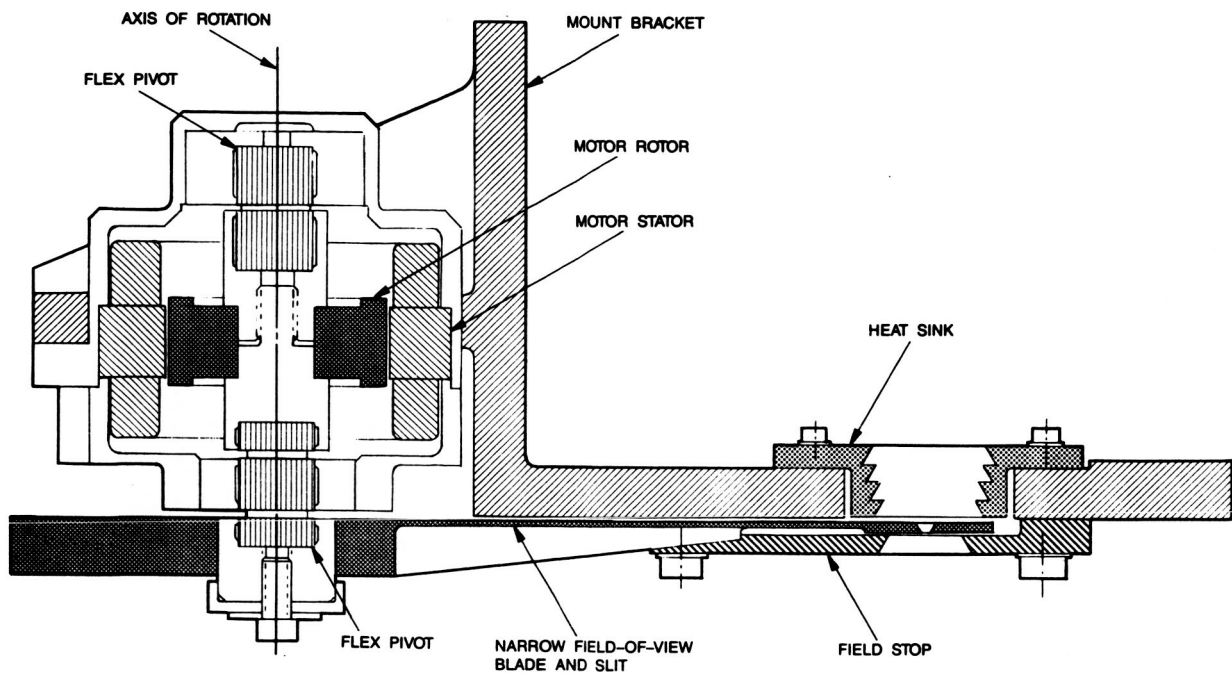


Figure 3 Field-of-View Selector - Cross Section

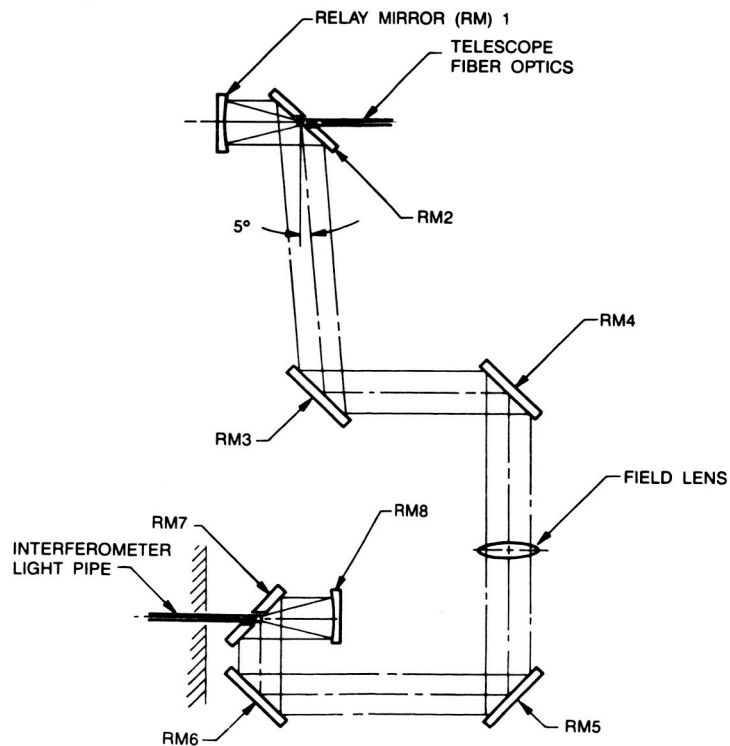


Figure 4 Relay Optics

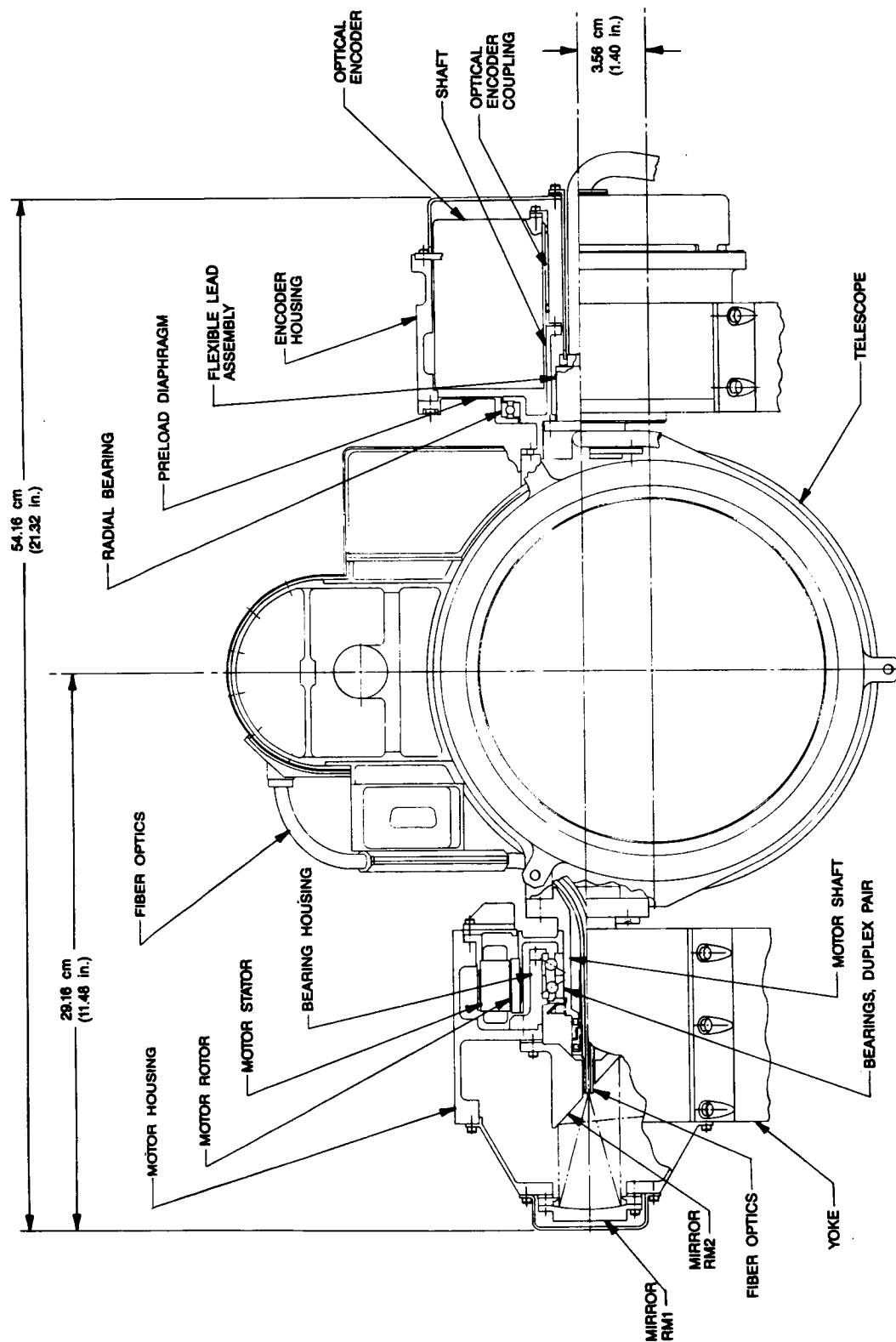


Figure 5 Zenith Drive Assembly

ORIGINAL PAGE IS
OF POOR QUALITY

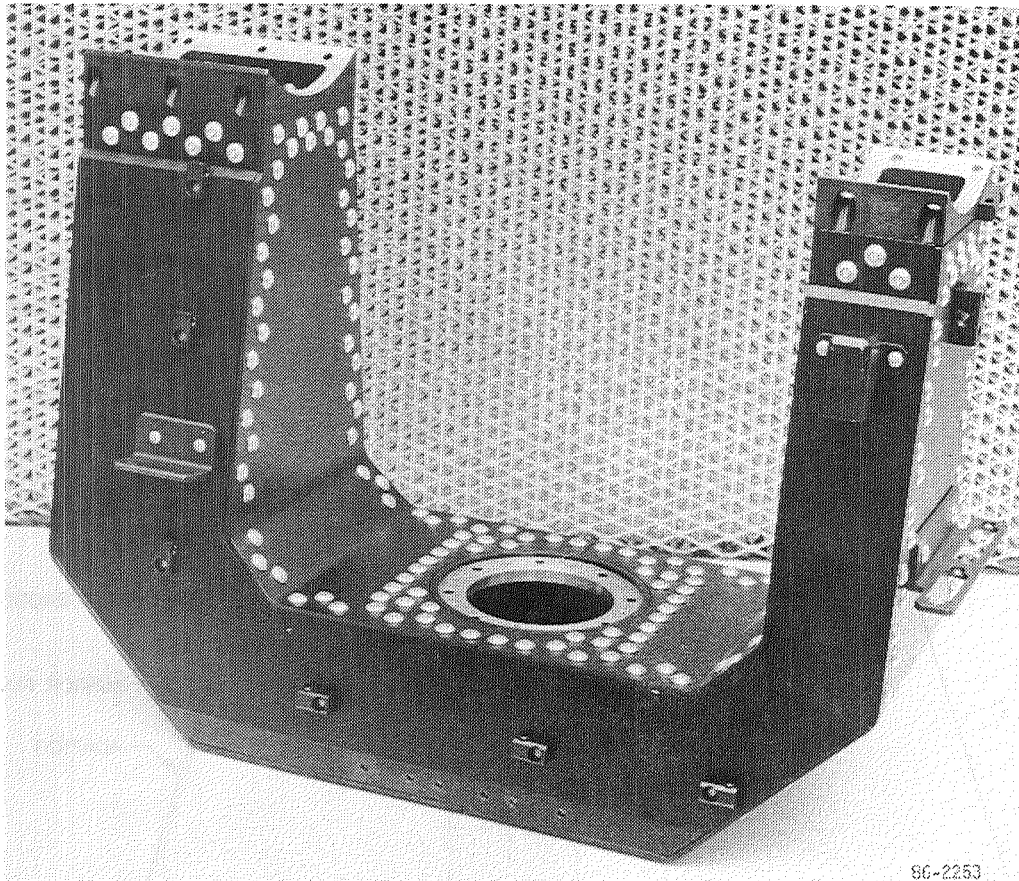


Figure 6 Yoke

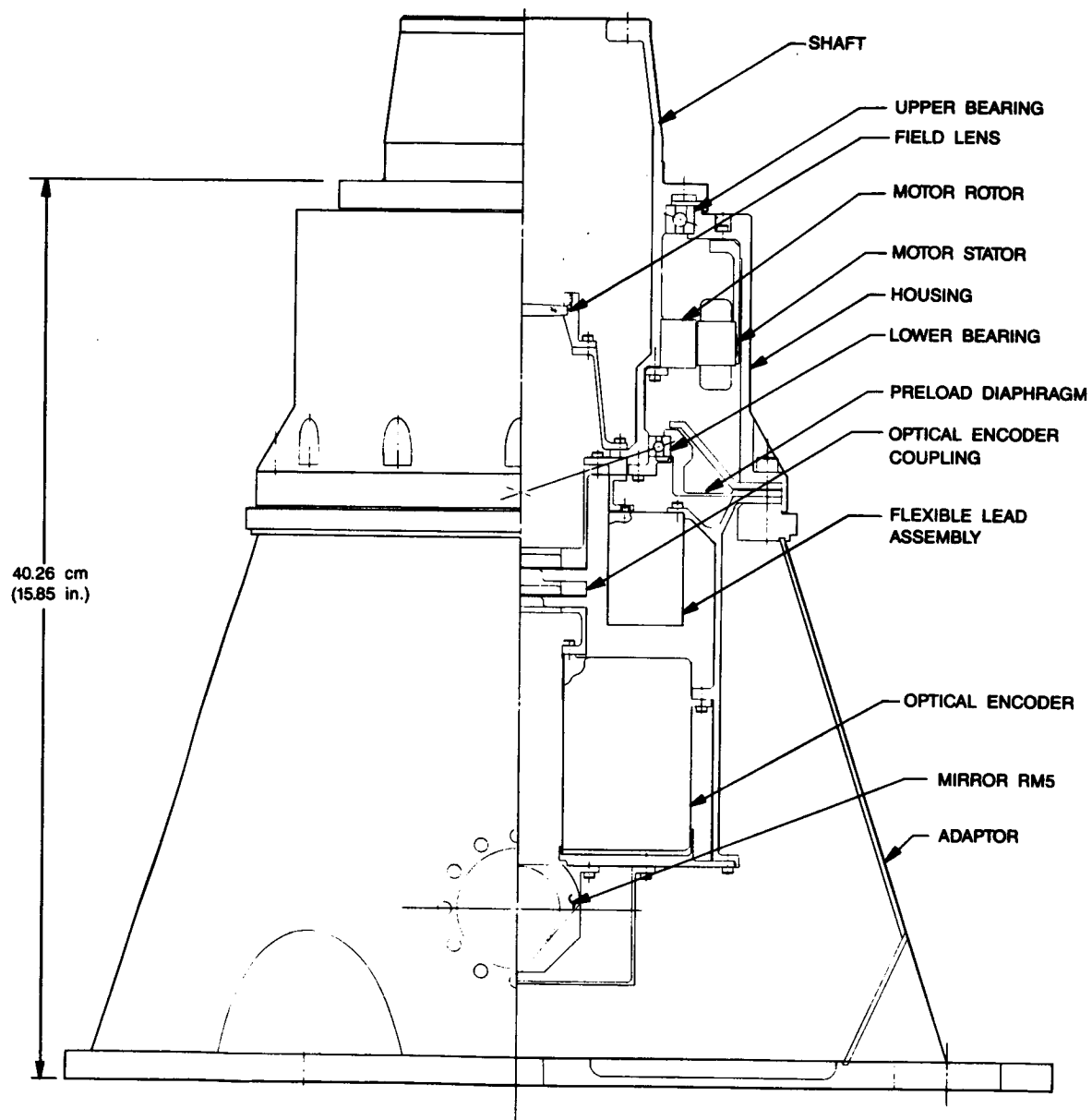


Figure 7 Azimuth Drive Assembly

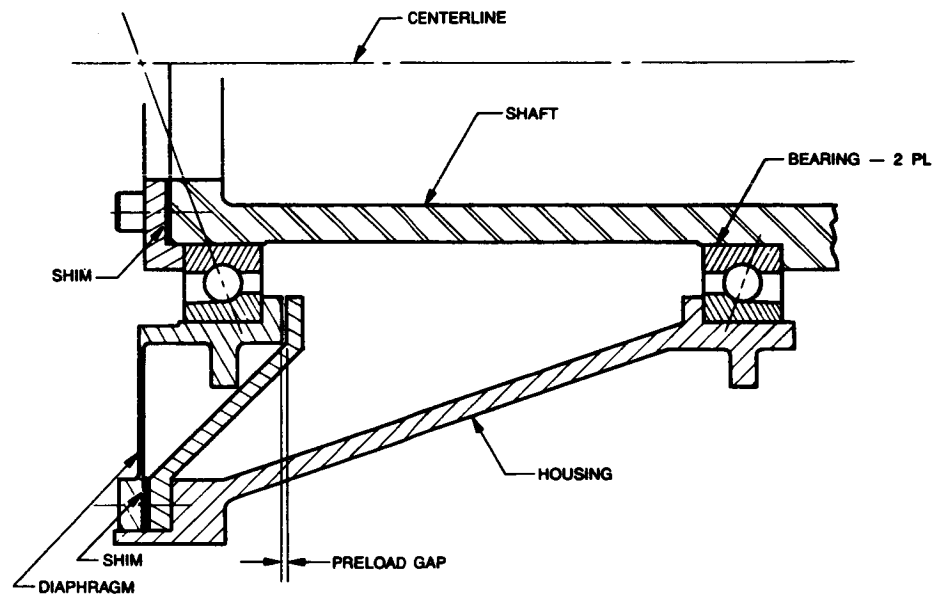


Figure 8 Bearing Diaphragm Placement

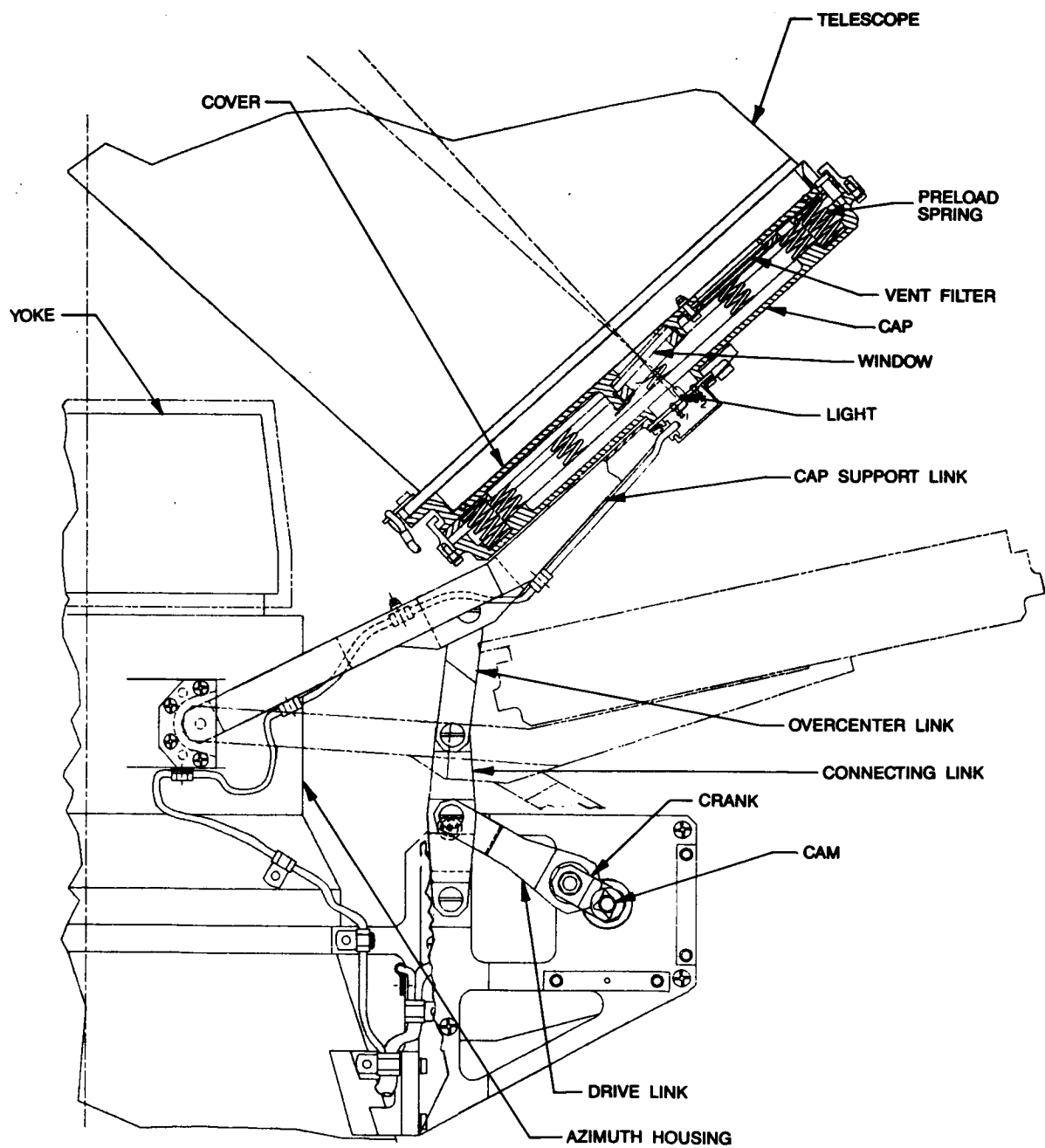


Figure 9. Cover and Caging Device

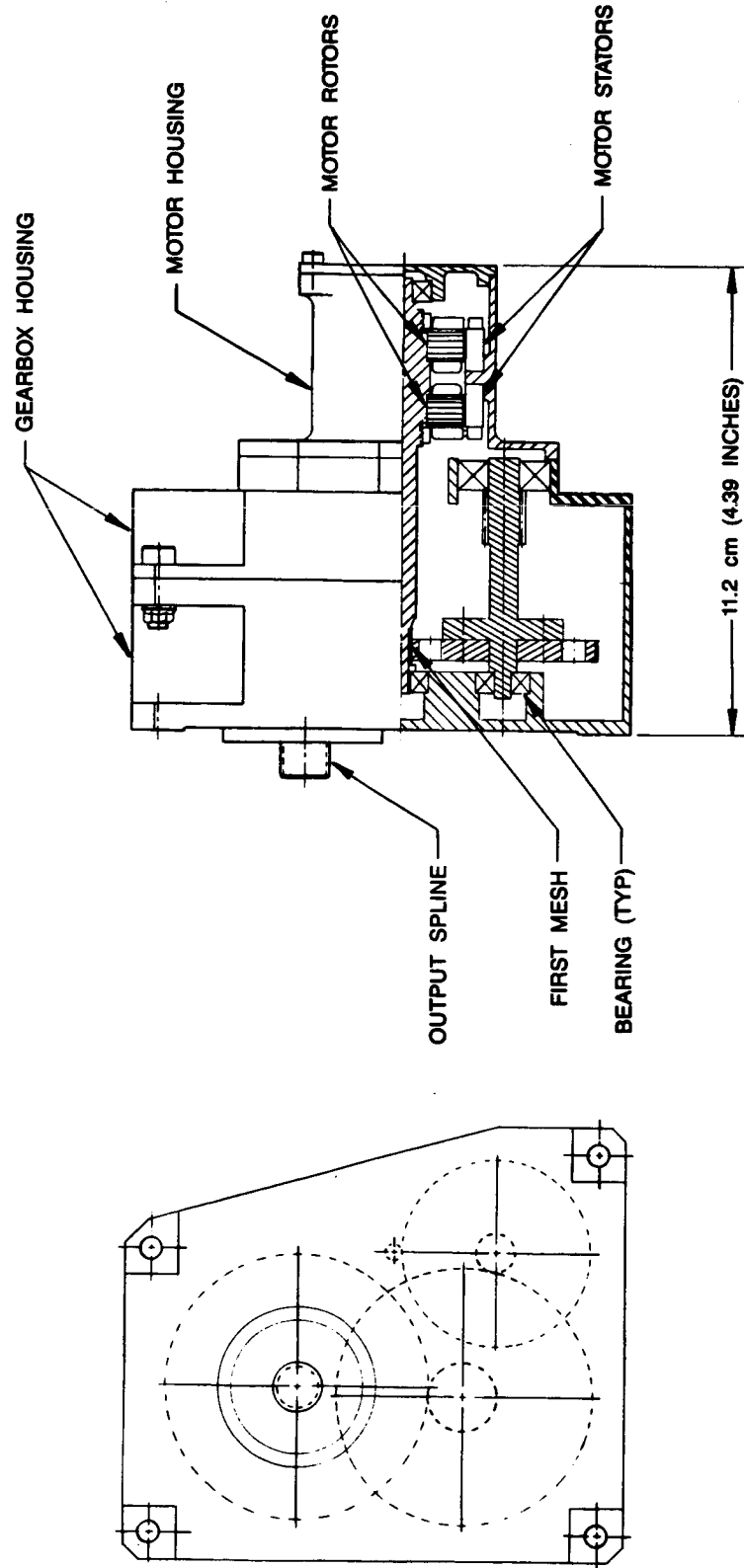


Figure 10 Caging Motor Gearbox Assembly

PASSIVE ISOLATION/DAMPING SYSTEM
FOR THE HUBBLE SPACE TELESCOPE REACTION WHEELS

Martin D. Hasha*

ABSTRACT

NASA's Hubble Space Telescope contains large, diffraction-limited optics with extraordinary resolution and performance far surpassing existing observatories. The need to reduce structural-borne vibration and resultant optical jitter from critical Pointing Control System components - Reaction Wheels - prompted the feasibility investigation and eventual development of a passive isolation system. Alternative design concepts considered were required to meet a host of stringent specifications and pass rigid tests to be successfully verified and integrated into the already-built flight vehicle. The final design employs multiple arrays of fluid-damped springs that attenuate over a wide spectrum, while confining newly-introduced resonances to benign regions of vehicle dynamic response. Overall jitter improvement of roughly a factor of 2 to 3 is attained with this system.

This paper presents the basis, evolution, and performance of the isolation system, specifically discussing design concepts considered, optimization studies, development lessons learned, innovative features, and analytical and ground test verified results. This predictable, readily adaptable mechanism is particularly suitable for application to sources requiring specialized vibration isolation to improve sensor and/or instrumentation pointing stability.

INTRODUCTION

The Hubble Space Telescope (HST) is a large, unmanned, versatile, free-flying, long-life telescope/spacecraft system developed for NASA (Fig. 1). Planned for Space Shuttle launch from Kennedy Space Center, its performance is centered near the visible portion (4000 to 7000 Å) of the electromagnetic spectrum, although it has a broad uninterrupted spectral range (Fig. 2). It will provide astronomers with data of a quality and quantity that greatly exceeds existing earth-based systems. Placed in a circular low-earth orbit, it will experience at least a 15 year service life, providing enhanced observations that are expected to be some of the most significant in the history of astronomy. The HST spacecraft is characterized by: (1) extremely high stability and pointing accuracy, (2) long-term thermal control and optical system alignment, (3) sophisticated onboard data processing to facilitate flexible multipurpose tasks, and (4) very long service life due to Space Shuttle support and capabilities for orbital maintenance and servicing by astronaut crews.

*Lockheed Missiles & Space Co., Sunnyvale, California

The diffraction-limited optical system resolution dictates very formidable pointing accuracy and stability requirements; 0.007 arc-sec RMS on single exposure times from 10 seconds (bright sources) to up to 24 hours on faintest targets. Efforts have been continually expended during HST development to control structural-borne vibration caused by operation of electro-mechanical onboard devices that perturb optical elements or sensitive detectors. Onboard systems are largely designed and built near the limits of conventional, proven state-of-the-art technology. Hardware modifications that show potential to achieve significant improvements in pointing performance or prevent eventual degradation are high priority items for further investigations, particularly reductions in Reaction Wheel Assembly (RWA) vibrations.

Pointing Control System Description

The HST has the most stringent pointing requirements imposed on any spacecraft to date: overall stability during science taking shall not exceed 0.007 arc-seconds RMS. This objective is met by using precision sensors and actuators, all with redundant backup systems. The Pointing Control System (PCS) provides a capability for autonomous maneuvers, target acquisition, and fine pointing based on time-tagged stored program commands, as well as the ability to accept real-time interactive commands from the ground control station. Control for maneuvering and maintaining precise pointing is achieved by onboard digital computer processing of attitude and rate sensor inputs. Gyro assemblies provide angular rate data which is supplemented by attitude data from a user-selectable combination of NASA-standard fixed-head star trackers and Fine Guidance Sensors (FGS's). The FGS's use photomultiplier tubes in an interferometric mode to provide a precise attitude reference on selected guide stars located within the optical system field of view. A momentum management system is used with database and sensor data inputs analyzing orbital magnetic fields to command four magnetic torquers that desaturate and minimize excess RWA momentum. The system also provides control capability for critical orbital phases involving operations close to the Space Shuttle. A diagram of the PCS is shown in Fig. 3.

Line-of-Sight Jitter

With such tight pointing requirements, reduction of even small amounts of vibration that might interfere with PCS performance is critical for HST objectives. This is especially true for RWA's which operate continuously, and for which no operational workarounds exist to counter debilitating vibrations. The PCS stability error requirement combines all motions of the target star at the optical system focal point with respect to attitude sensor(s). Additional errors are due to internal control system sources, disturbance torques and forces internal to the spacecraft, and external or environmental torques and forces. Jitter error budgets are arranged in categories of error generating sources characterized by frequency of disturbance.

These categories are (1) "Random," consisting of line-of-sight (LOS) jitter contributions due to detector photon noise and gyro electrical noise; (2) "Fast Sine," including electromechanical device vibrations such as those emanating from tape recorders, movable antennas, solar array drives, and Reaction Wheels; (3) "Slow Sine," including longer term cyclic effects with periods from many seconds to minutes; and (4) "Exponential," which are thermal-mechanical deformations in more massive structural elements caused by significant changes in spacecraft thermal conditions during large attitude maneuvers or earth eclipse. Only the Reaction Wheels and the High Gain Antenna (HGA) dishes are planned to operate continuously during science taking, and thus require special attention to limit their induced jitter. Also, infrequent short-term disturbance phenomenon such as Reaction Wheel stimulation of structural-optical resonances have to be fully accounted for rather than averaging them out over long sample times. Figure 4 shows graphical representations of various error producing sources as functions of time. RWA Induced-Vibration (I-V) test results were put into jitter analyses in 1982 (Fig. 5), and indicated that the RWA's could, under certain conditions, individually exceed error budget allocations for all four RWA's together. This, coupled with some uncertainties present in the analyses, prompted exploratory study of alternatives for reducing RWA vibration (Fig. 6). Key study goals for promising alternatives were:

- Significant (target factor of 2) reduction of overall RWA jitter in speed range needed for fine pointing (0 to 1200 RPM), by reducing primarily high-frequency axial direction vibrations;
- Small impact for integration into existing vehicle hardware;
- Capable of full flight certification within limited schedule;
- Noninterference with PCS system configuration and performance.

HST REACTION WHEEL ASSEMBLIES

General Description

The four RWA's (Fig. 7) are the constantly operating and torque producing components critical to the PCS. They are sized to encompass both the maximum torque needed for target-to-target maneuvering and the small precise control torques required during fine pointing. An RWA is similar in design and operating principle to Control Moment Gyro's (CMG's) except that RWA's are mounted in distinct orientations, rather than being gimbaled. They alter overall vehicle angular momentum by combined variations in their individual rotational speeds produced in response to PCS computed commands. They are basically electrically driven flywheels and nominally slowly sweep their speeds to counteract small vehicle disturbance torques (primarily aerodynamic drag and gravity gradient torques). Their constant operation produces minute structural-borne sinusoidal vibrations which must be controlled with very tight criteria. Key design goals for minimizing RWA mechanical vibration output noise are: (1) extremely precise dynamic balancing of the rotor-bearing assembly, and (2) state-of-the-art mechanical bearing manufacture, quality control and selection process.

RWA's are grouped in pairs, and located in box-like bays in HST's Support Systems Module (Fig. 8). Each RWA outwardly resembles a flying-saucer-shaped oblate spheroid. Spin axes are skewed ± 20 degrees from the plane normal to the HST optical axis and pairs are 90 degrees apart. Underlying mounting structures are at the heart of the HST primary load bearing structure and are hence very stiff.

Vibration Characteristics and Optical Jitter Impact

When powered and rotating, each RWA emits mechanical vibrations parallel to its spin axis and in directions radially outward in its equatorial rotational plane. The generation of these force and moment disturbances are caused by combinations of: (1) motor ripple/cogging, (2) electronic and resolver imbalance, and (3) rotor-bearing mechanical unbalance/geometry error. These vibrations emanate at the rotor rotational frequency and at other set harmonic ratios of rotational speed (e.g. 2.0, 2.8, 4.0, 5.2). These harmonic ratios are caused by minute bearing alignment and surface irregularities (specifically rotor imbalances, bearing raceway and ball geometric imperfections, and ball-retainer interaction). The precise ratios all have their basis in consistent physical parameters of the bearing-rotor assembly, and have been empirically verified by Induced Vibration (I-V) testing (Fig. 5). Any isolation or attenuation scheme must be capable of addressing the entire range of harmonics as well as the primary unbalance harmonic (1.0). Early RWA induced jitter analyses indicated that key harmonics that create the most deleterious optical system jitter were mid-ratios (primarily 2.8 and 5.2) producing vibratory motion along the RWA spin axes (Fig. 5), so these are the characteristics targeted for reduction.

Basis for Isolation System Development

As stated, jitter analyses in 1982 were displaying a worrisome increasing trend in RWA induced jitter. Certain concerns were raised about uncertainties in the analyses and applicability of the RWA disturbance level input data (Fig. 6). Additionally, the operational nature of the RWA's - continuous sweeping with no workarounds - caused high priority efforts to be expended to study alternatives (Fig. 6). A list of preliminary requirements (Fig. 9) was created to serve as a starting point for surveying existing damping devices, and assessing basic feasibility/viability. This initial exploration of existing damping device capabilities and manufacturer's experience led to a development program. Some major concerns were: (1) dynamic performance at such low throughput load levels, (2) obtaining target ratios of lateral to axial stiffness, (3) control of large excursions under launch conditions without harming the RWA's, and (4) placement of new isolator resonances.

ISOLATION SYSTEM DEVELOPMENT

Development Program and Evolution of Preferred Design

The development program consisted of three phases which combined analysis and test data to adequately resolve areas of concern:

- Phase I- proof-of-concept prototype unit development and tests (to demonstrate that alternative concepts exhibit acceptable stiffness and damping at small force/displacement levels);
- Phase II- flight-like engineering/qualification unit development and testing (to establish confidence in the candidate isolator design's ability to meet or exceed all flight requirements);
- Phase III- flight unit buildup, test, and certification (to verify that final as-built devices meet all requirements and are acceptable for final installation/integration into the HST).

Each phase required sufficient indication that the proposed system could be made to meet the final stringent flight specifications to proceed.

Feasibility/optimization analyses were performed at LMSC to help establish specification of key isolator dynamic parameters (Fig. 10). Specifications and qualification/acceptance test plans for procuring and testing prototype units were prepared and requests for proposals were transmitted to manufacturers of commercial damping products. The strong inclination for off-the-shelf or modified commercial designs was driven by the extremely tight timetable then available. After review of the refined specifications and schedule, candidate prototypes were produced for evaluation. Relaxation in schedules prompted Sperry to also propose and test a concept (Fig. 11). After evaluation, the Sperry concept was chosen for further development.

Subsystem Tests

A thorough series of tests (Fig. 12) was performed, and the Sperry concept was chosen for a flight unit build. I-V tests were conducted using an RWA, and output forces and moments were recorded. Results showed that the device functions as second-order spring-damper system (Fig. 13). As an added benefit, the isolators reduced vibration exposure for RWA's (Fig. 14).

Isolation System and Device Description

The isolator system was designed to attenuate disturbances while maintaining support stiffness. An important requirement is that the isolation system appear transparent to the PCS. The central element is basically a viscous fluid damped coil spring suspension system shown in Fig. 15. This design configuration provides a dual-acting, multi-directional isolation system for controlling displacements of the RWA's. A three unit set suspends each RWA (Fig. 16). Stiffness is provided by steel springs sandwiched between the central washer-like piston support plate and the retainers. Damping is provided by a low volatility silicone-based fluid (Dow Corning 200 series), confined by metal bellows to internal cavities. Spin axis direction energy dissipation (damping) is provided, and is generated by differential motion. The degree of damping is very deterministic for axial motion, while radial damping has proven to be less deterministic. In both axial and radial cases, damping has been demonstrated to be remarkably independent of the motion amplitude. Fig. 17 shows axial and radial direction transfer function curves for small displacements. The configuration of the design effectively fixes the internal fluid volume as far as dynamic motion is concerned. Volumetric change is also provided to accommodate temperature induced expansion. The outer shell/housing provides protection of inner components and a labyrinth seal. Also, this design provides electrical grounding through the isolators and incorporates features that enhance safety for nearby space-suited astronauts during orbital maintenance activities.

FULL VEHICLE GROUND TESTS

The four sets (consisting of 3 isolator units each) of flight qualified/accepted isolators were installed with their corresponding complement of RWA's on the assembled HST vehicle (Fig. 18). This was accomplished at the LMSC facilities in Sunnyvale, CA prior to scheduled system jitter performance/modal testing. The HST vehicle was suspended vertically by cables from an array of three air bags. This nearly complete vehicle was instrumented with sensitive accelerometers, and perturbed with shakers and onboard equipment to simulate actual orbital operations and predicted situations.

The performance/modal test consisted of four segments:

- Line-of-Sight (LOS) Transfer Function Test, using shakers to induce sufficient force levels to verify optical system response;
- Jitter Performance Test, measuring small optical component motions to compute overall system jitter;
- Modal Survey, to locate and characterize basic structural mode shapes, frequencies, and damping for finite element models;
- PCS Transfer Function Test, measuring response and thereby check amounts of structural feedback.

Example results from this last test are displayed in Fig. 19, and help confirm the pretest predicted isolator performance in the full vehicle. Measured dynamic responses of isolator related modes agreed well with results from finite element models. However, early LOS Transfer Function Test data produced results showing that some RWA isolators may be "bottomed" in the ground test configuration. Tests were devised to statically check isolation system clearances. The reduced Transfer Function test results showed an isolation mode at 19 Hz, with confirmation data from another transducer device agreeing within 10%. A review of PCS stability analyses found that the presence of the measured isolator dynamics in the PCS loop is acceptably stable (Fig. 20). Perhaps the most dramatic illustration of the isolator system effectiveness at minimizing or eliminating high-frequency vibrations is shown in Fig. 21, which is the axial direction I-V plot of the RWA sweeping from 0 to 3000 RPM with the spectral analyzer set to record the peak response.

ORBITAL PERFORMANCE PREDICTIONS

Based on ground test results (I-V tests) on the four flight RWA's, output forces and moments are known as a function of RWA rotational speed and can be input to HST structural dynamic math models. Figure 22 shows results of a jitter analysis in which the test-verified RWA outputs are introduced directly into the stiff mounting structure model (i.e. no isolation) with the response computed at the focal plane of the Optical Telescope Assembly (OTA). Figure 23 shows results from the same input, but with the dynamic model altered to duplicate each RWA's isolation system. The performance improvement of this critical HST parameter is evident, with average and peak jitter in the nominal RWA operating speed range of 0 to 10 Hz (0 to 600 RPM) typically decreasing by 55 and 70% respectively. The contingency RWA speed range of 0 to 20 Hz (0 to 1200 RPM) also benefits significantly with typical decreases in average and peak jitter of 60 and 75%. The ability to achieve this high level of improvement in a crucial HST performance parameter in such a short-term, cost-effective development program is the primary success of this effort.

SUMMARY AND STATUS

A passive isolation system was successfully developed, built, verified, and integrated into the existing HST flight vehicle in a short timespan: 9 months from proof-of-concept proposal to flight hardware delivery for installation. The development program attained a significant improvement in a critical pointing stability performance parameter - RWA jitter - with a cost-effective solution, and the system is awaiting launch. The isolator design met or exceeded the numerous requirements/constraints imposed by the HST application. However, the isolator design is relatively compact and lends itself to readily predictable adaptation. It is suitable for a potentially wide range of situations and applications where the use of off-the-shelf or modified commercial isolators may not be satisfactory.

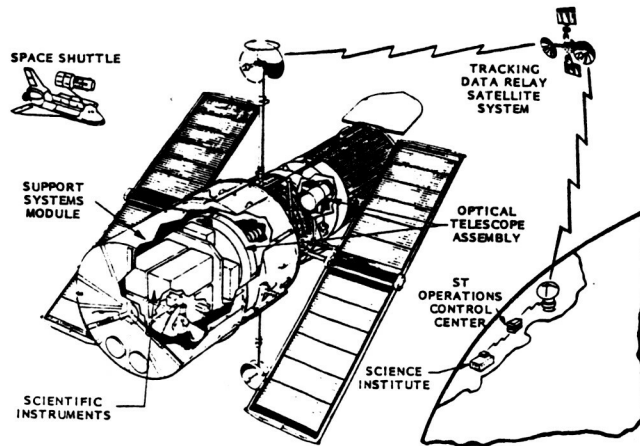


Figure 1. - Hubble Space Telescope - deployed and on station.

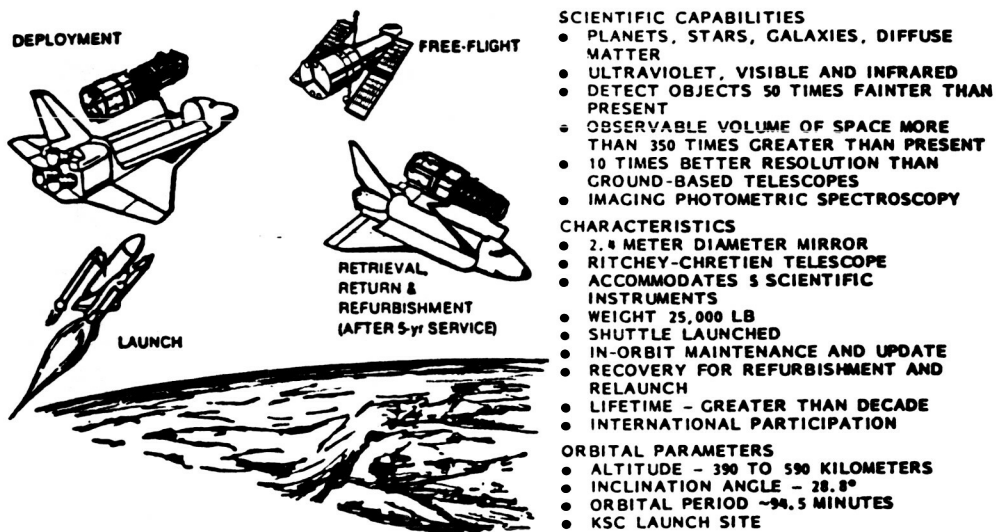


Figure 2. - Hubble Space Telescope System description.

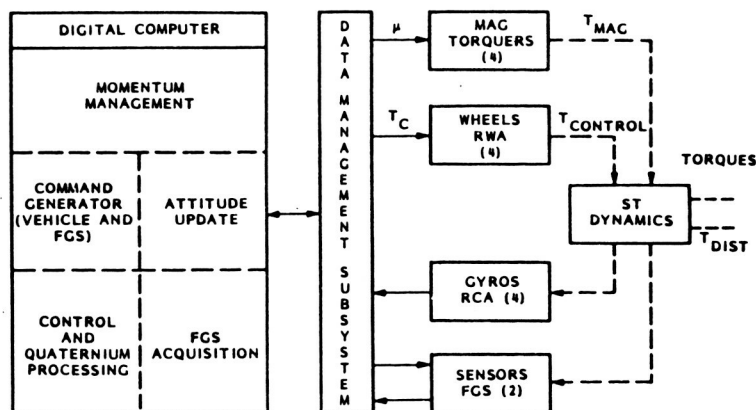


Figure 3. - Pointing Control System functional diagram.

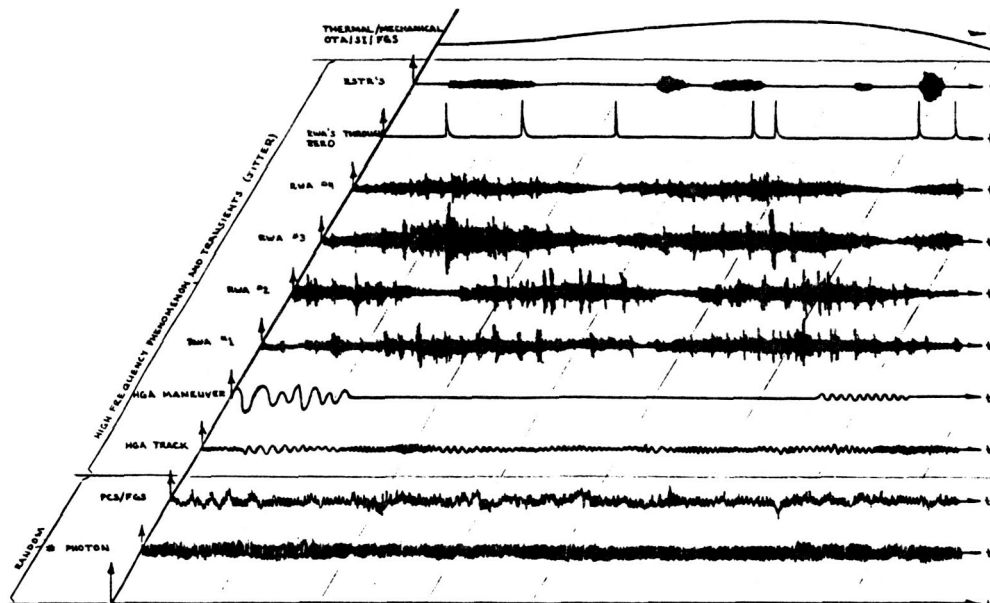


Figure 4. - Jitter categories sources, and characteristics.

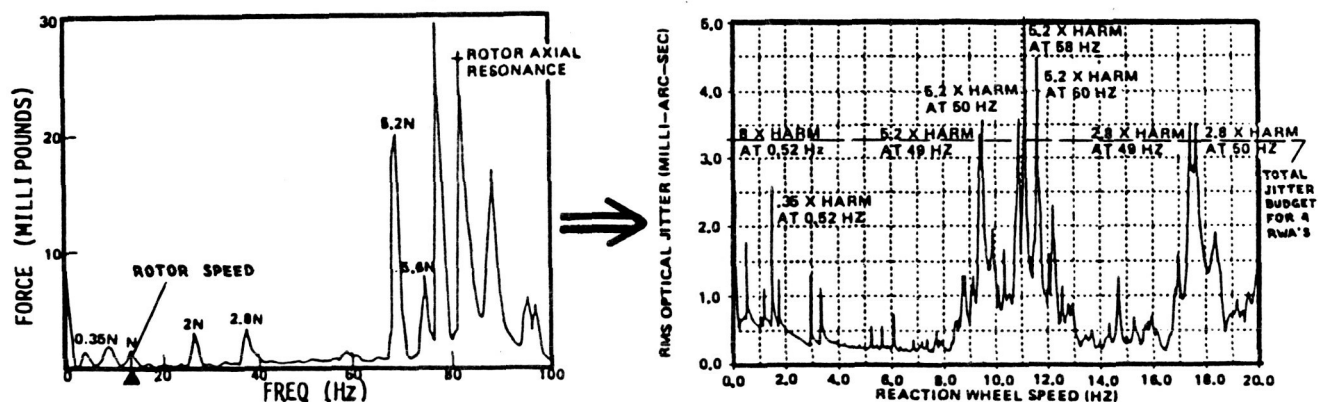
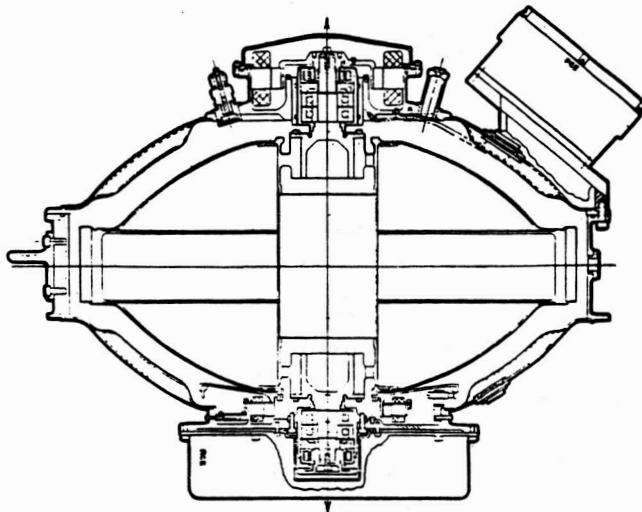


Figure 5. - Reaction Wheel Assembly Induced Vibration Test results and jitter.

HARDMOUNTED ANALYSIS ISSUES/UNCERTAINTIES	POTENTIAL SOLUTIONS	REMARKS
<ul style="list-style-type: none"> ANALYSES SHOW SMALL MARGINS: INDIVIDUAL RWA JITTER CAN EXCEED FULL BUDGET UNDER CERTAIN CONDITIONS AND CIRCUMSTANCES ALTHOUGH FORCING FUNCTIONS ARE WELL KNOWN, DYNAMIC MODEL VERIFICATION PLAN IS NOT IDEAL AND OCCURS LATE IN PROGRAM UNCERTAINTIES EXIST CONCERNING THE REALISTIC EXTENT OF RWA OPERATING CONDITIONS THAT MAY BE ENCOUNTERED DURING HST ORBITAL LIFETIME ALTHOUGH RWA BEARING ASSEMBLY ROUGHNESS LIFE TESTS ARE ENCOURAGING, NO FULL "END-TO-END" LIFE-VIBRATION TESTS ARE PLANNED DYNAMIC MODELS LOSE FIDELITY AND ACCURACY OF JITTER PREDICTION FOR HIGH FREQUENCY JITTER 	<p>QUIETER RWA BEARINGS</p> <p>STRUCTURAL MODIFICATION OF HST TO ALTER MODAL RESPONSE CHARACTERISTICS</p> <p>INCREASE STRUCTURAL DAMPING BY APPLYING DAMPING MATERIAL TO STRUCTURE/EQUIPMENT</p> <p>LOCALLY ISOLATE ALL RWA'S</p>	<p>EFFECTIVE BUT REACHED POINT OF GREAT EXPENSE AND DIMINISHING GAINS IN JITTER PERFORMANCE</p> <p>FEASIBILITY STUDIES INDICATE ONLY MINOR IMPROVEMENT FOR GREAT COST, SCHEDULE IMPACT & WEIGHT INCREASE</p> <p>SMALL IMPROVEMENT; LARGE AMOUNT OF ELASTOMERIC MATERIAL REQUIRED IS UNACCEPTABLE FOR CONTAMINATION PREVENTION WITH ORBITAL CONDITIONS</p> <p>PREFERRED ALTERNATIVE IF OBSTACLES CAN BE OVERCOME; PROTECTS AGAINST POSSIBLE RWA LONG-TERM DEGRADATION</p>

Figure 6. - Basis for exploration of isolator alternative.



- TORQUE: 0.82 N-M
- MOMENTUM: ± 264 N-M-SEC
- BANDWIDTH: 50 Hz
- SIZE: 63 Cm DIA., 51 Cm HEIGHT
- WEIGHT: 467 N (105 Lb)
- POWER: 45 WATTS QUIESCENT, 400 WATTS PEAK (0.0 N-M AND 3000 RPM)
- DIGITAL INPUT: ± 0.82 Nm, SIGN + 11 BITS MAG.
- ANALOG INPUT: -0.82 TO + 0.82 N-M (0-5 VDC)
- COMMANDS: POWER ON/OFF, ANALOG ENABLE/DISABLE

- ANALOG:
- TORQUE COMMAND: -0.7 TO +0.7 N-M
 - TEMP: 2 SPIN BRG., ELECTRONICS
 - MOTOR CURRENT: +30 A (Max.)

DIGITAL: 16-BIT WHEEL SPEED PULSE TRAIN (640 PPR)

Figure 7. - Reaction Wheel Assembly cutaway and description.

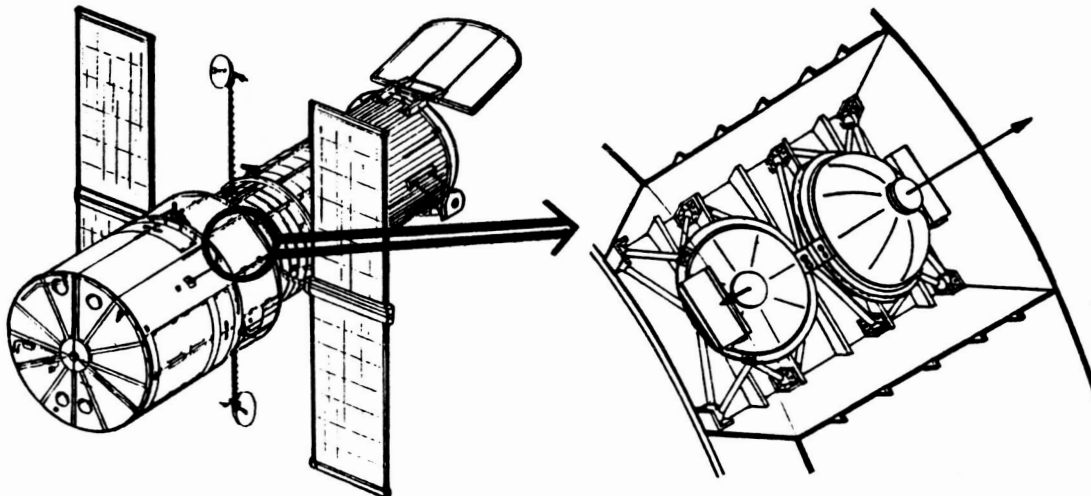


Figure 8. - Reaction Wheel location and mounting.

- ISOLATE AXIAL TRANSLATION: $F < 50$ Hz (ACTUAL)
 $Q < 10$ (VALUE TBD)
- NO EFFECT ON PCS TORQUE MODE: $F > 50$ Hz
 $Q = \text{ANY}$
- TRANSMITTED FORCES - ON ORBIT 0.001 TO 0.10 LB
0 TO 280 Hz
- LIFTOFF $14G's \times 102 \text{ LB} \times (8/6 \text{ OFFSET})$
 $= 1904 \text{ LB}$
- OPERATIONAL TEMPERATURE RANGE: 0 TO 100°F
- PHYSICAL SIZE PER UNIT: 2 X 1.5 X 7.5 INCHES
- LIFE: AT LEAST 3 YEARS ON ORBIT
- INTERFACE DEFINED FOR RWA TAB BOLT ON
- "NO" CONTAMINATION
- ORU COMPATIBLE: RECENT ADDED REQUIREMENT

Figure 9. - Preliminary isolation system requirements for development.

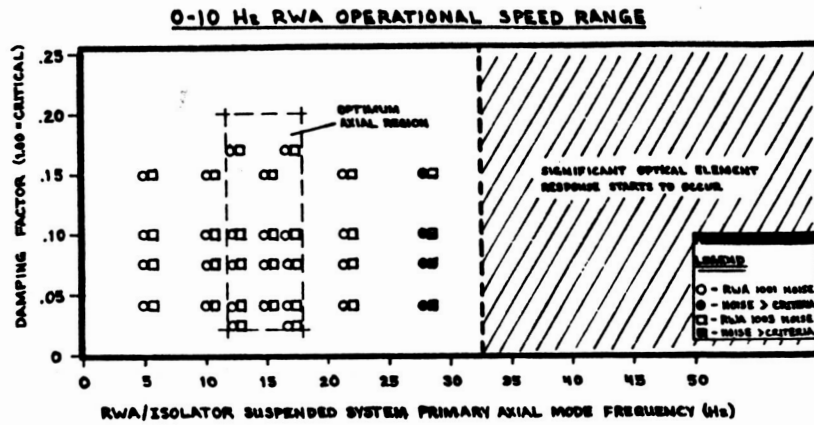


Figure 10. - Isolation system optimization study results.

ORIGINAL PAGE IS
OF POOR QUALITY

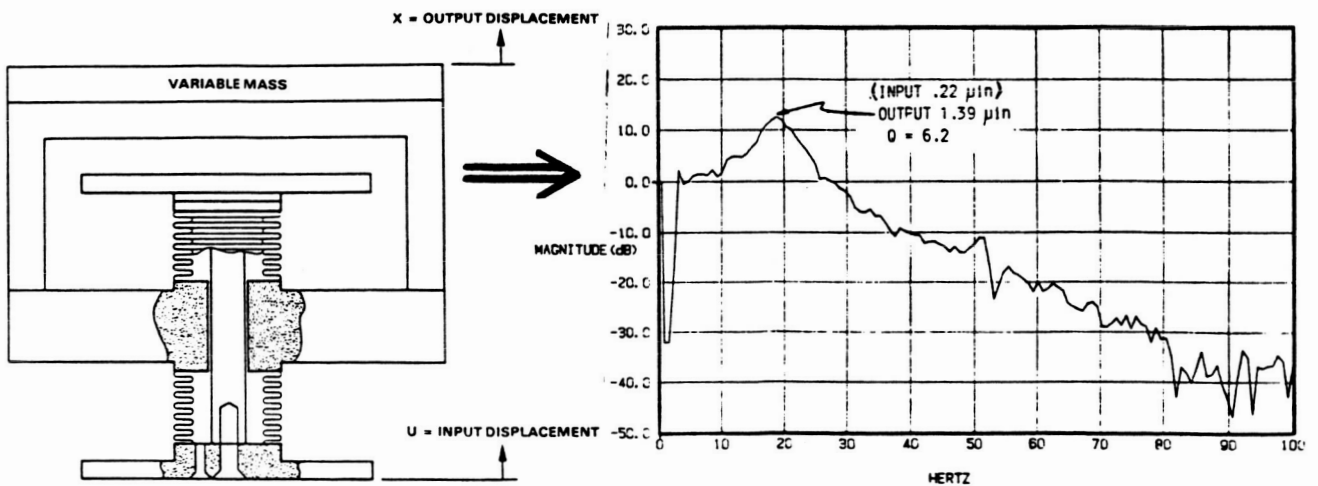


Figure 11. - Sperry's isolator concept and encouraging results.

ORIGINAL PAGE IS
OF POOR QUALITY

- PROTOTYPE PARAMETRIC INVESTIGATION
 - DIMENSIONAL PARAMETER EFFECT ON DAMPING
 - FLUID VISCOSITY EFFECT ON DAMPING
 - LOW AND HIGH LEVEL STIFFNESS CHARACTERIZATION
- COMMAND TORQUE CHARACTERIZATION
- FATIGUE LIFE INVESTIGATION
- I-V TRANSFER FUNCTION AND PEAK ENVELOPE RWA SWEEP RUNUP
- THERMAL-VACUUM EXPOSURE
- I-V TRANSFER FUNCTION AND PEAK ENVELOPE RWA SWEEP RUNUP REPEAT
- HIGH LEVEL VIBRATION
- FINAL I-V TRANSFER FUNCTION AND PEAK ENVELOPE RWA SWEEP RUNUP

Figure 12. - Engineering development and qualification tests.

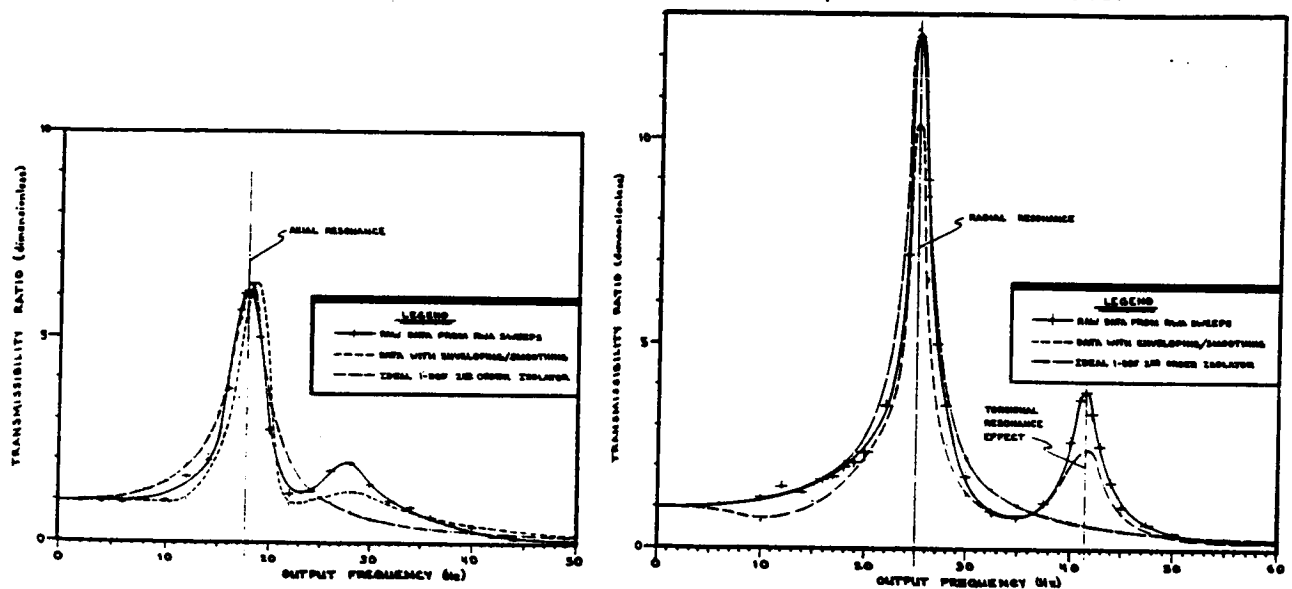


Figure 13. - Isolation system measured axial and radial response characteristics.

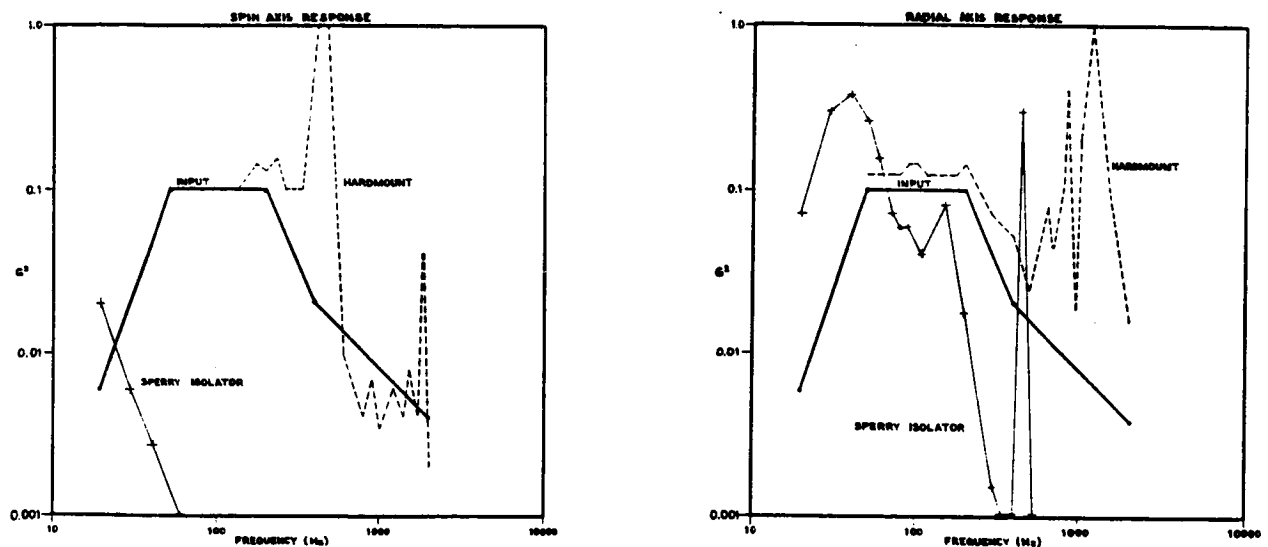


Figure 14. - Isolation attenuation of high-level axial and radial random vibration.

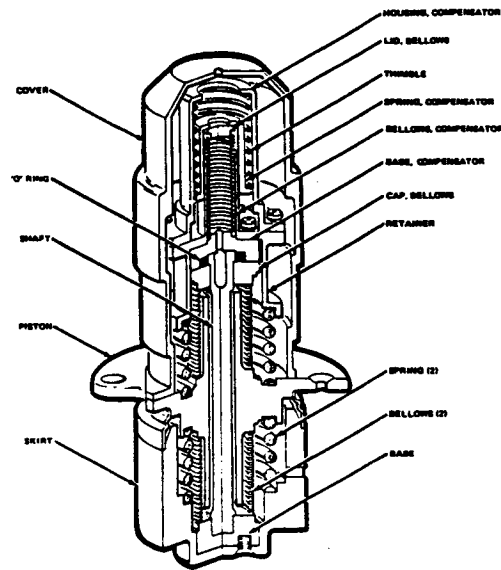
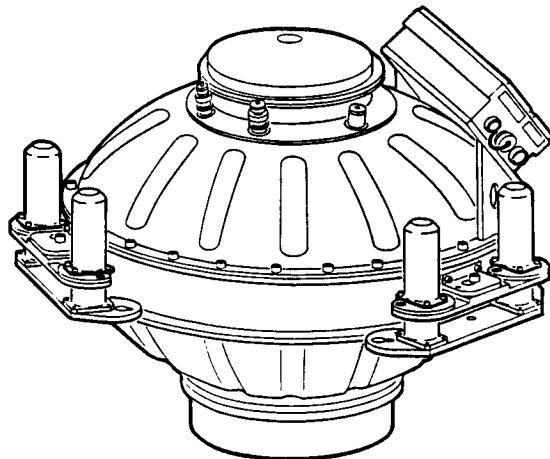


Figure 15. - Isolator spring-damper element cutaway.



PARAMETER	REQUIREMENT
• AXIAL STIFFNESS	670-910 LB/IN
• LATERAL STIFFNESS	1380-1870 LB/IN
• AXIAL DAMPING	.170-.025 (Q = 3 TO 20)
• LATERAL DAMPING	.170 - .025 (Q = 3 TO 20)
• MEET DYNAMIC PROPERTIES WITH STATIC LOAD ON 3 UNITS -1G	37.0 LB AXIAL 102.0 LB RADIAL
• ENVIRONMENT	TEMP: -20°F TO +120°F PRESSURE: 810 to 10 ⁻¹³ TORR ACCEL.: 9.2 g's FOR 1.5 min. RANDOM VIB: 6.18 g (rms) OVERALL
• LIFE	UNIT: 2 YEARS GROUND 5 YEARS ORBITAL DAMPING ELEMENT: 7 YEARS
• WEIGHT	5.0 LBS MAX PER ISOLATOR

Figure 16. - Full isolation system with Reaction Wheel and description.

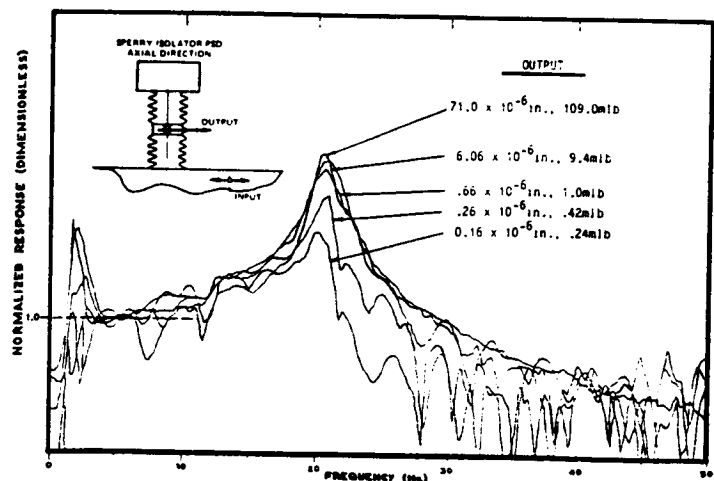
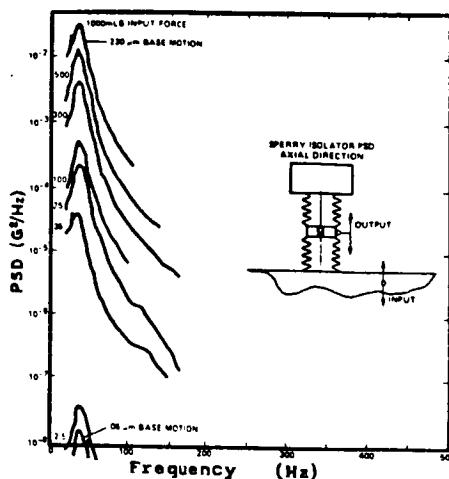


Figure 17. - Measured system axial and radial response at different levels.

ORIGINAL PAGE IS
OF POOR QUALITY

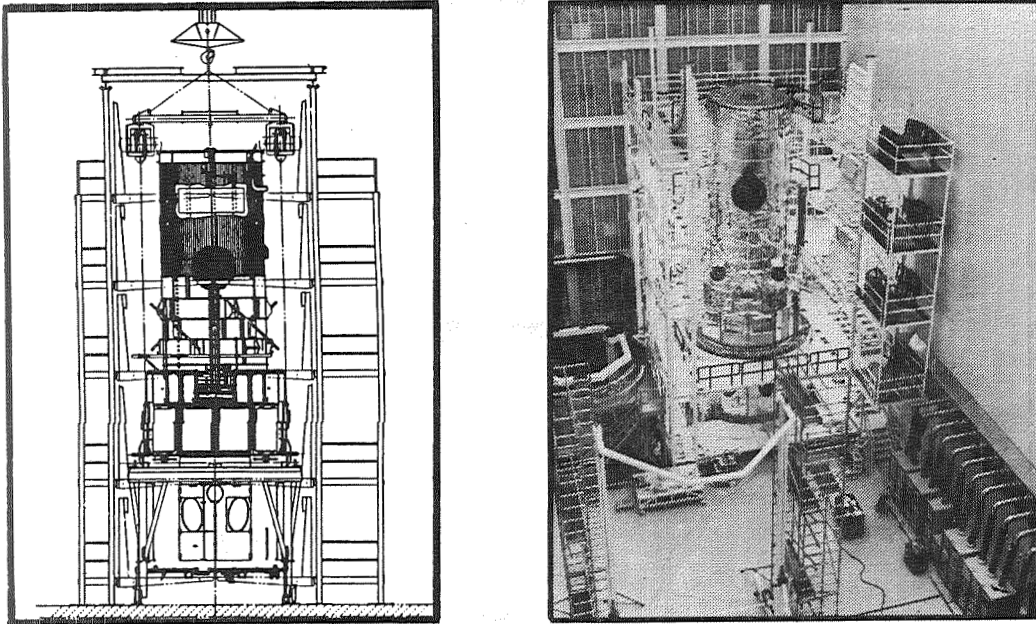


Figure 18. - Hubble Space Telescope in stand for ground vehicle tests.

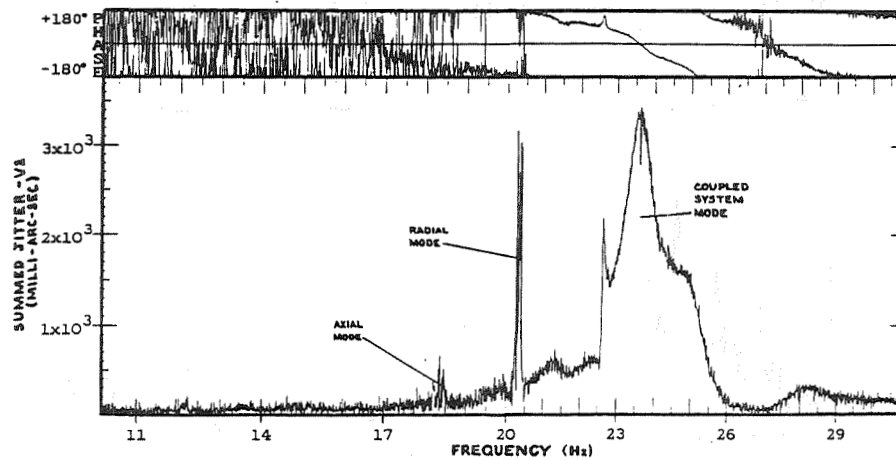


Figure 19. - Results from PCS Transfer Function test measuring LOS jitter.

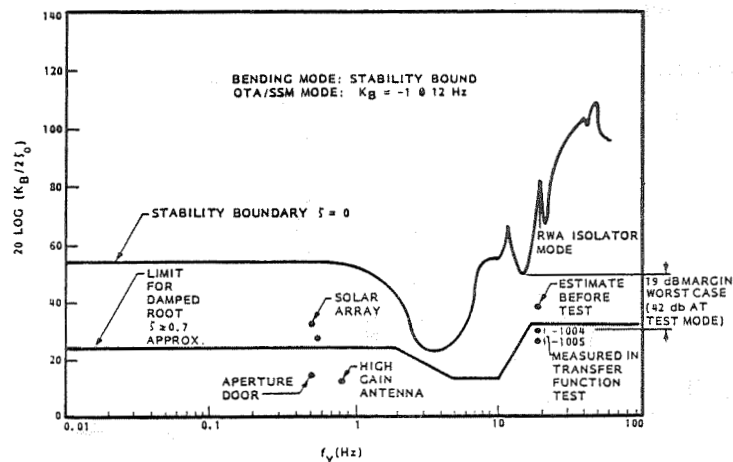


Figure 20. - Results from PCS stability analysis of isolation in PCS loop.

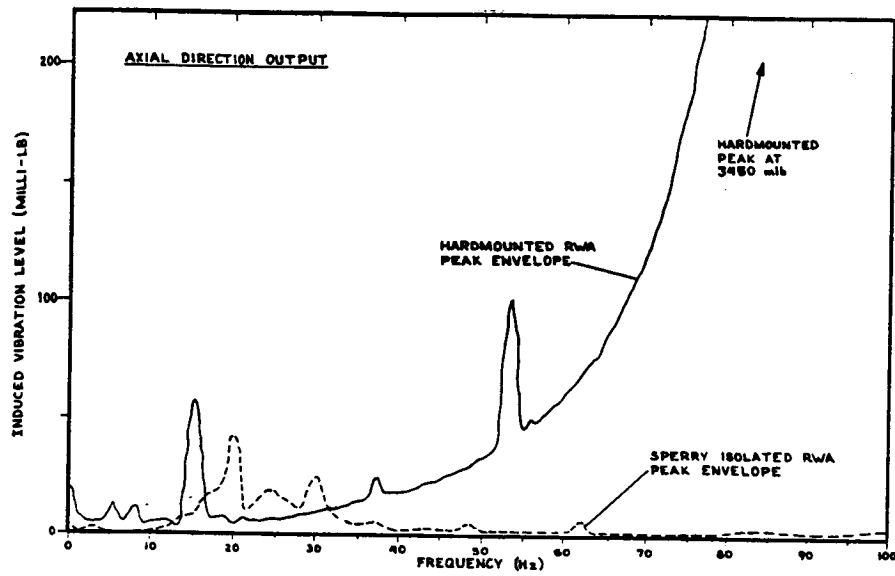


Figure 21. - Comparative peak envelope axial I-V: hardmounted and isolated RWA.

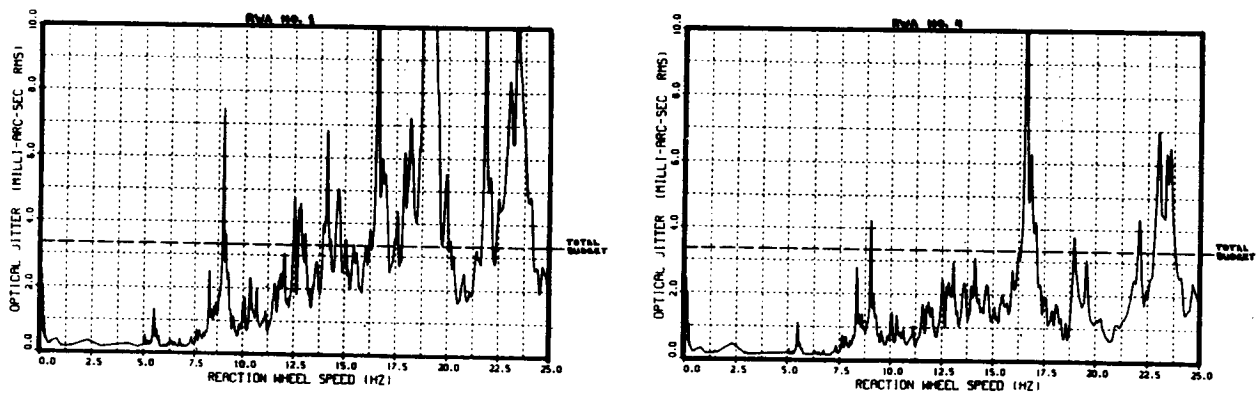


Figure 22. - Orbital LOS jitter analysis results for hardmounted RWA's.

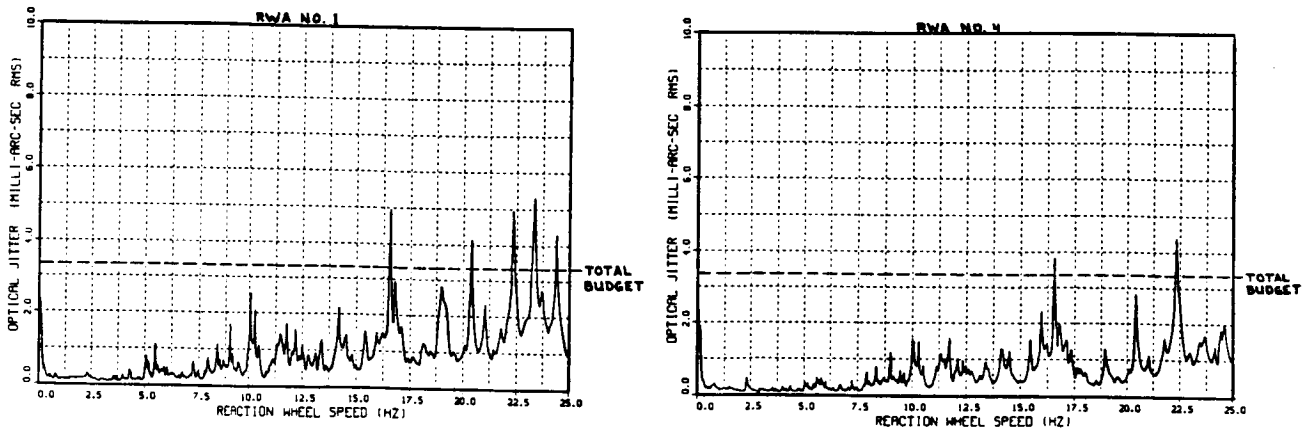


Figure 23. - Orbital LOS jitter analysis results for isolated RWA's.

A MULTIPURPOSE SATELLITE EJECTION SYSTEM

Michael B. Moore*

ABSTRACT

A design is presented for a pneumatic ejection system capable of ejecting a spin stabilized satellite from the cargo bay of the space shuttle vehicle or other space vehicles. This system was originally designed for use on the Spacelab 6 shuttle mission, but is now being considered for use with expendable rockets for launching satellites. The ejection system was designed to launch a 150-lb satellite at an initial ejection velocity of 32 ft per second with a spin rate of 30 revolutions per minute.

The ejection system consists of a pneumatic cylinder, satellite retaining mechanism, and bearing assembly to allow the satellite to rotate during the spin-up phase. As the cylinder is pressurized rapidly causing movement of the actuation piston, the mechanism automatically releases the spinning satellite by retracting a pneumatic locking pin and three spring-loaded holddown pins. When the piston reaches the end of its stroke, it encounters a crushable aluminum honeycomb shock absorber which decelerates the piston and retaining mechanism. The assembly is designed for multiple uses except for the crushable shock absorber and pyrotechnic valves.

The advantage of the design is that it has the ability to meet a variety of ejection requirements by varying the pressurization rate of the pneumatic cylinder and the speed of the direct current spin motor, thus giving the system a high degree of flexibility and versatility. This device was awarded U.S. Patent No. 4554905 on November 11, 1985.

BACKGROUND INFORMATION

This multipurpose satellite ejection system (MPSES) was initially conceived to eject a series of flight experiments in formation from the shuttle cargo bay. The experiment, the magnetospheric multiprobe (MMP), was proposed for observations of the Sun's vector magnetic fields. Figure 1 shows the MMP satellite cluster that was to be mounted in the orbiter payload bay.

OVERALL DESIGN

This mechanism was designed to launch satellites from the orbiter cargo bay with some pre-determined translational acceleration and rotational velocity, which can be varied with different mission requirements. Translational acceleration is accomplished by the pneumatic piston system shown in Figure 2, which shows a preliminary flight configuration. Figure 3 shows a test configuration. A pneumatic system was chosen over a simpler spring system for the aforementioned capability to vary the translational acceleration for

*George C. Marshall Space Flight Center, Huntsville, Alabama

different missions, and for safety and damping considerations. The piston is hollow on the gas side for an accumulator effect, damping out the shock effect created by the sudden entrance of gas into the cylinder at the beginning of the ejection sequence. Rotational velocity is accomplished by rotating the satellite and its cradle with a spin motor (Fig. 3). The satellite is retained on the cradle by three spring-loaded retaining pins, which rotate with the cradle inside a retainer cup, and are deactivated near the beginning of the piston stroke. Figure 4 shows the interface where these elements are located. The spin motor drives a pinion gear, which in turn drives an inner ring gear attached to the cradle. The momentum of the piston after ejection is absorbed by a honeycomb shock absorber (Fig. 2), which is crushed by the impact of the piston. The honeycomb shock absorber can be removed at the end of the mission and replaced with a new one in preparation for another mission.

Support hardware includes a pneumatic locking pin for cradle retention (Fig. 2); spin motor support structure (Fig. 3 shows the correct orientation); tripod struts for pneumatic cylinder support (Fig. 2); a universal joint (rod end clevis, Fig. 2) as a support base for the pneumatic cylinder; a hold down latch (Fig. 2) for satellite retention during launch; and the MPSES support structure. The rod end clevis allows the cylinder, and thus the satellite, to be mechanically aligned with the orbiter by manipulation of turnbuckles on the tripod struts. Additionally, a spring-loaded retaining latch is located on the cylinder to retain the piston at the top of its stroke after satellite ejection (Fig. 2). The MPSES support structure, which is for support of the MPSES during launch and landing and prevention of hardware contamination, is shown in Figure 2.

The indexing pin (Fig. 2) is a pyrotechnically actuated mechanism that stops the cradle/satellite from rotating if the ejection is aborted due to some mechanism failure after the hold down latch is unlatched and the spin motor is started.

EJECTION SEQUENCE

A central controller (not shown in figures) located on the system hardware will command the sequencing. The controller will be initiated by commands from the crew cabin. The pneumatic system pressure sphere (see Fig. 2) will be pressurized through the fill line. After the spin motor is started, the pyrotechnically actuated valve is opened, allowing pressurization of the pneumatic locking pin and the pneumatic cylinder. The gas line running from the pyrotechnically actuated valve to the pneumatic locking pin is sized so that the locking pin is unlocked before the piston begins acceleration. Releasing the locking pin frees the pneumatic piston, the cradle, and the satellite for ejection. As the piston moves upwards, it allows the spring-loaded retaining pins to release when they clear the retainer cup, then accelerates the satellite out of the cargo bay. The satellite is held on the cradle by acceleration loads, until the piston reaches the end of its stroke. At this point, the spring-loaded retaining latch locks the piston, preventing it from freely moving and damaging itself.

ANALYSIS

A mathematical model of the pneumatic system was developed to predict the g-force created by the ejection system on the experiment. The model incorporates the following variables: system weight (including satellite), design separation velocity, gas constant, specific heat ratio, and absolute gas temperature, sphere volume, sphere pressure, cylinder inlet line diameter, initial cylinder volume, cylinder diameter, vent orifice area, and piston stroke. The model yielded these parameters: stroke time, percent stroke, cylinder pressure, ejection acceleration, and ejection velocity. Figures 5 through 8 show the latter four parameters as functions of time.

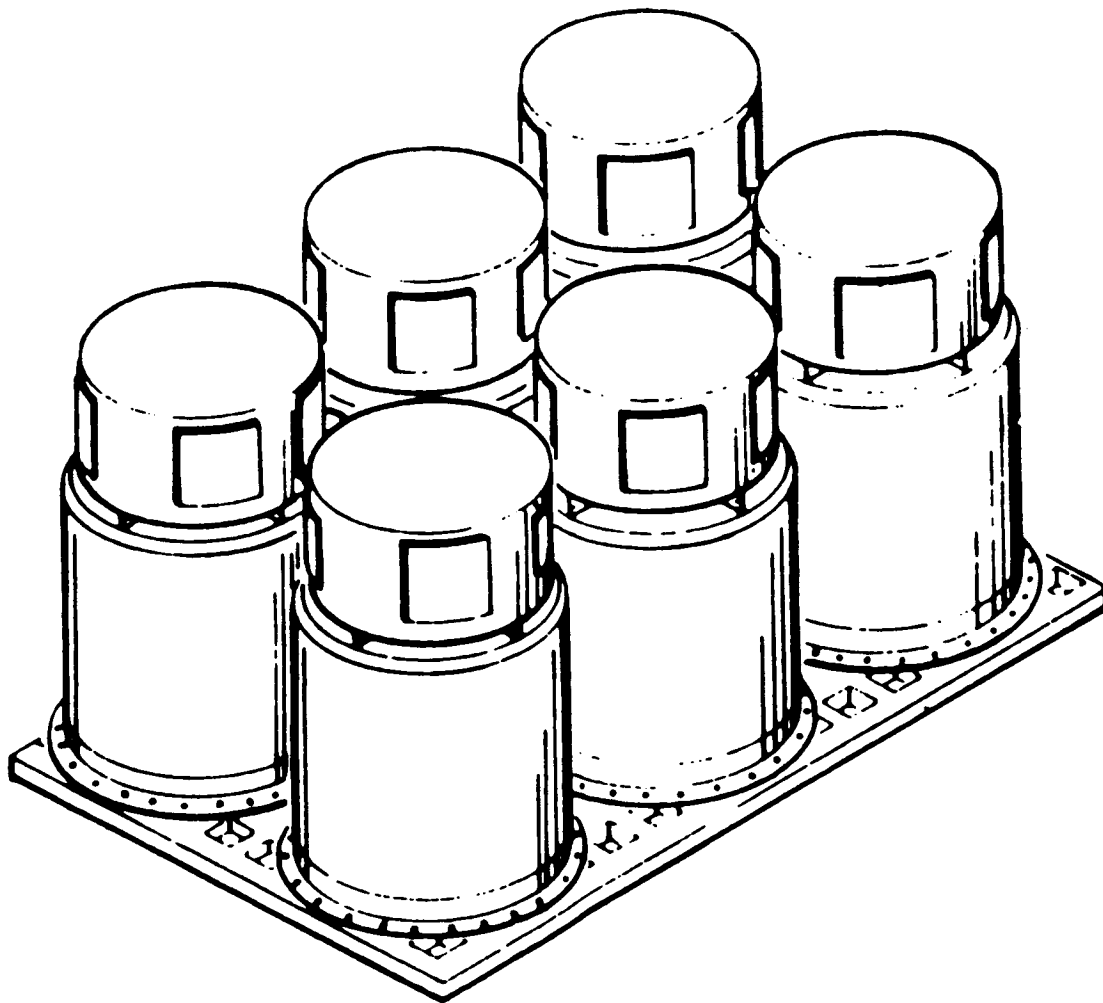


Figure 1. MMP Satellite Cluster.

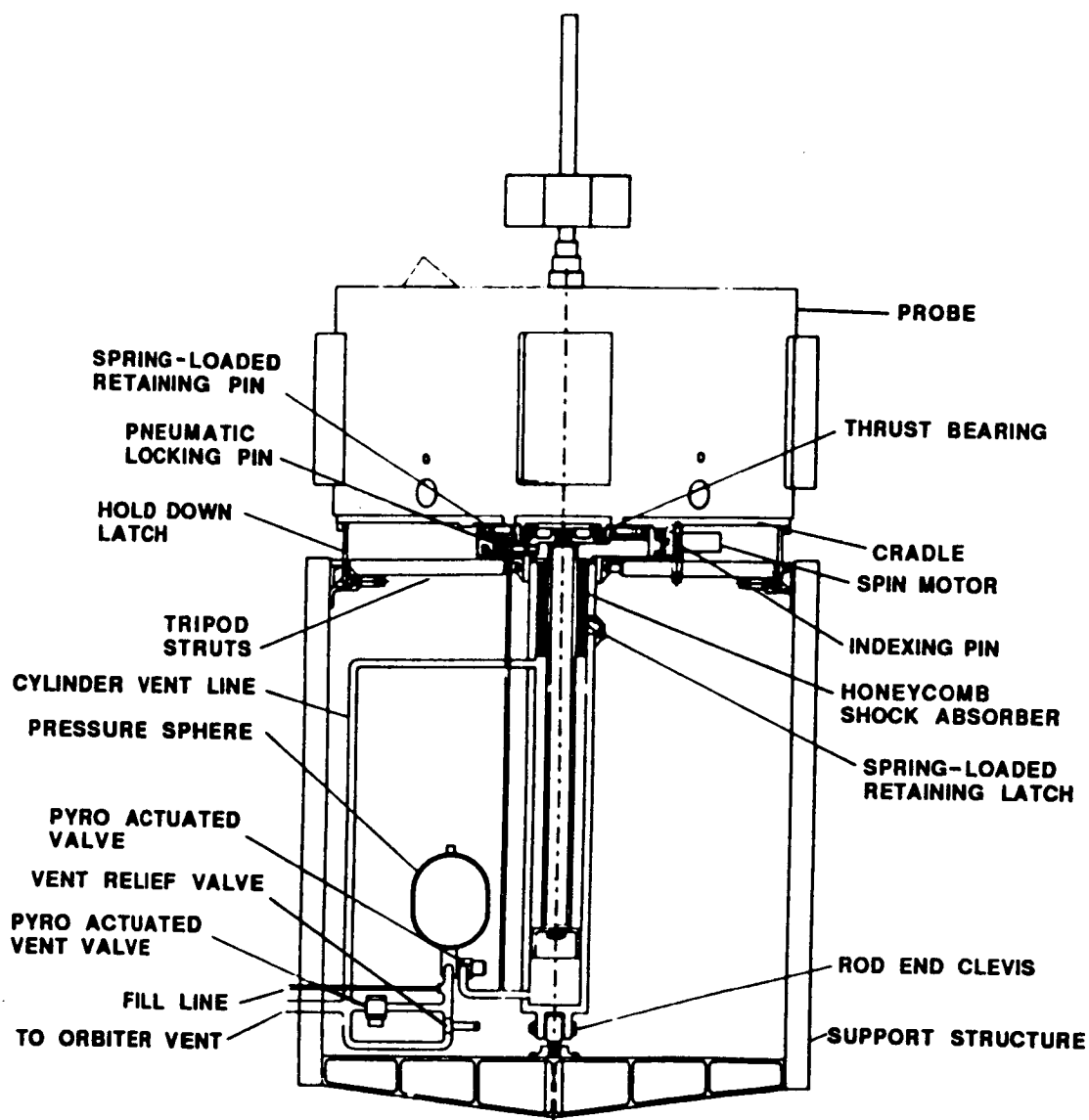


Figure 2. MPSES Flight Configuration.

ORIGINAL PAGE 15
OF POOR QUALITY

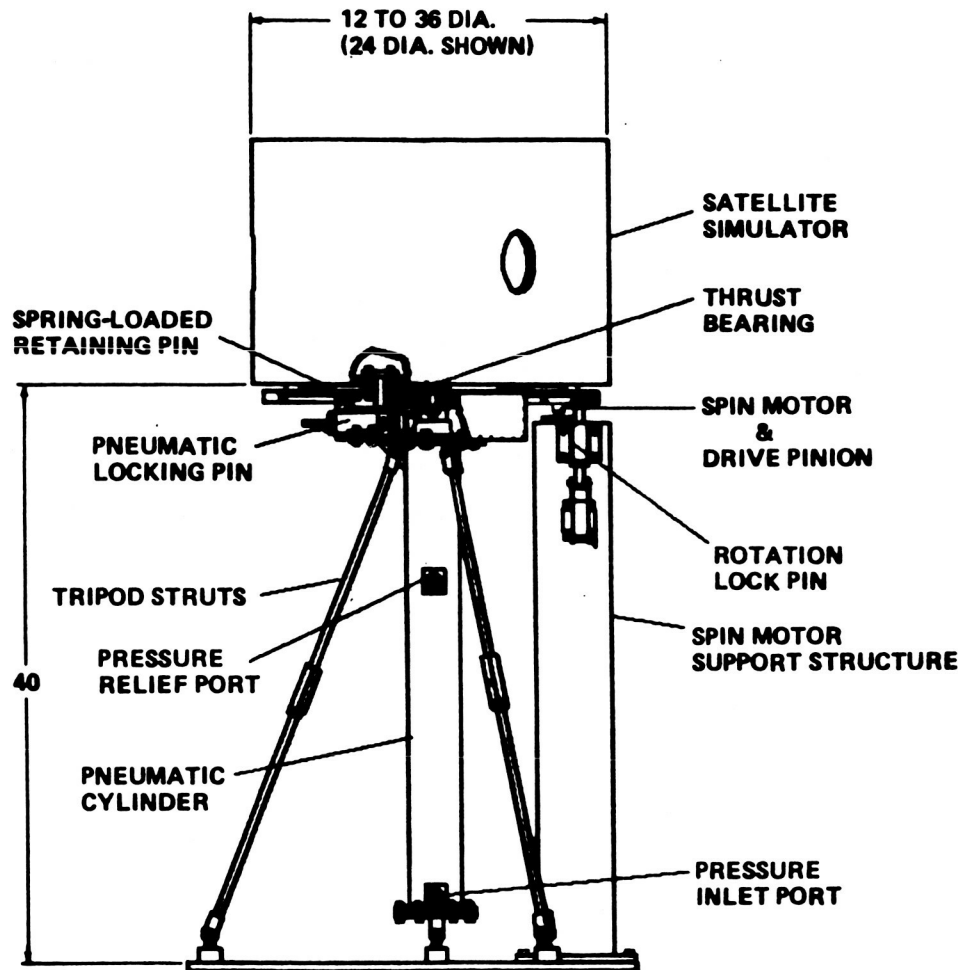


Figure 3. MPSES Test Configuration.

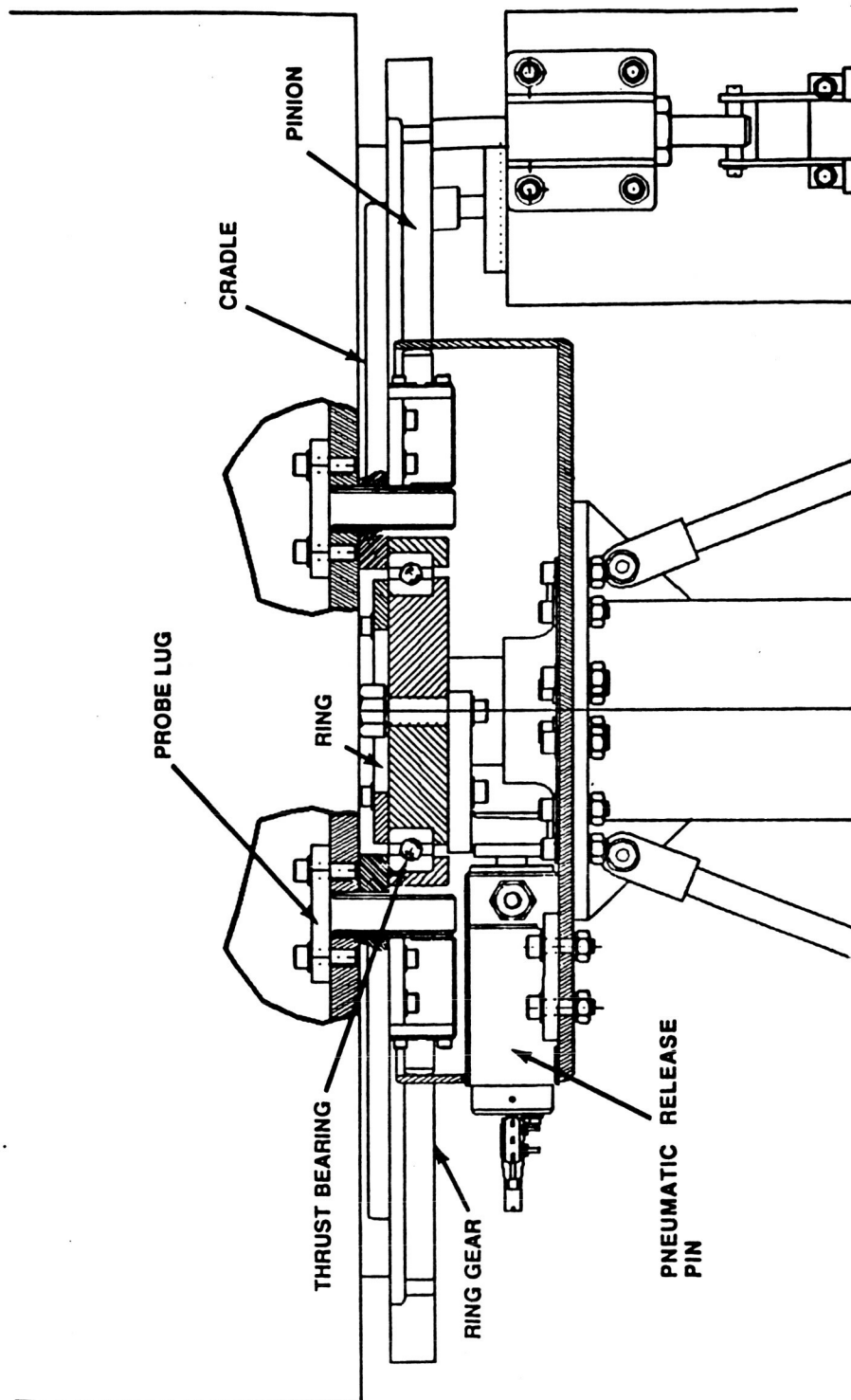


Figure 4. Critical Interface of MPSES Test Configuration.

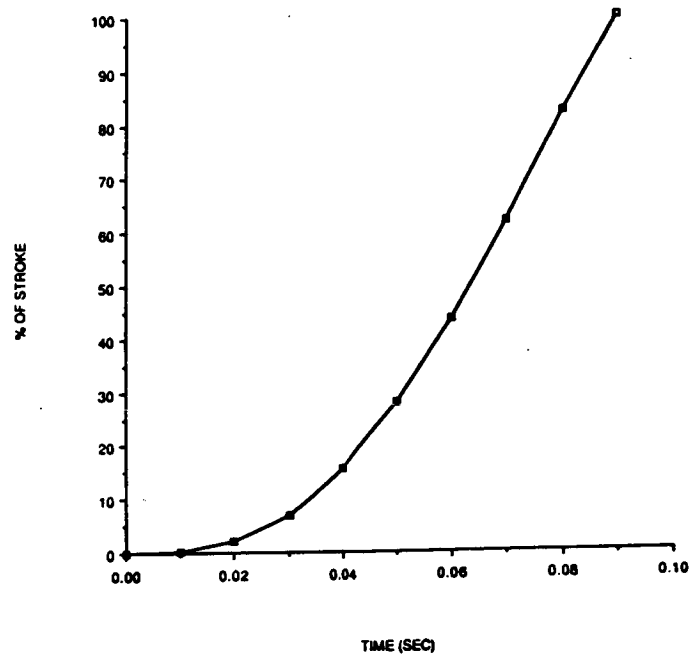


Figure 5. Percent of Stroke Versus Time.

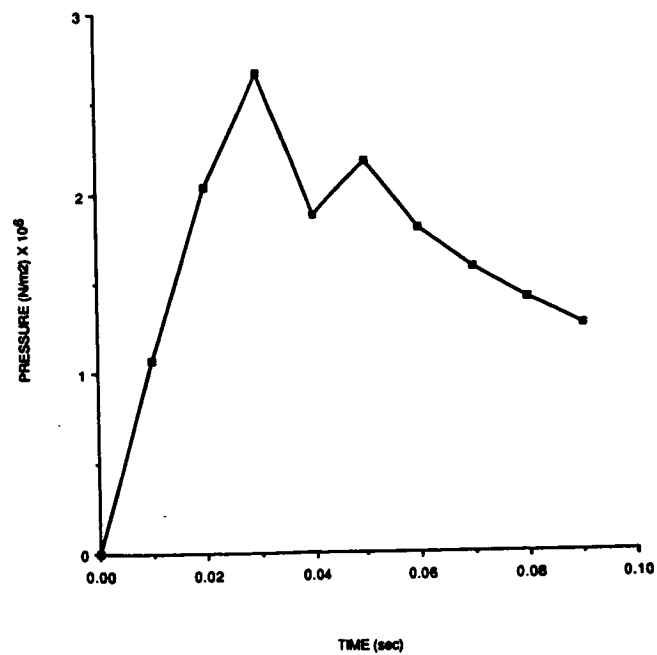


Figure 6. Cylinder Pressure Versus Time.

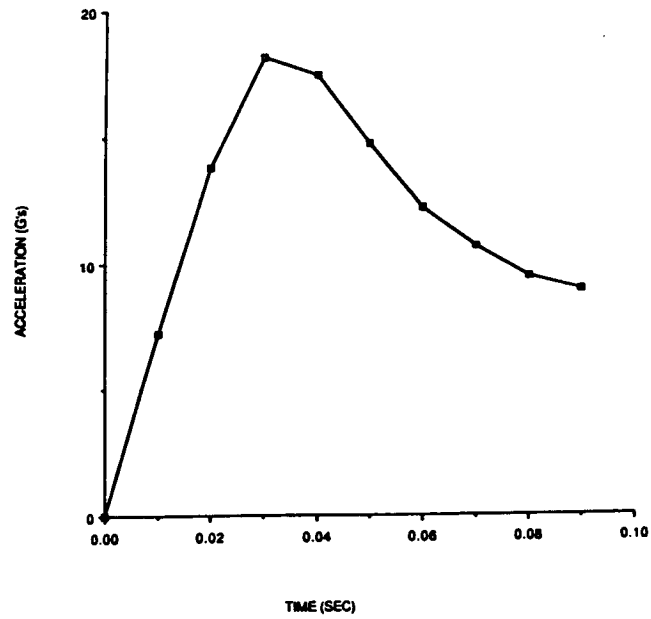


Figure 7. Acceleration Versus Time.

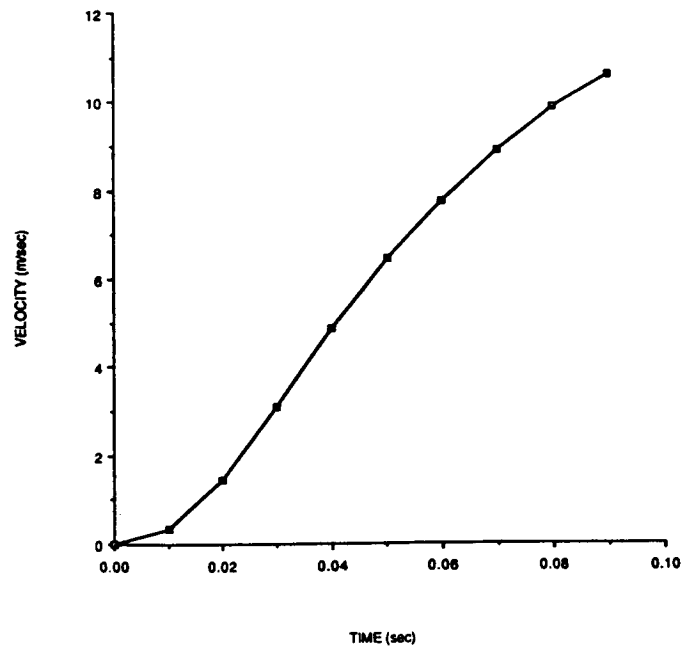


Figure 8. Ejection Velocity Versus Time.

A CAD/CAE ANALYSIS OF PHOTOGRAPHIC AND ENGINEERING DATA

S. Michael Goza* and Wayne L. Peterson*

ABSTRACT

In the investigation of the STS 51-L accident, engineers within the Advanced Programs Office (APO) of the NASA Johnson Space Center were given the task of visual analysis of photographic data extracted from the tracking cameras located at the launch pad. An analysis of the rotations associated with the right Solid Rocket Booster (SRB) was also performed as part of the study. The visual analysis involved pinpointing coordinates of specific areas on the photographs. The objective of the analysis on the right SRB was to duplicate the rotations provided by the SRB rate gyros and to determine the effects of the rotations on the launch configuration. To accomplish the objectives of the investigation, Computer Aided Design and Engineering (CAD/CAE) was employed. The solid modeler, GEOMOD, inside the Structural Dynamics Research Corporation (SDRC) I-DEAS package, proved invaluable to the study. This paper will discuss the problem areas that were encountered in the course of the study and the corresponding solutions that were obtained.

The first problem addressed was the need for an accurate model of the STS launch configuration. A brief description detailing the construction of the computer generated solid model of the STS launch configuration is given. Positioning of the model in coordinate space was also a concern. A discussion of the coordinate systems used in the analysis is provided for this purpose. One coordinate system was used in the assembly of the solid model and for the rotations on the right SRB while another coordinate system was used in duplicating photographic orientations. Secondly, the mathematics involved in determining the eye position for correct photographic matching as well as the area of perspective viewing with respect to telephoto lenses are also presented. The final section of the paper describes the techniques and theory used in the model analysis. The use of GEOMOD abilities to extract coordinates and to place markers on the solid model to match photographic areas of interest is presented along with the discussion on the interaction between the right SRB and the rest of the launch vehicle due to the rotations applied to it. A description of the process employed in rotating the SRB on the solid model is given along with the assumptions used in the analysis.

*Advanced Programs Office, NASA Johnson Space Center, Houston, TX

INTRODUCTION

The NASA Johnson Space Center Advanced Programs Office (APO) is in a unique situation. The APO is concerned with the design of future concepts. That is to say, the APO is responsible for the conceptual design of next generation space transportation systems, heavy lift launch vehicles, space platforms, lunar bases, Mars bases, and the vehicles to get personnel and materials to these places. The work is varied, complex, and extremely visual. Two years ago, the Structural Dynamics Research Corporation (SDRC) I-DEAS software package was chosen to perform the math modeling and to provide the visual capabilities. The precise surface definition provided by solid modeling as well as the excellent color shading and display options are invaluable to our work.

Recently, with Space Transportation System (STS) 51-L accident, the APO was required to use I-DEAS in a new way. The APO was required to match solid models of the STS launch configuration to photographic data acquired from various cameras located around the launch pad and the Florida coast. This paper will discuss the problems involved with matching solid models created with I-DEAS GEOMOD to photographs. Some of the problem areas were orientation matching, perspective, and scaling. This paper will also briefly discuss how the computer model was used in the engineering analysis.

MODEL DESCRIPTION

The first task to be addressed in the STS 51-L accident investigation was the need for an accurate computer solid model of the STS launch configuration. A GEOMOD model of the Orbiter was created by SDRC previously for a demonstration tape and the remaining components were created to complete the launch configuration. These components included both SRB's, the External Tank (ET), and all of the attachment hardware. Enough detail was modeled into the SRB's and ET to assist in coordinate extraction from the screen point picking function.

Several coordinate systems were used in setting up the model for analysis. The launch configuration was modeled using the shuttle launch configuration coordinate system. This is a right handed cartesian coordinate system. The tip of the ET is located at $X=8.31$ meters (327.22 in.), $Y=0$ meters, and $Z=10.16$ meters (400 in.). The X-axis is the longitudinal axis where the positive direction is toward the aft end of the configuration. The lateral axis is the Y-axis where the positive direction is out the right wing of the Orbiter if looking from the tail. The Z-axis is the vertical axis where all elevations are positive. Figure 1 depicts the shuttle launch configuration coordinate system. For the orientation matching part of the analysis, two coordinate systems

were used; the aries-mean of 1950 (M50) and the navigation body system. The M50 coordinate system is an inertial coordinate system. It is fixed in space and time. See figure 2 for description. The navigation body (NB) coordinate system is the standard coordinate system used for aircraft by navigation, guidance, and control analysts. The NB coordinate system is shown in figure 3.

ORIENTATION MATCHING

The first problem encountered after creation of the model was to match the orientation of the GEOMOD model of the STS launch configuration to that of the photograph. To compound the problem further, there were thousands of photographs, all at different times and from different cameras. Also, speed in generation was of the essence. The investigation was on a strict time line and could not afford to wait days for output. Therefore, an algorithm for computing the view orientation had to be developed. Guessing or eyeballing the view was tried, but it was too crude and slow a method for analysis. Rotation angle errors, as much as ten degrees could be induced with no visibly detectable change. This was due to the poor photography on some pictures. Therefore, orientation and position data of the stack and cameras versus time had to be acquired. The Best Estimated Trajectory (BET) data was used for the stack. This data is extrapolated from measurements made by the inertial measurement unit (IMU) on board the Orbiter. It contains orientation matrices, euler angles, and position of the stack in various coordinate systems. The camera positions were at known fixed latitudes and longitudes.

Since the algorithm would be used by other computer systems, a generic method had to be derived. Rotating the model itself was discarded because GEOMOD would not do euler angles simply nor would it allow input of direction cosine matrices. Also, different computer systems handle rotations differently. It was decided that the position of the eye vector would be the only method used to obtain the correct view. With this criteria in hand, the following algorithm was devised.

For a specified time and camera, the position in M50 coordinates of the camera and the origin of the NB coordinate system can be extracted from data generated for us by TRW, Inc., and the BET, respectively. By subtracting the stack position from the camera position, the resultant vector is the eye position in M50 coordinates. Multiplying by the orientation direction cosine matrix going from M50 to NB coordinates, which is also extracted from the BET, gives the new eye position in NB coordinates. If the GEOMOD stack model and the NB coordinate system are coincident, then inputting this new eye position will reveal a view with the correct orientation for the specified photograph. The equation is shown in figure 4. An example of the output product is shown

in figure 5. This method was automated through the use of FORTRAN programs and I-DEAS program files. With this, views of photography could be generated in minutes which aided tremendously in speeding up the analysis process.

VIEWING PARAMETERS

After the orientation problem was eliminated, scaling and perspective became a problem. Scaling the computer image to the photograph was and continues to be a problem. There seems to be no way mathematically to match the two. The guessing method gets close and the use of optical means yields better results. It was eventually decided to disregard scaling, not by choice, but due to the complexity and the lack of speed.

Perspective also posed an interesting problem. The cameras used were automatic focus, zoom, speed, and F stop. The depth of field function in GEOMOD attempts to handle some of the operations, but the value changes when you zoom in on the image. It would have been advantageous if GEOMOD was capable of imitating telephoto lense attributes. For our purposes, though, the distances involved were so immense that the effects of perspective were negligible. Therefore, perspective was turned off in GEOMOD for all images.

ANALYSIS

The analysis of the images proved very fruitful. The GEOMOD software was flexible enough that its features could be exploited to expedite the analysis. The analysis consisted of pinpointing the exact coordinates of specified areas of interest which are visible on the photography. The analysis proceeded in the following manner. A flash of light or puff of smoke would be detected on a photograph. The computer model would be oriented to that photographic view. The GEOMOD software was then utilized with the crosshair screen point picking function to extract the coordinate off the model. These coordinates were then checked against the known positions of access ports, structural joints, etc. If a known opening was nearby, the point was moved to that location, and an arrow marker would be positioned appropriately to highlight the area. The image would then be rechecked against the photograph as well as other views from different cameras. An iterative process would continue until a probable opening was found. An example of the marking method is shown in figure 6. The arrow is pointing out the surface of the solid rocket booster at the propellant segment joint.

An analysis was performed on the right SRB in order to duplicate the rotations provided by the SRB rate gyros. During the analysis an assumption was made that one of the three lower attachment struts between the right SRB and the ET failed. The theory in

this assumption was that the flame plume emerging from the SRB casing burned through the strut or that the forces generated by the thrust of the plume caused the strut to fail. Under this condition the SRB is free to pivot about the remaining two struts and the forward SRB attachment fitting. Thus, the right SRB on the solid model was rotated about an axis passing through the forward attachment fitting and a point bisecting the remaining lower two struts. Rotation angles of 5, 10, and 32 degrees were applied to the booster and interference between the booster and the ET was checked. Since the SRB was being rotated towards the Orbiter, an interference check between the SRB and the Orbiter wing was also investigated.

The results of the rotations established that the right SRB interfered with the ET right above the forward SRB fitting in the intertank area of the ET. The actual angle of rotation for initial contact was not verified, but it was shown that a small interference volume existed when the SRB was rotated through a 32 degree angle. Interference did not occur for the 5 degree rotation, but it was felt that the severe binding that occurs in the forward attachment fitting during the 10 degree rotation would cause the thrust ball fitting to fail. Figure 7 depicts a top view and a side view of the launch configuration after a SRB rotation of 32 degrees. The location of the interference volume between the SRB and the ET is highlighted by an arrow. The figure also shows that the SRB does not come into contact with the Orbiter.

CONCLUSION

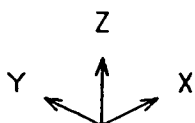
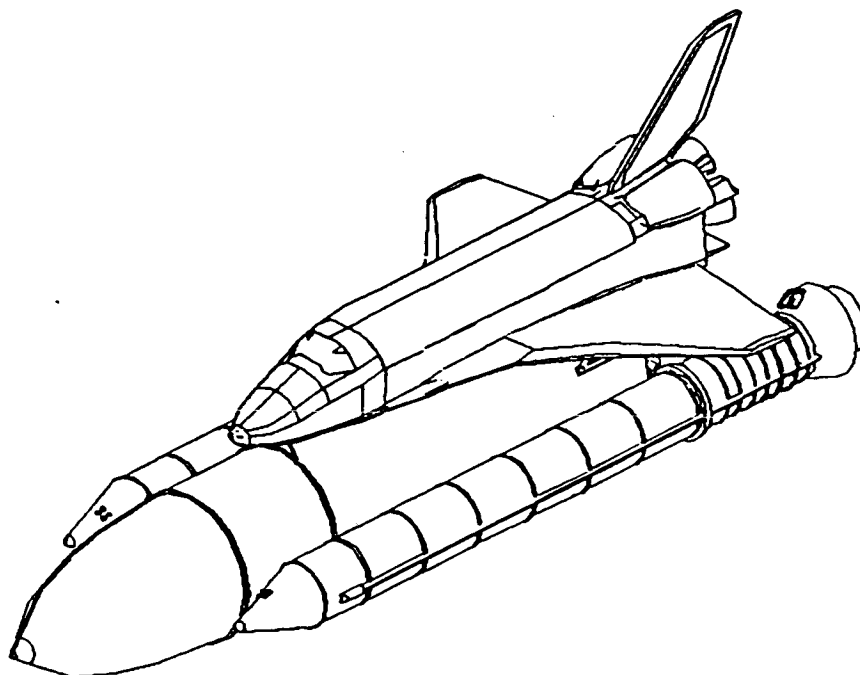
In conclusion, the SDRC GEOMOD software proved invaluable to the performance of the analysis. The computer images enhanced the photography and provided insight into what the photography was actually depicting. These images helped focus the analysis effort to specific areas thereby reducing the engineering work load and they aided tremendously in presentations. The computer images were examined on two occasions by the Rogers Commission for the STS 51-L investigation, and documented in the NASA/JSC Visual Analysis Sub Team (VAST) Final Report. A discussion of the study and the results were also published in Aviation Week and Space Technology, as well as Design Graphics World. The computer image results could have been improved if GEOMOD was able to model the effects of regular and telephoto camera lenses as well as the scaling. Otherwise, the software performed flawlessly.

The algorithm was also a success. It was adopted as the official method for reproducing photographic views on the computer systems involved at the Johnson Space Center. The algorithm was also published in the VAST Final Report.

The analysis of the SRB rotations helped to explain the appearance of dense vapor clouds in the ET intertank region in photographs taken by the tracking cameras. A bright flash near the SRB forward attachment is visible in the photographic data which is the region of impact predicted by the rotational analysis. Thus, the CAE analysis helped to visually understand the mechanics of the accident.

BIBLIOGRAPHY

1. Computer Graphics Depict Events Leading to Explosion. Aviation Week and Space Technology, March 24, 1986, pp. 74-75.
2. Oft Ascent/Descent Ancillary Data Requirements Document. Mission Planning and Analysis Division. JSC-14370, 78-FM-40, Rev. 1, February, 1980.
3. STS 51-L JSC Visual Data Analysis Sub-Team Report. JSC-22175, Final, June 1986. Figure 1 - Aries-mean-of-1950 coordinate system.
4. Aerodynamic Design Data Book, Volume 2, Launch Vehicle. IVBC-3, August, 1983.
5. NASA and CAD: The Way Back to Space. Design Graphics World, December, 1986, pp. 14-19.



NAME: Shuttle Launch Configuration coordinate system.

ORIGIN: -8.31 meters (-327.22 in.) in X, 0.0 meters in Y, -10.16 meters (-400 in.) in Z from the tip of the External Tank.

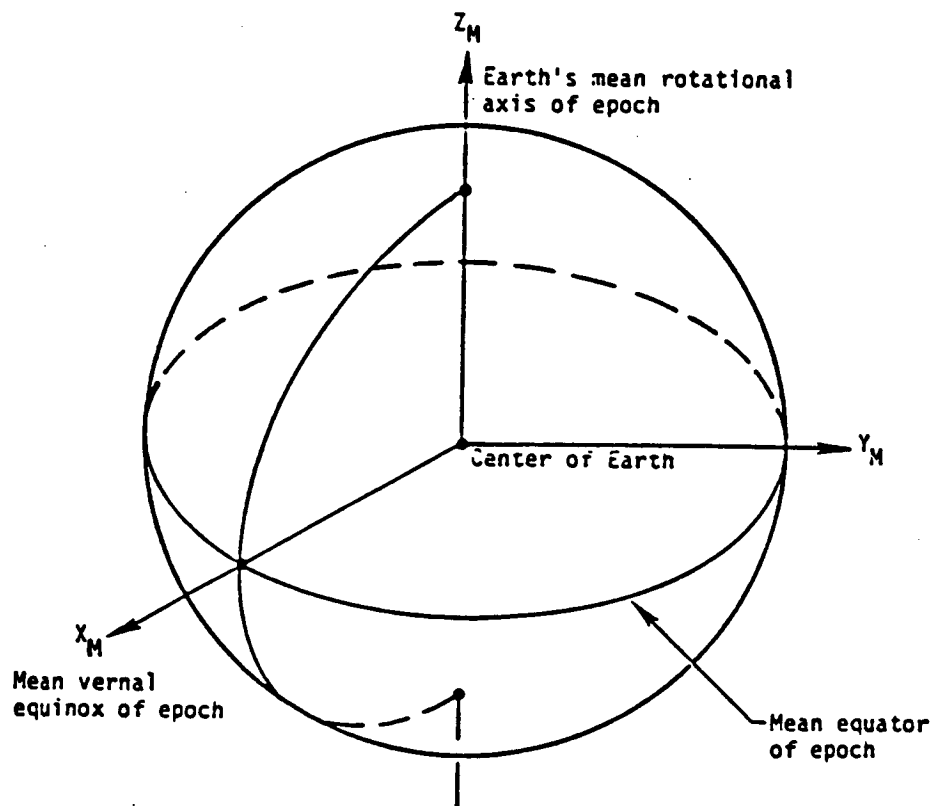
ORIENTATION: The X axis (longitudinal axis) is positive towards the aft end of the configuration.

The Y axis is positive out the right wing of the Orbiter.

The Z axis is the vertical axis where all elevations are positive.

CHARACTERISTICS: Right-handed, Cartesian system.

Figure 1 - Shuttle Launch Configuration coordinate system.



NAME: Aries-mean-of 1950, Cartesian, coordinate system.

ORIGIN: The center of the Earth.

ORIENTATION: The epoch is the beginning of Besselian year 1950 or Julian ephemeris date 2433282.423357.

The X -Y plane is the mean Earth's equator of epoch.

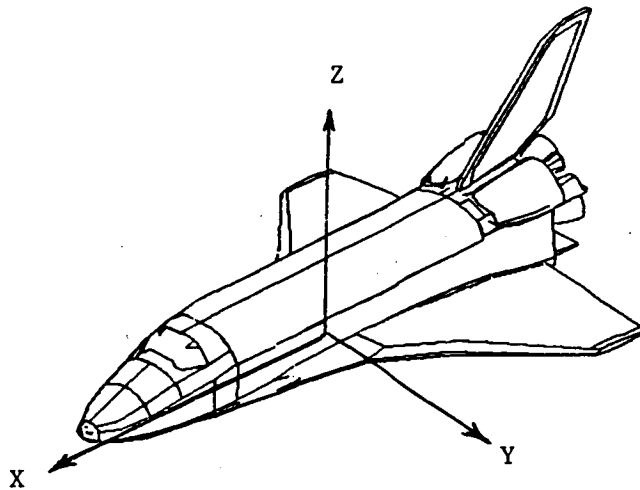
The X axis is directed towards the mean vernal equinox of epoch.

The Z axis is directed along the Earth's mean rotational axis of epoch and is positive north.

The Y axis completes a right-handed system.

CHARACTERISTICS: Inertial, right-handed, Cartesian system.

Figure 2 - Aries-mean-of-1950 coordinate system



NAME: Navigation Base coordinate system.

ORIGIN: The center of the inertial measurement unit.

ORIENTATION: The X axis is positive out the nose of Orbiter.

The Y axis is positive out the left wing of the Orbiter.

The Z axis is positive going up through plane of the vertical tail.

CHARACTERISTICS: Right handed cartesian coordinate system.

Figure 3 - Navigation Base coordinate system.

$$\begin{bmatrix} X_{ENB} \\ Y_{ENB} \\ Z_{ENB} \end{bmatrix}_{3 \times 1} = \begin{bmatrix} DC \end{bmatrix}_{3 \times 3} \begin{bmatrix} X_c - X_s \\ Y_c - Y_s \\ Z_c - Z_s \end{bmatrix}_{3 \times 1}$$

WHERE

DC = ORIENTATION DIRECTION COSINE TRANSFORMATION MATRIX
FROM BET

s = STACK POSITION IN M50 COORDINATES

c = CAMERA POSITION IN M50 COORDINATES

ENB = EYE POSITION IN NAVIGATION BASE COORDINATES

Figure 4 - Eye position algorithm.

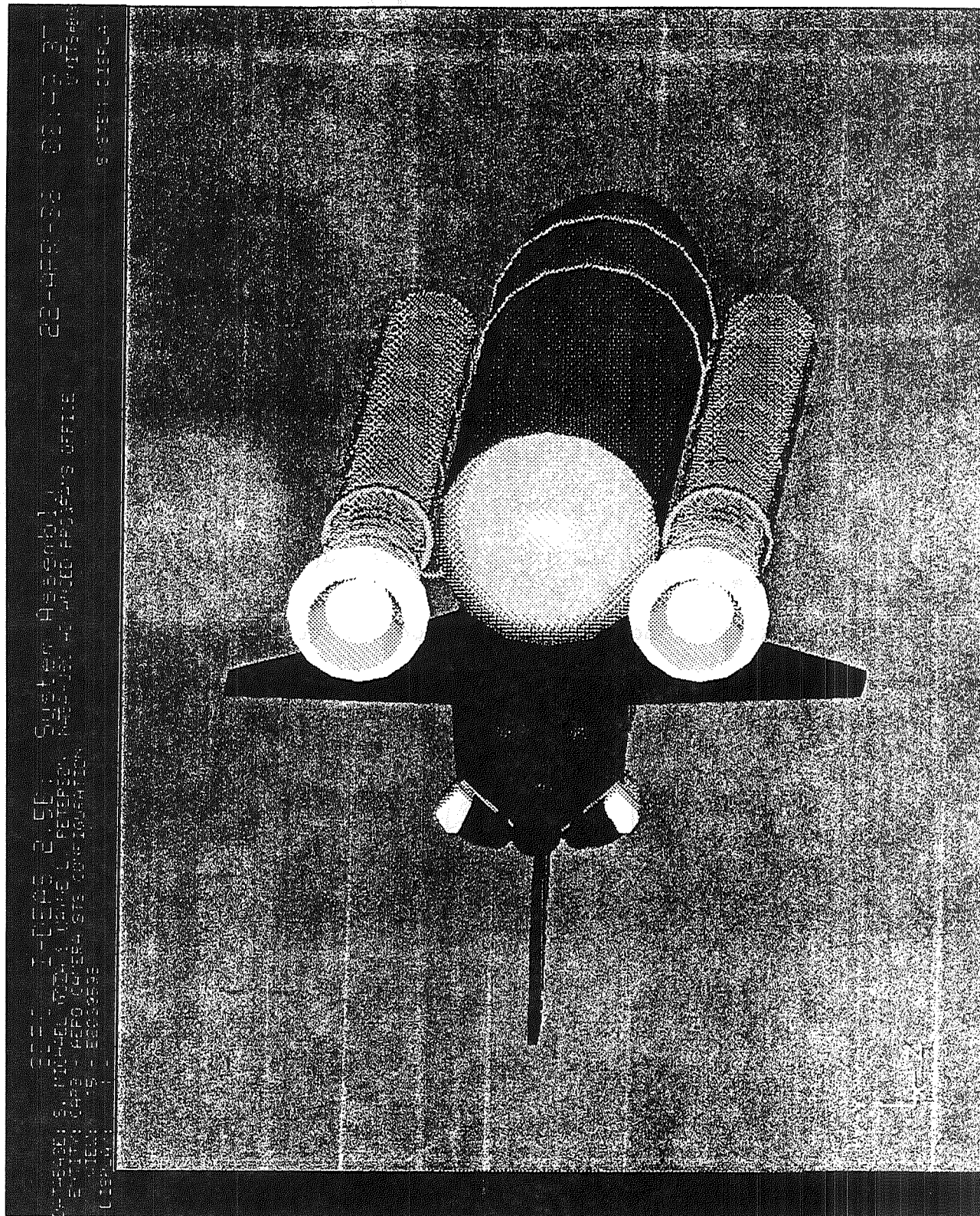
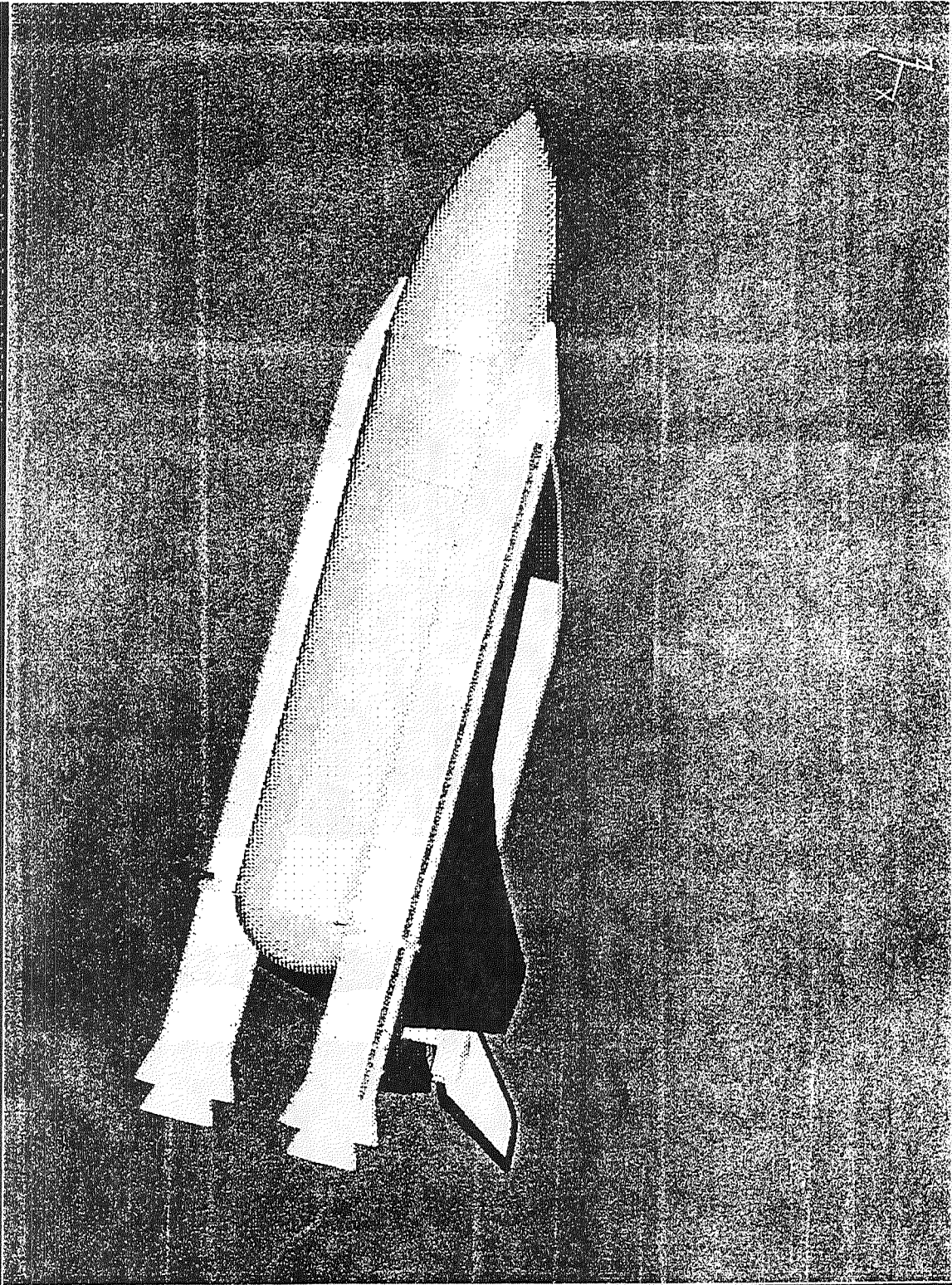


Figure 5 - Computer generated image

[illegible]

245

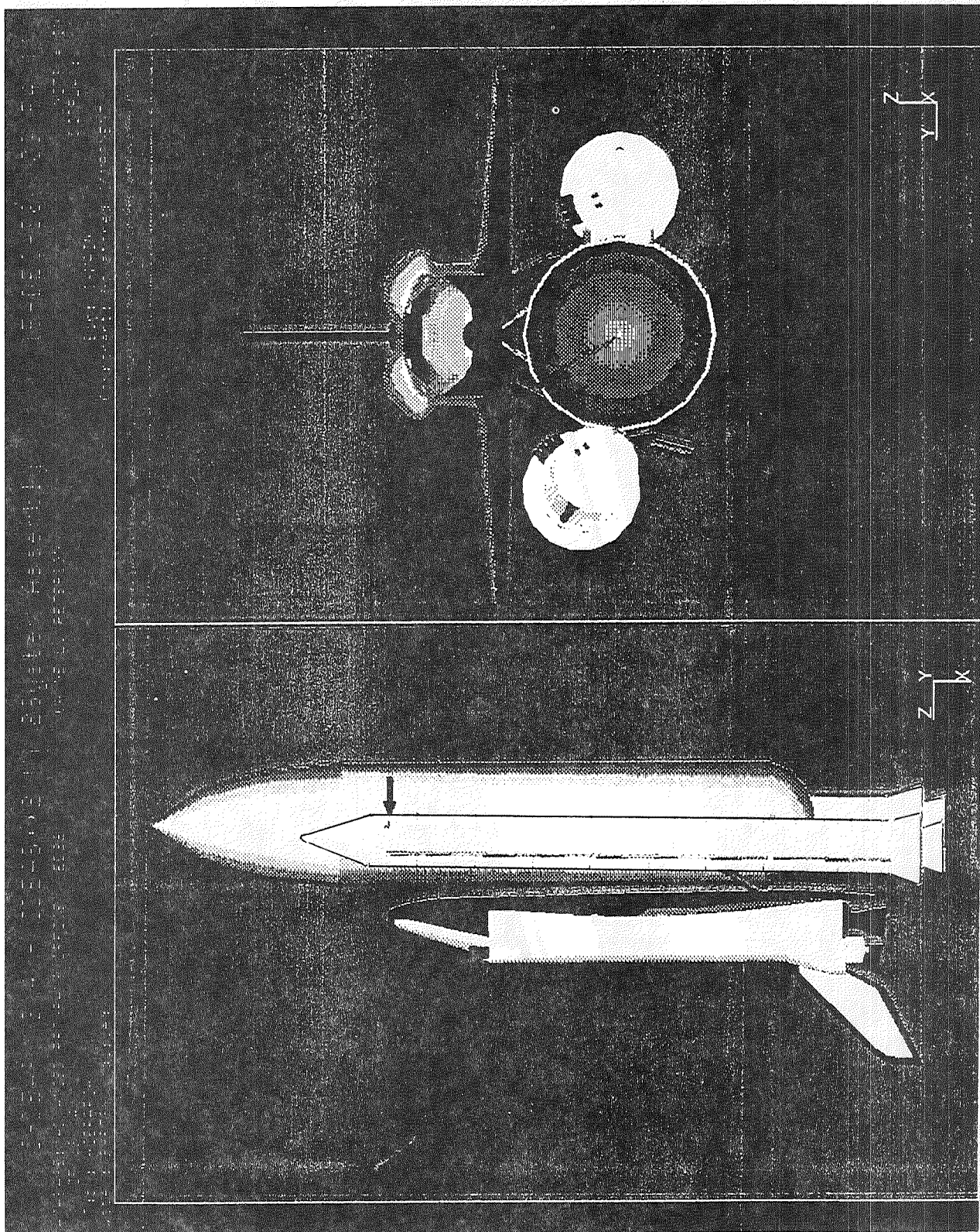


Figure 7 - Computer generated image with SRB rotation

THE PRELOADABLE VECTOR SENSITIVE LATCH FOR ORBITAL DOCKING/BERTHING

William R. Acres and John J. Kennedy *

ABSTRACT

This paper describes the workings and function of the "Preloadable Vector Sensitive Latch" designed by Mr. W. R. Acres of NASA JSC. A discussion of docking systems used in U. S. manned space flight programs is included to show how docking systems have evolved, and to highlight the potential advantages of a preloadable vector sensitive latch in such systems.

INTRODUCTION

To fully appreciate the potential advantages of this latching system, it is necessary to understand what has been done in the past relative to docking.

U.S. Manned space flight docking history:

The ability to dock two vehicles in space was first demonstrated during project Gemini in 1966 when Gemini 8 docked with an Agena target vehicle. The docking system in this demonstration is shown in Figure 1. It utilized the rendezvous and recovery section of the capsule to engage a cone interface attached to the Agena. Latching was accomplished by maneuvering an indexing bar located on the capsule nose, into a V-groove on the Agena cone. A latch in the cone then secured the bar in the groove. Release was accomplished by firing reverse thrusters located on the Gemini capsule. The Gemini program proved that rendezvous and docking in space was possible.

In the Apollo program, docking was facilitated by use of a probe and drogue system. This system (see Figure 2) used a probe, located in the command module tunnel, to mate with a cone or drogue, located in the lunar module tunnel. Once the two vehicles were joined with this system, structural latches located radially around the command module tunnel were activated. The probe and drogue were then removed from the tunnel to allow passage from one vehicle to the other. Storing the probe and drogue after removal was difficult due to volumetric constraints.

* NASA JOHNSON SPACE CENTER, HOUSTON, TEXAS

Neither the Gemini nor the Apollo docking systems were androgynous. Each vehicle being mated carried a different docking interface. Two Apollo command modules could never dock with each other since both carry only the probe portion of the docking system. This was also true for the Gemini, Agena and Lunar Module since each carried only a male or female portion of a docking system.

One of the prime objectives of Apollo-Soyuz Test Program (ASTP) was to demonstrate the ability of one vehicle to dock with and rescue the crew from another vehicle. To facilitate this, an androgynous system was required. This system (see Figure 3) used three guides attached to a ring in order to correct small angular and translational misalignments. A set of capture latches (protruding thru the guides) was engaged once the two rings made contact. These latches in turn held the rings together until the structural latch system (located radially around the tunnel) could be engaged.

The docking/berthing system concepts currently being studied for Orbiter to Space Station operations are all ring and guide systems. These concepts differ from ASTP by using four docking guides and an attenuation systems on each docking ring as opposed to three guides and an attenuation systems on ASTP. The latching system to be used has not yet been selected. A preloadable vector sensitive latch is one contender for this system.

There are several advantages of a preloadable vector sensitive latch system over the ASTP latching system. One of these advantages is an automatic release feature. If during docking separation, some latches fail to disengage, the remaining latches will automatically release when the ring rotates .14 rad (8 deg) relative to its mating interface. The ASTP structural latch system drove all latches with a cable mechanism. In the event of an inflight failure, manual release of a cable system would be difficult during an EVA while a preloadable latch system would provide easy accessibility. The final advantage of the new latch design is the reduced weight, cost and complexity associated with eliminating one set of latches.

DESCRIPTION

The preloadable vector sensitive latch is an over center locking mechanism which accomplishes both the capture and structural latching of the mating interfaces. As its name implies, it can be preloaded to withstand pressure, moment and seal compression loads being transferred across the mating docking/berthing interface. The loading requirements per latch is 1336 kg (2950 pounds) for docking and 4236 kg (9340 pounds) for worst case Orbiter-to-Station moment loading after docking. Vector sensitivity refers to an automatic latch release that occurs when the vector angle of the applied force on the latch changes significantly.

Each latch is secured in a latch housing located between the primary member and the docking/berthing guide as shown in Figure 4. The latch protrudes thru the guide prior to contact between the two docking vehicles (Figure 4a). During the docking/berthing process, the latch is pushed into its supporting housing within the guide by the front surface of the other vehicles docking interface (Figure 4b). As the latched member moves closer to the primary member, the latch moves around the latched member and finally comes to rest on the 45 degree chamfer along the back side (Figure 4c). Compression loads between the latch and primary members are created by exerting a compression loads on the member chamfer by the latch roller (see Figure 4d). As originally envisioned, there would be eight latches on each member ring, two per guide.

The system consists of three links, one actuator, a bearing surface roller, a sliding pin joint, a housing and a return spring mechanism (see Figure 5). Figure 6 shows the forces acting on the latch system during docking. The force "L2" is a frictional force between the sliding pin and housing caused by resultant force "L1." For this pin to housing interface, a static friction coefficient of 0.1 was assumed. The following equations are used when summing forces and moments on the main link:

- (i) $Q = \text{ARCOS} \left(\frac{B^2 + C^2 - A^2}{2*B*C} \right)$
- (ii) $H = \text{ARCOS} \left(\frac{C^2 + A^2 - B^2}{2*C*A} \right)$
- (iii) $I1 = Q - (.785 \text{ RAD} - G) + J = Q - (45 \text{ deg} - G) + J$
- (iv) $M1 = M*C*\text{SIN}(D) - K*A*\text{SIN}(N8)$
- (v) $Fx = M*\text{SIN}(D) - K*\text{SIN}(I1) - L1 + Fs = 0$
- (vi) $Fy = K*\text{COS}(I1) + L2 - M*\text{COS}(D) = 0$
- (vii) $L2 \leq (0.1*L1)$

Known Variables

I1 = release angle
 K = designed latch load
 Fs = known spring force
 L2 = pin frictional force

Unknown Variables

M = yoke force
 D = yoke angle
 L1 = bearing pin force

By assuming values for angle "D" in equation (iv), corresponding values of "M" can be computed. These values when substituted into equation (v) produce values for "L1." Using these values for "D" and "M", the force "L2" can be obtained from equation (vi). To remain latched, the value of "L2" from equation (iv) must be less than or equal to the normal force "L1" times the static friction coefficient equation (vii). Either a decrease in angle "D" or an increase in angle "I1" causes equation (vii) to be violated and the latch automatically releases. (Figure 7)

DEVELOPMENT TESTING

Several variables effect release operation of the latch. These variables include friction within the pinned joints, deviation from the assumed static friction coefficient, and the force imposed by the return spring. To aid in evaluating the effects of these variables, a series of tests has been developed. Results of these tests are intended to prove the following:

- (i) The latch will release by rotating the yoke to a given release position (angle "D" is decreased).
- (ii) The latch will collapse when contacted at angles greater than the release angle (angle "I1" is increased).
- (iii) The latch will withstand the design loads.
- (iv) The latch will automatically release when the load angle is rotated .14 rad (8 deg), from $-.79$ rad (-45 deg) to $-.65$ rad (-37 deg) (angle "I1" is increased).
- (v) The latch can be released while loaded to the design release load by rotating the yoke to the release position.
- (vi) Clearance between the latch roller and mating docking ring can be removed and the desired preload can then be applied.

During testing of objective (iii), the latch was to be loaded to 4236 kg (9340 pounds) while measuring deflections on the upper pin joints of the main link. Movement exceeded design limits resulting in rotation of the yoke to the release position. When the applied load reached 4073 kg (8980 pounds), the latch released.

Further testing was conducted until the cause of the premature release could be investigated.

ANALYSIS OF RESULTS

From preliminary analysis of the test results, objectives (i) and (ii) have been achieved. The third objective was also partially achieved.

Objective (i) was proven by loading the latch to approximately 45.3 kg (100 pounds) at a force vector of $-.79$ rad (-45 deg) as shown in Figure 8. The yoke angle "D" was then decreased until the latch released. The resulting value for "D" was slightly less than the calculated value. Once this angle was established, the latch was set at this angle and loaded to determine the

actual force required to collapse the latch. The average value for this force is 36.2 kg (80 pounds). This testing demonstrated the ability of the latch to release when the yoke is rotated to a given release position.

Objective (ii) was demonstrated by loading the mechanism at angles ranging from $-.52$ rad (-30 deg) to 1.83 rad (105 deg) in $.26$ rad (15 deg) increments (see Figure 6). The forces required to release the mechanism ranged from 11.3 kg (25 pounds) to 1.8 kg (4 pounds) with higher loadings required in the $-.52$ rad (-30 deg) to $.26$ rad (15 deg) and 1.31 rad (75 deg) to 1.83 rad (105 deg) angle ranges and lower loads in the $.26$ rad (15 deg) to 1.31 rad (75 deg) range. These results demonstrate that the latch will collapse when contacted at angles greater than the release angle.

The ability of the latch to handle the design loads (objective iii) was partially demonstrated by loading the mechanism to 96% of the design load prior to latch release. Inspection of the links indicated no permanent deformation in any member. Although the design load was not achieved, the ability of the latch to handle high loading while in the latched position was successfully demonstrated.

Preliminary analysis indicates that premature release of the latching mechanism occurred when the yoke rotated to the release position. This rotation was due to the movement of the main link relative to the fixed yoke position. Potential causes for this relative rotation are:

- (i) Movement of the latch housing (relative to the test base) due to bolt hole tolerances.
- (ii) Movement of the sliding pin prior to final release.
- (iii) Movement of the yoke caused by tolerances in the turnbuckle assembly.

FUTURE TESTING

Tests done to date will be repeated after several changes to the test hardware are completed. These modifications will allow measurement of the sliding pin motion and determination of latch housing movement relative to the base plate. Alterations to the turnbuckle assembly (load application test fixture) will be made to allow more accurate control of yoke movement.

Further tests will be performed to verify testing objectives (iv), (v) and (vi) listed above. The latch will be loaded with the force vector applied at $-.79$ rad (-45 deg) and release when the latch is rotated $.14$ rad (8 deg) while under a constant load of 1336 kg (2950 pounds). The latch will then be released by rotating the yoke to its release position with a constant load of 1336 kg (2950 pounds) applied to the roller. The latch will also remove $.31$ cm ($.125$ in) of clearance and then be preloaded to 4231 kg (9340 pounds) by applying a relatively small load on the yoke.

CONCLUSION

The concept of a vector sensitive latch has been demonstrated in tests with the property of locking and releasing when loaded at predetermined angles. The ability of preloading this latch to carry structural loads has also been demonstrated. Additional testing is required to prove the clearance removal and preload features of the design.

The potential advantages in reliability, safety, serviceability, weight and cost reduction provided by this latch system offer improvements in future docking/berthing systems.

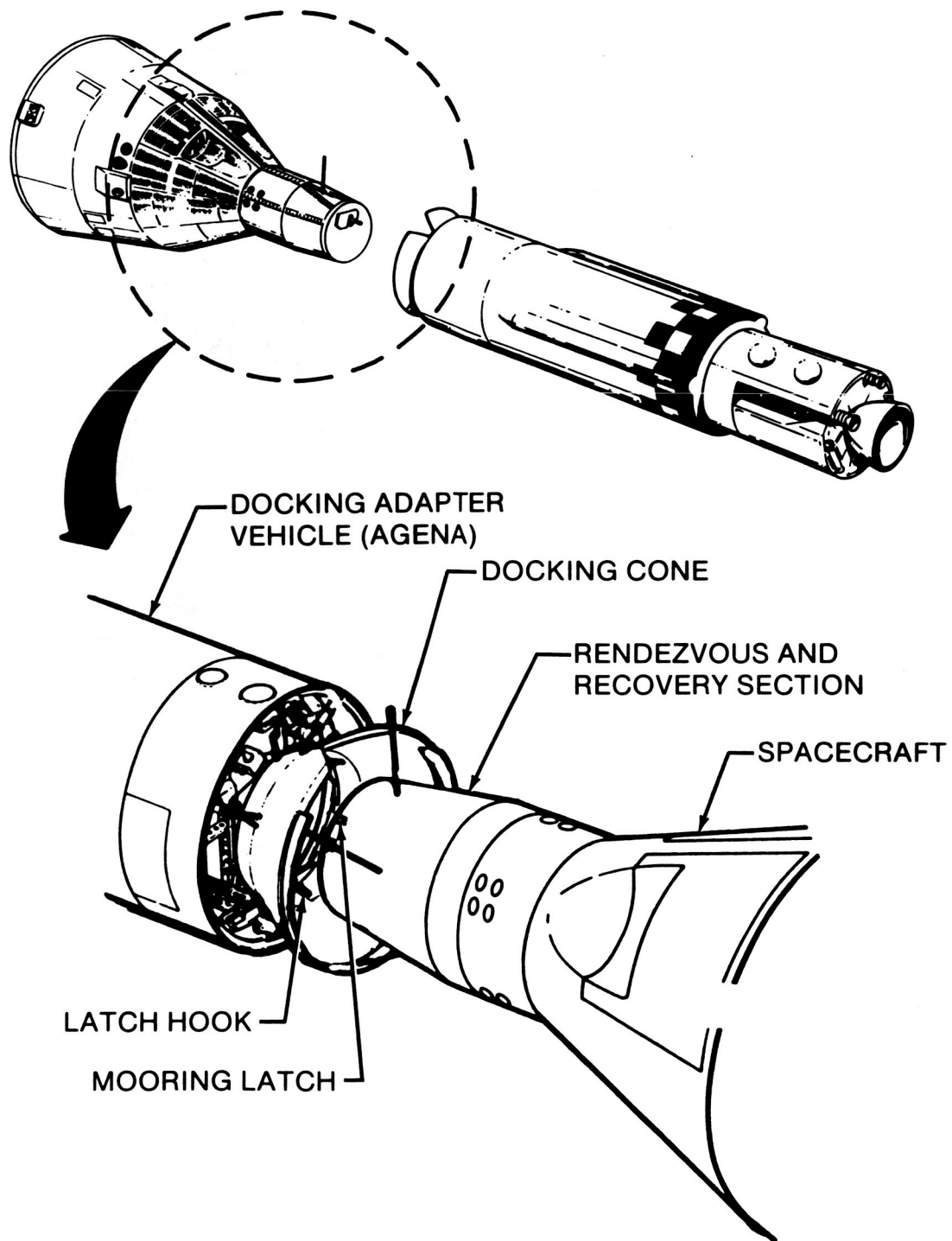


Figure 1. Gemini docking system.

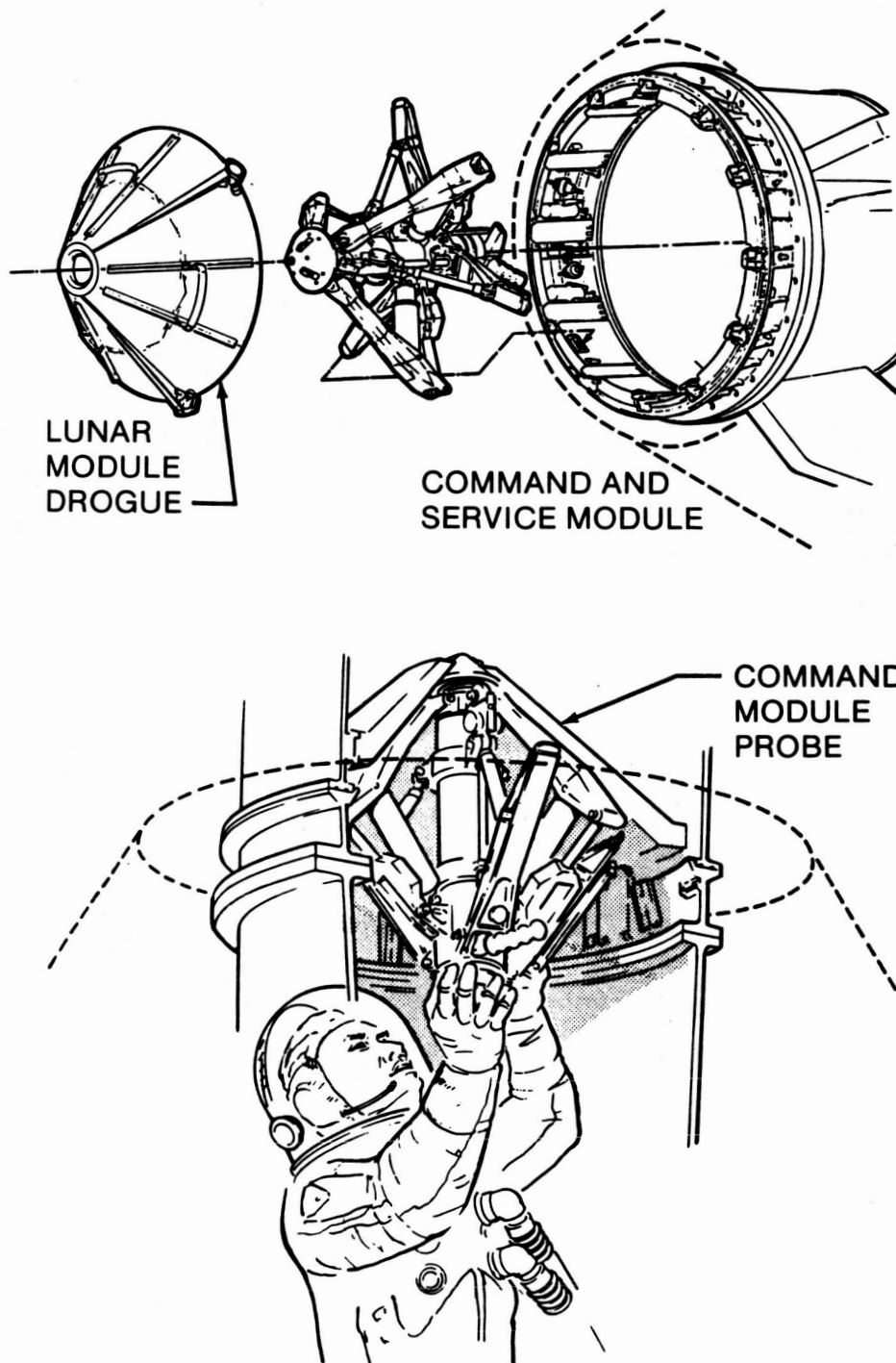


Figure 2. Apollo docking system.

ORIGINAL PAGE IS
OF POOR QUALITY

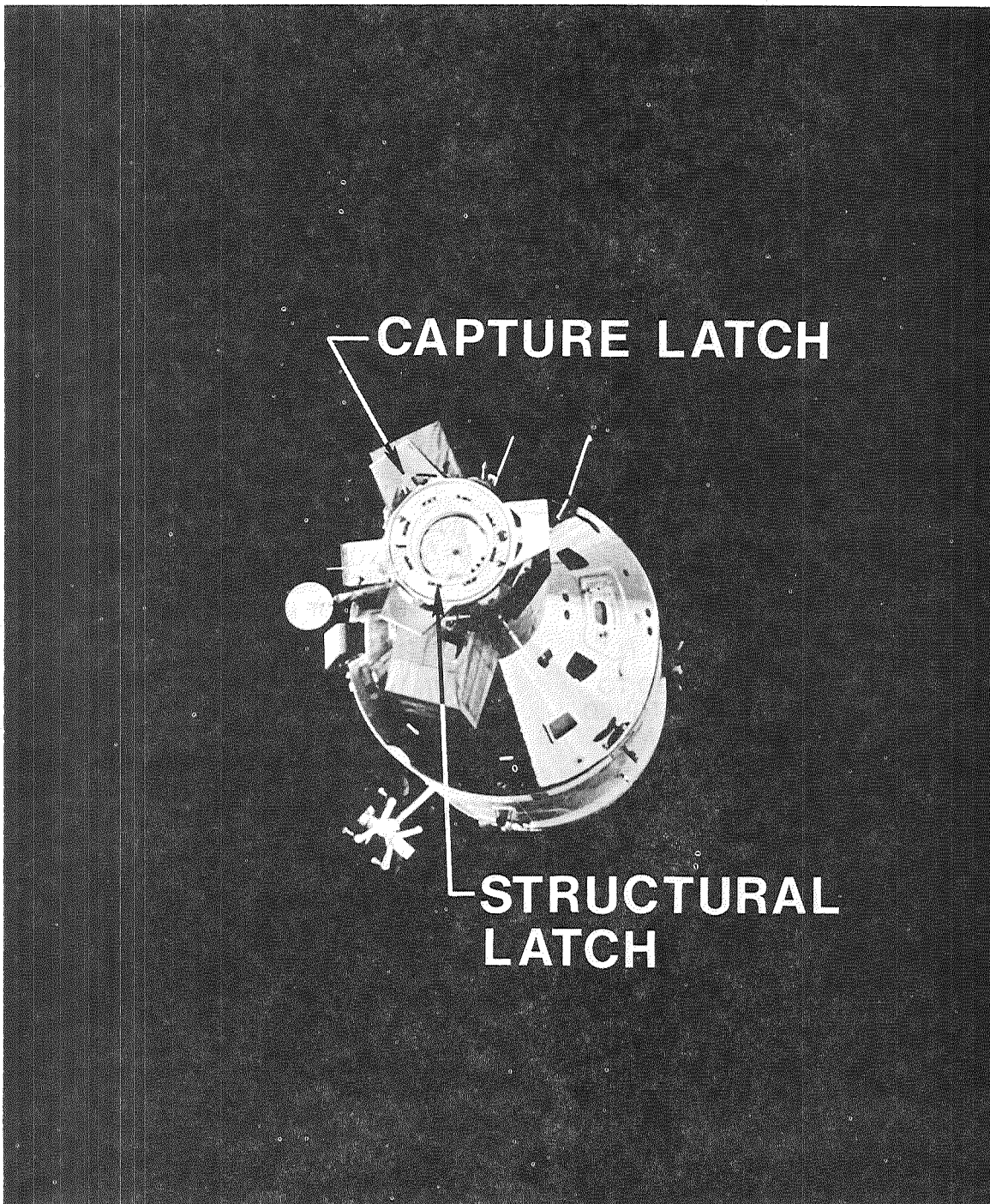


Figure 3. ASTP docking system.

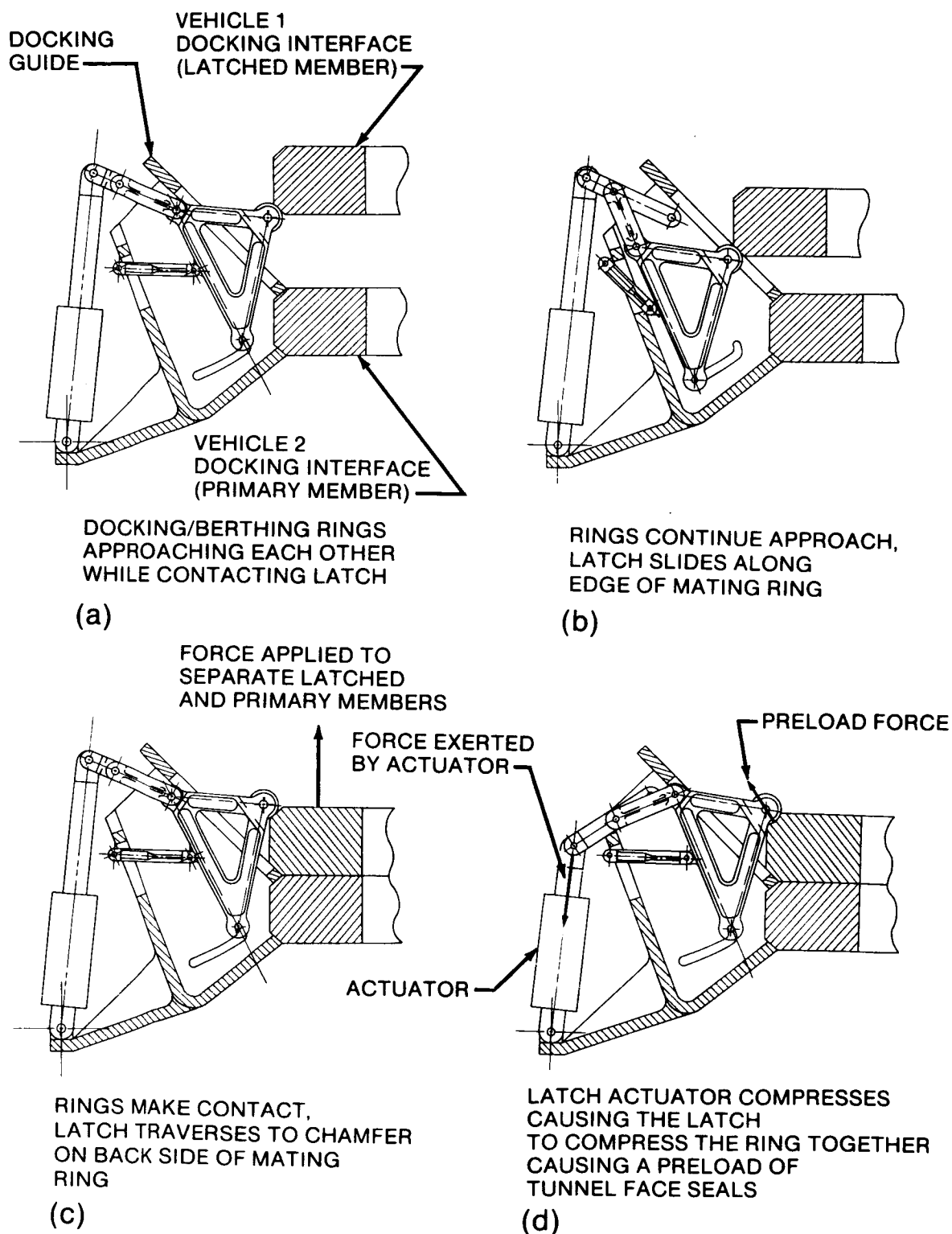


Figure 4. Functional sequence of preloadable vector sensitive latch during docking. (a) Docking/berthing. (b) Latch being compressed. (c) Latched. (d) Preload.

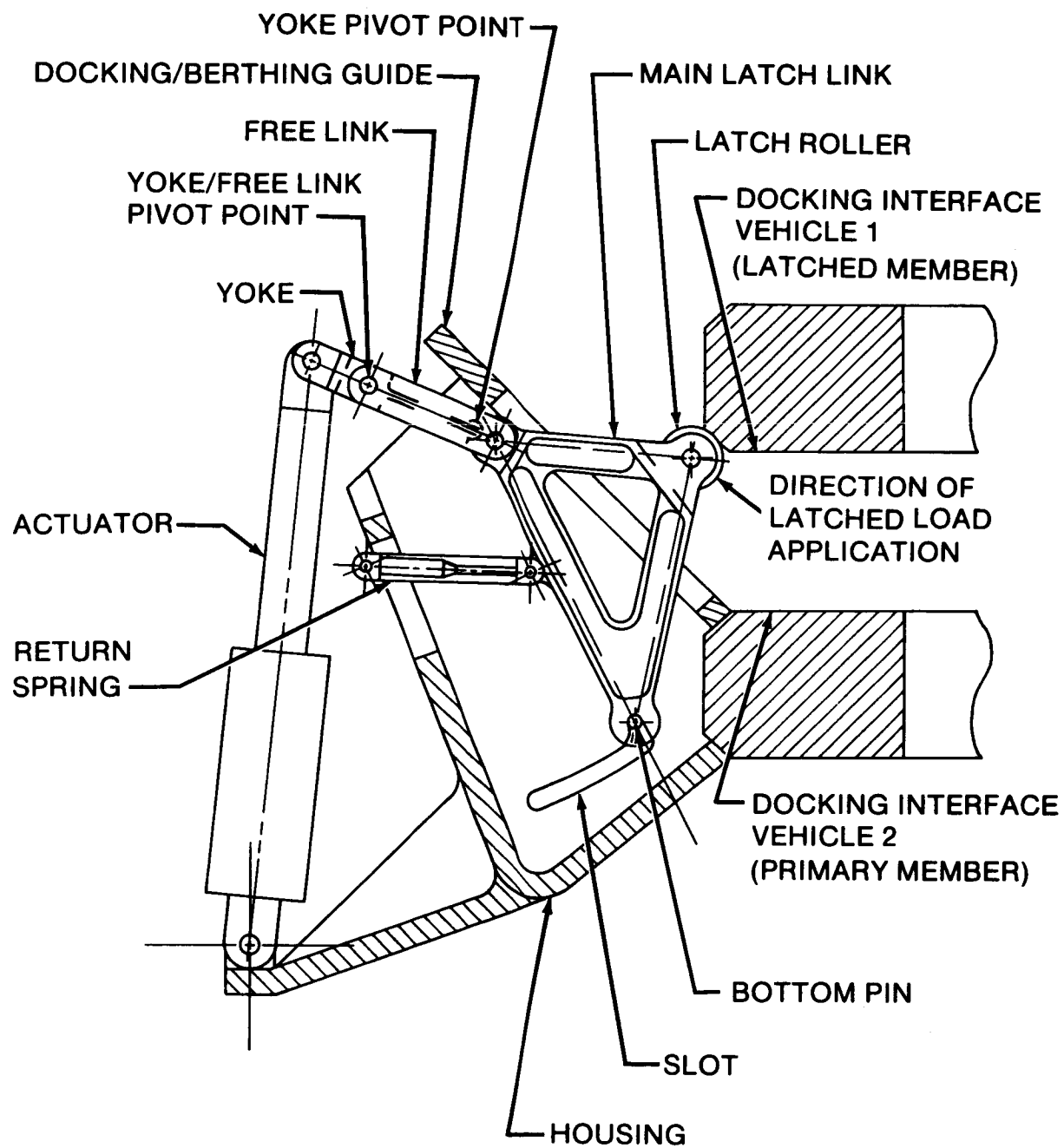


Figure 5. Latch components.

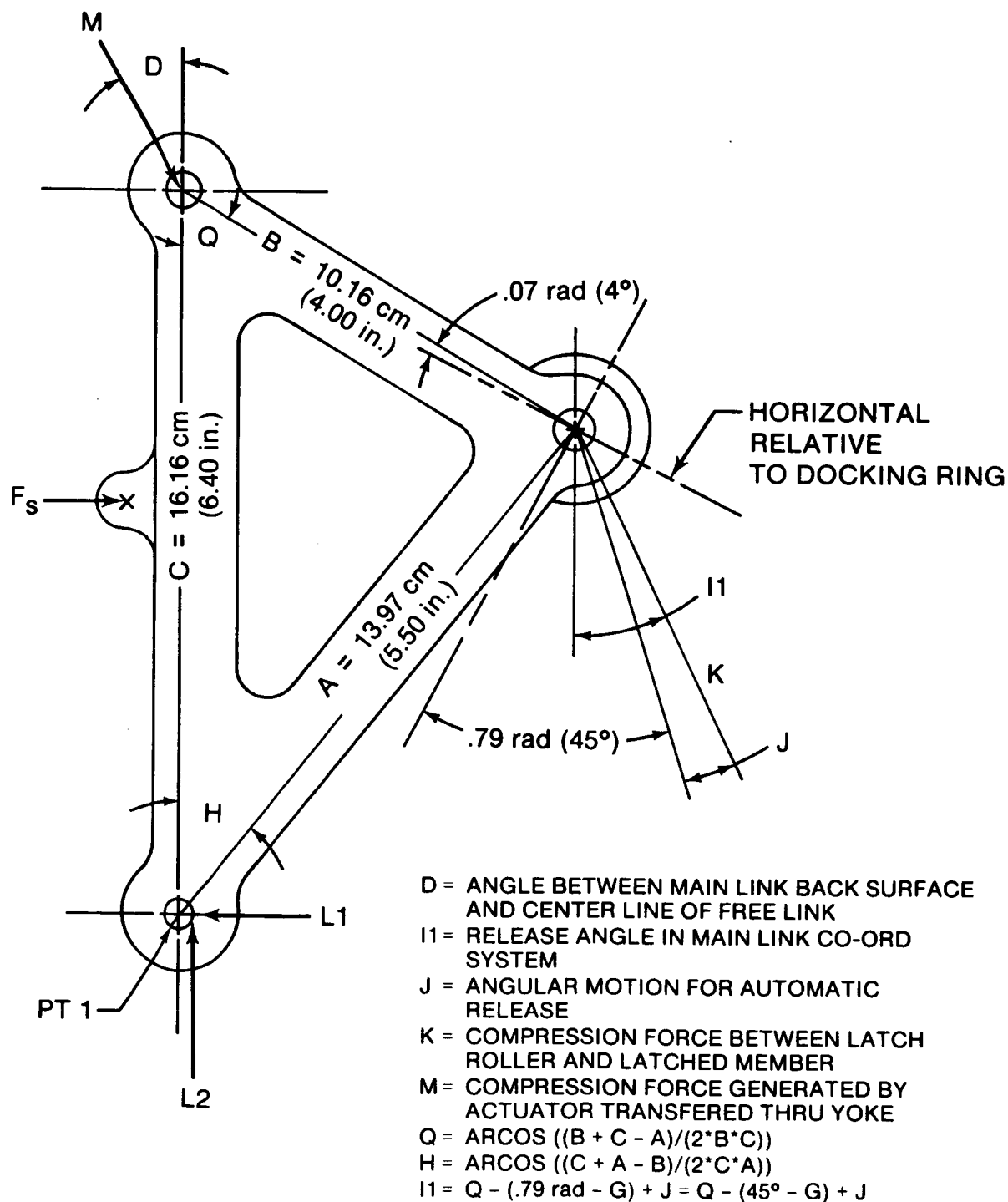


Figure 6. Latch main link.

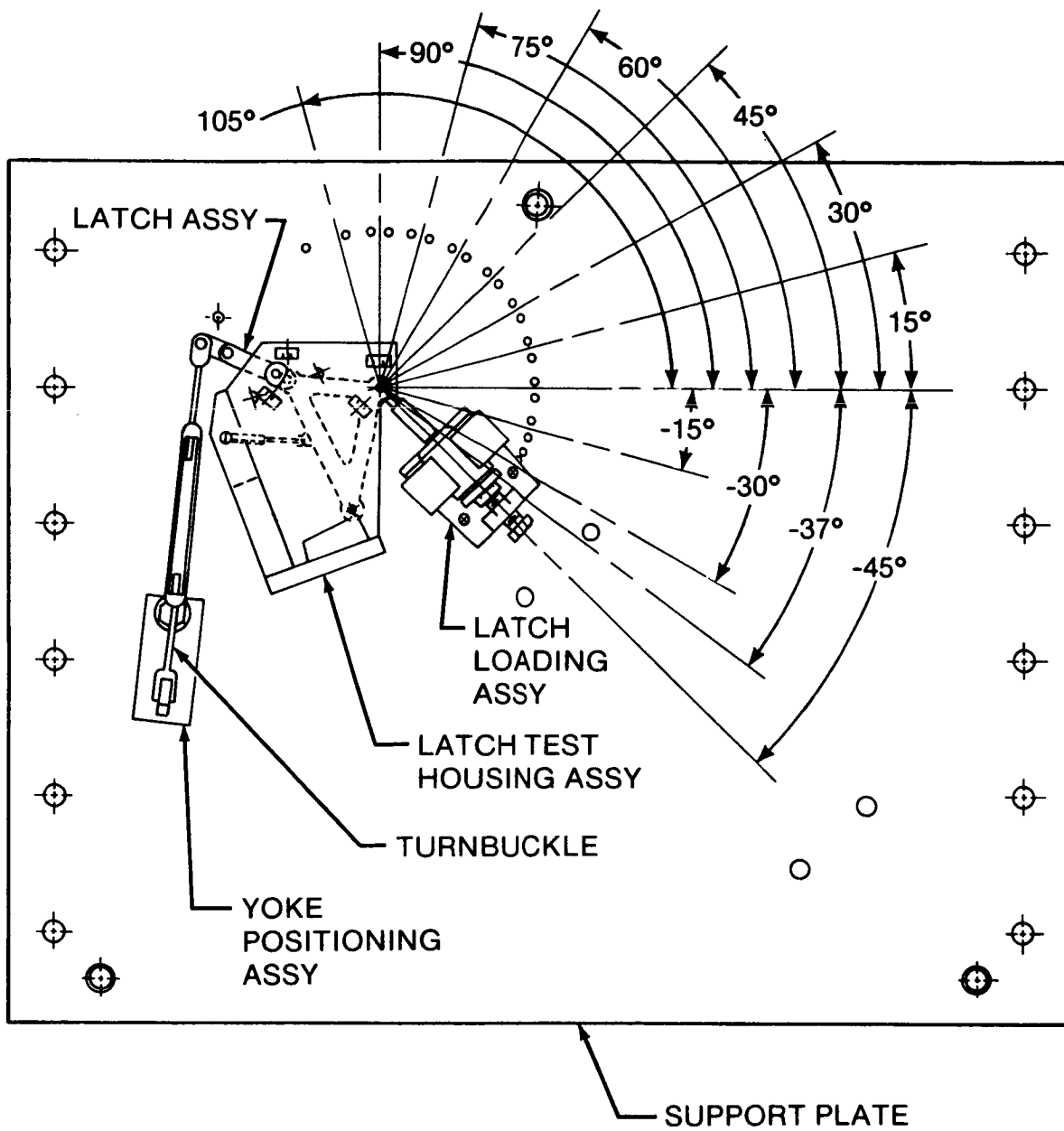


Figure 7. Yoke release position, latch loading.

SPACE STATION BASED OPTIONS FOR ORBITER DOCKING/BERTHING

Daniel J. Hoover*

ABSTRACT

This paper describes conceptual efforts to develop a Space Station based system for docking and/or berthing the NSTS Orbiter. Past docking and berthing systems are reviewed, the general requirements and options for mating the Orbiter and Space Station are discussed, and the rationale for locating the system on the Station is established. One class of Station-based system is developed in several variations and evaluated with respect to weight distribution, loads, safety, reliability, viewing, and maintainability. An evolutionary presentation of the variations provides insight into the development process and the problems encountered. An overall evaluation of the Station-based variations compared to an optimized Orbiter-based system demonstrates the potential benefits of this approach as well as the issues that must be resolved to realize the benefits.

INTRODUCTION

Orbital activities have included the mating and demating of vehicles throughout the last twenty years, since the Apollo program used separate vehicles for translunar flight and lunar landing. Two basic approaches to vehicle mating have since emerged; docking and berthing. Docking refers to the connection made when the approach vehicle flies directly into the target vehicle, where the docking mechanism engages on impact and secures the vehicles together. Docking systems were developed for the Gemini, Apollo, and Apollo-Soyuz programs.

The Apollo system, shown in Figure (1), utilized a probe and drogue capture mechanism. The probe was mounted on the Command Module (CM) and the drogue on the Lunar Module (LM). With the probe extended, either vehicle could fly into the other, where the impact forced the probe into alignment and allowed capture latches to engage the drogue. The probe was then retracted and structural latches actuated around the interface perimeter to provide a pressurizable interface between the vehicles. The probe and drogue were removable from within the vehicles to permit crew transfer.

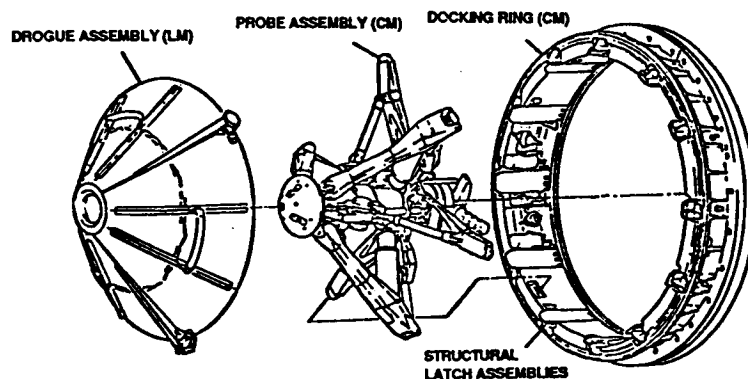


Figure 1. Probe-Drogue Capture Mechanism Provided Apollo Docking Capability

*Rockwell International, Space Station Systems Division, Downey, California

The probe and drogue system was combined with a new one for the Apollo-Soyuz interface, shown in Figure (2). The active portion of the Soyuz interface consisted of a capture ring with alignment petals mounted on hydraulic struts. An identical interface without struts was provided on the Soyuz spacecraft. As the interfaces were driven together, the petals interlocked and forced the interface rings into alignment, where capture latches around the perimeter secured the rings together. The hydraulic struts acted as shock absorbers and allowed the active ring to "float" during impact and alignment relative to the supporting structure. After damping, the active ring was retracted with a cable system and structural latches engaged to provide a pressurizable interface. Both Apollo and Soyuz interface systems depended on the closing velocity between vehicles to provide the force necessary to align the capture mechanisms.

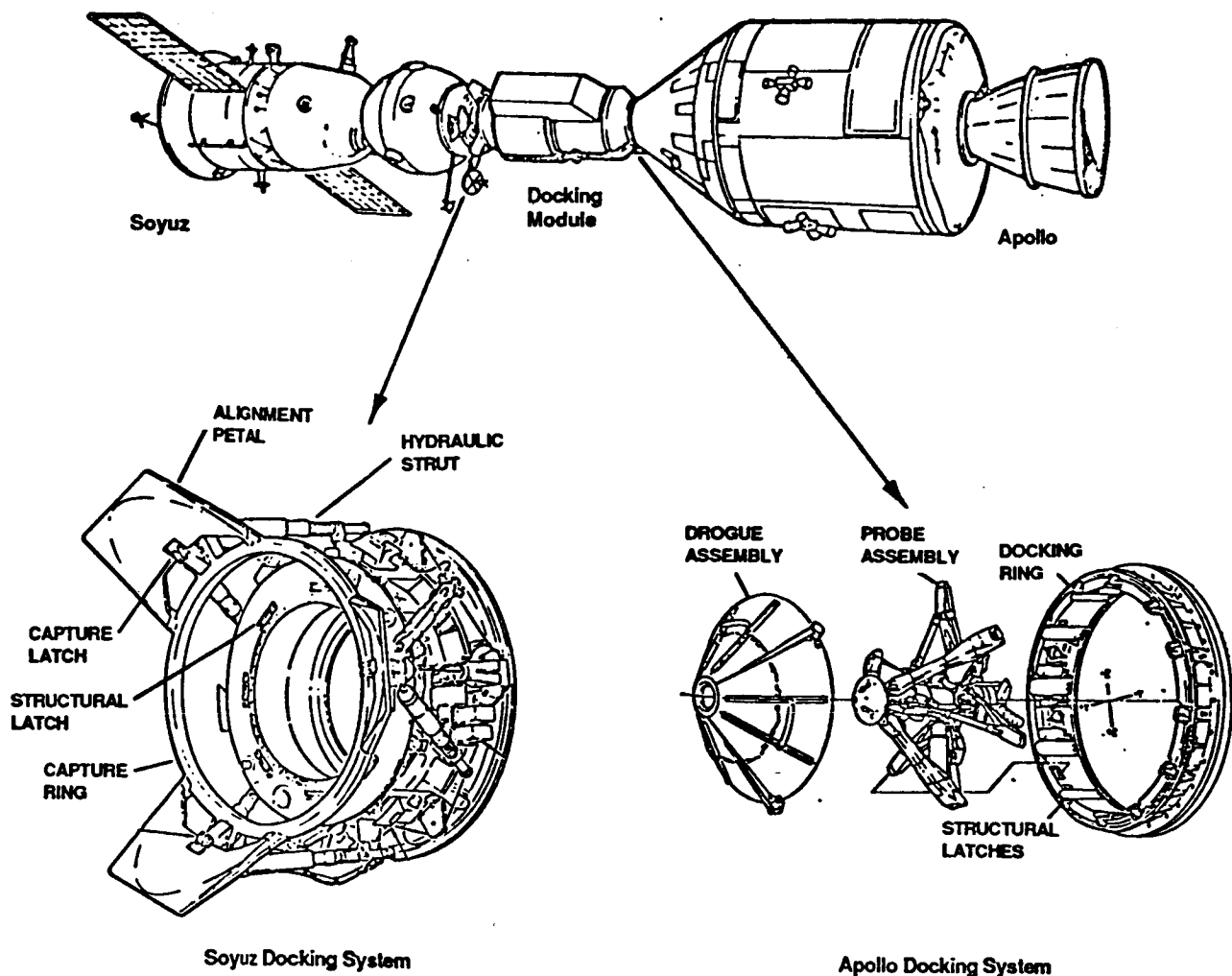


Figure 2. Ring/Petal Capture System Developed for Apollo-Soyuz Docking

ORIGINAL PAGE IS
OF POOR QUALITY

With the advent of the Shuttle Orbiter and the Shuttle Remote Manipulator System (SRMS), berthing of space vehicles became possible. Berthing refers to the use of an intermediate mechanism, typically a manipulator, to capture the target vehicle and perform the maneuvers required to position the vehicles for the desired interface.

Berthing operations to date have included the capture and placement of satellites in the Orbiter payload bay, Figure (3), and the deberthing and deployment of satellite and other payloads, such as the 22,000 pound Long Duration Exposure Facility (LDEF). In a typical satellite berthing operation, the arm tracks and captures the satellite and stops any relative motion. The arm then performs the maneuvers necessary to place the satellite within the reach of the interface system in the payload bay. Capture latches engage the satellite, the arm is switched to a "limp" mode, the latches complete the interface, and the arm is disengaged.

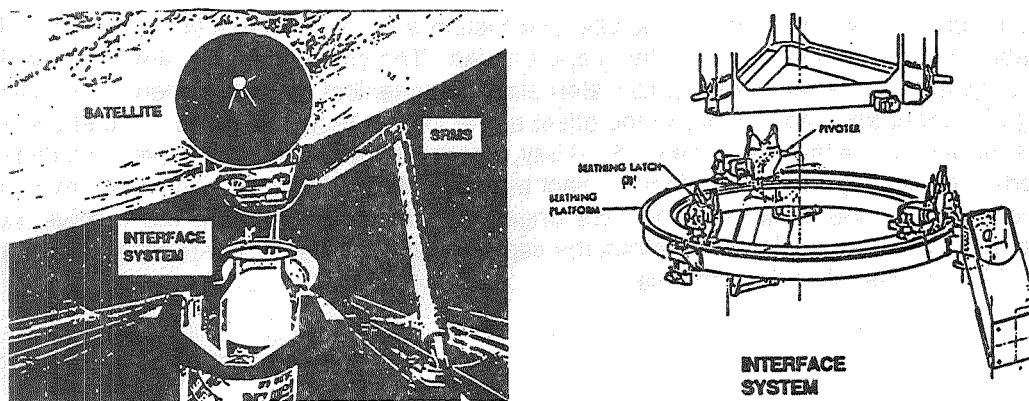


Figure 3. Manipulator Berthing Provides Controlled Mating Operations

The berthing approach is an attractive alternative to docking because no closing velocity is required for capture, reducing the risk of collision. In addition, manipulators are designed for accurate placement, and should be able to perform interface alignment more efficiently and without the contamination problems of jet thrusting. The disadvantage is that although the vehicle to vehicle interface may be simplified, the arm itself is an extremely complex element.

THE ORBITER-SPACE STATION INTERFACE

The interface between the Orbiter and the Space Station will be a critical one. The Station is planned to operate for 30 years or more and will depend on the Orbiter for consumables resupply and crew and payloads exchange. The type of interface selected will depend on a number of issues; the ability of the Canadian supplied Station manipulators to handle the mass of the Orbiter and to provide adequate reliability, and the tolerance of Station operations to docking related loads and contamination. Most importantly, the choice must resolve the risks associated with orbital operations and the mating of two vehicles each weighing in excess of 250,000 pounds. Berthing seems to represent the least risk approach, but Orbiter manipulator limitations make berthing totally reliant on the Station manipulators, which could make Station access impossible in the event of a catastrophic failure. Finally, the commercial nature of the Station will require an interface system with minimal overall cost, from development to operations and maintenance.

An example of a typical Orbiter-based interface system is shown in Figure (4). The mechanism is compatible with both docking and berthing approaches. The configuration is similar to the Soyuz interface system, although more sophisticated electromechanical struts are required to complete docking alignment and capture due to the offset of the Orbiter center of mass. The struts extend the capture ring and petals out of the payload bay, where interface contact and petal interlock force the interfaces into alignment. Interface contact may be initiated by direct fly-in or by manipulator placement. When the capture latches are engaged, the struts attenuate the relative motion, especially the induced rotation, and retract the capture ring onto the Orbiter transfer tunnel, where structural latches complete the interface.

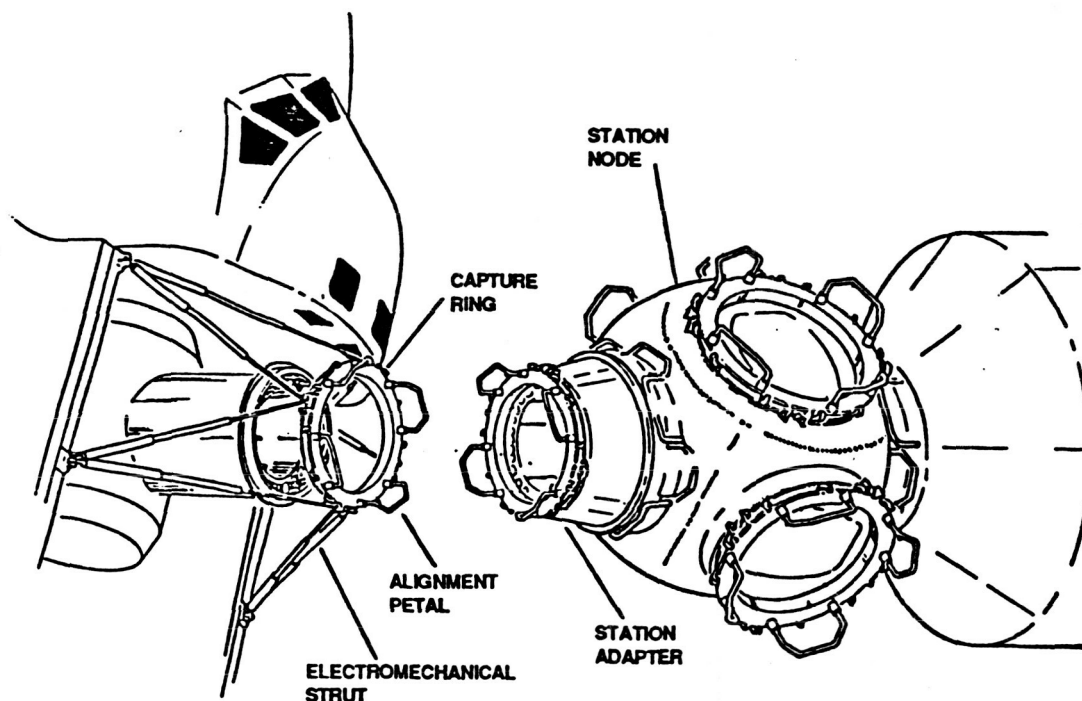


Figure 4. Typical Orbiter-Space Station Interface Concept Uses Modified Apollo-Soyuz Approach

This type of system has a number of unique features: the long struts eliminate the need for a separate tunnel extension mechanism and provide a large capture envelope. The Station mounted adapter reduces the likelihood of collision damage to the pressurized portion of the Station and allows the Orbiter transfer tunnel to be smaller in diameter than the Station port. However, like most of the systems proposed over the last ten years, the bulk of the interface system is based in the Orbiter payload bay. Although this locates most of the control with the Orbiter, which reduces reliance on Station performance, it requires a substantial portion of the available payload bay volume and launch weight. The system shown will take up roughly one-tenth of the weight that is available for cargo. This penalty has prompted a reevaluation of interface concepts where the bulk of the system can remain on-orbit.

STATION-BASED INTERFACE SYSTEMS

A Station-based interface system requires one of two approaches. The interface system may be similar to the Orbiter-based system, but stored and installed on-orbit, or an entirely new configuration may be developed where the bulk of the system remains permanently with the Space Station. The first approach, shown in Figure (5), is operationally complex. System transfer and installation requires either dual manipulator operations, as shown, or some application of EVA or remote vehicle operations. Because the second approach is potentially less complex, it was selected for investigation in this study.

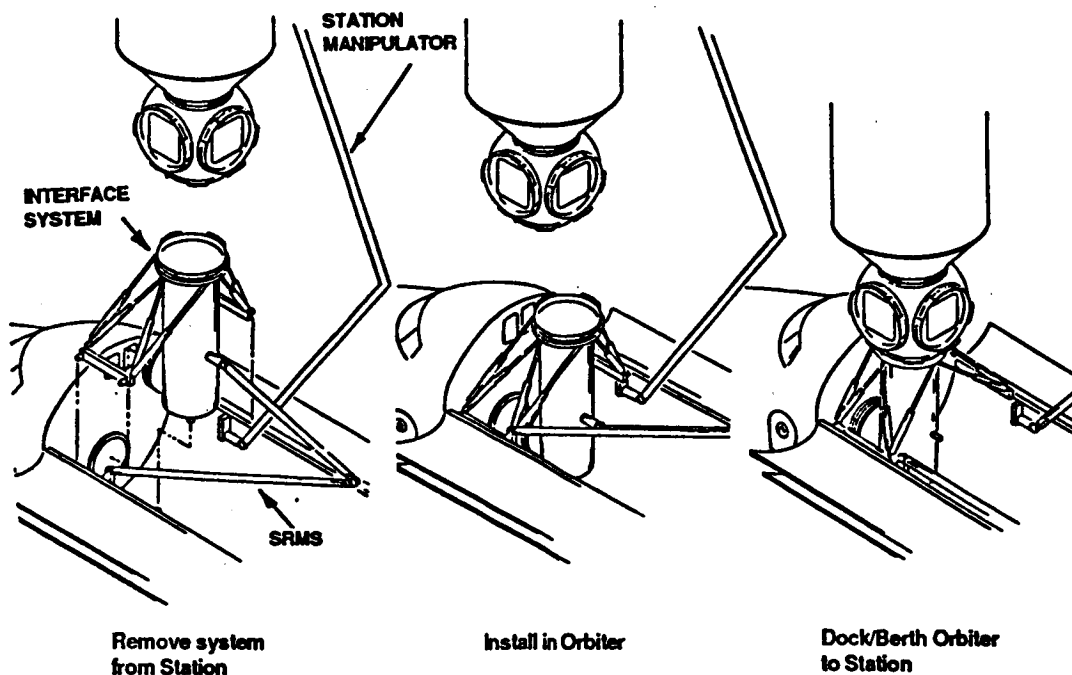


Figure 5. Orbital Transfer Requires Complex Installation Operations

The concept used as a starting point is shown in Figure (6). The basic system consists of a rigid transfer tunnel mounted on the target port and an alignment/capture/tunnel insertion assembly. The assembly consists of telescoping struts with alignment/capture mechanisms mounted on the ends. Ideally, the only hardware carried on the Orbiter is that required to attach to the capture mechanisms and to seal the transfer tunnel to the airlock hatch area. The telescoping struts have sufficient stroke to complete capture and attenuation before the bottom of the transfer tunnel approaches Orbiter structure. After attenuation, the telescoping retraction allows a controlled insertion of the tunnel into the payload bay. By using a primarily telescoping action and limiting the other degrees of freedom, the risk of joint runaway and collision, common to manipulator operations, is reduced.

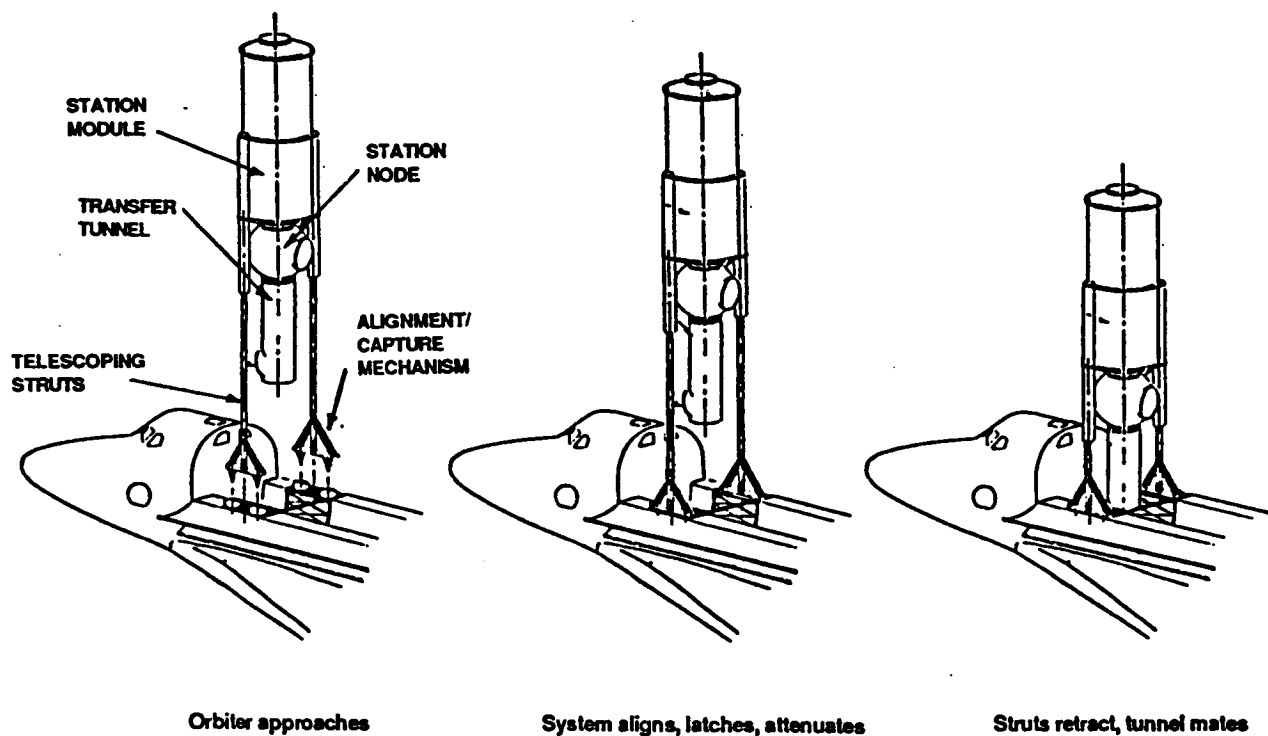


Figure 6. Telescoping Struts Provide Orbiter Capture and Station Tunnel Insertion

Concept 1. The first version of the Station-based system is shown in Figure (7). To minimize development costs, existing payload retention latches are used for the capture mechanism on the Orbiter, with two trunnion fittings on one strut and one on the other. The combination of two on one strut provides the ability to withstand pitching moments. The struts are mounted to the station through structure on existing ports. As the node is sized to fit in the payload bay, this configuration places the axes of the struts and the attached trunnions close to the Orbiter longerons and retention latches, minimizing the structure required to bring them into alignment. In addition, this configuration permits the entire strut assembly to be mounted to the node on the ground, avoiding on-orbit assembly.

ORIGINAL PAGE IS
OF POOR QUALITY

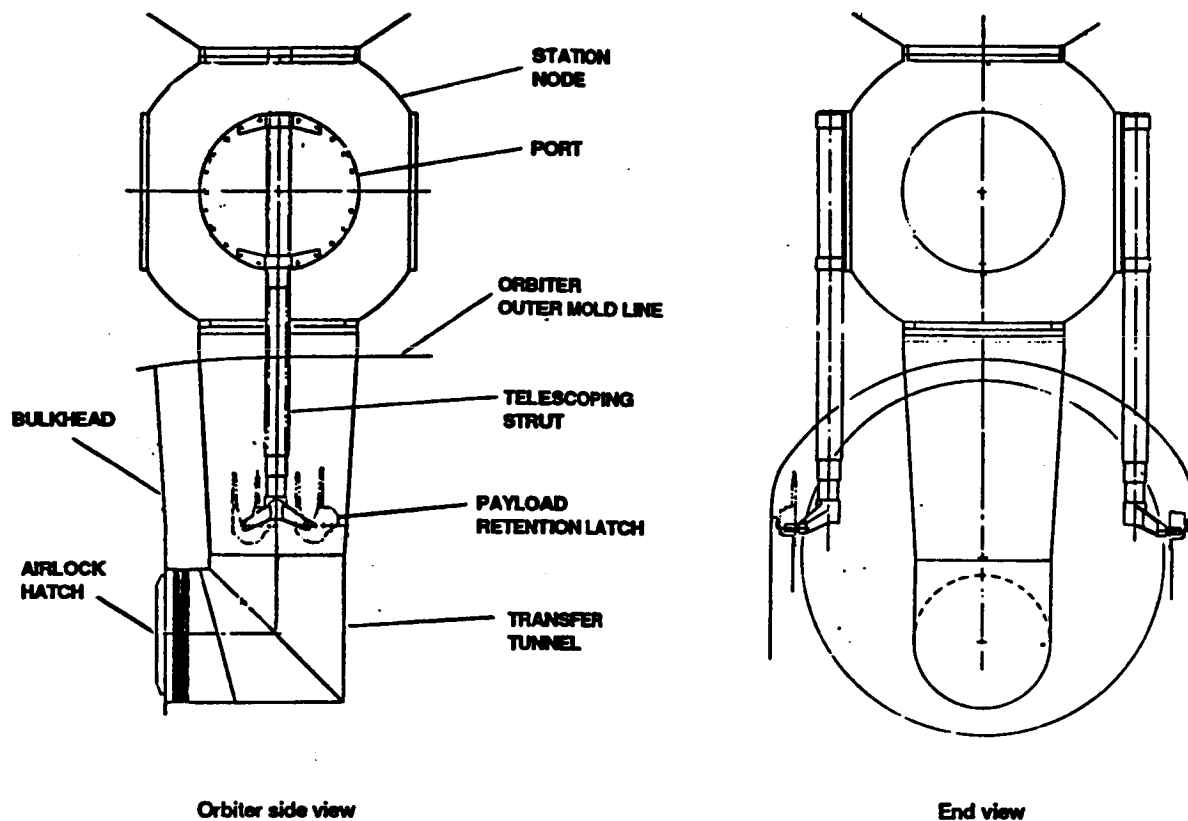


Figure 7. Existing Payload Retention Latches Provide Alignment and Capture Capability

The transfer tunnel assembly, Figure (8), is composed of two segments. The Orbiter portion incorporates a load isolating bellows element to prevent miscellaneous loads from being transferred into the Orbiter bulkhead. The bellows assembly also moves the interface away from the bulkhead, improving clearance between the Station tunnel and the bulkhead during insertion. The canted interface simplifies alignment and mating of the Orbiter and Station tunnel sections with the vertical insertion technique used.

Although the system is well packaged and uses proven hardware at the latching interface, the latches themselves limit system performance. Because latch actuation time is a minimum of 30 seconds, the system is suitable only for berthing operations, where the latch and trunnion can be held in proximity until the latches have engaged the trunnions sufficiently. To provide docking capability, latch actuation must be very rapid to insure capture before significant rebound occurs. For the Orbiter/Space Station interface this problem is especially acute because the contact point is roughly 40 feet from the Orbiter center of mass. Thus, although the large inertias of the Orbiter and the Station will tend to force the interface together, the resulting contact force will induce a substantial pitch moment and rotation on the Orbiter, complicating alignment and capture.

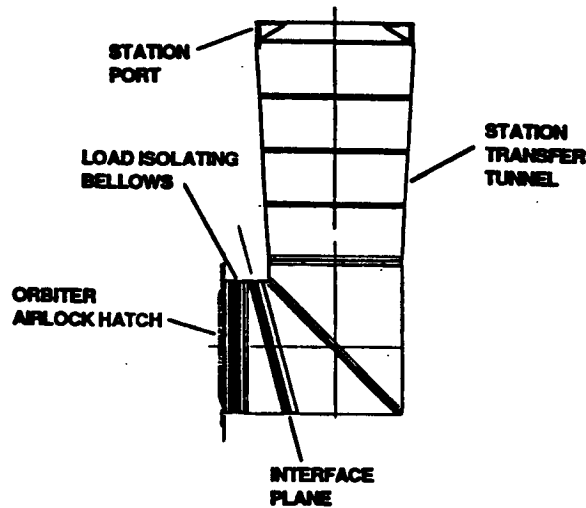


Figure 8. Tunnel Interface Simplifies Alignment, Isolates Loads

One way to insure capture is to replace the payload retention latch system with a probe and drogue interface like that used for Apollo, as shown in Figure (9). This modification provides rapid latch actuation, although the latch system will be somewhat complicated by the need to withstand the pitching moment while still providing misalignment tolerance. Some of the alignment may be accomplished by flexing of the telescoping struts themselves; sufficient attenuation stroke could soften the impact and reduce the induced pitching moment to make such a technique practical.

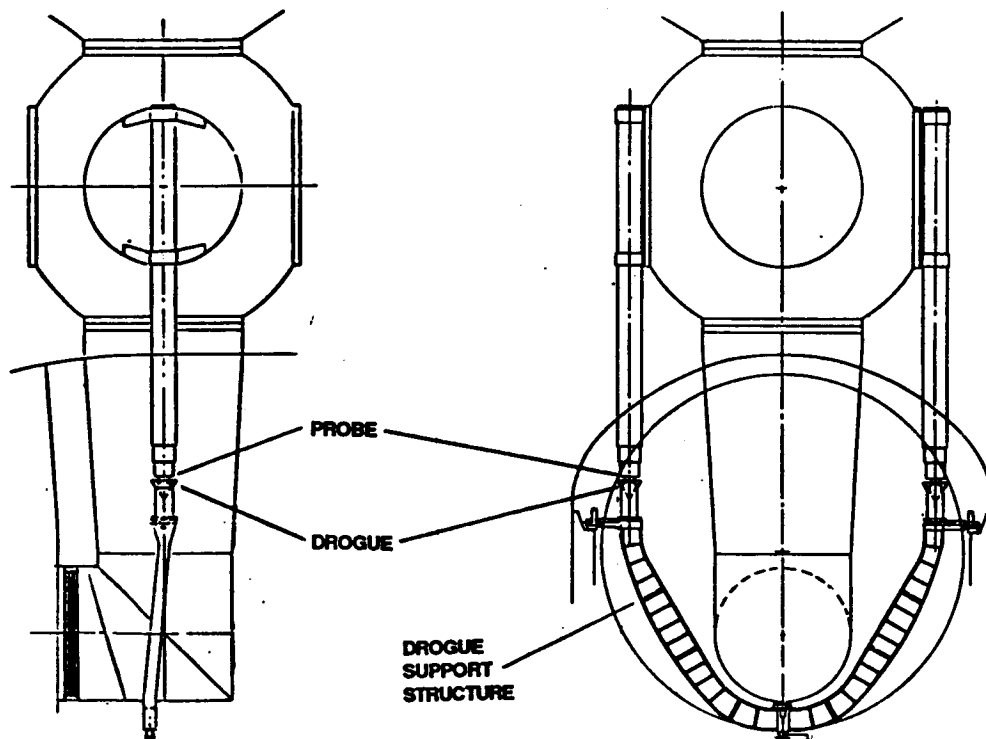


Figure 9. Probe-Drogue Capture Provides Docking Capability

The structural attachment between the latches and the Orbiter must also carry the induced pitch moment. This could be accomplished by mounting the support structure to two payload retention latches on one side, as in the first concept. However, because the two drogues must be fixed in all degrees of freedom to provide a stable target, a beam like the one shown can be incorporated to provide both latch support and moment transfer.

Replacing the payload retention latches with probe and drogue latches produces a configuration with both berthing and docking capability. Unfortunately, it does so at the expense of considerable additional hardware that must be carried in the Orbiter. Fortunately, further investigation of the Orbiter payload retention system revealed the possibility of bolting the latch support structure directly into the Orbiter longerons, as shown in Figure (10). This approach eliminates the retention latches, the supporting bridge and keel fittings, and the connecting beam. Additionally, it can be accomplished without Orbiter modifications as bolt locations are already available where the longeron bridges would otherwise be mounted.

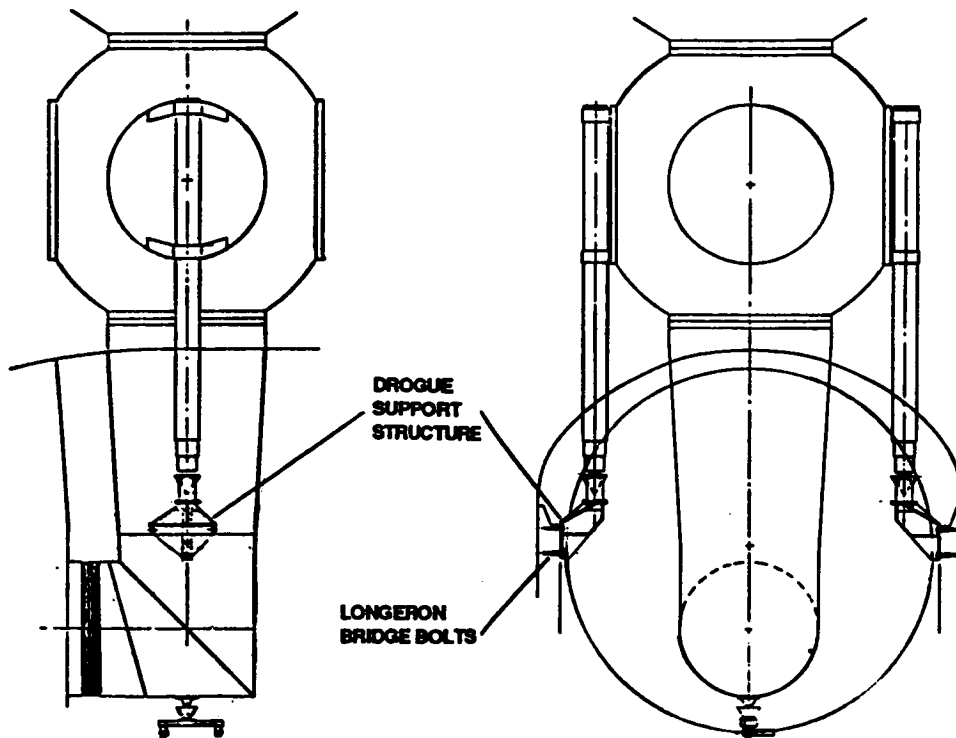


Figure 10. Direct Longeron Mounting Reduces Latch Support Requirements

Concept 2. The three versions of Concept 1 each represent a more or less viable means of attaching the Orbiter through struts that are symmetrical with respect to the target node and the Orbiter. Although the symmetry demonstrates certain advantages, it also has inherent drawbacks. The first is that mounting the struts on the node ports obstructs the ports themselves and prevents them from being attached to other pressurized elements. The second is that the basic strut configuration is not well suited to the expected load distribution, especially the pitch moment. For the symmetrical configuration, the entire moment must ultimately be taken out by strut bending.

An option that addresses these two concerns is shown in Figure (11). By locating the two struts fore and aft, the moment is taken out by strut tension and compression rather than bending. Also, moving the strut mounting from the port faces to the areas between the ports releases the port for attachment to other pressurized elements. With these improvements, however, come certain penalties. It is now impossible to preassemble the struts to the node because of packaging constraints, and the relocation of the struts moves them further from the Orbiter longerons so that additional structure is required to position the drogues. Finally, the superior pitch capability is traded for an induced roll, so that again some load will be taken in strut bending, and additional structure may be required to adequately transfer the roll moment from the latches to the Orbiter.

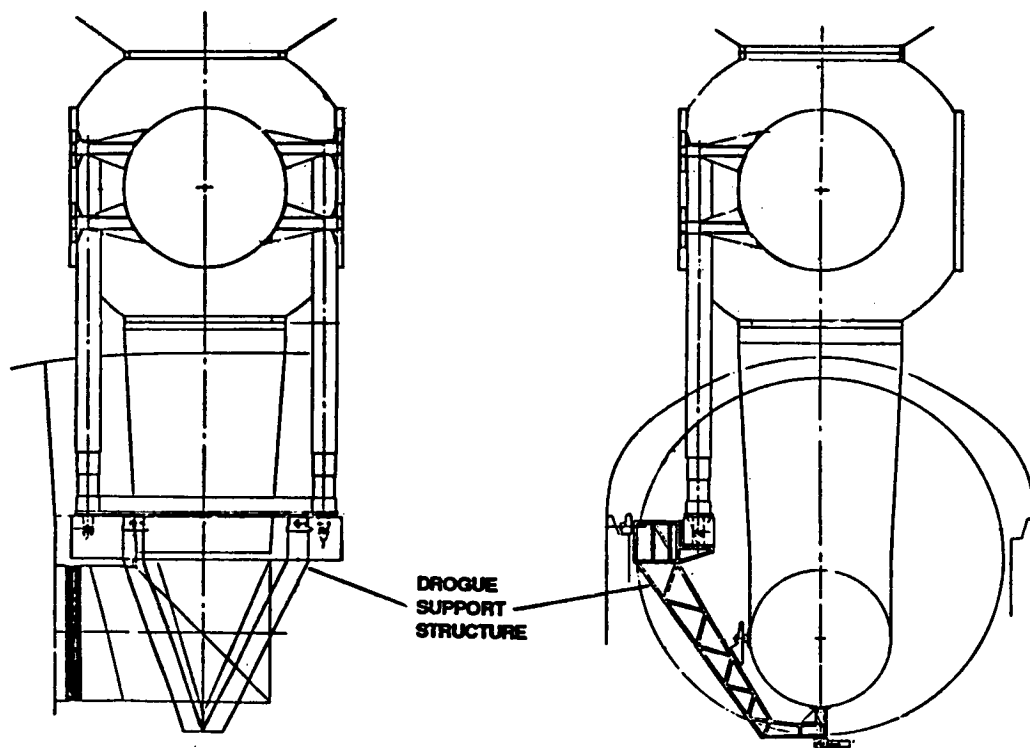


Figure 11. Fore/Aft Strut Placement Improves Pitch Load Capability

Concept 3. Both Concepts 1 and 2 suffer from some unsymmetrical loading which will require the telescoping mechanisms to resist the induced moment by bending. This limits their ability to utilize strut flex as an alignment technique and may drive the sizing of the struts. An alternative is shown in Figure (12). Four point contact provides symmetrical loading for both pitch and roll, and could allow alignment flex to drive strut sizing rather than moment capability. This configuration also differs from the previous two in that the drogues are now deployable. By raising them out of the payload bay the contact points are no longer close to Orbiter structure, where a missed capture could result in collision and damage. Although missed capture is a potential problem for the two strut configurations as well, the problem is more severe for the four strut approach because of the larger distance between probes and the increased difficulty of monitoring four points simultaneously.

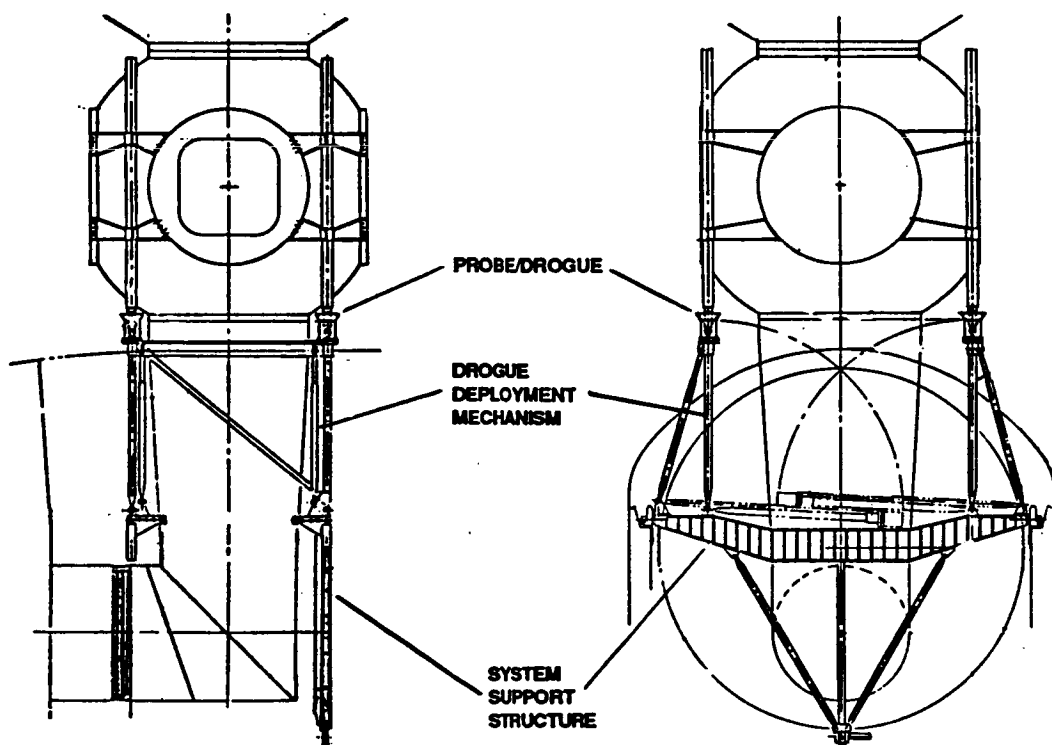


Figure 12. Raised Four-Point Contact Provides Symmetrical Loading, Reduced Collision Risk

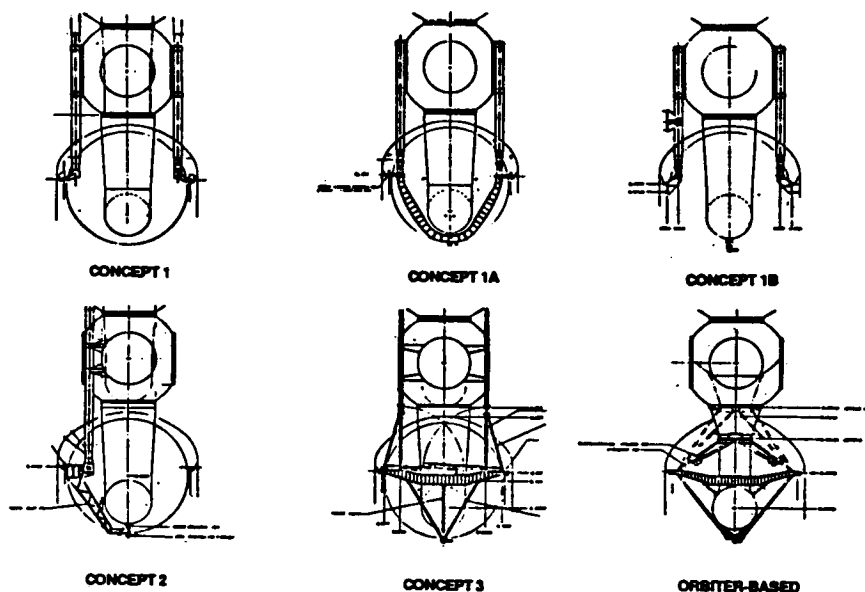
As with the other concepts, variations of this configuration may be possible which would reduce some of the structure required on the Orbiter, but the need for four, or at least three, contact points will require some additional hardware compared to a two strut approach. Another potential disadvantage with this particular configuration is that the support structure required occupies significantly more payload bay volume than the two strut options.

CONCEPT COMPARISON

The purpose of this study was to develop variations of the basic Station-based system, and to use the concepts developed to evaluate the potential of this type of system. To evaluate these concepts against the Orbiter-based system a number of discriminators were selected.

The key argument for a Station-based system is the weight distribution, so the most important factor is the amount of weight that must be carried by the Orbiter on each flight. In addition, the overall cost of the system depends on total weight, on system reliability, which defines maintenance requirements, and on maintainability, which affects the cost of the maintenance actions. The amount of risk inherent in the design is also crucial, as well as the efficiency with which the configuration handles mating loads. Finally, viewing was included as it affects the risk of collision and the ease with which the crew can monitor system operations. Although the list is by no means comprehensive, it represents a sampling of factors that can be used to perform a preliminary evaluation.

A summary of the approximate system weights and scorings for the other factors is shown in Figure (13). The scorings were on a subjective scale of 1 to 10 with 10 being the best. The top score in each category is boxed. Where the Orbiter-based system has the highest rating, both the Orbiter-based and highest Station-based score are boxed for comparison.



CONCEPT	TOTAL WEIGHT	STATION WEIGHT	ORBITER WEIGHT	LOADS	SAFETY	RELIAB.	VIEWING	MAINT.
1	3319	2275	1044	3	4	5	3	4
1A	3398	2277	1121	4	4	6	4	4
1B	2896	2277	619	4	4	6	4	5
2	3156	2293	863	5	4	6	5	4
3	3219	1348	1771	7	6	4	3	3
ORBITER-BASED	3430	667	2763	6	7	5	5	7

Figure 13. Station-Based Options Competitive with Orbiter-Based

In the area of Orbiter weight, Concept 1B is a dramatic improvement over the Orbiter-based system and most of the other Station-based concepts. Concept 3 offers the most efficient configuration for loads due to the large distance between latching points and the symmetry for both pitch and roll loads. Safety was evaluated based on the potential for collision after a missed capture; although the four point system provides capture at the same level above the Orbiter as the Orbiter-based system, the separate struts could allow capture of one or more points while missing with others, which makes the integral ring contact on the Orbiter-based system a slightly safer option. The reliability evaluation is based on the number and complexity of mechanisms required. Because Concepts 1A, 1B, and 2 all use two probe and drogue latches as opposed to four for Concept 3 and motor driven elements for Concept 1 and the Orbiter-based system, they should have somewhat better reliability. For viewing, Concept 2 is superior because both contact points are easily visible from the aft crew compartment windows within a small field of view. The other systems require scanning and, for Concept 3 and the Orbiter-based system, contact is made above the viewing plane. Finally, although the minimum amount of hardware required for Concept 1B makes it the most maintainable of the Station-based options, the ground maintainability of the Orbiter-based system is a clear advantage.

CONCLUSIONS

For the concepts identified and the discriminators selected, although no one concept is universally superior, the Station-based approach appears competitive with the Orbiter-based system. Although potentially substantial weight savings have been demonstrated, realization of this potential will depend on a number of issues. The real value of the recovered cargo capability is one: if the full capacity of the payload bay is not needed on every flight, then some of the potential savings are imaginary. A final assessment of the approach also will require an accurate evaluation of the increased costs of maintaining a Station-based system. Additional concerns are the significance of the loss of Orbiter operational autonomy and the need for detailed evaluation of the mechanisms required for alignment and capture. Nonetheless, in this preliminary evaluation, it appears that this type of Station-based system may provide a viable alternative to the more traditional Orbiter-based approach.

ACKNOWLEDGEMENTS

The author would like to acknowledge the contributions of those who participated in this project. Many helpful discussions and suggestions resulted in the development of the basic approach and options. In particular, the project could not have been completed without the assistance of Pete Buck, Bill Creasy, John Lewis, Gerry Malloy, and Warren Woolf.

AN ELECTROMECHANICAL ATTENUATOR/ACTUATOR FOR SPACE STATION DOCKING

LeBarian Stokes,* Dean Glenn,* Monty B. Carroll**

ABSTRACT

The development of a docking system for the Space Station and beyond has identified the need for reusable and variably controlled attenuators/actuators for energy absorption and compliance. One approach to providing both the attenuator and the actuator functions is by way of an electro-mechanical attenuator/actuator (EMAA) as opposed to a hydraulic system. The use of the electromechanical devices is considered to be more suitable for a space environment because of the absence of contamination from hydraulic fluid leaks and because of the cost-effectiveness of maintenance. A smart EMMA that uses range/rate/attitude sensor information to preadjust a docking interface to eliminate misalignments and to minimize contact and stroking forces is described. A prototype EMMA has been fabricated and is being tested and evaluated at the NASA Lyndon B. Johnson Space Center Robotics and Mechanical Systems Laboratory. Results of preliminary testing and analysis already performed have established confidence that this concept is feasible and will provide the desired reliability and low maintenance for repetitive long-term operation typical of Space Station requirements.

INTRODUCTION

A technology development task titled "Construction Equipment/Soft Docking Technology" was sponsored by the NASA Office of Aeronautics and Space Technology to study Space-Shuttle-Orbiter-based construction equipment required to support space construction, assembly, and satellite servicing. Later, this task was expanded with emphasis on docking and berthing. Requirements were proposed for minimum-disturbance (low force) docking with large flexible structures and with satellites having sensitive operating systems. This study was concentrated on the docking/berthing function, with emphasis on isolating the requirements for, and exploring the technology of, soft docking/berthing.

The methodology of this study comprised a simultaneous evaluation of mission requirements, hardware design concepts, and systems performance. The central study element was a combined conceptual-design/dynamic-performance analysis that produced the identification of docking/berthing component technology needs.

* NASA Lyndon B. Johnson Space Center, Structures and Mechanics Division, Houston, Texas.

**Lockheed Engineering and Management Company, Houston, Texas.

System design specialists reviewed the design evolution of past docking hardware to maximize the benefit of that experience. In reviewing component technology efforts, two key areas were identified for immediate component development activity needs. Achieving soft docking for a range of spacecraft masses and contact velocities requires the use of smart attenuator/actuators which can provide variable force/stroke characteristics and highly accurate proximity sensors to provide the necessary intelligence. These design specialists identified sensors and smart attenuator/actuators as the key components of the docking system that warrant proof-of-concept development testing.

A prototype smart electromechanical attenuator/actuator (EMAA) was fabricated for proof-of-concept development testing to support the Construction Equipment/Soft Docking Technology study. The development of a laboratory prototype microprocessor-controlled smart EMAA from which the development technology can be applied to Space Shuttle Orbiter and Space Station docking/berthing systems is described.

SOFT DOCKING SYSTEM OVERVIEW

A smart EMAA is one of four subsystems of a soft docking system concept consisting of (1) a laser docking sensor (LDS) subsystem, (2) an androgynous, four-fingered, ring-and-guide docking interface subsystem, (3) the EMAA subsystem, and (4) a docking microcomputer system (DMS) (Figure 1). The LDS provides position, velocity, attitude, and attitude-rate data of the approaching vehicle. The androgynous, four-fingered, ring-and-guide docking interface provides the rigid structural coupling of the two docking vehicles and permits 90° interval indexing of the two mating ports, while providing two axes of inverse symmetry that coincide with the two major axes of the vehicles. The DMS queries the LDS subsystem for data necessary to process the kinematic equations that are required to position the EMAA's. The EMAA's preadjust the docking interface. As a result, intolerable misalignments are eliminated, and contact forces are minimized. The DMS performs real-time processing to provide the EMAA's with data including energy absorption, fault detection, and error management during the attenuation process. The DMS also provides interface to embedded Space Station management subsystems and crew systems. The EMAA performs the soft docking energy absorption (attenuation) and actuation for the system. The EMAA receives high-level control instruction and attenuator/actuator performance characteristics from the DMS and transmits status information back to the DMS.

EMAA DESIGN REQUIREMENTS

The requirements for the smart EMAA were baselined upon the likely event of soft docking an Orbiter weighing 108 775 kg (240 kips) to the Space Station weighing 181 292 kg (400 kips) using a conceptual-design soft docking interface system from the Construction Equipment/Soft Docking Technology study. This interface system accommodates four pairs of smart EMAA's to control the docking interface relative to the base ring. The

following are the general smart EMAA requirements for soft docking:

1. Absorb the relative kinetic energy necessary for the docking interface between the two vehicles with typical approach velocity of 0.003 m/s (0.01 ft/s) to 0.031 m/s (0.10 ft/s)
2. Draw the docking interface with mating vehicle together for structured connection
3. Assure durability for repeated docking and undocking
4. Provide both attenuation and actuation functions
5. Change attenuation performance characteristics in real time

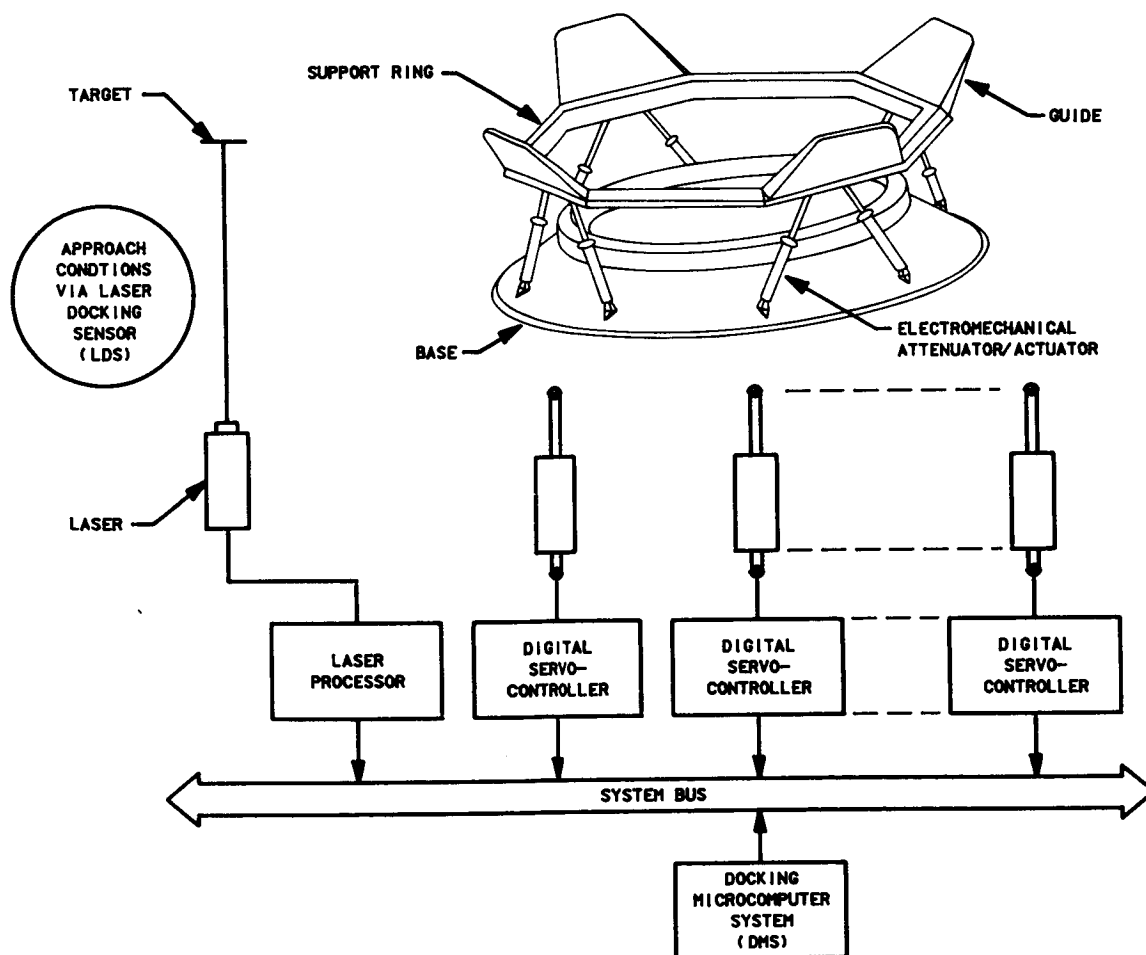


Figure 1 Soft Docking Interface System

6. Require little or no maintenance for long-term operations
7. Provide precise position control for prealignment of docking interface
8. Allow 0.457 M (18 in.) of attenuation/actuation stroke
9. Provide constant force attenuation

EMAA COMPONENT DESCRIPTION

The eight components of an EMAA are (1) a digital servocontroller, (2) a digital-to-analog converter (DAC), (3) an amplifier, (4) a direct-current (dc) motor, (5) an optical encoder, (6) a gear pair, (7) a roller screw, and (8) a mechanical housing (Figure 2).

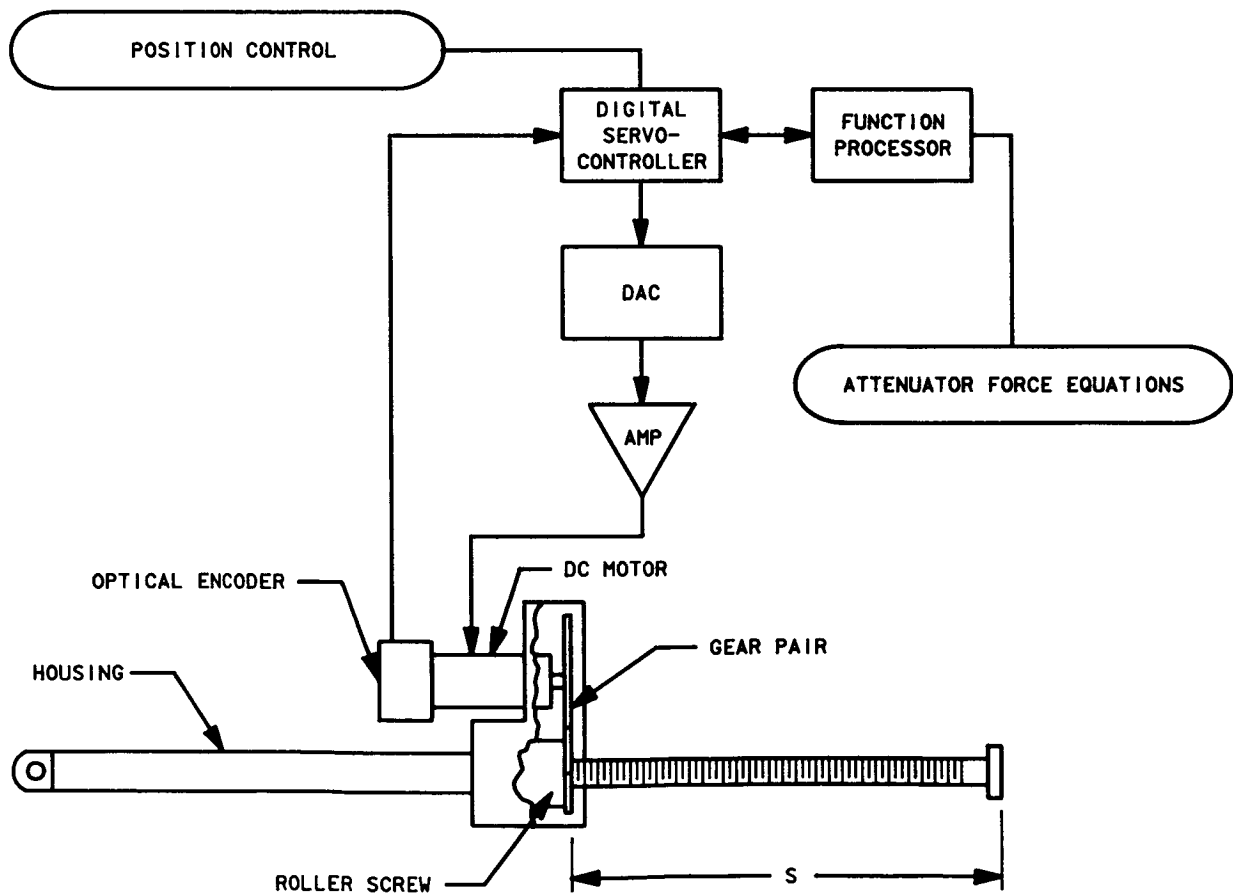


Figure 2 EMAA Components

The digital servocontroller is a 16-bit microcontroller based on a register-to-register architecture which allows digital filter control algorithms to execute faster than in accumulator-based architecture in which data transfer is bottlenecked. The controller receives data from both the DMS and the optical encoder, calculates a digital voltage command, and reports the current status and error conditions back to the DMS. This digital voltage command is converted to an analog voltage by the DAC, a 12-bit bipolar voltage-output device. The voltage is then applied to the amplifier and held constant until the controller completes another sampling period.

The pulse-width-modulated (PWM) amplifier receives the analog voltage from the DAC and provides the electrical power to drive the motor. Based on the average polarity of the amplified voltage, the dc motor will respond by rotating clockwise or counterclockwise. A permanent-magnet-field dc servomotor, with a peak rated torque of 0.490 N-m (70 oz-in.), converts the electrical power into rotary motion, which drives the optical encoder and the gear pair.

Shaft position feedback is determined by a 500-count-per-revolution optical incremental encoder. Two channels in quadrature are transmitted by the optical encoder to the controller, which resolves rotational direction by determining that channel "A" leads "B," or vice versa. By counting encoder increments or decrements and knowing the lead of the roller screw, the shaft's linear position can be determined.

Through the 1:1 gear pair, the mechanical motion from the dc motor is applied to the roller screw. One of the gears is attached to the motor shaft, and the other is attached to the nut of the roller screw.

The high-efficiency (0.845) roller screw with a lead of 0.005 m (0.2 in.) consists of a threaded shaft and an internally threaded nut with threaded rollers. The nut assembly rotates at a fixed location in the mechanical housing so that only the shaft is allowed to translate. Rotation of the shaft is restrained by a keyed bushing located at the end of the shaft sliding in the mechanical housing.

An aluminum structure mechanically supports the dc motor/encoder assembly and the roller screw. The housing is built to be easily mounted to a test fixture so that performance evaluations can be made.

EMAA FUNCTION

The smart EMAA is unique in its capability to provide programmable attenuator forcing functions. The digital servocontroller permits real-time, external-sensor data inputs to its attenuator force equations and allows for real-time performance parameter changes. Most attenuator forcing functions can be implemented using only position control and an algorithm to calculate a position profile of that function as it relates to

energy absorption. This discussion will be limited to constant force attenuation using position control.

In position control, a digital servocontroller will often command a motor to move and lock onto a final position. This action is accomplished by the controller determining a desired position and then calculating the position error, the difference between the desired position and the actual position. The position error is then digitally filtered, and the filtered output is applied to a motor through a DAC and an amplifier.

Constant velocity of a motor using position control is obtained by changing the desired position by constant discrete amounts every sampling period. Since the desired position is changing, a controller can take position feedback and compare it to the new desired position to obtain position error. A smooth constant velocity is sustained by minimizing this error through a digital filter. The controller follows the constant discrete changes allowing the filter to maintain stable motion.

Position control can also be used to accelerate or to decelerate a motor. The method is similar to the previous constant velocity control, except that the discrete changes in desired position are not constant. Again, the digital filter minimizes position error and maintains a stable acceleration or deceleration position profile.

Constant force attenuation is obtained from the EMAA using only position control. The force F can be expressed using Newton's second law of motion

$$F = ma$$

where m is the combined mass of the capture mechanism and the approaching body, and the acceleration a is defined by the deceleration position profile. The total work required to absorb the kinetic energy of the combined mass with a velocity v is expressed as

$$1/2 mv^2 = Fs$$

where s is the differential displacement (EMAA stroke) of the combined mass. Figure 3 best illustrates this method. Figure 3a is a velocity versus time ($v(t)$) profile of the roller screw shaft, and Figure 3b is the shaft's parabolic position profile ($s(t)$), the double integral of the constant acceleration. In phase A, the roller screw is accelerating to match the velocity of the approaching mass. Phase B shows the constant deceleration of the roller screw during the capture and the constant force attenuation of the mass. This parabolic position profile is generated by the digital servocontroller and applied to the dc motor, which drives the roller screw to provide constant force attenuation.

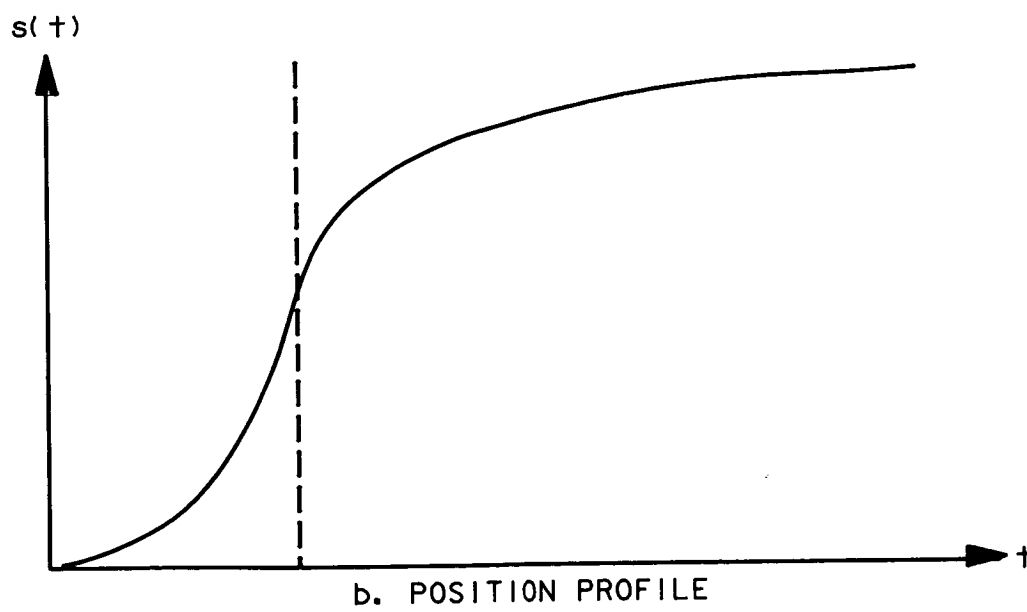
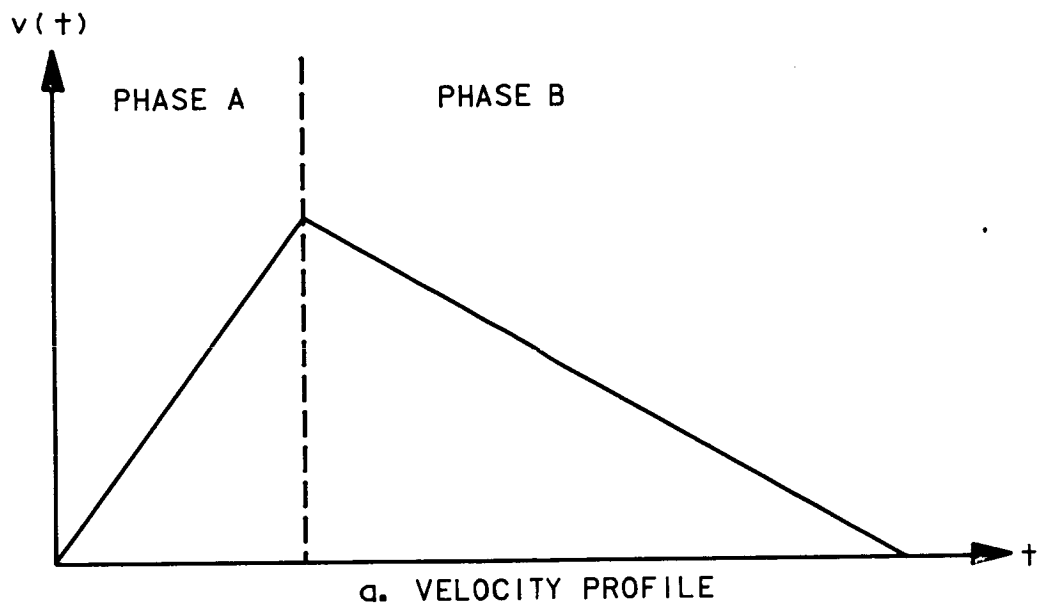


Figure 3 Capture and Attenuation Profile

EMAA TESTBED EVALUATION

A smart EMAA testbed was developed to test a single-axis EMAA system. The testbed is shown in Figure 4. It consists of (1) a test stand, (2) the load cells, (3) a mass simulator, (4) the EMAA, (5) a sonar ranging system (similar to the LDS), (6) a docking computer (a scaled-down DMS), and (7) a data acquisition system.

The mass simulator is an independently computer-controlled electro-mechanical mechanism similar to the EMAA. It drives the mating surface to simulate a free-moving mass in space. The mass-simulator computer receives force information from the load cell and uses the selected mass value to calculate a deceleration position profile to drive the mating surface.

Testing and verifying the soft docking concept required the fabrication of the single-axis EMAA system. The docking computer coordinates the data between the sonar and the EMAA; then, using the sonar range-rate data, the computer sends control parameters to the EMAA to capture and attenuate the mass. The sonar is an inexpensive system which is used only in this test setup for proof-of-concept purposes. In proximity, it provides range rate information similar to that of a laser sensor.

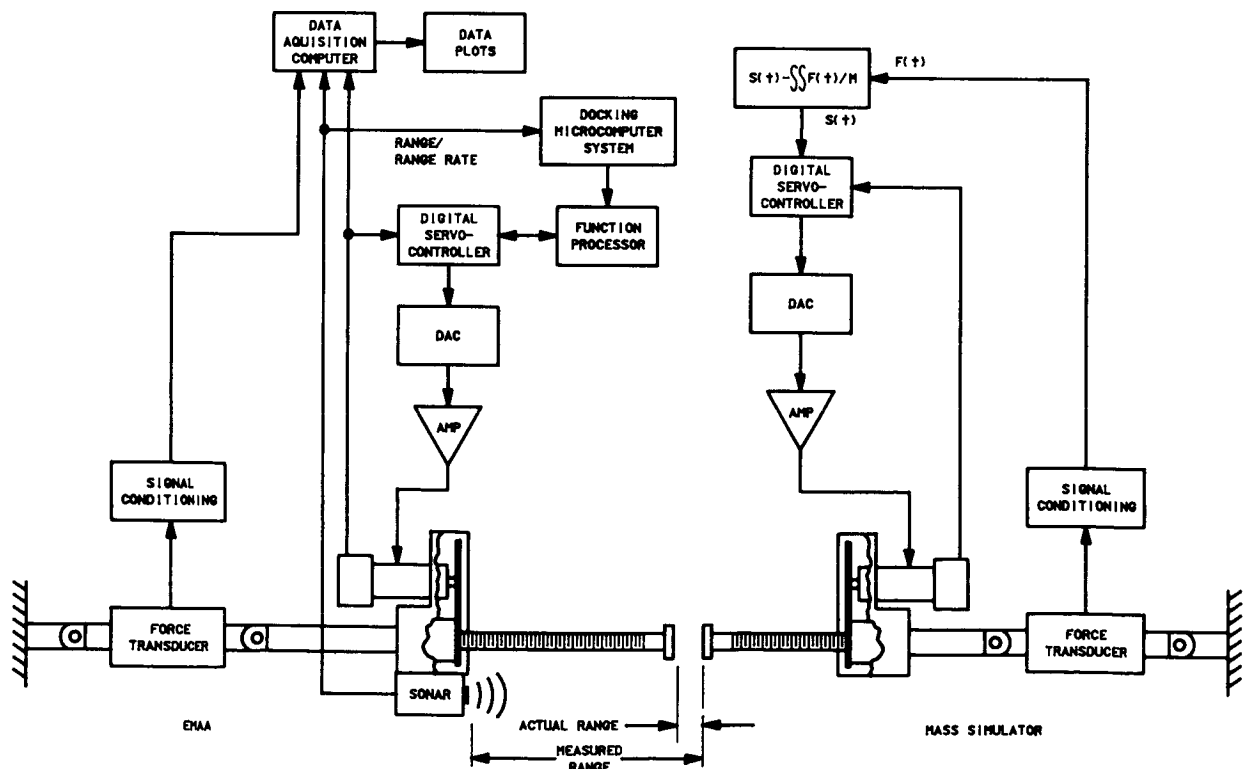


Figure 4 EMAA Testbed

The digital servocontroller, employing a position control system, was breadboarded and tested with laboratory equipment to verify the DAC update time, which corresponds to the sampling period of the position control algorithm.

In order to establish torque versus speed curves, the dc servomotor was first dynamometer tested at voltages ranging from 5 to 40 volts dc. Peak torque established the maximum constant force output of the attenuator. In its current configuration, this output was found to be 515 N (115 lbf).

The roller screw selected provides a 0.457-m (18 in.) stroke and the capability to withstand a 5440-N (1223 lbf) axial load (safety factor 3). Load-handling capability was obtained from the manufacturer's published specifications, and after numerous EMAA tests, no degradation has been observed. Also, from analysis of the load data based on a six-degree-of-freedom, three-body simulation program (SOFTDOCKSIM), it was concluded that these actual force loads to the roller screw shaft in a docking ring configuration would not be exceeded.

The data acquisition system obtained force-versus-time, position, velocity, and motor-current data from the soft docking attenuation process. These data verified the performance requirements of the smart EMAA.

CONCLUDING REMARKS

A proof-of-concept smart EMAA system has been described. The technology derived was based on current off-the-shelf components and can be applied to present and future space docking systems. Special new designs have been considered that incorporate a brushless dc motor around the roller screw and include a permanent-magnet rotor attached directly to the roller screw nut. This concept will eliminate the use of gears by producing a more compact size with reduced friction and inertia of moving parts. The attenuation technique, which uses a position controller to provide a motion profile, gives a high degree of flexibility to any attenuator/actuator system. This technology applies not only to a docking system, but also to berthing and to positioning and holding aids by controlling the motion of large, massive objects.

Some inherent, unresolved difficulties remain which include both the complexity of coordinated control of an overconstrained multiaxis system and the instability and mechanical binding of a coupled system. The control system development for the soft docking system will be the prime instrument in overcoming the difficulties of stability and control.

This unique concept has great potential for current and future docking/berthing systems. The use of microcomputers enables the real-time updating of attenuator/actuator parameters and allows for programmable attenuator forcing functions. This capability greatly enhances the

performance of the docking/berthing system because of the high degree of flexibility and programmability of the microcomputer.

ACKNOWLEDGMENTS

The authors wish to express their appreciation to the NASA Office of Aeronautics and Space Technology and to members of the Robotics and Mechanical Systems Laboratory at the NASA Lyndon B. Johnson Space Center.

REFERENCES

1. Construction Equipment/Soft Docking Technology. NASA Lyndon B. Johnson Space Center 506-64-27, November 1982.
2. LASER Docking Sensor (LDS) System. NASA Lyndon B. Johnson Space Center, JSC-22031, January 1986.
3. Tal, J.: Motion Control by Microprocessors. Galil Motion Control, 1984.
4. Soft Dock Simulator (SOFTDOCKSIM). NASA Lyndon B. Johnson Space Center, LEMSCO-21763, JSC-20624, January 1986.

SPACE STATION LUBRICATION CONSIDERATIONS

Lubert J. Leger* and Keith Dufrane**

ABSTRACT

Future activities in space will require the use of large structures and high power availability in order to fully exploit opportunities in Earth and stellar observations, space manufacturing and the development of optimum space transportation vehicles. Although these large systems will have increased capabilities, the associated development costs will be high, and will dictate long life with minimum maintenance. The Space Station provides a concrete example of such a system; it is approximately one hundred meters in major dimensions and has a life requirement of thirty years. Numerous mechanical components will be associated with these systems, a portion of which will be exposed to the space environment. If the long life and low maintenance goals are to be satisfied, lubricants and lubrication concepts will have to be carefully selected. Current lubrication practices are reviewed with the intent of determining acceptability for the long life requirements. The effects of exposure of lubricants and lubricant binders to the space environment are generally discussed. Potential interaction of MoS₂ with atomic oxygen, a component of the low Earth orbit environment, appears to be significant and further study of the specific interactions is suggested.

INTRODUCTION

Examination of planned future space activities shows a significant increase in the need for large space structures. Within the American civil space program, the Space Station seems to be developing into a mature objective and future defense systems could also benefit from the use of large space structures. The cost of developing such systems will dictate long life, thirty years in the case of the Space Station. Designing for a specific life, rather than accepting system or component life limitations, will be implemented for the first time. These large systems will be launched in packaged form and deployed on orbit and therefore, will be lightweight and thin walled. Large, rotating joints of unique design will be required to orient the solar power systems.

The unique design, size, and life requirements for the Space Station mechanical systems, combined with a need to minimize in-space repair or refurbishment activities, dictates careful lubricant selection. Two lubricant selection considerations, which seem unique to large space systems, are the long life requirement, and effect of lubricant exposure to the space environment. This paper addresses both of these issues, but

*NASA Lyndon B. Johnson Space Center, Houston, Texas

**Battelle Columbus Laboratories, Columbus, Ohio

emphasizes the latter issue by applying information gathered on the effects of the space environment on materials over the last few years to lubricant systems. Some of the anticipated effects have not been considered before, but appear to be life limiting for lubricants in certain mechanism designs. This information is presented to make the designer aware of such effects and emphasize the need for further study of the potential interaction between lubricants and the space environment, rather than provide definitive solution guidelines. General issues which must be addressed in selection guidelines are outlined.

SPACE ENVIRONMENT EFFECTS

The Space Station's long life requirement demands that issues which may not have been important for relatively short-lived spacecraft operating in the low Earth orbital environment be reconsidered. Exposure of lubricated surfaces to the space environment may result in lubricant changes severely limiting component life and producing maintenance requirements which will be difficult, at best, to satisfy. A discussion of each aspect of the environment which may be important to lubricant life and performance, therefore, is appropriate.

Thermo-Vacuum

In a period of thirty years, Space Station components will be exposed to 175 000 thermal cycles. The depth of these thermal cycles will be controlled primarily by the optical properties of the surface in question unless active thermal control is provided. It may be difficult to provide the required lubricating and thermo-optical properties simultaneously for exposed lubricated surfaces. This difficulty, combined with a desire to conserve energy, certainly indicates that lubricants which perform over a large temperature range will be advantageous.

The vacuum environment, to which the lubricants will be exposed, is another important consideration. Although this subject area has been extensively addressed in both lubricant studies, as well as spacecraft design, the extended exposure may be life limiting for liquid film lubricants. For example, some of the best liquid film lubricants have vapor pressures as shown in Fig. 1, ref. 1, and by using the Langmuir expression (ref. 2), shown below, the evaporation rates of lubricant films can be estimated.

$$R_{\text{evap}} = \frac{P}{17.14} \left(\frac{M}{T} \right)^{1/2}$$

P = vapor pressure (mm of Hg)

M = molecular weight (assume 15 000)

T = temperature of lubricant (°K)

Assuming an average molecular weight of 15 000 for this material and using the vapor pressure data, the time necessary to evaporate a film of 2.5×10^{-4} cm is shown on the upper axis of Fig. 1. As can be seen from the figure, the loss rate is a strong function of temperature. This is the worst case loss rate and can be reduced by enclosing the lubricant within the lubricated joint. Significant loss of lubricants in confinement will be complicated by the large size, long life, and thermal exposure of moving surfaces.

Outgassing from liquid film lubricants can produce contamination on sensitive optical systems and must be considered as part of the lubricant selection process. The acceptability of the use of liquid film lubricants near such optical systems will depend upon the characteristics of the lubricant involved and mechanism design. Contamination requirements for the Space Station (contained in ref. 3) should be used as general guidelines for lubricant contamination assessment. These requirements address three items, vacuum volatility, molecular deposition, and particle production, which are pertinent to lubricant selection.

Another aspect of joining or moving materials relative to each other in space that was once considered important and must be reconsidered for Space

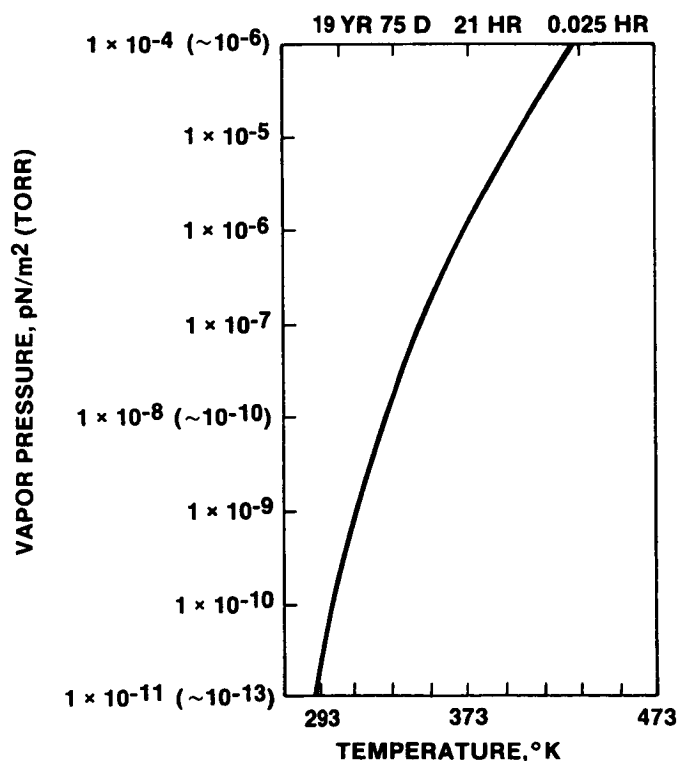


Figure 1. Vapor Pressure of High-Performance Liquid Lubricant

Station application is cold molecular welding. Impact of this consideration on past spacecraft has been limited in some cases because of short life and high localized pressure (contamination) associated with joint design. Both of these considerations will not be operative for the Space Station because of the long life requirement. Outgassing will be significantly reduced for two reasons, stringent contamination requirements, and long exposure to the thermo-vacuum environment. Cold molecular welding is even an important consideration for structural member, end fitting joints which must be capable of being disassembled at any point for repair of micrometeorite or debris damage. Certifying a coating for these joints, which would preclude cold molecular welding for thirty years, will surely be a challenge.

Ultraviolet Radiation

Some surfaces on the Space Station, such as the rotating joints (associated with the solar power systems) or tracks (for large remote manipulators), will be exposed to as much as twelve years of constant solar radiation during a thirty year life. Current data on ultraviolet exposures of materials is limited to one year exposure for a minimal number of materials. Lubricant changes on exposure to this environment have not been assessed, but will certainly be important for liquid film and organic based solid film lubricants.

Atomic Oxygen Effects

Atomic oxygen, the major constituent in the low Earth orbit (LEO) environment, has only recently been recognized (refs. 4 and 5) as being an important consideration in the design of surfaces of long-lived spacecraft. Several experiments have been conducted on Space Shuttle missions to quantify material degradation caused by atomic oxygen. Experiments on two of these missions, Space Transportation System (STS) 5 and STS-8, provide essentially all of the quantitative data available to date (see ref. 4). Of the two general classes of materials, metals and non-metals, the metals are the least reactive to atomic oxygen. More than 20 metal surfaces have been exposed during these Shuttle flight experiments and, of these, only three: carbon, silver, and osmium, interact quickly enough to produce macroscopic changes. Carbon interacts with atomic oxygen to form volatile oxides. Silver forms heavy oxide layers typical of oxidative attack, which results in loss of material by flaking and spallation. Osmium loses mass apparently through the formation and loss of OsO_4 , which has a relatively high vapor pressure. Generally, all of the other metals have significantly lower interaction rates than carbon, silver, or osmium.

All organic materials such as epoxies, polyurethanes, and polyimides, which are commonly used on spacecraft surfaces are reactive with the LEO environment. Reaction efficiency does not seem to be strongly dependent on chemical structure. However, additives do seem to be significant, since they are often oxides or other less reactive components which shadow the organic matrix from the incoming ambient oxygen atmosphere. Reaction efficiencies for a representative set of materials are shown in Table I.

These efficiencies (expressed as the volume of material lost per incident oxygen atom) are derived by normalizing material recession by exposure fluence.

TABLE I.- REACTION EFFICIENCIES OF SELECTED MATERIALS WITH
ATOMIC OXYGEN IN LOW EARTH ORBIT

<u>Material</u>	<u>Reaction Efficiency, cm³/Atom</u>
Kapton	3×10^{-24}
Mylar	3.4
Tedlar	3.2
Polyethylene	3.7
Polysulfone	2.4
Graphite/epoxy	
1034C	2.1
5208/T300	2.6
Epoxy	1.7
Silicones	<0.02*
White paint A276	0.3 to 0.4*
Black paint Z302	2.3*
Perfluorinated polymers	
Teflon, TFE	<0.05
Teflon, FEP	<0.05
Carbon (various forms)	0.9 to 1.7
Silver (various forms)	Heavily attacked

*Units of mg/cm² for STS-8 mission. Loss is assumed to occur in early part of exposure; therefore, no assessment of efficiency can be made.

To determine the effect on Space Station surfaces, only the total atom fluence and material description or reactivity is necessary. The fluences shown in Table II are derived by grouping the surfaces into three types of orientations relative to the velocity vector: forward facing, solar inertial, and deep space inertial, using the current constant drag Space Station flight approach (ref. 5). Assuming an exposed lubricant surface with an epoxy-based lubricant binder and a reaction efficiency of 1.7×10^{-24} cm³/atom, the recession shown in Table II can be expected for a full thirty year exposure. Because a typical dry film lubricant application uses approximately 2.5×10^{-4} cm thick films, some of which are predominantly epoxy based, this type of lubricant would be lost or severely affected in less than ten days. For such thin and relatively reactive lubricants, even scattered atomic oxygen may become life limiting to organic binders used in lubricant films.

Other, nonorganic, lubricant binder systems should be less reactive than the epoxy system discussed above. Perfluorinated based polymers, which are used as both binders and lubricants, are considerably less reactive than their organic counterparts, as shown in Table I. Even with this lower reactivity, thin films ($\sim 2.5 \times 10^{-4}$ cm) could be totally removed in one year. Silicate, and glasses in general, are not reactive with atomic oxygen because of their highly oxidized state, and should, therefore, be adequate for use as binders for lubricant systems.

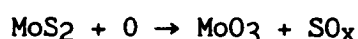
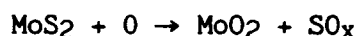
Examination of the reactivity of lubricating agents with the space environment indicates a need for additional study. The data from Table I represents the general reactivity of some lubricating agents. For example, perfluorinated oils and greases may be sufficiently stable to atomic oxygen so as not to preclude their use, consistent with the volatility limitations discussed earlier. Silicone based oils and greases have similar volatility limitations, but, in addition, are reactive, producing silicates in the process and possible changes in physical properties. Carbon, although not a candidate space lubricant, is reactive and should not be used in exposed configuration.

TABLE II.- SURFACE RECESSION PREDICTIONS FOR SPACE STATION COMPONENTS

<u>Materials</u>	<u>Lifetime, Yr</u>	<u>Fluence, Atoms/cm²</u>	<u>Recession*, cm (Mil)</u>
Forward facing surface	30	1.5×10^{23}	0.25 (100)
Solar inertial	30	8.2×10^{22}	0.14 (55)
Deep space pointing	30	9.5×10^{22}	0.16 (64)

*Assumes an epoxy-based surface.

Study of the behavior of the mainstay space system lubricating agent molybdenum disulfide (MoS_2) in the atomic oxygen environment is required in order to properly define its potential for lubricating long life systems. Although no evaluation of the reactivity of MoS_2 to atomic oxygen has been conducted, it is known that MoS_2 does form molybdenum oxides in oxygen containing environments at elevated temperatures; therefore, reaction with atomic oxygen can be expected. If reaction proceeds to complete oxidation, two oxides, MoO_2 and MoO_3 , are products that can be produced by the general reactions shown below.



Because of the high kinetic energy of the impacting atomic oxygen, it is not possible to predict the specific product of reaction. It is known, however, that MoO_2 is highly abrasive (ref. 6), and therefore, defining the reaction pathway is very important in determining the performance of MoS_2 . Even conversion to the MoO_3 could change the lubricating properties significantly.

It is not possible, in the limited scope of this paper, to discuss the specific reactivities of all lubricating agents of interest. The examples covered describe lubricant interaction possibilities, which must be considered to ensure known life, and, hopefully, known long life. Generally, to ensure good performance, the oxidative stability must be carefully considered. Additionally, data on specific lubricants for use on the Space Station must be obtained to provide the basis for a thorough evaluation.

SUMMARY OF LUBRICANT SELECTION CONSIDERATIONS

The potential interactions of lubricants discussed in the sections above are summarized in this section to provide a more succinct set of issues to be addressed in lubricant selection. The discussion is divided into two parts; it addresses sealed mechanisms, and mechanisms in which lubricants may be exposed to space.

Sealed Mechanisms

Sealed mechanisms do not present any special lubricant problems, except for long life. Long life for certain mechanisms, such as the solar power system rotating joint, may be twenty to thirty years, or full life, in the ideal case. The alternative to this full life objective is refurbishment, which, in turn, requires the development of in-space repair or refurbishment techniques. Although on the surface this approach may appear to be the most expedient, such activities are found to be difficult, a safety concern if the crew is involved, and as a minimum, requires crew time. At this point in time, such activity should be relegated to emergency conditions only, and

all efforts should be directed to selecting lubricants and joint designs which provide full life. Such an approach, which applies to both sealed and exposed mechanisms, will provide maximum programmatic benefits.

Mechanism Open to Space

The issues which should be considered for lubricants exposed to space, in their use configurations, are shown in Table III. Lubricants have been categorized into five different types, generally covering all lubricants appropriate to space system application. The issues applicable to each type of lubricant are listed. Except for the standard functional performance and long life issue, the importance of each issue is proportional to the extent of lubricant exposure to the environment; specific assessment for a given mechanism depends upon more mature design information. These issues should be considered early in mechanism design, eliminating life limiting effects.

ADDITIONAL STUDIES

As indicated earlier, studies of the effects of atomic oxygen on lubricants have not been conducted. In light of the potential interactions of MoS₂ with atomic oxygen, this represents a severe shortcoming in the lubricant data base which must be addressed. Providing sufficient information in time to support Space Station design will be difficult because of limited capabilities for simulating the atomic oxygen effects expected for a twenty to thirty year life. This limitation is further complicated by the need for rather large samples of exposed lubricants to perform lubricant performance evaluations. The initial step should examine chemical changes in specific lubricants when exposed to atomic oxygen.

Two opportunities exist for obtaining information on chemical changes in a limited number of lubricants. A flight experiment conducted in support of the Space Station and referred to as Evaluation of Oxygen Interaction with Materials III (EOIM III) represents one approach. The other approach is to perform exposure experiments in atomic oxygen beam facilities which are designed to simulate the space environment. Several facilities are currently under development (ref.7). Detailed chemical analysis of exposed samples should reveal major reaction pathways, for example, the loss of sulfur in the case of MoS₂, and may even provide kinetic information on important reactions. Identification of the specific products of reaction may be more difficult, especially in the case of MoS₂. As simulation facilities become more mature, extensive evaluations, including coefficient of friction, should be possible.

CONCLUSIONS

The brief examination of issues related to Space Station lubricant selection indicates the importance of space environment interactions in defining lubricant performance in mechanisms which are open to space. Under

long life conditions, vacuum volatilization will certainly have to be considered for oil and grease based lubricants. Reaction of atomic oxygen with exposed, or partially exposed mechanisms, will be important for organic based lubricating agents and binders and may react with MoS₂, producing significant changes in lubrication performance. These interactions need to be understood as soon as possible to ensure support of Space Station design activities to be conducted over the next several years.

TABLE III.- SPACE STATION LUBRICATION SELECTION CONSIDERATIONS

<u>Lubricant Type</u>	<u>Not Exposed to Environment</u>	<u>Exposed to Environment</u>
Liquid films (low vapor pressure)	<ul style="list-style-type: none"> ● Functional performance ● Long life 	<ul style="list-style-type: none"> ● Loss of lubricant by vaporization ● Contamination of nearby systems ● Reactivity with atomic oxygen ● Effects of UV radiation ● Functional performance and long life
Dry films with organic binders	<ul style="list-style-type: none"> ● Functional performance ● Long life 	<ul style="list-style-type: none"> ● Reactivity of binder and lubricating agent with atomic oxygen ● Particle release ● Functional performance and long life ● Effects of UV radiation
Dry films with inorganic binders	<ul style="list-style-type: none"> ● Functional performance ● Long life 	<ul style="list-style-type: none"> ● Reactivity of lubricating agent with atomic oxygen ● Particle release ● Functional performance and long life
Metal or metal oxide films	<ul style="list-style-type: none"> ● Functional performance ● Long life 	<ul style="list-style-type: none"> ● Functional performance and long life
Polymer films and liners	<ul style="list-style-type: none"> ● Functional performance ● Long life 	<ul style="list-style-type: none"> ● Reactivity with atomic oxygen ● Effects of UV radiation ● Functional performance and long life

REFERENCES

1. Personal Communication with Richard Kelly. Castrol, Bray Products Division, Irvine, CA, December 1986.
2. Dushman, S.: Scientific Foundations of Vacuum Technique. Second Edition, John Wiley and Sons, Inc., New York, NY, 1962, p. 18.
3. Space Station Induced Environment Requirements. JSC 30426, 1986.
4. Leger, L. J., Visentine, J. T., and Schliesing, J. A.: A Consideration of Atomic Oxygen Interactions with Space Station. AIAA 23rd Aerospace Sciences Meeting, January 14-17, 1985, AIAA Paper 85-0476.
5. Leger, L. J., Visentine, J. T., and Santos-Mason, B.: Selected Material Issues Associated with Space Station. SAMPE 18th International Technical Conference, October 7-9, 1986, Seattle, WA, pp. 1015-1026.
6. Giltrow, J. P. and Lancaster, J. K.: The Role of Impurities in the Abrasiveness of MoS₂. ASLE Proceedings - International Conference on Solid Lubrication, Denver, CO, 1971, p. 82.
7. SAMPE 18th International Technical Conference, October 7-9, 1986, Seattle, WA, pp. 722-779.

**GIOTTO'S ANTENNA DE-SPIN MECHANISM: ITS LUBRICATION AND
THERMAL VACUUM PERFORMANCE**

M J Todd^{*} and K Parker^{*}

Abstract

Except in the near-Earth phase of Giotto's mission to Comet Halley, the HGA (high gain antenna) on board Giotto was the only designed means of up/down communications. The spacecraft spin stabilisation required that the HGA be "de-spun" at the same rotational rate of nominally 15rpm in order to keep the HGA pointing accurately to Earth. A dual servomotor de-spin mechanism was designed and built by SEP of France for this purpose.

The expected thermal environment suggested that dry lubrication was preferable to wet for the ball bearings but there existed no relevant data on the torque noise spectrum of candidate solid lubricants. Therefore *ad hoc* torque noise tests were run with two solid lubricants: ion-plated lead film plus lead bronze cage (retainer) and a PTFE- composite cage only. The lead lubrication showed the better spectrum up to the mission lifetime point so it was selected for continued test over some 20 times the Halley mission life, with periodic torque spectrum monitoring. The spectrum remained well within the pointing error budget over the 100 million revolutions covered.

* European Space Tribology Laboratory, Risley Nuclear Power Development Lab., UKAEA, Risley, Cheshire, England

Following the bearing test, an engineering model of the de-spin mechanism, driven via a feedthrough outside the vacuum chamber, yielded transmitted torque spectra in which harmonics of the rotational frequency dominated over the nearly-white noise from the bearings.

The effect of these harmonics was quantified during a later thermal vacuum (TV) test of the complete energised mechanism, with dummy antenna, which was carried out a few months before launch in July 1985. Besides allowing functional checks of the servo-system, this test yielded the reacted torque spectra at all thermal states in the correct vacuum and inertial conditions. At particular motor speeds there was high and sustained reacted torque, implying out-of-tolerance undamped resonance of the antenna.

1. Introduction

GIOTTO, the ESA scientific probe to comet Halley, made its planned close encounter with the comet in March 1986.

GIOTTO was built by a consortium of European industries, the prime contractor being British Aerospace. The spacecraft was spin-stabilised and its high gain antenna (HGA) had to point off-axis towards Earth, Fig. 1.

A de-spin mechanism (DSM) drove the antenna to cancel out the spin. This mechanism was a new development and its correct function was crucial to the whole mission.

The DSM was designed and manufactured by the Societe Europeenne de Propulsion (SEP) of Vernon, France. It consisted of a stepper motor drive (operated in the synchronous mode by sin/cos waveforms) and a redundant motor on the rotating shaft supported upon flexibly preloaded angular contact bearings. During launch and perigee motor firing the bearings were offloaded.

The Earth-pointing accuracy required of the HGA (maximum constant error ± 0.1 degrees, maximum jitter ± 0.05 deg.) between design speeds of 14 to 16 rpm, together with the anticipated range of working temperature of the DSM - from -20C

to +40C - imposed limits upon the tolerable torque noise, part of which would be generated by the bearings. There was very little information on the torque spectrum of ball bearings or on how significant other sources of torque noise might be.

This paper therefore discusses the supporting experimental work on: long-term torque noise behaviour of solid-lubricated ball bearings in vacuo; the transmitted torque spectrum of an externally driven DSM and; the subsequent thermal vacuum testing of the energised DSM and HGA (dummy) with associated spectra of reacted torque, ie. that experienced by the spacecraft itself.

2. Description Of DSM And Control Of Speed

A description of the DSM has already been given by SEP (ref. 1) and by ESA (ref. 2) and a paper in this Symposium discusses design and dynamics of control for the GIOTTO DSM (ref. 3).

The cross-section in Fig. 2 shows the arrangement of bearings, motors and offload device, the HGA itself (not shown) being attached to the interface flange (1).

After launch and the release of the offload device (items 3,6,8 and 9), the two angular contact bearings (5) of 55mm ID carried a preload of 300N supplied by the membrane, 7. Of the two synchronous stepper motors (4) to drive the shaft, only one of the motors was normally energised.

Antenna spin-up after injection into heliocentric orbit was accomplished by a ramping sequence. When the desired speed was attained it was controlled by a servosystem relying upon the counting of internal clock pulses. These pulses measured the time difference between the actual and the desired position of the antenna. Because the time difference (as a number of clock pulses) was used only once per revolution to correct the motor speed over the next revolution, controller performance was necessarily sensitive to the fluctuation in angular velocity caused by torque variation within the DSM. That is, too much resistive torque variation during "coasting" in each revolution would produce a false error signal which might lead to control instability or to excessive HGA jitter.

From discussion with SEP in the early stage of the development, an overall limit on the torque noise from the bearings, regarded at that time as the chief cause of noise, was prescribed as 0.12Nm rms over the frequency range 0.01 to 12Hz. In addition, no prominent torque spectral peaks were to be contributed by the bearings over the frequency range of 1 to 3Hz which was regarded as the "sensitive" region by virtue of the expected antenna torsional resonance.

3. Choice of Lubricant

The criteria for the DSM bearing lubrication were:

- long-term stability in space vacuum
- low torque noise over the mission life
- insensitivity of mean torque to temperature change
- validity of accelerated testing
- simplicity in design, ie, preferably no lubricant reservoirs or molecular seals

The last criterion implied that greases or oils were not welcome since their supply and containment would inevitably lead to complexity of design. Additionally the known sensitivity of wet lubricants to temperature was an important factor in this application and so was the validity of accelerated testing.

A solid lubricant was thus favoured and the long experience in Europe with ion-plated lead film (ref. 4) made it a strong contender for this duty. Another solid lubricant - transferred PTFE film from a composite cage (retainer)- was also interesting.

Although early work in the UK on lead-plated bearings (refs. 5,6) had yielded time domain data on the torque noise over very long lives, eg. 300 million revs. of ref. 6, there was apparently no information on frequency domain noise (spectrum) with such solid lubricants in this type of duty. Existing

applications, eg. mainly to solar array drives and to other limited cycle ball bearings did not approach the continuous duty of several million revolutions required of the DSM bearings.

4. Accelerated Torque Spectrum Test of Solid Lubricated Bearings

4.1 Experimental Conditions

Bearing pairs of the same type as in the DSM were lubricated either by:

ion-plated lead with cast lead-bronze cage

or

PTFE-composite cage (PTFE/glass fibre/MoS₂)

The bearings were mounted as shown in Fig. 3 in a small vacuum chamber and their housing was driven round via a vacuum feedthrough. An inductive torque transducer restrained the shaft from rotating and measured the transmitted torque of the bearings only (the torque transducer having no bearings).

After a short 10000 revs. test in air to reproduce likely ground testing, the chamber was evacuated to a pressure of < 1 microtorr and the main test was begun. A target of 10^7 revolutions was initially set but this was later extended, in the case of the lead-plated bearings, to 10^8 revs. to give some 20 times the duty in the Halley mission ($4 - 6 \cdot 10^6$ revs.).

To fit this test into a reasonable timescale, we chose a speed of 100 rpm, with regular reduction to a nominal de-spin speed of 16 rpm for the recording of torque spectrum. Since, with these solid film lubricants, temperature was known to have little effect on bearing torque, all the tests described here were done at a nominal ambient temperature of 20C.

4.2 Results and Discussion of Torque Spectra From Bearings Alone

A comparison of the power spectral density (PSD), in units of $(Nm)^2/Hz$, at a similar number of revolutions, between the ion-

plated lead film/bronze caged bearings and the PTFE-composite caged bearings is shown in Figs. 4 and 5. There are many more peaks in the latter spectrum, probably because of the thick, uneven transfer of the PTFE film to the ball and raceways. On the grounds of the prominent peaks in the "sensitive" bandwidth of 1-3Hz the test on the PTFE-caged bearings was discontinued.

The typical spectrum in Fig. 4 from the lead-plated bearings at a stage equivalent to the Halley mission lifetime ($6 \cdot 10^6$ revs.) shows peaks from the cage rotational frequency (<0.1 Hz) and from debris impact frequencies ca. 2Hz. Such peaks were features of all recorded spectra but their amplitude varied over the test. At end of test, 10^8 revs., we show the spectrum in Fig. 6. The background level has increased to approx. $3 \cdot 10^{-7}$ Nm^2/Hz but there is rather less variation in PSD than in Fig. 4, ie. the noise appears to become "whiter" with time.

We may now set these bearing torque spectra in context by comparing them with the acceptable level of torque noise for the DSM. The above-specified maximum rms value of 0.12Nm over the frequency range 0.01 to 12 Hz implies, if it were pure white noise, a constant power spectral density of $1.2 \cdot 10^{-3}$ $(\text{Nm})^2/\text{Hz}$. This level is many times greater than observed from the lead-plated bearings.

In fact the highest individual peak observed at any point in the test was $<10^{-4}$ $(\text{Nm})^2/\text{Hz}$. In the time domain, the highest rms torque monitored during the test was 0.009Nm at $80 \cdot 10^6$ revs. - to be compared with the limit of 0.12Nm quoted above.

The lead-lubricated bearings themselves thus generated far less torque noise than the limit set for this application.

5. Torque Behavior of Driven DSM (Engineering Model)

5.1 Test Conditions

The first accelerated "thermal vacuum" life test on a model (EM) of the DSM was carried out at ESTL in the arrangement shown in Fig. 7.

In Fig. 7 an electric motor drives a feedthrough shaft which

passes through the vacuum chamber lid, through a central hole in a piezo-electric torque transducer and is then connected to the interface flange of the DSM shown in the lower part of Fig. 7. The torque transmitted from the drive to the housing of the DSM is sensed by the torque transducer to which the DSM body (housing) is attached. The slip rings shown at the top are used for thermistors on the rotating shaft.

The mechanism was externally driven, with no energisation of the stepper motors, mostly at 200 rpm except for periods of torque measurement and analysis which were at 15rpm.

Thermal conditions were as follows: shaft 20C, housing 20C; shaft 20C, housing 40C and shaft -25C, housing -3C.

Torque spectra were taken in all these temperature states every $5 \cdot 10^5$ revs. until a total of $6 \cdot 10^6$ revs had been accumulated.

5.2 Results And Discussion Of Driven DSM Test

We show a typical power spectrum of the driven DSM torque in Fig. 8 at a comparable number of revolutions to those in Fig. 4 by the lead-plated bearings alone. The most obvious difference between these spectra is the prominent set of harmonics of the rotational frequency ($0.25\text{Hz} = 15\text{rpm}$) in Fig. 8. Since Fig. 4 shows a much quieter spectrum and no such harmonics, it was concluded that they must arise from the stepper motors themselves. However the reason for this effect was not investigated further by the present authors. A discussion of motor-induced oscillations is given in ref. 1.

No significant effect of temperature state or of gradient was seen in the observed torque spectra.

6. Reacted Torque Behaviour Of Energised DSM (PM1)

6.1 Introduction

Following the "driven DSM" tests described above and after some further development work, it was decided to measure directly

in vacuum the reacted (or reaction) torque, ie. that torque which would be experienced by the spacecraft in driving the antenna. We shall describe one of these thermal vacuum tests on the DSM (FM1) carried out at ESTL a few months before launch in July 1985.

6.2 Test Arrangement

To accommodate the dummy antenna of the same polar moment of inertia (1.85 kgm^2) as the actual HGA, the DSM was mounted in a vacuum chamber of 1m diameter with the DSM supported by a piezo-electric torque transducer as in Fig. 9a. This configuration allowed the reacted torque to be measured as the DSM drove the HGA dummy. The DSM is shown in Fig. 9b (without the HGA dummy) mounted on the lower half of the vacuum chamber, prior to this test.

The thermal control surfaces in Fig. 9a were used to impose different temperature states in which the motor power, pointing accuracy, run-up and run-down times were measured by staff from SEP. These data will not be discussed here; we will confine ourselves to the reacted torque data.

6.3 Reacted Torque Spectrum From Speed Sweep

6.3.1 In Vacuum (Average Level: 3.10^{-8} Torr)

We show in Fig. 10 a typical "quiet" spectrum of reacted torque over the DSM speed range of 14 to 16 rpm. Fig. 10 was recorded at 15 rpm and the fundamental of 0.25Hz is visible as a small peak. The natural resonance frequency of the antenna, which can be regarded as a torsional pendulum with the (non-linear) restoring torque being the magnetic stiffness of the energised stepper motor, occurs at $1.8375 \pm 0.0125 \text{ Hz}$ in the conditions of Fig. 10. There is seen to be some excitation of the resonance by a nearby harmonic (the 7th) of the rotational frequency. These harmonics are clearly visible in Fig. 8 from the test on the driven DSM.

Corresponding to Fig. 10, the time-domain trace of torque is seen in Fig. 11. The beat frequency between the two major peaks

of Fig. 10 is evident in the envelope of the torque/time record. However the maximum rms torque is only ca. 0.01Nm which implies a pointing jitter of the HGA amounting to not more than 0.004 degree, ie. well below the tolerance level of 0.05 degree. For this reason we referred to the spectrum as "quiet".

As the rotational speed was varied, the exciting motor harmonics moved proportionately to speed and when the resonance and exciting frequencies coincided (this occurred at 15.527 rpm at 20C isothermal) a very strong oscillation was seen - Fig. 12.

It is to be noted that the resonance frequency had itself shifted from the value shown in Fig. 10 to 1.8125 ± 0.0125 Hz. Thus the resonance frequency was a function of oscillation amplitude, because of the non-linear stiffness of the motor (as noted in ref. 1). In Fig. 12 the energy content of the peak is some 10^3 times that of the quiet spectrum of Fig. 10. Note the change of ordinate scale between Fig. 10 and Fig. 12.

The time-domain record of this strong, undamped oscillation is seen in Fig. 13 which may be contrasted with Fig. 11. The rms torque has risen to 0.25Nm which can be roughly translated into a pointing jitter of 0.1 degree. This is twice the tolerance limit for jitter (0.05 degree).

Because of the closeness to launch and consequent time pressure, detailed sweeps through the resonance at all thermal states were not possible. However, from the torque spectra showing strong excitation in other temperature conditions, it was possible to find the speeds at which the 6th, 7th and 8th harmonics of rotational frequency would coincide with the natural frequency and thereby cause excessive antenna jitter. Table 1 shows the observed resonances at hot and cold conditions and the corresponding excitation speeds from the harmonics given.

In the mission itself a spin rate of 15.007 rpm was set (ref. 7), and the behaviour of the antenna (pointing accuracy) suggested that there was never any significant resonance excitation at this speed.

6.3.2 In Atmospheric Nitrogen

The torque behaviour in one atmosphere of dry nitrogen contrasted greatly with that in vacuum. Fig. 14 shows the spectrum under otherwise identical conditions to those in Fig. 12 where the strong oscillation occurred in vacuum. It is seen that the strength of the resonance peak is much attenuated from Fig. 12. This result illustrates the great importance of gas damping forces.

7. Concluding Remarks

The lubrication and thermal vacuum evaluation of GIOTTO's de-spin mechanism have provided some new information on this type of drive in space.

Though the use of lead ion-plated bearings and in particular their torque noise characteristics were originally perceived as problematic, we have shown experimentally that this lubricant was easily capable of meeting the mission life and that its noise spectrum was always rather insignificant compared with the tolerable noise.

With the externally driven DSM, the transmitted torque spectrum of the stepper motors was found to be dominant over the bearing spectrum and contained strong harmonics of the rotational frequency.

The subsequent thermal vacuum test of the complete energised DSM with its dummy inertia (all in high vacuum) quantified the effect of the stepper motor harmonics in exciting a strong, undamped torsional resonance of the antenna at certain motor speeds. Much weaker resonance was seen in atmospheric nitrogen because of gas damping. The frequency of the resonance depended not only upon temperature (because of the thermal change in electromagnetic stiffness of the motor), but also upon the amplitude of the oscillation. It was possible to identify de-spin speeds at different thermal states where the resonance would be excited.

The tests identified a safe operating regime for the GIOTTO de-spin mechanism and contributed to the eventual mission success.

This work underlines the importance of a full simulation of the flight environment. It also illustrates the usefulness of the reacted torque technique.

Acknowledgements

We are indebted to Dr R H Bentall and Mr F Felici of ESTEC for funding and support of part of this work. Mr M Humphries, BAe and Ms. G Turin and G Atlas of SEP worked in collaboration with us, enabling the driven EM and the FM1 TV testing to be done at ESTL. The authors are also grateful to the following ESTL staff for their contribution: John Duvall, Allan Thomas, Christine White and Alan Garnham.

References

1. Turin, G Giotto de-spin mechanism subsystem-general loop design and pointing aspects. Proc. 2nd Europ. Symposium on space mechanisms and tribology 1985 ESA SP231
2. Felici, F The Giotto mechanisms and their function. Proc. 1st Europ. Symposium on space mechanisms and tribology 1983 ESA SP196
3. Atlas, G and Thomin, G
The experiences of CNES and SEP on space mechanisms rotating at low speed. 1987 21st Aerospace Mech. Symposium
4. Sheppard, J S Some tribological problems in space mechanisms. Tribology in Aerospace. Proc. I Mech E Seminar 1985
5. O'Donnell, P J Lubrication by lead films. Proc. 1st European Space Tribology Symposium. Frascati 1975
6. O'Donnell, P J Progress report on the lubrication of bearings in vacuum. ESA CR 830 1977

7. Reinhard, R The Giotto encounter with comet Halley. Nature
Vol 321 15 May 1986

Table 1

**Resonance Frequencies Of HGA And Corresponding Excitation
Speeds**

Thermal state		Natural frequency	de-spinspeed (rpm) for excitation by harmonics:		
Shaft (°C)	Housing (°C)		6th	7th	8th
-18	7	1.75	17.5	15.0	13.13
20	20	1.8125	18.12	15.53	13.59
40	40	1.85	18.5	15.86	13.88

Note: at each of these temperature states a strong resonance was observed (peak torque power density at least $0.2 \text{ (Nm)}^2/\text{Hz}$). At other temperature states the resonance frequencies were less reliable since the excitation was much less.

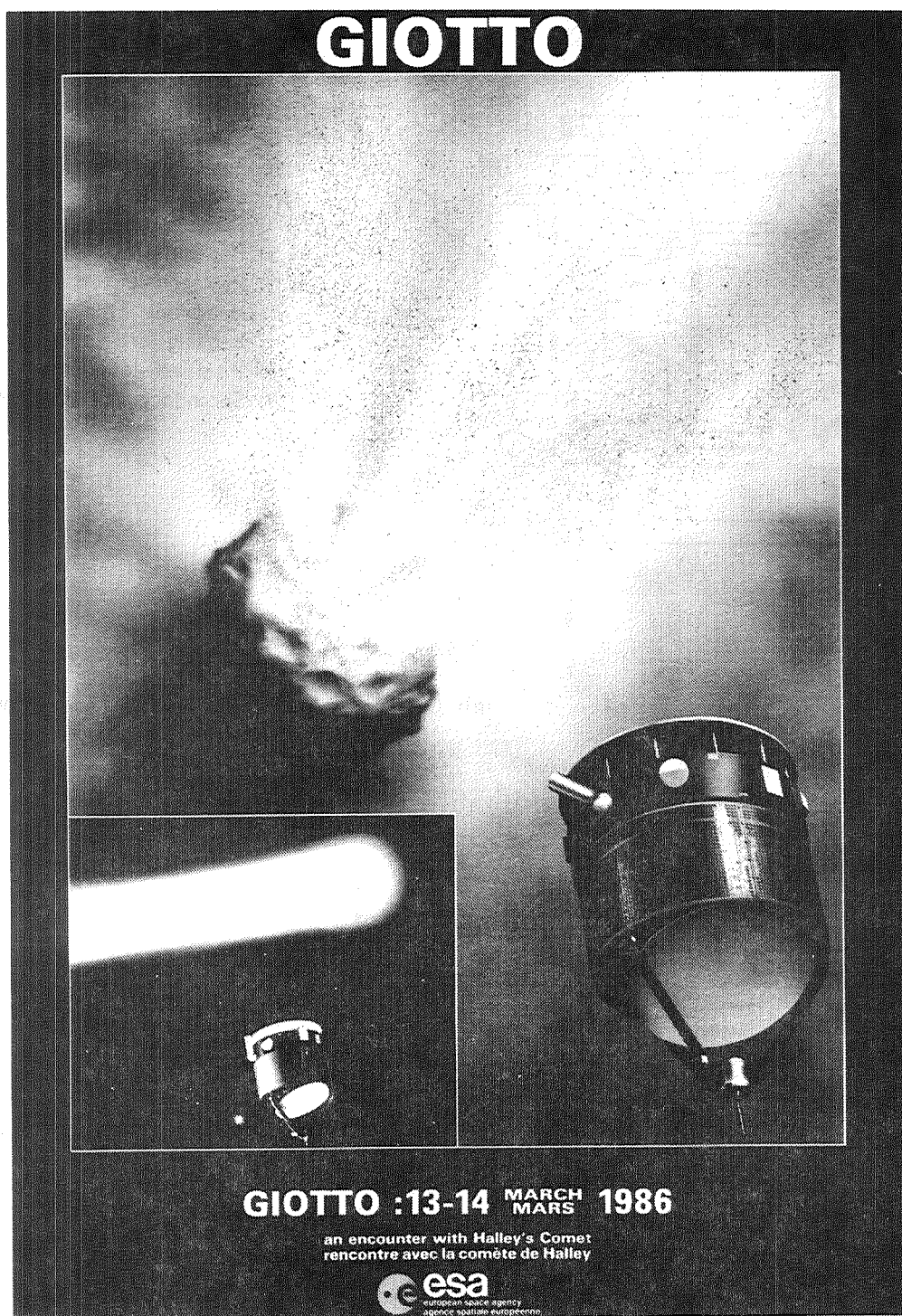


Fig. 1 GIOTTO approaching comet Halley (artist's impression)
showing Earth-pointing high gain antenna

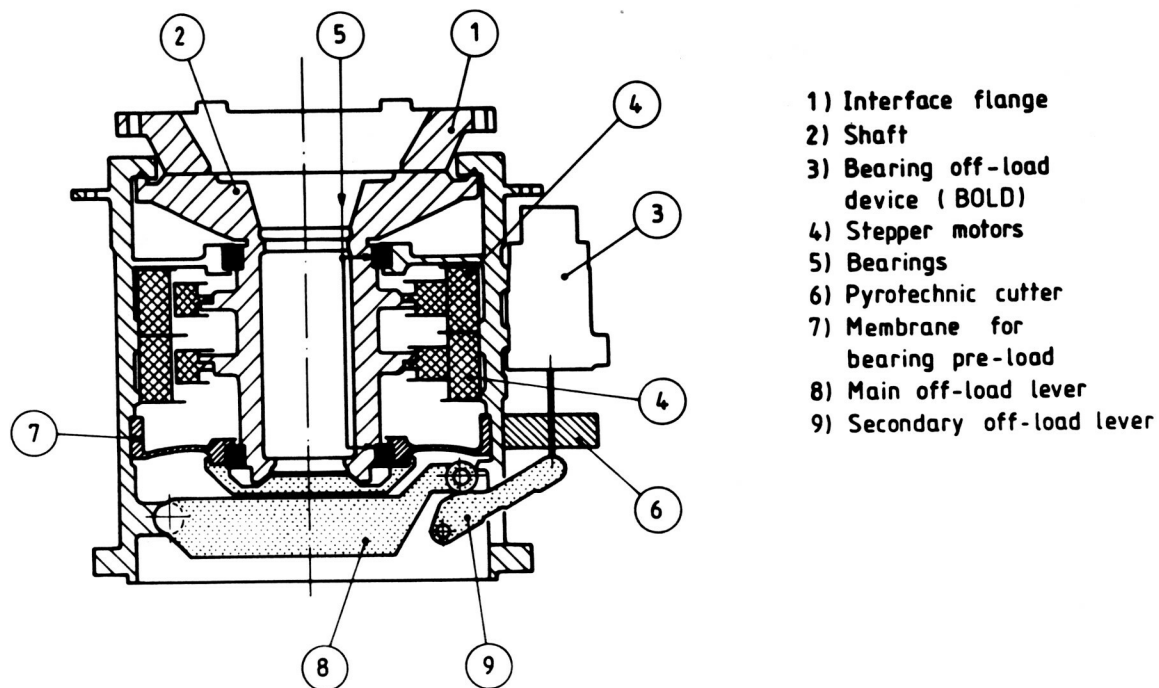


Fig. 2 Cross section through GlOTTO's de-spin mechanism (DSM)

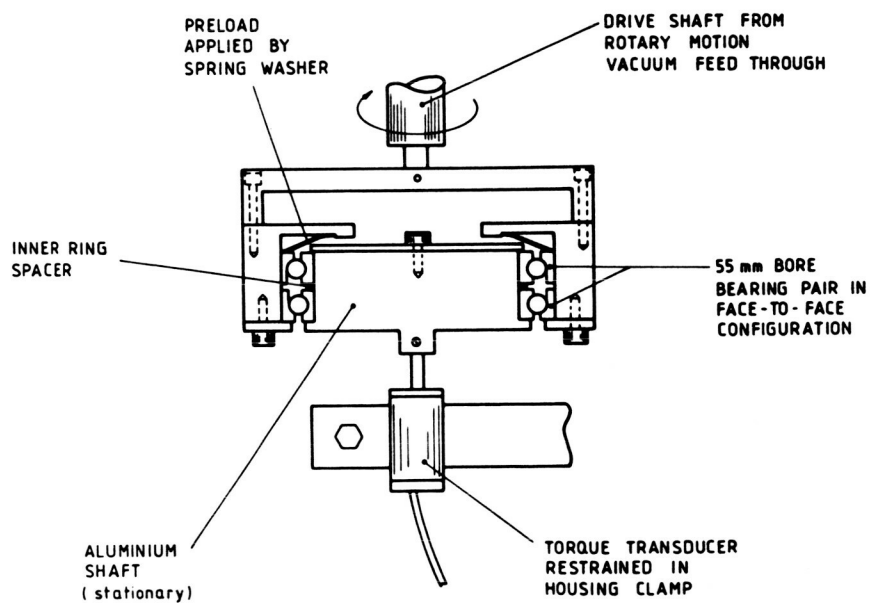


Fig. 3 Section through experimental rig for bearings-only torque test

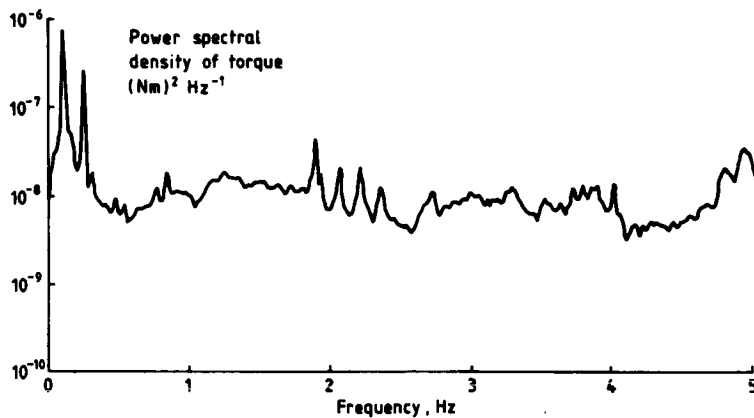


Fig. 4
Power spectrum of torque from lead-plated bearings at ca. Halley mission lifetime (6.7 million revs.)

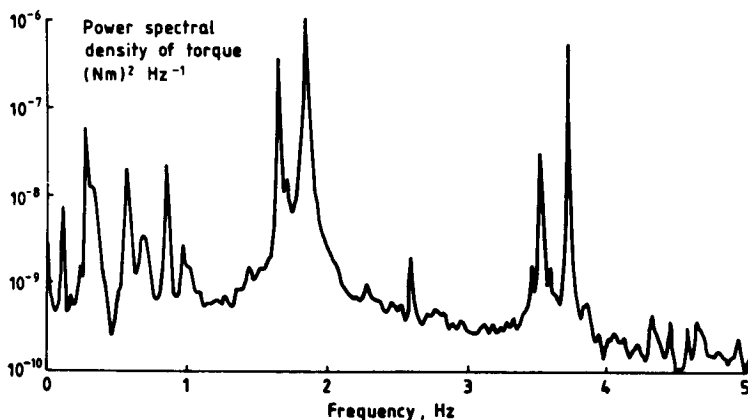


Fig. 5.
Torque spectrum from PTFE-composite-caged bearings at ca. Halley mission lifetime (6.9 million revs.)

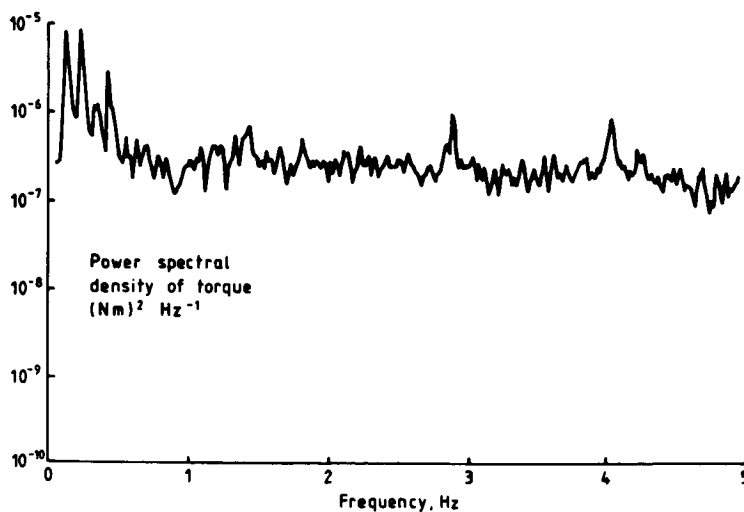


Fig.6
Torque spectrum at 10⁸ revs. from lead-plated bearings

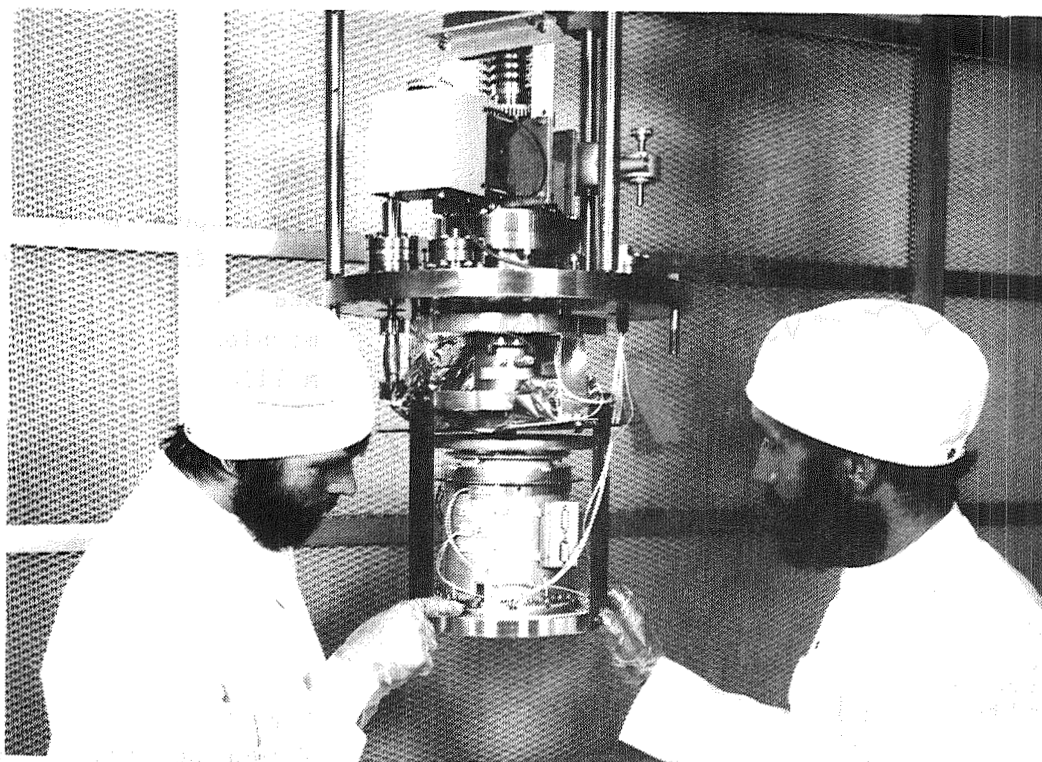


Fig. 7 Photo of DSM (Engineering Model) being prepared for thermal vacuum test

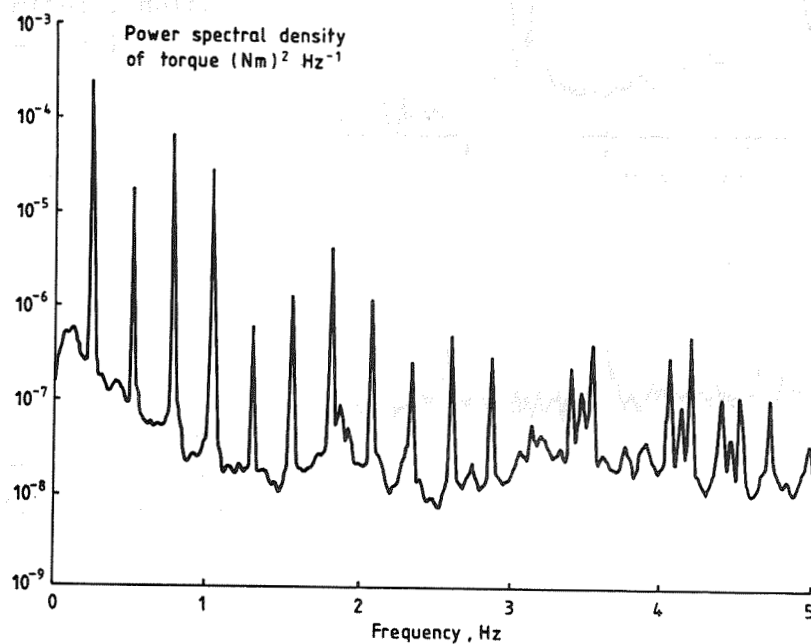


Fig. 8 Typical torque spectrum from driven DSM.

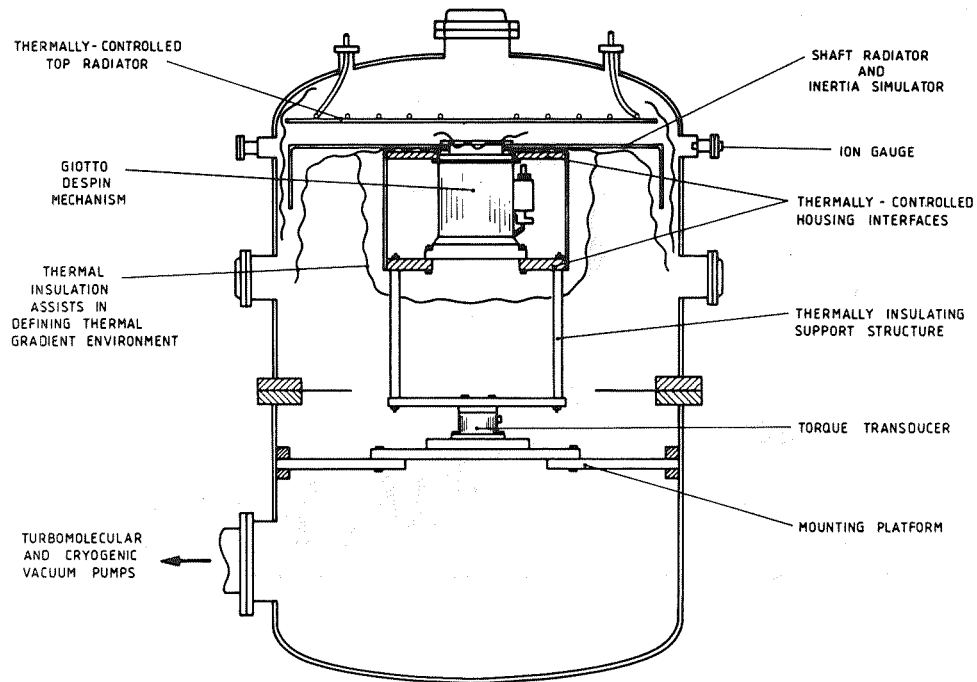


Fig.9a Arrangement of DSM (Flight Model 1) with dummy antenna in thermal vacuum chamber

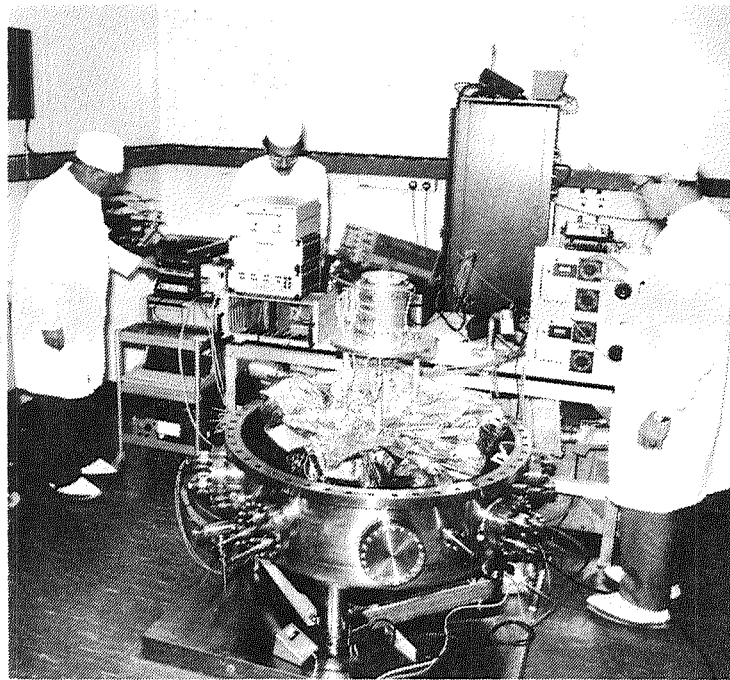


Fig. 9b GIOTTO FM1 DSM being installed in ESTL test chamber

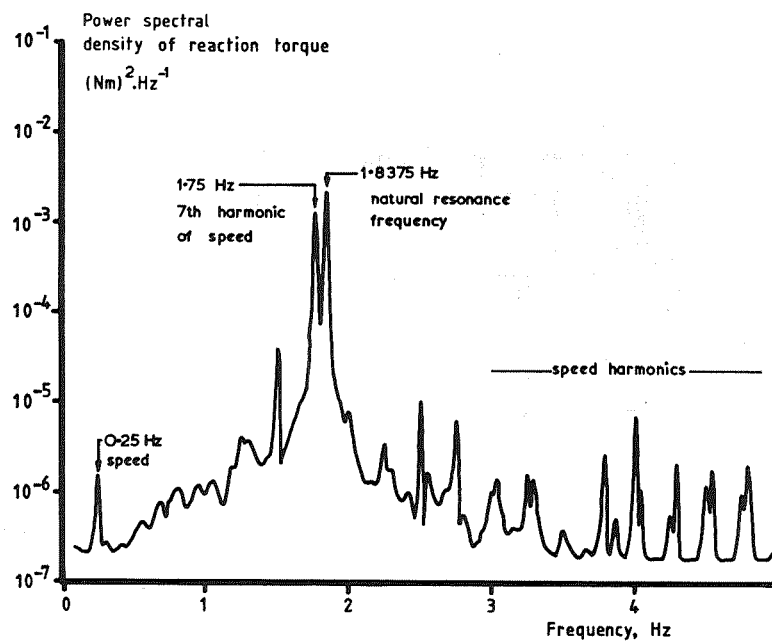


Fig. 10 Typical "quiet" power spectrum of reacted torque from DSM(FM1) in vacuum

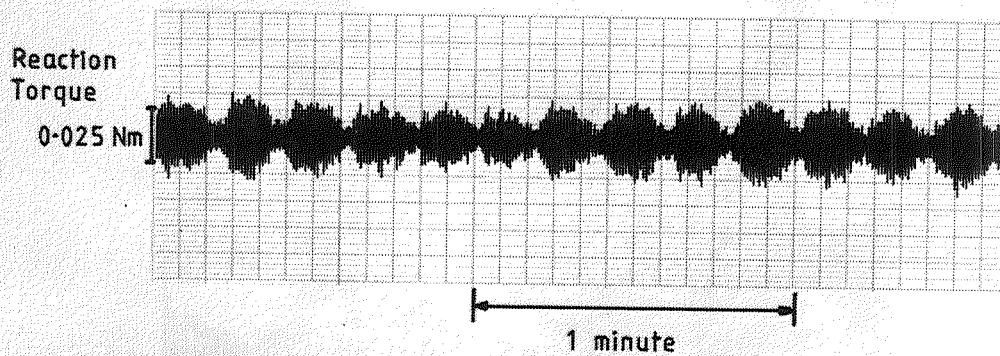


Fig. 11 Corresponding time-domain trace of reacted torque in Fig. 10

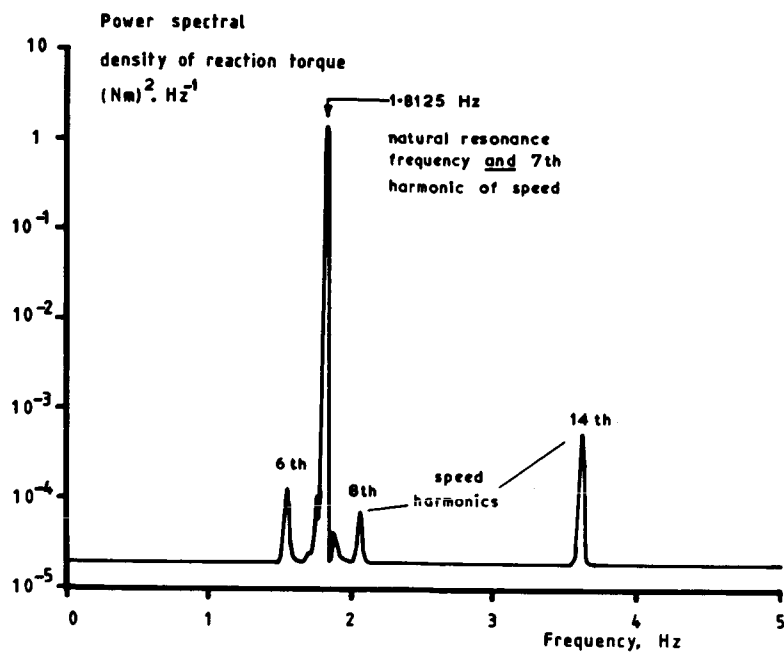


Fig. 12 Power spectrum at resonance condition from DSM (FM1) in vacuo

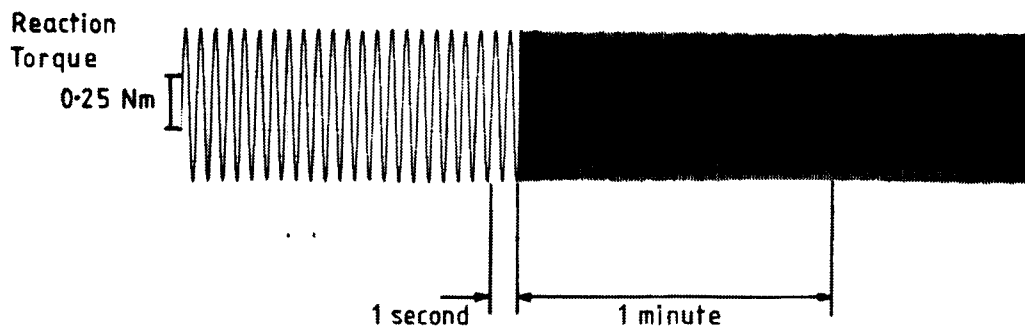


Fig. 13 Time-domain trace corresponding to torque spectrum of Fig. 12

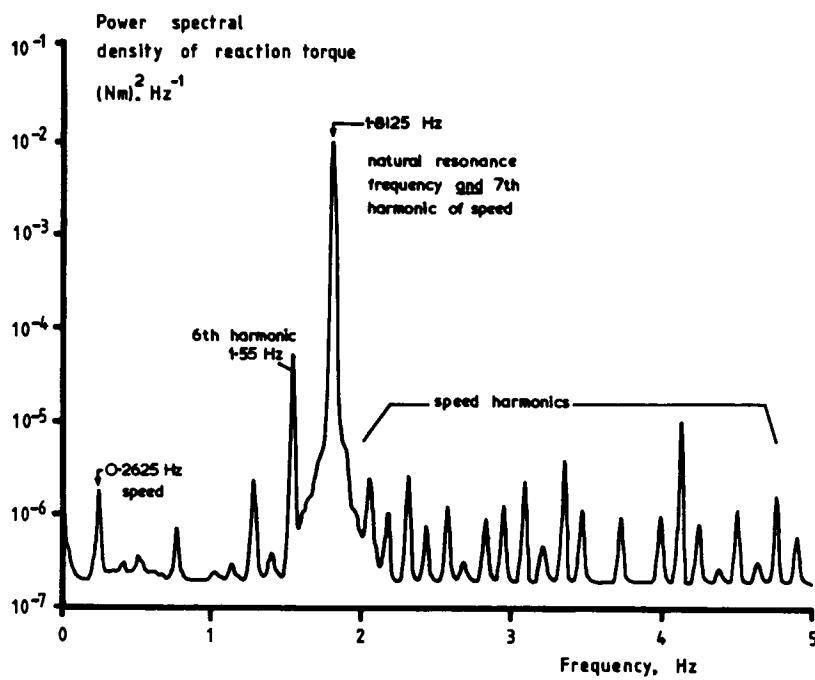


Fig. 14 Power spectrum at resonance condition from DSM (FM1) in atmospheric nitrogen

ANATOMY OF A BEARING TORQUE PROBLEM

Damon D. Phinney*

INTRODUCTION

In the early 1970s, Ball Aerospace Systems Division developed an antenna despin drive for the Messerschmitt Boelkow Blohm (MBB) solar science satellite HELIOS. This paper discusses a problem with high bearing drag torque that was encountered on the two flight models of this drive, after successful tests were completed on twelve bearings, an engineering model, and the qualification unit.

HELIOS was spin-stabilized at 60 RPM and was to be launched into a highly elliptical orbit which would take it 70 percent of the distance to the sun and then back within a million km of Earth, two times a year. The Despin Drive Assembly (DDA) mission was to point a parabolic antenna continuously toward Earth during the entire orbit. The shaft of the inside-out DDA was fixed to the spacecraft, supporting the antenna feed at its outboard end, while the antenna was attached to the housing. The specified DDA temperature range was -50°C to 60°C , and minimum lifetime was to be 18 months.

Our torque troubles occurred at the low end of the temperature range. The problem was insidious because it offered no clues of its existence in our usual tests until we went to low temperature, and the measures taken to correct it gave no indication of their effectiveness at normal temperatures.

DESCRIPTION OF DESPIN DRIVE ASSEMBLY

A flight DDA is pictured from the outside, with its mounting end up, in Figure 1, with internal details illustrated in Figure 2. Salient construction features that are discussed in the following account are shown in greater detail in Figure 3. They are:

- A three-piece shaft assembly, consisting of a 7075-T652 aluminum tube 7.8 in. long with 6Al-4V titanium stubshafts at each end. Bearing journals were on the stubshafts, whose function was to isolate the bearings from the high expansion rate of the aluminum tube. The stubshaft at the left end of Figure 3 has 16 studs on a flange outside the bearing, by which the DDA was mounted on the spacecraft.
- A three-piece housing assembly. The main housing was aluminum, with an 8-in. ribbed titanium plate at one end, and a short cylindrical titanium member at the other. The titanium pieces carried the bearing outer rings, isolating them from the aluminum member.

* Ball Aerospace Systems Division, Boulder, Colorado

- The aluminum shaft and housing were made from bar stock. The titanium end plate was probably made from 1 in. plate. (The drawing is ambiguous and production records are no longer available.) Other titanium pieces were made from bar stock.
- Two angular contact ball bearings were spaced 6.4 in. apart with outer race thrust shoulders facing each other. All bearing rings were slight interference fits except for the outer race of the right hand bearing. This was slip-fitted and acted on by a set of coil springs with a force of 5 lb. The springs were in a carrier machined to length at assembly to produce an end play of 0.0055/0.0065 in. Because of the mix of aluminum and titanium pieces in the shaft and housing, the end play would be reduced by 4 mils at -50°C.
- The 440C bearings were lubricated with a thin film of MoS₂ approximately 1/4 micron thick, and had inner-land-riding Rulon-A separators with full cylindrical pockets. The normal ball complement was reduced from 42 to 38 to provide additional separator material between pockets and increased dimensional stability.

Additional DDA features, for information, include:

- Non-redundant resolver-commutated brushless DC motor
- Magnetic pickups for rate and position
- An electronics assembly with motor drive circuitry, magnetic pickup output conditioning and a motor current feedback circuit. MBB closed the rate and position loops.

EARLY EXPERIENCE AND FLIGHT UNIT PROBLEM

DDA requirements included operation between -50°C and 60°C (-60°C and 75°C for qualification) with a maximum drag torque of 5 oz-in. In addition to the bearings, the only significant drag source was motor hysteresis (1.3 oz-in.).

To confirm bearing lubrication, a thermal vacuum life test on six bearing pairs had been run at 60 RPM for 18 months. Temperatures were -35°C, 10°C, and 60°C. Torques varied from 0.5 to 1.5 oz-in. with brief excursions to 2.5 oz-in. on two sets at 22°C.

An 18-month thermal vacuum life test had also been conducted on an engineering model DDA at 60 RPM and temperatures of -40°C, 22°C, and 50°C. After some fixturing problems were corrected, drag torque varied between 2 and 4 oz-in. There were two brief excursions as high as 8 oz-in. at 22°C and 120 RPM while we were catching up after some down-time.

The qualification unit had shown drag torques of 6.4 and 4.5 oz-in. at -60°C and 75°C. The 6.4 oz-in. reading, although above the 5 oz-in. limit,

was rationalized away on the basis of a probable adverse temperature gradient (housing warmer than shaft) unlikely to occur during flight. An excessive gradient would have completely eliminated end play and caused an increase in bearing load.

With this favorable experience preceding acceptance tests of the two flight DDAs, we were rudely surprised when drag torque climbed to 20 oz-in. on the first unit while it was being taken down to -50°C .

TESTS TO OBTAIN MORE INFORMATION

It took nearly three months to find out how to fix the drive and implement the changes. We ran 29 low-temperature tests on the DDA, several tests on the bearings by themselves, and distortion measurements at low temperature on several components, as well as making up special test samples of two of the drive parts involved.

The first step was to measure torque vs. temperature with the drive cooling down. These data were not taken during acceptance testing. The rotating housing was instrumented and the cooling rate, in soft vacuum, was adjusted so that the housing followed the shaft within 10°C . Torque was determined from motor current.

Curve 1 on Figure 4 shows results with the DDA in its normal mounting position, shaft vertical and big end down. In this position, the lower bearing carries the weight of the drive housing (several lb) and also the bearing preload force of 5 lb. Although this test indicates a peak torque of only 13 oz-in. at -50°C , and suggests that limiting the housing-to-shaft temperature gradient was helpful, it clearly shows a problem.

Curve 2 on Figure 4 gives results with the drive inverted. Torque exceeded 20 oz-in. at -56°C . In this position, the bearing now on top is essentially unloaded and the bottom bearing is subject to the preload force only, with the housing weight close to the preload spring force. This removes approximately 10 lb of total bearing load and explains the reduction in drag torque at room temperature, correlating well with results of bearing torque vs. preload tests. The shift in the knee of the torque curve to a lower temperature is not explained. As will be seen, our corrective actions were taken at the big end of the drive where it was usually attached to the mount, which was also a cooling plate. With the sensitive end of the shaft no longer attached to the cooling plate, it may not be surprising that response to low temperature is somewhat different.

Bearing Tests

The next step was to check out the bearings themselves. The inner land-riding separators were Rulon-A, which has a coefficient of thermal expansion (CTE) of $32 \times 10^{-6}/^{\circ}\text{F}$, more than five times the bearing ring CTE. Furthermore, the material had shown a tendency to go slightly out-of-round after machining.

We had land clearance sufficient to accommodate the CTE difference and some out-of-round, and used a thermal stabilizing process to minimize machining distortion. Additionally, life test results had demonstrated satisfactory separator design. Nevertheless, we tested our spare separator stock to find ones that had the least drag torque down to -60°C and retrofitted them into the flight DDA bearings. These bearings were then tested by themselves in a fixture, showing a torque of 1.6 oz-in. at -60°C .

If high torque occurred with these bearings in the DDA, it would not be due to the bearings by themselves.

DDA Retest in CO_2 Gas-Cooled Cold Chamber

With the reworked bearings back in the DDA, a cold test was performed in an atmospheric pressure cold chamber, using CO_2 gas as the coolant, to speed up the test and minimize temperature gradients. All subsequent tests were run in the cold chamber until the problem was solved.

This test indicated high torque again (Curve 3 on Figure 5) and proved that there was a problem other than in the bearings.

Bearing Slip-Fit Tests

The upper bearing outer race was a nominal 0.001 in. loose in its housing. CTEs for 440C steel and 6 Al-4V titanium are 5.8 and $4.8 \times 10^{-6}/^{\circ}\text{F}$ respectively. Therefore, the 3.88 in. bearing ring should have become 0.5 mil looser as the unit cooled down. Loss of the slip fit should not have been the problem unless severe out-of-roundness was taking place, or unless the bearing ring was much warmer (30°C) than the housing.

This DDA had 0.0061 in. of end play measured at room temperature. The aluminum shaft was 7.8 in. long and the aluminum housing was 3.8 in. long. Titanium parts and the steel bearings made up the other 4 in. Because of the difference in CTEs for aluminum and titanium (4.8 and $12.7 \times 10^{-6}/^{\circ}\text{F}$), end play would be reduced about 4 mils at -50°C , assuming uniform temperature. If the shaft cooled faster than the housing, another 0.5 mil would be lost for every 10°C of temperature gradient. In the cold box, with cooling by circulating CO_2 gas, the housing should have been colder than the shaft and loss of end play should not have been the problem.

Nevertheless, a simple fixture was made with which we could manually feel end play with the drive stopped. In the first test, we could no longer detect any play at -25°C and torque was up to 8 oz-in. A new preload ring giving 9 mils of end play was installed. Now some play was still detectable at -33°C but torque had reached 10 oz-in. (see Curve 4, Figure 5). Since all subsequent tests will be run with increased end play, Curve 4 will be used as a baseline for evaluating effects of changes.

These tests showed that loss of end play or sliding fit of the upper bearing was not the problem. The unit was then tested upside down with increased

end play. Torque was only 3.5 oz-in. at -50°C (see Curve 5, Figure 5). Comparing results with Curve 2, Figure 4, when the drive was upside down in a thermal vacuum test, it appears that increased end play and/or the difference in cooling method caused a major improvement. We did not determine the reasons for this improvement.

Torque Noise Determination

For the preceding test, we had started to record the motor current signal. The drive was being run open-loop, with a fixed voltage across the motor. Voltage was manually adjusted from time to time, as average torque changed, to maintain a nominal 60 RPM.

In this operating mode, when a transient torque rise occurs, the drive slows down. The lower speed causes reduced back EMF, permitting more current to flow. Since motor torque is proportional to current, operation is basically stable. Furthermore, the motor current trace gives a direct indication of the frequency of torque disturbances and an indirect indication of their amplitudes.

During the tests with greater end play, motor current recordings showed that drag torque was fluctuating cyclically and that the frequencies were ones characteristic of the bearings. It was also discovered that, with the drive upside down, torque noise amplitude was only about 10 percent of the right side up value.

Correlation of torque noise frequency to the bearings was to be expected, but these results caused us to focus our attention on the lower bearing mounts. We knew that the bearing by itself did not cause high torque, and we knew that, when it ran essentially unloaded (drive upside down), overall torque stayed low, at least in the cold chamber.

Test With Two New Lower Bearing Mounts

Because we now suspected the lower bearing mounting hardware, a new, simple outer ring mounting plate (end plate) was made from mild steel, and a spare engineering model stubshaft was located. Both bearing ring fits were made nominally 0.001 in. loose instead of line-to-line to tight, as on the flight hardware, and end play was adjusted to 9 mils. As shown by Curve 6 in Figure 6, these changes were magic! Torque was below 4 oz-in. at -50°C with the DDA right side up. We now had to discover why.

Test With Different Stubshaft Alone

The next experiment was to try the new stubshaft by itself, with the flight end plate. Again torque stayed low, perfectly duplicating results of the previous test with both lower bearing mounts changed. Data points from this test (x's) mingle with the ones of the previous test (o's) on Curve 6.

From this test result, we concluded that the end plate did not enter into the problem, but later we came to a different conclusion.

Lower-Bearing Inner-Ring Fit Test

The engineering model stubshaft which presented such favorable results had an undersize bearing journal that resulted in a 1-mil clearance with the bearing. To find out if this was making such a significant difference, the bore of a spare bearing was ground out to a 1-mil clearance with the flight stubshaft. When this combination was evaluated with the flight end plate, torque was again high and duplicated Curve 4, Figure 5 (7.6 oz-in. at -25°C).

This test showed that the snug inner ring fit of the lower bearing did not cause the problem.

Tests With New End Plate Alone

Going back to both flight bearings, we tried the flight stubshaft with the special steel end plate. We had already shown that the combination of flight end plate and special stubshaft was just as good as the special end plate and special stubshaft, so we might have expected that the new configuration would bring us all the way back to our original high torque curve. This did not occur. The special end plate used with the regular stubshaft somehow significantly reduced the adverse effect of the flight stubshaft (see Curve 7, Figure 6). We then rotated the special end plate 90 degrees and found that this greatly reduced the improvement (8.1 oz-in. at -36°C). Returning it to its original position resulted in repetition of Curve 7 results.

We now saw that the end plate might contribute to or ameliorate the torque problem, depending on its angular location with respect to the main aluminum housing to which it was attached.

Tests With Regular End Plate in Different Positions

With this new knowledge, a series of tests with the flight end plate in different angular positions was conducted. We discovered that flight end plate position did indeed affect low temperature torque, and that results at any position were quite repeatable. Furthermore, the position for the as-built DDA was the worst one - somebody's law at work! In its most favorable position, the drag torque was as shown by Curve 8, Figure 7. Instead of over 20 oz-in. at -50°C , we had only 7.5 oz-in., and the sharp knee in the curve was gone. Compare Curve 8 with baseline Curve 4, which has been repeated in Figure 7, for reference.

Stubshaft Tests

Results by this time led to close scrutiny of the flight stubshaft. The first test was to rotate it 180 degrees with respect to the main aluminum shaft. Results essentially duplicated Curve 8 (7.4 oz-in. at -46°C). We then

made a series of measurements on the flight and engineering model stubshafts to try to discover any significant differences (see Figure 8 for stubshaft details):

- Axial distortion between shaft flange and bearing thrust shoulder as temperature was reduced to -50°C . On the flight part, we found 0.0001 in. and 0.0002 in. change in two locations, while the engineering model stubshaft was worse (0.0004 in.).
- Changes in two bearing journal diameters, 90 degrees apart, between room temperature and -50°C . Both diameters on both parts changed the same amount (-0.0016 and -0.0017 in.).
- Roundness of bearing journals. The flight journal was round within 0.0001 in. while the engineering model part was off as much as 0.0004 in. Since the latter journal was intentionally undersize and a loose fit, any effect of the poor journal roundness would have been suppressed. Excellent roundness of the flight journal indicated that it could not be a problem.
- Concentricity between bearing journal and pilot diameter. Flight part concentricity was within 0.0003 in. while the engineering model part showed 0.0001 in. This difference seemed negligible.
- The flight journal was larger than the engineering model journal, and was also 0.4 mil over the drawing dimension. This diametral difference had already been discounted by test results.
- Parallelism between the shaft flange face and the bearing thrust shoulder. The engineering model stubshaft showed essential parallelism, but the flight part was off 0.0007 in. For the 3.2 in. diameter of the thrust shoulder, this corresponds to an angular deviation of 0.8 arcminute.

The only significant difference that was worse on the flight stubshaft was the seemingly insignificant reduced parallelism between flange and bearing thrust shoulder. With the bearing ring slightly tight on the journal, so that it should only bottom out on the high point of the shoulder, it hardly seemed possible that this could make any functional difference. Nevertheless, we promptly made a mild steel stubshaft, duplicating the flight bearing journal diameter with its tight fit to the flight bearing, but holding parallelism of the two critical surfaces within 0.0001 in. When this part was tried out in the DDA, Curve 9, Figure 7, we had found another piece in the puzzle. The new stubshaft was noticeably better, bringing -50°C torque down to the 6-7 oz-in. range.

With this finding, we had the flight stubshaft thrust face trued up on a jig grinder (measured parallel to the shaft flange within 0.3 arcminute) while removing 0.0005 in. from the journal. The DDA now tested even better than

with the new steel stubshaft, illustrated by Curve 10, Figure 7, after being cleaned up and made ready to repeat some of the formal acceptance tests. At -50°C , torque was 5 oz-in., just meeting the original specification requirement.

Improving parallelism between the bearing thrust shoulder and shaft flange, and slightly opening the inner bearing ring fit, had made a further significant reduction in -50°C torque.

Acceptance Test and Other Results - Complete Success

During acceptance tests, drag torque was measured in vacuum at 22°C and -51°C , where it was 2.6 and 3.4 oz-in. Curve 11 on Figure 7 shows these final results.

The second flight DDA also had high torque when cold. It was corrected exactly the same way, by trueing the stubshaft and finding the best position for the end plate.

HELIOS B was operational for four years until a TWT failure occurred. HELIOS A was still going in December 1984, ten years after launch. We were told that its drive had been turned off for 29 days during 1982 to conserve battery power, because solar cell degradation had occurred. Apparently the DDA whose travails are discussed here ran nearly continuously at 60 RPM for ten years. It may still be running as this is written in December 1986, twelve years from launch.

CONCLUSIONS

The preceding sections have ended with "what" conclusions, when applicable. It remains to decide the "whys." As soon as the problem was corrected, no more funds were available from this fixed price program for further investigation, so the only evidence to work with is summarized here.

The lower bearing inner race seat was not quite perpendicular to the shaft axis, after assembly. (This is presumed from the piece-part measurement.) With this bearing on top, so that it was unloaded, the small deviation made no difference. At room temperature and with a 10-lb load, there was no difference, but at -50°C the difference was significant. Improving the perpendicularity error from 0.8 arcminute to 0.3 arcminute dropped bearing drag at -50°C about 40 percent. Why?

With a steel end plate, which had a slip fit for the lower bearing outer race, and a stubshaft that did not have the bearing shoulder perpendicularity error, the torque problem disappeared. Replacing the new end plate with the flight plate did not affect these favorable results. The problem must have been with the stubshaft alone. Yet, when we then combined the original stubshaft with the new end plate, torque was much better than with the flight plate. Furthermore, rotating the plate to a different position with respect

to its mating housing changed results substantially. Then we discovered that rotating the regular flight end plate to different positions on the housing caused even greater effects on torque. In the most favorable position, torque was greatly reduced. Why?

Starting with the end plate, one must assume thermal distortion caused by anisotropic properties. But then, since the plate rotated at 60 RPM, why would its position relative to the aluminum housing make a difference? Distortion in the housing must also have occurred. Since torque was sensitive to the relative position of both parts, both must have distorted and there was some position where effects were compensating, or largely so. This also indicates that the distortions were not rotationally symmetrical. Since neither the engineering nor qualification models showed the problem, it is also clear that it was not inherent in the design. Both the end plate and housing must have been anisotropic and we were fortunate that the effects were compensating at some position of the two.

The stubshaft is more puzzling. This piece, with short axial dimensions, was fastened to a long aluminum tube with great axial rigidity by twelve screws. The tube should have been dominant, yet there were very significant performance differences between two quite similar parts. Apparently valid thermal distortion measurements on these parts in the free state showed the part that performed better was, if anything, slightly less isotropic. Did the seemingly small perpendicularity problem on the flight part add to some thermal change on the shaft and just carry the assembly over a critical threshold? It appears that this must have been the case.

ORIGINAL PAGE IS
OF POOR QUALITY

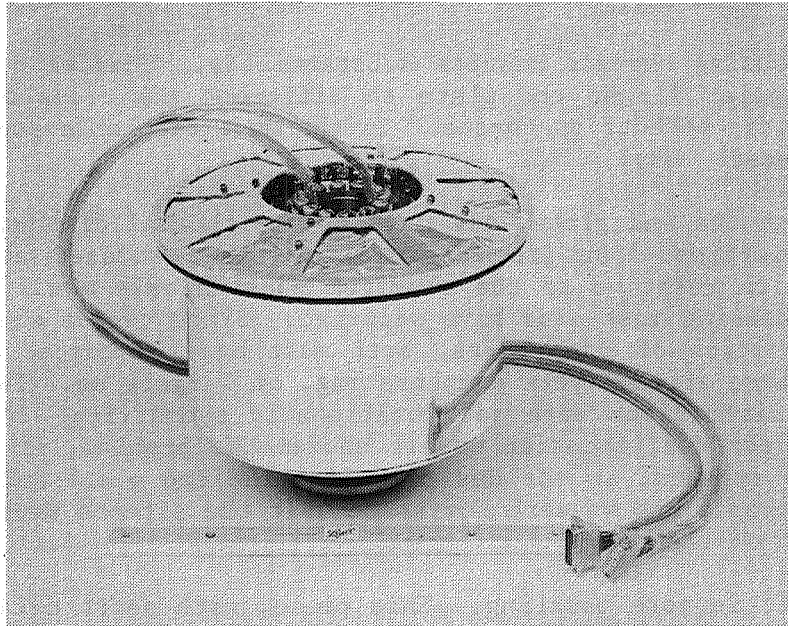


Figure 1 Despin drive assembly

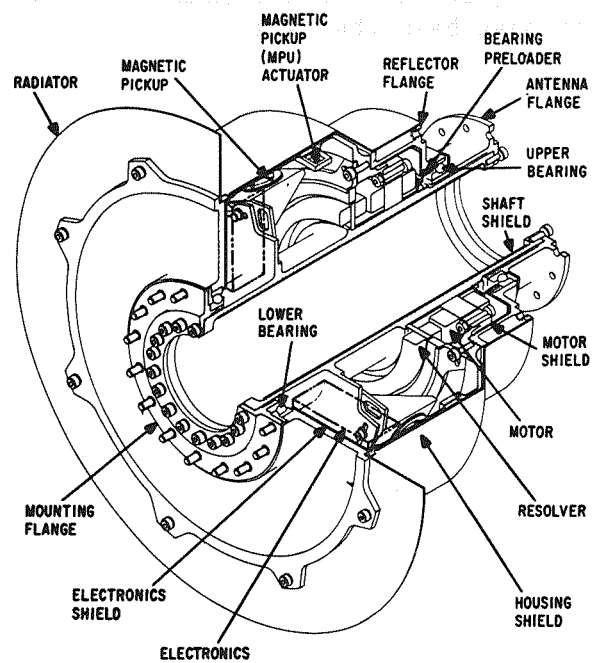
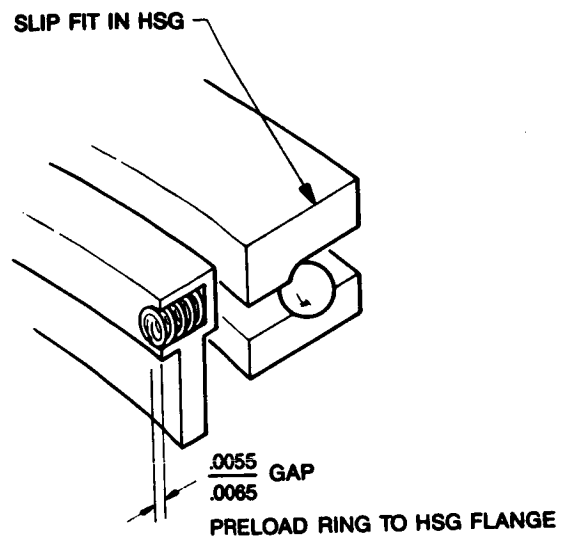


Figure 2 EMS-331 despin drive assembly



DETAIL A

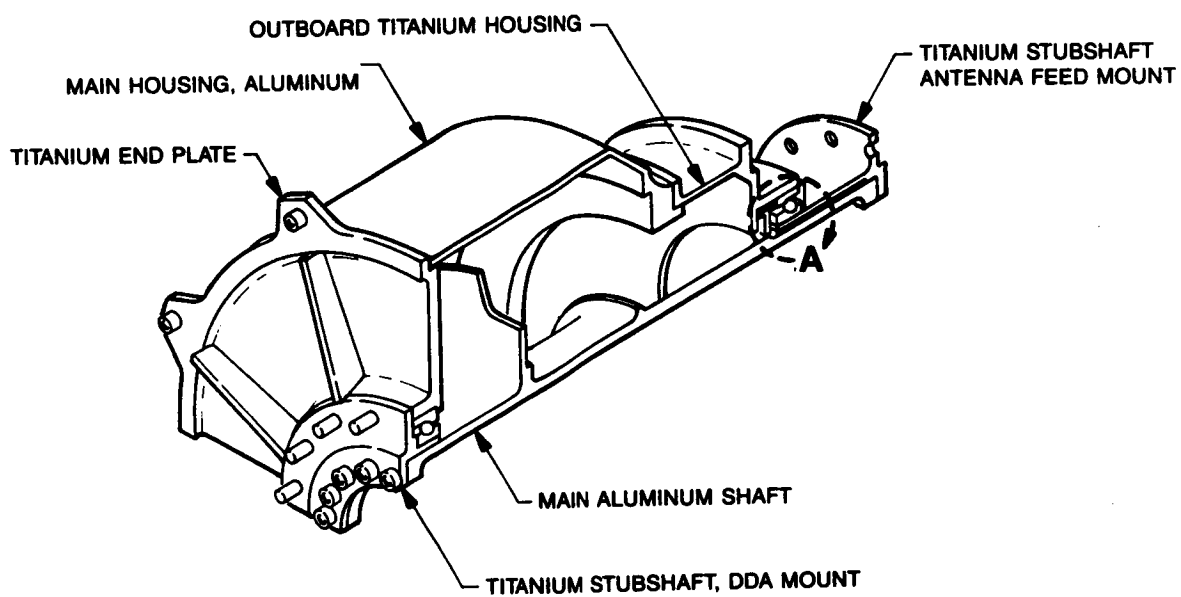


Figure 3 Bearing installations

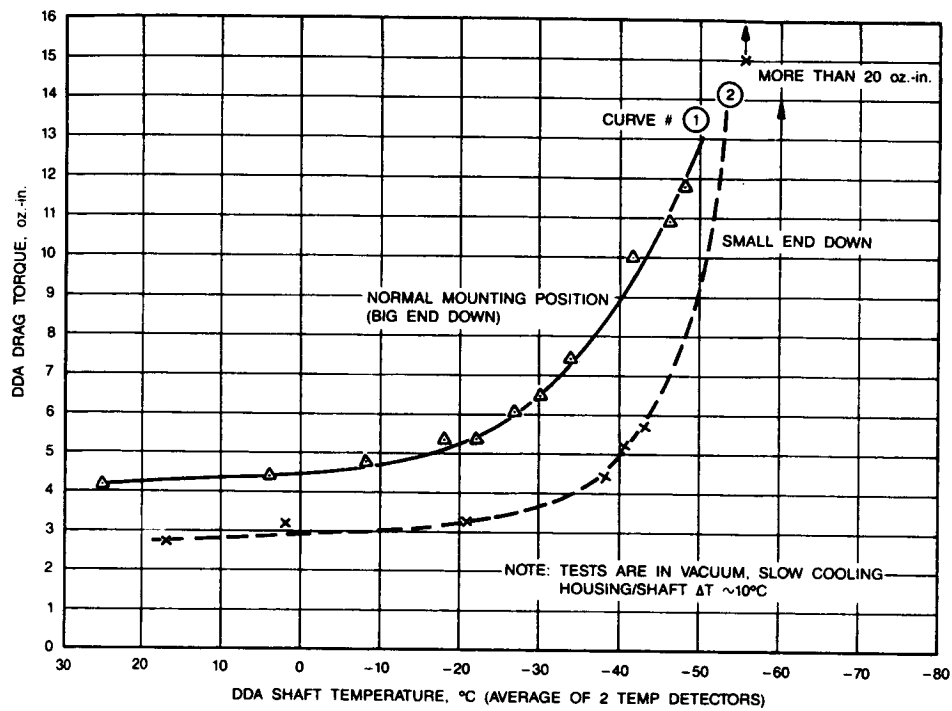


Figure 4 Torque vs. temperature, 1st flight DDA in thermal vacuum chamber

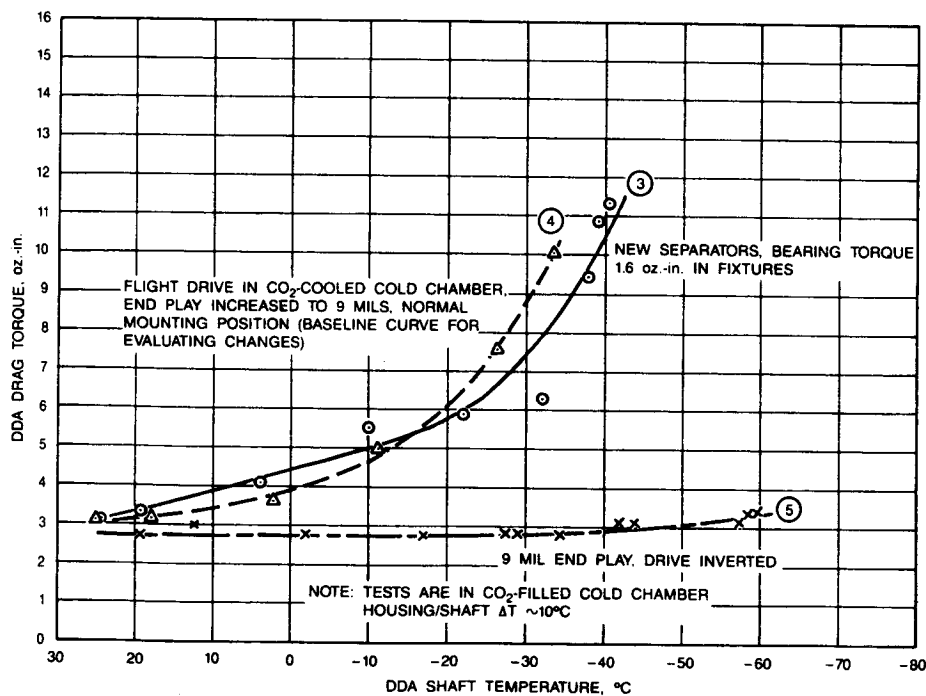


Figure 5 Cold chamber test results with new bearing separators and increased end play

ORIGINAL PAGE IS
OF POOR QUALITY

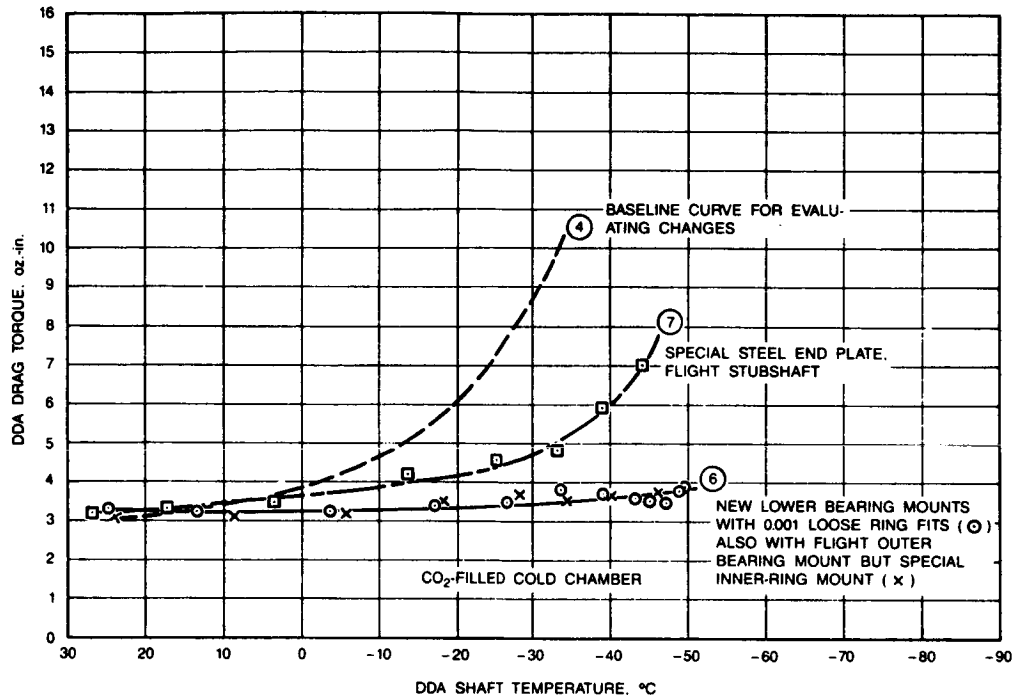


Figure 6 Performance with new lower bearing mounts

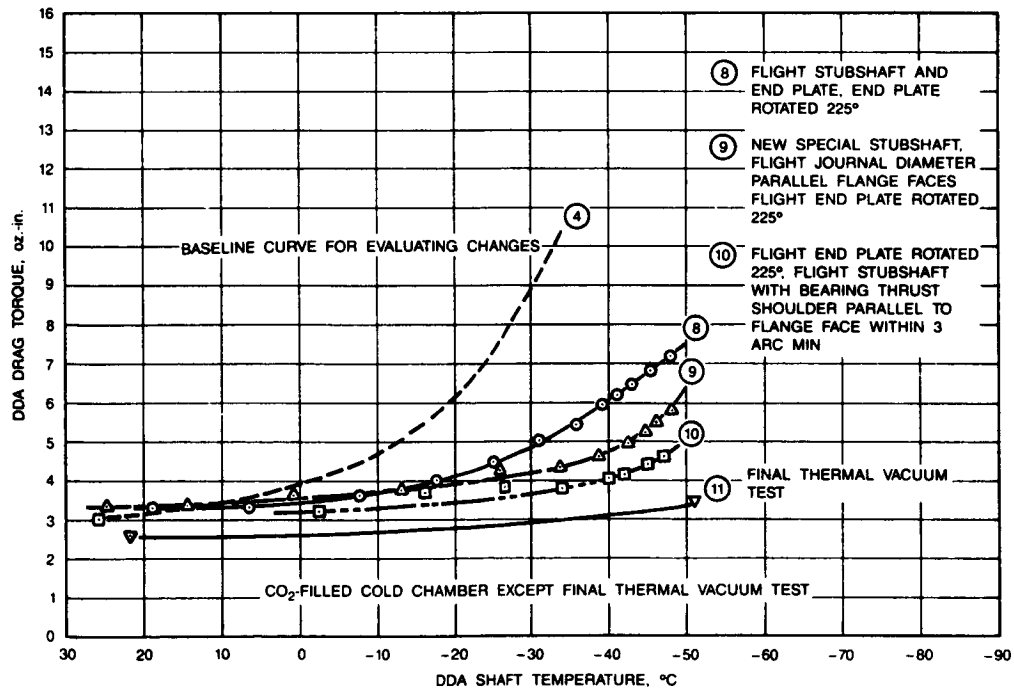


Figure 7 Performance with bearing mount changes that corrected the problem

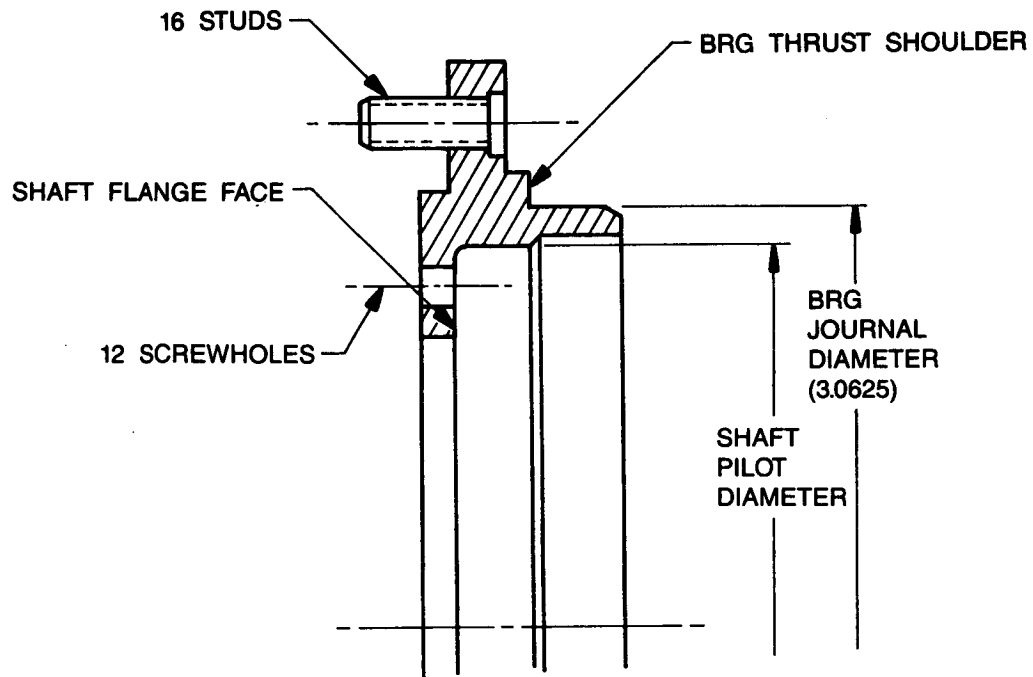


Figure 8 Lower stubshaft configuration

SPACE STATION ALPHA JOINT BEARING

Michael R. Everman^{*}, P. Alan Jones^{*}, Porter A. Spencer^{**}

ABSTRACT

Perhaps the most critical structural system aboard the Space Station is the Solar Alpha Rotary Joint which helps align the power generation system with the sun (Figure 1). The joint must provide structural support and controlled rotation to the outboard transverse booms as well as power and data transfer across the joint. The Solar Alpha Rotary Joint is composed of two transition sections and an integral, large-diameter bearing. Alpha joint bearing design presents a particularly interesting problem because of its large size and need for high reliability, stiffness, and on-orbit maintainability.

The discrete roller bearing developed is a novel refinement to cam follower technology (Figure 2). It offers thermal compensation and ease of on-orbit maintenance that are not found in conventional rolling element bearings. This paper is a summary of how the bearing design evolved. Driving requirements are reviewed, alternative concepts assessed, and the selected design is described.

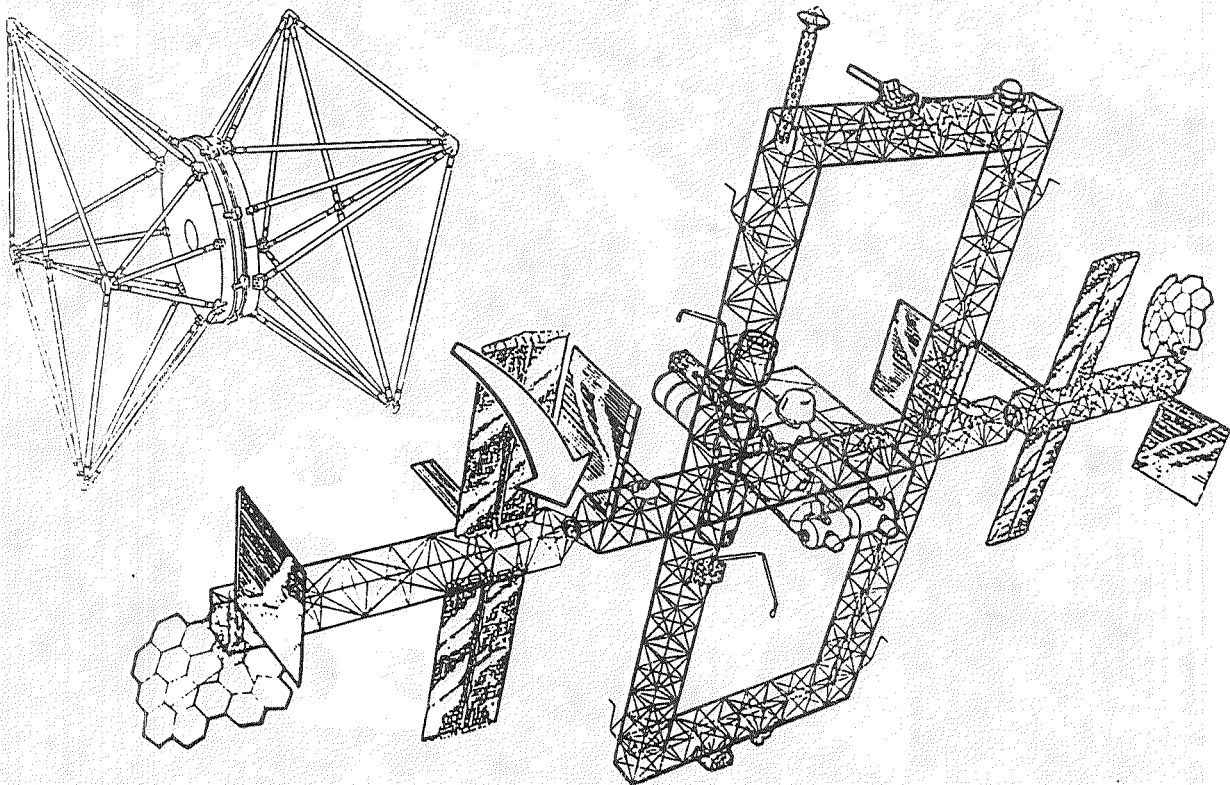


Figure 1: Dual Keel Space Station

^{*}AEC-Able Engineering Co., Goleta, CA

^{**}Lockheed Missiles and Space Co., Sunnyvale, CA

ORIGINAL PAGE IS
OF POOR QUALITY

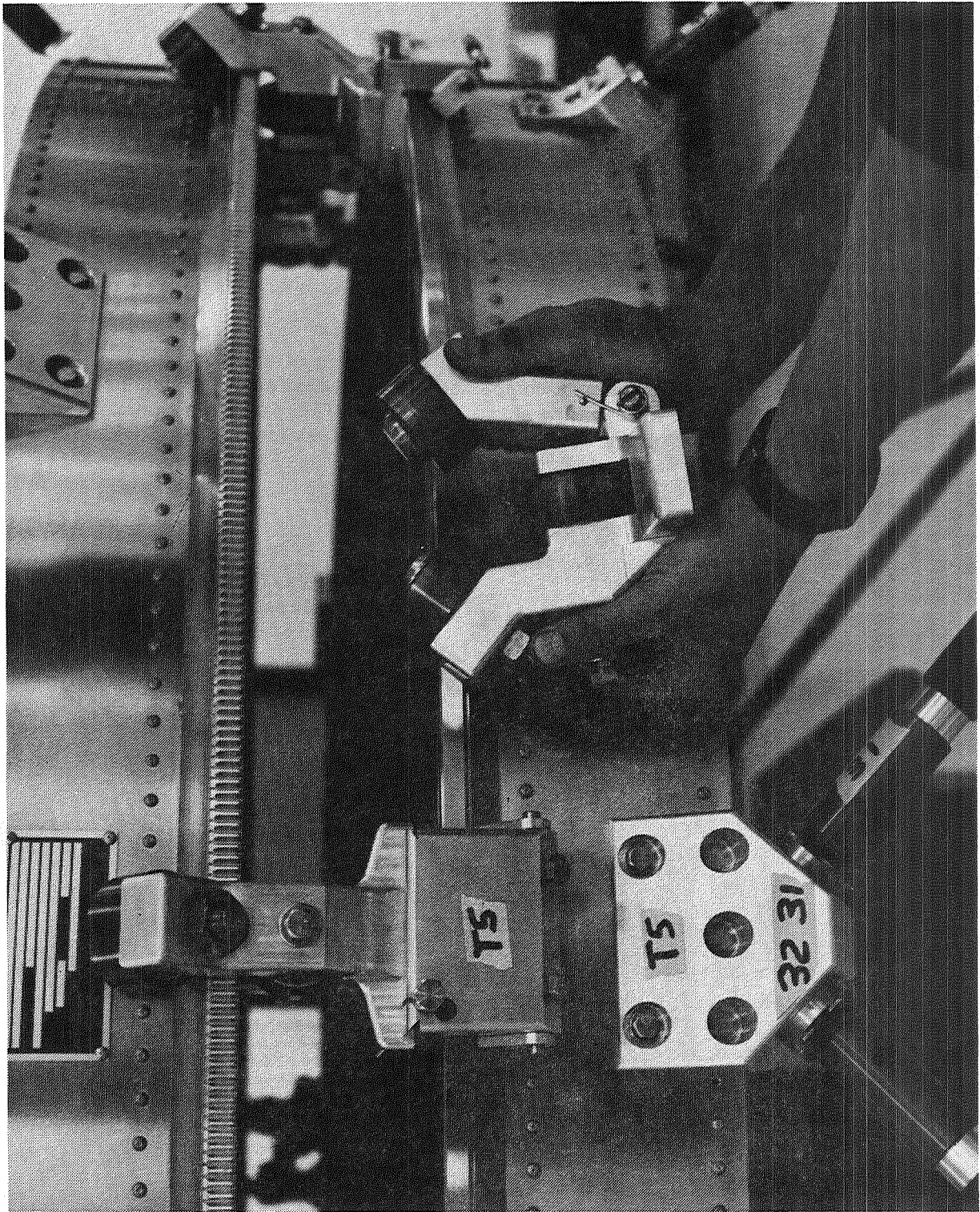


Figure 2: Discrete Roller Bearing

REQUIREMENTS

The alpha joint is designed to meet the performance requirements presented in Table 1.

Table I: Alpha Joint Requirements

Travel	360°	360°
Operational Life	Indefinite	Indefinite
Pointing Accuracy (degree)	±3.0	±3.0
Rotation Rate (deg/min)		
Maximum Slew/		
Nominal Tracking	30/3.8	30/3.8
Acceleration (deg/sec ²)	0.005	0.005
Bending Loads		
Maximum	47,451 (N-m)	420,000 (in.-lb)
Nominal	14,122 (N-m)	125,000 (in.-lb)
Shear Loads		
Maximum	2224 (N)	500 (lb)
Nominal	890 (N)	200 (lb)
Torsional Loads		
Maximum	20,336 (N-m)	180,000 (in.-lb)
Nominal	3107 (N-m)	27,500 (in.-lb)
Inertia Loads	5.15 x 10 ⁶ kg-m ²	3.8 x 10 ⁶ (slug-ft ²)
Stiffness		
Bending	1.81 x 10 ⁸ (N-m/rad)	1.6 x 10 ⁹ (in.-lb/rad)
Torsion	4.745 x 10 ⁷ (N-m/rad)	4.2 x 10 ⁸ (in.-lb/rad)
Shear	1.243 x 10 ⁷ N/m	7.1 x 10 ⁴ (lb/in.)

While loads, acceleration rates and inertias have a definite influence, the thermal environment, high stiffness, and need for a highly reliable and maintainable system became the primary design drivers.

Because the bearing is so large (3.05 m) (120 inches) in diameter, tolerances and clearances are critically sensitive to thermal deformation. During operation the bearing is heated by solar irradiation on one side while being exposed to deep space on the opposite side. In addition, a power transfer module located coaxially within the bearing is a source of waste heat that tends to warm the interior of the bearing. With these

factors in mind it was determined that the bearing must be tolerant to both out-of-round and inner race expansion conditions.

The alpha joint structurally supports the large power generation system wing. Stiffness of the joint is important because as stiffness is degraded the fundamental frequency of the wing lowers and introduces dynamic conditions that are more difficult to control.

The Space Station is designed for a twenty year life, extendable indefinitely through maintenance. The alpha joint is critical to mission success because, in the event of failure, power generation capability and mission capability would be severely degraded: payloads would have to be shut down and mission activities would have to be curtailed in an effort to conserve power. Therefore, ease of on-orbit maintenance is desirable.

BEARING TRADE STUDIES

The bearing concepts selected for analysis were four point contact, crossed roller, three row roller, and discrete follower. The four point contact was discarded due to an intolerable wear condition under a bending moment load. To meet the requirement of thermal compatibility the remaining bearing concepts were modified to provide added radial compliance to induced thermal strains (Figure 3). This passive approach to thermal compatibility is less complex and less costly than an active approach. The crossed roller and three row roller designs were discarded because they are difficult to maintain and prohibitively complex to manufacture. A failure of a continuous race bearing requires partial station disassembly, significant loss of power generation and myriad support equipment to replace the entire bearing. Manufacturers of large diameter bearings declined to bid on the thermally compensated designs citing excessive risk. The discrete follower bearing was then selected for detailed design and development.

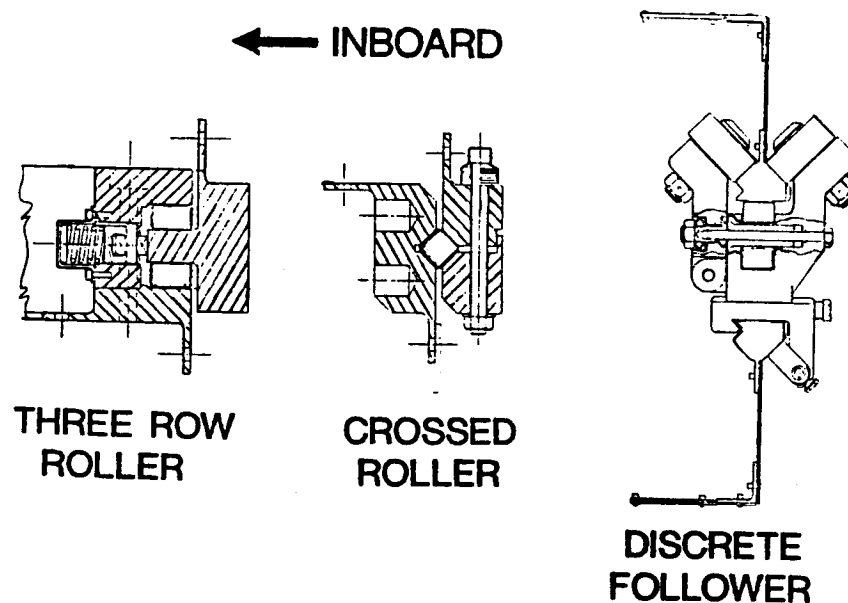


Figure 3: Temperature Compensating Bearing

DISCRETE ROLLER BEARING DESCRIPTION

Discrete Roller Package

The geometry of this system is such that the rotating and non-rotating structures are identical (Figure 4). Reasons for this are: (1) the two structures have matched thermal expansion properties, (2) a redundant ring race is provided, and (3) identical transition structures may be used, saving cost by increasing commonality.

Bearing packages are composed of the three roller bearings, a preload arm, yoke, and dovetail mount. The package spring preload reduces the drive torque variance should there be any variance in the race cross-section. The individual rollers are chosen for low Hertzian stress between the roller outside diameter and the ring race surface. Life expectancy of these bearings is in excess of the system lifespan. Each roller contains a self-alignment feature that provides a degree of freedom such that line contact is maintained at all times with the ring race.

The roller package is installed radially with a dovetail mount. Tightening of the main attachment bolt initiates the full predetermined preload. This bolt cannot change the preload if overtightened. Each roller package is allowed to align itself on the diameter of the rolling race before the dovetail is tightened down. The dovetail mounting is then tightened down to complete the change-out. The mounting block is attached to the triangular ring race on the non-rotating side of the joint. In case of a roller failure, the package can be easily replaced by extravehicular activity (EVA) without sophisticated aligning techniques. Should the rotating race be damaged, then all mounting blocks can be removed sequentially and placed on the formerly-rotating race to utilize the redundant race.

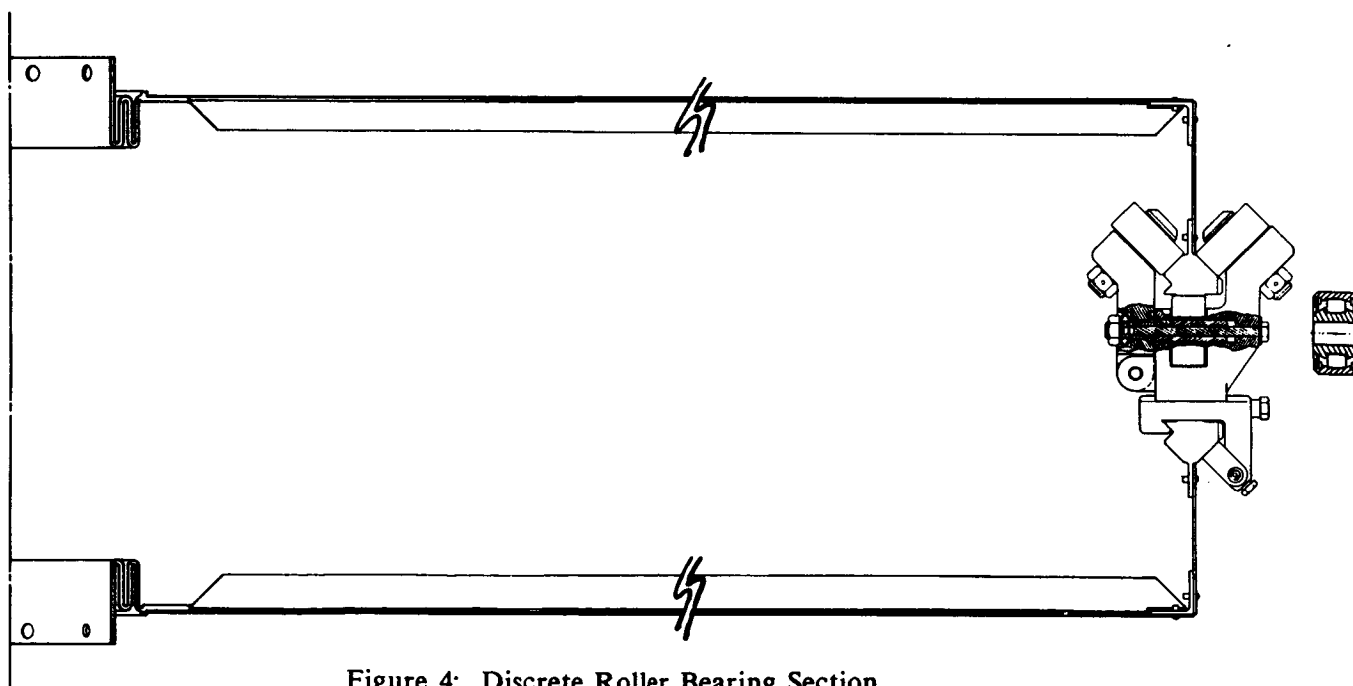


Figure 4: Discrete Roller Bearing Section

Bearing Race and Skirts

The skirts which support the triangular bearing races serve two functions: (1) their height and thickness provide axial stiffness between load inputs and (2) their radial compliance lessens the impact of thermal distortions and manufacturing out-of-roundness.

Shear Panel

Each half of the alpha joint transition structure must have a radial stiffener for two reasons. First, because of the offset between the bearing diameter and the main truss, the transition struts must join the bearing at some angle and therefore transmit load radially as well as axially. Second, since the bearing skirts are designed to be radially compliant (to reduce roller loads in response to thermal gradients and manufacturing tolerances) the transition radial loads must be accommodated for above the skirt. The shear panel is the only area in which radial stiffness is important, i.e., resolving the radial component of bending moment load.

DISCRETE FOLLOWER ANALYTICAL CONSIDERATIONS

Roller Bearing

One of the critical design parameters is the fatigue life at the race to roller interface. Since there are fewer load carrying elements than a similar continuous rolling element bearing, the loads per roller are greater. To determine these loads it was assumed that under a bending moment load the bearing races remained planar and thus produced a linear load distribution. The maximum operational roller axial load of 3389 kg (762 pounds) occurs at zero degrees of transition structure offset.

Now the amount of bearing preload can be defined. The preload spring constant can be deleted from the system stiffness calculation if the preload is larger than the expected operational load. This is possible since, as the preloaded package is loaded, the preload arm does not move and therefore the loads in the outboard rollers are constant. With the application of a tension load the preload on the center roller reduces to maintain equilibrium. A compressive load directly increases the load on the center roller. In this way the axial loads are "accommodated" by a variation of the center roller preload. Due to the geometry of the preload arm, the load at the springs must be 4408 N (991 pounds) to obtain a 1696 N (381 pound) load at the outboard rollers. This results in a 3389 N (762 pound) normal preload on the center roller. To obtain the 4408 N (991 pounds) of spring force, two serial rows of three parallel 1.27 cm (one half inch) inner diameter Belleville washers are used.

With the internal load distribution defined, it is possible to calculate contact stresses by¹:

$$\sigma_c = 0.798 \{ \bar{P} / D_R W_R [(1 - \nu_R^2) / E_R + (1 - \nu_r^2) / E_r] \}^{1/2} \quad (1)$$

where

D_R, W_R	...Roller dimensions
ν_R, ν_r	...Poisson's ratio
E_R, E_r	...Material modulus
P	...Load

The loading, \bar{P} , that the race experiences varies with time. In order to determine the mean and alternating stress levels a time averaged loading must be determined. Resulting loads are:

race loads			
mean	=	89 N	(20 lb)
alternating	=	2157 N	(485 lb)

Roller loads			
mean	=	342 N	(77 lb)
alternating	=	2157 N	(485 lb)

The fatigue life requirements of the race material are determined by the requirement that the alpha joint system rotate for 20 years at 1 revolution every 94 minutes. The resulting required lives are:

L10 RACE	=	1.40×10^6 cycles
L10 ROLLER	=	1.05×10^7 cycles

These values include a safety factor of 1.5.

Expected fatigue lives were determined from the mean and alternating contact stress levels. From those results the race material was selected to be Al 7075-T7351 and the roller was selected to be Ti 6Al-4V. This choice gives a race life margin of 0.51 and a roller margin of 0.50.

Drive Requirements

The alpha joint drive system must impart enough torque to the system to overcome the various frictional losses as well as accelerate the system at the required rate. Table I

1. Roark, R. J., Formulas for Stress and Strain, McGraw-Hill, 4th Edition, 1965, p. 320.

gives the maximum rotational acceleration as 0.005 deg/sec². The required torque can then be expressed as:

$$T_{REQ} = I\alpha + 8(R\mu\sum F_{pre}) + T_{RR} \quad (2)$$

where

- α ...Rotational acceleration.
- I ...Inertial load outboard of alpha joint.
- R ...Bearing radius.
- μ ...Frictional coefficient of roller bearing.
- $\sum F_{pre}$...Summation of trundle preload forces (8184 N/1840 lb)
- T_{RR} ...Torque loss of roll ring power transfer (6.8 N-m/60 in.-lb)

Lowenthal² gives the roller frictional coefficient as 0.003 which when coupled with a 60.0 radius and the inertial load in Table I gives:

$$T_{REQ} = 1065 \text{ N-m (9398 in-lb)}$$

This includes a margin of 1.0 on frictional losses. This torque corresponds to a total drive shear force requirement of 697 N (157 lb) at the bearing race.

Temperature Gradient Capability

The loading of the roller packages due to a thermally-induced strain is dependent on the stiffnesses of the skirt and the race ring. When the races are thermally displaced, three deformations occur (Figure 5). The skirt will experience a bending which creates a distributed shear load at the race. This shear load transmitted through the offset roller packages creates a moment that induces additional radial and angular deflection. Deformation must occur in the ring race as it is strained to match the skirt deflection at the eight roller locations. The coupled radial stiffness for this deformation is given as:

$$K_R = \frac{(\pi D R^4 \beta / 2EI) + (2/\lambda^3) + (1/\lambda^2)}{\beta R^3 / 2EI [(4/\lambda^3) + (4I/\lambda^2) + (2I^2/\lambda)]} \quad (3)$$

where

- D = $Et^3/12(1 - \nu^2)$
- λ = $[3(1 - \nu^2)/R^2t^2]^{1/4}$
- β = $(1/\sin^2\Theta)[(\Theta/2) + (\sin\Theta\cos\Theta/2)] - 1/\Theta$
- E Material modulus
- t Skirt thickness
- ν Material poisson's ratio
- R Bearing diameter
- Θ Half the angular gap between packages
- I Ring race moment of inertia

2. Lowenthal, S. H., and Schuller, F. T., "Feasibility Study of a Discrete Bearing/Roller Drive Rotary Joint for the Space Station", NASA Lewis TM-88800, July 1986.

When evaluated for the baseline design, the radial stiffness is:

$$K_R = 12067 \text{ N/cm (6891 lb/in.)}$$

For a temperature gradient, ΔT , the induced radial strain is:

$$\delta_R = R \cdot \Delta T \cdot \text{CTE} \quad (4)$$

and the amount of tolerable temperature gradient is

$$\Delta T_{\max} = F_{\text{pre}} / K_R \cdot R \cdot \text{CTE} \quad (5)$$

For a preload force of 1696 N (381 pounds), this corresponds to a maximum thermal gradient of 21.6 °C (70.9 °F). However, this value is not the only constraint on the permissible thermal gradient. As the race to race offset becomes greater, structural stability to the axial loads decreases. This factor must be considered when defining a maximum permissible thermal gradient.

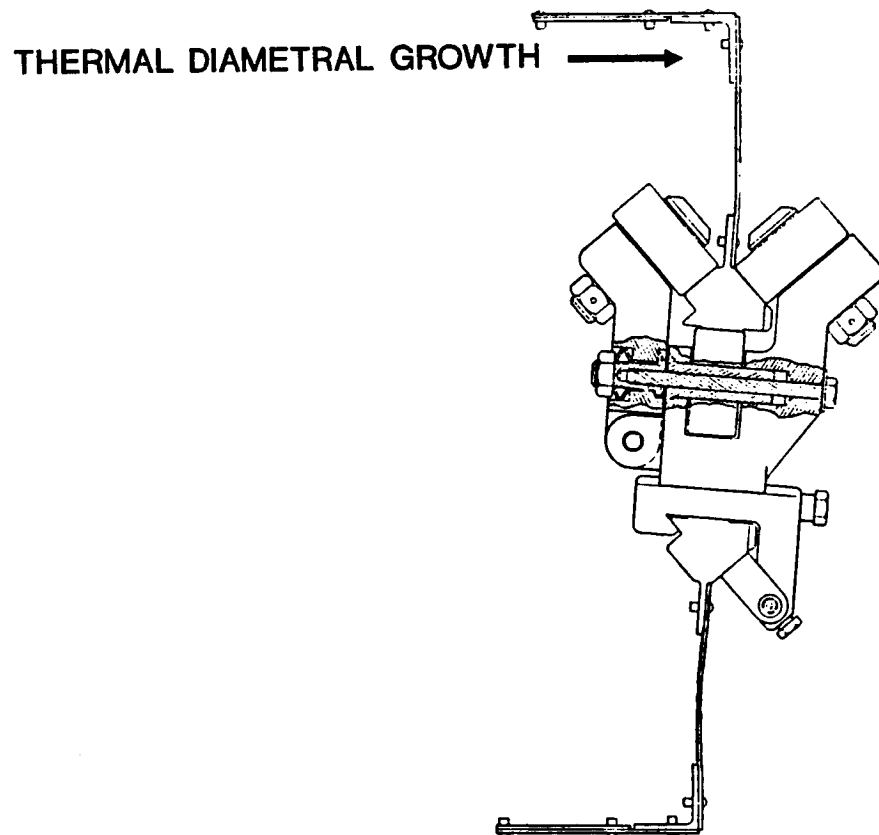


Figure 5: Thermally Strained Bearing

Alpha Joint System Analysis

In order to predict the global response of the alpha joint, finite element techniques were used. The basic method used was to separately model complicated mechanisms such as the race follower package and transition tube and fittings and then integrate their influence coefficients into a global model as general stiffness elements. Also incorporated into the model were standard structural elements. Stiffness predictions are given in Table II for various transition clockings.

Table II: Discrete Follower Analysis

	Transition Offset (Degrees)	Stiffness (N-m/rad) (in.-lb/rad)		Design Margin
Bending	22.5	1.81×10^8	1.60×10^9	0.0
Bending	0.0	3.60×10^8	3.19×10^9	0.099
Bending	45.0	3.46×10^8	3.06×10^9	0.091
Torsion	45.0	2.36×10^8	2.09×10^9	3.98
Shear	45.0	1.31×10^7 (N/m)	7.5×10^4 (lb/in.)	0.06

STRUCTURAL MODEL TESTING

Due to the uniqueness of the discrete roller bearing design and the importance of its application, it was deemed necessary to conduct a structural test program in the early phases of design development. To this end, a half-scale engineering model was designed, manufactured, and tested at AEC-Able Engineering Co. (Figure 6).

The primary objective of this testing program was to provide "real data" verification of the analytical techniques developed to characterize the discrete bearing design and to determine the presence of any hidden failure modes. In this light, analytical predictions were made for the half-scale model's stiffness. Corresponding structural tests were then performed. Results are presented in Table III and compared to predicted values. Figure 7 gives a sample chart of joint bending versus applied moment for the 22.5° transition offset configuration.

ORIGINAL PAGE IS
OF POOR QUALITY

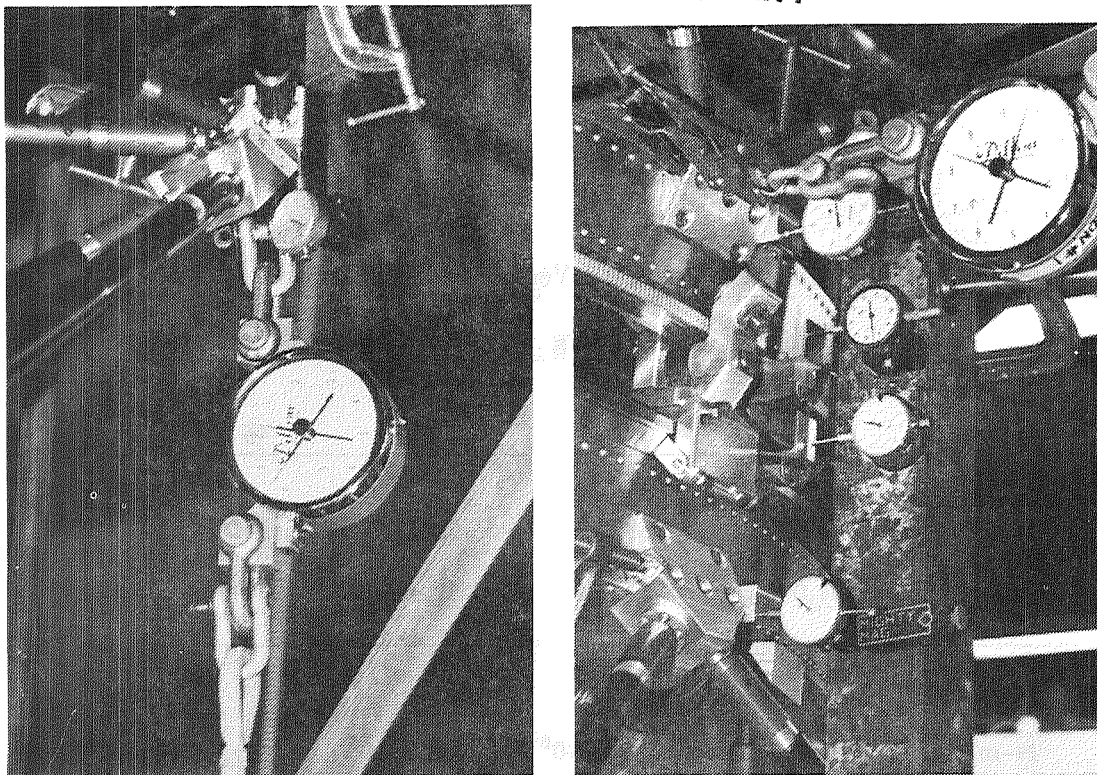


Figure 6: Bending, Shear Test Set-Ups

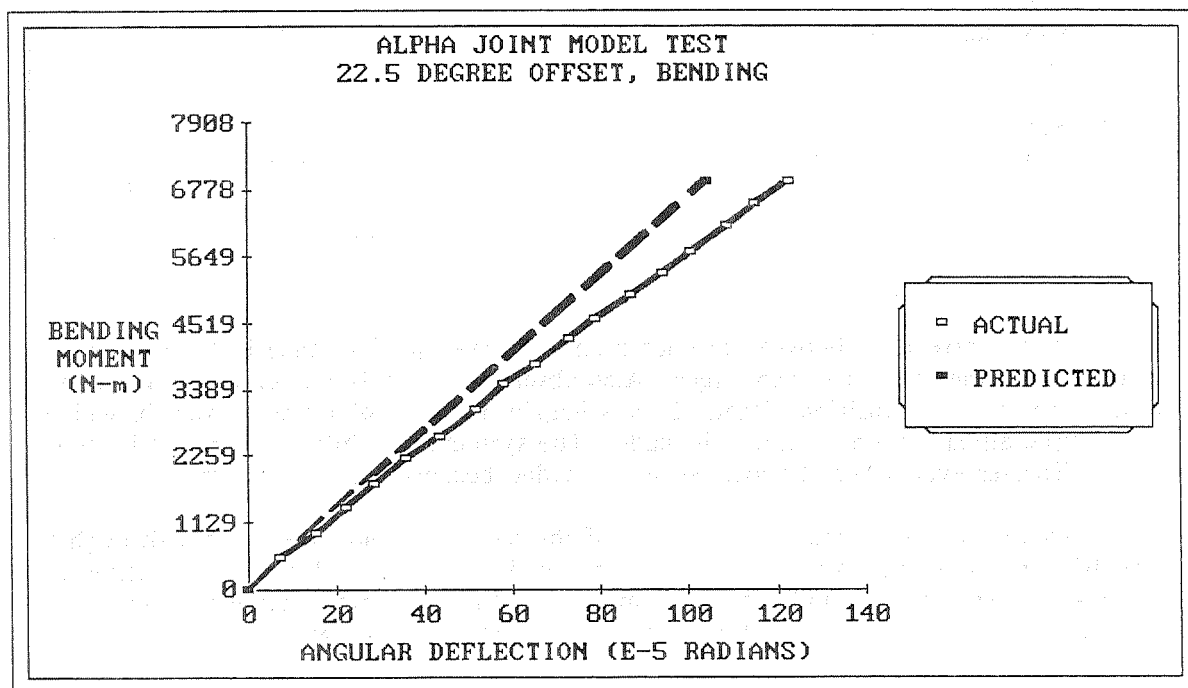


Figure 7: Bending Stiffness Test Results

Table III: Predicted Versus Actual Stiffness

	Bending	Bending	Bending	Torsional	Shear
Offset					
Degrees	22.5	0.0	45	45	45
Maximum Load					
N-m	6892	6892	6892	3451	
N					1334
in.-lb	61,000	61,000	61,000	30,547	
lb					300
Predicted Stiffness					
N-m/rad	6.47×10^6	7.3×10^6	7.3×10^6	1.05×10^7	
N-m					4.78×10^6
Actual Stiffness					
8 Packages					
N-m/rad	6.59×10^6	6.43×10^6	6.17×10^7	9.5×10^6	
N-m					4.32×10^6
7 Packages					
N-m/rad	5.10×10^6	6.05×10^6	5.84×10^6	-----	
N-m					3.82×10^6

The resulting correlation between predicted and observed performance instilled high confidence in the analytical techniques. Also observed was only moderate variation in joint stiffness with transition offset. This is helpful for control system design in which an isotropic alpha joint assumption is made. The system's reliability is verified by the high stiffnesses even when the most severely loaded bearing package is removed.

To verify the thermal compatibility of the bearing design, the current through a gear drive motor was monitored as the thermal load was varied. Both top-to-bottom and side-to-side temperature gradients were imposed. Minimal current variation was observed for either condition and a sample of the test data is shown in Figure 8 for the top-to-bottom thermal loading.

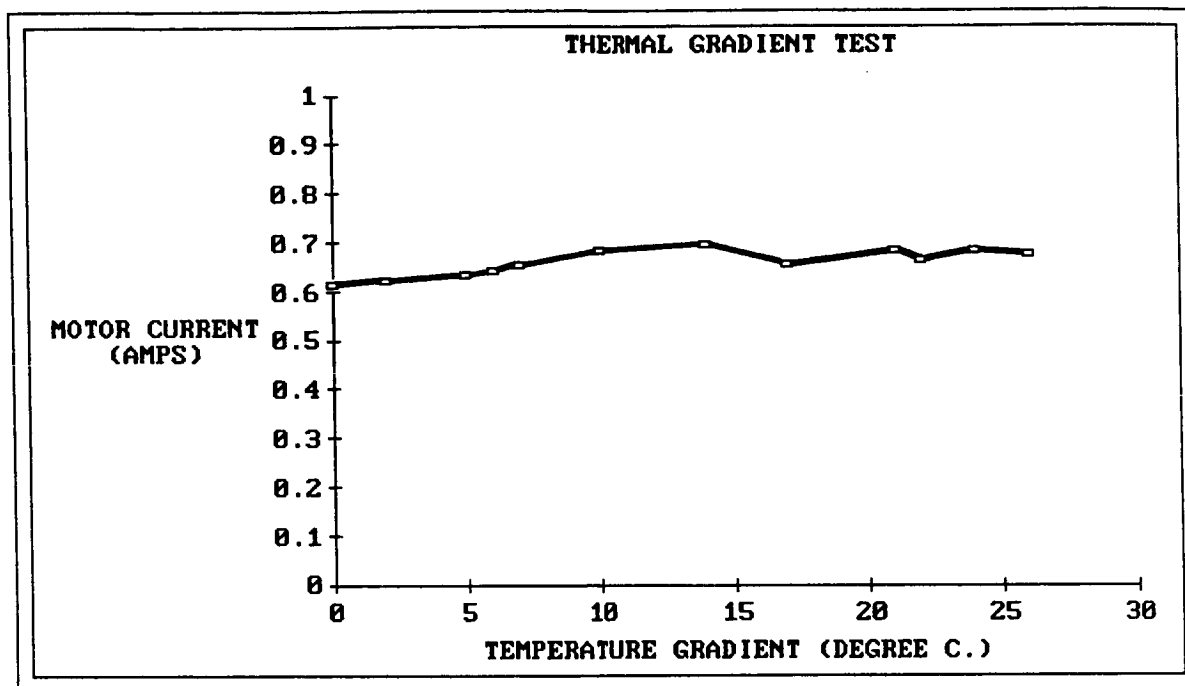


Figure 8: Thermal Gradient Test Results

In order to test the characteristics of the race-roller interface a straight rail tester was designed and built (Figure 9). The frictional load required to drive the race section through the roller packages was measured with a load cell as preload and temperatures were varied. Figure 10 depicts the variation of the drive friction with temperature. The room temperature value of the frictional coefficient (0.0029) verified that used in Equation 2 (0.003).

Lessons Learned

After prolonged running of the 162.5 cm (64 in.) diameter engineering model, minute aluminum deposits could be found on the inboard portions of the rollers. Tapering the rollers will eliminate this condition which is twice as extreme on the model than it would be at full scale. Further improvement can be made by installing finger guards around the rollers for safety. Further work shall include astronaut assembly simulation to provide inputs to maximize serviceability.

ORIGINAL PAGE IS
OF POOR QUALITY

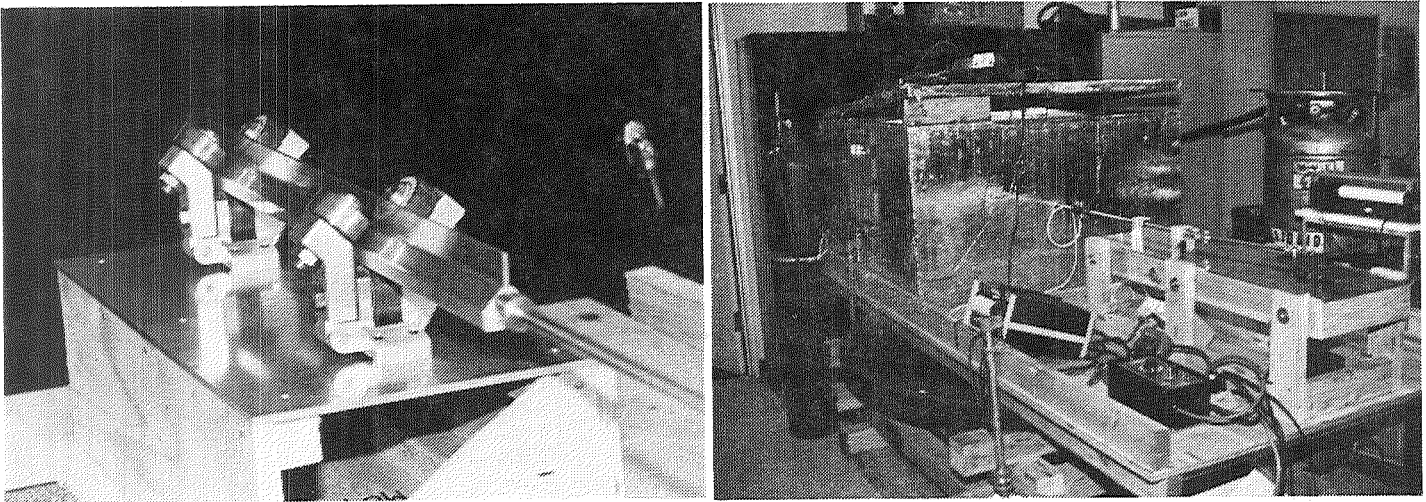


Figure 9: Straight Rail Test Set-Up

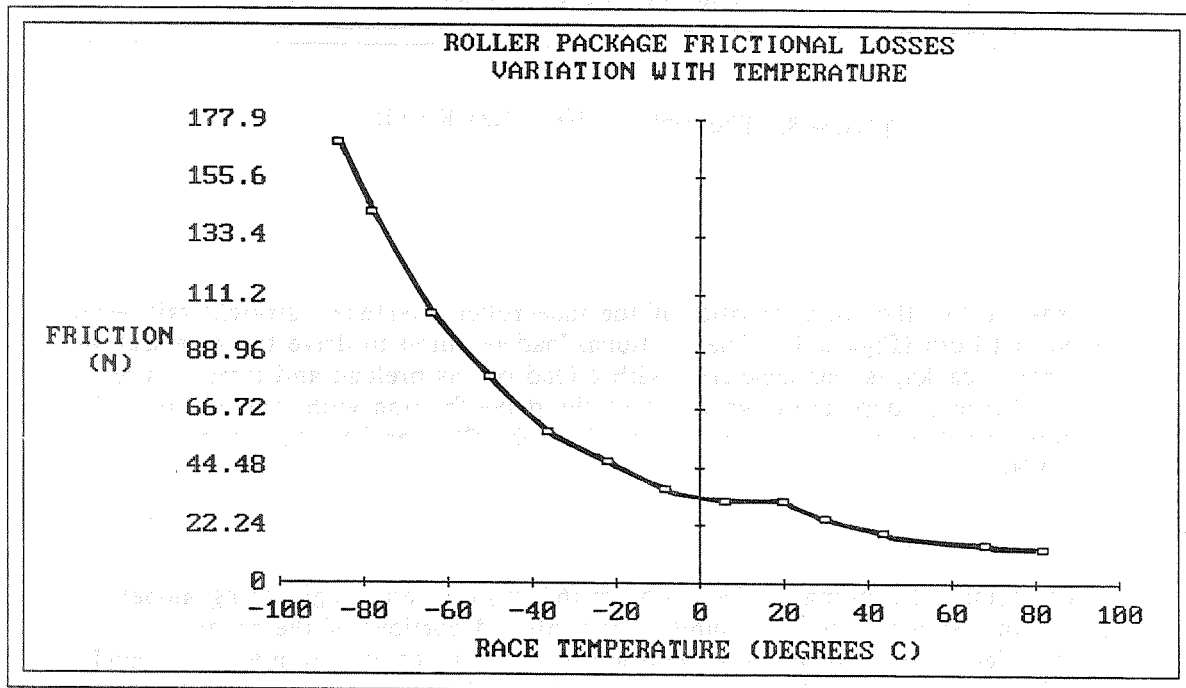
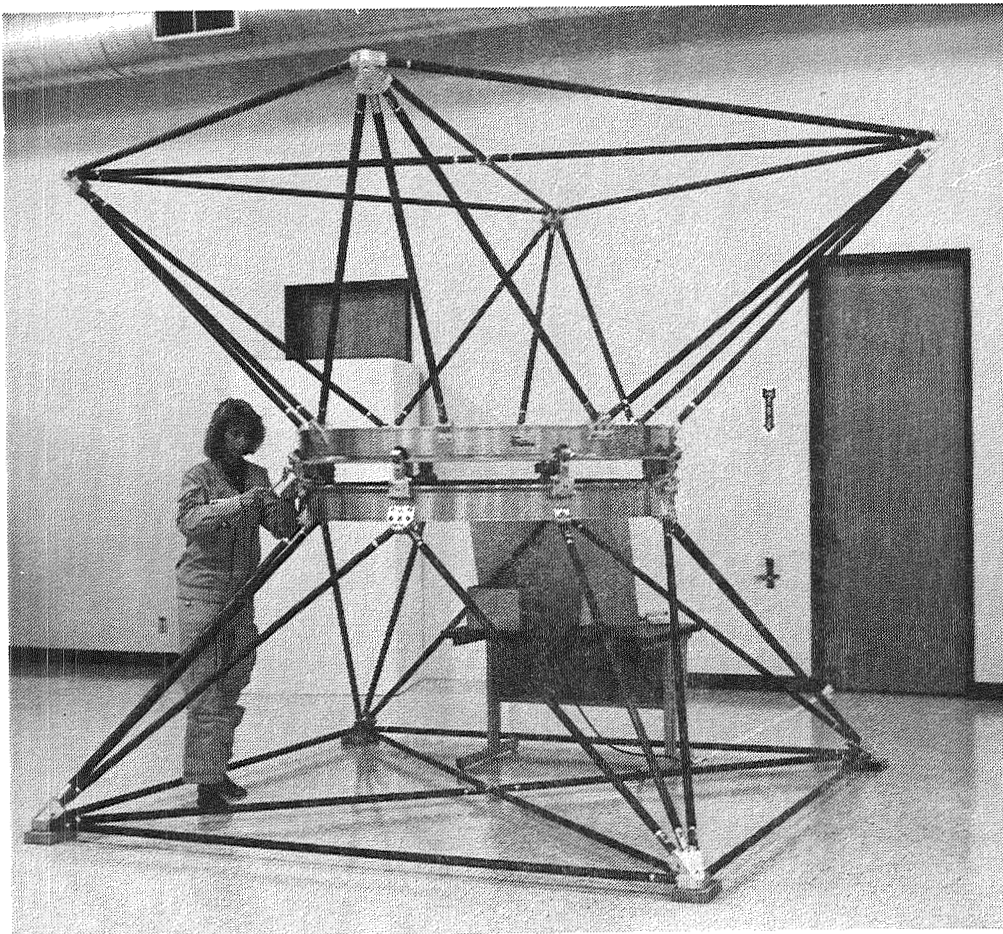


Figure 10: Roller Package Frictional Loss

ORIGINAL PAGE IS
OF POOR QUALITY

SUMMARY

A highly reliable and quality performing Alpha Joint is vital to successful Space Station operation. After conducting detailed trades, analyses, concept designs, and after building and testing hardware, the discrete follower bearing concept is clearly best suited to meet the Space Station requirements. The requirements found to be driving the design are reliability, thermal considerations, stiffness and load-carrying capability. Testing of the half-scale engineering model shows a good correlation between analytical predictions and test data. Key features and advantages of this bearing over conventional large-diameter bearings are the ability to accommodate thermal deformations and thermally-induced loads, ease of on-orbit maintenance, and reasonable cost while providing adequate structural strength and stiffness.



Engineering Model

APPENDIX

SUMMARY

20TH AEROSPACE MECHANISMS PANEL DISCUSSIONS

NASA LEWIS RESEARCH CENTER

MAY 8, 1986

PRECEDING PAGE BLANK, NOT FILMED

March 25, 1987

SUMMARY OF
"FUTURE DIRECTIONS IN MECHANISMS"

20th Aerospace Mechanisms Symposium, May 8, 1986

As reported by: Douglas A. Rohn, NASA Lewis Research Center, and
Otto H. Fedor, Lockheed Space Operations Co.

The first organized panel discussion since 1970 was held during the 20th Aerospace Mechanisms Symposium at the NASA Lewis Research Center. The organizing committee selected a general theme of "Future Directions in Mechanisms" and charged H. Mervyn Briscoe with the task of organizing the subtopics and moderating the actual panel discussion.

The panel was organized into several topics with an invited expert in each area to lead the discussions. Each topic was introduced by a panelist, who presented overview material and comments for stimulating discussion between the audience and members of the panel. This turned out to be a successful format based on the lively discussions that often followed.

Mr. Briscoe, retired from ESTEC, brought to the panel his background in mechanisms and space tribology. He, as moderator, was served well with a natural stage presence and thespian flair. Dr. Werner Auer, from Teldix GmbH, contributed his extensive experience in space mechanisms and gyros. Daniel Kuban, from Oak Ridge National Lab., has a strong background in robotics and manipulators as well as general mechanism design. Philip Studer, from NASA Goddard, brought to the discussion his considerable background in electro-mechanical and electromagnetic mechanisms for spacecraft. The following areas were addressed:

<u>TOPIC</u>	<u>INTRODUCED BY</u>
ELECTRO-MECHANICAL ACTUATORS, MOMENTUM WHEELS, DRIVES, GEARBOXES	Dr. WERNER AUER
TRIBOLOGY AND POWER TRANSFER	MERVYN BRISCOE
CAD FOR DESIGN AND ANALYSIS	DANIEL KUBAN
DEPLOYABLE STRUCTURES AND THEIR MECHANISMS: SHAPE CONTROL OF LARGE STRUCTURES	PHILIP STUDER
ROBOTICS AND AUTOMATION: TELEPRESENCE	DANIEL KUBAN
PHILOSOPHICAL ASPECTS: COMMUNICATION BETWEEN MECHANISM ENGINEERS, CONFIDENTIALITY (GOVERNMENT AND COMMERCIAL), THE FUTURE	MERVYN BRISCOE

At the beginning of the session, Mr. Briscoe introduced the panelists and outlined the basic objectives. These were: (1) to outline where the aerospace mechanism community stands today in the several topic disciplines, (2) to identify future needs and (3) to clarify philosophy. As previously mentioned, audience involvement was encouraged and turned out to be quite a bit more lively than anticipated. What follows in this write-up is a summary of the comments, questions, and disagreements which were brought out in the two-hour session.

Dr. Werner Auer

The first topic was Actuators, Momentum Wheels, Drives and Gearboxes. Dr. Auer began with a presentation of "lessons learned," with the overall objective of improving performance and lowering costs. Specific points included: avoid the use of caging, use simple bearing arrangements, use less parts, employ motors with no additional axes, use simple redundancy schemes, and combine pick-offs with drive elements. Care should be taken to define mechanical and electrical interfaces, and to select materials for their ability to be easily fabricated, not just for mass and strength properties.

During the panel-audience interaction, a question arose as to the best way to apply bearing preload and the use of Belleville washers. Dr. Auer suggested that a carefully calculated solid preload is best and Mr. Briscoe commented that it is difficult to get uniform circumferential loading with Bellevilles. A comment was made that diaphragm springs with off load stops have worked.

A question was asked: "Why not use graphite composites instead of beryllium? Is anyone using them now?" Mr. Briscoe answered that the potential is there, but more work needs to be done. He pointed out that each composite material has manufacturing difficulties to overcome. A thermoplastic resin with carbon fiber reinforcement has been used by SPAR on an STS boom deployment, but some bending stiffness was sacrificed. PEEK is being investigated for future use. It looks good in theory, but manufacturing and availability difficulties persist. A general panel recommendation was to exploit the use of onboard computers and adaptive control instead of changing mechanism designs.

Mr. H. Mervyn Briscoe

The next topic, Tribology and Power Transfer, was introduced by Mr. Briscoe. His opening remarks indicated that from the early days, the goal of good space lubrication was to prevent cold welding and avoid the loss of lubricants by evaporation. He discussed the current state-of-the-art in dry and liquid lubes. Good dry lubricants were listed: MoS₂, solid polymer transfer films (PTFE, PTFE + MoS₂, etc.) and soft metals (gold, lead, silver but avoid Indium). Lead has been found to be an excellent long-life rolling-element bearing lubricant, while gold has had spotted success. Liquid lubricants include hydrocarbon oils, synthetics and greases. Some are no longer available, silicones are to be avoided. Specifically Fromblin Z25 and Kytox have some great properties, but Mr. Briscoe warned that there are still

limitations, such as polymerization in some cases. Recommendations also include BP 2110 and Bray 601 (3L38RP) grease. Mr. Briscoe mentioned that brushes and slip rings still have problems and that no material is good in both air and vacuum applications.

An active discussion followed on slip ring and lubrication needs. A general lack of good materials and lubricants and the need to involve manufacturers was cited. Mr. Briscoe emphasized that lubricant availability is an international problem. He raised the following question: "Should we abandon liquid lubrication all together?" The audience response was that each design requires a decision as to which to use. It was suggested that researchers should strive to define regions of application for each type so that the designers can pick the best. An important area for future lubricant/actuator problems was identified in the hypersonics program, where extreme temperatures (cryo to 800°F) and both air and vacuum are encountered. An active discussion was generated, treating the infancy of this technology, and that we need to first develop technology then design the vehicle system.

Several attendees made general remarks regarding lubrication and slip rings. A need for long-life, high-speed, cryogenic slip rings was cited. An attendee mentioned good experience with conventional lubricants, and noted trouble with MoS₂ at lower speeds (approx. 6 RPM) that wasn't present at 30 RPM. Mr. Studer suggested consideration of electrical commutation to replace slip rings and magnetic bearings for long-life. Mr. Briscoe asked if we should abandon brush-commutation altogether. Dr. Auer cited the relative higher cost of brushless DC motors and others had opinions both ways.

Mr. Daniel Kuban

Mr. Kuban began the CAD topic with the observation that CAD is like a large carrot dangling in front of us. He noted that one of the basic problems is in the current state of rapid change in the CAD industry. As prices come down and capabilities go up, the distinction between micro-based and mainframe-based systems will be blurred and the day may come when every designer has a CAD workstation on his desk. The need for artificial intelligence will grow, currently we need more AI help in design selections and dimensioning. Kuban summarized his experience as follows: CAD allows very easy isometric-type drawing creation and CAD is only as good as the operator - an inexperienced, non-careful operator can make the design process more expensive. He also offered the advice to potential users to rent a system rather than making a sizeable capital investment, considering how fast the technology is evolving. He also advised to carefully evaluate archiving capabilities before acquisition.

Many significant observations were brought up by the audience. One attendee's experience was that initially CAD took longer in the design process, but a good data base was generated for the future so that changes became quicker down the line. Another attendee mentioned the need for a common operating system and the current lack of a good integrated package of

CAD, solid modelling, dynamic analysis and NASTRAN. An attendee pointed out the need for a large data base to make it more than just an electronic interactive drafting machine. Someone in the audience stated that one needs a large manufacturing interface and a large population of parts in order to justify CAD/CAM costs. It was mentioned that there is a trend away from big systems, and that many needs can be satisfied by a PC-based CAD system.

Mr. Philip Studer

The panel session continued with the introduction of Deployable Structures and Shape Control by Philip Studer. He pointed out that space systems in general are becoming more mechanized and space structures are becoming deployable and retractable. As mechanisms become more numerous and more complex, the field requires interdisciplinary efforts, involving electronics, controls and reliability needs. Studer suggested the term "Mechatronics" which is used elsewhere to describe the coexistence of mechanical and electrical elements. Future space structures will require adaptive control, on-board alignment, and sensors and actuators with a tremendous dynamic range of displacement, frequency and G-level. Shape control and alignment by electromechanical actuators instead of reliance on geometry will become increasingly more common. He also pointed out that tremendous strides in permanent magnet technology have been made recently. He also mentioned the need for better docking, latching and release mechanisms with improved damping devices.

Mr. Studer's remarks triggered reactions from the audience and other panelists. It was brought up that magnetic bearings seem attractive, but a definite comparison to rolling-element bearings with respect to cost and complexity is needed. Mr. Studer pointed out that at least one and usually two servos are needed per axis on magnetic bearings. He said the hardware costs today are low, but the engineering costs are high to develop a new system. Mr. Briscoe commented that European magnetic bearing systems seem to be ahead of that in the U. S., and that while still complex, the costs are coming down. He predicted that momentum wheels and micro-gravity applications may be the first to make substantial use of magnetic bearings for their "no stick-slip" characteristics. Mr. Studer commented there's no point in replacing a ball-bearing that works, but we should consider magnetic bearings in applications which can utilize their advantages.

A question was raised whether shape control is geometric only or frequency related as well. Mr. Studer's answer was that static alignment control is shape control, and that adaptive control is sensitive to frequencies above basic attitude control. He further pointed out that software solutions alone don't always do the job.

One attendee was concerned about fluid transfer across hinge joints. The Space Station Program is currently investigating convoluted flex hoses for hinge joints and developing continuous rotary transfer methods for rotary joints.

An active discussion acknowledged the fact that control engineers want a system with structural resonance at least 10 times the control bandwidth. Mr. Studer summarized the problem by stating that large structures will have too low natural frequencies and that we must consider passive damping along with active damping to reduce resonant peaks. Comments followed on the need to reduce or overcome backlash in deployable structure joints. Other points were made with respect to the use of tensile (guy-wire) systems and deployable column stowing.

Mr. Daniel Kuban

Robotics, Automation and Telepresence was then discussed by Mr. Kuban. He pointed out that we currently have a trade-off between autonomy and adaptability in the field of robotics. The essence of adaptability is symbolized by a human, while industrial assembly line robots typify autonomy. He suggested that a "telerobot," which combines features of both adaptability by having a man in the loop and autonomy by having some built-in "intelligence," is what is needed next in space. An extremely lively discussion followed Mr. Kuban's provocative question to the group: "When will we recognize telerobots' hand-in-space capability for maintenance and get away from concentrating so much on reliability?" Many sharply disagreed, saying that in space we cannot accept the consequences of a failure and that we want future missions to be used for new opportunities, not "flat-tire fixes" or scheduled maintenance. On the other hand, it was argued that many things can be maintained and that in spite of reliability efforts, failures are still possible. Mr. Kuban suggested that we could possibly lower costs by putting our money and effort into designing for repairability instead of high reliability. Some resistance to this was apparent. It was agreed that there is a definite role for robotics in space, especially for tasks which are too hazardous or inefficient for astronauts to do.

Mr. H. Mervyn Briscoe

The final topic of Philosophical Aspects was handled by Mr. Briscoe. Although the participants seemed eager for more discussion, the remaining time abbreviated discussion on this topic. Mr. Briscoe got the ball rolling by wondering if we, the Aerospace Mechanisms community, should have our own publication. He also mentioned the general concern of confidentiality, safeguarding of proprietary information and pros and cons of patenting. Response from the audience was centered around the availability of information. It was pointed out that detailed information on materials or components from vendors is often not available because the vendor believes we will become a competitor instead of a user of the product. A question was raised as to the idea of a mechanisms data base so that each company does not have to reinvent the wheel. A comment was made on good experience with NASA Tech Briefs and the STAR system. A final question regarding Soviet involvement in the Aerospace Mechanisms Symposium was raised. Dr. Coale answered that any such involvement would likely precipitate withdrawal of papers and attendees by many companies.

CONCLUDING REMARKS

The enthusiastic, free-flow of ideas and comments during the course of the panel discussion exemplify the Symposium's goal to provide an open forum for designers and users of mechanisms. Despite significant progress on many fronts, the discussion revealed that our work as developers of aerospace mechanisms is far from complete. There are many challenging new and continuing problems and few, if any, old hat solutions. Cost and performance continue to be major drivers. A brief review of the previous summary will bring out only a few of the many important issues and problems: electromechanical actuators need to be simpler and more easily manufactured; space lubrication is still an ongoing battle between available materials and the environment; CAD/CAM is a powerful tool, but overall cost savings shouldn't be taken for granted; space structures are becoming larger with greater demands on actuators, mechanisms and controls; robotics and automation have a great potential in space; and the technical problems are not the only issues - philosophical ones also remain. These areas and others demand our continued efforts.

1. Report No. NASA CP-2470		2. Government Accession No.		3. Recipient's Catalog No.	
4. Title and Subtitle 21st Aerospace Mechanisms Symposium				5. Report Date May 1987	
				6. Performing Organization Code 999-15-00-00-72	
7. Author(s)				8. Performing Organization Report No. S-560	
				10. Work Unit No.	
9. Performing Organization Name and Address Lyndon B. Johnson Space Center Houston, TX 77058				11. Contract or Grant No.	
				13. Type of Report and Period Covered Conference Publication	
12. Sponsoring Agency Name and Address National Aeronautics and Space Administration, Washington, DC 20546; California Institute of Technology, Pasadena, CA 91109; and Lockheed Missiles & Space Co., Inc., Sunnyvale, CA 94088				14. Sponsoring Agency Code	
15. Supplementary Notes					
16. Abstract Papers presented at the 21st Aerospace Mechanisms Symposium, hosted by the NASA Lyndon B. Johnson Space Center, Houston, Texas, on April 29 to May 1, 1987, are documented herein. During the 3 days, 24 technical papers were presented by experts from The Netherlands, the United Kingdom, the United States, France, Italy, and Japan. Panel discussions on robotics for space and large space structures also were held but are not documented herein. Technical topics addressed include deployable structures, electromagnetic devices, tribology, actuators, latching devices, positioning mechanisms, robotic manipulators, and automated mechanisms synthesis. A summary of the 20th Aerospace Mechanisms Symposium panel discussions is included as an appendix.					
17. Key Words (Suggested by Author(s)) Actuators Latching devices Deployable structures Positioning Robotic manipulators mechanisms Traction drives Space lubricants Tribology Computer analysis			18. Distribution Statement Unclassified - Unlimited Subject Category 39		
19. Security Classif. (of this report) Unclassified		20. Security Classif. (of this page) Unclassified		21. No. of Pages 357	
				22. Price*	

* For sale by the National Technical Information Service, Springfield, Virginia 22161

**National Aeronautics and
Space Administration
Code NIT-4**

**Washington, D.C.
20546-0001**

Official Business
Penalty for Private Use, \$300



National Aeronautics and
Space Administration

Washington, D.C.
20546

**SPECIAL FOURTH CLASS MAIL
BOOK**

Postage and Fees Paid
National Aeronautics and
Space Administration
NASA-451

Official Business
Penalty for Private Use \$300



NASA Headquarters
Code NTT-3/K. Carroll
Washington, DC 20546-0001

MAY 21 REC'D

(1 copy)



**POSTMASTER: If Undeliverable (Section 158
Postal Manual) Do Not Return**